ELSEVIER

THEORETICAL AND COMPUTATIONAL CHEMISTRY 15

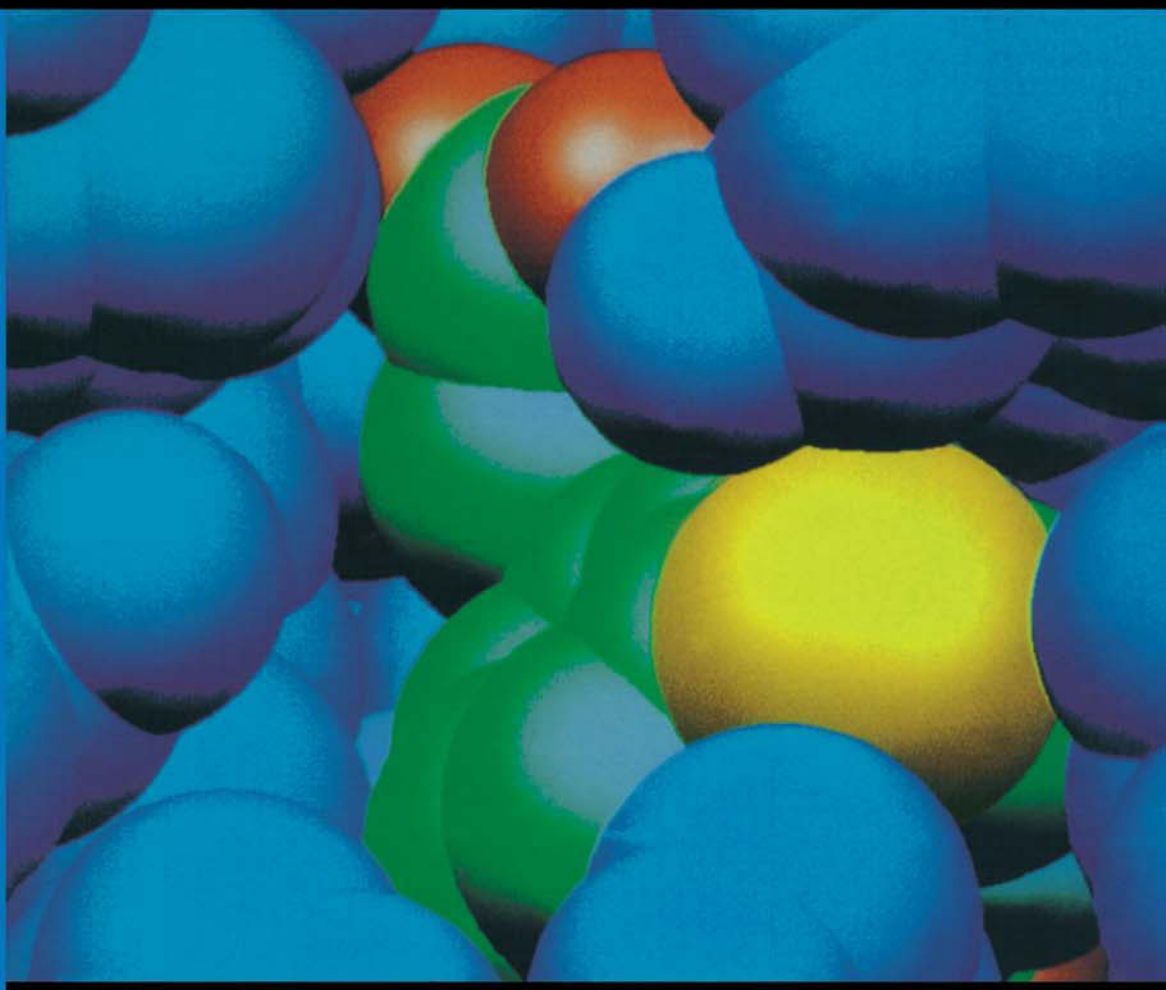

Computational Materials Science

Jerzy Leszczynski
editor

15
THEORETICAL AND COMPUTATIONAL CHEMISTRY

Computational Materials Science

THEORETICAL AND COMPUTATIONAL CHEMISTRY

SERIES EDITORS

Professor P. Politzer
Department of Chemistry
University of New Orleans
New Orleans, LA 70148, U.S.A.

Professor Z.B. Maksić
Rudjer Bošković Institute
P.O. Box 1016,
10001 Zagreb, Croatia

VOLUME 1
Quantitative Treatments of Solute/Solvent Interactions
P. Politzer and J.S. Murray (Editors)

VOLUME 2
Modern Density Functional Theory: A Tool for Chemistry
J.M. Seminario and P. Politzer (Editors)

VOLUME 3
Molecular Electrostatic Potentials: Concepts and Applications
J.S. Murray and K. Sen (Editors)

VOLUME 4
Recent Developments and Applications of Modern Density Functional Theory
J.M. Seminario (Editor)

VOLUME 5
Theoretical Organic Chemistry
C. Párkányi (Editor)

VOLUME 6
Pauling's Legacy: Modern Modelling of the Chemical Bond
Z.B. Maksic and W.J. Orville-Thomas (Editors)

VOLUME 7
Molecular Dynamics: From Classical to Quantum Methods
P.B. Balbuena and J.M. Seminario (Editors)

VOLUME 8
Computational Molecular Biology
J. Leszczynski (Editor)

VOLUME 9
Theoretical Biochemistry: Processes and Properties of Biological Systems
L.A. Eriksson (Editor)

VOLUME 10
Valence Bond Theory
D.L. Cooper (Editor)

VOLUME 11
Relativistic Electronic Structure Theory, Part 1. Fundamentals
P. Schwerdtfeger (Editor)

VOLUME 12
Energetic Materials, Part 1. Decomposition, Crystal and Molecular Properties
P. Politzer and J.S. Murray (Editors)

VOLUME 13
Energetic Materials, Part 2. Detonation, Combustion
P. Politzer and J.S. Murray (Editors)

VOLUME 14
Relativistic Electronic Structure Theory, Part 2. Applications
P. Schwerdtfeger (Editor)

VOLUME 15
Computational Materials Science
J. Leszczynski (Editor)

15

THEORETICAL AND COMPUTATIONAL CHEMISTRY

Computational Materials Science

Edited by

J. Leszczynski

The Computational Centre for
Molecular Structure and Interactions
Jackson State University
Jackson, MS, USA

ELSEVIER

2004

Amsterdam – Boston – Heidelberg – London – New York – Oxford – Paris
San Diego – San Francisco – Singapore – Sydney – Tokyo

ELSEVIER B.V.	ELSEVIER Inc.	ELSEVIER Ltd	ELSEVIER Ltd
Sara Burgerhartstraat 25	525 B Street, Suite 1900	The Boulevard, Langford Lane	84 Theobalds Road
P.O. Box 211,1000 AE	San Diego, CA 92101-4495	Kidlington, Oxford OX5 1GB	London WC1X 8RR
Amsterdam, The Netherlands	USA	UK	UK

First edition 2004

Library of Congress Cataloging in Publication Data
A catalog record is available from the Library of Congress.

British Library Cataloguing in Publication Data
A catalogue record is available from the British Library.

ISBN: 0-444-51300 0
ISSN: 1380 - 7323 (Series)

♾ The paper used in this publication meets the requirements of ANSI/NISO Z39.48-1992 (Permanence of Paper).
Printed in The Netherlands.

PREFACE

There are perhaps only a few examples of complex molecules that had been first designed based on theoretical considerations and only afterward identified by experimental techniques. Fullerene is the most famous illustration of such successful predictions. In addition to being a perfectly symmetrical, beautiful molecule, the synthesis and characterization of C_{60} elevated expectations of its utilization in many basic and industrial applications. However, only a limited number of fullerene-containing products have come to market because they are still more expensive than gold. This should change in near future since the Frontier Carbon Corporation announced recently (Chemical & Engineering News, August 11, 2003) their business plan to produce fullerenes in large quantities. In collaboration with TDA Research, based in Wheat Ridge, Colorado, USA, they developed a new, unique combustion technique that is quite different from the processes used by other commercial companies. The Frontier Carbon Corp. predicts that they will soon sell fullerenes for less than $300 per kg. The current price of their products is about $4,000 per kilogram which is a sharp decrease from $40,000 per kg price tag based on older technologies. The availability of cheap fullerenes will definitely stimulate the development efforts of industrial researchers which might include new applications ranging from electronic compounds to pharmaceuticals.

Computational tools have been permanently deposited into the toolbox of theoretical chemists. The impact of new computational tools can hardly be overestimated, and their presence in research and applications are overwhelming. Theoretical methods such as quantum mechanics, molecular dynamics, and statistical mechanics have been successfully used to characterize chemical systems and to design new materials, drugs, and chemicals. There is no doubt that Computational Chemistry not only contributes to a better understanding of classical chemical problems but also introduces new dimensions in different areas of science and technology.

The need for efficient computational performance is crucial not only in basic science but also in almost all areas of technological applications. The design and production of cluster materials is a rapidly growing area in the fields of applied science and technology. Such an approach allows a new way of producing materials with unusual properties which are expected to be potential candidates for new building units of future electronics to be revealed. Nanotechnology has been

deemed the one most important contemporary development in materials research as it is likely to impact virtually every area of future technology, from microelectronic fabrication to surgical procedures in medicine. At its very core, nanotechnology includes the exploration and characterization methods that allow for the design of materials and devices on an atomic scale. Of essential relevance for the success of these efforts are realistic and innovative models for nanotechnological systems. These models rely on the methods of Computational Chemistry.

The volume on Computational Material Sciences covers selected examples of notable applications of computational techniques to material science. They include discussions of the phenomenon of chaos in chemistry, reaction network analysis, and mechanisms of formation of clusters. More practical applications contain reviews of computational design of new materials and the prediction of properties and structures of well known molecular assemblies. Also current developments of effective computational methods which will help in understanding, predicting, and optimizing periodic systems, nanostructures, clusters and model surfaces are covered in this volume. However, as always, one volume cannot provide a comprehensive review of such a broad area as material science. As usual few people were unable to contribute; therefore, some important work must have been overlooked. The editor hopes that despite its incompleteness, this collection of chapters not only demonstrates the enormous progress that has been made in this area but also will provide impetus for future research activities.

I would like to thank all authors for the excellent contributions and fine collaborations. The very efficient technical assistance of Dr. Manoj K. Shukla in putting together this volume is greatly appreciated.

Jerzy Leszczynski

TABLE OF CONTENTS

This Page Intentionally Left Blank

J. Leszczynski (Editor)
Computational Materials Science
Theoretical and Computational Chemistry, Vol. 15

Chapter 1

Chaos and chemistry: simple models to understand chaos in chemistry

J.-M. André

Facultés Universitaires Notre-Dame de la Paix, Laboratoire de Chimie Théorique Appliquée, 61, rue de Bruxelles, 5000 Namur, Belgium

1. INTRODUCTION

A particularly good definition for the subject of this paper can be found in a dictionary such as "Merriam Webster's Collegiate Dictionary" [1]: *CHAOS 1 obs: CHASM, ABYSS 2 a often cap: a state of things in which chance is supreme; esp: the confused unorganized state of primordial matter before the creation of distinct forms b:* ***the inherent unpredictability in the behavior of a natural system*** *(as the atmosphere, boiling water, or the beating heart) 3 a: a state of utter confusion b: a confused mass or mixture.* The inherent unpredictability in the behavior of a natural system is the concept that we will develop in the next sections in close connection with non-equilibrium thermodynamics of chemical systems.

The article is conceived as a puzzle of a few large pieces which, at first sight, seem to concern different domains but which offer a simple understanding of non-linear effects in chemistry from different disciplines. To keep this introduction as simple as possible, the detailed proofs are developed in the Appendix.

2. VERHULST'S LOGISTIC MODEL OF POPULATIONS (1844)

At the beginning of the 19th century, the Belgian mathematician Pierre François Verhulst (1804-1849) dedicated an important research work to the study of the growth of populations. At that time, Flanders was undergoing a very dramatic economic crisis. Verhulst extended the basic ideas of Malthus by adding to the idea of an exponential growth the notion of inhibitory factors. By using rates of birth (b) and of mortality (m) that, respectively, decrease ($b = b_0 - k_b X$) or grow ($m = m_0 + k_m X$) in parallel with the population (X), he proposed his so-called

J. Leszczynski (Editor)
Computational Materials Science
Theoretical and Computational Chemistry, Vol. 15

Chapter 1

Chaos and chemistry: simple models to understand chaos in chemistry

J.-M. André

Facultés Universitaires Notre-Dame de la Paix, Laboratoire de Chimie Théorique Appliquée, 61, rue de Bruxelles, 5000 Namur, Belgium

1. INTRODUCTION

A particularly good definition for the subject of this paper can be found in a dictionary such as "Merriam Webster's Collegiate Dictionary" [1]: *CHAOS 1 obs: CHASM, ABYSS 2 a often cap: a state of things in which chance is supreme; esp: the confused unorganized state of primordial matter before the creation of distinct forms b:* ***the inherent unpredictability in the behavior of a natural system*** *(as the atmosphere, boiling water, or the beating heart) 3 a: a state of utter confusion b: a confused mass or mixture.* The inherent unpredictability in the behavior of a natural system is the concept that we will develop in the next sections in close connection with non-equilibrium thermodynamics of chemical systems.

The article is conceived as a puzzle of a few large pieces which, at first sight, seem to concern different domains but which offer a simple understanding of non-linear effects in chemistry from different disciplines. To keep this introduction as simple as possible, the detailed proofs are developed in the Appendix.

2. VERHULST'S LOGISTIC MODEL OF POPULATIONS (1844)

At the beginning of the 19th century, the Belgian mathematician Pierre François Verhulst (1804-1849) dedicated an important research work to the study of the growth of populations. At that time, Flanders was undergoing a very dramatic economic crisis. Verhulst extended the basic ideas of Malthus by adding to the idea of an exponential growth the notion of inhibitory factors. By using rates of birth (b) and of mortality (m) that, respectively, decrease ($b = b_0 - k_b X$) or grow ($m = m_0 + k_m X$) in parallel with the population (X), he proposed his so-called

"logistic" model

$$\frac{dX}{dt} = b\,X - m\,X$$
$$= (b_0 - k_b\,X)\,X - (m_0 + k_m\,X)\,X$$
$$= k\,(K - X)\,X$$

This very interesting equation will be the main thread running through this introduction to the theory of chaos. Indeed, Verhulst's logistic equation is a separable differential equation of the first order. For an initial population of X_0, the solution obtained by direct integration is:

$$X = \frac{K}{1 + \left(\frac{K}{X_0} - 1\right) e^{-kKt}}$$

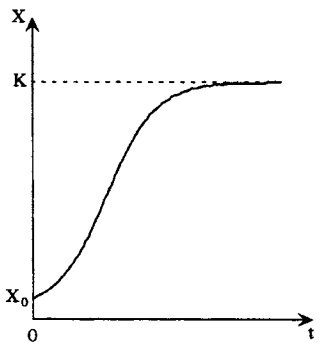

Fig.1. Logistic model of population.

In biology, a negative value of K ($\propto b_0 - m_0$) means a situation of high mortality ($b_0 < m_0$) whereas situations of a high birth rate ($b_0 > m_0$) correspond to a positive K parameter. K = 0 defines the transition (the "bifurcation") between the two regimes. Examples of applications of the logistic equation on various scales of time are given in numerous textbooks of biology [2] and of mathematics applied to biology and experimental science [3]. Note also that by its shape and its solution, the logistic equation is a kind of contraction of the simple model of exponential growth and of the opposite model of saturation of populations.

Verhults's logistic equation is an analytically soluble non-linear differential equation. Indeed, besides the linear term kKX, it contains the quadratic (harmonic) term - kX^2:

$$\frac{dX}{dt} = kKX - kX^2$$

Exponential Growth	Saturation
$\frac{dX}{dt} = kX$	$\frac{dX}{dt} = k(K-X)$
$X = X_0\, e^{kt}$	$X = K - (K-X_0)\, e^{-kt}$

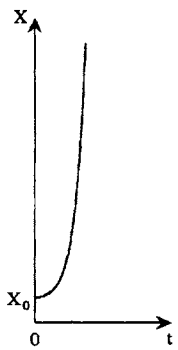

Fig.2. Exponential and saturation models of population.

The most important fact to remember for the discussion we present in this paper is that, in chemistry, the equation is the complete kinetic equation of the simplest auto-catalytic reaction:

$$K + X \Leftrightarrow 2X$$

An auto-catalytic reaction is one in which it is necessary to have reagent X to supply more product X. Auto-catalytic behavior is a universal characteristic observed in all oscillating chemical and biochemical reactions. It is the simplest chemical reaction to show instabilities. One auto-catalytic step is necessary to obtain instabilities, as shown by de Donder, Onsager, and later by Prigogine, in order to fight against the second principle, and to achieve order and auto-organization.

3. BELOUSOV (1950) AND BELOUSOV-ZHABOTINSKI OSCILLATORY REACTION (1963)

In 1959, the Russian chemist Boris Pavlovich Belousov published in the proceedings of a scientific meeting entitled "Short Communications on Radiation Medicine" a paper dedicated to the curious observation of chemical oscillations during the oxidation of citric acid by BrO_3^- catalyzed by the redox couple Ce^{4+} / Ce^{3+} in a homogeneous acid solution. At the beginning of the 1950s, his original article had been refused twice for publication in local Russian scientific journals amidst claims that oscillatory reactions contradict the second principle of thermodynamics. This statement is true for an isolated system but is not valid for an open thermodynamic system. This short paper [4] is Belousov's only publication on the oscillatory reactions. He states about his reaction. In the 1960's, Anatole Zhabotinski repeated and confirmed Belousov's experiments in his PhD thesis, substituting malonic acid for citric acid. The latter reaction is called the Belousov-Zhabotinski (BZ) reaction. Zhabotinsky and Belousov never met each other. However, they shared the 1980 Lenine Prize, a posthumous award for Belousov who passed away in 1973.

Field, Körös and Noyes [5] proposed the FKN mechanism (reflecting the initials of their last names) to analyze the BZ reaction. The mechanism involves 18 chemical reactions implicating 21 different compounds. It can be rationalized as a set of three successive processes [6]:

Process A

$Br^- + BrO_3^- + 2\ H^+ \Leftrightarrow HBrO_2 + HOBr$
$Br^- + HBrO_2 + H^+ \rightarrow 2\ HOBr$
$3[Br^- + HOBr + H^+ \Leftrightarrow Br_2 + H_2O]$

$5\ Br^- + BrO_3^- + 6\ H^+ \rightarrow 3\ Br_2 + 3\ H_2O$

$3[Br_2 + CH_2(COOH)_2 \rightarrow BrCH(COOH)_2 + Br^- + H^+]$

$2\ Br^- + BrO_3^- + 3\ CH_2(COOH)_2 + 3\ H^+ \rightarrow 3\ BrCH(COOH)_2 + 3\ H_2O$

The effect of this first process is the disappearance of Br^- and the production of brominated malonic acid $BrCH(COOH)_2$.

Process B

$$HBrO_2 + BrO_3^- + H^+ \Leftrightarrow 2\ BrO_2^{\cdot} + H_2O$$
$$2[BrO_2^{\cdot} + Ce^{3+} + H^+ \Leftrightarrow Ce^{4+} + HBrO_2]$$

$$HBrO_2 + BrO_3^- + 3\ H^+ + 2\ Ce^{3+} \Leftrightarrow 2\ Ce^{4+} + 2\ HBrO_2 + H_2O$$

$$2[HBrO_2 + BrO_3^- + 3\ H^+ + 2\ Ce^{3+} \Leftrightarrow 2\ Ce^{4+} + 2\ HBrO_2 + H_2O]$$
$$HBrO_2 + HBrO_2 \rightarrow HOBr + BrO_3^- + H^+$$

$$BrO_3^- + 4\ Ce^{3+} + 5\ H^+ \Leftrightarrow 4\ Ce^{4+} + HOBr + 2\ H_2O$$

This process corresponds to single-electron oxidation by BrO_2 and to the autocatalytic production of $HBrO_2$. At the same time, we have the oxidation of Ce^{3+} (colorless) to Ce^{4+} (yellow) that provokes the periodic change of color. The last process will regenerate the bromide and reduce the ceric ions. It can be summarized by:

Process C

$$4\ Ce^{4+} + 3\ CH_2(COOH)_2 + BrCH(COOH)_2 + HOBr + 3\ H_2O \rightarrow 4\ Ce^{3+} + 2\ Br^- + 4\ HOCH(COOH)_2 + 6\ H^+$$

4. DISSIPATIVE STRUCTURES (1950s), BRUSSELATOR (1967) AND OREGONATOR (1972)

While Belousov was describing his experiments into oscillatory chemical reactions, Ilya Prigogine in Brussels was developing theoretical models of non-equilibrium thermodynamics and ended with the notion of "structure dissipative" for which he was awarded the 1977 Nobel Prize in Chemistry. The concept of "Dissipative Structure" is explicitly mentioned in the Nobel quotation: "The 1977 Nobel Prize in Chemistry has been awarded to Professor Ilya Prigogine, Brussels, for his contributions to non-equilibrium thermodynamics, particularly the theory of dissipative structures". In the first half of the 1950s, Glansdorff and Balescu defined with Prigogine the thermodynamic criteria necessary for oscillatory behavior in dissipative systems [7]. Nicolis and Lefever then applied these to models of autocatalytic reactions [8].

The "Brusselator" model contains only two variables (X and Y). It corresponds formally to a system of four coupled chemical reactions in a complete non-equilibrium situation:

$$A \xrightarrow{k_1=1} X$$

$$B + X \xrightarrow{k_2=1} Y + C$$

$$2X + Y \xrightarrow{k_3=1} 3X$$

$$X \xrightarrow{k_4=1} D$$

Since the existence of the BZ reaction was not known in the west at that time, the Brusselator should not be taken as a model of that reaction. It is a simple model but it is capable of presenting an organization far from the equilibrium.

The solutions offered by the Brusselator present a variety of behaviors according to the respective values of the parameters A and B. The linear mathematical analysis given in Appendix A shows that if the concentration of reactant B in the system is lower than a critical value B_c, the system is stable and returns to the stationary state. If $B = B_c$, the system becomes unstable. If B is more than the critical value B_c, the system will not return to the stationary state. In this case, the linear analysis cannot give a correct indication concerning long-term behavior. A correct answer is obtained by numerically integrating the differential equations. In a diagram of concentrations X and Y, the system will evolve by oscillation towards a limit cycle, i.e. a closed trajectory S as shown in Figure 3.

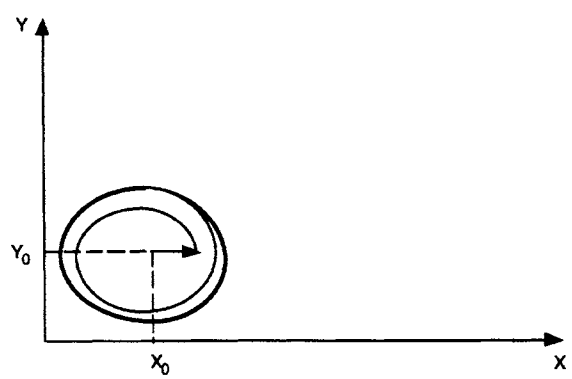

Fig.3. Evolution towards a limit cycle.

The limit cycle is stable because all the points of the plan converge on the curve. The resulting oscillation is defined by the physico-chemical conditions and is a thermodynamic characteristic of the system. It is a dissipative structure in the sense meant by Prigogine who says concerning the origin of the concept of dissipative structure: "In strong non-equilibrium conditions, the system attains "ordered states" that possess spatial and temporal organization. The oscillations are the result of chemical reactions. That means the result of dissipative processes that, in a closed system, wipe out inhomogeneities and derive the system to a stationary, timeless homogeneous state of equilibrium. Since the creation and the maintenance of organized non-equilibrium states are due to dissipative processes, Prigogine gave the name of dissipative structures to these organized states.

An explicit BZ model has been developed at the University of Oregon. It is referenced in the literature as the "Oregonator" according to the geographic origin of the laboratory of Noyes. The Oregonator models the three processes of the FKN mechanism in a simple way:

$2\ H^+ + Br^- + BrO_3^- \rightarrow HOBr + HBrO_2$

$H^+ + HBrO_2 + Br^- \rightarrow 2\ HOBr$

$2\ Ce^{3+} + BrO_3^- + HBrO_2 + 3H^+ \rightarrow 2\ Ce^{4+} + 2\ HBrO_2 + H_2O$

$2\ HBrO_2 \rightarrow HOBr + BrO_3^- + H^+$

$4\ Ce^{4+} + BrCH(COOH)_2 + 2\ H_2O \rightarrow 4\ Ce^{3+} + Br^- + HCOOH + 2\ CO_2 + 5H^+$

We recognize the disappearance of bromide (process A), the oxidation of Ce^{3+} cerium concomitant to the autocatalytic production of $HBrO_2$, and the regeneration process.

The Oregonator contains three variables X,Y, and Z according to the scheme:

Process A	$A + Y \rightarrow X + P$	$BrO_3^- + Br^- \rightarrow HBrO_2 + HOBr$
	$X + Y \rightarrow 2P$	$HBrO_2 + Br^- \rightarrow 2\ HOBr$
Process B	$A + X \rightarrow 2X + Z$	$BrO_3^- + HBrO_2 \rightarrow 2\ HBrO_2 + Ce^{4+}$
	$2X \rightarrow A + P$	$2\ HBrO_2 \rightarrow BrO_3^- + HOBr$
Process C	$Z \rightarrow hY$	$Ce^{4+} \rightarrow h\ Br^-$

Note that the reduction of the 18 steps of the FKN mechanisms to the 5 kinetic equations of the Oregonator does not allow the correct stoechiometry to be obtained. We note the analogy of the first step of the process B ($A+X \rightarrow 2X+Z$) with the "chemical" interpretation of Verhulst's logistic equation ($A+X \rightarrow 2X+Z$) described in section 2.
Like the Brusselator, the Oregonator exhibits limit cycle and confirms the existence of dissipative structures in the BZ reaction.

Finally we note that, from a conceptual viewpoint, there must be a change in the mathematical nature of the solutions of the Brusselator and of the Oregonator. This change defines what is called a bifurcation point, a concept that will be of utmost importance in the sections below.

5. LORENZ'S ATMOSPHERIC MODEL (1963)

In his paper on "Deterministic Nonperiodic Flow" [9], F.N. Lorenz studies the behavior of the ground atmosphere. The paper did not attract much attention at the time of its publication. Lorenz models the atmospheric behavior via non-linear equations using three variables:

1 ° the amplitude of the convection motion: x(t),

2 ° the difference in temperature between ascending and descending currents: y(t), and

3 ° the temperature deviation with respect to a linear profile: z(t):

$$\frac{dx}{dt} = a(y-x)$$

$$\frac{dy}{dt} = yz+ax-y$$

$$\frac{dz}{dt} = xy-bz$$

These strongly non-linear equations require a numerical solution. The random nature of the numerical solving of this problem helped Lorenz to discover the chaotic behavior of the solutions in the sense of a strong dependency with respect to the initial conditions as given by the Webster definition quoted in Section 1. Indeed, the computer used by Lorenz encountered - as was common at that time - a breakdown. In 1963, the size of internal memories did not allow

numerous data to be stored. The tradition thus was to print out any important intermediate results. Lorenz rebooted the system and restarted the calculation using the intermediate printed data. The comparison of the first series of results with the second showed no significant difference at the beginning of the simulation but the differences became more marked tending towards an exponential difference with increasing time. Lorenz had just discovered what would later be known as the "butterfly" effect. Indeed, both series of results were calculated from slightly different input data since a loss of significant figures with regard to the "exact" numerical values stored in the core memory of the computer is inevitable when printing intermediate data. Lorenz explicitly noted this significant finding in the summary of his paper: "It is found that nonperiodic solutions are ordinarily unstable with respect to small modifications so that slightly differing initial states can evolve into considerably different states". Furthermore, by representing the three variables of his model in the same diagram, he obtained a "strange" figure that David Ruelle would later baptize "strange attractor" in his paper of the same title published in 1980 [10].

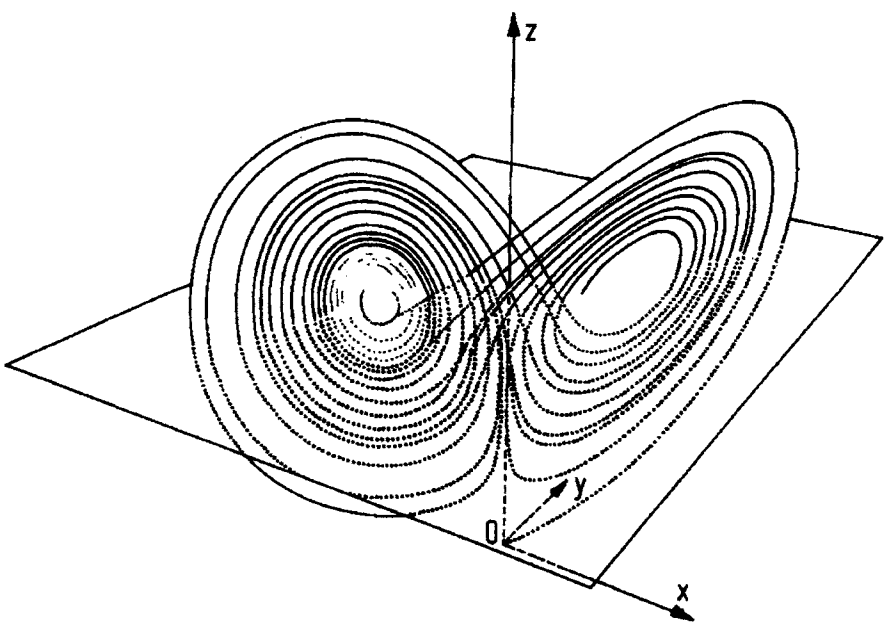

Fig. 4. Loren'z strange attractor.

6. BIFURCATIONS IN VERHULST'S LOGISTIC MODEL (1974)

In 1974, McNeil and Walls [11] applied to the logistic model the same techniques of stability analysis that Prigogine and his group had used for the case of the Brusselator. As shown in Appendix B, they proved the existence of a bifurcation at K = 0. If K is negative (mortality greater than the birth rate), only a zero population $X_0 = 0$ is stable. It is the domain of extinction of the populations. If K is positive, two solutions exist: an extinguished population $X_0 = 0$ and a stationary population $X_0 = K$. The stability analysis shows that the solution $X_0 = 0$ becomes unstable whereas the stable situation corresponds to $X_0 = K$. The point K = 0 is thus a bifurcation point characteristic of a deep change in the nature of the mathematical solutions.

Realistic examples of this type of bifurcation do exist. If an animal species is absent in a region which is ecologically favorable to that species, the import of very few individuals will provoke a brutal move towards the maximum population. There will be invasion.

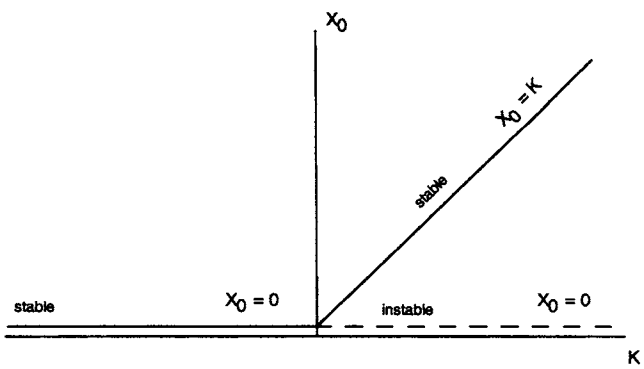

Fig.5. Bifurcation in the logistic model.

Thus, it is clear that Verhulst's logistic model exhibits the phenomenon of bifurcation. Nevertheless, it is a non-creative bifurcation. If the system is subject to a modification of the external parameters, the system can only shift from one stable branch to another.

7. PERIOD DOUBLINGS IN NUMERICAL SOLUTIONS OF VERHULST'S LOGISTIC MODEL (1976)

Again, luck allowed Robert May to discover a chaotic behavior in the numerical simulation of Verhulst's logistic equation. As shown in Appendix C, May proposed a numerical equivalent of the logistic equation where the population of a given generation (n+1) is related to the population of the previous generation (n) by the iterative formula:

$$x_{n+1} = \mu\, x_n\,(1-x_n)$$

May's conclusions were published in a reference paper entitled "Simple Mathematical Models with very Complicated Dynamics" [12]. A parameter μ replaces the parameter K of the original equation. Let us note only that the bifurcation between the situations of positive and negative values of K takes place at the value of $\mu = 1$. Furthermore, if the domain of variation of K was $-\infty < K < +\infty$, that of μ is restricted to the values $0 < \mu < 4$.

According to the values of μ, May observes various behaviors, both oscillatory and not, periodic and chaotic. Some examples of successive generations are given in the next table. The reader can easily reproduce these results by means of a simple pocket calculator.

The mathematical analysis (given in Appendix C) shows that we first find the bifurcation of McNeill and Walls at the point $\mu = 1$ ($K = 0$). If $0 < \mu < 1$, the successive generations decrease in intensity to complete extinction. When $1 < \mu < 3$, the populations tend by oscillations to a stationary population.

By gradually increasing the value of μ beyond 3, May discovered a new phenomenon with regard to the behavior of bifurcations as previously described. If $3 < \mu < 3.4495$, he observes an oscillation between two values (doubling of the period). The stationary population is no longer unique. The mathematical analysis shows a pitchfork bifurcation. The stable branch issued from the bifurcation at $\mu=1$ produces three branches. One of them is the unstable continuation of the stable branch and two new stable branches are produced. The two branches observed between $\mu=1$ and $\mu=3$ are now four branches (two stable and two instable).

Table 1
Population evolution according to the values of μ.

$\mu = 0.8$	$\mu = 2.7$	$\mu = 3.1$	$\mu = 3.5$	$\mu = 3.8$
$x_0 = 0.4$	$x_0 = 0.4$	$x_0 = 0.4$	$x_0 = 0.4$	$x_0 = 0.4$
$x_1 = 0.1920$	$x_1 = 0.6480$	$x_1 = 0.7440$	$x_1 = 0.84$	$x_1 = 0.9120$
$x_2 = 0.1241$	$x_2 = 0.6158$	$x_2 = 0.5904$	$x_2 = 0.4704$	$x_2 = 0.3050$
$x_3 = 0.0870$	$x_3 = 0.6388$	$x_3 = 0.7496$	$x_3 = 0.8719$	$x_3 = 0.8055$
$x_4 = 0.0635$	$x_4 = 0.6230$	$x_4 = 0.5818$	$x_4 = 0.3908$	$x_4 = 0.5954$
$x_5 = 0.0476$	$x_5 = 0.6341$	$x_5 = 0.7543$	$x_5 = 0.8332$	$x_5 = 0.9154$
$x_6 = 0.0363$	$x_6 = 0.6264$	$x_6 = 0.5746$	$x_6 = 0.4862$	$x_6 = 0.2943$
$x_7 = 0.0290$	$x_7 = 0.6319$	$x_7 = 0.7578$	$x_7 = 0.8743$	$x_7 = 0.7892$
$x_8 = 0.0217$	$x_8 = 0.6281$	$x_8 = 0.5691$	$x_8 = 0.3846$	$x_8 = 0.6322$
$x_9 = 0.0170$	$x_9 = 0.6307$	$x_9 = 0.7602$	$x_9 = 0.8284$	$x_9 = 0.8836$
$x_{10} = 0.0134$	$x_{10} = 0.6289$	$x_{10} = 0.5651$	$x_{10} = 0.4976$	$x_{10} = 0.3908$
$x_{11} = 0.0106$	$x_{11} = 0.6302$	$x_{11} = 0.7619$	$x_{11} = 0.8750$	$x_{11} = 0.2154$
$x_{12} = 0.0084$	$x_{12} = 0.6293$	$x_{12} = 0.5624$	$x_{12} = 0.3829$	$x_{12} = 0.6422$
$x_{13} = 0.0066$	$x_{13} = 0.6299$	$x_{13} = 0.7629$	$x_{13} = 0.8270$	$x_{13} = 0.8732$
$x_{14} = 0.0053$	$x_{14} = 0.6294$	$x_{14} = 0.5607$	$x_{14} = 0.4976$	$x_{14} = 0.4207$
$x_{15} = 0.0042$	$x_{15} = 0.6298$	$x_{15} = 0.7636$	$x_{15} = 0.8750$	$x_{15} = 0.9261$
$x_{16} = 0.0033$	$x_{16} = 0.6295$	$x_{16} = 0.5596$	$x_{16} = 0.3829$	$x_{16} = 0.2600$
$x_{17} = 0.0027$	$x_{17} = 0.6297$	$x_{17} = 0.7640$	$x_{17} = 0.8270$	$x_{17} = 0.7312$
$x_{18} = 0.0021$	$x_{18} = 0.6296$	$x_{18} = 0.5590$	$x_{18} = 0.5008$	$x_{18} = 0.7470$
$x_{19} = 0.0017$	$x_{19} = 0.6297$	$x_{19} = 0.7642$	$x_{19} = 0.8750$	$x_{19} = 0.7182$
$x_{20} = 0.0014$	$x_{20} = 0.6296$	$x_{20} = 0.5586$	$x_{20} = 0.3828$	$x_{20} = 0.7690$
$x_{21} = 0.0011$	$x_{21} = 0.6296$	$x_{21} = 0.7644$	$x_{21} = 0.8269$	$x_{21} = 0.6750$
$x_{22} = 0.0009$	$x_{22} = 0.6297$	$x_{22} = 0.5584$	$x_{22} = 0.5009$	$x_{22} = 0.8336$
$x_{23} = 0.0007$	$x_{23} = 0.6296$	$x_{23} = 0.7644$	$x_{23} = 0.8750$	$x_{23} = 0.5271$
$x_{24} = 0.0006$	$x_{24} = 0.6296$	$x_{24} = 0.5582$	$x_{24} = 0.3828$	$x_{24} = 0.9472$
$x_{25} = 0.0004$	$x_{25} = 0.6296$	$x_{25} = 0.7645$	$x_{25} = 0.8269$	$x_{25} = 0.1900$
$x_{26} = 0.0004$	$x_{26} = 0.6296$	$x_{26} = 0.5581$	$x_{26} = 0.5009$	$x_{26} = 0.5848$
$x_{27} = 0.0003$	$x_{27} = 0.6296$	$x_{27} = 0.7645$	$x_{27} = 0.8750$	$x_{27} = 0.9226$
$x_{28} = 0.0002$	$x_{28} = 0.6296$	$x_{28} = 0.5581$	$x_{28} = 0.3828$	$x_{28} = 0.2712$
$x_{29} = 0.0002$	$x_{29} = 0.6296$	$x_{29} = 0.7645$	$x_{29} = 0.8269$	$x_{29} = 0.7511$
$x_{30} = 0.0001$	$x_{30} = 0.6296$	$x_{30} = 0.5581$	$x_{30} = 0.5009$	$x_{30} = 0.7105$

The results are schematized in Figure 6:

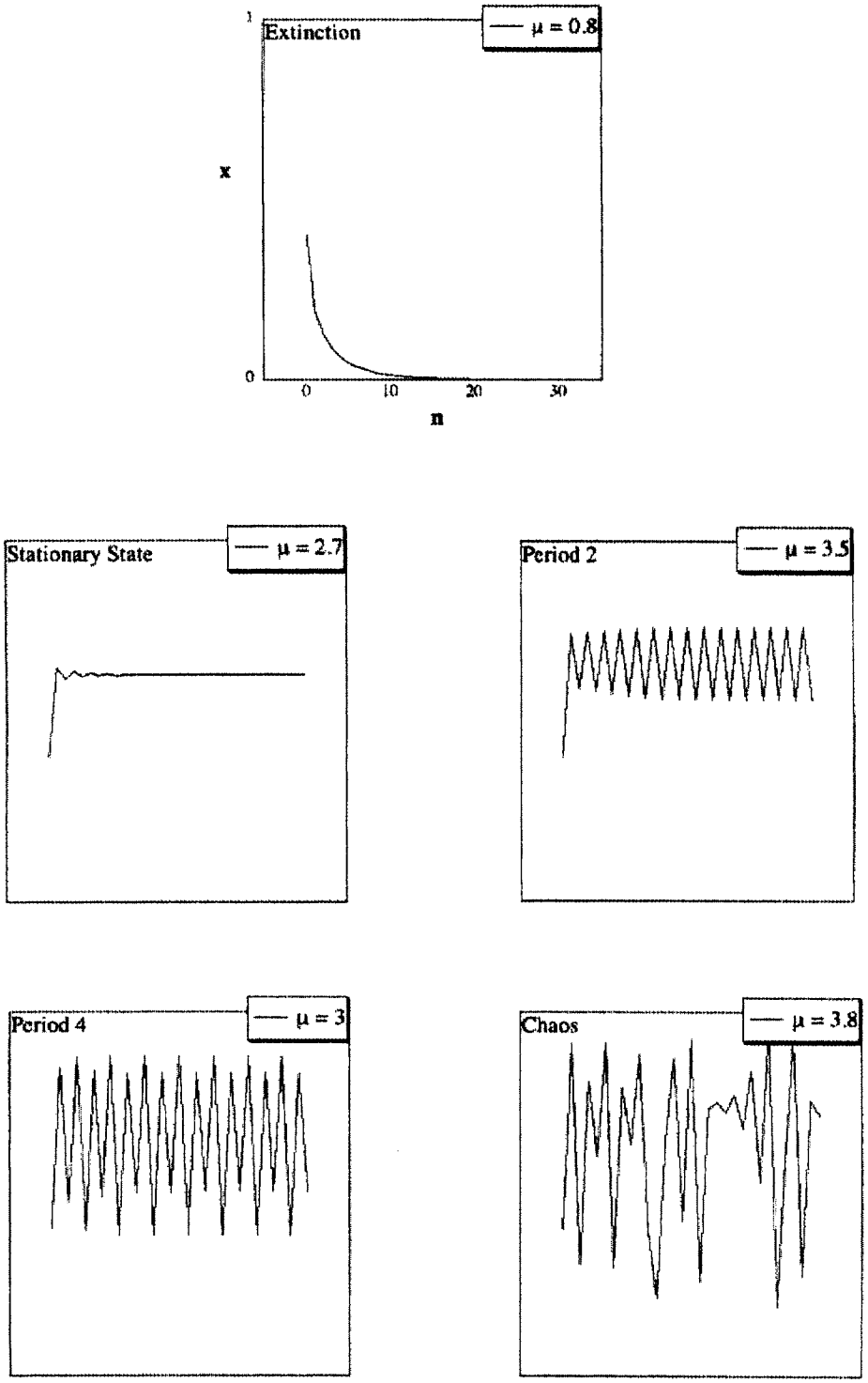

Fig.6. Time evolution in the logistic model for various values of μ

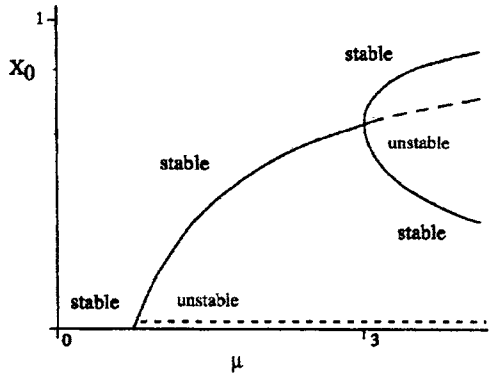

Fig.7. Sketch of bifurcations in May's numerical logistic model.

By increasing the value of the parameter μ, the four branches will generate eight branches (four stable and four unstable states), followed by sixteen branches (eight stable and eight unstable states) and so on (32, 64, 128, etc.). Thus the *Pitchfork* bifurcation process leads to an infinite sequence of cycles of period 2^n ($n \to \infty$). The stability domains of each cycle are progressively reduced:

period 0: $1 < \mu < 3$

period 2: $3 < \mu < 3.4495 = 1 + \sqrt{6}$

period 4: ...etc.

The converging process is limited by value, $\mu_\infty = 3.5699456$. Beyond this value of μ, the overlap of various periods is so great that we observe a chaotic behavior. Above a critical point, there exists an infinite amount of overlapping bifurcations and behaviors of varying periodicity and as well as an infinite amount of initial points x_0 which lead to completely aperiodic trajectories. The behavior of the trajectories is never the same even if the measurement times are infinitely large. This type of behavior is classified as "chaotic" in the famous paper by Li and Yorke (1975): "period three implies chaos" [13]. Close to the bifurcation points, natural fluctuations or very slight changes in initial conditions play a role of increasing importance. The system must "choose" between distinct branches and become increasingly sensitive to very weak perturbations. As a consequence, the values for a given step, x_n, are never reproduced. The band formed by stable x* turns into a continuum; this is the beginning of the chaos. This series of period doublings also makes it impossible

in practice to obtain analytical solutions, while numerical solutions are very easily obtained on a pocket calculator.

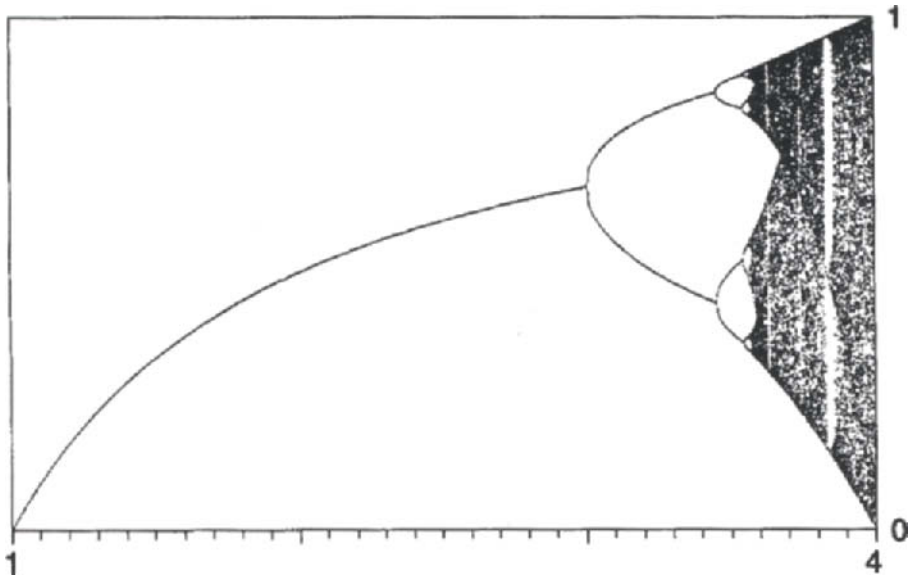

Fig.8. Bifurcations in May's numerical logistic model.

Poincaré was the first to assume the possibility of "irregular" or "chaotic" behavior of solutions of differential equations. From very slightly different initial conditions, resulting from errors in experimental measurements for example, the solutions can exponentially deviate over time resulting in extreme sensitivity to the initial conditions. The state of a system becomes effectively impossible to predict or "chaotic". This was the result observed in 1963 by Lorenz.

The reader can check this behavior in May's numerical equation of the logistic model. If we change slightly the initial value in the domain of stability (for example, $\mu = 2.7$), the population converges to the same value of 0.6296. This point acts as an attractor. In the chaotic region, a similar weak variation gives way to completely different successive evolutions. This is an indication of the "butterfly" effect.

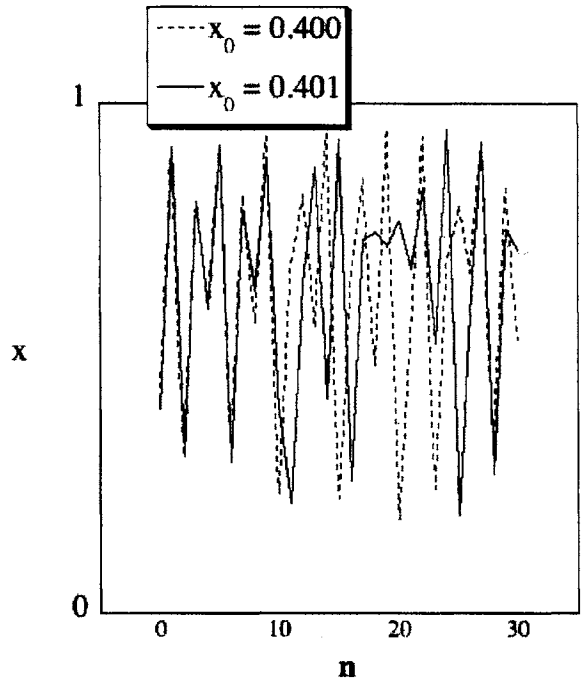

Fig.9. Chaotic time evolution in the logistic model.

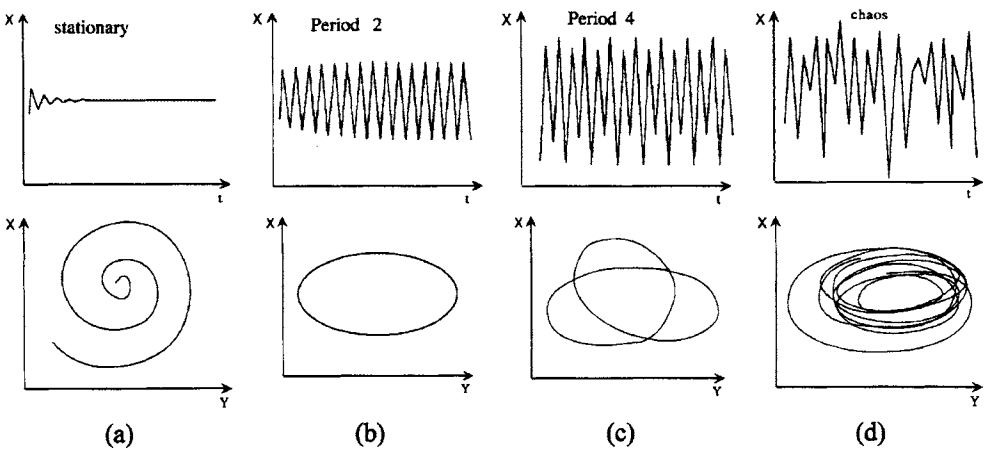

Fig.10. X-concentration as a function of time (first line) and of Y-concentration (second line) (a) in a stationary state, (b) in a doubling period regime, (c) in a quadrupling period regime d. in a chaotic regime.

Table 2

Population evolution in stable ($\mu = 2.7$) and chaotic ($\mu = 3.8$) regimes.

$\mu = 2.7$	$\mu = 2.7$	$\mu = 2.7$	$\mu = 3.8$	$\mu = 3.8$
$x_0 = 0.02$	$x_0 = 0.4$	$x_0 = 0.401$	$x_0 = 0.4$	$x_0 = 0.401$
$x_1 = 0.0529$	$x_1 = 0.6480$	$x_1 = 0.6485$	$x_1 = 0.9120$	$x_1 = 0.9128$
$x_2 = 0.1353$	$x_2 = 0.6158$	$x_2 = 0.6154$	$x_2 = 0.3050$	$x_2 = 0.3026$
$x_3 = 0.3159$	$x_3 = 0.6388$	$x_3 = 0.6390$	$x_3 = 0.8055$	$x_3 = 0.8019$
$x_4 = 0.5835$	$x_4 = 0.6230$	$x_4 = 0.6228$	$x_4 = 0.5954$	$x_4 = 0.6036$
$x_5 = 0.6562$	$x_5 = 0.6341$	$x_5 = 0.6343$	$x_5 = 0.9154$	$x_5 = 0.9092$
$x_6 = 0.6092$	$x_6 = 0.6264$	$x_6 = 0.6263$	$x_6 = 0.2943$	$x_6 = 0.3136$
$x_7 = 0.6428$	$x_7 = 0.6319$	$x_7 = 0.6319$	$x_7 = 0.7892$	$x_7 = 0.8180$
$x_8 = 0.6199$	$x_8 = 0.6281$	$x_8 = 0.6281$	$x_8 = 0.6322$	$x_8 = 0.5657$
$x_9 = 0.6362$	$x_9 = 0.6307$	$x_9 = 0.6307$	$x_9 = 0.8836$	$x_9 = 0.9336$
$x_{10} = 0.6249$	$x_{10} = 0.6289$	$x_{10} = 0.6289$	$x_{10} = 0.3908$	$x_{10} = 0.2356$
$x_{11} = 0.6328$	$x_{11} = 0.6302$	$x_{11} = 0.6302$	$x_{11} = 0.2154$	$x_{11} = 0.6844$
$x_{12} = 0.6273$	$x_{12} = 0.6293$	$x_{12} = 0.6293$	$x_{12} = 0.6422$	$x_{12} = 0.8209$
$x_{13} = 0.6312$	$x_{13} = 0.6299$	$x_{13} = 0.6299$	$x_{13} = 0.8732$	$x_{13} = 0.5588$
$x_{14} = 0.6285$	$x_{14} = 0.6294$	$x_{14} = 0.6294$	$x_{14} = 0.4207$	$x_{14} = 0.9369$
$x_{15} = 0.6304$	$x_{15} = 0.6298$	$x_{15} = 0.6298$	$x_{15} = 0.9261$	$x_{15} = 0.2248$
$x_{16} = 0.6291$	$x_{16} = 0.6295$	$x_{16} = 0.6295$	$x_{16} = 0.2600$	$x_{16} = 0.6621$
$x_{17} = 0.6300$	$x_{17} = 0.6297$	$x_{17} = 0.6297$	$x_{17} = 0.7312$	$x_{17} = 0.8501$
$x_{18} = 0.6294$	$x_{18} = 0.6296$	$x_{18} = 0.6296$	$x_{18} = 0.7470$	$x_{18} = 0.4842$
$x_{19} = 0.6299$	$x_{19} = 0.6297$	$x_{19} = 0.6297$	$x_{19} = 0.7182$	$x_{19} = 0.9491$
$x_{20} = 0.6295$	$x_{20} = 0.6296$	$x_{20} = 0.6296$	$x_{20} = 0.7690$	$x_{20} = 0.1837$
$x_{21} = 0.6297$	$x_{21} = 0.6296$	$x_{21} = 0.6296$	$x_{21} = 0.6750$	$x_{21} = 0.5699$
$x_{22} = 0.6296$	$x_{22} = 0.6297$	$x_{22} = 0.6297$	$x_{22} = 0.8336$	$x_{22} = 0.9314$
$x_{23} = 0.6297$	$x_{23} = 0.6296$	$x_{23} = 0.6296$	$x_{23} = 0.5271$	$x_{23} = 0.2427$
$x_{24} = 0.6296$	$x_{24} = 0.6296$	$x_{24} = 0.6296$	$x_{24} = 0.9472$	$x_{24} = 0.6984$
$x_{25} = 0.6296$	$x_{25} = 0.6296$	$x_{25} = 0.6296$	$x_{25} = 0.1900$	$x_{25} = 0.8004$
$x_{26} = 0.6296$	$x_{26} = 0.6296$	$x_{26} = 0.6296$	$x_{26} = 0.5848$	$x_{26} = 0.6671$
$x_{27} = 0.6296$	$x_{27} = 0.6296$	$x_{27} = 0.6296$	$x_{27} = 0.9226$	$x_{27} = 0.9065$
$x_{28} = 0.6296$	$x_{28} = 0.6296$	$x_{28} = 0.6296$	$x_{28} = 0.2712$	$x_{28} = 0.3222$
$x_{29} = 0.6296$	$x_{29} = 0.6296$	$x_{29} = 0.6296$	$x_{29} = 0.7511$	$x_{29} = 0.8299$
$x_{30} = 0.6296$	$x_{30} = 0.6296$	$x_{30} = 0.6296$	$x_{30} = 0.7105$	$x_{30} = 0.5364$

8. CHEMISTRY AND DETERMINISTIC CHAOS

Back to chemistry. We have already shown that the Brusselator leads to the existence of a limit cycle. In more elaborate models, this cycle can be subdivided into various periodicities to eventually give rise to a strange attractor.

Several groups have shown the existence of a strange attractor in the BZ reaction. The representation below was taken from the work of Györgi, Rempe and Field [14].

Thus, it is well established that deterministic chaos plays a role in chemistry. It has been analyzed in different chemical processes. Asked about the importance of chemical oscillations and chaos in the chemistry of mass industrial production, Wasserman, former director of research at Dupont de Nemours and past-president of the American Chemical Society in 1999, said [15]: "*Yes. The new tools of nonlinear dynamics have allowed us a fresh viewpoint on reactions of interest*". Dupont has identified chaotic phenomena in reactions as important as the conversion of the p-xylol in terephtalic acid or the oxidation of the benzaldehyde in benzoic acid.

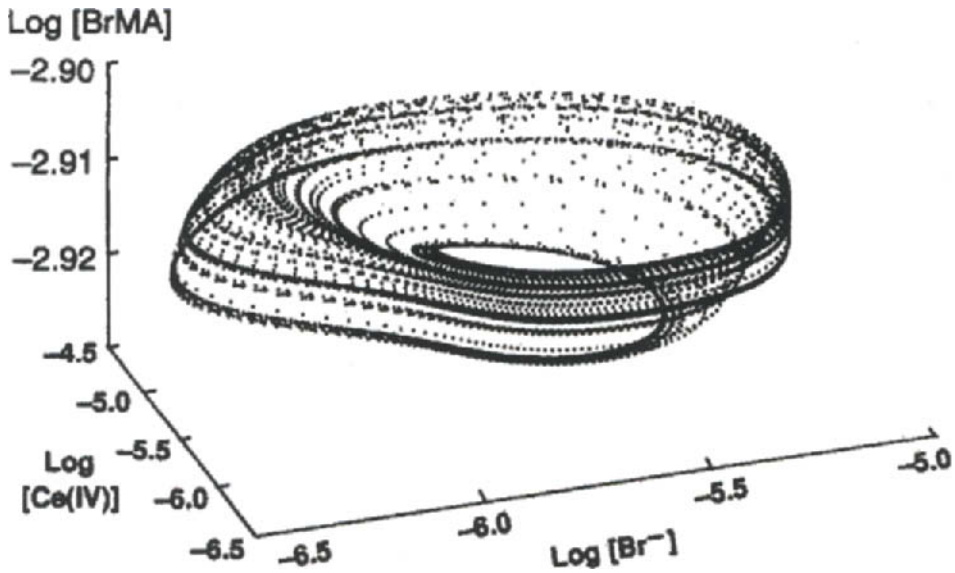

For the interested reader, various theoretical [16] and experimental [17] models are described in the literature related to these non-linear complex behaviors.

9. PERSPECTIVES AND CONCLUSIONS

What are the prospects for future science when taking into account the complexity we have described in this paper? They are summarized by John Maddox [18], editor of "Nature" for in excess of 25 years: "Science is at present a curious patchwork. Fundamental physics is perhaps the oddest: the research community is divided into those who believe that there will be a "theory of everything" very shortly and those who suspect (or hope) that the years ahead will throw up some kind of "new physics" instead. History is on the side of the second camp, to which I belong".

The intention of this article was to show that non-linear dynamics is important in chemistry and that it throws up new aspects. Fractal geometry is another way of interpreting the chaotic phenomena discussed. The appearance of new universal constants as shown by Feigenbaum [19] is further proof of the importance of non-linear behavior. Contemporary chemistry thus opens up new horizons.
It is also stresses the interesting point that chaos only appears in the numerical form of the logistic equation and not in its analytical one. Should this be connected with the question of continuity versus discontinuity. It is to note that the equations of classical mechanics are obtained from relativity when the speed of light is equal to infinity ($c = \infty$) and, on the opposite, from quantum mechanics when the Planck constant is equal to zero ($h = 0$). Feynman has written something similar: "Another way of describing this difficulty (the renormalization process) is to say that perhaps the idea that two points can be infinitely close together is wrong – the assumption that we can use geometry down to the last notch is false." [20]. In chemistry, the equations should be discontinuous due to the granular character of molecules and atoms.

The main contribution of non-linear chemistry is the pitchfork bifurcation diagram. A stable state becomes unstable and bifurcates into two new stable branches. We are unable to foresee which one of these states will be chosen by the nature of the physico-chemical reaction. The multiplicity of choices gives its full importance to the evolution of the systems. This paper has aimed to show the extent to which the concepts of non-equilibrium and of deterministic chaos sublimate the fundamental physical laws by leading us to the creation of new structures and to auto-organization. Chemistry is no exception to this rule. The final conclusion is given by Jean-Marie Lehn [21], Nobel Prize Winner in

Chemistry in 1987: "The essence of chemistry is not only to discover but to invent and above all to create. The book of chemistry is not only to be read but to be written. The score of chemistry is not only to be played but to be composed."

APPENDIX A: SOLUTIONS OF THE BRUSSELATOR MODEL

The Brusselator system of two equations depends on two variables X and Y:

$$\dot{X} = \frac{dX}{dt} = A + X^2 Y - B X - X$$
$$\dot{Y} = \frac{dY}{dt} = B X - X^2 Y$$

The stationary state is characterized by the stable concentrations X_0 and Y_0:

$$\frac{dX}{dt} = 0 = A + X_0^2 Y_0 - B X_0 - X_0 \qquad X_0 = A$$
$$\frac{dY}{dt} = 0 = B X_0 - X_0^2 Y_0 \qquad Y_0 = \frac{B}{X_0} = \frac{B}{A}$$

Its stability is studied by slightly changing the stationary concentrations by small quantities x and y:

$$X(t) = X_0 + x\, e^{\omega t} \qquad \frac{|x|}{|X_0|} << 1$$
$$Y(t) = Y_0 + y\, e^{\omega t} \qquad \frac{|y|}{|Y_0|} << 1$$

After algebraic transformations and neglecting second-order (and third-order) terms that imply crossed concentrations such as xx, yy or xy, one obtains:

$$(B - 1 - \omega)\, x + A^2\, y = 0$$
$$-B\, x + \left(-A^2 - \omega\right) y = 0$$

Its non-trivial solutions ($x \neq 0$ et $y \neq 0$) are obtained as the roots of the secular determinant:

$$\begin{vmatrix} B-1-\omega & A^2 \\ -B & -A^2-\omega \end{vmatrix} = \omega^2 + (A^2 - B + 1)\omega + A^2 = 0$$

The Brusselator solutions have five specific behaviors according to the respective values of the concentrations of A and B:

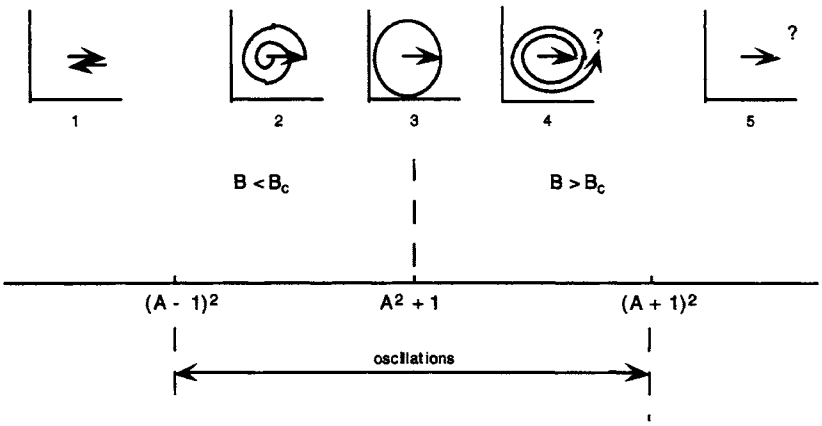

Fig.A1. Stable (1,2), metastable (3), instable (4,5), and oscillatory (3,4,5) regimes in the Brusselator model.

The oscillatory behaviors are obtained when the value of the discriminant is negative:

$$\begin{aligned} (A^2 - B + 1)^2 - 4A^2 &= a^2 - b^2 \\ &= (a+b)(a-b) \\ &= [A^2 - B + 1 + 2A][A^2 - B + 1 - 2A] \\ &= [(A^2 + 2A + 1) - B][(A^2 - 2A + 1) - B] \\ &= [(A+1)^2 - B][(A-1)^2 - B] \end{aligned}$$

i.e. when:

$$(A-1)^2 < B < (A+1)^2$$

In the limits $(A-1)^2 < B < (A+1)^2$, ω has both real and imaginary components:

$$\omega = \alpha + i\beta$$
$$= \alpha - i\beta$$

$$\mathrm{Re}\,\omega = \alpha = -\frac{(A^2 - B + 1)}{2}$$

If its real part is positive, the system becomes unstable. The bifurcation takes place at the point:

$$\alpha = 0 = A^2 - B_c + 1$$
$$\Rightarrow B_c = A^2 + 1$$
$$\Rightarrow \mathrm{Re}\,\omega = \tfrac{1}{2}(B - B_c)$$

If $B < B_C$, the system is stable. The real component of ω is negative. The oscillations are dampened. If $B = B_C$, the system becomes unstable.

In short,
1° if $B < B_C$, the system returns to a stationary state. In an X-Y diagram, this return to the starting point will correspond to a spiral if there is an imaginary component.

2° if $B = B_C$, the system oscillates; one observes marginal stability such as that found in the Lotka-Volterra prey-predator model.

3° if $B > B_C$, the perturbed system does not return to the stationary state but will diverge from it. The linear theory of stability is unable to give a correct answer since its analysis is limited to first-order terms and its results are not significant when $\exp(\omega t)$ becomes significant. A correct answer is given by the bifurcation theory. The correct solution obtained by numerical integration shows that the system tends towards a limit cycle i.e. to Prigogine's dissipative structure.

APPENDIX B: STABILITY ANALYSIS OF THE LOGISTIC MODEL

The stationary state of the logistic model is defined by:

$$\frac{dX}{dt} = 0 = k X_0 (K - X_0)$$

with the two stationary populations:

$$X_0 = 0$$
$$X_0 = K$$

When applying the perturbation:

$$X(t) = X_0 + x\, e^{\omega t}$$
$$\frac{dX}{dt} = x\, \omega\, e^{\omega t}$$

one obtains the equations that will define the stable or unstable behavior of the stationary solution:

$$\omega\, x\, e^{\omega t} = \frac{dX}{dt}$$
$$= k\, X(K - X)$$
$$= k\left[X_0 + x\, e^{\omega t}\right]\left[K - (X_0 + x\, e^{\omega t})\right]$$
$$= k\, x(K - 2X_0)e^{\omega t}$$

$$\omega = k(K - 2\, X_0)$$

First case: $K < 0$

The mortality rate is greater than the birth rate. One of the two stationary solutions has a physical meaning: $X_0 = 0$. The other solution would correspond to a negative population and thus has no physical meaning. The $X_0 = 0$ solution is stable and would return to extinction under the effect of a perturbation:

$$\omega = k\, K = -|\omega_R| < 0$$
$$X(t) = X_0 + x\, e^{-|\omega_R| t}$$

Second case : $K > 0$

The birth rate is greater than the mortality rate. The two solutions have a physical meaning. The $X_0 = 0$ branch becomes unstable while the stable branch corresponds to $X_0 = K$. One observes a bifurcation at point $X_0 = 0$:

$$X_0 = 0$$

$$\omega = kK = +|\omega_R| > 0$$

$$X(t) = X_0 + x\, e^{+|\omega_R|t}$$

$$X_0 = K > 0$$

$$\omega = kK - 2kX_0 = -kK = -|\omega_R| < 0$$

$$X(t) = X_0 + x\, e^{-|\omega_R|t}$$

APPENDIX C: TRANSFORMATION OF VERHULST'S ANALYTICAL EQUATION INTO MAY'S NUMERICAL EQUATION

The analytical equation is transformed into its numerical equivalent using the following steps:

$$\frac{dX}{dt} = k\,(K - X)\,X$$

If using normalized populations: p = X/K:

$$\frac{dX}{dt} = k\,(K - X)\,X$$

$$\Rightarrow \frac{d\left(\frac{X}{K}\right)}{dt} = Kk\,\frac{(K - X)}{K}\,\frac{X}{K}$$

$$\Rightarrow \frac{dp}{dt} = r(1 - p)p$$

The discrete equivalent of the differential equation is thus::

$$p_{n+1} - p_n = rp_n(1 - p_n)$$

which is strictly equivalent to:

$$x_{n+1} = \mu x_n(1 - x_n)$$

by the transformations:

$$x_n = \frac{r}{r+1}p_n$$

$$x_{n+1} = \frac{r}{r+1} p_{n+1}$$

$$\mu = r + 1$$

as shown by the following proof:

$$\left(\frac{r+1}{r}\right) x_{n+1} = \left(\frac{r+1}{r}\right) x_n + r\left(\frac{r+1}{r}\right) x_n \left[1 - \left(\frac{r+1}{r}\right) x_n\right]$$

$$x_{n+1} = x_n + r x_n \left[1 - \left(\frac{r+1}{r}\right) x_n\right]$$

$$= [1 + r - (r+1) x_n] x_n$$

$$= \mu [1 - x_n] x_n$$

APPENDIX D: MATHEMATICAL ANALYSIS OF MAY'S NUMERICAL MODEL

The quadratic function $f_\mu(x) = \mu x(1-x)$ has a maximum in the interval [0-1] and is zero at the extremities $f_\mu(0) = f_\mu(1) = 0$. The maximum is obtained at x_m=1/2 from the differentiation:

$$f'_\mu(x) = \mu(1-2x) = 0$$

$$x_m = \tfrac{1}{2}$$

The maximum of the curve corresponds to a maximum population of:

$$f_\mu\left(\tfrac{1}{2}\right) = \mu x_m (1 - x_m) = \frac{\mu}{4}$$

In all cases, the population must lie between 0 and 1. If μ increases, the function becomes increasingly peaked. Since the maximum normalized population is given by $\mu/4$, the value of μ cannot exceed four and thus μ must be defined within the limits $0<\mu<4$. The stationary population is obtained from the condition $x_{n+1}=x_n=x^*$ in the numerical equation:

$$x^* = \mu x^* (1 - x^*)$$

with the two solutions:

x*=0, a solution valid for all values of m, and

$$x^* = 1-\frac{1}{\mu}$$

The latter solution has a physical meaning only if $\mu>1$. If $\mu<1$, it would correspond to an impossible negative population. We find here at the point $\mu=1$, the bifurcation already met in the analytical model of the logistic equation at the value K=0. For the first two examples given in Section 7, one obtains from this relationship the values:

$$x^* = 1-\frac{1}{\mu} = 1-\frac{1}{2,7} = 1-0,3704 = 0,6296$$

The stability of the stationary point is ensured if it is an attractor, i.e. if:

$$\begin{aligned} x(n) &= x^* + \varepsilon(n) \\ x(n+1) &= x^* + \varepsilon(n+1) \end{aligned} \quad \rightarrow \quad \frac{|\varepsilon(n+1)|}{|\varepsilon(n)|} < 1$$

This establishes from a Taylor series expansion that the slope must be less than 45°:

$$x(n+1) = x^* + \varepsilon(n+1) = f[x(n)] = f[x^* + \varepsilon(n)]$$

$$\xrightarrow{\text{TaylorSeriesExpansion}} \quad \begin{aligned} x^* + \varepsilon(n+1) &\approx f(x^*) + \varepsilon(n)f'(x^*) \\ &= x^* + \varepsilon(n)f'(x^*) \end{aligned}$$

$$|f'(x^*)| < 1$$

This latter condition implies that the stationary population is stable if:

$$\begin{aligned} f'_{\mu}(x^*) &= \mu(1-2x^*) \\ |f'_{\mu}(x^*)| &= |\mu(1-2x^*)| < 1 \\ |f'_{\mu}(x^*)| &= \left|\mu\left(1-2\left(1-\frac{1}{\mu}\right)\right)\right| \\ &= |-\mu+2| < 1 \end{aligned}$$

If $x^*=0$, the previous condition only implies that $|\mu|<1$. This is a trivial solution of extinct population as long as it is the only possible solution. When $x^*\neq 0$, the same condition implies that μ will not be greater than 3. The stability condition in this case is $1<\mu<3$. It is the explanation of the bifurcation according to McNeill & Walls.

The origin of the second bifurcation, the first pitchfork bifurcation, at point $\mu=3$ can be found by comparing the values of the populations for two successive generations:

$$x_{n+1} = F(x_n)$$
$$x_{n+2} = F(x_{n+1}) = F[F(x_n)]$$

The stationary populations are given by solving the 4th-degree equation:

$$x = \mu^2 x(1-x)[1-\mu x(1-x)]$$
$$\mu^2 x(1-x)[1-\mu x(1-x)]-x = 0$$

which has four roots:

$$x^*_0 = 0$$
$$x^*_1 = 1-\frac{1}{\mu}$$
$$x^*_2 = \frac{1}{2\mu}\left[1+\mu+\sqrt{\mu^2-2\mu-3}\right]$$
$$x^*_3 = \frac{1}{2\mu}\left[1+\mu-\sqrt{\mu^2-2\mu-3}\right]$$

The last two roots x^*_2 and x^*_3 have imaginary components if $1<\mu<3$ and thus have no physical meaning in this region where x^*_0 is unstable and x^*_1 stable. x^*_2 and x^*_3 become meaningful when $\mu\geq 3$, a domain in which they are stable while x^*_0 and x^*_1 have become unstable. In the numerical example given in the text ($\mu=3.1$), one observes an oscillation that "pitchforks" the value previously obtained:

$$x^*_1 = 1-\frac{1}{\mu} = 0.6774$$
$$x^*_2 = \frac{1}{2\mu}\left[1+\mu+\sqrt{\mu^2-2\mu-3}\right] = 0.7645$$

$$x^*_3 = \frac{1}{2\mu}\left[1+\mu-\sqrt{\mu^2-2\mu-3}\right] = 0.5581$$

If we continue the analysis, the roots of double periodicity will become unstable and the cycle of period 2 will bifurcate to a cycle of period 4. The stability analysis shows that this bifurcation takes place at the value $1+\sqrt{6} = 3{,}4495$. It becomes increasingly difficult to continue the analytical study while the numerical solutions are straightforwardly obtained from a pocket calculator.

ACKNOWLEDGMENTS

The author would like to thank Dr. Marie-Claude André for the page setup of the manuscript, Dr. Eric Perpète and Denis Jacquemin for their help in the drawing of the figures, and Mrs. Joanne O'Donnel for the proofreading of the full paper. He also acknowledges the support from the Interuniversity Attraction Poles Programme on "Supramolecular Chemistry and Supramolecular Catalysis (IUAP N° P5-03)". – Belgian State- Federal Office for Scientific, Technical and Cultural Affairs.

REFERENCES

[1] See, for example: Merriam Webster's Collegiate Dictionary, Tenth Edition, 1993

[2] N.A. Campbell, Biologie, p. 1095-1097, Editions du renouveau pédagogique, Saint Laurent (1995)

[3] R. De Sapio, Calculus for the Life Sciences, p. 416-455, W.H. Freeman, San Francisco (1976)
P.B. Kahn, Mathematical Methods for Scientists and Engineers, Linear and Nonlinear Systems, p. 250-254, Wiley, New York (1990)

[4] B.P. Belousov, Ref. Radiats. Med. Moscow (1958). An English translation of the communication: B.P. Belousov, A periodic reaction and its mechanism, is published in: R.J. Field, M. Burger (eds), Oscillations and travelling waves in chemical systems, Wiley, New York (1985)

[5] R.J. Field, J. Chem. Educ., 49,308 (1972)
R.J. Field, R.M. Noyes, Nature 237,390 (1972)
R.J. Field, E. Körös, R.M. Noyes, J. Am. Chem. Soc., 94, 8649 (1972)

[6] R.J. Field, F.W. Schneider, J. Chem. Educ., 66, 195 (1989)

[7] P. Glansdorff, I. Prigogine, Physica, 20, 773 (1954)
I. Prigogine, R. Balescu, Bull. Acad. Roy. Belg., 41, 917 (1955)

[8] I. Prigogine, G. Nicolis, J. Chem. Phys., 46, 3542 (1967)
I. Prigogine, R. Lefever, J. Chem. Phys., 48, 1695 (1968)
R. Lefever, G. Nicolis, J. Theor. Biol., 30, 267 (1971)
[9] Edward N. Lorenz, Journal of Atmospheric Sciences, 20, 130 (1963)
[10] D. Ruelle, The Mathematical Intelligencer, 2, 126 (1980)
[11] K.J. McNeil, D.F. Walls, J. Statis. Phys., 10, 439 (1974)
[12] R. May, Nature, 261, 459 (1976)
[13] T.Y. Li, J.A. Yorke, American Mathematical Monthly, 82, 985 (1975)
[14] L. Györgyi, S.L. Rempe, and R.J. Field, J. Phys. Chem.,95,3159 (1991)
See also, Chemical Engineering News, Jan.21, 28 (1991)
[15] E. Wasserman, in Chemical Engineering News, Jan.21, 25 (1991)
[16] See, for example, D. Kondepundi, I. Prigogine, Modern Thermodynamics, From Heat Engines to Dissipative structures, Wiley, New York (1998)
M.M.C. Ferreira, W.C. Ferreira Jr., A.C.S. Lino, M.E.G. Porto, *Uncovering* Oscillations, Complexity, and Chaos in Chemical Kinetics Using Mathematica, J. Chem. Educ., 76, 861 (1999)
[17] O. Benini, R. Cervellati, P. Fetto, J. Chem. Educ., 73, 865 (1996)
P. Strizhak, M. Menzinger, J. Chem. Educ., 73, 868 (1996)
[18] J. Maddox, What Remains to be Discovered, Martin Kessler Books, (1998)
[19] M.J. Feigenbaum, Universal Behavior in Nonlinear Systems, Los Alamos Science, 1, 4 (1980)
[20] R. Feynman, *QED*, the strange theory of light and matter, p. 129, Princeton University Press (1985)
[21] J.M. Lehn, Supramolecular Chemistry, Concepts and Perspectives, VCH (1996)

J. Leszczynski (Editor)
Computational Materials Science
Theoretical and Computational Chemistry, Vol. 15

Chapter 2

Reaction network analysis. The kinetics and mechanism of water-gas-shift reaction on Cu(111)

I. Fishtik, C. A. Callaghan, R. Datta

Fuel Cell Center, Department of Chemical Engineering, Worcester Polytechnic Institute, Worcester, MA 01609, USA

1. INTRODUCTION

First principles quantum mechanical (QM) calculations of elementary reaction energetics are becoming an increasingly indispensable and incisive tool of the catalytic chemist [1]. We can now virtually "see" how molecules rearrange themselves on metal surfaces, and can calculate the corresponding reaction energetics of elementary processes with increasing accuracy, although still not accurate enough for predicting kinetics. Actually, there are available semi-theoretical methods [2] that can predict reaction energetics of elementary catalytic reactions with acceptable accuracy. It is, thus, only a matter of time before we have a very basic understanding of the molecular events involved in important catalytic processes and their energetics. However, this is only the first step toward unraveling the mechanism and kinetics of overall catalytic reactions. This chapter is concerned with using the thus predicted kinetic information on individual molecular events or elementary reaction steps to determine the kinetics and mechanisms of overall reactions comprising such steps. The general approach presented here is, in fact, more widely applicable and, in principle, may be utilized for the analysis of non-catalytic reaction networks as well as the functioning of cellular machinery. Furthermore, a deeper understanding of these reaction systems might eventually allow systematic molecular theory-based design, e.g., of catalytic materials.

There are currently two available different ways in which one might use the predicted kinetic information on elementary reaction steps: 1) the conventional Langmuir-Hinshelwood-Hougen-Watson (LHHW) approach [3], in which an explicit rate expression might be derived based on the common, but rather arbitrary,

assumptions such as the rate-determining step (RDS), quasi-steady-state (QSS) approximation, most abundant reactive intermediate (MARI), etc., and 2) the microkinetic approach [4,5], wherein no assumptions are made, but only numerical results are possible. The former approach is approximate, while the latter is opaque. In fact, the latter approach is already utilized in the computational modeling of combustion and atmospheric pollution systems comprising of hundreds of species and elementary reactions.

We propose an alternate approach [6] that begins with a rigorous microkinetic analysis based on predicted kinetics of elementary steps, but then utilizes a systematic network analysis in analogy to electrical networks, with De Donder's affinity as the driving force akin to voltage and reaction rate akin to current, in order to elucidate the major pathways followed by deliberate reduction of the network to arrive at simpler mechanisms and explicit but precise rate expressions containing predicted rate constants. Within this approach the reaction network may be envisioned in terms of a revisited version [6,7] of the conventional reaction route (RR) theory [9-12]. The capabilities of the new reaction network approach are illustrated by applying it to the analysis of a 15 elementary reaction microkinetic mechanism of the water-gas shift reaction (WGSR) developed by us earlier [13,14].

2. NOTATION AND DEFINITIONS

We consider the general case of a multiple chemical reaction system. The species comprising the elementary reactions that describe the detailed chemistry of the process are divided into the surface active sites S, the surface intermediates I_1, I_2, ..., I_q, and the gaseous terminal species (reactants and products) T_1, T_2,...,T_n. Thus, the mechanism is described by a set of p elementary reactions

$$s_j = \alpha_{j0}\mathrm{S} + \sum_{k=1}^{q} \alpha_{jk}\mathrm{I}_k + \sum_{i=1}^{n} \beta_{ji}\mathrm{T}_i = 0 \; ; \qquad j = 1, 2, \ldots, p \qquad (1)$$

The stoichiometric coefficients of the active sites α_{j0} (j = 1,2,...,p), the surface intermediates α_{jk} (j = 1,2,...,p; k = 1,2,...,q) and the terminal species β_{ji} (j = 1,2,...,p; i = 1,2,...,n), by convention, are assumed to be positive for products and negative for reactants. Because the active sites and the surface intermediates are linearly related (see Eq. (5) below), the stoichiometric coefficients of the active sites in the overall stoichiometric matrix ν may be omitted

$$\mathbf{v} = \begin{bmatrix} \alpha_{11} & \alpha_{12} & \cdots & \alpha_{1q} & \beta_{11} & \beta_{12} & \cdots & \beta_{1n} \\ \alpha_{21} & \alpha_{22} & \cdots & \alpha_{2q} & \beta_{21} & \beta_{22} & \cdots & \beta_{2n} \\ \cdots & \cdots & \cdots & \cdots & \cdots & \cdots & \cdots & \cdots \\ \alpha_{p1} & \alpha_{p2} & \cdots & \alpha_{pq} & \beta_{p1} & \beta_{p2} & \cdots & \beta_{pn} \end{bmatrix} \tag{2}$$

It is further assumed that $rank\, \mathbf{v} = m \leq p$, i.e., the elementary reactions are not necessarily linearly independent. We further define the stoichiometric submatrix

$$\boldsymbol{\alpha} = \begin{bmatrix} \alpha_{11} & \alpha_{12} & \cdots & \alpha_{1q} \\ \alpha_{21} & \alpha_{22} & \cdots & \alpha_{2q} \\ \cdots & \cdots & \cdots & \cdots \\ \alpha_{p1} & \alpha_{p2} & \cdots & \alpha_{pq} \end{bmatrix} \tag{3}$$

In what follows, this matrix is referred to as the *intermediates* matrix. It is assumed that the surface intermediates are linearly independent, i.e., $rank\, \boldsymbol{\alpha} = q$. If this is not the case, then the linearly dependent columns in the intermediates matrix may be arbitrarily omitted.

Each of the elementary reactions is characterized by its affinity A_j, defined by [15]

$$\mathcal{A}_j = \frac{1}{RT} \mathrm{A}_j = \ln K_j - \alpha_{j0} \ln \theta_0 - \sum_{k=1}^{q} \alpha_{jk} \ln \theta_k - \sum_{i=1}^{n} \beta_{qi} \ln P_i \; ; \qquad j = 1, 2, \ldots, p \tag{4}$$

Here K_j is the equilibrium constant of the j-th elementary reaction (as the ratio of the forward and reverse rate constants), $\theta_0, \theta_k (k = 1,2,...,q)$ are the surface coverages of the active sites and surface intermediates, respectively, and P_i (i = 1,2,…,n) represents the partial pressure of each terminal species. The surface coverages are subject to the site balance constraint

$$\theta_0 + \sum_{k=1}^{q} \theta_k = 1 \tag{5}$$

The net rate of the elementary reactions r_j (j = 1,2,...,p) in terms of rates of the forward $\vec{r}_j$ and reverse $\overleftarrow{r}_j$ reaction is

$$r_j = \vec{r}_j - \overleftarrow{r}_j \tag{6}$$

On the other hand from chemical thermodynamics we have

$$\mathscr{A}_j = \ln \frac{\vec{r}_j}{\overleftarrow{r}_j} \tag{7}$$

Combining Eqs. (6) and (7) gives

$$r_j = \vec{r}_j - \overleftarrow{r}_j = \vec{r}_j \left[1 - \exp\left(-\mathscr{A}_j\right) \right] \tag{8}$$

The rate equations in the form of Eq. (8) are typically referred to as the De Donder relation.

3. REACTION ROUTES

A reaction route (RR) is defined simply as a linear combination of the elementary reaction steps s_1, s_2, ..., s_p that eliminates a specified number of species (surface intermediates and terminal species) thus resulting in an overall reaction (OR) involving only a specified number of terminal species. Mathematically, a RR may be represented as

$$RR = \sum_{j=1}^{p} \sigma_j s_j \tag{9}$$

where $\sigma_1, \sigma_2, ..., \sigma_p$ is a set of real numbers, called stoichiometric numbers. Since here we are interested in a single-OR, it is sufficient to define a RR as a linear combination of a specified number of elementary reactions that eliminates *all* of the surface intermediates. Following Milner [11], we require the RRs to be direct, that is, the number of elementary reaction steps involved in a RR will be minimal. By "minimal" is meant that if an elementary reaction is omitted from the RR, then there is no way to eliminate all of the surface intermediates by linearly combining the remaining elementary reactions. More specifically, for a single OR, a direct RR is defined as a RR that involves no more than $1 + rank\ \boldsymbol{\alpha} = q + 1$ linearly independent elementary reactions. Clearly, more than one RR is possible, and indeed likely, for an OR. Of course, not all of these are independent.

Let the $q + 1$ *linearly independent* elementary reactions that are involved in a RR be $s_{i_1}, s_{i_2}, ..., s_{i_q}, s_{i_{q+1}}$, where the subscripts $i_1, i_2, ..., i_q, i_{q+1}$ represent an ordered set of $q + 1$ integers satisfying the condition $1 \le i_1 < i_2 < ... < i_q < i_{q+1} \le p$. A RR is denoted by $RR(s_{i_1}, s_{i_2}, ..., s_{i_q}, s_{i_{q+1}})$ thus specifying the elementary reactions, $s_{i_1}, s_{i_2}, ..., s_{i_q}, s_{i_{q+1}}$, that are involved in the given RR. Thus, the general equation of a RR is given by

$$RR(s_{i_1}, s_{i_2}, ..., s_{i_q}, s_{i_{q+1}}) = \sigma_{i_1} s_{i_1} + \sigma_{i_2} s_{i_2} + ... + \sigma_{i_q} s_{i_q} + \sigma_{i_{q+1}} s_{i_{q+1}} \tag{10}$$

where the stoichiometric numbers are obtained from [8]

$$\sigma_{i_k} = \begin{vmatrix} \alpha_{i_1,1} & \alpha_{i_1,2} & \dots & \alpha_{i_1,q} & 0 \\ \alpha_{i_2,1} & \alpha_{i_2,2} & \dots & \alpha_{i_2,q} & 0 \\ \dots & \dots & \dots & \dots & \dots \\ \alpha_{i_{k-1},1} & \alpha_{i_{k-1},2} & \dots & \alpha_{i_{k-1},q} & 0 \\ \alpha_{i_k,1} & \alpha_{i_k,1} & \dots & \alpha_{i_k,q} & 1 \\ \alpha_{i_{k+1},1} & \alpha_{i_{k+1},1} & \dots & \alpha_{i_{k+1},q} & 0 \\ \dots & \dots & \dots & \dots & \dots \\ \alpha_{i_q,1} & \alpha_{i_q,2} & \dots & \alpha_{i_q,q} & 0 \\ \alpha_{i_{i+1},1} & \alpha_{i_{i+1},1} & \dots & \alpha_{i_{i+1},q} & 0 \end{vmatrix} \tag{11}$$

The OR produced by this RR is

$$\rho = \sum_{i=1}^{n} \begin{vmatrix} \alpha_{i_1,1} & \alpha_{i_1,2} & \dots & \alpha_{i_1 q} & \beta_{i_1,i} \\ \alpha_{i_2,1} & \alpha_{i_2,2} & \dots & \alpha_{i_2,q} & \beta_{i_2,i} \\ \dots & \dots & \dots & \dots & \dots \\ \alpha_{i_q,1} & \alpha_{i_q,2} & \dots & \alpha_{i_q,q} & \beta_{i_q,i} \\ \alpha_{i_{q+1},1} & \alpha_{i_{q+1},2} & \dots & \alpha_{i_{q+1},q} & \beta_{i_{q+1},i} \end{vmatrix} \mathrm{T}_i = 0 \tag{12}$$

A similar equation is valid for the overall affinity of the OR in terms of affinities of reaction steps

$$\mathcal{A} = \sigma_{i_1}\mathcal{A}_{i_1} + \sigma_{i_2}\mathcal{A}_{i_2} + \ldots + \sigma_{i_q}\mathcal{A}_{i_q} + \sigma_{i_{q+1}}\mathcal{A}_{i_{q+1}} = \begin{vmatrix} \alpha_{i_1,1} & \alpha_{i_1,2} & \ldots & \alpha_{i_1 q} & \mathcal{A}_{i_1} \\ \alpha_{i_2,1} & \alpha_{i_2,2} & \ldots & \alpha_{i_2,q} & \mathcal{A}_{i_2} \\ \ldots & \ldots & \ldots & \ldots & \ldots \\ \alpha_{i_q,1} & \alpha_{i_q,2} & \ldots & \alpha_{i_q,q} & \mathcal{A}_{i_q} \\ \alpha_{i_{q+1},1} & \alpha_{i_{q+1},2} & \ldots & \alpha_{i_{q+1},q} & \mathcal{A}_{i_{q+1}} \end{vmatrix} \tag{13}$$

One way to enumerate the complete set of RRs is to consider each of the possible combinations of $q + 1$ elementary reactions from a total of p. Hence, the total number N of such combinations does not exceed

$$N = \frac{p!}{(q+1)!(p-(q+1))!}$$

Within this algorithm of RR enumeration, three different scenarios are possible:

a) The selected $q + 1$ elementary reactions are linearly independent. Then, there results a *full* RR, i.e., an OR and affinity different from zero. For simplicity, in what follows a full RR is simply referred to as a RR.
b) The selected $q + 1$ elementary reactions are linearly dependent. Then, the resulting RR is an *empty* RR (ER) that produces a *zero* OR, i.e., an OR in which the stoichiometric coefficients of all the terminal species are zero.
c) The selected $q + 1$ elementary reactions are linearly dependent and there are two or more RRs or ERs that involve a subset of the same $q + 1$ elementary reactions. Then, the resulting RR is a *zero* RR (ZR), i.e., a RR in which all of the stoichiometric numbers are equal to zero. A zero RR produces a zero OR.

4. QUASI-STEADY STATE CONDITIONS AND REACTION ROUTES

According to the QSS approximation, the rates of formation and consumption of the surface intermediates are approximately equal, so that the time derivatives of the coverages of the intermediates may be set equal to zero

$$\frac{d\theta_k}{dt} = \sum_{j=1}^{p} \alpha_{jk} r_j = 0 \ ; \qquad k = 1, 2, \ldots, q \tag{14}$$

In matrix form, this may be written as

$$\boldsymbol{\alpha}^{\mathrm{T}}\mathbf{r} = \begin{bmatrix} \alpha_{11} & \alpha_{21} & \dots & \alpha_{p1} \\ \alpha_{12} & \alpha_{22} & \dots & \alpha_{p2} \\ \dots & \dots & \dots & \dots \\ \alpha_{1q} & \alpha_{2q} & \dots & \alpha_{pq} \end{bmatrix} \begin{pmatrix} r_1 \\ r_2 \\ \dots \\ r_p \end{pmatrix} = 0 \tag{15}$$

Eqs. (14) and (15) may be referred to as the conventional formulation of the QSS approximation conditions. The QSS conditions may be expressed in a more useful form by employing the theory of RRs. Consider an arbitrary set of l linearly independent RRs

$$\begin{pmatrix} RR_1 \\ RR_2 \\ \dots \\ RR_l \end{pmatrix} = \begin{bmatrix} \sigma_{11} & \sigma_{12} & \dots & \sigma_{1p} \\ \sigma_{21} & \sigma_{22} & \dots & \sigma_{2p} \\ \dots & \dots & \dots & \dots \\ \sigma_{l1} & \sigma_{l2} & \dots & \sigma_{lp} \end{bmatrix} \begin{pmatrix} s_1 \\ s_2 \\ \dots \\ s_p \end{pmatrix} \tag{16}$$

According to the Horiuti-Temkin theorem [9,10], the number of linearly independent RRs is equal to $l = p - rank\boldsymbol{\alpha} = p - q$. Now, let $J_1, J_2, \dots, J_l$ be the corresponding rates (or, the RR fluxes) along the arbitrarily selected set of linearly independent RRs, namely $RR_1, RR_2, \dots, RR_l$. Then, within the QSS approximation the following relation between RR fluxes and the rates of individual elementary reaction steps is valid

$$\begin{pmatrix} r_1 \\ r_2 \\ \dots \\ r_p \end{pmatrix} = \begin{bmatrix} \sigma_{11} & \sigma_{21} & \dots & \sigma_{l1} \\ \sigma_{12} & \sigma_{22} & \dots & \sigma_{l2} \\ \dots & \dots & \dots & \dots \\ \sigma_{1p} & \sigma_{2p} & \dots & \sigma_{lp} \end{bmatrix} \begin{pmatrix} J_1 \\ J_2 \\ \dots \\ J_p \end{pmatrix} \tag{17}$$

A particular set of l linearly independent RRs may always be selected from the list of enumerated direct RRs as follows. Because the rank of the intermediate matrix $\boldsymbol{\alpha}$ is equal to q, at least one determinant of order q in $\boldsymbol{\alpha}$ is different from zero. Without loss of generality, we assume that

$$\sigma = \begin{vmatrix} \alpha_{11} & \alpha_{12} & \dots & \alpha_{1q} \\ \alpha_{21} & \alpha_{22} & \dots & \alpha_{2q} \\ \dots & \dots & \dots & \dots \\ \alpha_{q1} & \alpha_{q2} & \dots & \alpha_{qq} \end{vmatrix} \neq 0 \tag{18}$$

Then, from Eqs. (10) and (11) it may be deduced that

$$\begin{pmatrix} RR_1 \\ RR_2 \\ \dots \\ RR_l \end{pmatrix} = \begin{bmatrix} \sigma_{11} & \sigma_{12} & \dots & \sigma_{1q} & \sigma & 0 & \dots & 0 \\ \sigma_{21} & \sigma_{22} & \dots & \sigma_{2q} & 0 & \sigma & \dots & 0 \\ \dots & \dots & \dots & \dots & \dots & \dots & \dots & \dots \\ \sigma_{l1} & \sigma_{l2} & \dots & \sigma_{lq} & 0 & 0 & \dots & \sigma \end{bmatrix} \begin{pmatrix} s_1 \\ s_2 \\ \dots \\ s_q \\ s_{q+1} \\ s_{q+2} \\ \dots \\ s_p \end{pmatrix} \tag{19}$$

where σ is given by Eq. (18) and

$$\sigma_{jk} = \begin{vmatrix} \alpha_{11} & \alpha_{12} & \dots & \alpha_{1q} & 0 \\ \alpha_{21} & \alpha_{22} & \dots & \alpha_{2q} & 0 \\ \dots & \dots & \dots & \dots & \dots \\ \alpha_{k-1,1} & \alpha_{k-1,2} & \dots & \alpha_{k-1,q} & 0 \\ \alpha_{k1} & \alpha_{k2} & \dots & \alpha_{kq} & 1 \\ \alpha_{k+1,1} & \alpha_{k+1,2} & \dots & \alpha_{k+1,q} & 0 \\ \dots & \dots & \dots & \dots & \dots \\ \alpha_{q1} & \alpha_{q2} & \dots & \alpha_{qq} & 0 \\ \alpha_{q+j,1} & \alpha_{q+j,2} & \dots & \alpha_{q+j,q} & 0 \end{vmatrix} ; j = 1, 2, \dots, p\text{-}q; \; k = 1, 2, \dots, q \tag{20}$$

With this selection of linearly independent RRs, Eq. (17) becomes

$$\begin{pmatrix} r_1 \\ r_2 \\ \cdots \\ r_q \\ r_{q+1} \\ r_{q+2} \\ \cdots \\ r_p \end{pmatrix} = \begin{bmatrix} \sigma_{11} & \sigma_{21} & \cdots & \sigma_{l1} \\ \sigma_{12} & \sigma_{22} & \cdots & \sigma_{l2} \\ \cdots & \cdots & \cdots & \cdots \\ \sigma_{1q} & \sigma_{2q} & \cdots & \sigma_{lq} \\ \sigma & 0 & \cdots & 0 \\ 0 & \sigma & \cdots & 0 \\ \cdots & \cdots & \cdots & \cdots \\ 0 & 0 & \cdots & \sigma \end{bmatrix} \begin{pmatrix} J_1 \\ J_2 \\ \cdots \\ J_l \end{pmatrix} \tag{21}$$

For the particular case of a single OR, with only one RR, Eq. (21) takes the form

$$J = \frac{r_1}{\sigma_1} = \frac{r_2}{\sigma_2} = \ldots = \frac{r_q}{\sigma_q} = \frac{r_{q+1}}{\sigma_{q+1}} \tag{22}$$

5. REACTION NETWORKS

Prior to providing the details, it is useful to visualize a reaction network as a trek across a mountain range with many peaks and valleys (Fig. 1). In keeping with the transition state theory, the valleys may be viewed as reactants, surface intermediates and products of a reaction while a single elementary reaction may be viewed as the trek from one valley to an adjacent one over a shallow or tall mountain pass, representative of the energy barrier for the reaction. Many such excursions constitute the overall trek or a reaction network. Clearly, almost an infinite variety of pathways or RRs exist for a given trek in going from the reactants to the products, including those involving ERs. The direct RRs are those that do not involve ERs and are finite and shortest, although still large in number.

Based on this analogy, we define a reaction network as an ordered, interconnected, directed and a finite sequence of elementary reaction steps that satisfies the following conditions:

a) There is one starting point (reactants) and one end point (products) in the network for a given OR. If there is more than one RR, there will always be parallel branches in the network.
b) Each elementary reaction in the network is reversible, i.e., it may proceed in either direction.
c) Any sequence of elementary reaction steps from the starting point to the end point is a RR. In other words, the production and consumption of every surface

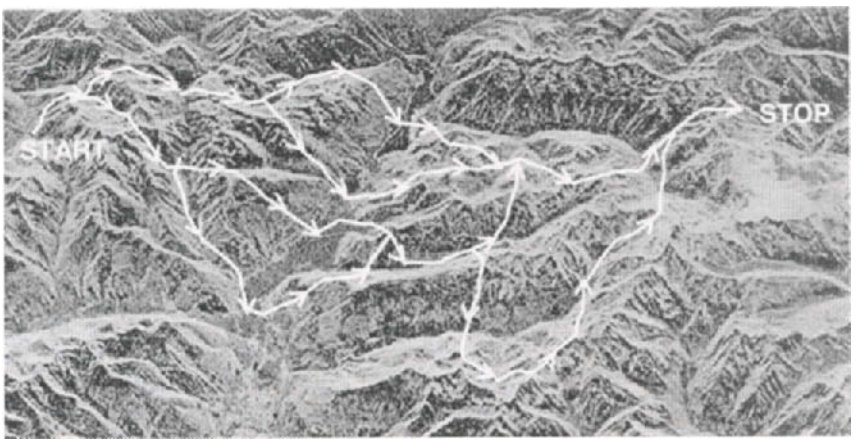

Fig. 1. The analogy between a mountain trek and a reaction network

intermediate along any RR are precisely balanced thus resulting in a net transformation of the reactants into products.

d) The algebraic sum of the affinities of the elementary reaction steps along each RR is equal to the overall affinity of the OR, $A_{overall}$, the overall driving force. From this viewpoint, the order of the reaction steps in the RR is unimportant.
e) The elementary reactions are interconnected at points called nodes. At each node the QSS conditions for the intermediates, Eq. (15), is satisfied; that is, the algebraic sum of the rates of the elementary reactions entering or leaving the node is equal to zero.
f) A RR that starts and ends at the same node is an ER. The algebraic sum of affinities of the elementary reactions along an ER is equal to zero. This means that there are slow steps or significant resistances in all significant parallel branches.
g) A reaction network for a given mechanism must be unique and include a complete set of direct RRs

There are several advantages in adopting this new viewpoint of a reaction network for its analysis, visualization and reduction. The main advantage is that within this representation a reaction network becomes analogous to a general linear electrical circuit network, so that the procedures of electric circuit analysis are applicable.

6. ELECTRICAL AND REACTION NETWORKS

Qualitatively, the analogy between the conventional electrical network theory and the reaction network defined above is quite transparent. To make this analogy quantitative, we introduce several additional concepts:

i) Each elementary reaction s_j (j = 1, 2,..., p) in the network is visualized as a single resistor with its characteristic resistance R_j (j = 1, 2,..., p) depending upon the local reaction conditions and the composition of the reaction mixture, including intermediates. Following Shiner [16], the resistance for each of the elementary reaction steps is defined as per the assumed linear constitutive equation in analogy to Ohm's Law

$$R_j \equiv \frac{\mathcal{A}_j}{r_j} = \frac{\ln \dfrac{\vec{r}_j}{\bar{r}_j}}{\vec{r}_j - \bar{r}_j} \tag{23}$$

It may be noticed that the resistance is necessarily a positive quantity. At equilibrium we have $r_j^0 = \vec{r}_j = \bar{r}_j$ where r_j^0 is the exchange rate of the j-th step and, hence, its resistance in the vicinity of equilibrium is simply equal to the inverse of the exchange rate

$$R_j^0 = \lim_{\substack{A_j \to 0 \\ r_j \to 0}} R_j = \lim_{\vec{r}_j \to \bar{r}_j \to r_j^0} \frac{d \ln \dfrac{\vec{r}_j}{\bar{r}_j}}{d\left(\vec{r}_j - \bar{r}_j\right)} = \lim_{\vec{r}_j \to \bar{r}_j \to r_j^0} \frac{\dfrac{d\vec{r}_j}{\vec{r}_j} - \dfrac{d\bar{r}_j}{\bar{r}_j}}{d\vec{r}_j - d\bar{r}_j} = \frac{1}{r_j^0} \tag{24}$$

This electrical analogy is appropriate, since each elementary reaction in a mechanism represents a different degree of resistance to the reaction progress. In fact, it is frequently assumed that all resistance resides in a single step, termed the rate-determining step.

ii) The net rates of the elementary reactions ($r_j = \vec{r}_j - \bar{r}_j$) are visualized as the currents (I) through the circuit while the affinities (A_j) are equivalent to the voltages (V); in this case, Eq. (23) may be considered as the analog of Ohm's Law. However, since the actual relation between rate and affinity is nonlinear (Eq. 8), the resistance of a reaction is not a constant, unlike Ohm's Law, but depends on reaction conditions.

iii) At the nodes, under QSS conditions, the algebraic sum of the rates (currents) of the elementary reactions are equal to zero; this is equivalent to Kirchhoff's Current Law (KCL) of electrical circuits.

iv) The algebraic sum of the affinities along each ER is equal to zero; this is equivalent to Kirchhoff's Voltage Law (KVL) of electrical circuits.

v) Electric power ($P = VI$) is considered analogous to the product of the affinity of a reaction and its rate, i.e., the rate of dissipation. In an arbitrary reaction network, the sum of powers dissipated in all reactions or branches is equal to the power delivered by the overall reaction, i.e.,

$$A_{overall} J_{overall} = \sum_{j=1}^{P} A_j r_j$$

which is always greater than or equal to zero [15]. This is analogous to Tellegen's theorem of electrical circuits.

From the above definitions it follows that the analogy between the electrical and reaction networks is rather exhaustive, the main difference being that the resistance is not a constant.

7. REDUCTION AND SIMPLIFICATION OF REACTION NETWORKS

A simple construction of the reaction network theory, even without a quantitative analysis, provides a powerful visualization tool as well as a deeper understanding of the reaction mechanism as compared to the traditional and computationally expensive analyses. Obviously, not all of the possible paths in a reaction network that transform the reactants, via intermediates, into products are equally important. In this respect, a key problem in the analysis of the reaction network is the discrimination among RRs, i.e., the determination of the dominant RRs, rate-determining and quasi-equilibrium steps and, ultimately, the derivation of a simple and accurate algebraic rate equation suitable for reactor analysis and design by employing the general methods used in the analysis of the electrical circuits. For our purposes, however, the most important from this plethora of methods are those that are based on the estimation of the overall resistances of elementary reactions connected in series and the overall resistances of parallel branches of the network. More specifically, we employ the following two properties of the reaction networks: a) in a sequence of elementary reactions connected in series the elementary reaction with the *highest* resistance is considered to be the RDS while the elementary reactions with *low* resistance may considered to be at quasi-equilibrium; and b) in a sequence of parallel branches in the reaction

network the dominant branches are those which possess the *least* resistance. More generally, these two properties of a reaction network may be reformulated in terms of a principle that, in what follows, is referred to as the *principle of extremum resistance.*

The theoretical background of the above formulated principle of extremum resistance may be deduced from the following considerations. Let us examine first a one RR mechanism

$$RR = \sum_{j=1}^{q+1} \sigma_j s_j \tag{25}$$

Obviously, all of the elementary reactions in this RR are connected in series and each elementary reaction s_j in the sequence occurs σ_j times. Thus, we can define a resistance of the RR (R_{RR}) as

$$R_{RR} = \sum_{j=1}^{q+1} \sigma_j^2 R_j = \sum_{j=1}^{q+1} \frac{\sigma_j^2 \mathcal{A}_j}{r_j} \tag{26}$$

The reasoning behind this definition is the following. Firstly, we observe that because the stoichiometric numbers are squared the resistance of a RR is necessarily positive. Secondly, Eq. (26) should be consistent with the QSS conditions. Indeed, once we have defined the resistance of the RR and the affinity of the OR, we can employ the analog of Ohm's law to define an overall rate of the reaction

$$r = \frac{\mathcal{A}_{overall}}{R_{RR}} = \frac{\mathcal{A}_{overall}}{\sum_{j=1}^{q+1} \frac{\sigma_j^2 \mathcal{A}_j}{r_j}} \tag{27}$$

At QSS, according to Eq. (22), we have

$$r_j = \sigma_j J \tag{28}$$

Inserting Eq. (28) into Eq. (27) and keeping in mind that

$$\mathcal{A}_{overall} = \sum_{j=1}^{q+1} \sigma_j \mathcal{A}_j \tag{29}$$

we obtain $r = J$. In other words, Eq. (26) is consistent with the QSS kinetics. Finally, because the resistances of the elementary reactions are inversely proportional to their rates, it follows that the fast elementary reactions (high rates) have small resistances while the slow elementary reactions (low rates) have large resistances. In particular, when the resistance of an elementary reaction, say s_j, far exceeds the resistances of all of the other elementary reactions in a sequence, the overall resistance may be approximated by

$$R_{RR} \approx \frac{\sigma_j^2 \mathscr{A}_j}{r_j} \tag{30}$$

In this case the remaining elementary reactions may be considered at quasi-equilibrium and may be lumped into a single, intermediate, quasi-equilibrated reaction [8]. This is similar to the case of the two-step mechanism of Boudart [28].

Similarly, the overall resistance in a set of parallel branches of elementary reactions may be estimated for the linear case in analogy to Ohm's Law according to

$$\frac{1}{R_{RR}} = \frac{1}{R_{RR_1}} + \frac{1}{R_{RR_2}} + \ldots = \frac{1}{\sum_{j=1}^{p} \frac{\sigma_{1j}^2 \mathscr{A}_j}{r_j}} + \frac{1}{\sum_{j=1}^{p} \frac{\sigma_{2j}^2 \mathscr{A}_j}{r_j}} + \ldots \tag{31}$$

From this relation, it is easily deduced that, in a set of parallel branches, the dominant are those with the least resistance, and having the highest reaction flux.

In complex reaction networks where the series and parallel branches are difficult to discern, the simplification and reduction of the network may be performed by analyzing the resistances of the individual RRs according to Eq. (26). Within this approach, the RRs with the least resistance are dominant.

8. APPLICATION TO WGSR

Now that the basic principles of the reaction network analysis have been enumerated, we proceed to analyze in detail the water-gas shift reaction (WGSR) microkinetic model. Due to its industrial significance, the catalysis and kinetics of the WGSR has been a key example in microkinetic modeling [17-26]. In the meantime, we have shown [13,14] that reliable microkinetic models for the WGSR on Cu(111) may be developed based on rather rudimentary kinetic considerations.

Thus, it is adequate to determine the energetic characteristics of the elementary reactions based on the Unity Bond Index-Quadratic Exponential Potential (UBI-QEP) method developed by Shustorovich [2], while the pre-exponential factors may be estimated simply from the transition-state theory [4,26]. Here we employ, for illustrative purposes, a simplified version of a microkinetic WGSR model developed by us earlier [14].

8.1 A microkinetic model of the WGSR

A microkinetic model for the WGSR has been developed based on the following considerations. Our starting point is a list of species (reactants, intermediates, and products), which for this system includes: H_2O and CO as reactants, H_2OS, COS, CO_2S, H_2S, HS, OHS, OS and HCOOS (q = 8) as surface intermediates, and CO_2 and H_2 as products (n = 4). Starting with these species, a plausible set of elementary reactions may be generated using an appropriate chemical reaction generator. The generation of elementary reactions is dictated further by the subsequent application of the UBI-QEP method [2] to calculate the energetics of these elementary reactions. In other words, the elementary reactions chosen are limited to those three types for which the UBI-QEP method provides the necessary formulae:

1. AB(g) + S = ABS
2. AB(g) + S = AS + BS
3. AS + BCS = ABS + CS

Here S represents a vacant site on the surface of the catalyst. The set of elementary reactions generated under these constraints for the WGS reaction is presented in Table 1. To simplify the resulting analysis, in what follows we further disregard two of the elementary reactions from this microkinetic model, namely

s_{13}: $H_2OS + OS = 2OHS$
s_{16}: $HCOOS + OHS = CO_2S + H_2OS$

Due to their high activation energy barriers, these elementary reactions have been shown [13,14] to have a negligible effect on the overall kinetics of the WGSR. Furthermore, these reactions present some difficulties in the analysis that are best avoided in this initial report.

The UBI-QEP method [2] was utilized to calculate the enthalpy changes as well as activation energies of these elementary reactions included in Table 1.

Table 1
A Microkinetic Model for WGSR on Cu((III) [14]

	$\vec{E}_j$	$\vec{A}_j$	Elementary Reactions	$\overleftarrow{E}_j$	$\overleftarrow{A}_j$
s_1:	0	10^6	$CO + S \leftrightarrows COS$	12.0	10^{14}
s_2:	0	10^6	$H_2O + S \leftrightarrows H_2OS$	13.6	10^{14}
s_3:	5.3	$4\ 10^{12}$	$CO_2S \leftrightarrows CO_2 + S$	0	10^6
s_4:	15.3	10^{13}	$HS + HS \leftrightarrows H_2S + S$	12.8	10^{13}
s_5:	5.5	$6\ 10^{12}$	$H_2S \leftrightarrows H_2 + S$	0	10^6
s_6:	25.4	10^{13}	$H_2OS + S \leftrightarrows OHS + HS$	1.6	10^{13}
s_7:	10.7	10^{13}	$COS + OS \leftrightarrows CO_2S + S$	28.0	10^{13}
s_8:	0	10^{13}	$COS + OHS \leftrightarrows HCOOS + S$	20.4	10^{13}
s_9:	15.5	10^{13}	$OHS + S \leftrightarrows OS + HS$	20.7	10^{13}
s_{10}:	0	10^{13}	$COS + OHS \leftrightarrows CO_2S + HS$	22.5	10^{13}
s_{11}:	1.4	10^{13}	$HCOOS + S \leftrightarrows CO_2S + HS$	3.5	10^{13}
s_{12}:	4.0	10^{13}	$HCOOS + OS \leftrightarrows CO_2S + OHS$	0.9	10^{13}
s_{13}:	29.0	10^{13}	$H_2OS + OS \leftrightarrows 2OHS$	0	10^{13}
s_{14}:	26.3	10^{13}	$H_2OS + HS \leftrightarrows OHS + H_2S$	0	10^{13}
s_{15}:	1.3	10^{13}	$OHS + HS \leftrightarrows OS + H_2S$	4.0	10^{13}
s_{16}:	0.9	10^{13}	$HCOOS + OHS \leftrightarrows CO_2S + H_2OS$	26.8	10^{13}
s_{17}:	14.6	10^{13}	$HCOOS + HS \leftrightarrows CO_2S + H_2S$	14.2	10^{13}

Further, the pre-exponential factors for the forward and reverse reactions $\vec{A}_j$ and $\overleftarrow{A}_j$ are estimated using the conventional transition-state theory [4]. Following Waugh [26], we thus assume an immobile transition state without rotation for all of the species, which results in a pre-exponential factor of 10^1 $Pa^{-1}s^{-1}$ for adsorption/desorption reactions, and 10^{13} s^{-1} for surface reactions. The resulting microkinetic model for the WGS reaction is summarized in Table 1. Fine-tuning of some of the pre-exponential factors of the adsorption/desorption reactions, however, was necessary in order to be consistent with the known thermodynamics of the overall reaction, i.e., for a RR, the activation energies of the forward and reverse reactions are related to the enthalpy change via

$$\sum_j \sigma_j \vec{E}_j - \sum_j \sigma_j \overleftarrow{E}_j = \Delta H^0_{OR} \tag{32}$$

whereas the pre-exponential factors of the forward and reverse reactions must conform to

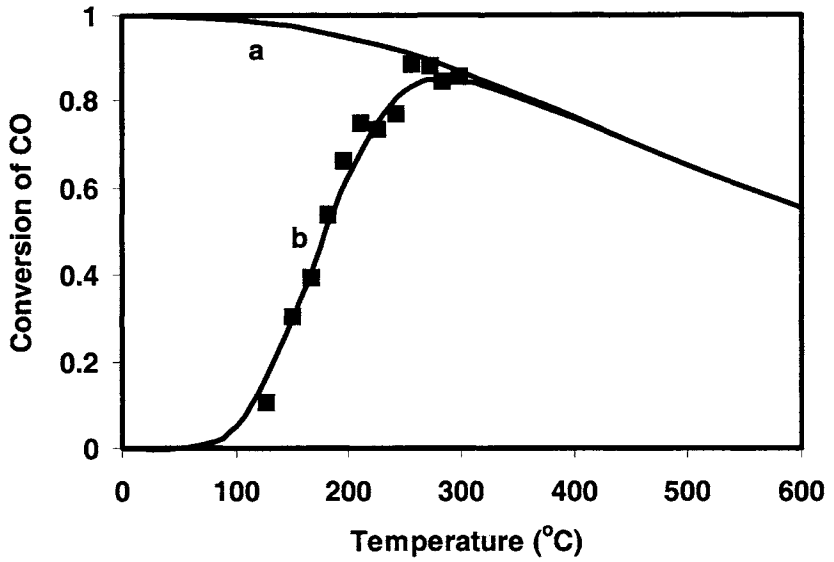

Fig. 2. The performance of the WGSR microkinetic model vs. experimental data. See the text for details.

$$\prod_j \left(\frac{\tilde{A}_j}{\bar{A}_j} \right)^{\sigma_j} = \exp\left(\frac{\Delta G^0_{OR} - \Delta H^0_{OR}}{RT} \right) \tag{33}$$

where ΔH^0_{OR} and ΔG^0_{OR} are the enthalpy and Gibbs free energy change of the OR. The disregarded steps, s_{13} and s_{16}, were considered at QE, as shown later, so that this does not affect the overall kinetics.

Numerical simulations and analyses were performed for both the continuous stirred-tank reactor (CSTR) and the plug-flow reactor (PFR). A comparison between the microkinetic model predictions for an isothermal PFR and the experimental results [13], is presented in Fig. 2 for the following conditions: commercial low temperature shift Cu catalyst loading of 0.14 g/cm^3; total feed flow rate of 236 cm^3 (STP) min^{-1}; residence time τ = 1.8 s; feed composition of H_2O(10%), CO(10%), CO_2(0%), H_2(0%) and N_2(balance). As can be seen, the model can satisfactorily reproduce the main features of the WGSR on Cu LTS catalyst without any further fine-tuning, e.g., coverage dependence of the activation energy, etc, which is remarkable and provides proof of the adequacy of the

methodology used to predict elementary reaction rate constants. Further insights and model reduction are accomplished in the next sections.

8.2 Enumeration of RR

The microkinetic model described above comprises $q = 8$ surface intermediates, namely, H_2OS, COS, CO_2S, H_2S, HS, OHS, OS and HCOOS. Consider the intermediates matrix

$$\boldsymbol{\alpha} = \begin{array}{c} \begin{matrix} H_2OS & COS & CO_2S & H_2S & HS & OHS & OS & HCOOS \end{matrix} \\ \begin{bmatrix} 0 & 1 & 0 & 0 & 0 & 0 & 0 & 0 \\ 1 & 0 & 0 & 0 & 0 & 0 & 0 & 0 \\ 0 & 0 & -1 & 0 & 0 & 0 & 0 & 0 \\ 0 & 0 & 0 & 1 & -2 & 0 & 0 & 0 \\ 0 & 0 & 0 & -1 & 0 & 0 & 0 & 0 \\ -1 & 0 & 0 & 0 & 1 & 1 & 0 & 0 \\ 0 & -1 & 1 & 0 & 0 & 0 & -1 & 0 \\ 0 & -1 & 0 & 0 & 0 & -1 & 0 & 1 \\ 0 & 0 & 0 & 0 & 1 & -1 & 1 & 0 \\ 0 & -1 & 1 & 0 & 1 & -1 & 0 & 0 \\ 0 & 0 & 1 & 0 & 1 & 0 & 0 & -1 \\ 0 & 0 & 1 & 0 & 0 & 1 & -1 & -1 \\ -1 & 0 & 0 & 1 & -1 & 1 & 0 & 0 \\ 0 & 0 & 0 & 1 & -1 & -1 & 1 & 0 \\ 0 & 0 & 1 & 1 & -1 & 0 & 0 & -1 \end{bmatrix} \end{array} \begin{matrix} s_1 \\ s_2 \\ s_3 \\ s_4 \\ s_5 \\ s_6 \\ s_7 \\ s_8 \\ s_9 \\ s_{10} \\ s_{11} \\ s_{12} \\ s_{14} \\ s_{15} \\ s_{17} \end{matrix} \tag{34}$$

Since $rank\,\boldsymbol{\alpha} = 8$, the surface intermediates are linearly independent and, hence, a direct RR involves no more that $q + 1 = 8 + 1 = 9$ elementary reactions. It is further observed that s_1, s_2, s_3, and s_5 (adsorption and desorption steps) should be involved in all full RRs. That is, it is not possible to obtain the OR by omitting these 4 elementary reactions. The remaining $9 - 4 = 5$ elementary reactions involved in a RR need to be selected from among s_4, s_6, s_7, s_8, s_9, s_{10}, s_{12}, s_{14}, s_{15} and s_{17}. Thus, the total number of RRs does not exceed the number of ways 5

elementary reactions may be selected from the remaining 10, i.e., 10!/5!/5! = 252. In reality, the number is considerably smaller by virtue of the fact that not all of the possible sets of 9 elementary reactions involved in a RR are linearly independent. As already mentioned above, in enumerating the RRs we may face three different scenarios. These are next illustrated with the help of examples. Consider the RR involving the elementary reactions s_1, s_2, s_3, s_4, s_5, s_7, s_{11}, s_{12} and s_{14} as our first example. Thus, according to Eqs. (10) and (11) we have

$RR(s_1, s_2, s_3, s_4, s_5, s_7, s_{11}, s_{12}, s_{14})$

$$= \begin{array}{c|cccccccc|c} & H_2OS & COS & CO_2S & H_2S & HS & OHS & OS & HCOOS & \\ \hline & 0 & 1 & 0 & 0 & 0 & 0 & 0 & 0 & s_1 \\ & 1 & 0 & 0 & 0 & 0 & 0 & 0 & 0 & s_2 \\ & 0 & 0 & -1 & 0 & 0 & 0 & 0 & 0 & s_3 \\ & 0 & 0 & 0 & 1 & -2 & 0 & 0 & 0 & s_4 \\ & 0 & 0 & 0 & -1 & 0 & 0 & 0 & 0 & s_5 \\ & 0 & -1 & 1 & 0 & 0 & 0 & -1 & 0 & s_7 \\ & 0 & 0 & 1 & 0 & 1 & 0 & 0 & -1 & s_{11} \\ & 0 & 0 & 1 & 0 & 0 & 1 & -1 & -1 & s_{12} \\ & -1 & 0 & 0 & 1 & -1 & 1 & 0 & 0 & s_{14} \end{array}$$

$$= 2s_1 + 2s_2 + 2s_3 + 2s_5 + 2s_7 + 2s_{11} - 2s_{12} + 2s_{14}$$
$$= 2(s_1 + s_2 + s_3 + s_5 + s_7 + s_{11} - s_{12} + s_{14})$$

In a more conventional format, this RR may be presented as

	σ_j
$s_1 = -$ CO - S + COS = 0	1
$s_2 = -$ H_2O - S + H_2OS = 0	1
$s_3 = -$ CO_2S + CO_2 + S = 0	1
$s_4 = -$ HS - HS + H_2S + S = 0	1
$s_5 = -$ H_2S + H_2 + S = 0	1
$s_7 = -$ COS - OS + CO_2S + S = 0	1
$s_{11} = -$ HCOOS - S + CO_2S + HS = 0	1
$s_{12} = -$ HCOOS - OS + CO_2S + OHS = 0	-1
$s_{14} = -$ H_2OS - HS + OHS + H_2S = 0	1
Net: $H_2O + CO \leftrightarrows CO_2 + H_2$	

Table 2
Stoichiometrically distinct RRs for WGSR on Cu(111)

Full Routes

$RR_1 = s_1 + s_2 + s_3 + s_4 + s_5 + s_6 + s_7 + s_9$
$RR_2 = s_1 + s_2 + s_3 + s_4 + s_5 + s_6 + s_{10}$
$RR_3 = s_1 + s_2 + s_3 + s_4 + s_5 + s_6 + s_8 + s_{11}$
$RR_4 = s_1 + s_2 + s_3 + s_4 + s_5 + s_6 + s_8 + s_9 + s_{12}$
$RR_5 = s_1 + s_2 + s_3 + s_4 + s_5 + s_6 + s_7 + s_{11} - s_{12}$
$RR_6 = s_1 + s_2 + s_3 + s_5 + s_6 + s_7 + s_{15}$
$RR_7 = s_1 + s_2 + s_3 + s_5 + s_6 + s_8 + s_{12} + s_{15}$
$RR_8 = s_1 + s_2 + s_3 + s_5 + s_7 + s_9 + s_{14}$
$RR_9 = s_1 + s_2 + s_3 + s_5 + s_{10} + s_{14}$
$RR_{10} = s_1 + s_2 + s_3 + s_5 + s_8 + s_{11} + s_{14}$
$RR_{11} = s_1 + s_2 + s_3 - s_4 + s_5 + s_7 + s_{14} + s_{15}$
$RR_{12} = s_1 + s_2 + s_3 + s_5 + s_7 + s_{11} - s_{12} + s_{14}$
$RR_{13} = s_1 + s_2 + s_3 + s_5 + s_8 + s_9 + s_{12} + s_{14}$
$RR_{14} = s_1 + s_2 + s_3 - s_4 + s_5 + s_8 + s_{12} + s_{14} + s_{15}$
$RR_{15} = s_1 + s_2 + s_3 - s_4 + s_5 + s_7 - s_{12} + s_{14} + s_{17}$
$RR_{16} = s_1 + s_2 + s_3 - s_4 + s_5 + s_8 + s_{14} + s_{17}$
$RR_{17} = s_1 + s_2 + s_3 + s_5 + s_6 + s_8 + s_{17}$
$RR_{18} = s_1 + s_2 + s_3 + s_5 + s_6 + s_{10} - s_{11} + s_{12} + s_{15}$
$RR_{19} = s_1 + s_2 + s_3 + s_5 + s_6 + s_{10} - s_{11} + s_{17}$
$RR_{20} = s_1 + s_2 + s_3 + s_5 + s_6 + s_7 - s_{12} + s_{17}$
$RR_{21} = s_1 + s_2 + s_3 + s_5 + s_6 + s_7 + s_9 - s_{11} + s_{17}$
$RR_{22} = s_1 + s_2 + s_3 + s_5 + s_6 + s_8 - s_9 + s_{11} + s_{15}$
$RR_{23} = s_1 + s_2 + s_3 + s_5 + s_6 - s_9 + s_{10} - s_{12} + s_{17}$
$RR_{24} = s_1 + s_2 + s_3 + s_5 + s_6 - s_9 + s_{10} + s_{15}$
$RR_{25} = s_1 + s_2 + s_3 + s_5 + s_7 + s_{11} + s_{14} + s_{15} - s_{17}$
$RR_{26} = s_1 + s_2 + s_3 + s_5 + s_8 + s_9 + s_{14} - s_{15} + s_{17}$

Empty Routes

$ER_1 = -s_{12} - s_{15} + s_{17}$
$ER_2 = -s_4 - s_{11} + s_{12} + s_{15}$
$ER_3 = -s_4 - s_{11} + s_{17}$
$ER_4 = -s_4 - s_6 + s_{14}$
$ER_5 = -s_4 + s_7 - s_{10} - s_{12} + s_{17}$
$ER_6 = s_4 - s_7 + s_{10} - s_{15}$
$ER_7 = -s_4 + s_7 - s_8 - s_{11} + s_{15}$
$ER_8 = -s_4 - s_7 + s_8 - s_9 + s_{17}$
$ER_9 = -s_4 + s_8 - s_{10} + s_{12} + s_{15}$
$ER_{10} = -s_4 + s_8 - s_{10} + s_{17}$
$ER_{11} = -s_4 - s_9 - s_{12} + s_{17}$
$ER_{12} = -s_4 - s_9 + s_{15}$
$ER_{13} = -s_6 + s_{11} - s_{12} + s_{14} - s_{15}$
$ER_{14} = -s_6 + s_{11} + s_{14} - s_{17}$
$ER_{15} = -s_6 - s_7 + s_{10} + s_{12} + s_{14} - s_{17}$
$ER_{16} = -s_6 - s_7 + s_{10} + s_{14} - s_{15}$
$ER_{17} = -s_6 - s_7 + s_8 + s_{11} + s_{14} - s_{15}$
$ER_{18} = -s_6 + s_7 - s_8 + s_9 + s_{14} - s_{17}$
$ER_{19} = -s_6 - s_8 + s_{10} - s_{12} + s_{14} - s_{15}$
$ER_{20} = -s_6 - s_8 + s_{10} + s_{14} - s_{17}$
$ER_{21} = -s_6 + s_9 + s_{12} + s_{14} - s_{17}$
$ER_{22} = -s_6 + s_9 + s_{14} - s_{15}$
$ER_{23} = -s_7 + s_{10} - s_{11} + s_{12}$
$ER_{24} = -s_7 + s_{10} - s_{11} - s_{15} + s_{17}$
$ER_{25} = -s_7 + s_8 + s_{12}$
$ER_{26} = -s_7 + s_8 - s_{15} + s_{17}$
$ER_{27} = -s_7 + s_8 - s_9 + s_{11}$
$ER_{28} = -s_7 - s_9 + s_{10}$
$ER_{29} = -s_8 + s_{10} - s_{11}$
$ER_{30} = -s_8 - s_9 + s_{10} - s_{12}$
$ER_{31} = -s_8 - s_9 + s_{10} + s_{15} - s_{17}$
$ER_{32} = -s_9 + s_{11} - s_{12}$
$ER_{33} = -s_9 + s_{11} + s_{15} - s_{17}$

Thus, $RR(s_1, s_2, s_3, s_4, s_5, s_7, s_{11}, s_{12}, s_{14})$ results in an OR and, consequently, is a full RR. On the other hand, the RR involving the elementary reactions s_1, s_2, s_3, s_4, s_5, s_7, s_8, s_9 and s_{11} is an ER, i.e.,

$RR(s_1, s_2, s_3, s_4, s_5, s_7, s_8, s_9, s_{11})$

	H_2OS	COS	CO_2S	H_2S	HS	OHS	OS	HCOOS	
	0	1	0	0	0	0	0	0	s_1
	1	0	0	0	0	0	0	0	s_2
	0	0	−1	0	0	0	0	0	s_3
	0	0	0	−2	1	0	0	0	s_4
=	0	0	0	0	−1	0	0	0	s_5
	0	−1	1	0	0	0	−1	0	s_7
	0	−1	0	0	0	−1	0	1	s_8
	0	0	0	1	0	−1	1	0	s_9
	0	0	1	1	0	0	0	−1	s_{11}

$= 0s_1 + 0s_2 + 0s_3 + 0s_4 + 0s_5 + 2s_7 - 2s_8 + 2s_9 - 2s_{11} = 2(s_7 - s_8 + s_9 - s_{11})$

or	s_7 = - COS - OS + CO_2S + S = 0	1
	s_8 = - COS - OHS + HCOOS + S = 0	-1
	s_9 = - OHS - S + OS + HS = 0	1
	s_{11} = - HCOOS - S + CO_2S + HS = 0	-1
	Net: 0 = 0	

A special situation is faced when considering the RR involving the elementary reactions s_1, s_2, s_3, s_4, s_5, s_6, s_7, s_9 and s_{10}. In this case all of the stoichiometric coefficients in the RR are zero

$RR(s_1, s_2, s_3, s_4, s_5, s_6, s_7, s_9, s_{10})$

	H_2OS	COS	CO_2S	HS	H_2S	OHS	OS	HCOOS	
	0	1	0	0	0	0	0	0	s_1
	1	0	0	0	0	0	0	0	s_2
	0	0	−1	0	0	0	0	0	s_3
	0	0	0	−2	1	0	0	0	s_4
=	0	0	0	0	−1	0	0	0	s_5
	−1	0	0	1	0	1	0	0	s_6
	0	−1	1	0	0	0	−1	0	s_7
	0	0	0	1	0	−1	1	0	s_9
	0	−1	1	1	0	−1	0	0	s_{10}

$$= 0s_1 + 0s_2 + 0s_3 + 0s_4 + 0s_5 + 0s_6 + 0s_7 + 0s_9 + 0s_{10} = 0$$

The occurrence of zero RRs is due to the fact that the elementary reactions involved in such RRs may produce at least two, either full or empty RRs. Thus, the elementary reactions involved in $RR(s_1, s_2, s_3, s_4, s_5, s_6, s_7, s_9, s_{10})$ are also involved in two RRs, namely, $s_1 + s_2 + s_3 + s_4 + s_5 + s_6 + s_7 + s_9$ and $s_1 + s_2 + s_3 + s_4 + s_5 + s_6 + s_{10}$ as well as in one ER $s_7 + s_9 - s_{10}$. Because any linear combinations of these RRs will result in new RRs, the zero RRs provides a way to preserve the uniqueness of the RRs.

A complete list of stoichiometrically distinct RRs, including ERs, for the WGSR is presented in Table 2.

8.3 Reaction network graph

Our starting point in the construction of a reaction network graph is the QSS conditions for the surface intermediates either in the conventional form, Eq. (15), or in terms of RRs, Eq. (16). These conditions, however, need to be presented in a special form that is suitable for a reaction network graph. First, let's present the QSS conditions in terms of RRs. A set of linearly independent RRs for the WGSR derived according to the algorithm proposed above is presented in Table 3. Notice that these RRs are direct. In particular, $RR_{\mathrm{I}} = RR_1$, $RR_{\mathrm{II}} = RR_2$, $RR_{\mathrm{III}} = RR_3$, $RR_{\mathrm{IV}} = LR_{25}$, $RR_{\mathrm{V}} = LR_9$, $RR_{\mathrm{VI}} = RR_6$, and $RR_{\mathrm{VII}} = RR_{17}$. Employing Eq. (21) we obtain

$$\begin{aligned}
r_1 &= J_{\mathrm{I}} + J_{\mathrm{II}} + J_{\mathrm{III}} + J_{\mathrm{VI}} + J_{\mathrm{VII}} & \qquad r_9 &= J_{\mathrm{I}} \\
r_2 &= J_{\mathrm{I}} + J_{\mathrm{II}} + J_{\mathrm{III}} + J_{\mathrm{VI}} + J_{\mathrm{VII}} & \qquad r_{10} &= J_{\mathrm{II}} \\
r_3 &= J_{\mathrm{I}} + J_{\mathrm{II}} + J_{\mathrm{III}} + J_{\mathrm{VI}} + J_{\mathrm{VII}} & \qquad r_{11} &= J_{\mathrm{III}} \\
r_4 &= J_{\mathrm{I}} + J_{\mathrm{II}} + J_{\mathrm{III}} - J_{\mathrm{V}} & \qquad r_{12} &= J_{\mathrm{IV}} \\
r_5 &= J_{\mathrm{I}} + J_{\mathrm{II}} + J_{\mathrm{III}} + J_{\mathrm{VI}} + J_{\mathrm{VII}} & \qquad r_{14} &= J_{\mathrm{V}} \\
r_6 &= J_{\mathrm{I}} + J_{\mathrm{II}} + J_{\mathrm{III}} - J_{\mathrm{V}} + J_{\mathrm{VI}} + J_{\mathrm{VII}} & \qquad r_{15} &= J_{\mathrm{VI}} \\
r_7 &= J_{\mathrm{I}} - J_{\mathrm{IV}} + J_{\mathrm{VI}} & \qquad r_{17} &= J_{\mathrm{VII}} \\
r_8 &= J_{\mathrm{III}} + J_{\mathrm{IV}} + J_{\mathrm{VII}}
\end{aligned}$$

From these relations we immediately obtain

$$r_1 = r_2 = r_3 = r_5 = r_9 + r_{10} + r_{11} + r_{15} + r_{17} \tag{35}$$

$$r_4 = r_9 + r_{10} + r_{11} - r_{14} \tag{36}$$

$$r_6 = r_9 + r_{10} + r_{11} - r_{14} + r_{15} + r_{17} \tag{37}$$

$$r_7 = r_9 - r_{12} + r_{15} \tag{38}$$

$$r_8 = r_{11} + r_{12} + r_{17} \tag{39}$$

According to Eq. (35), the adsorption/desorption steps, i.e., s_1, s_2, s_3 and s_5 must be connected in series. These steps, however, should be located at different places in the reaction network. Namely, the adsorption steps s_1 and s_2 constitute the starting point, node n_1, while desorption steps s_3 and s_5 constitute the terminus, node n_8.

Combining Eqs. (35) and (37) we further obtain

$$r_2 = r_6 + r_{14} \tag{40}$$

Which is the QSS condition for the adsorbed water, H_2OS, i.e., adsorbed water is formed in s_2 and consumed in s_6 and s_{14}. Hence, at this point, node n_2, the reaction

Table 3
A set of linearly independent RRs for WGSR on Cu(111)

		RR_{I}	RR_{II}	RR_{III}	RR_{IV}	RR_{V}	RR_{VI}	RR_{VII}
s_1:	$CO + S \leftrightarrows COS$	1	1	1	0	0	1	1
s_2:	$H_2O + S \leftrightarrows H_2OS$	1	1	1	0	0	1	1
s_3:	$CO_2S \leftrightarrows CO_2 + S$	1	1	1	0	0	1	1
s_4:	$HS + HS \leftrightarrows H_2S + S$	1	1	1	0	-1	0	0
s_5:	$H_2S \leftrightarrows H_2 + S$	1	1	1	0	0	1	1
s_6:	$H_2OS + S \leftrightarrows OHS + HS$	1	1	1	0	-1	1	1
s_7:	$COS + OS \leftrightarrows CO_2S + S$	1	0	0	-1	0	1	0
s_8:	$COS + OHS \leftrightarrows HCOOS + S$	0	0	1	1	0	0	1
s_9:	$OHS + S \leftrightarrows OS + HS$	1	0	0	0	0	0	0
s_{10}:	$COS + OHS \leftrightarrows CO_2S + HS$	0	1	0	0	0	0	0
s_{11}:	$HCOOS + S \leftrightarrows CO_2S + HS$	0	0	1	0	0	0	0
s_{12}:	$HCOOS + OS \leftrightarrows CO_2S + OHS$	0	0	0	1	0	0	0
s_{14}:	$H_2OS + HS \leftrightarrows OHS + H_2S$	0	0	0	0	1	0	0
s_{15}:	$OHS + HS \leftrightarrows OS + H_2S$	0	0	0	0	0	1	0
s_{17}:	$HCOOS + HS \leftrightarrows CO_2S + H_2S$	0	0	0	0	0	0	1
Net:	RR_{I}: $H_2O + CO \leftrightarrows CO_2 + H_2$	J_{I}						
	RR_{II}: $H_2O + CO \leftrightarrows CO_2 + H_2$	J_{II}						
	RR_{III}: $H_2O + CO \leftrightarrows CO_2 + H_2$	J_{III}						
	RR_{IV}: $0 = 0$	J_{IV}						
	RR_{V}: $0 = 0$	J_{V}						
	RR_{VI}: $H_2O + CO \leftrightarrows CO_2 + H_2$	J_{VI}						
	RR_{VII}: $H_2O + CO \leftrightarrows CO_2 + H_2$	J_{VII}						

network is partitioned into two parallel branches. In one, H_2OS dissociates into OHS and HS according to

s_6: $H_2OS + S \leftrightarrows OHS + HS$

while in the other branch, H_2OS reacts according to

s_{14}: $H_2OS + HS \leftrightarrows OHS + H_2S$

Next, consider the pathways producing/consuming H_2S. The combination of Eqs. (36) and (37) gives

$$r_6 = r_4 + r_{15} + r_{17} \tag{41}$$

This relation, in fact, expresses the interrelation between HS and H_2S, node n_3, i.e., HS that is formed in s_6 is transformed into H_2S via s_4, s_{15} and s_{17}.

Consider further the consumption/production pathways of OHS. From Eq. (36) we have

$$r_4 + r_{14} = r_9 + r_{10} + r_{11} \tag{42}$$

which is the modified QSS condition for OHS. To prove it, we observe (Table 1) that OHS is formed in s_6 and s_{14}. One of these elementary reactions, namely, s_6 also produces HS while the other, s_{14} forms H_2S. To make them compatible at the point of intersection, node n_4, we need to ensure that these sequences produce the same products, i.e., either OHS and HS or OHS and H_2S. We choose the second option. This means that s_6 should be followed by s_4 so that

i)	s_6:	$H_2OS + S \leftrightarrows OHS + HS$	1
	s_4:	$HS + HS \leftrightarrows H_2S + S$	1
	s_{14}:	$H_2OS + HS \leftrightarrows OHS + H_2S$	

Once all of the paths in which OHS are formed are accounted for, we consider next all of the remaining paths in which OHS is consumed, i.e., s_8, s_9 and s_{10}

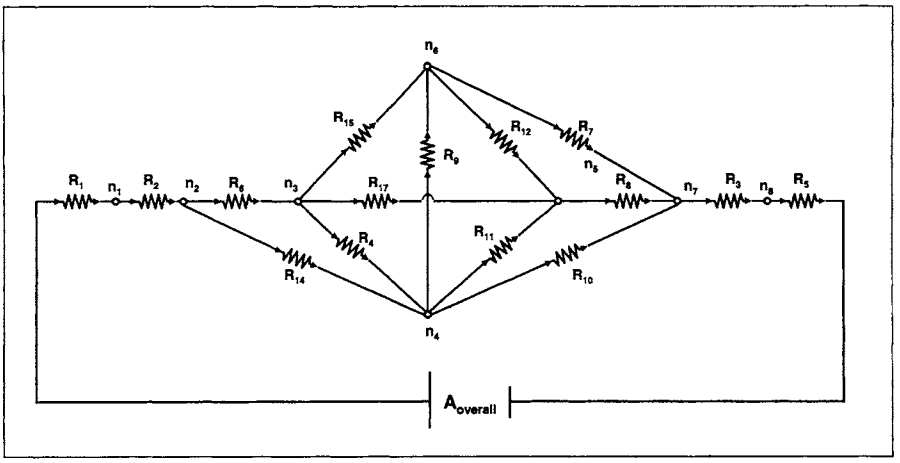

Fig. 3. The electrical circuit analog of the reaction network for the WGSR

s_8: COS + OHS ⇆ HCOOS + S
s_9: OHS + S ⇆ OS + HS
s_{10}: COS + OHS ⇆ CO_2S + HS

From these 3 paths only the last one, s_{10}, leads directly to the adsorbed products, CO_2S and HS. The two remaining paths, s_8 and s_9, lead to two other surface intermediates, namely, HCOOS and OS. We, therefore, need to consider further all the pathways by which the two intermediates HCOOS and OS are produced/consumed so as to produce the adsorbed products, CO_2S and HS. These paths are easily visualized from Eqs. (38) and (39). Indeed, according to Eq. (39), HCOOS is formed in s_8 and consumed in s_{11}, s_{12} and s_{17} thus resulting in node n_5. Similarly, from Eq. (38) it is seen that OS is produced in s_9 and s_{15} and consumed in s_7 and s_{12}. This gives us the node n_6.

The complete reaction network graph obtained in this manner is shown in Fig. 3. An inspection reveals that the reaction network involves all of the direct RRs (including ERs) enumerated above using the conventional algorithm (Table 1) [14]. However, the network is far more revealing in terms of the pathways taken by reactants to form products.

8.4 Simplification and reduction of the reaction network

As already stated above, the reaction network may be simplified and reduced by employing the principle of extremum resistance. The most substantial simplification of the reaction network may be achieved by evaluating and

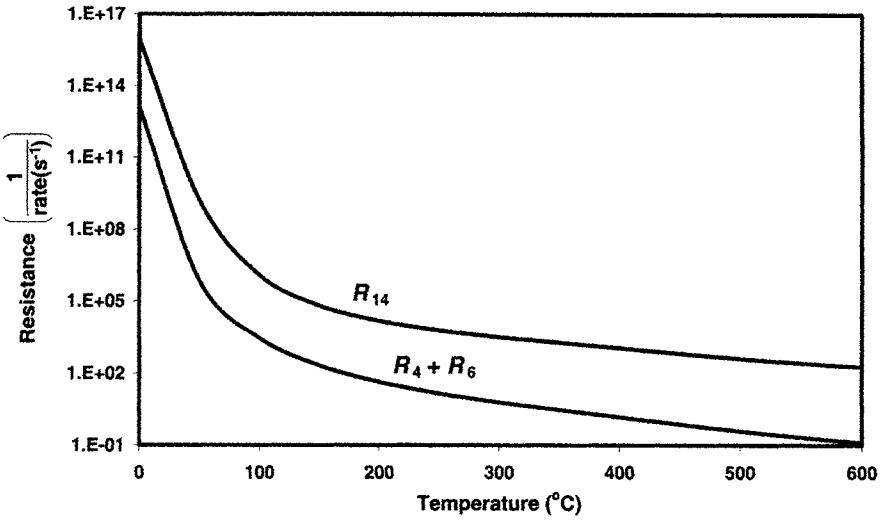

Fig. 4. R_{14} vs. $R_4 + R_6$ as a function of temperature for the following conditions: commercial low temperature shift Cu catalyst loading of 0.14 g/cm^3; total feed flow rate of 236 cm^3 (STP) min^{-1}; residence time τ = 1.8 s; feed composition of H_2O(10%), CO(10%) and N_2(balance)

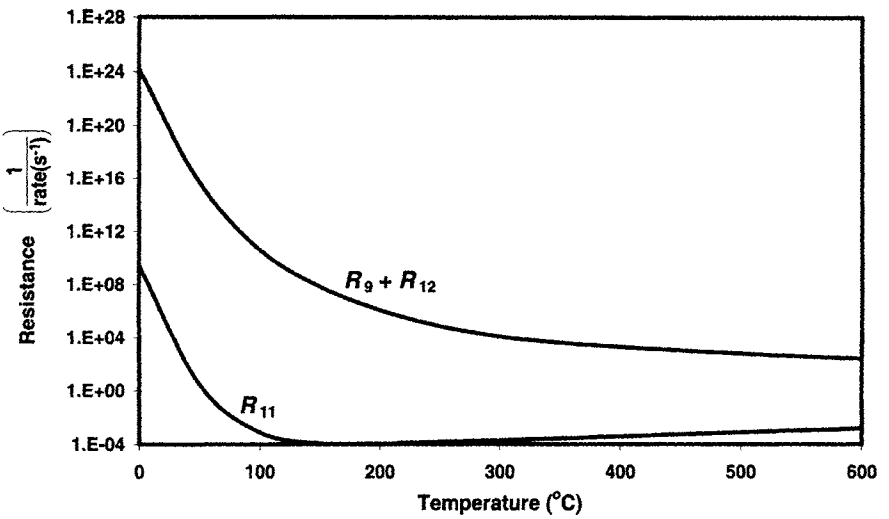

Fig. 5. $R_9 + R_{12}$ vs. R_{11} as a function of temperature for the following conditions: commercial low temperature shift Cu catalyst loading of 0.14 g/cm^3; total feed flow rate of 236 cm^3 (STP) min^{-1}; residence time τ = 1.8 s; feed composition of H_2O(10%), CO(10%) and N_2(balance)

comparing the resistances of the two parallel branches between nodes n_2 and n_4, i.e., the two parallel paths that produce OHS. The first branch involves only one resistance, R_{14}. The second branch involves a sequence of two series resistors, R_4 and R_6 so that its overall resistance is $R_4 + R_6$. An example of numerical simulations of these two resistances as a function of temperature is presented in Fig. 4. It is seen that the R_{14} is several orders of magnitude higher than $R_4 + R_6$ at all temperatures. Thus, there is ample reason to neglect s_{14}, which simplifies the network (Fig. 7b).

The next step in the simplification is to consider the two parallel branches between nodes n_4 and n_5, that is, R_{11} and $R_9 + R_{12}$. From numerical simulations it may be concluded (Fig. 6) that path s_{11} is much faster than path $s_9 + s_{12}$ and, consequently, the latter may be disregarded (Fig. 7c).

Finally, we compare the resistances of the two parallel branches between nodes n_3, and n_5. One of these two parallel branches involves only one resistance, R_{17}. The other one involves resistances R_4 and R_{11} connected in series with an overall resistance equal to $R_4 + R_{11}$. Based on numerical simulations (Fig. 5) we conclude that the resistance R_{17} is much higher than the resistance $R_4 + R_{11}$ and, hence, the consumption of HCOOS via s_{11} is much faster as compared to the consumption of HCOOS via s_{17}. In other words, the path via s_{17} may be neglected (Fig.7d).

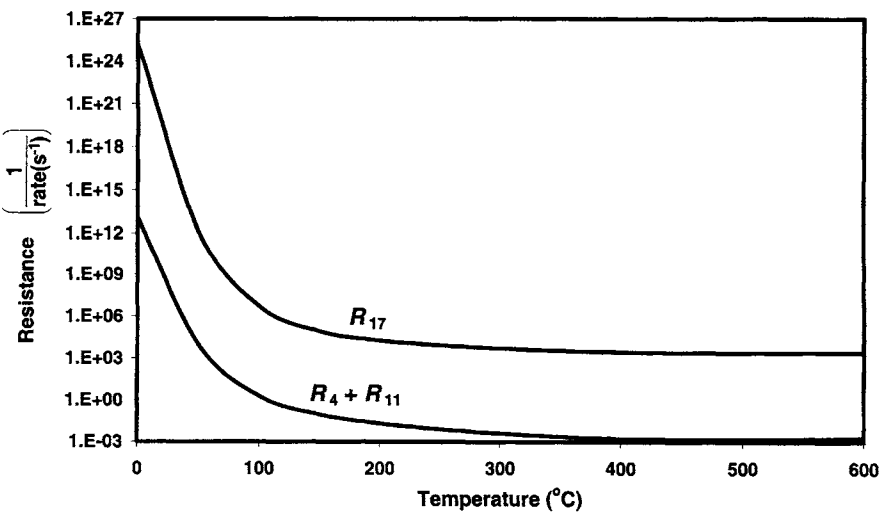

Fig. 6. $R_4 + R_{11}$ vs. R_{17} as a function of temperature for the following conditions: commercial low temperature shift Cu catalyst loading of 0.14 g/cm^3; total feed flow rate of 236 cm^3 (STP) min^{-1}; residence time τ = 1.8 s; feed composition of H_2O(10%), CO(10%) and N_2(balance)

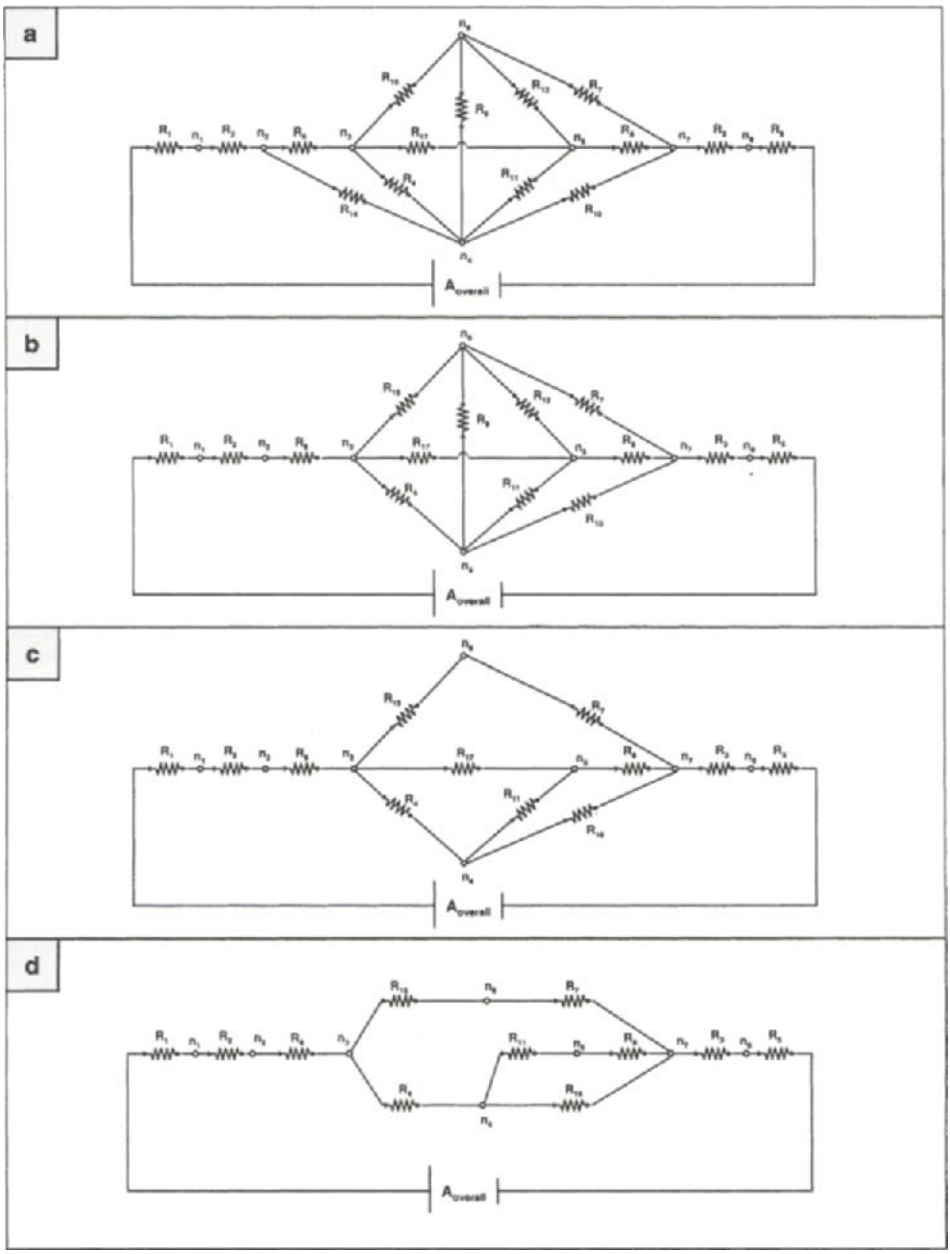

Fig. 7. Reduction of the reaction network as described in the text.

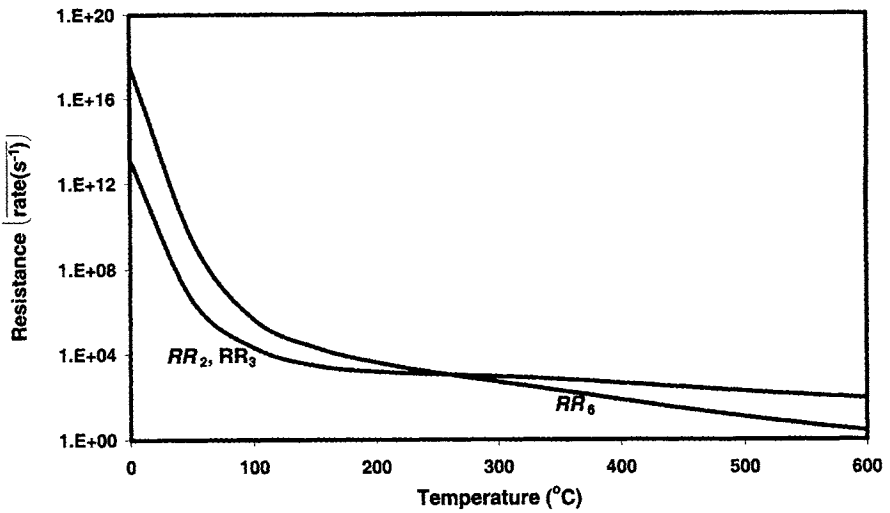

g. 8. Resistances of the dominant RRs vs. temperature for the following conditions: commercial w temperature shift Cu catalyst loading of 0.14 g/cm^3; total feed flow rate of 236 cm^3 (STP) in^{-1}; residence time τ = 1.8 s; feed composition of H_2O(10%), CO(10%) and N_2(balance)

The above simplifications leave us with a reduced network comprising 11 lementary reactions and 3 RRs, namely, RR_2, RR_3, RR_6 (Fig. 7d). The overall esistances of these RRs according to Eq. (26) are equal to

$$R_{RR_2} = R_1 + R_2 + R_3 + R_4 + R_5 + R_6 + R_{10}$$
$$R_{RR_3} = R_1 + R_2 + R_3 + R_4 + R_5 + R_6 + R_8 + R_{11}$$
$$R_{RR_6} = R_1 + R_2 + R_3 + R_5 + R_6 + R_7 + R_{15}$$

As can be seen from Fig. 8, RR_2 and RR_3 are dominant at lower temperatures while, at higher temperatures, the mechanism is dominated by RR_6.

8.5 The rate of the overall reaction

We are now in a position to consider the rate of the overall reaction. First, we write a formal rate equation for the kinetics of the reduced reaction network, Fig. 7d, by employing the electrical circuit analogy and the linear rate law analogous to Ohm's law. Thus, the overall rate (overall current) is the ratio of the affinity of the OR and the overall resistance of the reaction network. The overall resistance of the reduced reaction network is

$$R = R_1 + R_2 + R_3 + R_5 + R_6 + \cfrac{1}{\cfrac{1}{R_7 + R_{15}} + \cfrac{1}{R_4 + \cfrac{1}{\cfrac{1}{R_{10}} + \cfrac{1}{R_8 + R_{11}}}}} \tag{43}$$

which gives the overall rate as

$$r = \frac{\mathcal{A}_{overall}}{R} = \cfrac{\mathcal{A}_{overall}}{R_1 + R_2 + R_3 + R_5 + R_6 + \cfrac{1}{\cfrac{1}{R_7 + R_{15}} + \cfrac{1}{R_4 + \cfrac{1}{\cfrac{1}{R_{10}} + \cfrac{1}{R_8 + R_{11}}}}}} \tag{44}$$

or, keeping in mind that $R_j \equiv \mathcal{A}_j / r_j$

$$r = \cfrac{\mathcal{A}_{overall}}{\cfrac{\mathcal{A}_1}{r_1} + \cfrac{\mathcal{A}_2}{r_2} + \cfrac{\mathcal{A}_3}{r_3} + \cfrac{\mathcal{A}_5}{r_5} + \cfrac{\mathcal{A}_6}{r_6} + \cfrac{1}{\cfrac{r_7 r_{15}}{\mathcal{A}_7 r_{15} + \mathcal{A}_{15} r_7} + \cfrac{1}{\cfrac{\mathcal{A}_4}{r_4} + \cfrac{1}{\cfrac{r_{10}}{\mathcal{A}_{10}} + \cfrac{r_8 r_{11}}{\mathcal{A}_8 r_{11} + \mathcal{A}_{11} r_8}}}}} \tag{45}$$

The expression can be further simplified if the smaller of the resistances in series can be neglected. Futhermore, the affinities of the elementary reactions in this equation are actually not linearly independent. Indeed, from Fig. 7d it is seen that the reduced reaction network incorporates three ERs, i.e., the affinities of the elementary reactions are interrelated via

$$\mathcal{A}_7 + \mathcal{A}_{15} = \mathcal{A}_4 + \mathcal{A}_{10}$$
$$\mathcal{A}_8 + \mathcal{A}_{11} = \mathcal{A}_{10}$$
$$\mathcal{A}_7 + \mathcal{A}_{15} = \mathcal{A}_4 + \mathcal{A}_{11} + \mathcal{A}_8$$

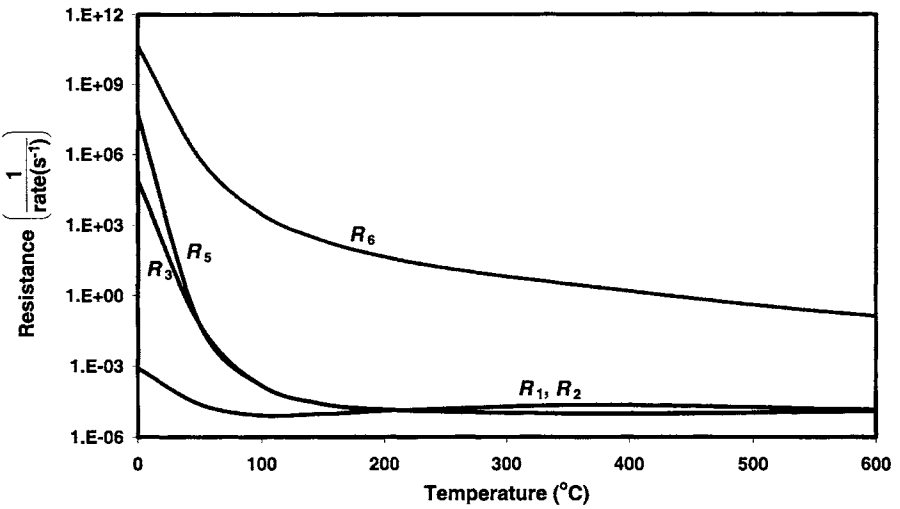

Fig. 9. R_1, R_2, R_3 and R_6 vs. temperature for the following conditions: commercial low temperature shift Cu catalyst loading of 0.14 g/cm^3; total feed flow rate of 236 cm^3 (STP) min^{-1}; residence time τ = 1.8 s; feed composition of H_2O(10%), CO(10%) and N_2(balance)

8.5.1 Explicit Rate Expression

While the above formal rate expression is adequate for numerical computation of the rate from numerically calculated resistances, it is more desirable to obtain, if possible, an explicit rate expression in terms of the terminal species composition. This is accomplished as follows.

Under the QSS assumption, the overall rate equation may be substantially simplified. Since s_9, s_{12}, s_{14} and s_{17} have been eliminated from the mechanism, there now remain only 3 linearly independent RRs in Table 3, namely, RR_{II}, RR_{III} and RR_{VI}. Thus, the QSS conditions now provide

$$
\begin{array}{lll}
r_1 = J_{II} + J_{III} + J_{VI} & r_6 = J_{II} + J_{III} + J_{VI} & r_{11} = J_{III} \\
r_2 = J_{II} + J_{III} + J_{VI} & r_7 = J_{VI} & r_{12} = 0 \\
r_3 = J_{II} + J_{III} + J_{VI} & r_8 = J_{III} & r_{14} = 0 \\
r_4 = J_{II} + J_{III} & r_9 = 0 & r_{15} = J_{VI} \\
r_5 = J_{II} + J_{III} + J_{VI} & r_{10} = J_{II} & r_{17} = 0
\end{array}
$$

Using these relations in Eq. (45) and keeping in mind that the affinities along all RRs are equal, after some algebra, we obtain

$$r = J_{II} + J_{III} + J_{VI} = r_8 + r_{10} + r_{15} \tag{46}$$

Table 4
A 11-step reduced mechanism for WGSR on Cu(111)

		RR_2	RR_3	RR_6	
s_1:	$CO + S \leftrightarrows COS$	1	1	1	EQ
s_2:	$H_2O + S \leftrightarrows H_2OS$	1	1	1	EQ
s_6:	**$H_2OS + S \leftrightarrows OHS + HS$**	**1**	**1**	**1**	**RDS**
s_7:	$COS + OS \leftrightarrows CO_2S + S$	0	0	1	RDS
s_8:	$COS + OHS \leftrightarrows HCOOS + S$	0	1	0	RDS
s_{10}:	$COS + OHS \leftrightarrows CO_2S + HS$	1	0	0	RDS
s_{11}:	$HCOOS + S \leftrightarrows CO_2S + HS$	0	1	0	RDS
s_{15}:	$OHS + HS \leftrightarrows OS + H_2S$	0	0	1	RDS
s_3:	$CO_2S \leftrightarrows CO_2 + S$	1	0	1	EQ
s_5:	$H_2S = H_2 + S$	0	0	1	EQ
$1/2(s_4 + s_5)$:	$HS \leftrightarrows 1/2H_2 + S$	2	2	0	EQ

Net: RR_1: $H_2O + CO \leftrightarrows CO_2 + H_2$ r_8
RR_2: $H_2O + CO \leftrightarrows CO_2 + H_2$ r_{10}
RR_3: $H_2O + CO \leftrightarrows CO_2 + H_2$ r_{15}
Overall rate = $r_8 + r_{10} + r_{15}$

This is precisely the same result as that obtained earlier based on a different approach [14].

An explicit overall rate equation may be deduced next by solving the QSS conditions for the surface intermediates. An analytical solution, however, cannot be obtained due to the nonlinear character of the QSS conditions. To avoid this difficulty, we apply the rate-determining step approximation formulated in terms of the principle of extremum resistance. Firstly, we compare the resistances R_1, R_2, R_3, R_5 and R_6 that are connected in series. Numerical simulations show (Fig. 9) that $R_6 >> R_1$, R_2, R_3, R_5. Thus, in this sequence, s_6 may be considered as rate-determining step with s_1, s_2, s_3 and s_5 at quasi-equilibrium. In a similar manner, we compare R_4 with $(R_8+R_{11})R_{10}/(R_8+R_{10}+R_{11})$ (the overall resistance of the parallel branch following R_4) and conclude that $R_4 << (R_8+R_{11})R_{10}/(R_8+R_{10}+R_{11})$ (Fig. 10). That is, s_4 may be also considered at quasi-equilibrium. Now, the quasi-equilibrium elementary reactions may be combined into intermediate reactions employing the formalism of intermediate RRs [8]. The resulting reduced microkinetic model is presented in Table 4. As can be seen, all the surface intermediates but OHS, OS and HCOOS may be determined using the quasi-equilibrium approximation. Using the QSS approximation for the above, the final simplified overall rate equations is

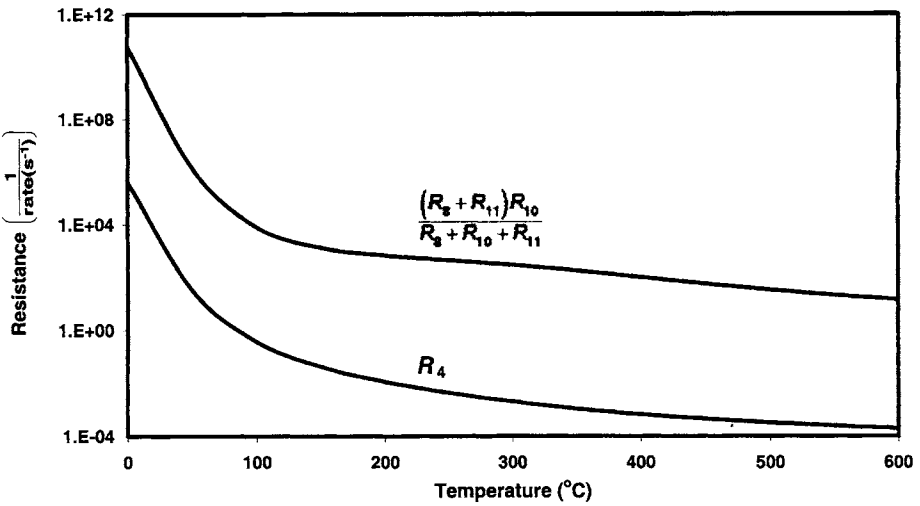

Fig. 10. R_4 vs. the resistance of the parallel branch involving R_{10}, R_8 and R_{11} as a function of temperature for the following conditions: commercial low temperature shift Cu catalyst loading of 0.14 g/cm^3; total feed flow rate of 236 cm^3 (STP) min^{-1}; residence time τ = 1.8 s; feed composition of H_2O(10%), CO(10%) and N_2(balance)

$$r = \frac{\vec{k}_6 K_2 P_{H_2O} \theta_0^2 \left[(\vec{k}_8 + \vec{k}_{10}) K_1 P_{CO} + \vec{k}_{15} (K_4 K_5)^{-1/2} P_{H_2}^{1/2} \right]}{\left(\frac{\vec{k}_6}{K_6} + \vec{k}_{15} \right) \frac{P_{H_2}^{1/2}}{(K_4 K_5)^{1/2}} + (\vec{k}_8 + \vec{k}_{10}) K_1 P_{CO}} \left(1 - \frac{P_{CO_2} P_{H_2}}{K P_{H_2O} P_{CO}} \right) \tag{47}$$

The error in the conversion of CO provided by this overall rate equation is virtually zero as compared with the exact microkinetic model, which points to the robustness of the reaction network analysis approach presented here.

9. DISCUSSION AND CONCLUDING REMARKS

Heterogeneous catalytic reactions proceed through a complex network of surface molecular events, or elementary reactions, involving the reactants, surface intermediates and products. Once the rate constants of all the elementary reactions comprising a microkinetic mechanism are known, the behavior and capabilities of the microkinetic model may be investigated through numerical simulations. However, a complete understanding of the model based simply on numerical computer outputs is difficult to achieve. A large variety of complementary

methods, both quantitative and qualitative, have been proposed in order to rationalize general features of complex microkinetic models. From this arsenal of theoretical methods, two have proved to be of special value in the analysis of microkinetic models. One of these is the RRs approach, and the other is the graph-theoretical approach. In fact, these two methods are closely interrelated. Indeed, there is a large number of publications discussing different graph-theoretical aspects of the theory of RRs. (For a review of the application of graph-theoretical methods in studying complex reaction mechanisms, see Ref. 27.)

A general feature of the graph-theoretical methods as applied to the analysis of reaction mechanisms is that the surface intermediates are shown on the nodes of the graph as key species. Although such a graphical representation is useful in studying many structural aspects of the mechanisms, it is not useful in the analysis of the kinetics of the system. As far as we are aware, there have been no attempts so far, except the simple case of linear mechanisms, to eliminate the surface intermediates from the graph. In this work we have shown for the first time that the elementary reactions comprising a complex, non-linear mechanism may be uniquely arranged into a reaction network so as to completely eliminate from the network any species, either surface intermediates or terminal species. The rules that govern the connectivity and directionality of the elementary reactions in such a reaction network are derived from the QSS conditions of the surface intermediates. The resulting reaction network incorporates a complete set of direct RRs including the ERs and may be considered as an additional and independent proof of the concept of direct RRs. A subsequent assumption involving the introduction of the resistance of an elementary reaction defined as the ratio between its affinity and rate, i.e., a linear relation in the spirit of Ohm's Law, makes the reaction network totally analogous to a linear circuit network. As a result, we are in a position to employ the methods of electrical network analysis including Kirchhoff's Current and Voltage Laws. In particular, the electrical circuit analogy suggests a systematic way of determining the dominant RRs and, hence, a substantial simplification and reduction of the mechanism.

The proposed theoretical methodology has been applied here to study and rationalize a 15 elementary reaction microkinetic mechanism for the WGSR on Cu(111) for illustrative purposes. A reaction network has been constructed that incorporates all of the 26 direct RRs that have been previously generated using the conventional methods. Using the electrical circuit analogy the reaction network was subsequently simplified and reduced to a reaction network involving only 3 dominant RRs. An overall rate equation has been developed that reproduces the complete microkinetic model precisely.

REFERENCES

[1] L.J. Broadbelt, R.Q. Snurr. Applied Catal. A: General 200 (2000) 23.
[2] E. Shustorovich, H. Sellers. Surf. Sci. Reports, 31 (1998) 1.
[3] M. Boudart, G. Djega-Mariadassou, Kinetics of Heterogeneous Catalytic Reactions, Princeton University Press, Princeton, 1982.
[4] J.A. Dumesic, D.F. Rudd, L.M. Aparicio, J.E. Rekoske, A.A. Trevino, The Microkinetics of Heterogeneous Catalysis, ACS, 1993.
[5] P. Stoltze, Prog. Surf. Sci. 65 (2000) 65.
[6] I. Fishtik, C. Callaghan, R. Datta. J. Catal. In preparation.
[7] I. Fishtik, R. Datta. Chem. Eng. Sci. 55 (2000) 4029.
[8] I. Fishtik, R. Datta. Ind. Eng. Chem. Res. 40 (2001) 2416.
[9] J. Horiuti, T. Nakamura, Adv. Catal. 17 (1967) 1.
[10] M.I. Temkin, Adv. Catal. 26 (1979) 173.
[11] P.C. Milner, J. Electroanal. Soc. 111 (1964) 228.
[12] J. Happel, P.H. Sellers, Adv. Catal. 32 (1983) 272.
[13] Fishtik, R. Datta. Surf. Sci. 512 (2002) 229.
[14] C.A. Callaghan, I. Fishtik, R. Datta, M. Carpenter, M. Chmielewski, A. Lugo. Surf. Sci. in press.
[15] T. De Donder, P. Van Rysselberg, Thermodynamic Theory of Affinity, Stanford University Press, 1936.
[16] J.S. Shiner, Adv. Therm. 6 (1992) 248.
[17] J. Nakamura, J. M. Campbell, C. T. Campbell. J. Chem. Soc. Faraday Trans. 86 (1990) 2725.
[18] C. N. Satterfield. Heterogeneous Catalysis in Industrial Practice, 2nd ed., McGraw-Hill, New York, 1991.
[19] E. Shustorovich, A. T. Bell. Surf. Sci. 253 (1991) 385.
[20] C. V. Ovesen, P. Stoltze, J. K. Norskov, C. T. Campbell. J. Catal. 134 (1992) 445.
[21] C. Rhodes, G. J. Hutchings, A. M. Ward. Catal. Today, 23 (1995) 43.
[22] K. M. Vanden Bussche, G. F. Froment. J. Catal. 161 (1996) 1.
[23] C. Lund. Ind. Eng. Chem. Res. 35 (1996) 2531.
[24] C. V. Ovesen, B. S. Clausen, B. S. Hammershoi, G. Steffensen, T. Askgaard, I. Chorkendorff, J. T. Norskov, P. B. Rasmussen, P. Stoltze, P. Taylor. J. Catal., 158 (1996) 170.
[25] E. Tserpe, K. C. Waugh. In: G. F. Froment, K. C. Waugh (Eds.), Dynamics of Surfaces and Reaction Kinetics in Heterogeneous Catalysis, Elsevier, Amsterdam 1997.
[26] K. C. Waugh. Catal. Today, 53 (1999) 161.
[27] O.N. Temkin, A.V. Zeigarnik, D. Bonchev, Chemical Reaction Networks: A Graph-Theoretical Approach, CRS Press, New York, 1996.
[28] M. Boudart, AIChE J, 18 (1972) 465

This Page Intentionally Left Blank

J. Leszczynski (Editor)
Computational Materials Science
Theoretical and Computational Chemistry, Vol. 15

Chapter 3

Clusters, the intermediate state of matter

Szczepan Roszak[a,b] and Jerzy Leszczynski[a]

[a]The Computational Center for Molecular Structure and Interactions, Department of Chemistry, Jackson State University, P.O. Box 17910 J.R. Lynch Street Jackson, Mississippi 39217 USA

[b]Institute of Physical and Theoretical Chemistry, Wroclaw University of Technology, Wyb. Wyspianskiego 27, 50-370 Wroclaw, Poland

1. INTRODUCTION

The studies of dispersed media such as colloids, aerosols, smokes, fogs, and clouds have a long history dating back to the nineteenth century [1,2]. Although much work has been done concerning the nucleation phenomenon [3-5], modern cluster science has been born only when clusters of carbon dioxide were detected in supersonic jets [6,7]. In recent years, cluster science has undergone an explosive growth, not only because of the large number of basic problems on which cluster studies may shed new light, but also due to the potential commercial perspectives for development of new materials. The driving force for cluster research is the need to understand how properties of aggregates vary as a function of size. The stepwise development of clusters allows the properties of consecutive attached particles in a wide range to be controlled. In addition it helps to bridge a gap between isolated molecules or ions and the condensed phase.

The presently available cluster materials may be divided into three categories [8]: magic clusters [9,10], nanophase materials, and discrete clusters covered by protective coatings. Available magic clusters represent the most stable species among the cluster materials. From two known classes: fullerenes [11] and metcars [12] - fullerenes are available commercially. Nanophase materials [13] and clusters covered by a protective coating [14] already have commercial and scientific applications.

Clusters, ultrafine particles of microscopic scale, often exhibit very unique physical and chemical properties that from one side are not present in the bulk solid phase and from the other side are absent in atoms, molecules, or ions. The specific properties of clusters often originate from their large surface-to-volume ratio. The large changes of thermodynamic properties versus size are related to this property [15]. In comparison to the bulk solid, nanocrystals still display the specific properties of clusters despite their extensive sizes [15]. For sizes below 10 nm and by the manipulation of the dimensions of nanoparticles composed from a single chemical compound, one may derive an enormous range of fundamental properties. For example, for CdS clusters the melting temperature varies from 400 to 1600 Celsius [16], and the band gap varies between 2.5 and 4 eV [17].

The unique properties of clusters, different from that of single molecules and the extended solids, are well illustrated in the case of semiconductor nanocrystals which exhibit strong variation in their optical and electrical properties with an increase in their volumes [18,19]. In the case of semiconductor nanoparticles, the density of the electronic energy levels possesses partially the characteristics of a molecular limit as discrete levels of electronic states and partially is represented by continuous bands present for the extended crystalline limit. In semiconductors, discrete electronic levels lie around the Fermi level, and these levels dominate the low-energy electrical behavior [15]. The effect of the size dependence is observed even for clusters containing ten thousand atoms. In the case of molecular or van der Waals crystals, interactions between neighbor molecules are weak; bands composed of atomic energy levels are narrow; little size dependence is observed; and clusters of sizes of ten to a few hundred units already resemble the bulk state [20].

The development of experimental techniques has allowed studies of clusters at the initial state of nucleation to be carried out, starting from the single molecule or ion through further formation of consecutive clusters with the size increasing toward the bulk phase [8,21-23]. The most extended sets of thermodynamic data have been obtained via the high-pressure mass spectrometry technique [24,25]. The use of lasers in the cluster ion dissociation spectroscopy allows the dynamics of photodissociation at the molecular level [21] to be unraveled. The high resolution spectroscopic studies are another important source of information concerning the properties of molecular and ionic extended complexes [26,27].

The differences in the sizes of the clusters that could vary from few to thousands of atoms, require development of different theoretical methods to model such systems. The smallest aggregates may be treated by the most

sophisticated computational techniques including ab initio and Car-Parrinello molecular dynamics methods. The ab initio studies have extensively contributed to the understanding of the chemistry of both weakly and strongly bound clusters [28-30]. In this chapter we focus on structures and properties of weakly bound ionic clusters, especially on building ionic aggregates by the consecutive addition of atoms or molecules coordinated to the charged ion. For this class of clusters the high level ab initio studies supplement experimental findings, enhance the interpretation of data, and provide valuable information not available from other sources.

2. THEORETICAL TOOLS FOR THE STUDY OF THE NATURE OF WEAKLY BOUND AGGREGATES

The basic properties of small clusters have been studied applying the standard quantum-chemical methods. The limitations of these approaches, regarding the size of complexes and the accuracy of the determination of the properties of interest, have been extensively discussed, and excellent guiding books are available [31]. Although studies of weak interactions have a long history, the corresponding theoretical approaches, even today, are not commonly used. Intermolecular interactions are well described within the perturbation theory, and a rigorous and elegant theory is available as the spin-adapted perturbation theory (SAPT) [32]. However due to the relative ease of adaptation, the approximate approaches based on the variational calculations are more popular. Probably the most successful partitioning scheme for the decomposition of the Hartree-Fock (HF) interaction energy was proposed by Kitaura and Morokuma [33]. In further developments the main modification to this scheme was the inclusion of the correction for the basis set superposition error [34-36]. The modern approaches are additionally supplemented by the correlation energy component which can be calculated at the second-order Møller-Plesset (MP2) or higher levels of theory [37].

In the aforementioned scheme the interaction energy is partitioned

$$\Delta E_{int} = \varepsilon_{el}^{(10)} + \varepsilon_{ex}^{HL} + \Delta E_{del}^{HF} + \varepsilon_{MP}^{(2)} \qquad (1)$$

where the physical components of the decomposition are as follows: electrostatic ($\varepsilon_{el}^{(10)}$), Heitler-London exchange (ε_{ex}^{HL}), delocalization (ΔE_{del}^{HF}), and correlation ($\varepsilon_{MP}^{(2)}$) interaction energies. The delocalization

term accounts mostly for the charge transfer and induction energies. For longer distances $\varepsilon_{MP}^{(2)}$ represents mostly dispersion interactions ($\varepsilon_{disp}^{(20)}$)[37].

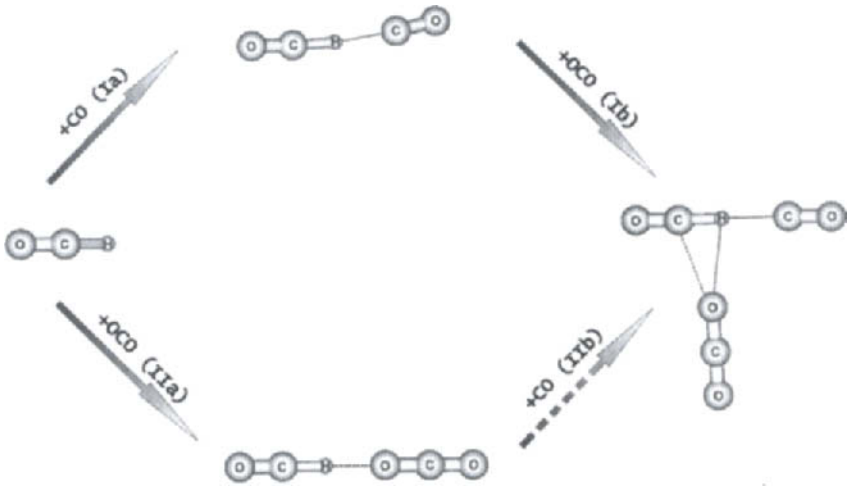

Figure 1. Structures of complexes for the reaction scheme of the $OCH^+(CO)OCO$ complex formation.

The popular concept of bonding taking into consideration the ionic and covalent nature of chemical bonds agrees well with the partitioning presented above. Electrostatic forces represent ionic, while the delocalization term represents the covalent character of chemical bonds or interactions. Modern studies often consider the exchange repulsion interactions as a third component of the ionic-covalent concept of bonding [38].

The requirement that the structures of the supermolecule (dimer) and the corresponding monomers possess the same geometry imposes limits on the applicability of the interaction energy concept. Substrates (subunits) may be significantly modified after the product (dimer) is formed. Large structural deformations due to the intermolecular interactions were observed in studies of $H_3^+Ar_n$ cluster growth [39]. Although there is no unique solution to this problem, the procedure to include the energy term accounting for the relaxation of the fragments has been proposed [40]. However the usefulness of this approach was questioned by others [41]. Clusters with a number of possible geometrical arrangements allow, in some cases, for the solution of the structure relaxation problem. The proposed procedure [42] for the estimation of the relaxation contribution to the interaction energy is based on Hess' law. The procedure is illustrated in the formation reaction of the protonated mixed clusters of CO and CO_2 (Figure 1). Reactions Ia, IIa, and

Ib proceed with little geometrical perturbations, and the interaction energy provides a meaningful interpretation of these processes. The reaction IIb proceeds with significant structural changes, and the interaction energy for the $OCH^+CO(OCO)$ complex is a poor representation of the molecular transformation. The interaction energy representing reaction IIb may be calculated from the thermodynamic cycle (IIb=Ia+IIa-Ib). In this procedure we assume that Hess' law is applicable to the interaction energy corrected for the BSSE. Such an assumption, although not rigorously satisfied, allows for a unique definition of the procedure. The procedure may be extended for the interaction energy decomposition terms. An illustration of the results is given in Table 1.

Table 1
The energy decomposition components for reactions of cluster growth (Figure 1). The components of the last column were calculated from the Hess' law. Energies in kcal/mol

Interaction energy components	$OCH^+ + CO$ Ia	$OCH^+ + OCO$ IIa	$OCH^+(CO) + OCO$ Ib	$OCH^+(OCO) + CO$ IIb
$\varepsilon_{el}^{(10)}$	-13.19	-14.48	-9.41	-8.12
ε_{ex}^{HL}	23.94	16.08	5.96	13.82
ΔE_{del}^{HF}	-20.71	-16.17	-5.45	-9.99
ΔE_{HF}	-9.96	-14.58	-8.91	-4.29
ΔE_{TOT}	-16.33	-14.06	-7.94	-10.21
D_e	15.72	14.64	9.07	10.15

3. PROPERTIES OF CHARGED CLUSTERS

3.1 Structures

The striking feature of small charged clusters is the arrangement of ligands into shells – locations that gather ligands characterized by the same properties. The aggregation proceeds through the successive filling of shells. The first evidence for the existence of solvation shells has been provided by thermochemical experiments [41,44]. However the obtained data allow only for speculations concerning the molecular structure of complexes. Direct information about structural details of ionic clusters arises from theoretical predictions. The results of ab initio calculations were calibrated on small, weakly interacting complexes for which experimental geometries are known [36]. Successful predictions for model systems assure that similar approaches can be safely extended to much more complex moieties.

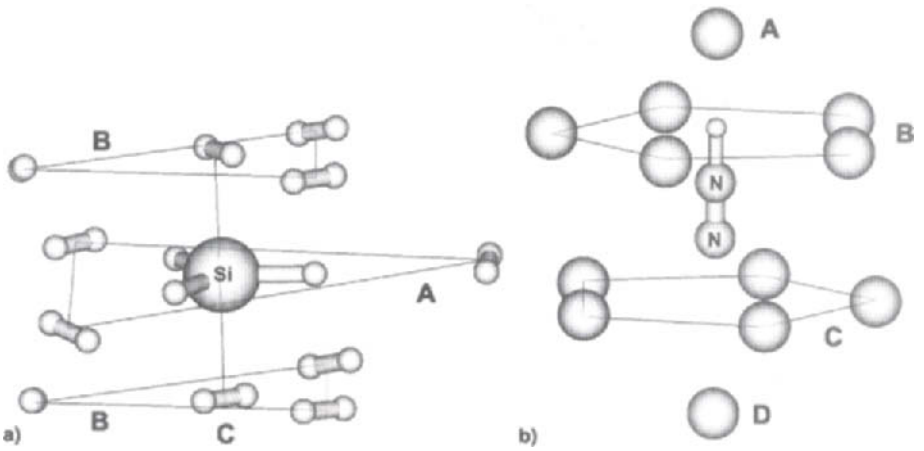

Figure 2. Molecular structures of $SiH_3^+(H_2)_{11}$ (a) and $N_2H^+Ar_{12}$ (b) clusters. Consecutive shells are denoted by capital letters.

At the first approximation, it is reasonable to assume that charged core-ligand and ligand-ligand interactions are additive [29]. For aggregates, in which the ligand-ligand interactions are negligible to a large extent, the molecular geometry of the complex is determined by the symmetry of the electric field of the central ion. The complexes with completely filled (closed) shells possess a symmetry defined by the central ion (Figure 2). The significant ligand-ligand interactions perturb the perfect symmetry of the complex, although the shell structure is still preserved (Figure 3). The capacity of the shells is restricted by the number of energetically favorable contacts which is controlled by the symmetry of the core (Figure 2a) [45-47] or by the lack of space in the shell to host an additional ligand (Figure 2b) [48,49].

The clusters originating from the core ions of the same symmetry possess very similar structures as was shown, e. g., for $SiH_3^+(H_2)_n$ and $GeH_3^+(H_2)_n$ [46,47] complexes and for $N_2H^+(H_2)_n$ and $N_2H^+Ar_n$ complexes [49,50]. It was also observed that different ligands attach topologically equivalent structures to the same core ion form [39,50]. More importantly, even the mixing of different ligands on one (or more) shells still preserves the geometry of the parent homogenous moieties. The shells observed in the $H_3^+Ar_n(H_2)_m$ moiety closely resemble the shells of the homogenous $H_3^+Ar_n$ and $H_3^+(H_2)_n$ complexes [39,50,51].

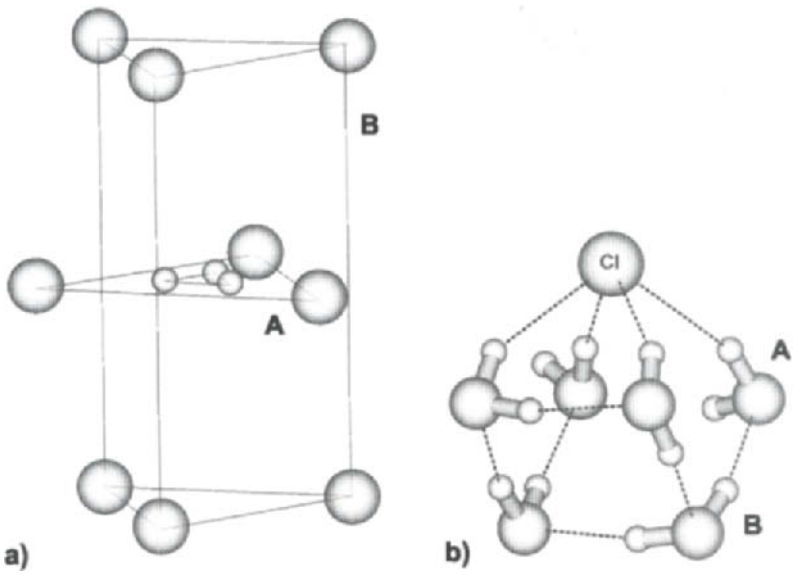

Figure 3. Molecular structures of $H_3^+Ar_9$ (a) and $Cl^-(H_2O)_4$ (b) complexes. The capital letters denote distinct shells.

Although the consecutive filling of shells is controlled energetically, the shells are often well separated, and different occupation patterns are possible and lead to a number of isomers. Because of the restricted capacity of shells in clusters with negligible ligand-ligand interactions, these clusters possess a limited volume [29], and only very few shells can be formed. A different situation is observed in clusters characterized by significant ligand-ligand interactions. The initial complex is formed due to the prevailing core-ligand interactions, and the further extension of complexes leads toward the ligand-ligand network observed in the bulk state of the solvent [52].

3.2 Thermodynamics of the cluster formation

Thermodynamical measurements were the first sources of energetic information concerning solvated cluster cations and anions [8]. Negative ion photoelectron spectroscopy is also an important technique leading to energetic information of complex ions [53]. Other sources of energetic data include spectroscopic experiments [27]. Pioneering works on high-pressure mass-spectrometry have generated data sets for consecutive complexes and, for the first time, have indicated the distinct organization of ligands into

groups according to the measured values of enthalpy and entropy of the reaction of the cluster formation [25]. The interpretation of available data led to the concept of shells. The discontinuities in otherwise smoothly changing enthalpies and entropies of the consecutive ligand binding as a function of the size led also to the definition of magic numbers [54]. As nucleation proceeds, the enthalpy of the binding slightly decreases within the shell (Table 2) [25]. Cases of anomalous behavior have also been discovered [50] and confirmed theoretically [48,49]. The agreement between theoretical values corresponding to determined structures and values found experimentally indicates the direct correlation between energetics and the geometry of extended complexes.

The consecutive occupation of shells leads to the restriction of motions due to the crowding of neighbors. As occupation increases the usually weaker bonding is overcompensated by the crowding of the shell, and successive entropies became more negative. Such an effect is especially visible for the closing of the shell and defines the "magic number." These experimental findings are supported by theoretical calculations. The variations of thermodynamic functions are directly related to geometrical structures of complexes as is well presented by quantum-chemical modeling. As was shown for $H_3^+Ar_n$ complexes, some local perturbations of shell occupation are possible (Table 2). According to the entropy value the closing of the shell takes place for the A(3)B(4) occupation. The theory, however, indicates that the B shell may still accept one more ligand, although such a situation is not energetically preferable.

Table 2

Theoretical [39] and experimental [71] consecutive dissociation energies (D_e), enthalpies (ΔH), and entropies (ΔS) of the $H_3^+Ar_{n-1}$-Ar bond dissociation. Energies in kcal/mol, entropy in cal/molK. The corresponding shell structure is given on Figure 3a.

n	Shell occupation	D_e	ΔH(calc.)	ΔH(expt.)	ΔS(calc.)	ΔS(expt.)
1	A(1)	6.37	6.97	6.69	16.2	13.4
2	A(2)	4.53	5.12	4.56	15.9	16.0
3	A(3)	3.81	4.40	4.28	17.9	17.3
4	A(3)B(1)	1.64	2.37	2.45	11.7	16.1
5	A(3)B(2)	1.66	2.25	2.27	13.8	16.7
6	A(4)B(2)	1.68	2.27	2.18	12.7	18.7
7	A(3)B(4)	0.98	1.57	1.56	23.0	23.0
8	A(3)B(5)	0.81	1.39		13.2	

3.3 Properties of clusters and the shell structure

The properties of clusters may be studied with a focus on the central ion or on its ligand environment. Due to the weak interactions, most of the properties of both mentioned components are preserved, and their modification due to the clustering process may be considered as perturbations of the bare ion or bare ligand properties. An often posed question regarding cluster evolution is: what is the number of ligands needed to change the cluster characteristics from molecular to that of the bulk phase? The answer is not general and varies for different species from a few to thousands of ligands. The Cl^- ion tends to stay on the surface of small water clusters, and more than ten water molecules are needed to form the cluster with the chlorine ion inside [52,55]. Bare H^- and NH_2^- anions have reversed basicities compared to their state in liquid ammonia. Only two interacting NH_3 ligands are required to change the order of basicities from the bare anion to that of liquid [56-58]. The IR spectra of the water dimer from vibrational predissociation of the H_2O clusters are significantly different from those of the bulk water, while trimer and larger complexes possess close similarity with the IR bands of liquid water [59,60].

Table 3
Calculated [62] and experimental [63] total stabilization energies ($SE=E(O^-Ar_n)-E(O^-)-nE(Ar)$) and vertical electron affinities (VEA) for the O^-Ar_n complex. Energies in eV.

n	SE(calc.)	SE(expt.)	VEA(calc.)	VEA(expt.)
0			1.44	1.465
1	0.096	0.097	1.54	1.562
2	0.190	0.183	1.56	1.648
3	0.261	0.252	1.71	1.717
4	0.326	0.313	1.77	1.778
5	0.383	0.363	1.82	1.828
6	0.453	0.416	1.90	1.881

An analysis of the interactions of ions with ligands leads to valuable information which is difficult to obtain otherwise. Important data for resolving the dynamical structure of the protonated methane cation CH_5^+ arises from the infra-red spectra of $CH_5^+(H_2)_n$ [45,61]. The topology of shells is projected on the properties of bare ions. The process of the consecutive electron photodetachment from the central anion indicates the existence of the well developed shell structure of complexes. The theoretically predicted electronic affinities for O^-Ar_n clusters calculated for theoretical structures of complexes agree with the known measured values (Table 3) [62,63]. The ionization potential of $CH_3^+Ar_n$ clusters is little

changed as an effect of the consecutive argon coordination (Table 4) [64]. The molecular beam photoionisation of $(H_2S)_n$ also indicates only small changes in the ionization potentials of the core due to the cluster formation [65].

Table 4
Theoretical and experimental [64] adiabatic ionization potential (IP) for the CH_3Ar_n (n=1-3) complexes. Ionization potentials in eV.

Molecular complex	IP(calc.)	IP(expt.)
CH_3	9.77	9.84
CH_3Ar	8.96	9.19
CH_3Ar_2	8.86	9.09
CH_3Ar_3	8.86	9.02

Because shells are principally determined by the central ion it is possible to utilize the almost 'one-to-one' ion–ligand relation to reveal the properties of the core ion through studies of the properties of attached molecules [61]. Examples include the IR spectra of $CH_3^+(H_2)_n$ cations that have been applied to the study of the structure of protonated methane. The frequencies of the CH_5^+ core are sensitive to a number of hydrogen molecules coordinated to this cation. The different possibilities for the occupation of shells are visible as complications in the observed infra-read bands. The statistical occupation of shells, due to many energetically possible isomers, leads to broad and complicated bands. The stretching modes of the H_2 ligand clearly display the shell structure of complexes. Both experimental and theoretical IR frequencies (Table 5) indicate the well separated vibration modes [45,61].

Table 5
Theoretical [45] and experimental [61] vibrational frequencies for the stretching modes of molecular hydrogen ligands for the different occupation of shells in $CH_5^+(H_2)_n$ complexes. Frequencies are given in $cm.^{-1}$

Cation	Shell occupation	B(1)	B(2)	C(1)	C(2)	C(3)	Expt.
$CH_5^+(H_2)$	B(1)	4073					4077
$CH_5^+(H_2)_2$	B(2)	4080	4089				4088
$CH_5^+(H_2)_3$	B(2)C(1)	4086	4092	4124			4099
$CH_5^+(H_2)_4$	B(2)C(2)	4084	4092	4125	4133		4106
$CH_5^+(H_2)_5$	B(2)C(3)	4089	4095	4125	4134	4134	4109

4. THE NATURE OF INTERACTIONS IN WEAKLY BOUND CLUSTERS

The structures and properties of the two simple charged complexes OCH^+Ar_3 and $OCH^+(CO)_3$ (Figure 4) indicate the rich chemistry of such moieties [42,48]. The position of argon atoms in the second solvation shell of OCH^+Ar_3 is determined by the argon-argon attraction, while the structure of the second shell in $OCH^+(CO)_3$ is controlled by the conjugation of π-π orbitals of the OCH^+ core and CO ligands. The interactions between CO ligands of the second shell of $OCH^+(CO)_3$ are repulsive, and the overall geometry is stabilized by covalent forces. The interplay between forces of differing natures, especially in larger clusters, causes significant structural consequences. At present, such subtle effects involving chemical bonds may be explained exclusively by theoretical models.

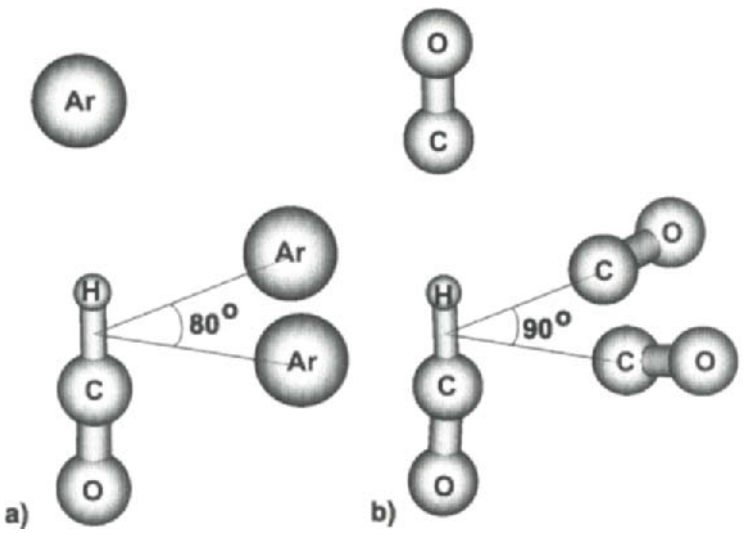

Figure 4. The structures of OCH^+Ar_3 (a) and $OCH^+(CO)_3$ complexes.

An atomic charge distribution, calculated theoretically using one of the available population analysis schemes, although arbitrary and method dependent, is a useful tool to study the electronic density distribution. The performed calculations indicate in most cases very little charge dispersion from the core ions to the ligand space. In the case of the $NO^-(H_2O)_2$ complex the calculated electron loss from NO^- amounts to 0.03 electron [66]. The similarity of the measured photoelectron spectra of NO^- and its complexes

with H_2O confirms indirectly the charge localization [67]. The differences between cationic and anionic clusters are small. In the former, the positive charge is more delocalized compared to anionic clusters even through the central ion is still the distinctly charged center [64]. Similar to other properties, it was found that the charge distribution also displays regularities in harmony with the shell structure of the clusters (Table 6).

Table 6

Calculated [46] and experimental [72] dissociation energies and molecular charge on core hydrogens (H_3) and on subsequently coordinated hydrogen molecules in $SiH_3^+(H_2)_n$ complexes. Energy in kcal/mol. Molecular charges, determined within the Mulliken population analysis, are given in electron.

Cation	Shell occupation	D_e(calc.)	ΔH (expt.)	H_3	A(1)	A(2)	B(1)	B(2)
SiH_3^+				-0.064				
$SiH_3^+(H_2)$	A(1)	13.70	14.2	-0.088	0.226			
$SiH_3^+(H_2)_2$	A(2)	5.16	4.8	-0.105	0.157	0.156		
$SiH_3^+(H_2)_3$	A(2)B(1)	0.85	1.5	-0.107	0.151	0.156	0.015	
$SiH_3^+(H_2)_4$	A(2)B(2)	0.84		-0.112	0.151	0.150	0.014	0.014

More detailed information concerning the nature of interactions in the charged ions may be deduced from the components of the interaction energy partitioning scheme presented in section 2. The values of components indicate a dramatic change in the character of binding of ligands occupying different shells. The change of characteristics is often not only quantitative but also qualitative. The linear ArH^+Ar cation is stabilized mostly due to the charge transfer interactions (the delocalization term) (Table 7), while the electrostatic interactions are repulsive [68]. However the occupation of the second shell is governed mostly by correlation forces.

Table 7

Consecutive dissociation energies and interaction energy components (for the definition see paragraph 2) for consecutive clusters of Ar_nH^+ [68]. Energies in kcal/mol.

Cation	D_e	$\varepsilon_{el}^{(10)}$	ε_{ex}^{HL}	ΔE_{del}^{HF}	ΔE_{HF}	$\varepsilon_{MP}^{(2)}$	ΔE_{TOT}
ArH^+-Ar	16.4	3.09	36.13	-58.58	-19.35	-5.18	-24.53
Ar_2H^+-Ar	2.1	-0.34	1.69	-1.62	-0.32	-1.34	-1.66
Ar_3H^+-Ar	2.3	-0.50	2.03	-1.55	-0.02	-1.75	-1.77
Ar_4H^+-Ar	2.3	-0.60	2.38	-1.49	0.29	-2.17	-1.88
Ar_5H^+-Ar	2.3	-0.63	2.45	-1.49	0.33	-2.24	-1.91
Ar_6H^+-Ar	2.6	-0.62	2.41	-1.37	0.42	-2.23	-1.81

The Ar-Ar electrostatic interactions, although weak, are also attractive. Due to the increased crowding of atoms occupying the shell, exchange repulsion forces increase with every new atom attached in the second shell.

5. UNUSUAL PROPERTIES OF WEAKLY BOUND CLUSTERS

Although there is no difference between the nature of interactions in clusters and in any other weakly bound complexes, the systematic formation of complex aggregates allows unexpected features to be detected. Gas phase clustering reactions $N_2H^+(H_2)_{n-1} + H_2 = N_2H^+(H_2)_n$ with n=1-13, measured by the pulsed beam mass spectrometer indicate anomalous changes of binding energies in the $N_2H^+(H_2)_n$ cluster ion; mainly the bond energies of $N_2H^+(H_2)_n$ increase with "n" changing from 2 to 5 [50]. The discovery was confirmed by theoretical studies [50]. The computational investigations additionally reveal the similar property of clustering in $N_2H^+Ar_n$ and OCH^+Ar_n moieties [48,49]. In the above complexes of the general formula AH^+-L_n, the A-H stretching vibration in the simplest AH^+-L moiety is red-shifted in comparison to the simple AH^+ cation. A further increase in the size of the cluster by the formation of a shell perpendicular to the A-H^+-L axes leads to the distinct blue shift of the AH^+ stretching vibrations. The effect continues when subsequent shells are being occupied. As expected, the blue shift of the AH vibration coincides with the shortening of the A-H bond leading to the relation between $\Delta\nu_{AH}$ and $\Delta r_e(AH)$ which satisfies the Badger's rule (Table 8) [69]. A reasonable and simple explanation of the above phenomenon was based on the balance of interactions between ligands in the first and the second shells [48]. The explanation proposed in the somewhat

Table 8

Enthalpies of formation (ΔH), molecular charges (from Mulliken population), N-H bond distances (R_e), and stretching vibrational frequencies of N-H (ν) for the $N_2H^+Ar_n$ complexes [49]. Enthalpies in kcal/mol, charges in electron, distances in Angstrom, and frequencies in $cm.^{-1}$

n	Shell structure	ΔH	Molecular charge on N_2H^+	R_e(N-H)	ν_{NH}
0	N_2H^+				3410.4
1	A(1)	7.16	0.785	1.088	2635.9
2	A(1)B(1)	1.13	0.790	1.086	2658.4
3	A(1)B(2)	1.67	0.758	1.084	2686.3
4	A(1)B(3)	1.73	0.730	1.081	2707.1
5	A(1)B(4)	1.96	0.702	1.080	2731.5
6	A(1)B(5)	2.13	0.664	1.078	2747.1

similar phenomenon of improper blue-shifting hydrogen bonding [70] suggests the important role of the dispersion energy in binding as a counter balance for electrostatic interactions. We expect that the advanced modeling of the observed phenomenon would probably result in the consideration of both discussed effects.

6. CONCLUSIONS

Despite technological problems with production of clusters of controlled sizes and stabilities, the cluster field has entered the commercial stage. Fullerenes and other cluster materials are available on the market. The extremely large size (surface) to volume ratio makes these moieties very efficient catalysts. Clusters offering new properties, not available in gas or condensed phase, form new species classified as intermediate states of matter. More importantly, as problems concerning the size and stability of clusters become more controllable, manipulations of these molecular aggregates could create a material with an enormous range of fundamental properties to be accessible by the preparation of a single chemical compound.

The ab initio methods supplement the current experimental studies by providing information not available from other sources. The experiments provide the energetic and spectroscopic data for the systematic enlargement of clusters. The ab initio calculations supplement the experimental findings and allow often present ambiguities to be removed. Probably, the most important property of weakly bound clusters is the organization of ligands into shells. The opening of new shell manifests as the sudden change in the otherwise smoothly changing property. The closing of the shell defines a maximum number of ligands that could be located in a given shell, known as "magic number." The existence of shells is directly visible in geometries of charged clusters, and in addition it is reflected in the number of properties such as enthalpy and entropy of formation, electron attachment and detachment phenomena, and spectroscopic properties such as vibrational spectra. The one-to-one correspondence between the central cation and ligands trapped in shells allows the behavior of the core ion to be controlled by manipulating the size of the cluster. Theoretical techniques such as the interaction energy decomposition schemas yield insight into the bonding of clusters and allow for the development of models useful for studying more extended systems for which the use of ab initio algorithms is not yet

feasible. The unique structure of clusters leads to the observation of patterns of unusual bonding properties and spectroscopic properties.

ACKNOWLEDGEMENT

This work was facilitated in part by NSF grant No. 9805465 & 9706268, ONR grant No. N00014-03-1-0498, Wroclaw University of Technology Grant, and the Army High Performance Computing Research Center under the auspices of the Department of the Army, Army Research Laboratory cooperative agreement number DAAH04-95-2-0003/contract number DAAH04-95-C-0008. This work does not necessarily reflect the policy of the government, and no official endorsement should be inferred. We would like to thank the Mississippi Center for Supercomputing Research, Poznan and Wroclaw Supercomputing and Networking Centers, and the Interdisciplinary Center for Mathematical and Computational Modeling of Warsaw University for a generous allotment of computer time.

REFERENCES

1. M. Coulier, J. Pharm. Chim. Paris 22(1875)165.
2. J. S. Thomas, Michael Faraday and The Royal Institution, Adam Hilger, Bristol, 1991.
3. K. Z. Oswatitsch, Angew. Math. Mech. 22(1942)1.
4. N. F. Ramsey, Phys. Rev. 74(1948)286.
5. S. A. Osch, R. E. Cote, and P. Kusch, J. Chem. Phys. 21(1953)459.
6. P. G. Bentley, Nature 190(1961)432.
7. W. Henkes, Z. Naturforsch. 16A(1961)842.
8. A. W. Castleman Jr. and K. H. Bowen Jr., J. Phys. Chem. 100(1996)12911.
9. S. N. Khanna and P. Jena, Phys. Rev. Lett. 69(1992)1664.
10. S. N. Khanna and P. Jena, Phys. Rev. Lett. 71(1993)208.
11. H. W. Kroto, J. R. Heath, S. C. O'Brien, R. F. Curl, and R. E. Smalley, Nature 318(1985)162.
12. B. C. Guo, K. P. Kerns, and A. W. Castleman Jr., Science 255(1992)1411.
13. R. L. Whetten, J. T. Khoury, M. M. Alvarez, S. Marthy, I. Vezmar, Z. L. Wang, P. R. Stephens, C. L. Cleveland, W. D. Luedtke, and U. Ladman, Adv. Mater. 8(1996)428.
14. R. P. Andres, R. S. Averback, W. L. Brown, L. E. Brus, W. A. Goddard III, A. Kaldor, S. G. Louie, M. Moscovits, P. S. Peersy, S. J. Riley, R. W. Siegel, F. Spaepen, and Y. Wang, J. Mater. Res. 4(1989)704.

15. A. P. Alivisatos, J. Phys. Chem. 100(1996)13226.
16. A. N. Goldstein, C. M. Echer, and A. P. Alivisatos, Science 256(1992)1425.
17. V. L. Colvin, A. P. Alivisatos, and J. G. Tobin, Phys. Rev. Lett. 66(1991)2786.
18. A. I. Ekimov and A. A. Onushchenko, Fiz. Tekh. Poluprovodn. 16(1982)1215.
19. R. Rosetti, S. Nakahara, and L. E. Brus, J. Chem. Phys. 79(1983)1086.
20. C. Ellert, M. Schmidt, C. Schmidt, T. Reiners, and H. Haberland, Phys. Rev. Lett. 75(1995)1731.
21. A. W. Castleman Jr. and R. G. Keesee, Acc. Chem. Res. 19(1986)413.
22. Z. Bacic and R. E. Miller, J. Phys. Chem. 100(1996)12945.
23. A. W. Castleman Jr. and R. G. Keesee, Acc. Chem. Res. 19(1986)413.
24. R. G. Keese and A. W. Castleman Jr., J. Phys. Ref. Data 5(1982)1011.
25. K. Hiraoka and S. Yamabe, in Dynamics of Excited Molecules (ed. S. Kachitsu), Studies in Physical and Theoretical Chemistry 82, Elsevier Science, Amsterdam, 1994, p. 399.
26. H. J. Neusser and K. Siglow, Chem. Rev. 100(200)3921.
27. E. J. Bieske and O. Dopfer, Chem. Rev. 100(2000)3963.
28. S. Roszak and J. Leszczynski, J. Phys. Chem. A 107(2003)949.
29. S. Roszak and J. Leszczynski, in Computational Chemistry – Reviews of Current Trends (ed. J. Leszczynski) Vol. 5, World Scientific, Singapore, 2001, p. 179.
30. J. A. Alonso, Chem. Rev. 100(2000)637.
31. W. J. Hehre, L. Radom, P. v. R. Schlayer, and J. A. Pople, Ab Initio Molecular Orbital Theory, Wiley-Interscience, New York, 1986.
32. K. Szalewicz and B. Jeziorski, in Molecular Interactions, from van der Waals to Strongly Bonded Complexes (ed. S. Scheiner), Wiley, Chichester, 1997, p. 3.
33. K. Kitaura and K. Morokuma, Int. J. Quant. Chem. 10(1976)325.
34. W. A. Sokalski, S. Roszak, P. C. Hariharan, and J. J. Kaufman, Int. J. Quant. Chem. 23(1983)847.
35. W. A. Sokalski, S. Roszak, and K. Pecul, Chem. Phys. Lett. 153(1988)153.
36. G. Chalasinski and M. M. Szczesniak, Chem. Rev. 94(1994)1723.
37. G. Chalasinski and M. M. Szczesniak, Mol. Phys. 63(19988)205.
38. J. Uddin and G. Frenking, J. Am. Chem. Soc. 123(2001)1683.
39. M, Kaczorowska, S. Roszak, and J. Leszczynski, J. Chem. Phys. 113(2000)3615.
40. S. S. Xantheas, J. Chem. Phys. 104(1996)8821.

41. K. Szalewicz and B. Jeziorski, J. Chem. Phys. 109(1998)1198.
42. J. J. Szymczak, S. Roszak, R. W. Gora, and J. Leszczynski, J. Chem. Phys. 000(2003)000.
43. W. A. Chupka, J. Chem. Phys. 30(1959)458.
44. P. Kaberle in Interactions Between Ions and Molecules (ed. P. Ausloos), Plenum, New York, 1974, p. 459.
45. S. Roszak and J. Leszczynski, Chem. Phys. Lett. 323(2000)278.
46. S. Roszak and J. Leszczynski, Chem. Phys. Lett. 314(1999)333.
47. S. Roszak, P. Babinec, and J. Leszczynski, Chem. Phys. 256(2000)177.
48. K. O. Sullivan and G. I. Gellene, Int. J. Mass Spectrom. 201(2000)121.
49. Y. Sheng, R. W. Gora, S. Roszak, M. Kaczorowska, and J. Leszczynski, J. Phys. Chem. A 106(2002)11162.
50. K. Hiraoka, J. Katsuragawa, A. Minamitsu, E. W. Ignacio, and S. Yamabe, J. Phys. Chem. A 102(1998)1214.
51. M. Kaczorowska, S. Roszak, and J. Leszczynski, J. Phys. Chem. A 105(2001)7938.
52. R. W. Gora, S. Roszak and J. Leszczynski, Chem. Phys. Lett. 325(2000)7.
53. S. T. Arnold, J. H. Hendricks, and K. H. Bowen in Reaction Dynamics in Clusters and Condensed Phases (ed. J. Jortner) Kluwer, Amsterdam, 1994, p. 37.
54. A. W. Castleman Jr. in Clustering Phenomena of Atoms and Molecules (eds. M. Brenner, T. Lonnroth, F. B. Malik) Springer-Verlag, Berlin, 1992, p. 99.
55. L. Perera and M. L. Berkowitz, J. Chem. Phys. 99(1993)4236.
56. J. T. Snodgrass, J. V. Coe, C. B. Freidhoff, C. B. McHugh, and K. H. Bowen, Faraday Discuss. Chem. Soc. 86(1988)241.
57. J. T. Snodgrass, J. V. Coe, C. B. Freidhoff, C. B. McHugh, and K. H. Bowen, J. Phys. Chem. 99(1995)9675.
58. S. Roszak, J. Chem. Phys. 105(1996)7569.
59. D. F. Coker, R. E. Miller, and R. O. Watts, J. Chem. Phys. 82(1985)3554.
60. M. F. Vernon, D. J. Krajnovich, H. S. Kwok, J. M. Lisy, Y. R. Shen, and Y. T. Lee, J. Chem. Phys. 77(1982)47.
61. D. W. Boo and J. T. Lee, J. Chem. Phys. 103(1995)520.
62. S. Roszak, R. W. Gora, and J. Leszczynski, Chem. Phys. Lett. 313(1999)198.
63. S. T. Arnold, J. H. Hendricks, and K. H. Bowen, J. Chem. Phys. 102(1995)39.

64. R. W. Gora, S. Roszak, and J. Leszczynski, J. Chem. Phys. 115(2001)771.
65. W. A. Walters and N. C. Blais, J. Chem. Phys. 75(1981)4208.
66. S. Roszak, Chem. Phys. Lett. 221(1994)255.
67. J. G.Eaton, S. T. Arnold, and K. H. Bowen, Int. J. Mass Spectrosc. Ion Processes 102(1990)303.
68. K. Giju, S. Roszak, and J. Leszczynski, J. Chem. Phys. 117(2002)4803.
69. R. M. Badger, J. Chem. Phys. 2(1935)710.
70. P. Hobza and Z. Havlas, Chem. Rev. 100(2000)4253.
71. K. Hiraoka and T. Mori, J. Chem. Phys. 91(1989)4821.
72. K. Hiraoka, J. Katsuragawa, and A. Minamitsu, Chem. Phys. Lett. 267(1997)580.

J. Leszczynski (Editor)
Computational Materials Science
Theoretical and Computational Chemistry, Vol. 15

Chapter 4

Computer simulation of fullerenes and fullerites

Ilya Yanov and Jerzy Leszczynski

Computational Center for Molecular Structure and Interactions (CCMSI),
Department of Chemistry, Jackson State University, Jackson, MS 39217, USA

1. INTRODUCTION

In 1985 Kroto and Smolly found the sharply prevailing peaks corresponding to the C_{60} and C_{70} clusters in the mass spectra of graphite vapors. To explain the high stability of C_{60}, which they called buckyball, it was assumed that it is a spherical molecule in which atoms are located in the tops of truncated icosahedra [1]. A considerable interest was piqued by buckyball (also known as fullerene) when the method of production of significant amounts of C_{60} by electric arch evaporation of graphite in a helium atmosphere had been discovered [2].

Like all closed geodesic structures, C_{60} (Fig. 1) has the 12 pentagons that are required to transform a two dimensional network of hexagons into a spheroid. The remaining carbon atoms are configured as 20 hexagons to form the molecule's soccerball shape. Fullerenes follow the net closing formula postulated by Leonhard Euler. He states that, for any polygon with **n** edges, at least one polyhedron can be constructed with **12** pentagons and **(n-20)/2** hexagons.

In order to characterize the highly symmetric C_{60}, it is necessary to determine only two independent geometrical parameters, for example, the lengths of the bonds between the sixfold rings (R_1) and the bonds sharing fivefold and sixfold rings (R_2). Experiments show that the average distance between the nearest neighbors in the structure are 1.40Å (R_1) and 1.45Å (R_2), and carbon atoms are located at the 3.51 Å from the center [3].

In Fig. 1 those two types of bonds are displayed. From a chemical point of view, bond alternation is an important feature of strained five-membered rings adjacent to benzenoid rings — the tendency to avoid forming double bonds in a pentagon ring [4]. The presence of double bonds shortens the bonds in the already strained ring, producing the Mills-Nixon effect [5].

The high symmetry of a fullerene molecule causes appearance of simple vibrational [6] and electronic spectra [7]. Isolated C_{60} has icosahedral symmetry I_h, the highest among the point groups.

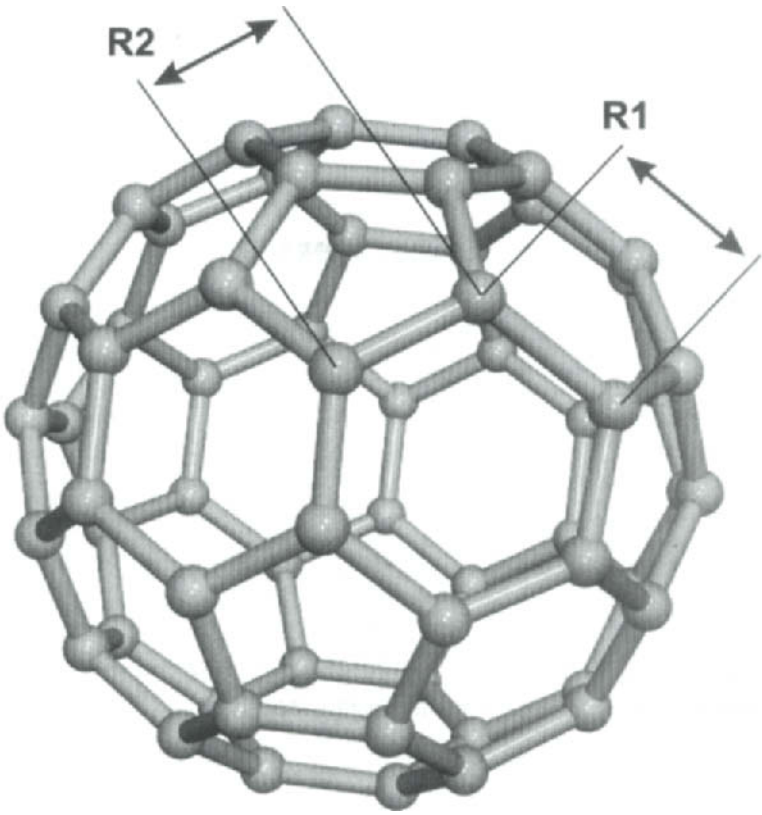

Fig. 1. Fullerene molecule. Two types of bonds are shown.

It results in a strong degeneration of the vibrational spectrum, and from a possible 174 vibrational modes only 46 are independent. Among them it is possible to observe experimentally four IR T_{1u} modes that are three times degenerated, two nondegenerated Raman A_g modes, and eight fivefold degenerated Raman H_g modes (Table 1).

The results of calculations of an electronic spectrum show that the HOMO is the fivefold degenerated h_u state completely occupied by 10 electrons. The LUMO orbital is the three times degenerated t_{1u} state separated from the HOMO orbitals by a gap of about 2 eV [8]. The cohesive energy of a fullerene molecule, defined as the difference of the total molecular energy and the sum of the energies of the isolated atoms, is 7.0 eV/atom (for comparison, the cohesive energy of a diamond is 7.4 eV/atom).

Table 1

Vibrational spectrum of C_{60}. IR and Raman modes

Vibrational modes	Experimental data (cm^{-1})	*Ab initio* data(cm^{-1}), [17]
$A_g(1)$	491[a]	537
$A_g(1)$	1469[a]	1680
$H_g(1)$	265[a]	249
$H_g(2)$	434[a]	413
$H_g(3)$	711[a]	681
$H_g(4)$	773[a]	845
$H_g(5)$	1100[a]	1209
$H_g(6)$	1255[a]	1453
$H_g(7)$	1427[a]	1624
$H_g(8)$	1575[a]	1726
$T_{1u}(1)$	528[b]	494
$T_{1u}(2)$	577[b]	643
$T_{1u}(3)$	1183[b]	1358
$T_{1u}(4)$	1429[b]	1641

[a] Data from Ref. 17.
[b] Data from Ref. 2.

The chemical properties of the fullerene molecule are also of interest. Unlike the majority of aromatic or unsaturated compounds, C_{60} is a reluctant donor of π-electrons. Even fluorine interacts with fullerene slowly and in several stages. On the other side, the fullerene molecule is a rather strong oxidizer. The first three electrons attach to fullerene easily and reversibly. Alkaline metals can give up to six electrons to the fullerene molecule. Therefore, fullerene possesses strong oxidizing properties in a closed electronic environment. Those features of an electronic structure provide high catalytic activity for fullerenes [9]. For example, $C_{60}Pd_n$ is an effective catalyst in the reaction of hydrogenization of olefins and acetylenes [10].

The unique properties of fullerene molecules allow for the assumption that in the future they will be widely used for the creation of new materials. Reports on the potential applications of fullerene structures have been recently published: soft ferromagnetics, three-dimensional organic conductors, lubricant materials, etc. [11,12]. Of special significance is the superconductivity discovered in fullerene films, doped with alkaline metals. The temperature of transition into the superconducting state achieved at the present time (about 45 K) is exceeded only by ceramic superconductors, but fullerene films have higher critical current values [13,14]. The fullerene molecule and some fullerene derivatives exhibit biological activity such as inhibition of HIV protease [15,16]. The application of materials on the fullerene basis for nano- and biotechnology is also of great interest.

Unlike any other molecules, the history of fullerene is strongly connected to computer modeling. The aim of this review is to reveal the role of computational methods in the solid state and material science investigations of fullerene and its selected derivatives and point out some recent developments in this field.

The first part of the chapter is devoted to non-carbon and fullerene-like clusters and describes the role of the fullerene molecule in cluster research. The second part addresses one of the most controversial questions concerning the mechanism of formation of the fullerene molecule. The third part reveals the role of of defects of the fullerene molecule and their possible applications. The results of molecular dynamic simulations show the possibility for the production of selected types of defects in the process of atomic implantation. Solid state properties of the fullerene molecule are discussed in the fourth part of the chapter.

Superconductivity in doped fullerites is one of their most intriguing properties from a theoretical point of view. Herein lies the greatest prospects concerning the practical application of fullerene compounds. The history of this phenomenon and the ways of enhancing of the superconductive properties of fullerene molecules are discussed in the fifth part.

A computational approach was not only very successful in fullerene research, but advances in these studies have created the demand for the development of new theoretical methods. The last part of this chapter describes the application of the non-equilibrium Green's function formalism to the investigation of the current-voltage dependence of the fullerene molecule. This method can be also applied to a wide range of nanomolecular devices.

2. NON-CARBON AND LAYERED FULLERENES. FULLERENE-LIKE CLUSTERS.

The discovery of fullerenes, carbon molecules with geodesic structures, has prompted a number of studies, both theoretical and experimental, devoted to the possible existence of non-carbon analogues of these species [18-21]. From a theoretical point of view this discovery opens the way toward the preparation of new forms of known substances. In addition to theoretical interests, such polyhedrons could facilitate a much more diverse chemistry than has been possible so far with carbon fullerenes.

It is now generally accepted that there are three distinct regions characterizing the carbon clusters mass spectrum [22]: 1) small clusters containing fewer than 25 atoms, consisting of chains and monocyclic rings; 2) a region between about 20 and 35 atoms in which species of any sort are observed; and 3) an even-numbered cluster distribution from the high 30s to well over 150 atoms.

In spite of the repeated recognition of fullerene-like polymorphs [23-25] it has so far been impossible to isolate them in amounts comparable to those obtained for C_{60} and C_{70}. There are only a few studies devoted to the fullerene-like structures, based on elements distinct from carbon or silicon [26-28]. The majority of investigations related to non-carbon clusters has been performed on silicon systems, perhaps because of silicon's applications in the microelectronic industry.

In contrast to experiments with C_N or $Alkali_N$ compounds, the abundance spectra of Si_N do not display the signatures of the magic numbers [29]. However, observation of the Si_N species ($10< N < 100$) reveals a very remarkable size selectivity of Si_N clusters. In a series of pioneering measurements, Smalley and co-workers studied the reactivity of these clusters with ammonia [30]. Chemisorption of ammonia yields reactivity minima for Si_N clusters with N=21, 23, 39, and 45 indicating a particularly high degree of saturation, corresponding to preferred geometric shapes for these "magic" numbers. As a common finding from all these measurements, Si_N clusters exhibit strong reactivity oscillation with size in the region $N \leq 47$. For larger systems, the dependence of reactivity on size is rather smooth.

A crucial experimental result concerning the shapes of Si_N was obtained by Jarrold et al. [31]. Investigating the mobilities of size-selected Si_N cluster ions in a helium atmosphere the authors conclude that the Si_N geometries undergo a transition around N=27 from prolate to quasi-spherical shapes. Photoionization spectra [32] reveal similar features for the clusters in the size range $18 \leq N \leq 41$, hinting at the possibility of a common bonding network for mid-sized Si_N clusters.

A comparison of the carbon and silicon compounds indicates that there is no favorable even-numbered distribution of silicon clusters, but there is a tendency for the clusters to form quasi-spherical shapes. The Si_N clusters differ significantly from the corresponding C_N species since there is no evidence for linear or cap structures for the silicon compounds.

A series of *ab initio* quantum-chemical investigations have been performed on Si_N systems. Si clusters ranging in size from three to 15 silicon atoms have been investigated by the Hartree-Fock and MP2 methods [33]. The tendency of such clusters towards the deformation of the original geodesic shell structures into configurations of lower symmetry which are composed of a negatively charged "core" and a positively charged "shell" is revealed. The energy difference between cage-like and ground state structures diminishes as one goes from N=4 to N=8, and the cohesive energy rises to a maximum for Si_{10}. From this observation, one may infer that small Si_N clusters with N=4, 6, 8, and 10 tend to adopt cage-like structures as N increases.

Intermediate-sized Si clusters, containing 20 to 33 atoms, have been studied using the first-principles methods based on the Local Density

Approximation [34]. The calculations reveal the complex relationships between the properties of the clusters and the cluster structures. Jackson studied three classes of structures over the entire size range including elongated structures formed by stacking a basic structural unit along a common axis, compact structures which attempt to minimize the cluster surface area, and single shell fullerene structures [34]. He found evidence suggesting a transition in stability from the elongated structures to the compact structures with a cluster size of N=26 atoms which is in good agreement with experimental results. The stability of the fullerene structures is intermediate over the whole size range studied. Therefore, the closed-shell silicon clusters, like fullerenes, do not necessarily prefer the most compact geometric arrangement, and the fullerene structures are intermediate in stability among the considered systems.

A number of theoretical studies have been devoted to the possible existence of the Si_{60} fullerene. It was concluded that the difference in total energy (HF/DZ+ECP) between the icosahedral Si_{24} and Si_{60} clusters per silicon atom is 10.3 kcal/mol in favor of Si_{60} [20]. This value approximately amounts to half of the corresponding value of 22.3 kcal/mol calculated for C_{60} using the HF/STO-3G method [35]. As a result of the larger Si-Si than C-C bond distances, Si_{60} has a hollow cage bigger than that of C_{60}. Bond orders of 1.078 and 1.101 (1.681 and 1.495) are obtained from AM1 calculations [21] for pentagonal bonds (hexagonal bonds) of Si_{60} and C_{60}, respectively. Therefore, the loss of delocalization in passing from C_{60} to Si_{60} is shown [21].

The calculated electronic structure of Si_{60} indicates [20] that the highest occupied molecular orbital and the lowest unoccupied molecular orbital display the same symmetry as those of C_{60}. In addition the HOMO-LUMO gap is approximately half as large as that for C_{60}. As predicted for smaller size clusters, the geodesic form is not the most stable structure of Si_{60} [36].

In summary, based on the available experimental and theoretical data, neither the existence nor the nonexistence of non-carbon fullerene polymorphs can be concluded. However, since sp^2 bonding is energetically more favorable for C_N than for Si_N, in the latter there are no caps and no plane structures which play a crucial role in fullerene formation. It seems that the mechanism of formation of such complexes for carbon and silicon is different. Taking into account the fact that the fullerene structure is not the global minimum for either carbon or silicon and in combination with the observable tendency of silicon clusters to have a spherical form, one can assume that under certain conditions processes similar to Stone-Wales rearrangement from polycyclic carbon structures to fullerene is also possible for silicon. Currently there is no common opinion on this issue. However, in addition to the notes about direct syntheses of non-carbon fullerenes, it is possible to specify some new synthetic approaches to the formation of silicon clusters.

The condensed analogues of the fullerenes have been produced in the well-crystallized hexagonal phases of Na-In-Z (Z=Ni, Pd, and Pt) [25]. A typical molecule in this new class has the formula of $Na_{96}In_{97}Z_2$, where Z represents nickel, palladium, or platinum. Such a cluster consists of an In_{74} cage surrounding a sodium cage which in turn encloses In_{10}-Z units.

Another way of constructing non-carbon, fullerene-like curved molecular surfaces has been proposed by Harada et al. [18]. Following their initial suggestion, it is possible to utilize C_{60} as the reactive core and to attach atoms of elements known to form strong carbide bonds onto the surface of C_{60}. Particularly, *ab initio* calculations have shown that the formation of the $C_{60}@Si_{60}$ complex is energetically favorable (Fig. 2) [19]. These investigations were extended into all isovalent IV main group fullerene-like compounds: C_{60}, Si_{60}, Ge_{60}, Sn_{60}, and Pb_{60} [37].

Tables 2 and 3 summarize the optimized geometry and energy parameters for C_{60}, Si_{60}, Ge_{60}, Sn_{60}, and Pb_{60} obtained at the Hartree-Fock and DFT levels. It is shown that absolute bond alternation increases from C_{60} to Sn_{60} and then significantly decreases for Pb_{60}.

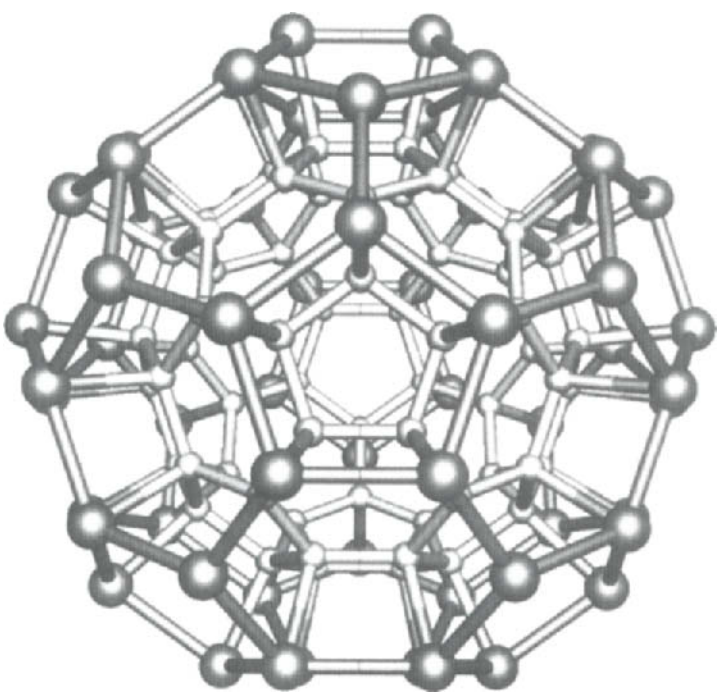

Fig. 2. Molecular structure of the $C_{60}@Si_{60}$ complex.

TABLE 2

Selected structural and energetic parameters for the C_{60}, Si_{60}, Ge_{60}, Sn_{60} and Pb_{60} compounds (HF/Lanl1DZ level). All distances are in angstroms; energies and HOMO-LUMO gaps are in atomic units

		HF/Lanl1DZ				
		C_{60}	Si_{60}	Ge_{60}	Sn_{60}	Pb_{60}
R_1	Distance	1.3797	2.1883	2.3137	2.6613	2.9184
	Mulliken overlap population	0.3177	0.4957	0.5217	0.4354	0.2180
R_2	distance	1.4559	2.2656	2.3981	2.7503	2.9613
	Mulliken overlap population	0.2738	0.3576	0.4242	0.3208	0.2092
bond alternation		0.0762	0.0773	0.0843	0.0890	0.0429
average diameter		7.080	11.091	11.736	13.473	14.601
total energy		-2271.09538	-224.81941	-219.20632	-195.64533	-200.81336
isolated atom energy		-37.59892	-3.61394	-3.53918	-3.17976	-3.28558
cohesive energy		-15.16015	-7.98244	-6.85535	-4.85938	-3.67797
HOMO-LUMO gap		0.2720	0.1610	0.1501	0.1322	0.0580

TABLE 3

Selected structural and energetic parameters for the C_{60}, Si_{60}, Ge_{60}, Sn_{60} and Pb_{60} compounds (B3LYP/Lanl1DZ level). All distances are in angstroms; energies and HOMO-LUMO gaps are in atomic units

		Becke3LYP/Lanl1DZ				
		C_{60}	Si_{60}	Ge_{60}	Sn_{60}	Pb_{60}
R_1	distance	1.4041	2.2196	2.3620	2.7232	2.9690
	Mulliken overlap population	0.3530	0.4199	0.3531	0.3076	0.1721
R_2	distance	1.4638	2.2769	2.4259	2.7903	2.9821
	Mulliken overlap population	0.3487	0.3254	0.2828	0.2539	0.1633
bond alternation		0.0596	0.0572	0.0638	0.0670	0.0131
average diameter		7.149	11.183	11.910	13.710	14.757
total energy		-2285.72151	-232.81672	-226.6558	-203.51826	-209.49898
isolated atom energy		-37.78697	-3.71926	-3.64561	-3.28343	-3.39247
cohesive energy		-18.50316	-9.66070	-7.91882	-6.51208	-5.95048
HOMO-LUMO gap		0.1038	0.0550	0.0364	0.0118	0.0113

The most important quantity for understanding the trends in the formation of fullerene-like molecules is the cohesive energy, defined as the difference of the total molecular energy and the sum of the energies of the isolated atoms. As expected, the cohesive energy decreases considerably from C_{60} to Pb_{60}. The maximum HF (B3LYP) value of -15.160 a.u. (-18.503 a.u) corresponds to C_{60}, and the minimum value -3.677 a.u. (-5.950 a.u.) corresponds to Pb_{60}. The other values lie in between and are relatively close to each other.

On the basis of the molecular orbital energies, all the non-carbon clusters considered seem to be better electron donors and better electron acceptors than C_{60}. They also possess lower electronically excited states and therefore should display enhanced nonlinear optical properties. Interestingly, the energy gap, which plays a direct role in the determination of the metallic behavior of the system, changes negligibly when one considers the HF level data for the semiconducting Si and Ge or the metal Sn type clusters.

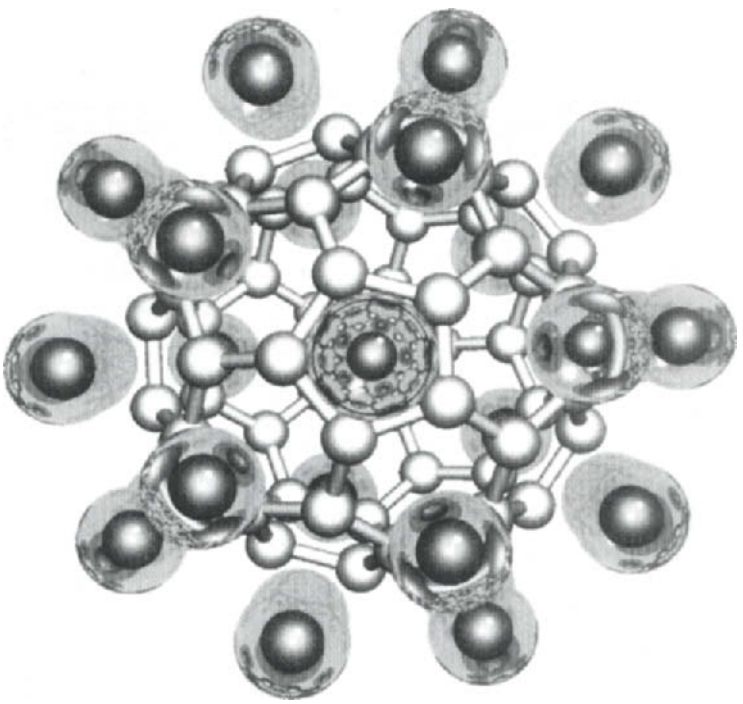

Fig. 3. Molecular structure of the $Ti_{12}@C_{60}$ complex.

As expected, for Ge_{60} the obtained data is rather similar to the one for Si_{60}, but it was also found that the molecular parameters for Sn_{60} are close to the appropriate values for both Si_{60} and Ge_{60}. In light of the method offered by Harada et al. [18], the given circumstance opens the opportunity for the synthesis of new metal-coated fullerenes like $Si_{60}@Sn_{60}$, $C_{60}@Ti_{32}$ (Fig. 3), and others with rather unusual properties which are interesting both from chemical and nanotechnological points of view.

3. FULLERENE FORMATION MECHANISM

A common technique of the macroscopic production of fullerenes is the arc-discharge method under the controlled pressure of an inert gas proposed by Haufler et al. [38]. Usually the generated fullerenes consist of 80% C_{60}, 15% C_{70}, and a small amount of the higher fullerenes.

In spite of the number of investigations, the formation mechanism of fullerenes is not clear. Several models have been proposed based on experimental insights and theoretical calculations (see, for example, the detailed review of Yamaguchi and Maruyama [39]). Haufler et al. [38] concluded that the growth of a hexagonal network is the result of the addition of carbon dimers and trimers. They stated that the pentagons are essential for curvature and for decreasing the number of dangling bonds. On the other hand, the interaction between two neighboring pentagons should result in a strain on the network system which is too high, so the "isolated pentagon rule" was assumed.

Quite different precursors to the fullerene structure, such as a piece of a graphite sheet [40] or a bucky tube, were also proposed [41]. Alternately, Heath [42] proposed a model for the clustering sequence in which there is a linear chain of carbon atoms up to C_{10}, rings in the C_{10}-C_{20} range, and a fullerene type structure for C_{30}. He claims that the successive C_2 additions follow until the isolated pentagon rule is satisfied. Recently, the drift tube ion chromatography experiments of laser vaporized carbon clusters show the existence of polycyclic rings and the possibility of annealing such a structure to a fullerene [43].

Although these models explain some experimental results, it is still difficult to decide which model is more realistic. Yamaguchi and Maruyama [39] have performed molecular dynamic calculations to simulate the clustering process of carbon atoms. The classical many-body potential function for carbon atoms developed by Brenner [44] was used. The clustering process was simulated under controlled temperature conditions. Translational, rotational and vibrational temperatures of each cluster were controlled to be in equilibrium. Special attention was paid to the structure and vibrational temperature of precursors. It was found that the structure of clusters obtained after simulations depends on the temperature T, the yielding graphitic sheet for $T< 2600$ K, the fullerene-like caged structure for $2600\ K < T < 3500$ K, and a chaotic 3-

dimentional structure for T > 3500 K. Through the detailed trace of precursors, it was revealed that the key feature of the formation of the caged structure is the chaotic 3-dimentional cluster of 40 to 60 atoms which has large vibrational energy. If precursors were kept under lower vibrational energy, the successful growth of 2-dimentional graphite-like structures was observed. The perfect fullerenes were finally obtained in the process of annealing at 2500 K after the Stone-Wales transformations (migration of pentagons without the change of the total number of pentagons and hexagons).

In summary, the main similarity among the proposed models is the concept that flat or caged polycyclic species are considered as precursors. It is also of interest that fullerenes are not the global minimum energy species under formation conditions and may exist in the whole range of the phase diagram [45], so the formation process of these compounds must be kinetically controlled. Therefore, the extraordinarily high temperature stability of caged structures is key to the preference of fullerene over diamond or graphite.

A molecular dynamic simulation of the collision of a carbon atom and a fullerene molecule was performed recently to demonstrate a new method of producting a fullerene molecule with defects [46]. Such simulations can be considered both a model of an artificial process of atomic implantation and a model of collisions which can occur in the hot carbon vapors.

Molecular dynamic calculations (on the basis of the semiempirical MNDO force field) were performed for two mutual orientations of a fullerene molecule and the direction of the implanting atom (Fig. 4a). Fig. 4b shows the dependence of the threshold energy of formation of the endohedral complex $C@C_{60}$ (vertical axis) for Orientation I. The obtained results show that the process of formation of endohedral complex proceeds as follows. The implanting atom passes a central part of a five-member (or six-member) ring, cavity of cluster, and is reflected from an opposite side of a cluster. This process continues since the basic part of kinetic energy is not transferred into the vibrational energy of a molecule. The vertical lines of Fig. 4 correspond to the head-on collisions of the implanting atom with the atoms of the five-member face of a molecule. At the top level of Fig. 4 the isolines of the same surface are presented.

Similar results were obtained for the second orientation of a molecule. The minimal kinetic energy of an implanting atom required for the penetration of a potential barrier and the formation of an endohedral complex is 6 eV for the direction through the center of a six-member face (11 eV for the direction through the centre of a five-member face). If the energy becomes greater than 16 eV for trajectories through the center of a five-member face (25 eV for a six-member face), implanting atoms do not reflect from the opposite side of a molecule and pass through it. If the kinetic energy of the implanting atom exceeds 40 eV, head-on collisions lead to the fragmentation of a fullerene. The

implanting atom knocks out two atoms of a fullerene on the opposite sides of the sphere, and rising instability results in the destruction of the system (Fig. 5c).

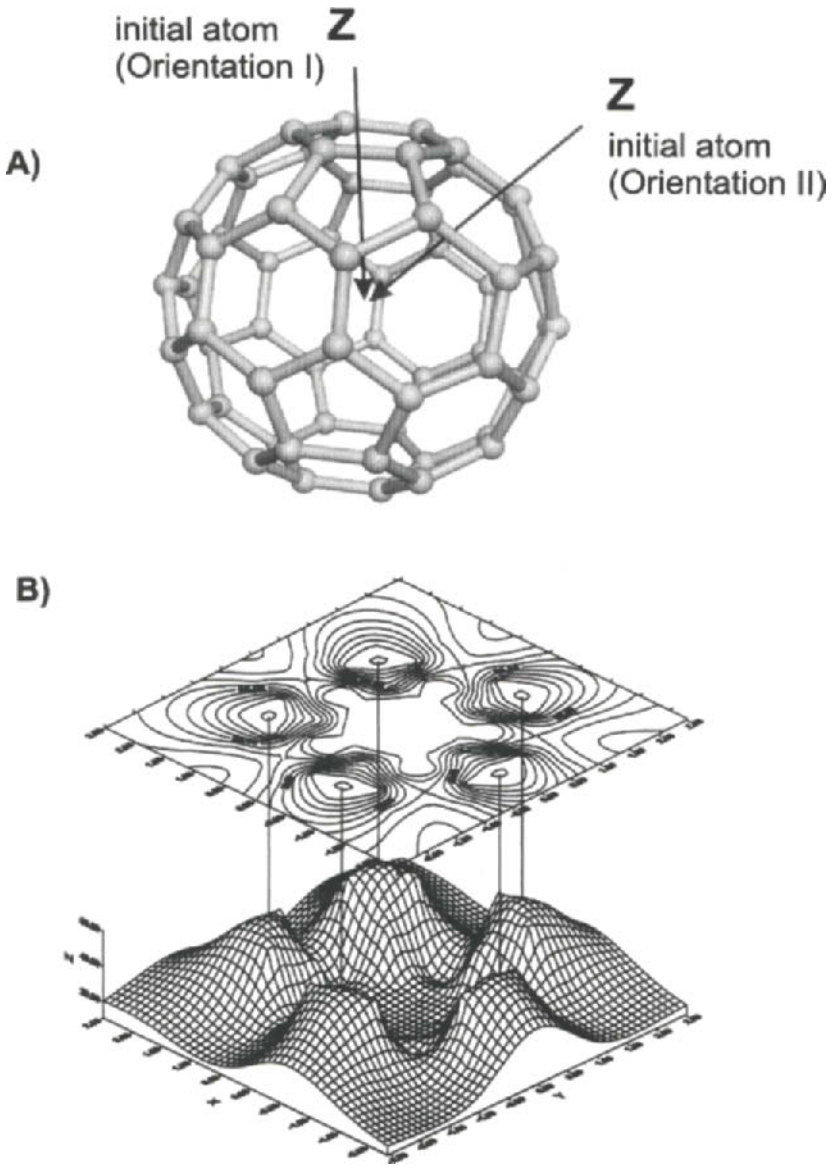

Fig. 4. Molecular dynamic calculations. (a) Mutual orientation of implanted atom and fullerene. (b) Pattern of penetration energy for the five-member ring.

Fig. 5 shows some other structures which are the result of molecular dynamic calculations: the C_{59} cluster (the Fig. 5a), the C_{58} cluster (Fig. 5b), and interesting cylindrical structures (Fig. 5d) which can be used as precursors for carbon nanotube.

Based on the discussed effects a new method for the creation of an artificial relief on the fullerite surface with accuracy up to 1 nm is offered. Because defects arise instead of molecules that have a strict identity, the geometrical characteristics of the required artificial structure can be controlled very precisely. It should be noted that such accuracy is far beyond the possibilities of contemporary lithographic techniques.

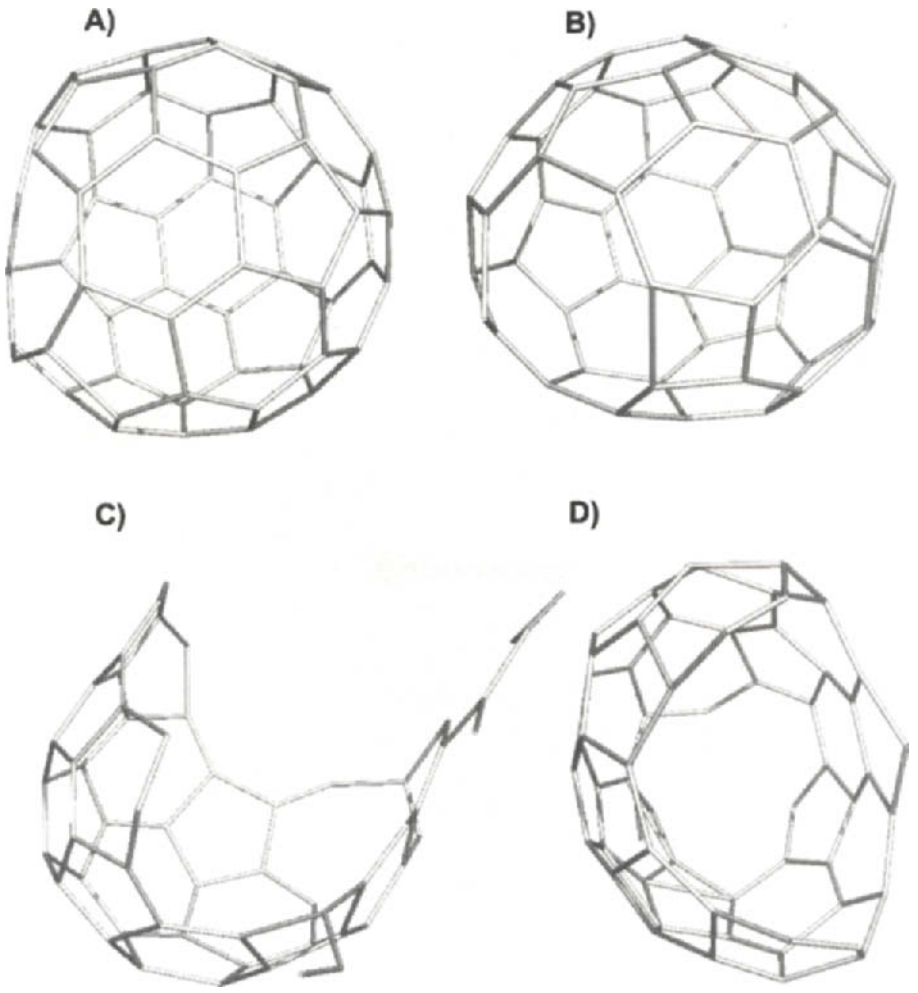

Fig. 5. Selected defects of C_{60} obtained during molecular dynamic simulations:
C_{59} cluster (a); C_{58} cluster (b); destroyed C_{60} (c); precursors for carbon nanotube (d).

4. FULLERENE MOLECULES WITH DEFECTS

The design and production of cluster assembled materials is a rapidly growing area in the fields of applied science and technology. Such systems provide a new way of producing materials with unusual properties. The unique properties of fullerene molecules allow for the assumption that they will be widely used in the future for the creation of such materials.

Crystal lattice defects and impurities significantly influence the properties of the traditional materials. For example, the dislocation structure changes the mechanical characteristics or pinning centres impact on superconductivity phase transition. In the case of solid C_{60} it is possible to expect that this influence is even more distinct because, along with the defects of a crystal lattice in fullerite, the various defects of molecules creating this lattice are observed [47,48]. The isomers of the C_{60} and C_{58} clusters, the $C_{59}M$ type clusters, and other carbon clusters have been synthesized but in insignificant quantities [49-51]. Also the strong influence on the electronic structure is rendered by endohedral inclusions in C_{60}. Since the radius of the fullerene molecule is about 3.5 angstrom, many atoms and small molecules can be placed inside the C_{60} sphere [52-54].

Despite the interesting properties and possible applications, details concerning the formation of such defects, their structures and influence on the physical and chemical properties remain scarcely investigated.

When graphite, impregnated with the salt of metal, is evaporated in the mass spectra corresponding to the formed carbon clusters, there are peaks that can be related to the $C_{60}M$ species (M=La, Cu, Na, K, U, etc.) where atoms of metal are located inside of C_{60} [55]. The formation of such endohedral complexes was also detected by other experiments [56-59].

In previous works [56,57] it is shown that during the collisions between C_{60}^+ and He with an impact energy of about 8 keV, C_nHe fragments (where n=46, 48, 50, 52, 54, 56, and 58) are formed. In works [58] and [59], in similar experiments the formation of the endohedral complexes $C_{60}He^+$, $C_{60}D_2^+$, $C_{60}Ne^+$ and $C_{60}Ar^+$ was also observed.

In the case when in a cavity of a fullerene molecule there is a potassium atom, the first principles calculations show that the 4s electron of the K atom passes to the external shell of C_{60} [8, 60]. If this cluster is in face centered cubic (f.c.c.) C_{60}, an additional electron will be delocalized around the fullerene. Thus, the $C_{60}K$ cluster can be used as the donor in a C_{60} semiconductor. Similarly, the atoms of halogens, located inside C_{60}, can act as acceptors. Such phenomenon opens the opportunity to create new materials in which fullerene molecules will play the role of atom-like building units.

In the work [61], a tight-binding method was used to study isomers of C_{60}. Fig.6 presents one of such species that preserves the general number of pentagonal and six-member faces of a molecule.

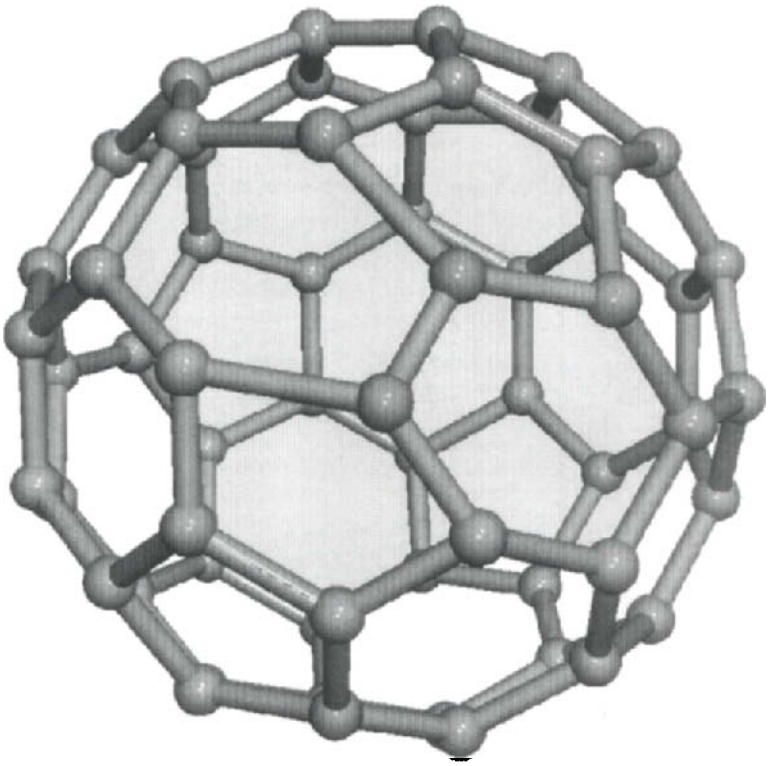

Fig. 6. The simplest isomer of C_{60} which preserves the general number of pentagonal and six-member faces of a molecule.

In order to create such a defect it is necessary that the atoms designated A and B move to positions A_1 and B_1. The calculated value of 1.3 eV represents the energy of formation of such structures.

In such isomers the degeneration of electronic levels is removed, and the gap between the occupied and free states decreases in comparison with the ideal fullerene molecule. It was found out that, if the fullerene molecule contains two defects of the type described above, the energy of their formation is approximately double the energy of formation of one defect (i.e., 2.6-2.7eV) and is practically independent of the relative positioning of these defects.

In recent studies [62, 63], closed shell defects of the fullerene molecule, C_{58}, C_{59}, and also the C_{60}@C endohedral complex, were considered. This class of defects is promising for technological applications because the investigated species are similar to the ideal C_{60}, do not change the neutral state of the material, and are thermodynamically stable.

Ab initio quantum-chemical calculations without symmetry restrictions have been performed to determine the structure and electronic spectra of the investigated complexes. The SCF MO calculations at the Hartree-Fock and hybrid DFT levels of theory were carried out. The STO-3G and 6-31G(d) basis sets were employed.

Fig. 7 and Tables 4 and 5 summarize the optimized geometry and energy parameters for the $C@C_{60}$ complex. Two different sites (Type A and Type B) for the endohedral carbon atom were found. The first position is near the center of the five-member faces of the fullerene molecule, while the second one is slightly shifted from the center of the six-member face in the direction of the neighboring five-member face (the B3LYP/6-31G(d) level of theory).

The formation of the endohedral complex leads to a significant change in the cohesive energy. The values of the Mulliken overlap populations underscore the fact that the formed bonds are much weaker than the bonds of a C_{60} cluster. The change in total energy of the system is caused basically by the symmetry break and local distortion of the molecular structure. The total energy of the Type A complex is slightly higher than the total energy of Type B.

Because of the small difference in total energy between complexes of Type A and B, the question arises of whether the transition of the atom from one stable position into another is possible under the influence of thermal fluctuation. Molecular dynamics calculations (with the MNDO force field model) show that the dynamic barrier of migration is only 0.12 eV for the transition from site A into site B and 0.16 eV for the transition between the sites of type A.

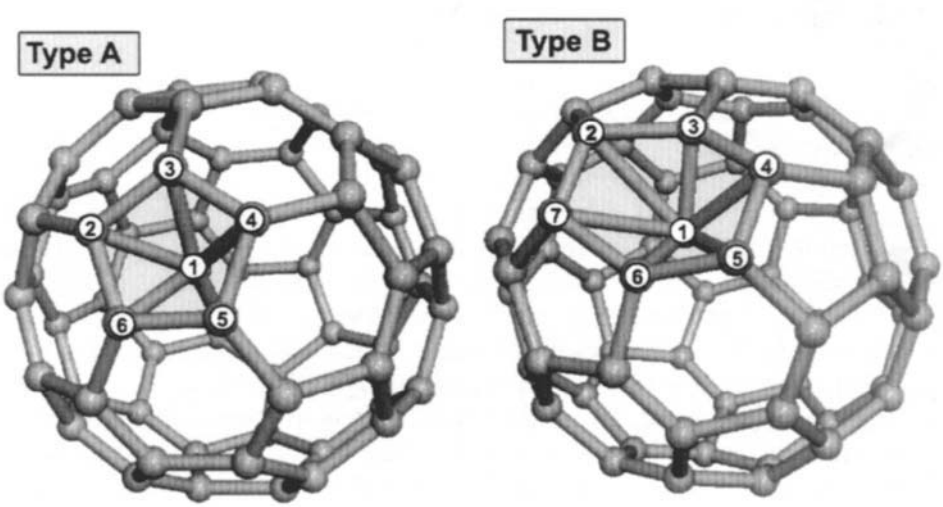

Fig. 7. Two different types of location for the carbon atom inside the fullerene molecule and atomic numeration scheme.

TABLE 4

Selected geometrical and energy parameters of the $C@C_{60}$. All distances are in angstroms; energies and HOMO-LUMO gaps are in atomic units

	Type A			Type B		
	HF/STO-3G	HF/6-31(d)	B3LYP/6-31G(d)	HF/STO-3G	HF/6-31G(d)	B3LYP/6-31G(d)
Bond length:						
$C_1 - C_2$	1.807	1.704	1.759	1.796	1.693	1.691
$C_1 - C_3$	1.805	1.719	1.758	1.795	1.693	1.691
$C_1 - C_4$	1.731	1.688	1.742	1.634	1.624	1.776
$C_1 - C_5$	1.731	1.688	1.742	-	-	-
$C_1 - C_6$	1.805	1.719	1.758	-	-	-
$C_1 - C_7$	N/A	N/A	N/A	1.634	1.625	1.776
HOMO-LUMO gap	0.21	0.25	0.04	0.27	0.20	0.06
Total energy	-2281.2679	-2309.3944	-2324.0102	-2281.3004	-2309.3939	-2324.0066

TABLE 5

Mulliken overlap population of the $C@C_{60}$ selected bonds

	Type A			Type B		
	HF/STO-3G	HF/6-31(d)	B3LYP/6-31G(d)	HF/STO-3G	HF/6-31G(d)	B3LYP/6-31G(d)
Mulliken overlap population:						
$C_1 - C_2$	0.068	.017	-.042	0.029	-.017	-.057
$C_1 - C_3$	0.064	.053	.005	0.029	-.017	-.057
$C_1 - C_4$	0.095	.033	-.026	0.240	.213	.069
$C_1 - C_5$	0.095	.033	-.026	-	-	-
$C_1 - C_6$	0.064	.053	.005	-	-	-
$C_1 - C_7$	N/A	N/A	N/A	0.240	.213	.069

Such findings indicate that even at room temperature a system with two metastable levels exists, and under certain conditions (for example, under the thermal fluctuations or at the expense of a laser pulse), the endohedral atom can migrate from one stable position in the molecular cage to another. This process is similar to the known effect of caging (easy migration) of the impurity atom in the lattice of heavier atoms; however in the case of the studied system all atoms are of the one type.

Fig. 8 displays the electronic levels of investigated complexes near the HOMO-LUMO energy gap obtained from the HF/6-31G(d) level calculations. Unlike an ideal fullerene molecule in which all sites of the atoms are equivalent, one can see a reduction in the degeneration of electronic levels. Thus, the higher the energy of formation for such defects, the larger the difference between the electronic structure of such species and the parent fullerene. Besides the reduction in the degeneration of states, the decrease of the energy gap between the HOMO and LUMO levels is also observed for all types of defects.

Full geometry optimizations were also performed for the C_{58} and C_{59} clusters. Optimized structures of these complexes are presented in Fig. 9. It is shown that in the case of the C_{59} cluster, distortions of the ideal structure are much larger than in the case of C_{58}.

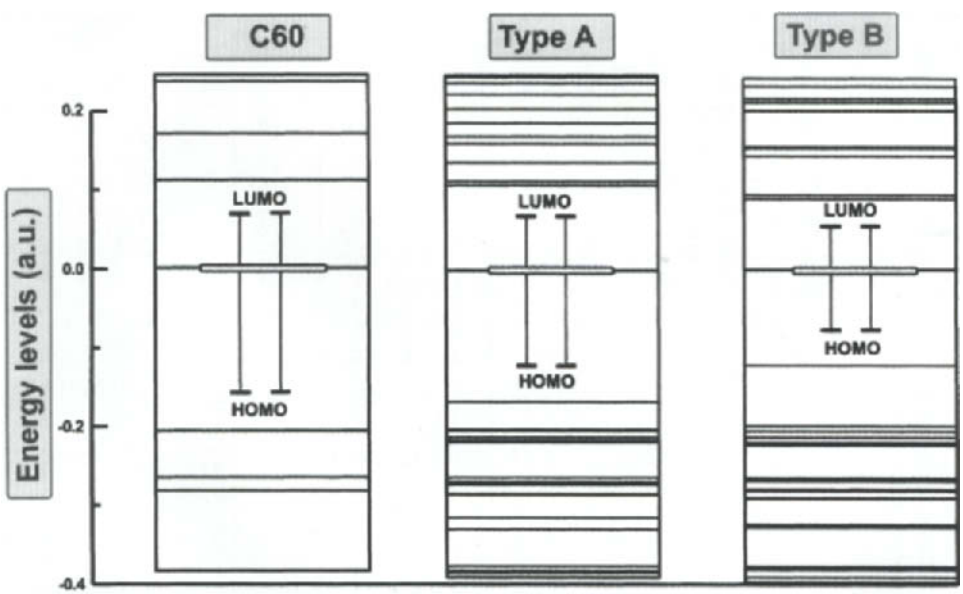

Fig. 8. Electronic energy levels of C_{60}, and $C@C_{60}$ near the HOMO-LUMO gap. HF/6-31G(d) level of theory.

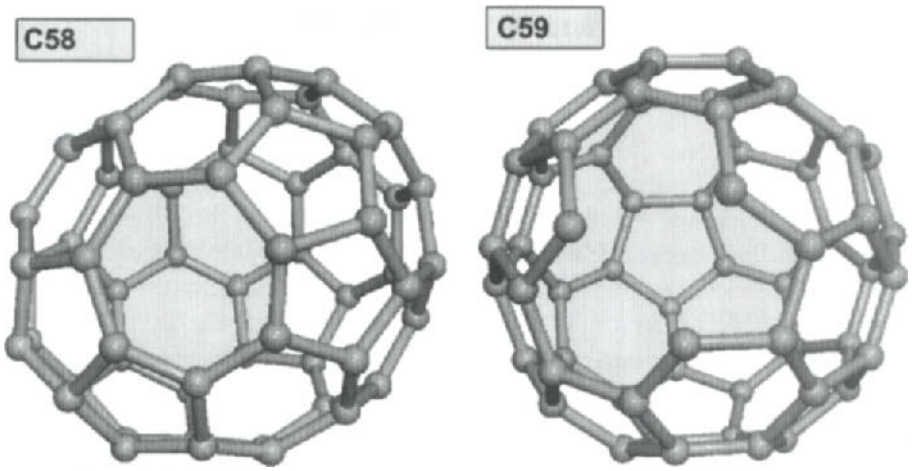

Fig. 9. Molecular structure of the C_{58} and C_{59} clusters.

In addition, carben-like terminal groups make such clusters extremely reactive. All of these factors result in a significantly lower value of cohesive energy. A comparison of the calculated energies for C_{60}, C_{58}, and C_{59} (Table 6) indicates that the more energetically favorable defragmentation of C_{60} is, in this situation, the simultaneous removal of a pair of atoms.

5. SOLID FULLERENE —FULLERITE

Solid fullerene displays interesting properties. After condensation, the C_{60} molecules forms a face centered cubic (f.c.c.) structure: fullerite. This is the only material which consists of quasi-spherical molecules, all atoms of which are of one kind. X-ray dispersion experiments show that fullerite forms a closely packed f.c.c. crystal in which the distance between the nearest molecules is 10.04 Å [2]. The least distance between two molecular surfaces is 2.9 Å, and the distance between the nearest atoms in a crystal is 1.42 Å. Thus, the experiments specify that the molecular structure of C_{60} is preserved in the solid. Strong orientational disorder is observed at room temperature [64] and this disorder decreases as the temperatures decreases.

TABLE 6
Total energy (atomic units) of the investigated complexes at the HF/6-31G(d) level of theory

	C58	C59	C60	C61 Type A	C61 Type B
	HF/6-31G(d)	HF/6-31G(d)	HF/6-31G(d)	HF/6-31G(d)	HF/6-31(d)
Total energy	-2195.9311	-2233.6285	-2271.8304	-2309.3944	-2309.3939

Ab initio DFT calculations using local-density approximation (LDA) reveal that the total energy of isolated C_{60} as a function of the lattice constant. The results of this study also provide details concerning the band structure of f.c.c. C_{60} [8]. They indicate that C_{60} molecules are condensed mostly by the weak van der Waals forces. The cohesive energy amounts to 1.6 eV per C_{60} which is much smaller than the energy typical for the C-C bond (~3 eV). It was also shown that the deeper electronic levels of C_{60} have very little dispersion when they form an f.c.c. crystal. These levels are considered to be the bonding states of the σ bonds. On the other hand, most electronic levels between –6 and +7 eV have considerable dispersion in f.c.c. C_{60}. The authors have assigned those levels as the π bond states because the π bonds spread outside the molecules more than σ bonds and have large intercluster overlap. Electronic levels above 7 eV again have little dispersion and correspond to the antibonding states of the σ bonds. The energy gap of the C_{60} molecules remains finite when C_{60} forms a solid. The recent calculations indicate that the f.c.c. C_{60} crystal is a direct-gap semiconductor with an energy gap of 1.5 eV [8]. The transition between the valence band top and the conduction band bottom is optically forbidden.

The first order phase transition from the low temperature simple cubic lattice to f.c.c. appears in solid C_{60} at T_C=249 K [65,73]. Treating the C_{60} molecule as an undistorted truncated icosahedron, the rotation angle G between them was found to be about 22° [68-70]. This arrangement of molecules implies that six of the 12 pentagonal faces of a molecule, characterized by the low charge density, face inter-pentagon "double" bonds on the neighboring molecules which possess high charge density. A "donor-acceptor" electrostatic interaction is invoked to explain this arrangement. This additional connecting mechanism is the reason for the sharp increase in the interacting potential. Therefore T_C is high despite the highly spherical shape of a molecule. Above T_C a molecule rotates irrespective of the neighbors.

There is also evidence concerning the presence of a "higher order" phase transition at about T_{C2}=90 K [69, 73]. The authors propose a two-state model to describe the low temperature ($T < T_{C2}$) structure of C_{60}, according to which any molecule has one of two possible orientations, designated I and II, corresponding to rotation for G_1=G and G_2=G+60°, respectively, where G=22°. In contrast to orientation I, which has been described above, orientation II implies that six hexagons on an origin molecule face "double" bonds on neighbors. The probability ***p*** that a given molecule has orientation I was found to be independent of temperature and equal to 0.835 for $T < 90$ K. This probability decrease with increasing T above 90 K, reaching a value of about 0.61.

The neutron scattering results can be directly compared with molecular dynamics simulations. A number of works [72-74] was devoted to molecular dynamic modeling of the orientational ordering in fullerite. Most of them used

the model of rigid C_{60} molecules with the atoms interacting according to classical potentials. The Lennard-Jones (12-6) potential, the Morse potential, and a potential with the angular part expanded in terms of spherical harmonics of the sixth order were used.

Original calculations using only the intermolecular van der Waals atom-atom interaction (Lennard-Jones potential) [72] predict that librations occur in a band of width ~0.8 meV which is centered at ~1.3meV. (The librations band was estimated from the density of phonon states as the result of the Fourier transformation of the velocity autocorrelation function.) These data indicate that the potential used in this work is about a factor of four too small and that it is not as rotationally symmetric as is indicated by the measurements [73]. Utilization of more complicated potential functions does not improve significantly the underestimated values of T_c obtained which confirms the model mentioned above. In order to improve predictions, the parameters should include, in an obvious way, the double bonds and electrostatic potentials in addition to van der Waals interactions. The modeling that includes these specific contributions to the intermolecular interaction was carried out in work [74] and allows obtaining a value of T_c which is close to the reality. However other quantitative characteristics, such as the rotational diffusion factor, were reproduced with a large error (about 100%). This is evidence for the essentially quantum character of the interaction among C_{60}.

Application of the modern technology of fullerite production yields a product where the main impurity in a material is C_{70} molecules. Distortions, which they cause in an ideal lattice, are important for practical applications. It was found, that carbon molecules of different sizes practically do not mix up in fullerite and form the precisely outlined areas similar to domains [75].

6. SUPERCONDUCTIVITY IN ALKALINE METAL DOPED FULLERITE

6.1. Mechanism of superconductivity

The crystal structure of fullerite has been well characterized [76-78]. There are freely available tetrahedral and octahedral voids in a crystal lattice of fullerite, and the metal ions can be located in such voids. For monocrystals, it is established that A_3C_{60} forms the f.c.c. lattice (lattice constant is 14.24 Å for A=K) and A_6C_{60} forms the body centered cubic (b.c.c.) lattice (lattice constant 11.39 Å for A=K) where A is an alkaline metal [76]. In the f.c.c. structure the ions of C_{60}^{-3} are randomly distributed between two orientations distinguished from each other by a 90^0 rotation, while in the b.c.c. phase the ions of C_{60}^{-6} are orientationally ordered at room temperature [77].

The f.c.c. lattice constant increases with the increasing alkali metal ion radius. The interstitial voids can accommodate K^+, Rb^+ and Cs^+ ions, but the f.c.c

structure becomes unstable for Cs_3 which possesses the Pm3n A15 structure and is only a superconductor under additional pressure [78]. Doping with the smaller Na^+ ion results in an ease rotation of C_{60} and leads to the orientationally ordered Pa3 structure at low temperature [79]. It was also found out that the C_{60}^{-3} molecules in these structures are polymerized (although probably incompletely) [80].

Fig. 10 presents the fragment of a lattice of a solid C_{60} (f.c.c. structure) and the sites into which the atoms of alkaline metals can be placed. For each C_{60} molecule there are two tetrahedral and one octahedral position for the interstitial atom, with radii of 1.12 Å and 2.06 Å, respectively [76]. The radii of ions of alkaline metals (0.97 for Na, 1.33 for K, and 1.47 Å for Rb) approximately coincide with the sizes of these sites and, when completely filled, result in the A_3C_{60} structure. The A_1C_{60} high temperature structure is similar to A_3C_{60}, but only the octahedral sites are occupied.

Additional doping results in the formation of the body centered tetragonal (b.c.t.) structure of A_4C_{60} and the b.c.c. phase A_6C_{60} (Fig. 11) in which the distinction between the tetrahedral and octahedral sites disappears, and for each fullerene molecule there exists six tetrahedral positions of interstitials. According to [76] the change of crystal packing from f.c.c. to b.c.c. is not accompanied by a significant displacement of C_{60} molecules. For equal numbers of fullerene molecules, the volume of the b.c.c. phase is only 9% larger than the volume of the f.c.c. phase.

A first principles DFT investigation of the electronic structure of potassium doped C_{60} was carried out by Saito and Oshiyama [60]. Three different positions of the potassium atom were considered: the endohedral center of C_{60} and the tetrahedral and octahedral interstitial sites. The most stable position has been predicted for the tetrahedral site with a cohesion energy of ~10 eV, followed by the octahedral site (~8 eV) and the center of the fullerene molecule (~6 eV). It was revealed that, in all cases, the 4s electron of the K transfers to the LUMO level of C_{60}. Thus, in the f.c.c. A_3C_{60} phase three valence electrons of alkaline metals transfer to the lowest unoccupied level of each fullerene molecule and form the half filled conductivity band. In the case of b.c.c. A_6C_{60}, the t_{1u} electronic level of fullerene is completely filled by electrons, and the material is not conductive.

At cooling films formed from fullerene, which was doped by potassium, and possess a K_3C_{60} structure, at T_c =18 K a transition into a superconductive state was detected [13]. Then for materials doped by Rb and Cs, a T_c of 33 K was achieved [6]. Currently, the maximum reporting temperature of a transition into a superconducting state amounts to 45 K [14] for fullerite doped by Rb and Ta. These values of T_c concede only to ceramic superconductors, but in comparison with the latter, doped fullerite has considerably higher values of critical currents.

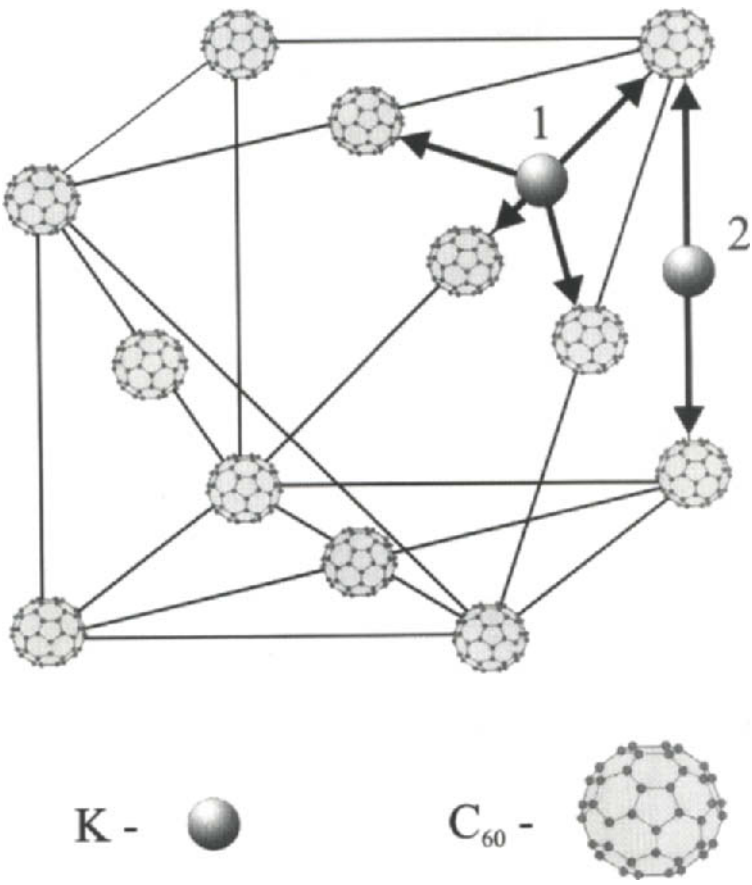

Fig. 10. Scheme of f.c.c. lattice. The tetraherdral (1) and octahedral (2) positions for a doped atom are shown.

The superconducting transition temperature in the class of A_3 materials is strongly correlated with the f.c.c. lattice parameter (although cubic symmetry is not required for superconductivity in the fullerites [78]).

As the mechanism of superconductivity in these doped fullerites was not clear, the greatest attention was directed to the standard mechanism of superconductivity. The conventional theory is based on the electron-phonon interaction and generalized in the Eliashberg equations which include the Bardeen, Cooper and Schrieffer (BCS) equation as a weak-coupling limit [78]. For real superconductors the ratio for the weak-coupling limit is close to the value of 3.52, and for stronger coupling materials it increases up to about 5.1 [78].

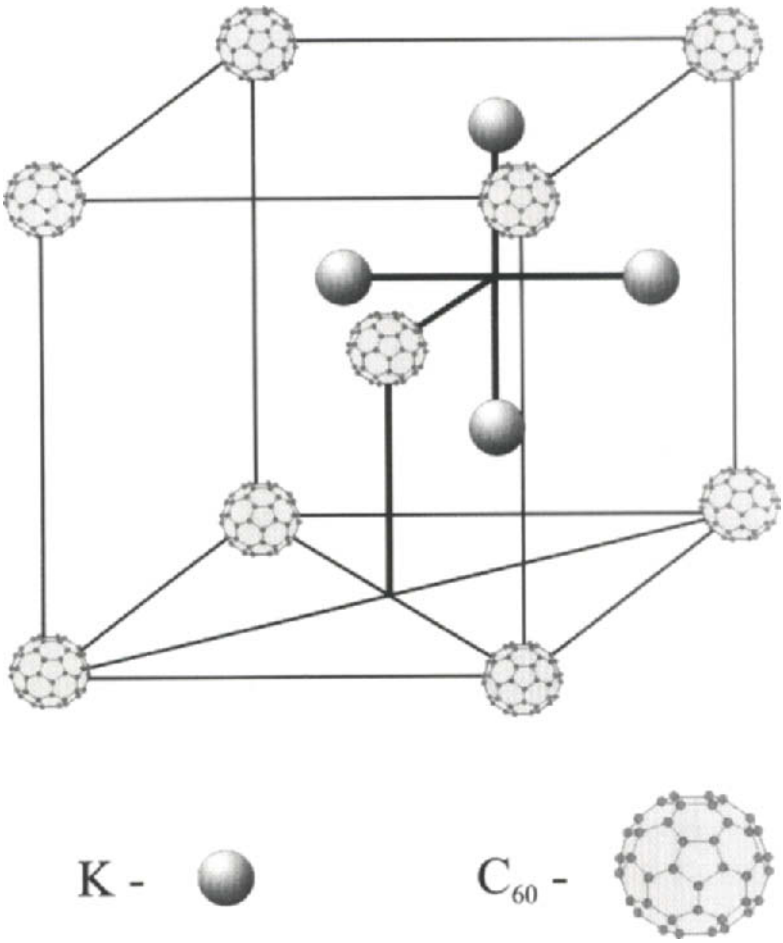

Fig. 11. Scheme of b.c.c. lattice. Some of the six tetraherdral position for doped atom is shown.

The contribution of the electron-electron Coulomb repulsion in fullerite is not well defined. The narrow conduction bands in the A_3C_{60} materials and the large values of the electron-electron Coulomb repulsion prompted development of the exotic all-electron pairing models [81]. In this model the electron screening under some conditions results in an effectively attractive interaction between electrons. However, nearly all observations can be understood by a conventional electron-phonon pairing mechanism [78] (although C_{60} based compounds do not satisfy Migdal's theorem).

In theoretical works [82, 83] the potential of coupling in solid C_{60} doped by alkaline metals was estimated. It was concluded that the coupling dominates in the vibrational modes of H_g and A_g symmetry. Thus the coupling is distributed

among the modes of low frequency, mainly radial and high-frequency — tangential.

Neutron scattering experiments [76] show that in the vibrational spectrum of K_3C_{60} and Rb_3C_{60} (in comparison with C_{60}), the 54 meV and 66 meV modes with H_g and T_{1u} symmetry disappear, probably because of electron-phonon interactions. This experiment confirms a theoretical picture [83]. At the same time the results of experiments [76] indicate that low energy librational modes do not have any abnormal shifts or changes of the form below T_c. This is evidence against the large contribution into electron-phonon coupling from the low energy librational modes that were predicted in [85].

Therefore, superconductivity observed in doped C_{60} can be explained in terms of the generalized BCS theory and electron-phonon interaction. The theoretical estimations using a tight-binding method have shown that with an increase in the lattice constant also the density of electronic states around the Fermi level grows. Therefore, the temperature of transition into a superconductive state is increased [60]. These facts are also evidence of the benefit of the traditional BCS mechanism of superconductivity.

It is necessary to note that if the lattice constant of doped fullerite grows it will result in a reduction in the gap between the states of conductivity electrons and internal electrons. In a limit, this gap becomes comparable with the value of Coulomb interactions of electrons of a fullerene molecule. In such a case the one-electron approximation is broken. Therefore, increasing a lattice constant by the introduction of ions of greater radii will increase the temperature of transition in a superconducting state only up to a certain limit [83].

6.2. Influence of fullerene structure defects on the properties of a superconductive state

One of the methods of rising critical currents in conventional superconductors is the introduction of defects of structure which work as the pinning centers for the vortex lattice. This method can also be applied for doped fullerite.

The defects of the C_{60} structure lower its symmetry. As a consequence some transitions between vibrational states that are forbidden for an ideal molecule become IR-active. Several works were devoted to the study of vibrational spectra of fullerene molecules for which some of the atoms were replaced by ^{13}C isotopes. They tried to address an important question concerning whether such replacement influences the physical properties of C_{60}. First of all, in view of the electron-phonon mechanism of superconductivity in doped fullerite, the question whether isotopical replacement results in a change in temperature of transition into a superconductive state was investigated.

In a previous work [86] the sharp reduction of T_c in isotopically mixed $^{13}C_n{}^{12}C_{60-n}$ (^{13}C contents — 60 %) was predicted. According to the authors, the

IR spectrum of such a sample contains many new intensive bands besides four IR active peaks corresponding to isotopically pure C_{60}. The authors explain this observation by the infringement of symmetry which makes originally inactive vibrations active. On the other hand, a study carried out with a sample containing about 30 % of ^{13}C has not confirmed the presence of any new IR-active bands (at least bands with significant intensity) [87]. It was found that the shift of vibrational frequencies of a molecule is inversely proportional to the square root of the mass of a molecule. Similar results were obtained in later studies [88, 89] (structure: 55 % ^{13}C) where the spectrum range between 500 and 600 cm^{-1} was investigated.

In a previous work [90] theoretical oscillator strengths, corresponding to IR-active vibrations of an isotopically mixed fullerene molecule, were calculated. The $^{13}C_n{}^{12}C_{60-n}$ structures (where n=10, 20, 30, 40, and 50) were considered. Two cases of isotopical replacement were investigated: atoms of ^{13}C were randomly distributed or were concentrated on the opposite poles of a C_{60} molecule. It was revealed that in the case when the vibrations of such molecules do not coincide with IR-active frequencies of homogeneous C_{60}, the oscillator strengths corresponding to these vibrations do not exceed 5 % of average value of IR peaks of isotopically pure C_{60}.

The effect of isotopical replacement was also investigated for the $^{13}C_1{}^{12}C_{59}$ structure corresponding to the natural contents of the ^{13}C isotope (about 1.1 %). Because of infringement of symmetry all vibrational frequencies of such molecules became IR active [90]. In line with the case of clusters characterized by large n considered above, the calculations have shown that the intensity of such peaks is very small in comparison with the intensity of the IR modes of a homogeneous fullerene molecule. Therefore, the most typical effect from replacement of one or several ^{13}C atoms in C_{60} is a smoothing of IR peak (about 1/6 from the initial value) corresponding to the vibration mode of T_{1u} symmetry [90].

In the same study [90] the influence of isotopical replacement on the temperature of transition into a superconductive state was also investigated. In linear approximations such replacement does not render the influence on coupling constants. Following is an estimation for transition temperature:

$$T_c=1.13\langle\omega\rangle_{log}\exp(-1/\lambda), \quad (1)$$

where T_c is proportional to the logarithmic average of normal vibrational modes [91].

According to [86] a reduction of T_c, corresponding to isotopical replacement, amounts to 0.6 °K for K_3C_{60} and 2 °K for Rb_3C_{60}. Therefore, supposing that the shift of T_c occurs only because of the change of logarithmic averages of intermolecular vibrations, for K_3C_{60}, the term given by $\langle\omega\rangle$log will

decrease by 3.4 % and for Rb_3C_{60} by 7.4 %. However, calculations [90] have shown that the predicted shift amounts to only 0.04%. Hence the aforementioned experimental results cannot be quantitatively explained by changes of $<\omega>_{log}$ term because of partial isotopical replacement.

Neglecting changes of normal modes of vibrations, $<\omega>_{log}$ is inversely proportional to the square root of the weight of a molecule. Thus, it is possible to write down:

$$T_c(BCS)=T_{c0}\sqrt{(M_0/M)}, \qquad (2)$$

where Tc_0 and M_0 are the temperature of transition into a superconductive state and the mass of an ideal fullerene molecule, respectively. M is the mass of an isotopically replaced molecule. In [90] the diagram of dependence dT_c/T_c from the number of ^{13}C atoms for the known experimental data was constructed. It was shown that this simple estimation is close to average for these results. Therefore, one can conclude that the strongly overestimated values of T_c are caused by discrepancies among the experiments.

The situation with isotopical replacement considered above is similar to what is observed in fullerene clusters with closed-shell defects: C_{61}, C_{58}, and isomers of C_{60} [46,63,92]. The introduction of additional (or the removal of existing) atoms in an ideal fullerene molecule also results in the removal of the degeneration of vibrational levels. As a consequence originally forbidden IR transitions became active (though unlike in the case of isotopical replacement the "constants of coupling" cannot be considered as constant).

Based on the results of calculations of the vibrational spectrum it is possible to estimate the influence of fullerene defects on the properties of the superconductive phase. As was mentioned above, T_c is proportional to the logarithmic average of normal vibrational modes. Because considered defects only locally distort the structure of the C_{60} shell, in the first approximation it is possible to consider coupling constants unchanged and therefore the $\exp(-1/\lambda)$ component as a constant.

Table 7 provides the values of $<\omega>_{log}/<\omega_0>_{log}$ term for several types of defect clusters (MNDO force field model) [93]. It is shown that for the defects of types A and B (Fig. 7) these values are rather large, and endohedral clusters significantly influence the properties of the superconductive state. However, utilization of endohedral clusters as the pinning centers requires further research because in the frame of this approach it is not possible to take into account electron-phonon interactions.

TABLE 7
Relative values of $\langle\omega\rangle_{log}$ (compared with the ideal C_{60}), %

	$\langle\omega\rangle_{log}/\langle\omega_0\rangle_{log}$, %
C_{61} Type A	-4.15
C_{61} Type B	-4.40
C_{61} Type C	-2.60
C_{58}	-0.97
Isomer of C_{60}	-1.41

7. ELECTRICAL CONDUCTIVITY OF THE FULLERENE MOLECULE

One of the most promising applications of fullerene molecules is nanoelectronics. Recently, several groups have reported the results of *ab initio* calculations of current-volt characteristics of the fullerene molecule [94,95]. These investigations were stimulated by scanning tunneling microscopy (STM) experiments in which the C_{60} molecules were adsorbed on metallic surfaces [96, 97] as well as the break-junction experiments [98] and the demonstration of a prototype of a molecular transistor on the basis of carbon nanotube [99].

The study of molecular scale devices has created the need for new theoretical tools which could be used for predictions of their structures and properties and to probe their new designs. Electronic devices are open systems with respect to electron flow, and a theoretical description of such devices should be done in terms of statistically mixed states which cast the problem in terms of quantum kinetic theory [100]. The only completely adequate theory that could currently address this task is the non-equilibrium Green's function formulation of many-body theory.

More practical approximations are based on the assumption of coherent movement of electrons throughout the device. According to Lang [101, 102] the solution can be obtained in the following way. First, within the framework of the density-functional formalism, the single-particle wave functions and self-consistent density distribution are found for the pair of bare metallic electrodes, assuming them to be identical in the presence of the bias voltage. Next, corresponding to each of these wave functions, a Lippmann-Schwinger equation

$$\Psi^{MA}(r) = \Psi^{M}(r) + \int d^3r' d^3r'' G^{M}(r,r')\delta V(r',r'')\Psi^{MA}(r'') \qquad (3)$$

involving a Green's function for the biased bimetallic junction

$$G^{M}_{Enn'} = \frac{(-1)^{n_X+n_Y+n'_X+n'_Y}}{2\pi^2 L^4}\int_0^\infty t dt g_{En_Z n'_Z}(t/L)\int_0^{\pi/2} d\phi \sin^2(t\cos\phi)\cos^2(t\sin\phi)$$
$$\times(t^2\cos^2\phi+\pi^2 n_X n'_X)(t^2\sin^2\phi+\pi^2 n_Y n'_Y) \qquad (4)$$
$$\times[(t^2\cos^2\phi-\pi^2 n_X^2)(t^2\cos^2\phi-\pi^2 n'^2_X)$$
$$\times(t^2\sin^2\phi-\pi^2 n_X^2)(t^2\sin^2\phi-\pi^2 n'^2_X)]^{-1}$$

should be solved to obtain a single-particle wave function for the total system consisting of the two electrodes plus the molecule. The superscripts M and MA refer, respectively, to the pair of bare biased metal electrodes and to the complete system consisting of the metal electrodes and the molecule between them.

These equations describe the motion of electrons scattered elastically by the potential $\delta V(r,r')$ which is the difference in potential between the complete system and the bare electrodes:

$$\delta V(r,r') = v_{ps}(r,r') + \left[v_{xc}(n^{MA}(r)) - v_{xc}(n^{M}(r)) + \int d^3r'' \frac{\delta n(r'')}{|r-r'|}\right]\delta(r-r') \qquad (5)$$

From these wave functions, the density distribution for the total system is obtained, and the problem is solved self-consistently using an iterative procedure. Finally, the electric current density in the full system is given by:

$$j^{MA}(r) = -2\int_{E_{FL}}^{E_{FR}} dE \int d^2K_{\parallel}\,\mathrm{Im}\{[\Psi^{MA}_{EK_{\parallel}-}(r)]^{*}\nabla\Psi^{MA}_{EK_{\parallel}-}(r),$$
$$\qquad (6)$$
$$\delta J = \int d^2R\bar{z}[j^{MA}(r) - j^{M}]$$

Implementation of this method to different structures shows that it can provide a qualitative description of quantum transport in nanostructures, but the jellium model of electrodes oversimplifies the molecule-electrode interaction which plays an important role in quantative theory.

To overcome this disadvantage another approach has been developed by Palasios et al. [94]. The main idea of this method involves performing a density-functional calculation of the molecule including part of the electrodes with the desired geometry (Fig. 12). For a sufficiently large number of atoms describing the electrodes, it is possible to represent the important properties of the bulk electrodes and to provide a correct description of the charge transfer. A crucial step of the method is to transform this finite system into an effectively infinite one. In order to do this, all but the *N* atoms forming the relevant atomic structure

of each electrode close to the molecule are removed from the Hamiltonian. The retarded Green's function associated with this reduced Hamiltonian is then transformed into the retarded Green's function of an infinite system:

$$G^r(\in) = (\in \hat{I} - \hat{H}_r + i\delta)^{-1} \longrightarrow [\in \hat{I} - \hat{H}_r - \hat{\sum}(\in)]^{-1} \tag{7}$$

Providing the initial system is large enough, a substitution of the fragment of the electrodes by effective self-energy should introduce no spurious effects, and it makes the system effectively infinite. The conductance can be calculated using the formula:

$$G = \frac{2e^2}{h} Tr[\Gamma_L G^r \Gamma_R G^a] \tag{8}$$

Although this method is suitable only for relatively small systems, the major advantage of this approach consists in the utilization of GAUSSIAN98 code which is well established in computational quantum chemistry.

The Palacios technique was recently applied to modeling STM experiments of the C_{60} molecule adsorbed on Al(111) electrodes with different geometries. Contacts from Al are not common in experiments, but in contrast to precious metals they create strong covalent bonds with carbon molecules. This is an important feature for practical implementations.

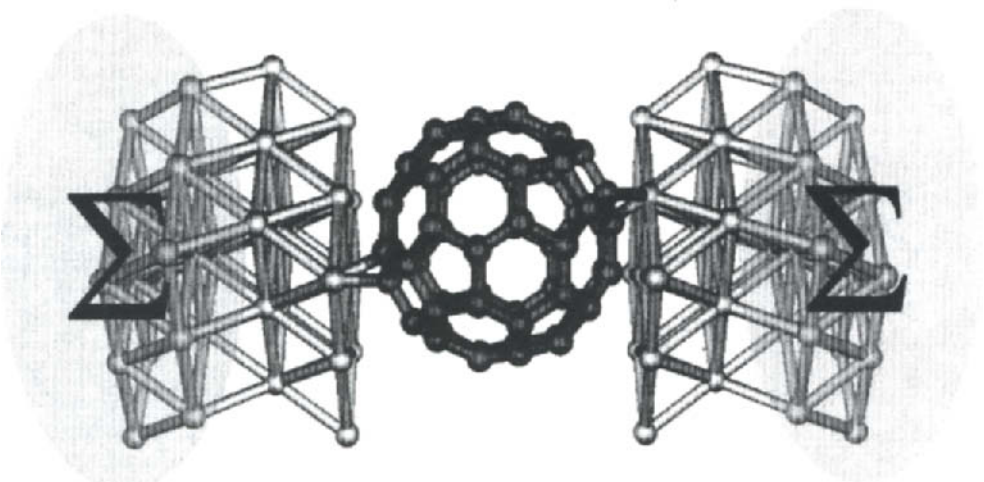

Fig. 12. Scheme of current-voltage calculations.

Molecular characteristics of the studied system have to be carefully defined. In Palacios' investigation, an initial geometry was chosen in such way that two opposite C atoms of the fullerene molecule were situated at the bonding distance to the apex Al atoms of the electrodes in the form of pyramids. The results of the calculations show that at several modes fullerene molecules can conduct ballistically ($G>e^2/h$). The HOMO-LUMO gap of the isolated fullerene reflects itself in the value of G vanishing below the Fermi level, and the LUMOs of the isolated molecule became partially occupied.

When two pyramids have been replaced by the Al(001) parallel surfaces the value of the conductance rises up to 2.5 e^2/h, right at the Fermi energy. It can be explained by the interaction of the fullerene molecule with the surface which opens more channels for the electron to travel between electrodes. The HOMO-LUMO gap still exists but is partially closed by the strong hybridization.

When the fullerene was allowed to relax, conductance is reduced drastically. Only the LUMO orbital preserves its extended character, while the rest of the orbitals become localized at the interfaces. A Mulliken population analysis and the integration of the local density of states show that the excess transferred charge (~3.3 e) concentrates mostly at the interface hexagons. Such a finding confirms that the details of the interactions between the metal-molecule contacts are the most important factors which determine the transport properties of the molecular bridges.

CONCLUDING REMARKS

Here we have presented a review of selected investigations of the fullerene species where computational methods were especially productive and have attempted to elucidate prospective directions for future researches. Interestingly, when the interest in fullerenes seems to decrease, there always appear new topics which maintain the continuing interests of scientists. Such milestones have been the discovery of superconductivity, carbon nanotubes, and recent advances in applications of fullerene-based materials in nanotechnology.

ACKNOWLEDGEMENTS

This work was supported by the Office of Naval Research grant No.00014-03-1-0498 and by the Army High Performance Computing Research Center under the auspices of the Department of the Army, Army Research Laboratory cooperative agreement number DAAD19-01-2-0014, the content of which does not necessarily reflect the position or the policy of the government, and no official endorsement should be inferred.

REFERENCES

[1] H.W. Kroto, J.R. Heath, S.C. O'Brien, R.F. Curl and R.E. Smalley, Nature, 318 (1985) 162.
[2] W. Kraetschmer, L.D. Lamb, K. Fostiropoulos and D.R. Huffman, Nature, 347 (1990) 354.
[3] D.M. Cox, S. Behal, M. Disco et al., J. Amer. Chem. Soc., 113 (1991) 2940.
[4] R. Taylor and D.R.M. Walton, Nature, 363 (1993) 685.
[5] W.H. Mills and I.J. Nixon, J. Chem. Soc., (1930) 2510.
[6] R.L. Cappelletti, J.R.D. Copley, W.A. Kamitakahara et al., Phys. Rev. Lett., 66 (1991) 3261.
[7] E. Manousakis, Phys. Rev. B, 44 (1991) 10991.
[8] S. Saito and A. Oshiyama, Phys. Rev. Lett., 66 (1991) 2637.
[9] R. Malhotra, D.F. McMillen, D.S. Tse et al., Energy Fuels, 7 (1993) 685.
[10] H. Nagashima, A. Nakaoka, S. Tajima et al., Chem. Lett., 7 (1992) 1361.
[11] D.B. Whitehouse and A.D. Buckingham, Chem. Phys. Lett., 207 (1993) 332.
[12] S.E. Campbell, G. Luengo, V.I. Srdanov, F. Wudl and J.N. Israelachvili, Nature, 382 (1996) 520.
[13] A.F. Hebard, M.J. Rosseinsky, R.C. Haddon, D.W. Murphy, S.H. Glarum, T.T.M. Palstra, A.P. Ramirez, and A.R. Kortan, Nature, 350 (1991) 600.
[14] Z. Iqbal, R.H. Baughman, B.L. Ramakrishna, S. Khare, N.S. Murthy, H.J. Bornemann, and D.E. Morris, Science, 254 (1991) 826.
[15] S.H. Friedman, D.L. DeCamp, R.P. Sijbesma, G. Srdanov, F. Wudl, G.L. Kenyon, J. Am. Chem. Soc., 115 (1993) 6506.
[16] P.M. Allemand, K.C. Khemani, A. Koch, F. Wudl, K. Holczer, S. Donovan, G. Gruner and J.D. Thompson, Science, 253 (1991) 301.
[17] G.B. Adams, J.B. Page, O.F. Sankey et al., Phys. Rev. B, 44 (1991) 4052.
[18] M. Harada, S. Osawa, E. Osawa and E.D. Jemmis, Fuller. Sci. Technol., 3 (1995) 225.
[19] D. Jemmis E. J. Leszczynski and E. Osawa, Fuller. Sci. Technol., 6 (1998) 271.
[20] M.C. Piqueras, R. Crespo, E. Orti and F. Tomas, Chem. Phys. Lett., 213 (1993) 509.
[21] S. Nagase and K. Kobayashi, Chem. Phys. Lett., 187 (1991) 291.
[22] R.E. Smalley in "Comparison of Ab Initio Quantum Chemistry with Experiment for Small Molecules" R.J. Bartlett (ed.). D. Reidel Publishing Company, Boston, 1985, 53.
[23] E.D. Jemmis and B. Kiran in "Computational Chemistry: Reviews of Current Trends," Vol.1, J. Leszczynski (ed.), World Scientific, Singapore, 1996, 175.
[24] R. Nesper, Angew. Chem. Int. Ed. Engl., 33 (1994) 843.
[25] S. Sevov and J. Corbett, Science, 262 (1993) 880.
[26] F. De Proft, C. Van Alsenoy and P. Geerlings, J. Phys. Chem., 100 (1996) 7440.
[27] S. Nagase, Polyhedron, 10 (1991) 1299.
[28] S. Nagase, Pure Appl. Chem., 65 (1993) 675.
[29] L.A. Bloomfield, M.E. Geusic, R.R. Freeman and W.L. Brown, Chem. Phys. Lett., 121 (1985) 3.
[30] J.E. Elkind, J.M. Alford, F.D. Weiss, R.T. Laaksonen and R.E. Smalley, J. Chem. Phys., 87 (1987) 2397.
[31] M.F. Jarrold, V.A. Constant, Phys. Rev. Lett., 67 (1991) 2994.
[32] K.D. Rinnen and M.L. Mandich, Phys. Rev. Lett., 69 (1992) 1823.
[33] F. Hagelberg, J. Leszczynski and V.J. Murashov, J. Mol. Struct. (THEOCHEM), 454 (1998) 209.
[34] K.A. Jackson, in Abstracts, 1995 March Meeting of the APS, 20-24 March 1995, San Jose, California, B26.01.

[35] J.M. Schulman, R.L. Disch, M.A. Miller and R.C. Peck, Chem. Phys. Lett., 141 (1987) 45.
[36] X.G. Gong and Q.Q. Zheng, in Abstracts, 1996 March Meeting of the APS, 20-24 March 1996, St. Louis, Missouri, G23.11.
[37] J. Leszczynski and I. Yanov, J. Phys. Chem. A, 396 (103) 1999.
[38] R.E. Haufler, Y. Chai, L.P.F. Chibante, J. Conceicao, C. Jin, L.-S. Wang, S. Maruyama and R.E. Smalley, Mat. Res. Soc. Symp. Proc., 206 (1991) 627.
[39] S. Maruyama and Y. Yamaguchi, Therm. Sci. Engng., 3, (1995) 105.
[40] D.H. Robertson, D.W. Brenner and C.T. J. White, Phys. Chem., 96 (1992) 6133.
[41] V. P. Dravid, X. Lin, Y. Wang, X.K. Wang, A. Yee, J.B. Ketterson and R.P.H. Chang, Science, 259 (1993) 1601.
[42] J. R. Heath, in "Fullerenes," G.S. Hammand and V.J. Kuck (eds.), American Chemical Society, Washington, D. C., 1992,1-23.
[43] J.M. Hunter, J.L. Fye, E.L. Roskamp, M.F. Jarrold, J. Phys. Chem., 98 (1994) 1810.
[44] D.W. Brenner, Phys. Rev. B, 42 (1990) 9458.
[45] R.E. Smalley and D.T. Colbert, in "Proceedings from NATO Advanced Research Workshop: Modular Chemistry", J. Michl (ed.), Kluwer Academic Publishers 1997.
[46] V.V. Kirsanov, E.I. Shamarina and I.Yu. Yanov in "Proceedings from NATO Advanced Research Workshop: Computer Modelling of Electronic and Atomic Processes in Solids" R.C. Tennyson, A. E. Kiv (eds.), Kluwer, 1997.
[47] V.V. Kirsanov and I.Yu. Yanov, Mol. Cryst. Liq. Cryst. Sci. Tech. Sect. C, Molecular Materials, 8 (1996) 149.
[48] V.V. Kirsanov and I.Yu. Yanov, Physics Letters A, 193 (1994) 188.
[49] P.W. Fowler and F. Zerbetto, Chem. Phys. Lett., 243 (1995) 36.
[50] D.E. Clemmer, J.M. Hunter, K.B. Shelimov and M.F. Jarrold, Nature, 372 (1994) 248-250.
[51] Y. Miyamoto, N. Hamada, A. Oshiyama and S. Saito, Phys. Rev. B, 46 (1992) 1749.
[52] M. Saunders, H.A. Jimenez-Vazquez, R.J. Cross and R.J. Poreda, Science, 259 (1993) 1428.
[53] M. Saunders, R.J. Cross, H.A. Jimenez-Vazquez, R. Shimshi and A. Khong, Science, 271 (1996) 1693.
[54] J. Cioslowski and E.D. Fleischmann, J. Chem. Phys., 94 (1991) 3730.
[55] D.E. Clemmer, J.M. Hunter, K.B. Shelimov and M.F. Jarrold, Nature, 372 (1994) 248.
[56] R.C. Mowrey, M.M. Ross and J.H. Callahan, J. Phys. Chem., 96 (1992) 4755.
[57] J.H. Ross and J.H. Callahan, J.Phys.Chem., 95 (1991) 5720.
[58] T. Weiske, J. Hrusak, D.K. Bohme and H. Schwarz, Chem. Phys. Lett., 186 (1991) 459.
[59] T. Weiske, J. Hrusak, D.K. Bohme and H. Schwarz, Helv.Chim.Acta, 75 (1992) 79.
[60] S. Saito and A. Oshiyama, Physica C., 185 (1991) 421.
[61] L. Goodwin, Phys. Rev. B, 44 1991, 11432.
[62] I. Yanov and J. Leszczynski, in "NATO ASI series "Mathematics, Physics and Chemistry": Molecular Low Dimensional and Nanostructured Materials for Advanced Applications" A. Graja, B.R. Bulka and Kajzar (eds.), Kluwer Academic Publishers (2002) 247-250.
[63] I. Yanov and J.Leszczynski, J. Molec. Graph. Modell., 19 (2001) 236.
[64] Q.M. Zhang, J.Y. Yi and J. Bernholc, Phys. Rev. Lett., 66 (1991) 2633.
[65] P.A. Heiney, J.E. Fisher, A.R. McGhie et al., Phys. Rev. Lett, 66 (1991) 2911.
[66] W.I.F. David, R.M. Ibberson, J.C. Matthewman et al., Nature 353 (1991) 147.
[67] P.A. Heiney, G.B.M. Vaughan, J.E. Fisher et al., Phys. Rev. B, 45 (1992) 4544.
[68] A.B. Harris, R. Sachidanandam, Phys. Rev. Lett., 70 (1993) 102.

[69] W.I.F. David, R.M. Ibberson, T.J.S. Dennis et al., Europhys. Lett., 18 (1992) 219.
[70] A. Cheng, M. Klein, J. Phys. Chem., 95 (1991) 6750.
[71] A. Cheng, M. Klein, Phys.Rev.B., 45 (1992) 1889.
[72] K.H. Michel, J.R.D. Copley, D.A. Neumann, Phys. Rev. Lett., 68 (1992) 2929.
[73] J.R.D. Copley, D.A. Neumann, R.L. Cappelletti, W.A. Kamitakahara, J. Phys. Chem. Solids, 53 (1992) 1353.
[74] M. Sprik, A. Cheng, M. Klein, J. Phys. Chem., 61 (1992) 348.
[75] S. Wang, P.R. Buseck, Chem.Phys.Lett., 182 (1991) 1.
[76] C. Christides, D.A. Neumann, K. Prassides et al., Phys. Rev. B, 46 (1992) 12088.
[77] P.J. Benning, J.L. Martins, J.H. Weaver et al., Science, 252 (1991) 1417.
[78] W.A. MacFarlane, Ph.D. thesis. Department of Physics and Astronomy University of British Columbia (1997).
[79] K. Prassides et al, Science, 263 (1994) 950.
[80] K. Prassides et al, J. Am. Chem. Soc., 119 (1997) 834.
[81] S. Chakravarty and S. Kivelson, Europhys. Lett., 16 (1991) 751.
[82] F.C. Zhang, M. Ogata and T.M. Rice, Phys. Rev. Lett., 67 (1991) 3452.
[83] M. Schluter, M. Lannoo, M. Needels et al, Phys. Rev. Lett., 68 (1992) 526.
[84] K. Prassides, C. Christides, M.J. Rosseinsky et al, Europhys. Lett., 19 (1992) 629.
[85] I.I. Mazin, O.V. Dolgov, A. Golubov and S.V. Shul'ga. Phys. Rev. B, 47 (1993) 538.
[86] A.A Zakhidov, K. Imaeda, D.M. Petty et al., Phys. Lett. A, 164 (1992) 355.
[87] T.W. Ebbersen, J.S. Tsai, K. Tanigaki et al., Nature, 355 (1992) 620.
[88] C.C. Chen and C.M. Leiber, J.Amer.Chem.Soc., 114 (1992) 3141.
[89] C.C. Chen and C.M. Leiber, Science, 259 (1993) 655.
[90] Y. Tanaka, M. Tokumoto and Y.Sugawara, Fullerene Science and Technology, 3 (1995) 179.
[91] M. Tinkham, "Introduction to Superconductivity", McGraw-Hill, New York, 1975
[92] V.V. Kirsanov and I.Yu. Yanov, Molecular crystal and liquid crystals science and technology Sect. C, Molecular Materials, 8 (1996) 149.
[93] Ilya Yanov, Ph.D. thesis, Tver State University, 1999.
[94] J. Palacios, E. Louis, A.J. Pérez-Jiménez and J. A. Vergés, Phys. Rev. B, 64 (2001) 115411.
[95] J. Taylor, H. Guo and J. Wang, Phys. Rev. B, 63 (2001) 121104.
[96] C. Joachim, J.K. Gimzewski, R.R. Schlitter, and C. Chavy, Phys. Rev. Lett., 74 (1995) 2102.
[97] D. Porath, Y. Levi, M. Tarabiah and O. Millo, Phys. Rev. B, 56 (1997) 9829.
[98] H. Park, J. Park, A.K.L. Lim, E. Anderson, A.P. Alivisatos, and P.L. McEuen, Nature, 407 (2000) 57.
[99] P.G. Collins, M.S. Arnold, and P. Avouris, Science, 292 (2001) 706.
[100] W.R. Frensley in "Quantum Transport," ch. 9 in "Heterostructure and Quantum Devices", a volume of VLSI Electronics: Microstructure, Science, N.G. Einspruch and W.R. Frensley (eds.), Academic Press, San Diego,1994.
[101] N.D. Lang, Phys. Rev. B, 52 (1995) 5335.
[102] N.D. Lang and P. Avouris, Phys. Rev. Lett., 84 (2000) 358.

J. Leszczynski (Editor)
Computational Materials Science
Theoretical and Computational Chemistry, Vol. 15

Chapter 5

Theoretical Approaches to the Design of Functional Nanomaterials

P. Tarakeshwar, Dongwook Kim, Han Myoung Lee, Seung Bum Suh and Kwang S. Kim*

National Creative Research Center for Superfunctional Materials
Department of Chemistry, Division of Molecular and Life Sciences
Pohang University of Science and Technology
San-31, Hyojadong, Namgu, Pohang 790-784, Korea.

1. INTRODUCTION

One of the fundamental issues in nanoscience and nanotechnology is the design of novel nanomaterials with specific and desirable properties [1-10]. While experimental measurements have made many important contributions over the years to enhance our understanding of these properties, theoretical methods have been instrumental in their ability to help understand the variation of chemical and physical properties as single atoms or molecules coalesce to form larger functional entities [1-10]. However, a theoretical description of these nanomaterials, which belong to the mesoscopic phase, is fraught with a number of problems because neither quantum chemical methods used to investigate the microscopic phase nor solid state physics methods used to investigate the macroscopic phase can adequately describe all the desired properties [1-3,8,11-12]. A judicious combination of both these methods apart from providing a detailed insight of the properties of these nanomaterials also aids the de novo design of novel molecular systems and functional materials [8]. Interest in molecular level functional materials and devices is high because they aid the development of extremely small and hence fast and highly powerful computers. Another area of interest is molecular recognition, wherein quantum chemical calculations aid the design of microscopic chemical/biochemical sensors/monitors such as DNA chips [9-10]. It is important to note that most of the above research thrives on ideas gleaned from condensed matter physics, chemistry, biology as well as computational science.

* Phone: +82 54 279 2110, Fax: +82 54 279 8137, E-mail: kim@postech.ac.kr

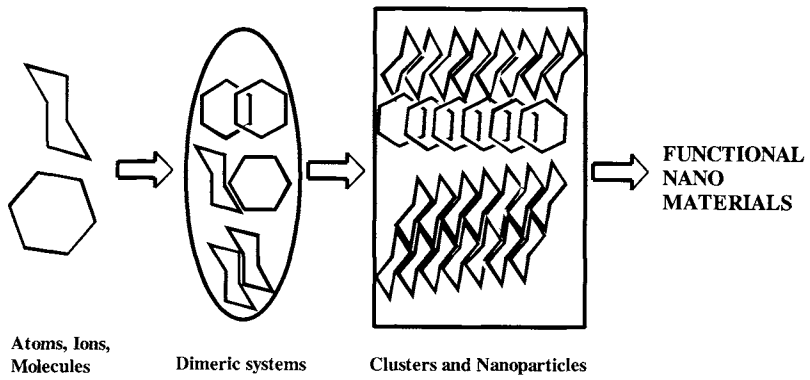

Figure 1. A step-wise approach to the design of functional nanomaterials.

Much of the recent successes in the computational design of materials can be attributed to the advent of fast computers together with the remarkable advances in new theoretical methodologies and computational algorithms [13-16]. Computational methods, apart from providing unique insights into experimental data, can also guide experimenters towards new materials with unique and important properties [3,15].

Calculations on systems described of Figure 1 yield important information which can aid the design of the desired functional nanomaterial. Thus, calculations on dimeric systems or complexes provide a detailed understanding of the nature of intermolecular interactions which in turn aid the construction of the geometries of the larger clusters or nanoparticles. Apart from providing information on the modulation of electronic characteristics, the calculations on the larger clusters also help understand the role of many body effects. Though one would also like to examine the role of external perturbations on both the geometries and electronic characteristics of the larger clusters or nanoparticles, the complexity of such calculations limits both the size and number of the systems which can be investigated.

The physical properties of most nanomaterials are a manifestation of several types of interatomic, intramolecular, and intermolecular interactions, which can be either cooperative or competitive [17-21]. As a result, the magnitude of each interaction term in the nanomaterial of interest is either enhanced or depleted. In particular, judicious combination of various types of intermolecular interactions would lead to self-assembly process of given molecular systems including self-synthesis, which would result in ideal molecular engineering process toward smart self-engineered functional molecular systems and nanomaterials.

In the course of this review, we examine how an effective combination of diverse theoretical methods ranging from traditional ab initio, density functional, tight binding, Monte Carlo to molecular dynamics simulations, have helped elucidate the nature of intermolecular interactions in a large number of widely disparate molecular complexes (aqueous and metal clusters, biomolecules), and

have also aided the design of novel nanomaterials (ionophores, receptors, endo/exohedral fullerenes, fullerides, nanotori, nanotubes, nanowires, and molecular devices). Before we do that, we briefly describe the methods employed in our calculations in the next section.

2. THEORETICAL METHODS

The nature of the intermolecular interactions in the dimeric complexes or larger clusters can be ascertained by using a judicious combination of supermolecular (SM) variational and perturbational methods [17,22]. The former method is employed to carry out the geometry optimizations and evaluate the vibrational frequencies. The evaluation of the vibrational frequencies is an integral component of most theoretical investigations of clusters because one can readily compare the calculated numbers with the experimentally observed frequencies or shifts. This in a way provides an effective way to test the efficacy of the theoretical method employed in the calculations. Presently, SM calculations are broadly based on either the (i) Hartree-Fock, (ii) Post Hartree-Fock methods like the Møller-Plesset level of theory (MP), configuration interaction (CI), complete active space self consistent field (CASSCF), coupled cluster singles and doubles (CCSD), or (iii) methods based on Density functional theory (DFT) [23-25]. Since the inclusion of electron correlation is vital to obtain an accurate description of most of the calculated properties, most of the SM calculations were carried out at either the second order Møller-Plesset (MP2) or the coupled-cluster with single, double, and perturbative triple substitutions [CCSD(T)] levels using basis sets composed of both diffuse and polarization functions [17].

Even though the SM method is conceptually and computationally simple, it does not provide a clear picture of the interaction forces responsible for the interaction. On the other hand, the perturbation method enables one to obtain a physical picture of the interactions prevailing between the various complex monomers. This is because of the fact that in the SM method, the interaction energy is evaluated as the difference of the energy of the complex and the energy of the isolated monomers. However, in the perturbational method, the interaction energy is obtained as a sum of the individual electrostatic, exchange, dispersion, and induction energies [26].

As the size of the system increases, it is impossible to carry out the calculations at the levels of theory employed in the investigation of the smaller systems. Therefore, DFT methods have been widely employed in a large number of studies because of the smaller computational resources needed to describe very large systems. In particular, they have been found to be effective in the description of systems dominated by hydrogen bonding interactions but their use in the description of weak intermolecular complexes is limited by the inability of most current functionals to describe dispersion energies [27,28].

Beyond a certain system size, even DFT methods using conventional basis sets become computationally very intensive. In such situations, we have employed the pseudopotential plane wave or tight-binding methods to obtain the various physical properties [14,27].

3. TYPES OF INTERMOLECULAR INTERACTIONS

An effective strategy for the theoretical design of novel functional nanomaterials also entails a detailed understanding of various types of intermolecular interactions. Though a large number of intermolecular interactions prevail in chemical and biological systems, we find it convenient to broadly classify them into five different types. These include, (i) hydrogen bonding, (ii) ionic interactions, (iii) intermolecular interactions involving π systems, (iv) metallic interactions, and (v) interactions involving quantum species. The physical properties of most nanomaterials are a manifestation of several of these intermolecular interactions, which can be either cooperative or competitive. As a result, the magnitude of each intermolecular interaction in the nanomaterial of interest is either enhanced or depleted. Thus, judicious combination of these interaction forces would be essential for the design of smart self-engineered functional molecular systems and nanomaterials.

3.1 Hydrogen Bonding

Hydrogen bonding is one of the most important intermolecular interactions, which is typically characterized by an equilibrium configuration involving a hydrogen atom donor D and an acceptor A [18,29]. The strength of the interaction, which allows one to classify them as weak, medium, and strong, ranges between 0-30 kcal/mol (~30 kcal/mol in case of the $F^{-}\cdots H\text{-}F$ interaction). Hydrogen bonding finds relevance in nanomaterial design because (i) the interaction is of intermediate strength and therefore reversible, (ii) the interaction is directional and therefore one-, two-, three- dimensional structures can readily be assembled by hydrogen bonding, and (iii) the assembly is often fast and specific. Since the hydrogen bonding interaction is much weaker than a covalent bond, the interaction can easily be reversed and hence error correction can be carried out.

In general hydrogen bonding is characterized by a dominant contribution from electrostatic energies. However the sum of the induction and dispersion energies is nearly equivalent to the total interaction energy. This implies that the attractive electrostatic contribution is to a large extent cancelled by the repulsive exchange energy. Indeed, it has been observed in the case of the water dimer and many other structures that the global minimum corresponds to a structure with the largest attractive contributions and a large exchange-repulsion term [18,30]. On the other hand, the multitude of local minima and transition states exhibit smaller magnitudes of attractive terms and repulsions with respect to their

values observed for the global minimum. It would be shown in subsequent sections that the magnitude of the repulsive term to a large extent governs the geometry of the equilibrium structure. Nearly all the characteristic experimental features of hydrogen bonding, viz. changes in the bond lengths, dipole moments, and red-shifting of vibrational frequencies, etc. can be explained using very simple theoretical models.

When a system possesses multiple hydrogen bonds, cooperativity is a particularly characteristic manifestation, which has important consequences in nanomaterial design [31,32]. While an explanation of the origin of cooperativity is beyond the purview of this review, it is useful to highlight some of the salient features of cooperative interactions. Foremost amongst them is the enhancement of the strength of hydrogen bond. Thus, in water clusters, the average energy of a hydrogen bond progressively increases with an increase in the cluster size. This enhancement of interaction energies leads to a progressive decrease in the intermolecular hydrogen bonding distance and hence significant geometry changes can also be noted.

In addition, we should mention special types of hydrogen bonds such as ionic hydrogen bonds, positively charged hydrogen bonds, negatively charged hydrogen bonds, short hydrogen bonds, short strong hydrogen bonds, and aromatic hydrogen bonds (π-H interactions), the details of which can be found from the literature [17,18,33,34].

3.2 Ionic Interactions

Since electrostatic energies dominate intermolecular interactions between cations and anions involving ionic species, these interactions are specially considered as ionic interactions. Since this cation-anion interaction is almost ubiquitous, and easy to understand, the details of this well-known interaction is not discussed here. However, it would be somewhat difficult to understand if this is a special class of hydrogen bonds, i.e. ionic hydrogen bonds, which are important for various types of self-assembly processes [35]. While we discuss these electrostatic interactions of ionic species in the section devoted to ionophore/receptor design [18,36-45], it is interesting to note that fundamental differences exist between interactions involving cations and anions. This is particularly true for theoretical calculations with interactions involving cations being described more easily than those involving anions [18]. It may be due to the fact that electrostatic interactions involving anions are much less effective because they have a lower charge to radius ratio than isoelectronic cations (Table 1) [46], while the polarization effect in anions is very large. Another critical reason is that a cation interacts with heavy non-hydrogen atoms (such as oxygen and nitrogen), while an anion interacts with hydrogen atoms which have extremely small van der Waals radius. In this case, the electron clouds of the anion can be more polarized toward the hydrogen atom anisotopically and directionally. Furthermore, in the case when an anion interacts with water or

ammonia molecules, the crowded hydrogen atoms in water or ammonia at very short van der Waals separation distances, tend to repel each other by the coulombic repulsions, and the full coordination is not easy, in contrast to the case of easy full coordination for a cation which can interact with many oxygen/nitrogen atoms at van der Waals separation distances between the anion and oxygen/nitrogen atoms [39-45].

Table 1. Ionic radii of cations and anions [46].

Cation	R (Å)	Anion	r (Å)
Na^+	1.16	F^-	1.19
K^+	1.52	Cl^-	1.67
Rb^+	1.66	Br^-	1.82
Cs^+	1.81	I^-	2.06

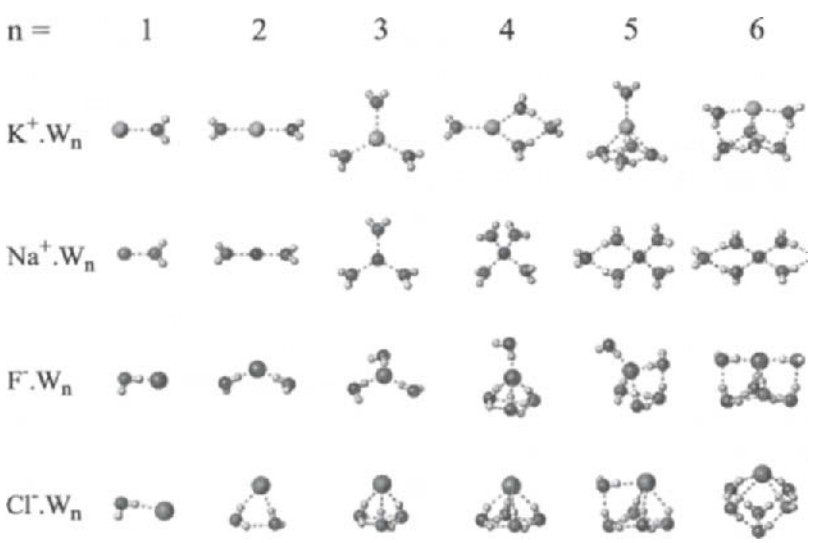

Figure 2. Optimized structures of the water cluster complexes of cations (K^+, Na^+) and anions (F^-,Cl^-). Note the differences in the structures as a result of both changes in the ion size and the charge.

In order to understand these differences, we examine the interaction of cations or anions with water molecules [30,47-55]. In cation-water clusters, the interaction between water molecules and cations is dominated by ion-dipole interactions at long range [30,52-55]. This results in the hydrogens of the water being oriented away from the ion. As the cation comes closer to the water molecule, electron transfer could play an important role in dictating the geometries and energetics. However, the limiting factor to the extent of electron

transfer is the size of the cation, because the repulsive interactions increase with a closer approach of the oxygen atom to the cation. As the oxygen lone pair is involved in the interaction with the cation, there is a marked decrease in both the number and strength of inter-water hydrogen bonds. Consequently, most cationic water clusters are symmetrically hydrated species.

The diffuse nature of the electron clouds of the anion and the involvement of the hydrogen of the water molecule in binding to the anion make them distinctly different from the corresponding cationic water clusters (Figure 2). In the context of the smaller anionic water clusters, there is a lot of debate on whether the anion is solvated within a shell of water molecules (internal state) or the anion is bound to a condensed phase network of water molecules (surface solvated ionic state) [30,47-51].

Given this background on structures, it is of interest to examine the efficacy of various theoretical approaches in reproducing both the geometries and interaction energies of these ionic clusters [30]. The rationale for such an exercise would become relevant in our discussion of ionophore design [36-45]. In general, the geometries and interaction energies of cationic-water clusters are nearly independent of the level of theory at which the calculations are carried out. Of course, the calculations involving the larger alkali cations like K^+, Cs^+, organic and transition metal cations yield more accurate results when electron-correlation is explicitly included [30]. In sharp contrast, the interaction energies of the anionic-water clusters are vastly underestimated at the Hartree-Fock level. This underestimation is more pronounced for water clusters of the larger anions like Cl^- and O_2^-. At the correlated levels of theory, both the MP2 and CCSD(T) calculations yield nearly equivalent interaction energies with the results obtained at the latter level being somewhat smaller than those obtained at the MP2 level. Based on the above discussion, it becomes evident that calculations on anion containing systems should explicitly include electron correlation. This inclusion of electron correlation becomes more important in intermolecular interactions involving π systems, because these interactions are mediated through the more diffuse π electron cloud [17,18].

3.3 Intermolecular interactions involving π systems

Amongst all the intermolecular interactions discussed herein, interactions involving π systems are one of the most relevant in the context of nanomaterial design [17,18]. Though these interactions are widely existent in biological and chemical systems, their importance was known only very recently [17,56]. This is because these interactions are perceptibly weak to be observed experimentally and their accurate description requires very high levels of theory [17,56,57]. Hence early theoretical studies which attributed these intermolecular interactions, involving the negatively charged electron cloud of the π system, to emerge from electrostatic energies, fail to explain the binding of rare gases or neutral molecules like methane or benzene to these π systems [17,58-60]. Given

the fact that a large number of nanosystems ranging from fullerenes to ionophores exhibit these interactions, it is of value to theoretically investigate the nature of these interactions [17,18]. Interactions involving π systems find relevance in the fabrication of nanodevices, because subtle changes in the electronic characteristics of the π systems can lead to dramatic effects in the structure and properties of the nanosystem [61-66] Apart from changes in the π system and the presence of substituents, the changes in the electronic characteristics can be brought about by electrochemical or photochemical means [66].

A broad classification of the nature of the interactions involving these π systems can be based on the nature of the countermolecule involved in the interaction. A combination of electrostatic and induction energies dominate the interaction when the countermolecule is a metal cation [17,18,67]. Dispersion energies predominate when the countermolecule is either a rare gas atom or a nonpolar molecule (gas dimers, hydrocarbons) [17,18,58,59]. When the countermolecule is either a polar molecule or Lewis acid, both electrostatic and dispersion energies govern the interaction [17,18,68-70]. The magnitude of the repulsive energies plays a vital role in governing the observed geometry of the π system containing cluster [58,67].

Given the relevance of some of our recent results obtained on the nature of these interactions in our subsequent discussion on nanomaterials, we thought it would be useful to highlight some of the salient features of these interactions. We begin with a discussion of the cation-π interaction, because it is many ways similar to the more well-known hydrogen bonding [67]. Early explanations of the cation-π interaction indicated that it primarily emerged from the interaction of a positively charged cation with the negatively charged π electron cloud. It soon became apparent that the variations in the electrostatic potential of the π system only mirrored the trends in the cation-π interaction energies. An accurate estimate of the interaction energies required the inclusion of other factors like the polarizability of the π system. These findings were reinforced by reports of the importance of dispersion energies in the binding of the tetramethyl ammonium cation to benzene.

In a recent study carried out in our group, we had shown that both electrostatic and induction energies are major contributors to cation-π interactions involving alkali metal cations [67]. The large induction energy can be attributed to the interaction between the highest occupied molecular orbital (HOMO) of the π system and the empty *s* orbital of the metal cation. Thus, this energy is electron-correlation driven induction energy. Consequently, systems exhibiting an enhanced overlap of the constituting MO's would exhibit larger induction and hence larger interaction energies. The size of the cation, apart from governing the magnitude of the dispersion energies, also governs the extent of orbital overlap. A smaller cation can approach much closer to the π system

because of the reduced exchange-repulsion. However as we see in case of the interaction of these π systems with transition metal cations like Ag^+, a closer approach of the small sized Ag^+ cation (1.26 Å) leads to a large increase in the repulsive energies. However, the higher charge density and the presence of d electrons lead to large interaction energies. One also notes that the nature of the π system has little effect on the nature and magnitude of the interaction energy.

The magnitudes of the electrostatic and induction energies in the case of the organic cation complexes of these π systems are much smaller than those observed in case of the π-alkali metal cation complexes, and hence the contribution of dispersion energies becomes vital. Apart from obtaining an accurate estimate of dispersion energies, the inclusion of electron correlation in calculations involving π systems and organic cations is important, because the inductive energies described by the π-σ* interaction (where π is the HOMO of the π system and σ* is the LUMO of the organic cation) are magnified. This magnification of the induction energies upon inclusion of electron correlation is due to the depletion in the electron density from the centers of the bonds and a concurrent increase in the shells around the atomic nuclei. Consequently the organic cation can have a closer approach to the π system and as a result both the induction and dispersion energies are magnified. Except for interactions involving transition metal cations, the nature of the π system influences the magnitude of each interaction energy component, with the pyrrole complexes exhibiting the largest electrostatic and induction energies because the π electron density of pyrrole is much higher than that of either benzene or ethene.

Given our discussion of the cation-water interactions in an earlier section, it is of interest to compare their characteristics with the cation-π interactions. It can be seen from Figure 3, that the total interaction energies of the cation-water complexes are comparable in magnitude to the corresponding cation-pyrrole complexes.

What however distinguishes the interactions of these cations with water and π systems is the magnitude of the electrostatic energies, with them being dominant contributors to the total interaction energy in case of the former [30,67]. This marked difference can be attributed to the difference in the nature of the donor, with the donor lone pair of the water oxygen atom being more localized than the diffuse electron cloud of the π system. This leads to a larger electrostatic contribution and a much smaller induction contribution in the case of the water complexes. The repulsive energies are higher in the case of the water complexes because the cation encounters another atom in contrast to a bond in ethene or the center of the aromatic ring (no atoms or bonds).

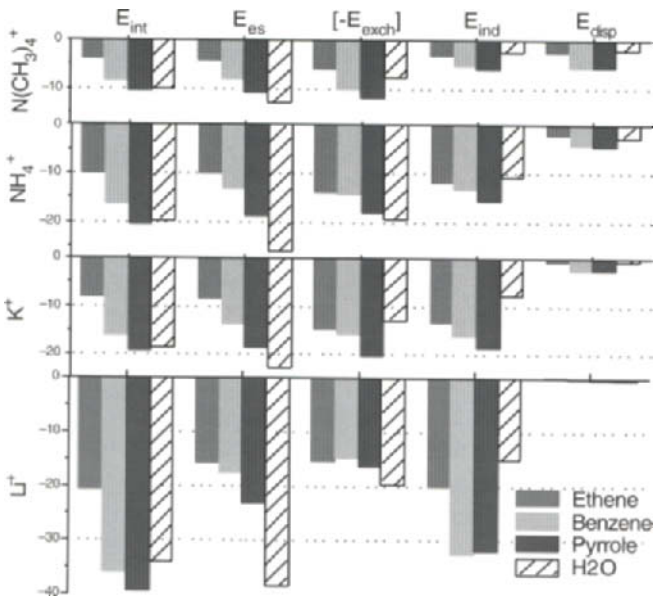

Figure 3. Comparison of cation-π and cation-water interactions. Notice the distinct differences in the various interaction energy components as a result of changes in the nature of the cation and the π-system.

In the context of nanomaterial design, these findings are significant because a greater electrostatic contribution implies that the magnitudes of the interaction energies are more susceptible to the dielectric of the environment. It was also shown in the course of our studies that the nearly similar interaction energies of the benzene with the ammonium and potassium cations result from a balance of dispersion and induction energies because the electrostatic and exchange energies are nearly similar and hence cancel out. However the ammonium cation complexes exhibit a larger contribution of dispersion energies [67,71,72]. In a subsequent section, we show on how suitable receptors specific for the ammonium cation could be designed by enhancing the contribution of the dispersion energies. In the context of the cation-π interactions, it is interesting to note that the anion-π interactions have recently been discovered [73-75].

In the order of decreasing magnitude, the interaction energies of the π-Lewis acid complexes follow the cation-π interactions [17,68-70]. Apart from a few experimental reports detailing the interaction of Lewis acids with π systems in the context of donor-acceptor complexes and electrophilic aromatic substitution reactions, little was known about either the magnitudes or the exact nature of their interaction. However, in the course of our extensive investigations, it was found that the halides of aluminium, boron, and hydrogen, form fairly strong non-covalent complexes with both benzene and ethene [69,70]. The magnitude

of the interaction depends on the nature of the Lewis acid, with the benzene complexes of aluminium halides exhibiting interaction energies (8~15 kcal/mol), which are significantly larger than the corresponding complexes of the boron halides (3~6 kcal/mol) [69,70]. As far as our knowledge goes, the interaction energies exhibited by the aluminium halide complexes of benzene are the highest for a neutral (uncharged species) binding to it. Recent work by Olah and Seddon highlight the importance of π-Lewis acid interactions in understanding the nature of catalysts and ionic liquids [76,77].

Complexes exhibiting the π-H interaction are of interest because they are the prototypes of a typical hydrogen bond [58,78,79]. Apart from their biological and chemical relevance, an investigation these interactions offer the best opportunity to highlight the distinct differences between olefinic and aromatic π-H interactions [56,58,80]. Our studies of the π-H interaction were done by carrying our theoretical investigations of the complexes of the first-row hydrides with ethene and benzene [58]. Most of these differences stem from the widely differing electron density profiles of ethene and benzene. Thus, in the benzene complexes, the hydride aims at the midpoint of the ring (where there are no nuclei or bonds), but in ethene, at the midpoint of the double bond. As we progress from CH_4 to HF, the increase in the repulsive exchange energies is more pronounced in the ethene than in the benzene complexes. This leads to a smaller variation in the intermolecular distances in the benzene complexes. Consequently, the magnitude of the dispersion energies is nearly independent of the nature of the hydride, because the magnitude of the dispersion energies is nearly proportional to the number of electrons participating in the interaction and the intermolecular distance. Similar to what is observed in the cation-π complexes; one also notes an increase in the magnitude of the induction energies of the hydride complexes of both ethene and benzene upon inclusion of electron correlation.

The π-π interactions are one of the most intriguing non-covalent interactions, in the sense that the negatively charged and diffuse electron clouds of the π systems exhibit an attractive interaction [17,21,60,81]. This interaction is predominated by dispersion interactions, when the π systems possess nearly similar electron densities. However, when one of the systems is electron-rich (benzene) and the other electron-deficient (hexafluorobenzene), the resulting complexes are bound by induction interactions with the negative charge being transferred from benzene to hexafluorobenzene [82,83]. The acetylene dimer is one of the simplest systems exhibiting a π-π interaction [84,85]. Though a parallel displaced conformer, which involves a stacking of the two acetylene π systems exhibit a π-π interaction, the most stable conformer is a T-shaped structure, which involves the interaction of hydrogen of acetylene with the π system of the other [84]. In the case of the ethene dimer, the most stable structure has a D_{2d} symmetry, which involves the formation of a quadruple

hydrogen bond [86,87]. The interaction of two benzene rings (benzene dimer) has been widely investigated both experimentally and theoretically. The experimental estimates of the interaction energy is of the order of ~2 kcal/mol, which indicates that the attraction is appreciable and significantly influences the interaction of phenyl rings in solution or other environments, in addition to other factors such as solvophobic effects [88-90]. The interaction is predominated by dispersion interactions and as in the case of the acetylene dimer, the benzene dimer can manifest itself in any one of the structural forms; Stacked, T-shaped, or parallel-displaced. The available evidence seems to indicate that the parallel displaced conformation is most stable [88]. However, it should be noted that the isolated benzene dimer is highly fluxional and can coexist in any of the three structural forms. In a subsequent section, we take advantage of the fact that the interconversion between the different conformers or the orientations of the two interacting π systems can be exquisitely controlled [60,65]. In order to have maximum control on this interconversion, we use the electrochemically and photochemically active π systems (quinone and hydroquinone) [65].

While we have investigated several other interactions involving π systems, we believe that they have little relevance in our subsequent discussion on nanomaterial design. Mention should however be made of the interaction of paramagnetic atoms with π systems, which is discussed in our account of A@C_{60} (A: N, P, As, O, or S) [91].

3.4 Metallic interactions

The interaction between metal atoms is of interest in the context of nanomaterial design because most metal systems exhibit very unusual properties when their lateral dimensions are decreased to the nano- or subnano-scale [18,92,93]. An example of this unusual behaviour can be noted from the properties of a lead (Pb) nanowire, which in contrast to what is observed in the bulk, is a better conductor than gold by an order of magnitude. Apart from changes in the conductivity, the tensile/cohesive strength of metallic nanomaterials is found to be much larger than that observed in bulk [93]. This is because, deformations in bulk metallic systems occur through dislocation motions, while structural rearrangements are the norm in materials at the subnanoscale.

The interactions in systems containing uncharged metallic species may be classified as either continuous transitions or metallic [18,92,94]. In the former interaction, there is a continuous shift from one type of bonding to another type as function of a chemical or physical variable. An interesting feature of this kind of transition is depicted in a covalent/ionic/metallic/van der Waals tetrahedron (Figure 4) [94].

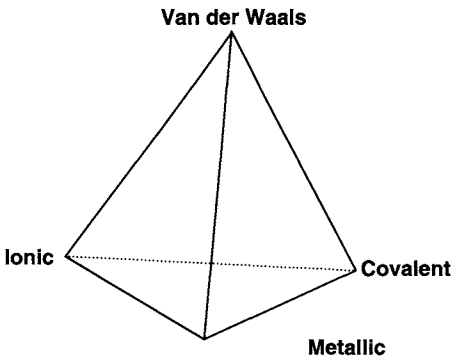

Figure 4. A tetrahedron depicting the interactions prevailing in metallic species [94].

Though there is no such thing as metallic bonding, metals could be regarded as systems with close-lying HOMO's and LUMO's and nearly all the properties of metals, conductivity, optical reflectivity, Friedel oscillations, etc. are consequences of these small HOMO-LUMO gaps [18,92]. In the metallic bonding, the electron correlation is very important. This has been extensively documented in the case of interactions involving d^{10} gold cations. Interestingly, these interactions are enhanced by relativistic effects and hence are more pronounced in systems containing heavy metals possessing large relativisitic effects [92]. The electron correlation energies have also been known to play an important role in the experimental observation of large enhancement of van der Waals forces between small silver particles [95].

3.5 Interactions involving quantum species

While most of the previous discussion on intermolecular interactions was involved in molecules, atoms, or stable closed shell cations or anions, the interactions involving quantum species like single electrons, photons, and paramagnetic atoms have been found to be of importance in understanding the modulation of properties by external stimuli. These stimuli could be from photochemical (involving photons), chemical (involving changes in ion and pH concentrations), to electrical (involving electrons) [18]. Most of the current work on intermolecular interactions involving quantum species has implications in nanomaterial design because it paves the way to several desirable goals like responsive and intelligent materials, smart sensors, molecular devices, etc. It should be however mentioned that the theoretical methods which can be used to tackle these problems are still in their infancy and are the focus of research of several groups in the world [4].

3.6 Cooperative and competing interactions

Since a vast majority of intermolecular interactions are weak, they are reversible. However, molecules possessing multiple complementary binding

sites provide a means to magnify the effect of very weak individual interactions [18,31,32]. This effect is more commonly known as cooperativity and is responsible for the physical characteristics of a vast majority of chemical and biological systems. The basis for cooperativity can entirely be explained by the additivity of the corresponding individual free energies and formation constants [96]. In most cases, the entropic effects need not be invoked to explain this phenomenon in nanoscale systems, due to their small contributions at low and non-high temperatures. In general, the existence of multiple binding sites in natural or synthetic receptors leads to greater efficiency and selectivity in complexation. What is interesting about cooperativity is that conformational changes occurring during the course of complexation can be harnessed to design functionally important systems [31,64,65].

One of the widely-known manifestations of cooperative effects, which is, of relevance to our discussion is self-assembly [18,31]. The most interesting aspect of self-assembly is that in a number of cases, the high affinity and selectivity arises from a complementarity of size and shape than from interactions involving charges. This aspect of self-assembly is well-illustrated in cucurbituril [31].

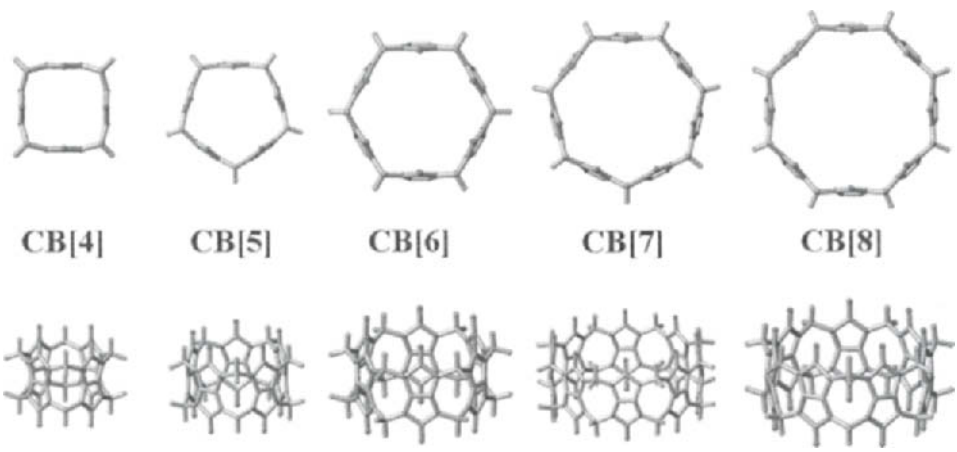

Figure 5. A nice example of self-assembly (cucurbiturils). The optimized structures depicted in this figure have been obtained at the B3LYP/3-21G level.

In fact, the large number of fascinating molecular architectures (Figure 5) formed from cucurbiturils lead to the concept of self-assembling capsules. These self-assembling capsules are receptors with enclosed cavities that are formed by the reversible noncovalent interaction of two or more, not necessarily identical, subunits. As would be in a subsequent section, the self-assembly of isolated calix[4]hydroquinone molecules leads to well-defined honeycomb architectures [64,65]. One of the advantages of these self-assembling capsules is that they can

encapsulate increasingly large guests or promote specific properties, like catalysis [97].

A number of studies on hydrogen bonding in organic molecular assemblies have revealed that certain classes of functional groups always form hydrogen bonds when complementary donors or acceptors are available, while other classes of functional groups only occasionally participate in hydrogen bonding [98]. This discussion on the concept of best donor and acceptor forming hydrogen bonds provides a cogent tool for controlling the composition and structure of molecular assemblies. Thus, novel molecular assemblies can be designed using complementary sets of strong and weak hydrogen bonds. It is interesting to note that this competition between hydrogen bonds in solid state mirrors those found in solution or in the gas phase.

While there is a marked preference for the formation of strong intermolecular interactions, it is of interest to note that weak interactions behave as steering interactions. Thus in case of hydrogen bonds, Desiraju demonstrated that weak hydrogen bonds other than those taking part in strong hydrogen bonds, play a crucial role in determining crystal packing [99]. We discuss this aspect in more detail in our discussion of the formation of calix[4]hydroquinone CHQ nanotubes [64,65].

4. APPLICATIONS

There are two aspects of nanomaterial design, which would be addressed in this section. These include theoretical investigations of known nanomaterials, and de novo theoretical design of new nanomaterials. Apart from an awareness of intermolecular interactions, investigations of the properties of known nanomaterials provide useful information on the level of theory required to investigate the nanomaterial. Thus, for example, systems containing a number of π systems would require the use of theoretical methods, which explicitly include electron correlation [17,18]. On the other hand, Hartree-Fock methods suffice in the investigation of systems dominated by hydrogen bonds [18,29].

4.1 Clusters and complexes

Clusters, in addition to offering several ways of making new materials, are exciting subjects for theoretical investigations [12,100-102]. In the following account, we discuss three different kinds of clusters, namely, hydrogen bonded clusters, metal clusters, and clusters containing π systems. The investigation of each of these clusters not only provides necessary information for nanomaterial design, but also highlights some of the important similarities and differences in their structures and properties.

Aqueous clusters have been the focus of a large number of theoretical investigations in the last few decades [30,103-113]. However, very few of these investigations have addressed their relevance in material design.

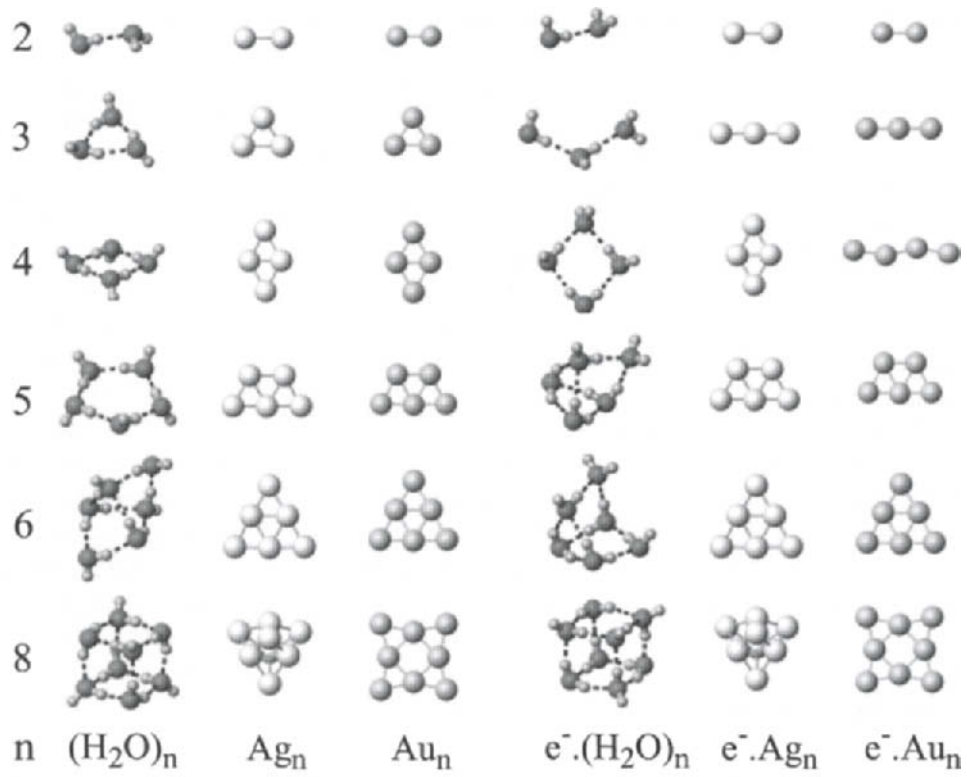

Figure 6. A structural comparison of hydrogen bonded and metallic clusters.The lowest-energy conformations of neutral and anionic clusters of water, gold, and silver $\{(H_2O)_{2\text{-}6,8}$, $(Au_{2\text{-}6,8})$, $(Ag_{2\text{-}6,8})\}$. Note that in both the cases, the presence of an extra electron either geometrically or energetically stabilizes the corresponding neutral structure.

There are several alluring features associated with these water clusters (Figure 6), which make them very relevant in the context of nanomaterial design. Foremost among them are the changes in their lowest-energy structures with an increase in their sizes. Thus the water dimer, which is composed of two water molecules, possesses a linear structure with the hydrogen of one of the water molecules forming a hydrogen bond with the oxygen of the other. As the size of the water cluster increases, there is initially a transition to two-dimensional cyclic structures (trimer, tetramer, pentamer). However, the hexamer heralds the onset of three-dimensional minimal energy structures (Figure 6), a trend which extends to the larger water clusters [30,103,109,111]. It should also be noted that this structural transition is associated with a sharp increase in the number of iso-energetic conformers. Consequently the prediction of the lowest-energy structures of the larger water clusters is complicated, a fact illustrated in more detail in recent studies of the water undecamer and dodecamer [112]. One of the interesting insights obtained about hydrogen

bonds, from investigations of the structures of water clusters is that energetic stability is not associated with the presence of more hydrogen bonds. Thus, the lowest-energy ring structure of the water pentamer has fewer hydrogen bonds than the pyramidal structure [30]. It is also interesting to note the drastic changes in structures of water clusters in the presence of an excess electron [114-125].

Against this background on clusters involving hydrogen bonding interactions, it is useful to examine the characteristics of noble metal clusters [12,126-130]. Small noble metal clusters are of interest because the dominance of quantum effects in such small dimensions alludes to the emergence of several interesting characteristics, like their catalytic properties, etc. Till very recently, most studies were concentrated on pure metallic clusters. However, recent observations indicate that mixed clusters exhibit unique electronic, magnetic, optical and mechanical properties. For example, mixed clusters of gold and silver have been found to exhibit enhanced optical nonlinearity over the corresponding bulk metals. Additionally, they also help understand the mechanism of alloying. As would be seen latter, such an understanding is useful in modulating the structural and physical characteristics of metallic nanowires. The theoretical methodology we have used in the investigation of these small gold and silver metal clusters ranges from density functional to coupled cluster methods. The relativistic effects prevalent in these metal clusters were accounted for, by employing basis sets containing pseudopotentials.

Our results for varying sizes of neutral and anionic gold (Au) and silver (Ag) clusters indicate that they exhibit an even-odd oscillation in their stability and electronic properties [130]. Thus, clusters which have an even number of atoms tend to be more stable in the neutral state, while those having an odd number of atoms tend to be more stable in the anionic state. Since the *6s* orbital energy of Au is almost as low as *5d* orbitals, the strong *s-d* hybridization in Au favours one-dimensional and two-dimensional structures in the case of the gold clusters. This structural preference, probably due to the relativistic effects, also explains the ductility of small gold clusters. In vivid contrast, silver clusters exhibit a strong preference to exist as three-dimensional structures with spherical coordination because the valence orbitals are predominantly of the *s*-type. However, one can distinctly note this preference for clusters larger than the hexamer. A similar argument can also be employed to explain the lower coordination number of the Au atom in the gold clusters as compared to the Ag atom in the silver clusters. This preference in coordination reflects itself in the location of the Au and Ag atoms in the corresponding binary clusters of gold and silver, with the Au atoms being located on the boundary, while Ag atoms are generally located on the inner side. In the anionic systems of both the pure and mixed clusters, there is marked tendency to adopt lower-dimensional conformations as compared to the corresponding neutral clusters. However, it should be noted that in the mixed clusters, the conformational preferences are strongly correlated to the number of Au and Ag atoms in the cluster. Given the

higher energy of the Ag *5s* as compared to the Au *6s* orbital, an electron transfer from the Ag to the Au atom can be noted in the mixed clusters. This together with the predilection for the Au atom to be located on the boundary indicates that the core of the mixed clusters is positively charged and the surface, negatively charged. The marked ease for the formation of the mixed gold-silver clusters and as a consequence their alloys, is due to the significant electrostatic stabilization accruing from the charge transfer from the Au to the Ag atom.

It has been recently suggested that π systems (graphite) promote the formation of nanometer-sized water clusters (nanodroplets) [131]. However, little is known about the nature of arrangement of the water monomers or their interaction with the surface of graphite. It is in this connection that we discuss our work on the structure and energetics of microsolvated aromatic π-systems [17,78,79,132-140]. Of course, these studies also aid the understanding of a wide variety of physical phenomena ranging from hydrophobicity, solvation, solvation induced catalysis to molecular recognition [57]. Apart from highlighting the role of substituents, our calculations carried out on a series of clusters containing a substituted benzene (*p*-difluorobenzene, fluorobenzene, benzene, toluene) with varying sizes of water clusters reveal several interesting facets on their optimal structures, binding energies, and vibrational frequencies. Thus, it can be seen from Figure 7, wherein we have depicted the optimal structures of the π-$(H_2O)_{1-4}$ clusters, that the water monomer and dimer complexes of fluorobenzene and *p*-difluorobenzene exhibit a σ-type of hydrogen bonding interaction involving the covalently bonded fluorine atom. However, with an increase in the size of the water cluster, there is a gradual transition from a σ-type of hydrogen bonding to a π-type of interaction [135].

The energetic changes accompanying this structural transition indicate that the water trimer is most strongly bound to these π systems (Figure 8). Since the water trimer with two parallelly oriented hydrogen atoms (i.e., two clustered dangling hydrogen atoms) is geometrically more strained than any of the other water clusters, we believe that its interaction with the π-system leads to a decrease in the repulsion between the two water molecules and hence decreases the strain of the intervening hydrogen bonds [135]. Even though the interaction energy of the fluorobenzene-water monomer complex is smaller than that of the water monomer complexes of benzene and toluene, the interaction energy of the fluorobenzene-water tetramer complex is much higher than that of the corresponding water tetramer complexes of benzene and toluene [136]. While this energetic stabilization is due to the presence of two stabilizing σ and π interactions in the fluorobenzene-water tetramer complex, the smaller interaction energies of the water tetramer complexes as compared to the water trimer complexes indicates that in the presence of the π-system, there is a gradual increase in the strength of the inter-water hydrogen bonding. This fact is supported by our calculations of the strengths of the hydrogen bonds.

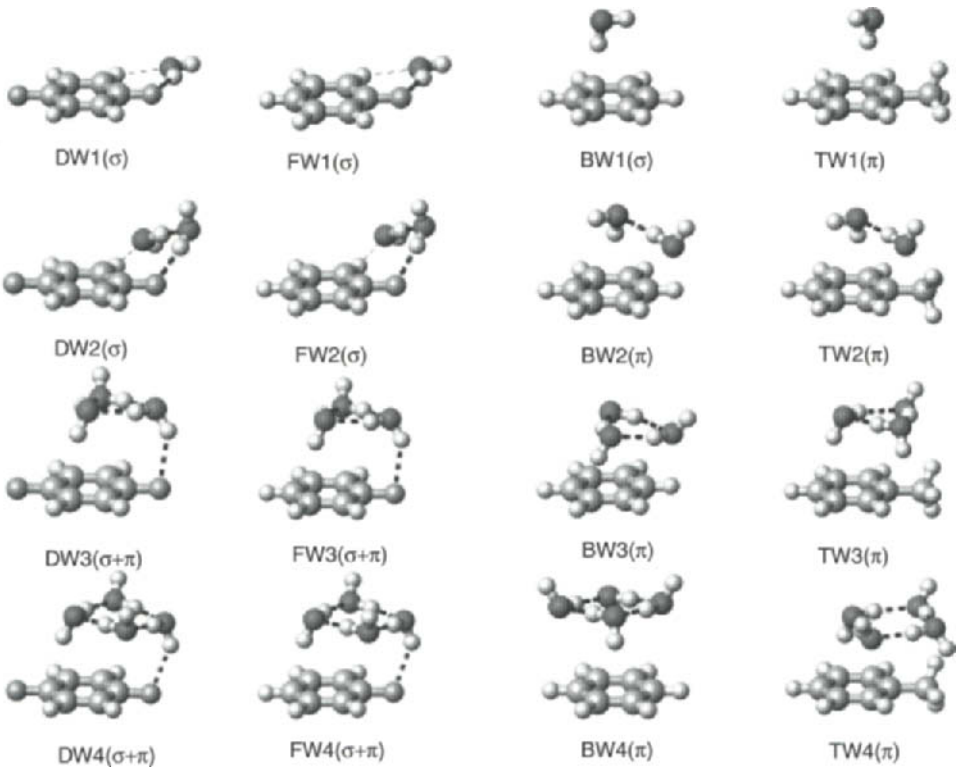

Figure 7. The optimal structures (MP2/aug-cc-pVDZ) of the π-$(H_2O)_{1\text{-}4}$ clusters (D: *p*-difluorobenzene, F: fluorobenzene, B: benzene, T: toluene, W: H_2O). Note the σ to π transition observed in the water trimer complexes of fluorobenzene and *p*-difluorobenzene.

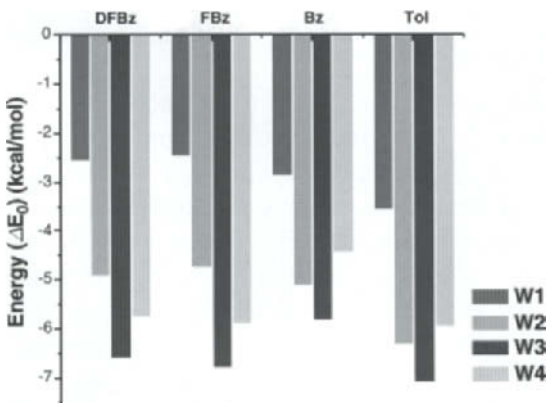

Figure 8. The interaction energies of the π-(H2O)$_{1\text{-}4}$ complexes. The energies have been evaluated at the MP2/aug-cc-pVDZ level and have been corrected for both zero point vibrational energies and basis set superposition errors. (Reproduced by permission of American Institute of Physics [136])

Most of our conclusions on the π-water cluster complexes, which are based on the structures, are supported by the excellent agreement of the calculated and the experimentally determined vibrational frequencies of the OH modes in these π-$(H_2O)_{1-4}$ clusters [136]. While we do not discuss the features of the vibrational frequencies of these systems here, it is useful to reiterate the salient insights obtained from our studies of clusters.

An important point, which has to be borne in mind for the success of any strategy in nanomaterial design, is that the presence of an excess electron, or for that matter, electronic charge, can dramatically change the structural, energetic and physical characteristics of the desired nanomaterial. This is amply illustrated in our studies of small water and metal clusters. Small metal clusters, exhibit very different physical characteristics as compared to the corresponding bulk. Hence, it is very difficult to predict the properties of nanometallic systems based on calculations of the corresponding bulk. As in the case of the bulk, a number of desirable physical characteristics can be imparted to a nanomaterial by alloying. This however to a large extent depends on the structural arrangement of various metals in the nanoalloy. In the presence of π systems, there is a marked tendency of molecules possessing polar binding sites or polar molecules to coalesce. This is an important observation in the context of weak molecular interactions behaving as steering interactions [99].

4.2 Ionophores/Receptors

Our quest in ionophore and receptor design emerged from one of the seemingly intractable problems of contemporary biochemistry; the selective recognition of the ammonium cation (NH_4^+) [141]. Much of the problem, as discussed in earlier section is due to the nearly equivalent sizes of NH_4^+ and the potassium cation (K^+) [67]. One also learns from our discussion of the cation-π interaction, that receptors providing improved dispersion stabilization are more selective for NH_4^+ [67,71,72].

In the following account, we describe our successful efforts in identifying a series of receptors with improved selectivity and affinity for NH_4^+ (Table 2) [40]. The first step in the receptor design was that high selectivity for NH_4^+ could be achieved, if the receptors have an optimal space to capture NH_4^+ and exhibit strong interactions towards NH_4^+. Since the ionic radius of K^+ is nearly similar that of NH_4^+, spatial differentiation is not very useful. However, the receptor should have an optimal space for both cations to have high affinities. Once the size in the ionophore is optimally chosen, the coordination differentiation would be very critical, because K^+ favors coordination number of 6, while NH_4^+ favors only 4. Our calculations indicated that an existing benzene based tripodal system with pyrazole arms (Table 2a) possesses both an optimal space and a good capability to distinguish between NH_4^+ and K^+, because the NH_4^+ ion interacting with the tripodal system has one vacant site available for

the interaction with only one solvent molecule, while the K^+ ion interacting with the tripodal system has three vacant sites for three solvent molecules.

Table 2. Schematic representation of designed ammonium receptors and their affinities

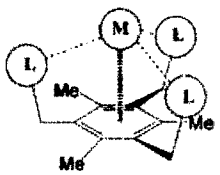

M = NH_4^+, K^+

Receptor (L)	E^R_{gas}	ΔE^R_{gas}	E^S_{gas}	ΔE^S_{gas}	E^π_{gas}	ΔE^π_{gas}	$\Delta E^{3S+\pi}_{gas}$	E^R_{sol}	ΔE^R_{sol}
(a) 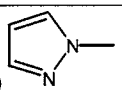	-63.34	-3.33	-24.29	-2.56	-15.24	3.45	-4.24	-21.3	-4.6
(b) 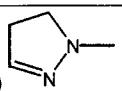	-64.48	-1.84	-23.99	-1.93	-15.31	3.78	-2.01		
(c) 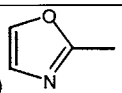	-67.26	-3.38	-22.71	-2.64	-14.91	4.16	-3.77		
(d) 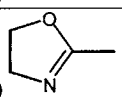	-68.48	-4.31	-24.94	-3.08	-15.11	4.01	-5.23	-24.1	-4.6
(e) 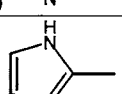	-72.58	-4.12	-29.84	-3.06	-15.65	3.43	-5.75	-24.6	-6.1
(f) 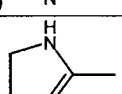	-80.94	-4.96	-30.04	-3.54	-15.82	3.29	-7.32	-36.9	-6.5
(g) 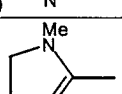	-80.67	-5.54	-30.78	-3.79	-15.97	3.16	-8.21	-33.1	-7.6

The above data have been obtained at the HF/6-31G* values and are in units of kcal/mol. Superscripts "R" and "S" denote receptor and subunit, respectively. E^R/E^S is the binding energy of the receptor/subunit with NH_4^+. E^π denotes the cation-π interaction energy. The sum of the binding energy component differences ($\Delta E^{3S+\pi} = 3\Delta E^S + \Delta E^\pi$) is correlated to the receptor binding energy difference ΔE^R, and therefore this analysis can be utilized to predict new receptors for NH_4^+. Induction energies are responsible for the smaller magnitudes of ΔE^R as compared to $\Delta E^{3S+\pi}$ (i.e., the subadditive effect). The values of E^R and ΔE^R for selected receptors in $CHCl_3$ solution [E^R_{sol} and ΔE^R_{sol}] were obtained using the IPCM method.

Thus, the predicted selectivity for NH_4^+ over K^+ ($10^{3.4}$ in $CHCl_3$ solution and $10^{2.4}$ in the gas phase) for the receptors with three subunits (Table 2a) is in

reasonable agreement with the experimental value ($10^{2.6}$ in $CHCl_3$ solution). As enunciated earlier, the origin of this selectivity and affinity can be explained by a combination of both ionic and cation-π interactions. In order to maximize the affinity and selectivity of these receptors for NH_4^+, it becomes important to maximize the π-electron density of the receptor. Indeed, as can be seen from Table 2, receptors with enhanced π-electron density exhibit much higher affinities and selectivities.

Given this background, we thought it would be interesting to extend this concept of receptor design to the biologically important molecule, acetylcholine [142]. Since the structure of acetylcholine is closed related to the tetramethyl ammonium cation (NMe_4^+), the receptor for acetylcholine should have a high affinity and selectivity for NMe_4^+ instead of NH_4^+. As in case of the receptors for NH_4^+, the benzene based tripodal system (Table 2) was chosen as the starting structure [44]. Since ionic interactions are more conducive to the binding of NH_4^+, a receptor specific for NMe_4^+ should exhibit enhanced dispersion interactions and diminished ionic interactions. These twin objectives are met in one stroke if we replace the pyrazole and imidazole arms of the NH_4^+ receptors with pyrrole and indole. The theoretical calculations also indicate that the presence of methyl groups on the benzene base leads to a large increase in steric repulsions.

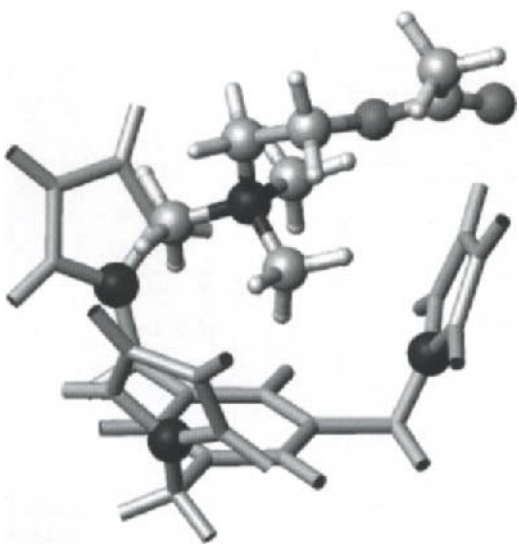

Figure 9. Optimized structure (B3LYP/6-31G*) of a complex of acetylcholine and a benzene based tripodal receptor with pyrrole arms.

Based on these calculational results, we inferred that a receptor with an unmethylated benzene base and pyrrole substituents (Figure 9) would exhibit

large affinities and selectivities towards acetylcholine. These theoretical inferences were confirmed by experimental determination of the binding affinities and selectivities using both nuclear magnetic resonance and ion-selective electrode measurements [44]

Hitherto, most of our discussion was focussed on the design of receptors for cations. It is therefore interesting to examine whether anion specific receptors can also be designed. We had mentioned in a previous section that intermolecular interactions involving anions are very different from those of cations. Since anions are more polarizable and so more susceptible to polar solvents than cations, it becomes important to take into account solvent effects. This further complicates the design of anion specific receptors. It was reported in recent studies that receptors with 1,3-disubstituted imidazolium groups bind anions by forming C-H···X^- hydrogen bonds between the imidazolium rings and the guest anion [143,144]. A simple approach of enhancing the anion binding strength is to increase the positive charge in the imidazolium ring. However, this enhanced anion binding strength could be dramatically diminished in the presence of polar solvents because of the inverse relation between electrostatic energy and the solvent dielectric. One can however increase the magnitude of the induction energies, by toying around with the dipole moments.

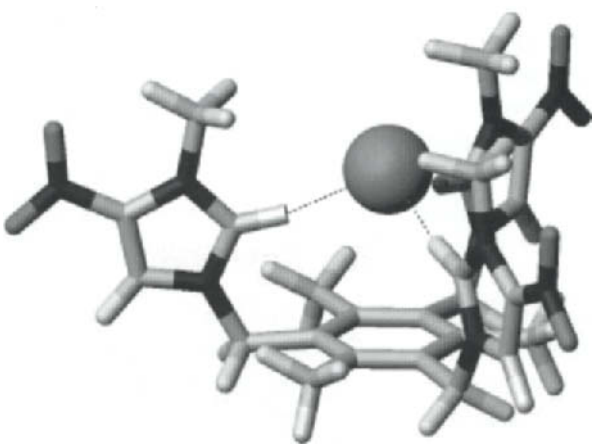

Figure 10. Optimized structure (HF/6-31G*) of a complex of chloride anion and a benzene based tripodal receptor with nitro-substituted imidazolium arms.

The impetus for such an approach emerged from a study of ion binding by crown ethers [37]. We realized that the charge-dipole interactions play a very important role in ion recognition. A simple method of modulating the dipole moments and hence the magnitude of induction energies is by attaching a strategically placed electron withdrawing group with a high dipole moment. Indeed, we found that by placing a nitro group at the C(4) position of the

imidazolium ring (Figure 10), the magnitude of both the electrostatic and induction energies could be magnified. Furthermore, the structure of the tripodal receptor containing three imidazolium groups helps preorganize the anion binding. Experimental evaluations of both the ion affinity and selectivity confirm this theoretical prediction [43,45].

As can be noticed, most of our previous discussion featured the benzene-based tripodal receptors. The fact that a single receptor with suitable substituents can exhibit affinity and selectivity for both cations and anions (amphi-ionophores), led us to theoretically investigate the possibility of other systems possessing similar characteristics [36,41].

Given the fact that host-guest complexation plays a central role in various biological processes together with the wide prevalence of several ion-binding proteins [142,145-152], we thought it would be interesting to investigate the ion binding characteristics of cyclic peptides. Though the initial choice of the system, cyclohexaglycyl (a cyclohexapeptide comprised of six glycine molecules) was dictated by computational limitations, we soon found that several cyclic peptides exhibit high affinities toward both cations and anions in the gas phase [36,41]. Since solvent effects play a very important role in determining the ion affinities and selectivities, we recently examined the binding characteristics of one such cyclic peptide, composed of six alanine molecules, with both anions (F^-,Cl^-,Br^-) and cations (Na^+, K^+) in the aqueous phase [41]. The calculations, which included molecular dynamics simulation in the presence of explicit solvent molecules reveals that in the presence of cations, the carbonyl groups of the peptide tend to orient toward the cations [41]. Interestingly, similar observations were made by Doyle et al. in explaining the binding of the potassium cation in biological ion channels and by one of the authors of this review in his investigations of the binding of the potassium ion to gramicidin [146,149-152].

In the discussion of all the ionophores/receptors till now, the binding of the cations or anions is mediated through the presence of oxygen or nitrogen atoms present on the receptor. Given our extensive investigations of cation-π interactions, we thought it would be appealing to explore the possibility of carbon based materials being used as ionophores [38,42,153]. There have been reports of the systems in which π-orbitals are oriented vertically to the plane of the rings, viz. belt-shape carbocyclic conjugated systems (annulenes, beltenes, cyclacenes, and collarenes) [154]. Interestingly, most of these systems are closely related to other carbon based systems containing curved surfaces. These include fullerenes and carbon nanotubes [155]. In an effort to unravel the ion binding characteristics of these carbon materials, we carried out ab initio calculations of collarenes (benzene rings linked by methylene linkages), cyclacenes (comprised of only benzene rings) and beltenes (ethene groups linked by methylene linkages) and their complexes with various cations (alkali, alkaline-earth metal and organic cations) in both the gas and aqueous phases

(Figure 11) [38,42,153]. Apart from an evaluation of the interaction energies, the cation selectivities in aqueous solution were investigated using Monte Carlo and molecular dynamics simulations. Our investigations revealed that both collarenes and beltenes exhibit excellent binding affinities and selectivities for metal cations [38,42]. However, beltenes have an added advantage because their cavity sizes are more flexible than collarenes [38]. Additionally, suitable substituents could also enhance their binding affinities and selectivities. In particular, the designed molecules could be modified to be soluble in polar solvents by adding hydrophilic groups on the edges of the molecules.

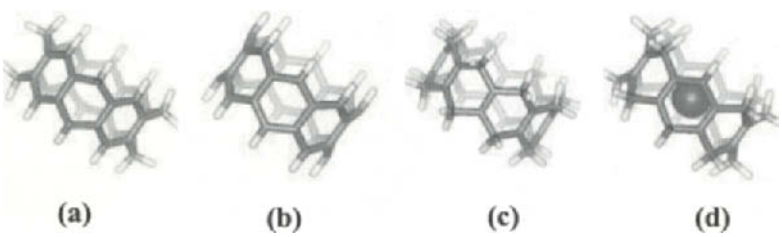

Figure 11. Structures of (a) collarenes, (b) cyclacenes, (c) beltenes, and (d) [8]beltene complexed to the rubidium cation.

4.3 Nanomaterials

Up to now, most of our discussion featured small molecules, complexes, or clusters. In this section, we examine on how these conclusions could be extended to the realm of functional assemblies and nanomaterials. We begin with examining the structures and physical characteristics of carbon containing systems. We then progress to a discussion of organic nanotubes, metallic and encapsulated nanowires, and finally, nanodevices.

4.3.1 Carbon based materials

Ever since the discovery of fullerenes and carbon nanotubes, a lot of effort has gone into the discovery of other interesting allotropes of carbon with unusual structural characteristics and novel physical properties [155]. Carbon nanotori are one of the best examples in this context. The structures of these systems were proposed by Dunlap and Itoh et al [156-159]. However, a practical exploitation of these carbon nanotori requires a detailed knowledge of various possible structures and their electronic properties. Towards this end, the geometries, electronic structures, and energetics of small carbon nanotori were investigated employing both tight-binding and semi-empirical quantum chemical methods [160]. We observed that their physical characteristics are intrinsically linked to the symmetry of their structures (Figure 11). Thus, tori of D_{5d} symmetry, which are energetically more favoured than the corresponding carbon nanotubes, exhibit semiconducting characteristics. On the other hand,

tori of D_{6h} symmetry, wherein the carbon linkages are more strained, possess metallic characteristics. While most of these calculations have been carried out closed-shell species in their ground states, it is important to note that most of the electrical and magnetic properties of nanomaterials are associated with either excited states or open-shell species. We discuss this issue of open-shell calculations in the context of our work on the magnetic properties of alkali-metal fullerides [161].

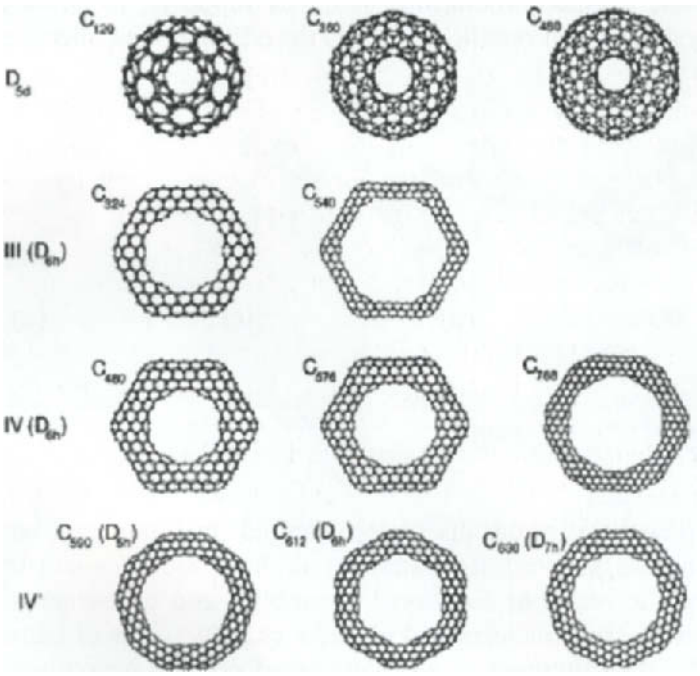

Figure 12. Optimized structures of various types of carbon nanotube tori. (Reproduced by permission of American Physical Society [160])

Alkali-metal fullerides (A_xC_{60}, A = Na, K, Rb, Cs) exist in two stable phases, a face centered-cubic (fcc) rocksalt structure comprised of freely rotating C_{60}^- monomers above ~400 K and an orthorhombic structure containing covalently bonded dianionic polymer chains below ~400 K [162,163]. The temperature dependent electrical and magnetic properties of the polymer phase, which exhibits characteristics of a quasi-one-dimensional metal, are in particular very interesting. Thus, this phase displays an abrupt transition from paramagnetic to diamagnetic susceptibility around 220-270K without hysteresis [162]. Since the individual C_{60} cages are connected by a [2+2] cycloaddition along the face diagonal to the fcc unit cell, we presumed that these changes can be linked to the changes in the electronic characteristics of $(C_{60})_2^{2-}$. Indeed, calculations carried out on different structures of $(C_{60})_2^{2-}$, which included several open-shell species, reveal that the ground triplet state (*d_D2h*) of the doubly

charged dimer is nearly degenerate with the excited singlet state (*s_C2h*) (Figure 13). These calculations were carrying out, employing a wide variety of theoretical methods ranging from semiempirical [unrestricted parametrized method (UPM3), restricted open shell parametrized method at the UPM3 optimized geometries (ROPM3//UPM3)], ab initio [restricted open shell Hartree-Fock methods using STO-3G basis sets (ROHF/STO-3G)], to density functional methods [restricted open shell density functional calculations using 4-21G basis sets employing either Becke's three parameter hybrid method using Lee-Yang-Parr correlation functional (ROB3LYP) or Perdew-Wang correlation functionals (ROPW91)]. Given the nearly similar energies exhibited by the two species (ground triplet, excited singlet), it is likely that all of them co-exist. Our results indicate that the stability of the singlet state of $(C_{60})_2^{2-}$ is significantly enhanced in the presence of cations, due to stronger Coulombic interactions. At low temperatures (~220 K), a single-bonded singlet structure is the dominant species, but with an increase in temperature, the population of the double-bonded triplet structure increases with a relatively small activation barrier (0.3–0.4 eV). The ease of this transformation from the single-bonded singlet to the double-bonded structure triplet structure explains the increased susceptibility of $(C_{60})_2^{2-}$, with an increase in temperature (i.e., the transition from the diamagnetic toward the paramagnetic state). Our calculations also indicate that the spin states of fullerenes doped with alkali metals are important factors, which govern the stability of various inter-fullerene bonding configurations and also explain the origin of the ensuing magnetic phase transition [161].

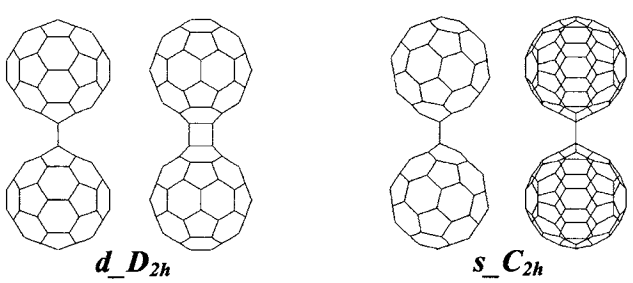

Figure 13. Optimized structures of the ground triplet (*d_D2h*) and excited singlet (*s_C2h*) states of $(C_{60})_2^{2-}$. Two views of the structures have been provided.

With this background on open-shell species, it is of interest to examine our work on the endohedral fullerenes [A@C_{60} (A: N, P, As, O, or S)] [91]. Interest in these kind of systems was kindled after the experimental observation of N@C_{60} in 1996 [164]. The most interesting aspect of the experimental investigation was the fact that the encapsulated nitrogen, which possesses three unpaired electrons and is paramagnetic in nature, is totally inert within C_{60}. While there have been a few attempts to explain the remarkable inertness of the highly reactive nitrogen atom with in the C_{60} cage, there were no detailed

theoretical investigations of the same [165,166]. As was mentioned earlier, investigations of systems containing open-shell species is computationally a very arduous task, and is fraught with a number of problems. A number of authors have advocated the use of multi-determinant wavefunctions to investigate open-shell systems, but it is computationally too expensive for these large systems [167]. While the use of single reference unrestricted Hartree Fock (UHF) wave functions is valid, if the spins are localized, one often encounters the problem of spin contamination. Fortunately, there was very little or negligible spin contamination in most of our calculations involving these endohedral fullerenes. Of course, it should also be mentioned that the use of restricted UHF wavefunctions can solve the problem of spin contamination but then that leads to symmetry breaking because of the neglect of spin polarization [167]. Since the available computational resources thwarted our attempts to carry out calculations at the MP2 level using basis sets larger than 6-31G*, we resorted to an ingenious method to obtain estimates of the interaction energy of the paramagnetic atom and C_{60}. We carried out calculations on the interaction of these paramagnetic atoms with benzene at several levels of theory using very large basis sets. A measure of the computational effort involved can be realized from the fact that MP2/aug-cc-pVQZ calculations of $^4N\cdots C_6H_6$ complex involves the evaluation of interaction energy of an open-shell system containing 836 basis functions. The interaction energy of 1.31 kcal/mol obtained for the $^4N\cdots C_6H_6$ complex at the MP2/aug-cc-pVQZ level, however indicated that a nearly 8-fold increase in the size of the basis set increases the interaction energy only by an order of two (MP2/6-31G* = 0.73 kcal/mol).

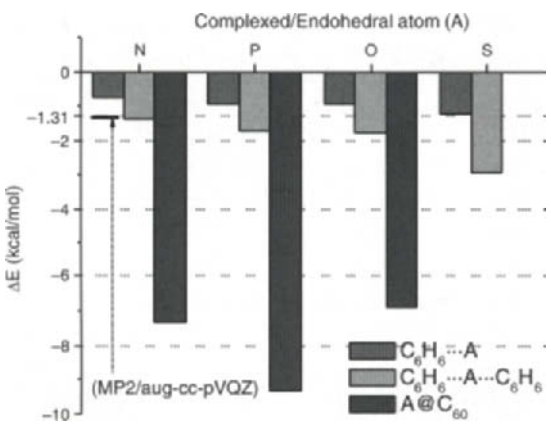

Figure 14. MP2/6-31G* interaction energies of $A\cdots C_6H_6$, $A\cdots C_6H_6\cdots A$, and $A@C_{60}$ (A = ^4N, ^4P, ^3S, ^3O) complexes.

The magnitudes of the MP2/6-31G* interaction energies obtained for the $A\cdots C_6H_6$, $A\cdots C_6H_6\cdots A$, and $A@C_{60}$ (A = ^4N, ^4P, ^3S, ^3O) complexes and displayed in Figure 14, indicate that the interaction energies of the $N@C_{60}$ and

P@C_{60} complex are nearly ~10 times the values exhibited by the corresponding A···C_6H_6 complexes [91]. The high interaction energies observed in the case of N@C_{60} are predominantly dominated by dispersion energies. An examination of the orbital maps of ^{4}N and ^{4}P in the endohedral C_{60} complexes revealed that there is no orbital interaction between the paramagnetic atom and the C_{60} cage. This is because the 2*p* and 3*p* orbitals of N and P lie far below the HOMO of either the uncomplexed C_{60} or its complex. Though we investigated the energy barriers for the formation of endohedral ^{3}O@C_{60}, we do not discuss it in the context of this review [91]. Given the current reports of the utility of endohedral fullerenes containing paramagnetic atoms in the design of quantum computers [168], we believe that the present investigations would be a step in that direction. The common thread running through all the nanomaterials discussed in this section is that the properties of most of these systems are a consequence of covalently formed bonds.

4.3.2 Organic Nanotubes and Peptide Helixes

There are several advantages in using hydrogen bonds to design nanomaterials [64,65,98]. We illustrate this in fine detail in this section, wherein we discuss the formation, stabilization, and characterization of organic nanotubes and unusual peptide helixes [64,65,169]. Given the potential applications of organic nanotubes as artificial biological channels, drug deliverers, nano-chemical reactors, and hosts for nanomaterials, there has been a lot of interest in designing hollow tubular self-assembled structures [170-175]. Early work on organic nanotubes was predominantly focused on variants of biological systems like tubular transmembrane channels, cyclic peptides and cyclodextrins [36,41,149-152,170-174]. However in a recent report, we had highlighted the self-assembly of an organic nanotube from non-tubular subunits of calix[4]hydroquinone (CHQ) [64]. One of the spectacular aspects of this report was that the theoretical design preceded the actual experiment of synthesis and investigation of the X-ray structure. Apart from highlighting the robustness of the theoretical approach, this study also provided several insights into the mechanism of self-assembly of these CHQ nanotubes.

We employed a wide array of theoretical methods in our investigations. The initial conformational searches were carried out using both empirical and molecular dynamics simulations. It should be mentioned that several existing force fields were not reliable in this regard. In the next step, we employed semiempirical methods (such as PM3) to obtain the initial geometries of various self-assembled structures [176]. These structures were then subject to full geometry optimizations employing the Becke three parameters with Lee-Yang-Parr density functionals (B3LYP) in conjunction with small (3-21G) and moderately sized (6-31G*) basis sets [177-180]. Given the limitations of density functional calculations in describing intermolecular interactions involving π systems, we also carried out second order Møller Plesset perturbation (MP2)

calculations using the 6-31G* and aug-cc-pVDZ basis sets to obtain insights into the competition between hydrogen bonds and π-π stacking interactions [181]. Incidentally the calculations of the octamer structure with bridging molecules involves 4704 basis functions, which we believe is one of the largest calculations ever carried out to date. We also carried out pseudopotential plane wave density functional theory (PW-DFT) calculations to obtain insights on the crystal structure of the CHQ nanotubes [27]. These PW-DFT calculations involve the use of a generalized gradient approximation (GGA) of Perdew and Wang and the Vanderbilt pseudopotential [182-185]. The cutoff energy for the plane wave basis set is 20 Ry. It should be mentioned that PW-DFT calculations are devoid of basis set superposition error (BSSE) [186], because plane wave basis sets uniformly cover all the space unlike Gaussian orbitals, which span only a local region. Though empirical and semiempirical methodologies are not very reliable, they help weed out several implausible structures. Given the size of the systems, the computational effort, and the relative reliability of various theoretical methodologies, we believe that the B3LYP/6-31G* method is well-suited for investigations of large molecular systems.

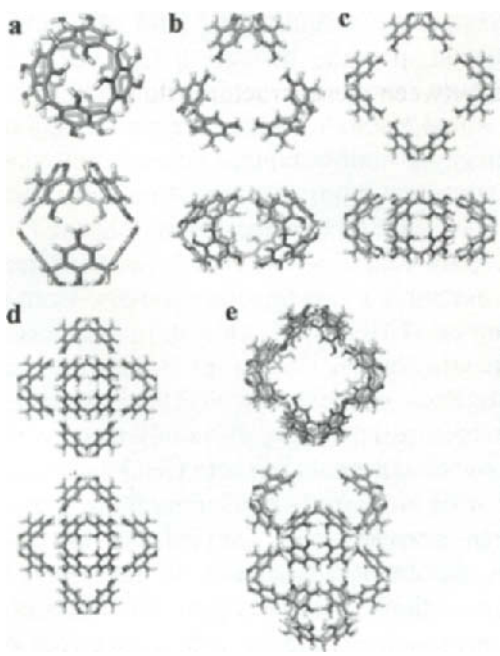

Figure 15. Calculated structures of *n*-oligomers in the absence of water molecules (top and side views): (a) CHQ dimer, (b) trimer, (c) tetramer, (d) octahedral hexamer, and (e) tubular octamer (B3LYP/6-31G* level). (Reproduced by permission of American Chemical Society [65])

In the discussion of our results on these CHQ nanotubes, we do not delve into our calculations on the individual monomers, because they are outside the

gambit of this review. The first-stage of the self-assembling study of CHQs began with calculations of various possible combinations of assembled structures. These included dimers, trimers, tertramers, hexamers, and polymers of CHQ (Figure 15). In the n-oligomer, we have 8n OH groups of which 4n OH groups form four-membered circular intramolecular hydrogen bonds. The remaining 4n free OH groups are therefore available for the formation of intermolecular hydrogen bonds. Thus, in the dimer (Figure 15a), CHQs form a capsule comprised of only 4 hydrogen bonds. On a similar note, the trimer (Figure 15b) and tetramer (Figure 15c) possess 6 and 8 hydrogen bonds to form cyclic structures, and the tubular octamer (Figure 15e) possesses 16 hydrogen bonds. On the other hand, the octahedral hexamer (Figure 15d) is comprised of 24 hydrogen bonds with no dangling hydrogen atoms. The calculated assembling energies per monomer of the dimer, trimer, tetramer, hexamer, and octamer (Figure 15a-e) at the BSSE-uncorrected B3LYP/6-31G*//B3LYP/3-21G level are 9, 8, 9, 21, and 11 kcal/mol. This indicates that the hexamer (Figure 15d) is the most favourable self-assembling structure because of full saturation of the dangling hydrogen atoms by hydrogen bonding. The numbers of the dangling hydrogen atoms in the dimer, trimer, tetramer, hexamer, and octamer are 4, 6, 8, 0, and 16, respectively. It should be emphasized that BSSE corrected values also exhibit similar trends, and hence the resulting relative assembling energies between these structures do not change significantly. While the above calculations were carried out in the absence of water molecules, it is interesting to examine the self-assembly trends in the presence of water molecules. Apart from highlighting the role of water molecules in the formation of intermolecular hydrogen bonds, this would also reflect the competition between hydrogen bonds involving water molecules and those involving CHQs. Our calculations reveal that the involvement of water molecules in the formation of bridging hydrogen bonds energetically stabilizes the assembly of oligomers. Thus, the tubular octamer and polymers are energetically more stabilized than the hexamer because the latter has no free hydrogen atoms to form hydrogen bonds with water. This can be noted from the B3LYP/6-31G* assembling energies per monomer of the dimer, trimer, tetramer, hexamer, and octamer of 44, 40, 37, 22, and 47 kcal/mol, respectively. Clearly, the involvement of the water molecules in the assembling process stabilizes the tubular octamer relative to the two tetramers, by about 10 kcal/mol. When the tubular octamer forms a linear chain with repeating units, the stability is further enhanced by almost the same amount (~10 kcal/mol-monomer) with the formation of hydrogen bonds between repeating units via bridging water molecules. These results strongly suggest that the formation of tubular polymeric structures is energetically favoured. Indeed, in experiments, the addition of water molecules to a mixture of CHQ in acetone results in the formation of a stable self-assembled tubular structure, which is in agreement with the theoretical predictions. A similar

tubular structure was also noted upon electrochemical reduction in the presence of water.

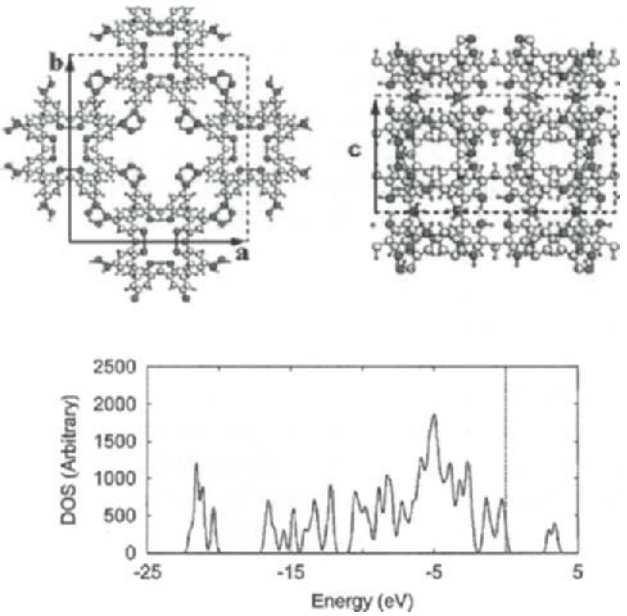

Figure 16. Calculated atomic structures (top and side views) and density of states (DOS) of CHQ nanotubes. The unit cell is drawn by the dashed lines (a = 23.30 Å, b = 25.04 Å, c = 11.63 Å, and $\alpha = \beta = \chi = 90°$). The HOMO energy is set to zero. The HOMO-LUMO energy gap is 2.9 eV. (Reproduced by permission of American Chemical Society [65])

We also carried out electronic structure calculations of the CHQ crystal to understand the structures and electronic properties of the organic nanotubes. Using the periodic boundary condition, the molecular structure was fully optimized without imposing any symmetry constraints within a unit cell, fixed to the X-ray characterized unit cell size [64]. Since the positions of hydrogen atoms are not available in the X-ray structure, they were determined by carrying out PW-DFT calculations (Figure 16). These calculations indicate the presence of infinitely long 1-D hydrogen bond arrays composed of hydroxyl groups of CHQs and water molecules and well-ordered intertubular π-π stacking pairs. The calculated distance between two HQ centroids is 3.76 Å (interplanar distance: 3.54/3.48 Å) and the angle between two π-ring planes is only 3.5°. These theoretically predicted geometrical parameters are in good agreement with the experimental values (3.63 Å, 2.9°; interplanar distance: 3.41/3.38 Å). Even though PW-DFT calculations do not adequately describe π-π interactions, the distance between two HQ centroids is in good agreement with the X-ray structure. We believe that this is due to the fact that the repulsion between the aromatic rings is small and PW-DFT calculations describe the hard wall region well. As a consequence, the crystal structure is well-reproduced by the PW-DFT

calculations. The calculated chemical bond lengths and angles are within 0.01 Å and ~3° from the X-ray data; the hydrogen bond distances are only slightly shorter (within ~0.08 Å) and the π-π interplanar distances are only slightly larger (within ~0.1 Å). An interesting feature of the one-dimensional hydrogen bond arrays is that the hydrogen bonds are particularly short for systems even in the absence of negative charges. The O-O distance is 2.61 and 2.58 Å for the water-HQ pair and the HQ-water pair, and 2.57 Å for the HQ-HQ pair, (which are in reasonable agreement with experimental values of 2.67 and 2.64 Å, respectively), is comparable to the distances observed in short strong hydrogen bonds (SSHB) length [33,34,187,188]. We believe that this indicates the significant role of hydrogen bond relays on hydrogen bonds lengths in one-dimensional systems. The predicted structure (with hydrogen atoms included) and the density of states (with respect to energy) are shown in Figure 16. The CHQ nanotubes are predicted to possess insulating characteristics because the band gap is 2.9 eV. The interaction energy per short hydrogen bond between HQ and water is calculated to be 10 kcal/mol, which is 4 kcal/mol larger than the average value (6 kcal/mol) of those of water-HQ, HQ-HQ, and HQ-water [65,140]. This enhanced hydrogen bond energy is due to the formation of short hydrogen bonds.

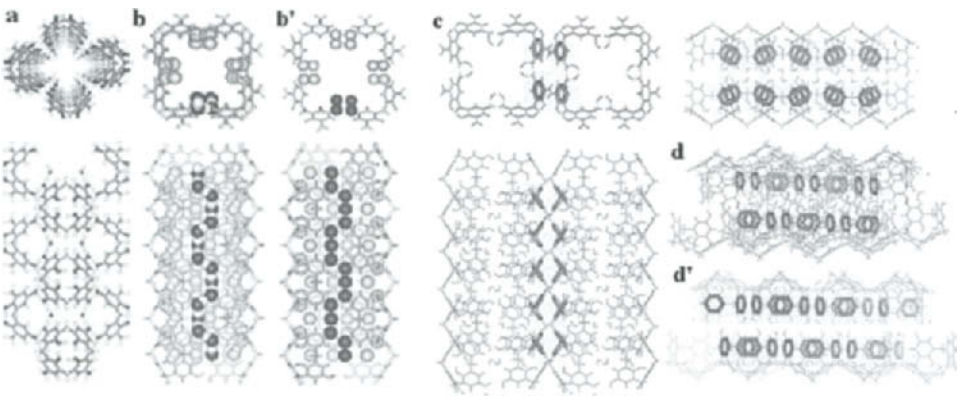

Figure 17. Longitudinal H-bond relay between CHQs and water molecules and intertubular π-π stacking interactions: (a) Four pillar frames of short H-bonds (in dark shade) are shown as the top view; (b) The space-filled part (with O atoms in dark shade and H atoms in white) represents a 1-D H-bonds relay comprised of hydroxyl groups (-OH) and water molecules, where only 1-D H-bonds array is clearly represented for visual aid; (b') the X-ray structure corresponding to (b); (c) Top view with two side views; (d) Projected view to show displaced stacks on aromatic rings plane; (d') the X-ray structure corresponding to (d). Note the similarity in the position of heavy atoms between the X-ray and PW-DFT structures, while the H atom positions are not given in the X-ray structutres. Figures b' and d' clearly demonstrate the striking features of the infinitely long 1-D H-bonds arrays and the exemplary displaced π-π stacks, respectively. (Reproduced by permission of American Chemical Society [65])

In the absence of water, for each CHQ monomer, the number of dangling hydrogen atoms is 4, and the number of aromatic rings available for π-π stacking interactions is also 4. Thus, four hydrogen bond pairs and four π-π stacking pairs can be formed by neighbouring dangling hydrogen atoms and HQ rings of other CHQ monomers, respectively. As the π-π stacking interactions are stronger than the normal hydrogen bonds, the π-π stacking would be favored [17,18]. On the other hand, in the presence of water, the CHQs form chains HQ-(water-HQ-HQ-)$_n$water comprised of the building units (water-HQ-HQ-). Thus for every CHQ monomer of the CHQ nanotube bundles, two water molecules are involved in the formation of two hydrogen bonds, with one of them behaving as an acceptor and the other as a donor. The hydroxyl groups of each HQ moiety are also involved in the formation of two hydrogen bonds (one as an acceptor by the oxygen atom and the other as a donor by the hydrogen atom). Since one bridging water molecule is present for two HQ moieties, the number of hydrogen bond partners is three times the number of π-π stacking partners. Although the strength of one-dimensional short hydrogen bonding interaction (~10 kcal/mol) is similar to the strength of the π-π stacking interaction (~9 kcal/mol), the assembling along the one-dimensional short hydrogen bonds relay should be much more favorable because the number of hydrogen bonds are three times the number of π-π stacks. Indeed, in the presence of water, CHQs are assembled to form long tubular structures with four infinitely long short strong hydrogen bond arrays (PW-DFT results in Figure 17a, b; X-ray results in Figure 17b'). Interestingly this feature can be related to the high-resolution transmission electron microscope (HRTEM) image of a single nanotube of 2-nm width loosely bound to a CHQ bundle. In the absence of water, we see laminar film-like structure of CHQs for which the numbers of both interaction pairs are the same, because the π-π stacking interactions (~9 kcal/mol) are stronger than the normal hydrogen bonding interactions (~6 kcal/mol). The CHQ tubes assembled to form long tubular structures in the presence of water form bundles with intertubular π-π stacking interactions (PW-DFT results in Figure 17c, d; X-ray results in Figure 17d'), resulting in crystals with well-ordered two-dimensional arrays of pores. We would be addressing the structures of these pores in the context of our discussion on encapsulated nanowires in the next section [189-191]. Interesting is a comparison of the predicted with the experimentally determined crystal structure. In the X-ray structure, the unit cell is comprised of 8 CHQ monomers (comprised of 32 HQ moieties) and 16 bridging water molecules, which involve the formation of 80 hydrogen bonds (48 for four one-dimensional bond arrays and 32 for four circular four-membered hydrogen bonds) and 16 π-π stacking pairs, where the double count due to the neighboring HQ partners in other unit cells is removed. The number of hydrogen bonds in the needlelike crystal is three times the number of π-π stacking pairs. A nanotube bundle exhibits the infinitely long one-dimensional hydrogen bonding

network between hydroxyl groups of CHQs and water molecules and well-ordered intertubular π-π stacking pairs (Figure 17). Figure 17d and 17d' shows clear projected views of the π-π stacks on the aromatic rings plane. The π-π stacks in PW-DFT calculations (Figure 17d) are very close to the π-π stacks in the X-ray structure (Figure 17d'). Thus, though the PW-DFT calculations do not properly account for π-π interactions, the packing effect (by fixing the unit cell size to the crystal data) resolves such problems, and the overall structure is in excellent agreement with the X-ray structure.

There are relatively few examples of self-assemblies of pure organic molecules exhibiting rectangular shapes and large pore sizes. However, the bundles of CHQ nanotubes form very large and novel chessboardlike rectangular structures. The apparent size of each inner square channel (with the van der Waals volume excluded) is 6 × 6 $Å^2$ in terms of apparent cross section on the projected plane. However, the real cross section (with the van der Waals volume excluded) is 8 × 8 $Å^2$ because atoms are located in zigzag shape, and the shortest distance between one atom on a wall in the tube and another atom on the other side of the wall is 11 Å. An annealing technique was employed to study the pore volume using classical molecular dynamics simulations (for 10 ps) [103]. Interestingly, this technique was also employed in our earlier investigations of ion-chanels [149-152]. When it is fully solvated, it has about 48 water molecules in a unit cell, which corresponds to the volume of 8 × 8 × 11.63 $Å^3$.

In order to investigate the effect of solvent on the one-dimensional hydrogen bonds, we carried out PW-DFT calculations of the CHQ crystal in the explicit presence of solvent water molecules (48 water molecules in a unit cell excluding the bridging water molecules) with periodic boundary conditions for the X-ray crystal unit cell. In this case, the binding energy per short hydrogen bond is evaluated to be 9 kcal/mol, as the nonadditive interaction energy was extracted from the PW-DFT results of both the real system with the nonadditive interaction energies and a hypothetical system with the PW-DFT pair interaction energies. The solvent effect reduces the short hydrogen bond strength, but the effect is rather small (1 kcal/mol). Thus, it can be seen that our theoretical investigations of the self-assembly of CHQ nanotubes provides a wealth of information, both on the use of different theoretical methods and on the relative roles of intermolecular interactions, viz. hydrogen bonding and π-π interactions. While we describe the experimental utility of these organic nanotubes in the next section, it is important to reiterate that the computational effort involved in these calculations is enormous.

One of the most unusual discoveries made during our investigations on the role of charges in hydrogen bonding, was the identification of the left-handed λ-helix secondary structural motif in peptides and proteins [169]. The reason for discussing this discovery in this section on the role of hydrogen bonded materials is our belief that the transition between left-handed and right-handed

helix motifs can be triggered by the presence of charged species near the end of the helix terminals (Figure 18). The possibility of such a transition would herald the development of new chiral switches.

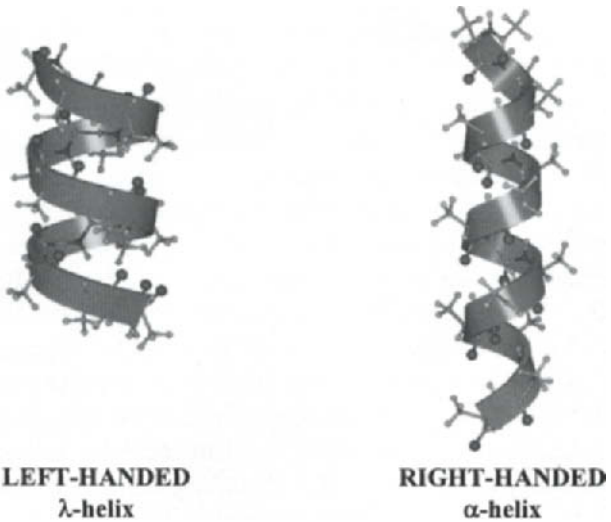

Figure 18. A left handed λ-helix vs. a right-handed α-helix.

In our initial investigations, we employed a poly-alanine peptide capped with neutral amino and methyl groups (CH_3-$(Ala)_n$-NH_2) [169]. Molecular dynamics simulations of this peptide under neutral terminal charge conditions yielded a right-handed α-helix pattern [192], in about ~1.8 ns. However, when the terminals are charged (NH_3^+-$(Ala)_{30}$-COO^-), we observed that a left-handed λ-helix is formed in about ~4.0 ns. During the formation of the left handed λ-helix, helix-nucleation first occurs at the terminal sites (in particular, near the N-terminus in the case of the left handed λ-helix) and it promotes the propagation of the helix pattern along the segment. It should be noted that in both the molecular dynamics simulations, only the terminal composition is different. Therefore, the handedness of the final conformation is related to the terminal charge conditions. The propagation of the helix pattern along the segment clearly shows that sequential local interactions determine the nascent folding patterns of the protein. The initial folding in the left-handed λ-helix arises from the electrostatic interactions of the positively charged NH_3^+ group with the adjacent carbonyl dipole moiety, followed by the dipole-dipole interactions between two adjacent carbonyl moieties. Similar conclusions were obtained from calculations using a density functional (B3LYP) approach.

4.3.3 Metallic and Encapsulated Nanowires

There is a lot of interest in the fabricating nanowires, with lateral dimensions smaller than 1 nm. Apart from being useful in building molecular

level devices, these subnanowires have been found to exhibit several unusual properties because of the predominance of quantum effects in such dimensions [93]. However, these subnanowires are difficult to make and even if they are made, they are not stable for long periods of time. In a previous section, we had described our theoretical investigations and experimental characterization of organic CHQ nanotubes. Of particular interest were the honeycomb like structure of the CHQ nanotubes and their pores (Figure 19).

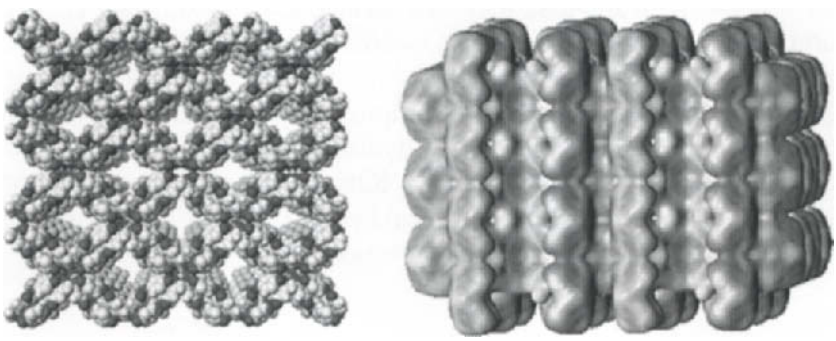

Figure 19. Cross-sectional views of the CHQ nanotube crystal structure with bridging water molecules: perspective view and side view showing solvent-accessible surface. The size of the pore (with the van der Waals volume excluded) is 6 × 6 $Å^2$ on the projected view. However, the actual pore size is 8 × 8 $Å^2$ because atoms are located in zigzag shape. The nearest distance between atoms on the opposite sides of the pore is 11 Å. (Reproduced by permission of American Chemical Society [65])

Given the pore size of 8 × 8 $Å^2$, we envisioned that they could be used as templates for nano-patterning. Hydroquinones are widely used as reducing agents; in particular, to reduce silver ions to form silver aggregates in acidic solution under photochemical conditions, because of the free energy gain through the reduction-oxidation process [193,194]. Interestingly, ultrathin silver nanowires can be formed within the pores, after the CHQ nanotubes were soaked in a 1M aqueous solution of silver nitrate and the resulting mixture was subject to ultraviolet irradiation [189]. The resulting nanowire is comprised of four dumbbells, each of which contains two silver atoms, superimposed on one another, and crisscrossed in their length. In the context of this review, it is useful to examine the theoretical characterization of these ultrathin silver nanowires.

We employed density functional calculations using the ultrasoft pseudopotential plane wave method to investigate the CHQ nanotubes and the encapsulated silver nanowires. The local density approximation (LDA) of Ceperley and Alder and Vanderbilt pseudopotential was employed and the cutoff energy of the plane wave basis set was 20 Ry [27,182-185]. Full-potential linearized augmented plane wave method calculations were also carried out on the isolated silver nanowire [195-197]. To check the reliability of our

methodology, we initially carried out all the calculations on bulk silver. Fortunately, we observe an excellent agreement between the experimentally determined and theoretical predicted values of the lattice constants, modulus constant, and cohesive energies in case of bulk silver [198].

Since we have already discussed the theoretical characterization of the CHQ nanotube in a previous section, we examine the reduced form herein. Upon reduction with silver nitrate, the CHQ nanotubes get transformed to the corresponding calix[4]quinone-hydroquinone (CQHQ) nanotubes, whose band gaps of 0.3 eV indicate that they are semiconducting in nature. The gross structural feature of CQHQ nanotubes is similar to that of CHQ nanotubes, with well ordered hydrogen bond arrays and inter-tubular π-π stacking pairs. In the CQHQ nanotubes, there are only two infinitely long one-dimensional hydrogen bond arrays per nanotube because two hydroxyl groups are transformed to the corresponding reduced forms (=O). Simultaneously, silver cations get transformed to metallic silver. The calculated O-O and π-π stacking distances are similar to those observed in the CHQ nanotubes.

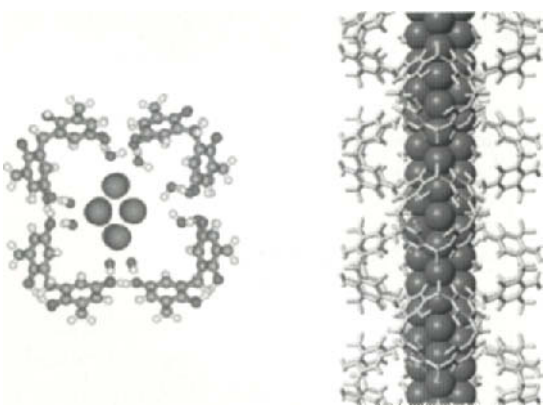

Figure 20. Top and side views of a silver nanowire inside a CQHQ organic nanotube. (Reproduced by permission of American Physical Society [191])

Upon reduction of the CHQ nanotubes, the silver atoms are located within the reduced CQHQ nanotube (Figure 20). Given the reports of an enormous enhancement of van der Waals forces between neutral silver particles possessing nanodimensions [95], it seems likely that the neutral silver atoms coalesce to form aggregates of eight silver atoms in a single unit cell. We have used a supercell geometry to simulate the silver nanowires because the neighboring nanowires are sufficiently separated by 5 times the wire width along the [110] and [001] directions. The predicted equilibrium properties of the 2/2 [110] silver nanowire indicates that its lattice constants along [001], [1 10], and [110] directions are 4.01, 2.79 and 2.78 Å. These are in good agreement with the experimental values (4.0 Å along the [110] direction and 2.75 Å along the [110]

direction). The calculated atomic layer spacing along the [110] wire axis (2.78 Å) is decreased by 4 % relative to the corresponding calculated bulk value (2.88 Å), in good agreement with the experimental value (2.75 Å) which is reduced by 4 % relative to the X-ray diffraction result of the bulk (2.89 Å) [64,191]. This compression is due to the reduced interaction from the outside of the surface, resulting in increased interaction toward inner atoms inside the surface, which can be seen in silver nanoclusters [127,130]. The interatomic spacing along [001] direction is predicted to be 4.01 Å, which is 2% smaller than the corresponding bulk value (4.09 Å). In the case of 2/2 nanowire, the predicted cohesive energy is 2.4 eV, which is 0.9 eV smaller than the bulk value. This indicates that the isolated 2/2 nanowire might not be stable. Even though it barely fits inside the cavity of the CQHQ nanotubes, we have explored the possibility of an encapsulated 4/3 silver nanowire. Our results indicate that the cohesive energy of the 4/3 nanowire is 2.6 eV. This indicates that the cohesive energy gain of the 4/3 over the 2/2 nanowire is only 0.2 eV, which is not significant in spite of three-fold increase in the number of atoms.

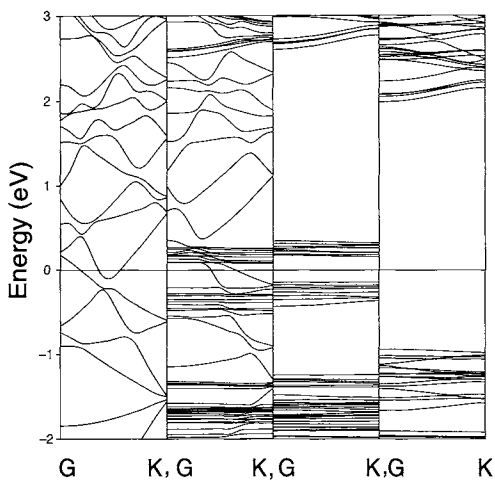

Figure 21. Band structure of an isolated silver nanowire (left-first), a silver nanowire encapsulated in a CQHQ nanotube (second), a CQHQ nanotube (third), and a CHQ nanotube (last). (Reproduced by permission of American Physical Society [191])

To obtain insight into the electronic structure of the encapsulated silver nanowire, we evaluated its band structure and compared it, with both an isolated silver nanowire and the parent CHQ and CQHQ nanotubes (Figure 21). It can readily be noted that the CQHQ tube is a semiconductor with small gap (0.3 eV) compared to the insulating CHQ nanotube. The encapsulation of a silver nanowire within the CQHQ nanotube leads to several additional states in the band gap region and is somewhat different from that of an isolated silver

nanowire. Thus the bands near the Fermi energy are shifted up in case of the encapsulated silver nanowire. This indicates that there is electron transfer from the silver nanowire to the CQHQ nanotube. The most interesting aspect of the band structure is the metallic and conducting character exhibited by the encapsulated nanowire. Additionally the fact that two *s* channels cross the Fermi energy level indicate the existence of quantum conductance. In an isolated silver nanowire, three *s* channels cross the Fermi energy level. One of the key issues which emerge from this study on the encapsulated silver nanowires is the structure and stability of isolated nanowires. We explore two different aspects in the context of stability of isolated nanowires, (i) dimensionality and (ii) role of alloying.

In order to obtain more insight into the role of dimensionality on the stability of nanowires, we investigated the electronic structure of copper, silver and gold in their one-, two-, and three-dimensional structures [199]. We observed that as we progress towards low-dimensional structures, there is a strong sharpening of the *d* bands, which sharply enhances the corresponding density of states and raises the band edges. This strong preference for lower-dimensional structures is in consonance with the experimental observation that the interatomic interactions progressively become stronger in low-coordinated systems.

It was seen in our discussion of gold clusters, that the presence of an excess charge promotes linearity [130]. Interestingly, it was experimentally noted that a wire of at least four gold atoms suspended between two gold electrodes is linear [93,200-202]. However, theoretical calculations of a free standing one-dimensional gold wire indicate that a zigzag structure is more stable [202]. Therefore, a subject of intense interest in the recent past is on methods to improve the linearity of gold wires. Our investigations were motivated by the observation that the heat of formation of low-dimensional clusters of alloys is much larger than that of the bulk alloy [130]. This in turn can be attributed to the charge transfer-induced electrostatic interaction between different species. As was mentioned in our studies of clusters, charge transfer generally originates from the gold atom. So, we thought it would useful to modulate the charge transfer in gold alloy nanowires by injecting *s* electrons into gold wire without distorting its band structure [203]. The *s* band of the alloying metal should therefore possess similar energy levels and dispersion as the *6s* orbital of gold. Of all the *s* band metals, beryllium, magnesium, zinc, cadmium, and mercury have their valence energy levels closest to that of the *6s* orbital of gold, and incidentally all these metals can form alloys with gold.

We therefore carried out density functional calculations with ultrasoft pseudopotentials of free-standing infinite monoatomic gold wires alloyed with both magnesium and zinc. In the alloy chains, the locations of the gold and zinc (or magnesium) atoms were alternated, and investigated as both linear and zigzag structures. In sharp contrast to pure gold nanowires, both the zigzag and

linear structures of both gold-magnesium and gold-zinc alloys are distinct minima in the plots of the cohesive energy. Additionally, the difference in the cohesive energies associated with these two minima is very small (~0.13 eV). This together, with the fact the energy barrier between the equilibrium zigzag and linear structures is 0.73 (gold-zinc) and 0.49 eV (gold-magnesium) indicate that the linear structures would be as stable as the zigzag structures. We note that both zinc *4s* and magnesium *3s* bands display *p* character near the Fermi energy. This *sp* hybridization, which is absent in pure gold nanowires, favours a linear structure in case of these alloyed nanowires.

4.3.4 Nanodevices

In a previous section, we had addressed the issue of employing the interaction of photons or electrons with molecular systems in the design of new nanodevices [66]. While photochemical and electrochemical switching devices have been extensively investigated, most of the photochemical switching devices are limited to the linear regime [204-206]. However, it would be of interest to use non-linear optical properties in the design of practical photochemical switching devices. In this regard, the general idea which has prevailed in the course of extensive studies on photoswitch memory devices is that an efficient memory device can be obtained, if the molecular entity obtained after photoswitching is nonlinearly optically active. We realized during our theoretical investigations of 1,2-*bis*-(3-thienyl)-ethene derivatives that their closed forms are π-conjugated after photoswitching [207]. The substitution of suitable donors and acceptors on certain strategic positions of these ethene derivatives however makes the closed form non-linear optically active and the resulting molecular system behaves as an efficient non-linear optical switch [207].

It would also be of interest to harness the subtle changes in the π-electron densities to obtain novel molecular systems with unusual characteristics [62,63,208]. It becomes evident from our discussion of organic nanotubes and encapsulated nanowires that quinones are ideal systems in this regard because their electronic characteristics can be electrochemically or photochemically controlled [64,65]. Based on a theoretical investigation of the conformational characteristics of *p*-benzoquinone-benzene complexes, we realized that the energy difference between the stacked and edge-to-face conformations of cyclophane molecules (Figure 22) is substantial. Thus, if one could subtly control the conformational characteristics of 2,11-dithio[4,4]metametaquinocyclophane (MQC) (stacked conformer is 7 kcal/mol more stable than the edge-to-faced conformer), and 2,11-dithio[4,4]metametahydroquinocyclophane (MHQC) (edge-to-face is 9 kcal/mol more stable than the edge-to-face conformer), either electrochemically or photochemically, we could have a very interesting model of a potential molecular device [66]. In order to examine these predictions, we synthesized

MQC and MHQC and tried to obtain their crystal structures. The crystal structure of MQC clearly indicated the prevalence of the stacked conformation. Unfortunately, we were unable to obtain the crystal structure of MHQC. Given the previous reports of crystal structures of 2,11-dithio[4,4]metametacyclophane, exhibiting the edge-to-face conformation, it is very much likely that MHQC would also exhibit an edge-to-face conformation [66].

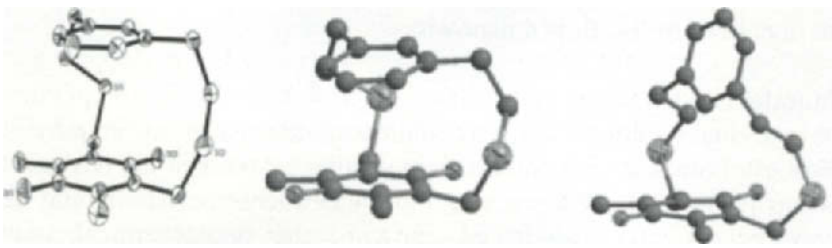

Figure 22. X-ray crystal structure of MQC (left) and ab initio (MP2/6-31G*) structures of MQC (middle) and MHQC (right). (Reproduced by permission of American Chemical Society [66])

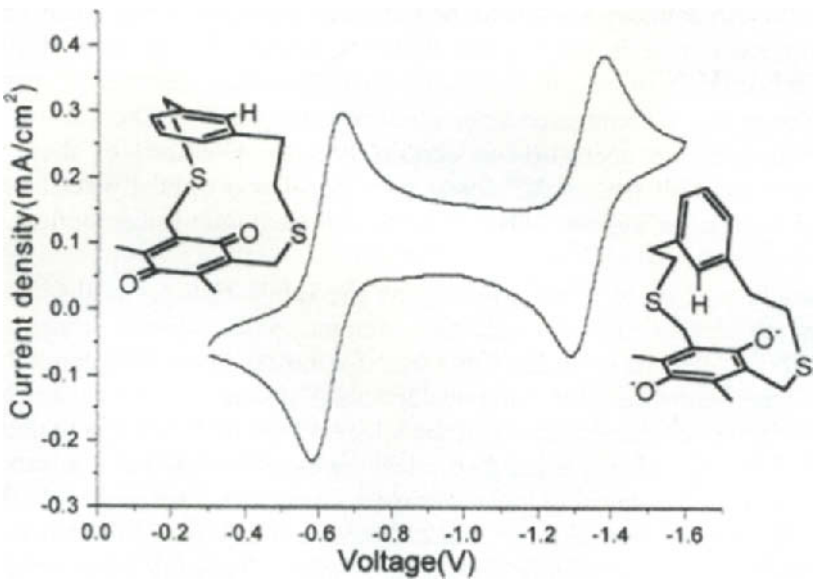

Figure 23. Cyclic voltammogram of **1** (1 mM) and tetrabutylammonium dihydrogen phosphate (0.1 M) in acetonitrile at 25°C (scan rate 100 mV/s). (Reproduced by permission of American Chemical Society [66])

While we characterized this conformational transition using nuclear magnetic resonance investigations, the cyclic voltammograms of MQC exhibits two clear reversible redox reactions (Figure 23). In aprotic media, quinones

exhibit two reduction peaks separated by 0.7 V, which corresponds to the formation of a radical anion species and a dianion species of quinones, respectively [209]. This is in agreement with the reduction characteristics of MQC. Two well-separated reduced states of MQC are formed in the aprotic solvent of acetonitrile upon reduction. Therefore, the electronic states of MQC and MHQC can be easily transformed into each other by simple electrochemical control of the redox reaction, which results in large conformational flapping motions due to a preference for the stable conformation caused by the change in the electronic state of the quinone moiety.

It can therefore be summarized that we were successful in designing a novel nanomechanical molecular cyclophane system composed of quinone and benzene rings that exhibits a flapping motion involving squeezing and thrusting motions in the presence of solvent molecules by electrochemical redox process. It shows the potential utility of harnessing the differences in the relative magnitudes of different kinds of intermolecular interactions to yield a nanomechanical device. We believe that the large flapping/flipping motion from the edge-to-face and stacked conformations and vice versa could be applied to design molecular hinges, molecular switches, and mobile nanomechanical devices as a first step toward a propelling molecular vessel or a molecular flipper that can be electrochemically controlled.

5. CONCLUSIONS

In this review, we have illustrated our efforts in nanomaterial design using a wide variety of examples. Apart from stressing the strengths and weaknesses of several theoretical methodologies, our extensive studies also highlight that an understanding of intermolecular interactions is very useful in nanomaterial design. Some of the salient conclusions which can be drawn from these investigations are listed below.

(1) Given the small size of the systems involved, energetic considerations take more precedence over thermodynamic considerations.

(2) Theoretical calculations involving nanomaterials should explicitly take into account electron correlation. Apart from providing accurate estimates of dispersion energies, which are widely prevalent in nanomaterials, the inclusion of electron correlation also influences the magnitude of other interaction energy components like induction energies. In systems involving large number of atoms, it is computationally not feasible to use very high-level theoretical methodologies. In such case, the use of density functional or semi-empirical methods is advocated. However, adequate care should be taken while interpreting the results.

(3) The magnitude of repulsive energies are very important in that the equilibrium structures of most nanomaterials, are the ones wherein the attractive energies are maximized and the repulsive energies, minimized.

(4) Quantitative estimates of the magnitudes of various intermolecular interactions and energy components are very useful in determining their relative importance. However, weak interactions are very important in the sense that they steer and promote much stronger interactions.
(5) Given the success of our approach in designing experimentally viable nanomaterials, we believe that the coming years would see the use of this approach in the development of novel nanosystems with potential applications in pharmaceuticals, optics, opto-electronics, information storage, sensors, biotechnology, nanomedicine, nanofluidics, and nanoelectronics. Furthermore, it would also provide vital information on the methods needed to harness these nanosystems as machines and devices and provide an increased understanding of the science behind most nanoscale processes.

Acknowledgements

This work was supported by the Korean Ministry of Science and Technology under the Creative Research Initiatives Program. We thank Professor Michael Laing (University of Natal) for allowing us to reproduce Figure 4.

REFERENCES

[1] J. R. Chelikowsky and M. A. Ratner, Comp. Sci. Eng. 3 (2001) 40.
[2] L. R. Reif, Lect. Notes Comput. Sc. 2380 (2002) 1.
[3] G. J. de A. A. Soler-Illia, C. Sanchez, B. Lebeau and J. Patarin, Chem. Rev. 102 (2002) 4093.
[4] D. R. Walt, Nature Materials 1 (2002) 17.
[5] V. Balzani, A. Credi and M. Venturi, Chem. Phys. Chem. 4 (2003) 49.
[6] J. R. Heath, Acc. Chem. Res. 32, 388 (1999).
[7] L. M. Greig and D. Philp, Chem. Soc. Rev. 30 (2001) 287.
[8] K. S. Kim, Curr. Appl. Phys. 2 (2002) 65; Bull. Kor. Chem. Soc. (in press).
[9] C. M. Niemeyer, Angew. Chem. Int. Edit. 36 (1997) 585.
[10] A. B. Ellis and D. R. Walt (eds.), Chem. Rev. 100 (2000) 2477-2738.
[11] M. Cohen, Ann. Rev. Mater. Sci. 30 (2000) 1.
[12] H. Haberland (ed.), Clusters of Atoms and Molecules, Springer-Verlag, Berlin, 1994.
[13] P. v. R. Schleyer, N. L. Allinger, T. Clark, J. Gasteiger, P. A. Kollman, H. F. Schaefer III and P. R. Schreiner (eds.), Encyclopedia of Computational Chemistry, John Wiley & Sons, Chichester, 1998.
[14] W. A. Harrison, Solid State Commun. 124 (2002) 443.
[15] A. J. Freeman, J. Comput. Appl. Math. 149 (2002) 27.
[16] N. Attig, R. Esser and M. Kremer, Comput. Phys. Commun. 147 (2002).
[17] K. S. Kim, P. Tarakeshwar and J. Y. Lee, Chem. Rev. 100 (2000) 4145.

[18] P. Tarakeshwar and K. S. Kim, In "Encyclopedia of Nanoscience and Nanotechnology", H. S. Nalwa (Ed.), American Science Publishers, California, 2003.
[19] C. V. K. Sharma, Cryst. Growth Des. 2 (2002) 465.
[20] H. Kuhn and H.-D. Försterling, Principles of Physical Chemistry: Understanding Molecules, Molecular Assemblies and Supramolecular Machines, John Wiley & Sons Inc., New York, 1999.
[21] D. Braga and F. Grepioni, Acc. Chem. Res. 33 (2000) 601.
[22] G. Chałasiński and M. M. Szczęśniak, Chem. Rev. 100 (2000) 4227.
[23] H. F. Schaefer III (ed.), Methods of Electronic Structure Theory, Plenum Press, New York, 1977.
[24] G. H. F. Diercksen and S. Wilson (eds.), Methods in Computational Molecular Physics, D. Reidel, Dordrecht, 1983.
[25] R. G. Parr and W. Yang, Density Functional Theory of Atoms and Molecules, Oxford Univ. Press, Oxford, 1989.
[26] K. Szalewicz and B. Jeziorski, In "Molecular Interactions - From van der Waals to Strongly Bound Complexes"; S. Scheiner (ed.), Wiley, New York, 1997, p. 3.
[27] G. Kresse and J. Furthmüller, Comput. Mater. Sci. 6 (1996) 15.
[28] K. Schwarz, P. Blaha and G. K. H. Madsen, Comput. Phys. Commun. 141 (2002) 71.
[29] S. Scheiner, Hydrogen Bonding: A Theoretical Perspective, University Press, Oxford, 1997.
[30] P. Tarakeshwar, H. M. Lee and K. S. Kim, In "Reviews in Modern Quantum Chemistry - A celebration of the contributions of R.G. Parr", K. D. Sen (ed.), World Scientific, Singapore, 2002, p. 1642.
[31] K. S. Oh, J. Yoon and K. S. Kim, J. Phys. Chem. A 105 (2001) 9726.
[32] H. S. Choi and K. S. Kim, J. Phys. Chem. B 104 (2000) 11006.
[33] W. W. Cleland and M. M. Krevoy, Science, 264 (1994) 1887.
[34] P. A. Frey, Science, 269 (1995) 104.
[35] K. R. Seddon and C. B. Aäkeroy, Chem. Soc. Rev. (1993) 397.
[36] K. S. Kim, C. Cui and S. J. Cho, J. Phys. Chem. B 102 (1998) 461.
[37] C. Cui, S. J. Cho and K. S. Kim, J. Phys. Chem. A 102 (1998) 1119.
[38] H. S. Choi, S. B. Suh, S. J. Cho and K. S. Kim, Proc. Natl. Acad. Sci. U. S. A. 95 (1998) 12094.
[39] C. Cui and K. S. Kim, J. Phys. Chem. A 103 (1999) 2751.
[40] K. S. Oh, C.-W. Lee, H. S. Choi, S. J. Lee and K. S. Kim, Org. Lett. 2 (2000) 2679.
[41] S. B. Suh, C. Cui, H. S. Son, J. S. U, Y. Won and K. S. Kim, J. Phys. Chem. 106 (2002) 2061.
[42] H. S. Choi, D. Kim, P. Tarakeshwar, S. B. Suh and K. S. Kim, J. Org. Chem. 67 (2002) 1848.

[43] H. Ihm, S. Yun, H. G. Kim, J. K. Kim and K. S. Kim, Org. Lett. 4 (2002) 2897.
[44] S. Yun, Y. -O. Kim, D. Kim, H. G. Kim, H. lhm, J. K. Kim, C.-W. Lee, W. J. Lee, J. Yoon, K. S. Oh, J. Yoon, S.-M. Park and K. S. Kim, Org. Lett. 5 (2003) 471.
[45] S. Yun, H. lhm, H. G. Kim, C.-W. Lee, B. Indrajit, K. S. Oh, Y. J. Gong, J. W. Lee, J. Yoon, H. C. Lee and K. S. Kim, J. Org. Chem. 68 (2003) 2467.
[46] R. D. Shannon, Acta Crystallogr. Sect. A 32 (1976) 751.
[47] J. Baik, J. Kim, D. Majumdar and K. S. Kim, J. Chem. Phys. 110 (1999) 9116.
[48] D. Majumdar, J. Kim and K. S. Kim, J. Chem. Phys. 112 (2000) 101.
[49] J. Kim, H. M. Lee, S. B. Suh, D. Majumdar and K. S. Kim, J. Chem. Phys. 113 (2000) 5259.
[50] H. M. Lee and K. S. Kim, J. Chem. Phys. 114 (2001) 4461.
[51] H. M. Lee and K. S. Kim, J. Chem. Phys. 117 (2002) 706.
[52] B. J. Mhin, J. Kim and K. S. Kim, Chem. Phys. Lett. 216 (1993) 305.
[53] B. J. Mhin, S. Lee, S. J. Cho, K. Lee and K. S. Kim, Chem. Phys. Lett. 197 (1992) 77.
[54] S. Lee, J. Kim, J. K. Park and K. S. Kim, J. Phys. Chem. 100 (1996) 14329.
[55] H. M. Lee, J. Kim, S. Lee, B. J. Mhin and K. S. Kim, J. Chem. Phys. 111 (1999) 3995.
[56] E. A. Meyer, R. K. Castellano and F. Diederich, Angew. Chem. Int. Ed. 42 (2003) 1210.
[57] B. Brutschy, Chem. Rev. 100 (2000) 3891.
[58] P. Tarakeshwar, H. S. Choi and K. S. Kim, J. Am. Chem. Soc. 123 (2001) 3323.
[59] P. Tarakeshwar, K. S. Kim, E. Kraka and D. Cremer, J. Chem. Phys. 115 (2001) 6018.
[60] B. H. Hong, J. Y. Lee, S. J. Cho, S. Yun and K. S. Kim, J. Org. Chem. 64 (1999) 5661.
[61] J. Y. Lee, S. B. Suh and K. S. Kim, J. Chem. Phys. 112 (2000) 344.
[62] J. Y. Lee, B. J. Mhin and K. S. Kim, J. Chem. Phys. 115 (2001) 9484.
[63] J. Y. Lee, B. J. Mhin and K. S. Kim, J. Phys. Chem. A J. Phys. Chem. A 107 (2003) 3577.
[64] B. H. Hong, J. Y. Lee, C.-W.Lee, J. C. Kim and K. S. Kim, J. Am. Chem. Soc. 123 (2001) 10748.
[65] K. S. Kim, S. B. Suh, J. C. Kim, B. H. Hong, E. C. Lee, S. Yun, P. Tarakeshwar, J. Y. Lee, Y. Kim, H. Ihm, H. G. Kim, J. W. Lee, J. K. Kim, H. M. Lee, D. Kim, C. Cui, S. J. Youn, H. Y. Chung, H. S. Choi, C.-W. Lee, S. J. Cho, S. Jeong and J.-H. Cho, J. Am. Chem. Soc. 124 (2002) 14268.
[66] H. G. Kim, C.-W. Lee, S. Yun, B. H. Hong, Y.-O. Kim, D. Kim, H. Ihm, J. W. Lee, E. C. Lee, P. Tarakeshwar, S.-M. Park and K. S. Kim, Org. Lett. 4 (2002) 3971.

[67] D. Kim, S. Hu, P. Tarakeshwar, K. S. Kim and J. M. Lisy, J. Phys. Chem. A 107 (2003) 1128.
[68] P. Tarakeshwar, S. J. Lee, J. Y. Lee and K. S. Kim, J. Chem. Phys. 108 (1998) 7217.
[69] P. Tarakeshwar, S. J. Lee, J. Y. Lee and K. S. Kim, J. Phys. Chem. B 103 (1999) 184.
[70] P. Tarakeshwar and K. S. Kim, J. Phys. Chem. A 103 (1999) 9116.
[71] K. S. Kim, J. Y. Lee, S. J. Lee, T.-K. Ha and D. H. Kim, J. Am. Chem. Soc. 116 (1994) 7399.
[72] J. Y. Lee, S. J. Lee, H. S. Choi, S. J. Cho, K. S. Kim and T. K. Ha, Chem. Phys. Lett. 232 (1995) 67.
[73] D. Quiñonero, C. Garau, C. Rotger, A. Frontera, P. Ballester, A. Costa and P. M. Déya, Angew. Chem. Int. Ed. 41 (2002) 3389.
[74] M. Mascal, A. Armstrong and M. D. Bartberger, J. Am. Chem. Soc. 124 (2002) 6274.
[75] I. Alkorta, I. Rozas and J. Elguero, J. Am. Chem. Soc. 124 (2002) 8593.
[76] M. J. Earle and K. R. Sedddon, Pure Appl. Chem. 72 (2000) 1391.
[77] G. A. Olah, B. Torok, J. P. Joschek, I. Bucsi, P. M. Esteves, G. Rasul and G. K. Suryaprakash, J. Am. Chem. Soc. 124 (2002) 11379.
[78] K. S. Kim, J. Y. Lee, H. S. Choi, J. Kim and J. H. Jang, Chem. Phys. Lett. 265 (1997) 497.
[79] P. Tarakeshwar, H. S. Choi, S. J. Lee, J. Y. Lee, K. S. Kim, T.-K. Ha, J. H. Jang, J. G. Lee and H. Lee, J. Chem. Phys. 111 (1999) 5838.
[80] P. Tarakeshwar and K. S. Kim, J. Mol. Str. 615 (2002) 227.
[81] T. Ren, Y. Jin, K. S. Kim and D. H. Kim, J. Biomol. Struct. Dyn. 15 (1997) 401.
[82] M. I. Cabaço, Y. Danten, M. Besnard, Y. Guissani and B. Guillot, J. Phys. Chem. B 102 (1998) 10712.
[83] A. P. West Jr., S. Mecozzi and D. A. Dougherty, J. Phys. Org. Chem. 10 (1997) 347.
[84] A. Karpfen, J. Phys. Chem. A 103 (1999) 11431.
[85] B. H. Cardelino, C. E. Moore, D. O. Frazier, D. G. Musaev and K. Morokuma, Int. J. Quantum Chem. 66 (1998) 189.
[86] M. C. Chan, P. A. Block and R. E. Miller, R. E. J. Chem. Phys. 102 (1995) 3993.
[87] S. Tsuzuki, T. Uchimaru and K. Tanabe, Chem. Phys. Lett. 287 (1998) 202.
[88] M. O. Sinnokrot, E. F. Valeev and C. D. Sherrill, J. Am. Chem. Soc. 124 (2002) 10887.
[89] H. Krause, B. Ernstberger and H. J. Neusser, Chem. Phys. Lett. 184 (1991) 411.
[90] J. R. Grover, E. A. Walters and E. T. Hui, J. Phys. Chem. 91 (1987) 3233.
[91] J. M. Park, P. Tarakeshwar, K. S. Kim and T. Clark, J. Chem. Phys. 116 (2002) 10684.

[92] P. Pyykkö, Chem. Rev. 97 (1997) 597.
[93] N. Agraït, A. Levy Yeyati and J. M. van Ruitenbeek, Physics Reports 377 (2003) 81.
[94] M. Laing, Educ. Chem. (1993) 160.
[95] H. Burtscher and A. Schmidt-Ott, Phys. Rev. Lett. 48 (1982) 1734.
[96] H.-J. Schneider, Angew. Chem. Int. Ed. 30, (1991) 1417.
[97] J.-S. Seo, D. Whang, H. Lee, S. I. Jun, J. Oh, Y. J. Jeon and K. Kim, Nature 404 (2000) 982.
[98] D. N. Chin, J. A. Zerkowski, J. C. MacDonald and G. M. Whitesides, In "Organized Molecular Assemblies in the Solid State", J. K. Whitesell (ed.), John Wiley & Sons Inc., New York, 1999, p 185.
[99] G. R. Desiraju, Acc. Chem. Res. 29 (1996) 441.
[100] A. W. Castleman Jr., and K. H. Bowen Jr., J. Phys. Chem. 100 (1996) 12911.
[101] P. Pyykkö and N. Runeberg, Angew. Chem. Int. Ed. 41 (2002) 2174.
[102] X. Li, B. Kiran, J. Li, H.-J. Zhai and L.-S. Wang, Angew. Chem. Int. Ed. 41 (2002) 4786.
[103] K. S. Kim, M. Dupuis, G. C. Lie and E. Clementi, Chem. Phys. Lett. 131 (1986) 451.
[104] K. S. Kim, B. J Mhin, U.-S. Choi and K. Lee, J. Chem. Phys. 97 (1992) 6649.
[105] B. J. Mhin, S. J.Lee and K. S. Kim, Phys. Rev. A 48 (1993) 3764.
[106] B. J. Mhin, J. Kim, S. Lee, J. Y. Lee and K. S. Kim, J. Chem. Phys. 100 (1994) 4484.
[107] J. Kim, B. J. Mhin, S. J. Lee and K. S. Kim, Chem. Phys. Lett. 219 (1994) 243.
[108] J. Kim, J. Y. Lee, S. Lee, B. J. Mhin and K. S. Kim, J. Chem. Phys. 102 (1995) 310.
[109] J. Kim and K. S. Kim, J. Chem. Phys. 109 (1998) 5886.
[110] J. Kim, D. Majumdar, H. M. Lee and K.S. Kim, J. Chem. Phys. 110 (1999) 9128.
[111] H. M. Lee, S. B. Suh, J. Y. Lee, P. Tarakeshwar and K. S. Kim, J. Chem. Phys. 112 (2000) 9759.
[112] H. M. Lee, S. B. Suh and K. S. Kim, J. Chem. Phys. 114 (2001) 10749.
[113] U. Buck and F. Huisken, Chem. Rev. 100 (2000) 3863.
[114] K. S. Kim, I. Park, S. Lee, K. Cho, J. Y. Lee, J. Kim and J. D. Joannopoulos, Phys. Rev. Lett. 76 (1996) 956.
[115] S. Lee, S. J. Lee, J. Y. Lee, J. Kim, K. S. Kim, I. Park, K. Cho and J. D. Joannopoulos, Chem. Phys. Lett. 254 (1996) 128.
[116] J. Kim, J. M. Park, K. S. Oh, J. Y. Lee, S. Lee and K. S. Kim, J. Chem. Phys. 106 (1997) 10207.
[117] K. S. Kim, S. Lee, J. Kim and J. Y. Lee, J. Am. Chem. Soc. 119 (1997) 9329.

[118] S. Lee, J. Kim, S. J. Lee and K. S. Kim, Phys. Rev. Lett. 79 (1997) 2038.
[119] J. Kim and K. S. Kim, J. Chem. Phys. 111 (1999) 10077.
[120] S. B. Suh, H. M. Lee, J. Kim, J. Y. Lee and K. S. Kim, J. Chem. Phys. 113 (2000) 5273.
[121] I. Park, K. Cho, S. Lee, K. S. Kim and J. D. Joannopoulos, Comput. Mater. Sci. 21 (2001) 291.
[122] H. M. Lee, D. Kim and K. S. Kim, J. Chem. Phys. 116 (2002) 5509.
[123] H. M. Lee and K. S. Kim, Mol. Phys. 100 (2002) 875.
[124] H. M. Lee, S. B. Suh and K. S. Kim, J. Chem. Phys. (in press).
[125] H. M. Lee, S. Lee and K. S. Kim, J. Chem. Phys. (in press).
[126] P. Schwerdtfeger, Angew. Chem. Int. Ed. 42 (2003) 1892.
[127] J. Yoon, K. S. Kim and K. K. Baeck, J. Chem. Phys. 112 (2000) 9335.
[128] H. Häkkinen, M. Moseler and U. Landman, Phys. Rev. Lett. 89 (2002) 033401.
[129] Y. Negishi, Y. Nakamura, A. Nakajima and K. Kaya, J. Chem. Phys. 115 (2001) 3657.
[130] H. M. Lee, G. Maofa, B. R. Sahu, P. Tarakeshwar and K. S. Kim, (submitted).
[131] D. Chakarov and B. Kasemo, Phys. Rev. Lett. 81 (1998) 5181.
[132] P. Tarakeshwar, K. S. Kim and B. Brutschy, J. Chem. Phys. 110 (1999) 8501.
[133] P. Tarakeshwar, K. S. Kim and B. Brutschy, J. Chem. Phys. 112 (2000) 1769.
[134] J. Y. Lee, J. Kim, H. M. Lee, P. Tarakeshwar and K. S. Kim, J. Chem. Phys. 113 (2000) 6160.
[135] P. Tarakeshwar, K. S. Kim and B. Brutschy, J. Chem. Phys. 114 (2001) 1295.
[136] P. Tarakeshwar, K. S Kim, S. Djafari, K. Buchhold, B. Reimann, H.-D. Barth and B. Brutschy, J. Chem. Phys. 114 (2001) 4016.
[137] C. Riehn, B. Reimann, K. Buchhold, H.-D. Barth, S. Vaupel, B. Brutschy,
[138] P. Tarakeshwar and K. S. Kim, J. Chem. Phys. 115 (2001) 10045.
[139] B. Reimann, K. Buchhold, H.-D. Barth, B. Brutschy, P. Tarakeshwar and K. S. Kim, J. Chem. Phys. 117 (2002) 8805.
[140] T. K. Manojkumar, H. S. Choi, P. Tarakeshwar and K. S. Kim, J. Chem. Phys. 118 (2003) 8681.
[141] P. Bühlmann, E. Pretsch and E. Bakker, Chem. Rev. 98 (1998) 1593.
[142] J. H. Sussman, M. Harel, F. Frolow, C. Oefner, A. Goldman, L. Toker and I. Silman, Science 253 (1991) 872.
[143] K. Sato, S. Arai and T. Yamagishi, Tetrahedron Lett. 40 (1999) 5219.
[144] E. Alcalde, C. Alvarez-Rúa, S. García-Granda, E. García-Rodriguez, N. Mesquida, L. Pérez-García, Chem. Commun. (1999) 295.
[145] R. Dutzler, E. B. Campbell, M. Cadene, B. T. Chait and R. Mackinnon, Nature 415 (2002) 287.

[146] D. A. Doyle, J. M. Cabral, R. A. Pfuetzner, A. Kuo, J. M. Gulbis, S. L. Cohen, B. T. Chait and R. MacKinnon, Science 280 (1998) 69.
[147] B. Roux and R. Mackinnon, Science 285 (1999) 100.
[148] J. Åqvist and V. Luzhkov, Nature 404 (2000) 881.
[149] K. S. Kim, D. P. Vercauteren, M. Welti, S. Chin and E. Clementi, Biophys. J. 47 (1985) 327.
[150] K. S. Kim and E. Clementi, J. Am. Chem. Soc. 107 (1985) 5504.
[151] K. S. Kim, J. Comput. Chem. 6 (1985) 256.
[152] K. S. Kim, H. L. Nguyen, P. K. Swaminathan and E. Clementi, J. Phys. Chem. 89 (1985) 2870.
[153] H. S. Choi and K. S. Kim, Angew. Chem. Int. Ed. 38 (1999) 2256.
[154] A. Schroeder, H.-B. Mekelburger, F. Voegtle, Top. Curr. Chem. 172 (1994) 179.
[155] M. S. Dresselhaus, G. Dresselhaus and P. C. Eklund, Science of Fullerenes and Carbon Nanotubes, Academic Press, San Diego, 1996.
[156] B. I. Dunlap, Phys. Rev. B 46 (1992) 1933.
[157] S. Itoh, S. Ihara and J. Kitakami, Phys. Rev. B 47 (1993) 1703.
[158] S. Itoh, S. Ihara and J. Kitakami, Phys. Rev. B 47 (1993) 12908.
[159] S. Itoh and S. Ihara, Phys. Rev. B.48 (1993) 8323.
[160] D.-H. Oh, J. M. Park and K. S. Kim, Phys. Rev. B. 62 (2000) 1600.
[161] K. S. Kim, J. M. Park, J. Kim, S. B. Suh, P. Tarakeshwar, K. H. Lee and S. S. Park, Phys. Rev. Lett. 84 (2000) 2425.
[162] G. Oszlányi, G. Bortel, G. Faigel, M. Tegze, L. Gránásy, S. Pekker, P. W. Stephens, G. Bendele, R. Dinnebier, G. Mihály, A. Jánossy, O. Chauvet and L. Forró, Phys. Rev. B 51 (1995) 12228.
[163] F. Bommeli, L. Degiorgi, P. Wachter, Ö. Legeza, A. Jánossy, G. Oszlanyi, O. Chauvet and L. Forro, Phys. Rev. B 51 (1995) 14794.
[164] T. A. Murphy, Th. Pawlik, A. Weidinger, M. Höhne, R. Alcala and J. Spaeth, Phys. Rev. Lett. 77 (1996) 1075.
[165] H. Mauser, N. J. R. van Eikema Hommes, T. Clark, A. Hirsch, B. Pietzak, A. Weidinger and L. Dunsch, Angew. Chem. Int. Ed. 36 (1997) 2835.
[166] J. Lu, Z. Zhang and X. Zhao, Chem. Phys. Lett. 312 (1999) 85.
[167] T. Bally and W. T. Borden, In "Reviews in Computational Chemistry", K. Lipkowitz and D. Boyd (eds.), Wiley-VCH, New York, 1999, Vol. 13, p 1.
[168] J. Twamley, arXiv:quant-ph/0210202 v1 (2002).
[169] H. S. Son, B. H. Hong, C.-W. Lee, S. Yun and K. S. Kim, J. Am. Chem. Soc. 123 (2001) 514.
[170] M. J. Krische and J. M. Lehn. Struct. Bond. 96 (2000) 3.
[171] D. T. Bong, T. D. Clark, J. R. Granja and M. R. Ghadiri, Angew. Chem. Int. Ed. 40 (2001) 988.
[172] V. G. Muchado, P. N. W. Baxter and J.-M. Lehn, J. Braz. Chem. Soc. 12, (2001) 431.

[173] L. G. Prins, D. N. Reinhoudt and P. Timmerman, Angew. Chem. Int. Ed. 40 (2001) 2383.
[174]F. Hof, S. L. Craig, C. Nuckolls and J. Rebek, Angew. Chem. Int. Ed. 41 (2002) 1488.
[175] E. Donath, S. Moya, B. Neu, G. B. Sukhorukov, R. Georgieva, A. Voigt, H. Bäumler, H. Kiesewetter and H. Möhwald, Chem. Eur. J. 23 (2002) 5481.
[176] J. J. P. Stewart, J. Comput. Chem. 10 (1998) 209; 10 (1998) 220.
[177] A. D. Becke, Phys. Rev. A 38 (1988) 3098.
[178] A. D. Becke, J. Chem. Phys. 98 (1993) 5648.
[179] J. P. Perdew, Phys. Rev. B 33 (1986) 8822; 34 (1986) 7406.
[180] C. Lee, W. Yang and R. G. Parr, Phys. Rev. B 37 (1988) 785.
[181] C. Møller and M. S. Plesset, Phys. Rev. 46 (1934) 618.
[182] Y. Wang and J. P. Perdew, Phys. Rev. B 43 (1991) 8911.
[183] J. P. Perdew and Y. Wang, Phys. Rev. B 45 (1992) 13244.
[184] D. M. Ceperley and B. J. Alder, Phys. Rev. Lett. 45 (1980) 566.
[185] D. Vanderbilt, Phys. Rev. B 41 (1990) 7892.
[186] S. F. Boys and F. Bernardi, Mol. Phys. 19 (1970) 553.
[187] K. S. Kim, K. S. Oh and J. Y. Lee, Proc. Natl. Acad. Sci. U. S. A. 97 (2000) 6373.
[188] K. S. Kim, D. Kim, J. Y. Lee, P. Tarakeshwar and K. S. Oh, Biochemistry 41 (2002) 5300.
[189] B. H. Hong, S. C. Bae, C.-W. Lee, S. Jeong and K. S. Kim, Science 294 (2001) 348.
[190] B. H. Hong, C.-W. Lee and K. S. Kim, European Patent No. EP 1264919, (2002).
[191] S. B. Suh, B. H. Hong, P. Tarakeshwar, S. J. Youn, S. Jeong and K. S. Kim, Phys. Rev. B (Rapid Commun.) (in press).
[192] N. J. Darby and T. E. Creighton, Protein Structure, Oxford University Press, Oxford, 1993, pp 9-16.
[193] E. Braun, Y. Eichen, U. Sivan and G. Ben-Yoseph, Nature 391 (1998) 775.
[194] T. A. Taton, C. A. Mirkin and R. L. Letsinger, Science 289 (2000) 1757.
[195] E. Wimmer, H. Krakauer, M. Weinert and A. J. Freeman, Phys. Rev. B 24 (1981) 864.
[196] M. Weinert, E. Wimmer and A. J. Freeman, Phys. Rev. B 26 (1982) 4571.
[197] H. J. F. Jansen and A. J. Freeman Phys. Rev. B 30 (1984) 561.
[198] J. Xie, S. de Gironcoli, S. Baroni, and M. Scheffler, Phys. Rev. B 59 (1999) 970.
[199] T. Nautiyal, S. J. Youn and K. S. Kim, Phys. Rev. B (in press).
[200] H. Ohnishi, V. Kondo and K. Takayanagi, Nature 395 (1998) 780.
[201] A. I. Yanson, G. R. Bollinger, H. E. van den Brom, N. Agräit and J. M. van Ruitenbeek, Nature 395 (1998) 783.
[202] V. Rodrigues, T. Fuhrer and D. Ugarte, Phys. Rev. Lett. 85 (2000) 4124.

[203] W.-T. Geng and K. S. Kim, Phys. Rev. B (in press).
[204] A. Troisi and M. A. Ratner, J. Am. Chem. Soc. 124 (2002) 14528.
[205] S. Mukamel, S. Tretiak, S. Wagersreiter and V. Chernyak, Science 277 (1997) 781.
[206] M. Irie, Chem. Rev. 100 (2000) 1685.
[207] D. Majumdar, H. M. Lee, J. Kim and K. S. Kim, 111 (5866) 1999.
[208] H. M. Lee, J. Kim, C.-J. Kim and K. S. Kim, J. Chem. Phys. 116 (2002) 6549.
[209] J. Q. Chambers, In "The Chemistry of Quinonoid Compounds", S. Patai and Z. Rappoport (eds.), Wiley, New York, 1988, pp 719-757.

J. Leszczynski (Editor)
Computational Materials Science
Theoretical and Computational Chemistry, Vol. 15

Chapter 6

Methods and Implementation of Robust, High-Precision Gaussian Basis DFT Calculations for Periodic Systems: the GTOFF Code

S.B. Trickey[a], J.A. Alford[a], and J.C. Boetgger[b]

[a]Quantum Theory Project, Departments of Physics and of Chemistry, P.O. Box 118435, University of Florida, Gainesville FL 32611-8435

[b]Group X-7, Los Alamos National Laboratory, Los Alamos NM 87544

1. APPROACH

1.1. Setting and Motivation

The 1998 Nobel Prize for Chemistry, awarded to a physicist for inventing modern Density Functional Theory (DFT), signaled widespread recognition of DFT as the pre-eminent many-electron theory for predictive, materials-specific (chemically specific) calculation of extended and molecular systems. The original papers of modern DFT are those of Hohenberg and Kohn [1] and Kohn and Sham [2] (preceded by seminal work of Thomas, Fermi, Dirac, Slater, Gáspár, Gombas, and others not of direct relevance). General references include [3–16].

We focus on periodic systems (1D → ordered polymers, 2D → slabs and ultra-thin films, 3D → crystals). A considerable variety of DFT implementations exists in codes for such systems, depending on the choice of basis set. (Somewhat confusingly for beginners, in solid-state physics the choice of a basis commonly has been called a "method", presumably because special techniques evolved to exploit the advantages and minimize the difficulties of each choice.) With few exceptions, modern codes are based on some approximate eigenvalue problem for an effective Hamiltonian, hence they expand the eigensolutions in linear combinations of one of four types of basis functions:

- plane waves (virtually always in conjunction with pseudopotentials); a typical example is [17]
- linearized augmented plane waves; a typical example is [18]
- linearized muffin-tin orbitals; a typical example is [19]
- gaussian-type orbitals; the topic of this paper.

The first three all are plane-wave based. They predominate in calculations on periodic systems (probably because of the ubiquity of plane-wave prefactors from Bloch's theorem). Quite the opposite is true for molecules and clusters. In them, gaussian basis sets are the de facto standard. The advantage of gaussian-type orbitals (GTOs) is that many of the matrix elements needed can be evaluated analytically and swiftly. Those that cannot be done analytically typically need only a well-behaved 1D numerical quadrature. This feature lends itself to indirect numerical quadrature methods via fitting-function techniques, an advantage discussed in greater detail below. The number of matrix elements can be large; 10^8 is routine.

In principle, a finite GTO basis can describe neither the free-space tail of an electronic orbital nor the nuclear cusp correctly. Because there are relatively few physically or chemically interesting properties that depend on detailed behavior of orbitals in an arbitrarily small neighborhood of a nucleus or at arbitrarily large distances from all the nuclei, the intrinsic deficiencies of a GTO basis have not proved to be a major drawback in practice. For most observables, a rich GTO basis obviates the formal limitations. More discussion of the long-ranged behavior issue is given below in connection with calculated work functions.

Compared to the other three basis types, GTO-based algorithms and codes for periodic systems have at least two advantages. As noted, GTOs are far and away the basis set of choice for high-precision, first-principles molecular calculations. (The other half of the 1998 Nobel Prize in Chemistry went to the founder of the well-known "Gaussian-9x" series of codes.) Therefore, minimizing intercode comparison error for predictions on different aggregation states (atoms → molecule/cluster → ordered systems) amounts to a practical *requirement* that one use GTO codes. The emergence of nano-featured surfaces and nano-particles as important systems makes the issue all the more pertinent. The point is a sharp one. One can show, for example, that an attempt to calculate a surface energy by using one code for a ν-layer (ultra-thin film, slab, with ν periodically ordered nuclear planes) and another code for the counterpart crystal will give an error in the calculated surface energy that diverges as ν increases [20, 21].

GTO-based algorithms also avoid the cellular decomposition of cartesian space that serves to define both the LMTO and LAPW bases. Such decompositions introduce discontinuities in radial derivatives of the basis functions higher than the first derivative. Cellular discontinuities are a particular nuisance, for example, when using gradient-dependent exchange-corrrelation functionals. Further, the relationship between the basis function inside the muffin-tin sphere and outside can cause the quality of the expansions to differ in different regions. In a GTO basis, the **only** parameters of choice are the basis functions themselves (number of each symmetry type and range and distribution of widths) plus the technical controls on precision regarding the behavior of those functions properly in recursions, sums, and quadratures. Proponents of cellular or plane-wave methods sometimes argue that the choices of types of GTOs (s, p, ...) and orbital exponents are both arbitrary. Certainly there is no simple GTO analogue of the plane-wave cutoff $\mathbf{K}_{max}$. Such a cutoff, though simpler than selecting a set of GTO exponents, is not fundamentally less arbitrary however. More detail on basis set selection is given below.

In any event, the historical dominance of plane-wave and cellular-based codes in surface and solid state physics continues today. There are relatively few GTO-based codes for crystals, slabs, and infinite periodic polymers (3D, 2D, and 1D periodicity respectively). Only some of those are purpose-built to exploit the fundamental properties of DFT. This paper describes the current state of development of the algorithms and implementation of a particular approach to DFT calculations for periodic systems, Gaussian Type Orbitals with Fitting Functions. The underlined letters yield the name of the code, "GTOFF", pronounced "gee-toff". The emphasis is on those methods which are unusual (even, perhaps, unique), so we do not give any detail on such more-or-less routine aspects as Brillouin Zone scans, SCF convergence methods, etc. We also give a brief comparative description of the relationship of GTOFF with other GTO periodic codes and give highlights of several examples of the application of GTOFF (and FILMS, its predecessor) to interesting systems.

1.2. Basics

The basic papers about GTOFF are Refs. [22–24]. The algorithms originated with Mintmire *et al.* [25–27] and evolved through a series of codes called "FILMS" [28], with major contributions from Birkenheuer and Rösch [29]. While GTOFF handles spin-density functional theory straightforwardly, for brevity most of our discussion will be for the non-spin- polarized case unless noted otherwise.

In DFT the electron number density n_e is given by

$$n_e(\mathbf{r}) = \sum_{i,\Gamma} n_{i,\Gamma} |\varphi_{i,\Gamma}(\mathbf{r})|^2 \tag{1}$$

where $n_{i,\Gamma}$ is the occupation number (from Fermi statistics and the aufbau principle) for Kohn-Sham orbital i with quantum numbers Γ. In periodic systems the Γs are symmetry-labeled wave vectors $\mathbf{k}$; for molecules/clusters they are molecular symmetry labels.

The Kohn-Sham (KS) equation is

$$\left\{ -\frac{1}{2}\nabla^2 + V_{eff}[n_e(\mathbf{r})] \right\} \varphi_{i,\Gamma}(\mathbf{r}) = \varepsilon_{i,\Gamma} \varphi_{i,\Gamma}(\mathbf{r}) \tag{2}$$

(Note the somewhat unconventional choice, at least for surface and solid state physics, of Hartree atomic units: $\hbar = |q_{electron}| = m_{electron} = 1$, 1 E_H = 27.2116 eV). The local potential $V_{eff}[n_e(\mathbf{r})]$ contains electron-electron Coulomb repulsion, exchange-correlation ("XC"), and nuclear-electron attraction terms that are the functional derivatives of the corresponding terms, E_{ee}, E_{XC}, and E_{Ne}, in the density functional $E[n_e]$

$$\begin{aligned} V_{eff} &= V_{ee}[n_e(\mathbf{r})] + V_{XC}[n_e(\mathbf{r})] + V_{Ne}[n_e(\mathbf{r})] \\ &= \delta(E_{ee} + E_{XC} + E_{Ne})/\delta n_e \end{aligned} \tag{3}$$

V_{eff} is a highly non-linear functional of n_e, so the KS equation is solved by iteration to self-consistency. Whatever the basis set, the KS orbitals $\varphi_{i,\Gamma}$ are expanded as linear combinations, thereby converting the one-electron differential equation into a linear algebra problem for the expansion coefficients.

For periodic systems, the GTO solution [24, 27] begins by defining Bloch-symmetrized gaussian basis functions $\chi_j^\ell(\mathbf{r}, \mathbf{k})$ for each primitive function G_j^ℓ of type ℓ as

$$\chi_j^\ell(\mathbf{r}, \mathbf{k}) = \sum_{\mathbf{R}} B_{\mathbf{k}}(\mathbf{R}) G_j^\ell(\mathbf{r} - \mathbf{R}) \tag{4}$$

where the sum runs over all nuclear sites $\mathbf{R}$. The B coefficients are Bloch phase

factors $N_{cell}^{-1/2}\exp(-i\mathbf{k}\cdot\mathbf{R})$, with N_{cell} the number of unit cells in the periodic region.

There are many types of GTO basis sets. They differ by the kind of function that multiplies the simple gaussian itself, that is, the functions indexed by ℓ in Eq. (4). A "*p*-type cartesian gaussian", for example, is of the form $z\exp(-\mu r^2)$. GTOFF uses so-called Hermite gaussians: each GTO is a spherical gaussian multiplied by a function closely related to a Hermite polynomial. A primitive function G_j^{ℓ} can be a fixed linear combination ("contraction") of several individual GTOs of the same type. Such contractions, especially for core levels, gain much of the speed-up commonly obtained via pseudopotentials, without introducing core-valence orthogonality issues. Further, the effect of any contraction can be evaluated exactly by the simple step of de-contracting.

The vectors **k** are 3D, 2D, or 1D for a crystal, slab, or periodic polymer respectively. Keep in mind that the nomenclature "nD" refers to the number of cartesian directions in which nuclei have periodic ordering. The electron density is *three-dimensional*, as is **r**, whatever the system periodicity. Thus, when we treat an ultra-thin film (UTF) with GTOFF, we are *not* doing a super-cell calculation on a fictitious crystal consisting of the UTF interspersed by "layers of vacuum". GTOFF can do such "super-cell" calculations but more importantly, it can handle the UTF as a free-standing object periodic in two Cartesian directions and of finite thickness in the third direction (conventionally *z*), subject to vacuum boundary conditions in *z*. Note also that a 2D GTOFF calculation does not require inversion symmetry with respect to *z*, hence can treat an even number of nuclear planes as readily as an odd number.

Once the "molecular orbitals" Eq. (4) are defined, much of the schematic code design is the same whether the systems are periodic or bounded clusters. The KS orbitals $\varphi_{i,\Gamma}(\mathbf{r})$ are expanded as

$$\varphi_{i,\mathbf{k}}(\mathbf{r}) = \sum_{j\ell} C_{j,\ell}^{i,\mathbf{k}} \chi_j^{\ell}(\mathbf{r},\mathbf{k}) \tag{5}$$

Standard linear variation theory applied to the KS Hamiltonian Eq. (2) yields a generalized eigenvalue problem for the eigenvalues $\varepsilon_{i,\mathbf{k}}$ and coefficients $C_{j,\ell}^{i,\mathbf{k}}$:

$$[H] - [\varepsilon][S] = 0 \tag{6}$$

$[H]$ and $[S]$ are the Hamiltonian and overlap matrices in the "MO" basis, as in Eq. (4).

Where GTOFF differs from many other codes is in a set of techniques, collectively called fitting function methodology [27, 30], that are used to obtain major speedups in this approach while retaining arbitrarily high precision (subject only to limits on computational cost which scale well). The speedups come in evaluating the two contributions to the matrix $[H]$ that depend non-linearly upon the electron charge density n_e, the classical Coulombic (or electron-electron repulsion) energy E_{ee} and its corresponding matrix elements $<\chi_i|V_{ee}|\chi_j>$ and the exchange-correlation term E_{XC} and corresponding matrix elements $<\chi_i|V_{xc}|\chi_j>$.

Electron-electron repulsion matrix elements have the form

$$[V_{ee}]_{ij} \propto \int d\mathbf{r}\chi_i(\mathbf{r})\chi_j(\mathbf{r}) \int d\mathbf{r}' n_e(\mathbf{r}')/|\mathbf{r}-\mathbf{r}'| \tag{7}$$

Comparison with Eqs. (1) and (4) shows immediately that in principle this is a four-center integral (basis functions at four nuclear sites contribute). The computational cost can be reduced greatly by mapping the problem to a sum of three-center integrals. The scheme is to expand, at each self-consistent iteration, the electron number density n_e in an auxiliary Hermite gaussian basis set $\{Q\}$ of the same type (but *not necessarily* the *identical* functions) as used to expand the KS functions:

$$n_e(\mathbf{r}) \approx \tilde{n}_e(\mathbf{r}) \equiv \sum_{s=1}^{N_q} q_s Q_s(\mathbf{r}) \tag{8}$$

The fitting coefficients q_s are determined by minimizing the spurious Coulomb energy associated with the difference between the fitted and exact densities. (Notice that the set $\{Q\}$ can and often does contain several different types of Hermite GTOs, e.g., those that correspond to s-, d- and p_z- type atomic symmetries.)

Discussion of aspects of variational Coulomb fitting that are specific to periodic systems are in Sect. 1.4. The particular variational Coulomb scheme we use was invented by colleagues at the University of Florida [31, 32], though it was anticipated by Whitten [33] in a paper that none of us knew about until many years later. Subsequently Mintmire et al. generalized it to periodic systems [25–27, 34], after which it was evolved by us, by our colleauges at Technische Universität München [35]), and elsewhere (*e.g.*, the work of Dunlap [30] and of Salahub

et al. [36]). Related work is found in the ADF (molecular) and BAND (periodic) codes of Baerends *et al.* [37] and the so-called Resolution of the Identity method as, for example, in TURBOMOLE [38].

In addition to the fitting, the long-ranged Coulomb lattice sums implicit in $[V_{ee}]_{ij}$ have to be handled accurately. GTOFF uses generalized Ewald techniques and a distributed array of neutralizing charges. We have found that approach to be more stable and rapidly converging than the multipolar scheme used previously. FILMS (the GTOFF predecessor) used multipolar expansions and other periodic GTO codes do also. However, we found them unreliable in practice. This was particularly the case when treating the energy changes associated with large structural changes in a relatively weakly bound system. The interplanar separation of the graphite bi-layer was the key example [39]. Implementation specifics of the generalized Ewald method coupled with variational Coulomb fitting scheme for extended systems never have been published, so we give careful attention to them in Subsects. **1.4.** and **1.5.**

The KS exchange-correlation potential V_{XC} also is a highly non-linear functional of $n_e(\mathbf{r})$, so analytical evaluation of the matrix elements

$$[V_{XC}]_{ij} \propto \int d\mathbf{r}\chi_i(\mathbf{r})V_{XC}[n_e(\mathbf{r})]\chi_j(\mathbf{r}) \tag{9}$$

is not possible. Either full numerical integration or an alternative must be employed. GTOFF uses the alternative of expanding V_{XC} in another auxiliary GTO basis $\{\Xi\}$

$$V_{XC}([n_e\mathbf{r}]) \approx V_{XC}([\tilde{n}_e\mathbf{r}]) \approx \tilde{V}_{XC}(\mathbf{r}) \equiv \sum_{s=1}^{N_{XC}} x_s\Xi_s(\mathbf{r}) \tag{10}$$

GTOFF is unusual, perhaps unique, in using the variationally *fitted* density $\tilde{n}_e(\mathbf{r})$ as the reference for the XC-fitting. Again the required matrix elements become integrals over sums of products of gaussians. The fitting coefficients x_s must be evaluated by numerical integration, but the integrands involved are relatively plain and well-behaved. This "fit-to-fit" procedure eliminates the extremely costly double sum over direct lattice vectors that would be necessitated by constructing the density $n_e(\mathbf{r})$ for use as the target of a direct fit of the XC quantities. Obviously fit-to-fit works only as well as the original density fitting but that is not an additional requirement. Further, GTOFF implements accuracy constraints

on the XC fitting [40]. Additional details are in Subsection **1.6.** below.

GTOFF development has emphasized robustness and precision. Though not an order-N (N = electrons per cell) code, GTOFF is relatively fast. In principle its run times should scale as N^3. The fitting and fit-to-fit approaches, the rapid convergence of the generalized Ewald scheme, various technical means to stabilize SCF convergence, and the intrinsically short-ranged character of the basis combine to give actual scaling $\approx N^{2.6}$. In its present, serial form and running on an older workstation (Sun SPARCstation 5), GTOFF can handle about 20 3d transition atoms per unit cell. On a *single, shared* 66 MHz POWER2 CPU of a shared, older IBM RS6000/SP, we did over a 100 configurations of α-quartz with a large basis in a few weeks. The present version of GTOFF is strictly serial; regarding parallel re-implementation see "Betterments and Enhancements" below.

The relativistic version of GTOFF [22, 41] uses the Douglas-Kroll-Hess (DKH) [42, 43] methodology developed for clusters and molecules by our colleagues at Technische Universität München [44]), with modifications to handle charge-neutrality-related technical issues in the periodic Madelung sums. (Implementation of those modifications is incomplete for the 1D case at this writing, but there is no fundamental barrier.) Since the DKH procedure is relatively unfamiliar in ordered systems, it is useful to summarize the features which distinguish it from the Koelling-Harmon scheme [45] more common in ordered systems. See the Subsection **1.7.** below.

It should be noted that the program BAND (see below) uses the formulation of scalar-relativity called the zeroth-order regular approximation (ZORA) [46]. That approach is closely related to the Koelling-Harmon approach but differs in that it exploits the fact that the eigenvalues ε are much smaller than the electronic rest mass energy to remove the dependence on ε exhibited by the one-electron operator in the former method. This "regularization" of the one-electron operator linearizes the relativistic Kohn-Sham equations, thereby allowing the use of an arbitrary basis set. The matrix elements in ZORA must, however, be evaluated numerically, which is incompatible with the design philosophy of GTOFF, to wit, to do as much of the matrix element evaluation as possible analytically.

In principle, relativistic exchange-correlation functionals should be used. However our TUM colleagues have shown [47] that ordinary exchange-correlation functionals (that do not incoroporate explicit relativistic corrections) are adequate for the study of material properties such as geometries, binding energies, and valence charge densities.

Inclusion of spin-orbit effects at zero magnetic field is critical primarily in two arenas, structure determination of light actinides (notably Pu) [48] and certain spectroscopic characterizations. At non-zero field their inclusion is clearly more important. Calculating spin-orbit effects however raises the computational requirements by approximately an order of magnitude because one must use double-group symmetries (complex-valued KS orbitals are already possible in GTOFF, which works with Hermitian matrices rather than real-symmetric ones). Therefore, a rapid, high-accuracy approximate scheme for inclusion of spin-orbit effects has been developed [48].

GTOFF calculations are not limited to just the DFT total energy, associated bulk modulus or pressure, and KS eigenvalues and eigenfunctions. We have formulated and implemented computationally tractable treatments of energy deposition by high velocity ions and by photons in films, surfaces, and crystals. The first major version of a radiation properties package as an auxiliary code to GTOFF has been completed [49]. It yields the spectral electron momentum density, which is the primary determiner of four key indices of irradiation effects: the proton stopping cross-section, the (e,2e) coincidence cross-section, the (γ,eγ) cross-section, and the directional Compton profile. We also recently implemented the first-principles calculation of the proton stopping cross-section in crystals via ab initio calculation of the microscopic dielectric function $\varepsilon_{Q,Q'}(\mathbf{q},\omega)$ from the Kohn-Sham orbitals and eigenvalues calculated in GTOFF. The calculation requires evaluation of ε over an unprecedentedly large range of energies ω [50].

1.3. Other Codes

Neither FILMS (the GTOFF predecessor) nor even Mintmire's original INTSRF/SCFSRF was the first gaussian orbital periodic code for DFT. That honor apparently goes to Callaway et al.'s BNDPKG [51]. BNDPKG originally calculated only the KS eigenvalues (energy bands) and did not include total energies until 1982 [52], two years after the first paper by Mintmire and Sabin [25]. The BNDPKG total energy scheme was unstable as published, but could be made robust [53]. BNDPKG also had cubic symmetry so deeply entwined in its design that it was prohibitively difficult to generalize the code to non-cubic symmetries [54]. Those barriers led to our decision to resume the line of development begun by Mintmire and Sabin.

At that time there was related LCGTO-FF work on UTFs by Hamann, Feibelman and co-workers [55–58]. Apparently, with one exception, those codes were

not developed further. The exception is the pair of codes QUEST and SeqQUEST [59, 60], which combine pseudopotentials and a gaussian basis. Since we focus upon all-electron calculations, QUEST and SeqQUEST are complementary.

Other codes came later. One was the implementation of DFT in the well-known CRYSTAL code [61], already mentioned. Originally CRYSTAL was a Hartree-Fock package. Suppported by a large development collaboration, CRYSTAL is widely distributed and has a much more user-friendly interface than GTOFF. At least with default settings and basis sets, however, CRYSTAL appears to give peculiar results sometimes. The most recent example is a predicted double minimum for the α-quartz equilibrium structure at very different molar volumes per formula unit [62]. No other DFT study of α-quartz equilibrium had found this behavior, but they were all plane-wave/pseudopotential or cellular basis. We do not find it either [63]. See discussion below.

Four other recent works have implemented periodic methodology resembling that in earlier versions of FILMS and GTOFF. These are by Jaffe and Hess [64], Hirata and Iwata [65], and Kudin and Scuseria [66]. The published results from both of the latter two are for 1D systems only, except for the very recent paper on UO_2 [67]. The Hirata-Iwata effort implements many of the techniques of many-body theory (e.g. coupled cluster) as well as time-dependent DFT. The Kudin-Scuseria work emphasizes order-N scaling. Finally there is BAND, the periodic counterpart to the well-known ADF molecular DFT code [37]. A detailed comparison is not possible in this space, but broadly the ADF approach is to focus on numerical methods, hence it is complementary to the GTOFF focus on purely GTO methodology.

1.4. Variational Coulomb Fitting of the Density

Variational Coulomb fitting for periodic systems has evolved quite a bit since the original work, yet the details and working equations have never been published systematically. That omission is remedied in this and the next Subsections.

In the usual notation, the DFT total energy is

$$E = T_s + E_{ee} + E_{XC} + E_{Ne} + E_{NN} \tag{11}$$

with T_s the Kohn-Sham kinetic energy, E_{ee}, E_{XC}, and E_{Ne} as defined above, and E_{NN} the nuclear-nuclear repulsion energy (in the clamped nucleus approximation). In a finite system with vacuum boundary conditions (atom, molecule) E

is finite. In an infinite system (thermodynamic limit: $\lim_{N_{cell}\to\infty, V\to\infty} N_{cell}/V =$ constant, N_{cell} = number of cells, V = system volume in 3D, area in 2D, length in 1D) that is periodic, $E \to \infty$ but E/N_{cell} is finite.

1.4.1. Charge Neutrality

The finiteness of E/N_{cell} involves a subtlety that can be missed in the informal language that "a solid is just a big molecule". For simplicity, take one atom per unit cell except where noted otherwise. Since we are working with single-particle basis functions that are rather well localized and are integrable, consider electron charge distributions $\mathcal{F}_n(\mathbf{r})$ each comprised of lattice sums of such localized functions $\bar{\mathcal{F}}_n(\mathbf{r})$:

$$\mathcal{F}_n(\mathbf{r}) = \sum_{\mathbf{R}} \bar{\mathcal{F}}_n(\mathbf{r}-\mathbf{R}) \tag{12}$$

The Coulomb repulsion of two of these is (except for a factor of one-half)

$$\mathcal{E}_{mn} = \int d\mathbf{r}_1\, d\mathbf{r}_2 \mathcal{F}_m(\mathbf{r}_1)\mathcal{F}_n(\mathbf{r}_2)/r_{12} = \sum_{\mathbf{R},\mathbf{R}'} \int d\mathbf{r}_1\, d\mathbf{r}_2 \bar{\mathcal{F}}_m(\mathbf{r}_1-\mathbf{R})\bar{\mathcal{F}}_n(\mathbf{r}_2-\mathbf{R}')/r_{12}$$

$$= \sum_{\mathbf{R},\mathbf{R}'} \int d\mathbf{r}\, d\mathbf{r}' \bar{\mathcal{F}}_m(\mathbf{r})\bar{\mathcal{F}}_n(\mathbf{r}')/|\mathbf{r}-\mathbf{r}'+(\mathbf{R}-\mathbf{R}')|$$

$$= N_{cell} \sum_{\mathbf{R}} \int d\mathbf{r}\, d\mathbf{r}' \bar{\mathcal{F}}_m(\mathbf{r})\bar{\mathcal{F}}_n(\mathbf{r}')/|\mathbf{r}-\mathbf{r}'+\mathbf{R}|$$

$$\mathcal{E}_{mn}/N_{cell} = \sum_{\mathbf{R}} \int d\mathbf{r}\, d\mathbf{r}' \bar{\mathcal{F}}_m(\mathbf{r})\bar{\mathcal{F}}_n(\mathbf{r}')/|\mathbf{r}-\mathbf{r}'+\mathbf{R}| \tag{13}$$

Though this looks like an extensive quantity, its thermodynamic limit is infinite if $\bar{A}_i := \int d\mathbf{r}\bar{\mathcal{F}}_m(\mathbf{r})$ is non-zero for both $i = m$ and $i = n$. (The Coulomb repulsion of an infinite set of monopoles is infinite.) The problem can be removed by including the nuclear Coulomb attraction. Consider the charge distribution $\mathcal{F}_m(\mathbf{r})$

interacting with a lattice of nuclei:

$$\mathcal{E}_{Ne,m} = -\int d\mathbf{r}\mathcal{F}_m(\mathbf{r})\sum_{\mathbf{R}} Z_{\mathbf{R}}/|\mathbf{r}-\mathbf{R}| = -\sum_{\mathbf{R},\mathbf{R}'}\int d\mathbf{r}\bar{\mathcal{F}}_m(\mathbf{r}-\mathbf{R}')Z_{\mathbf{R}}/|\mathbf{r}-\mathbf{R}|$$

$$= -\sum_{\mathbf{R},\mathbf{R}'}\int d\mathbf{r}\bar{\mathcal{F}}_m(\mathbf{r})Z_{\mathbf{R}}/|\mathbf{r}-\mathbf{R}+\mathbf{R}')| = -N_{cell}\sum_{\mathbf{R}}\int d\mathbf{r}\bar{\mathcal{F}}_m(\mathbf{r})Z_{\mathbf{R}}/|\mathbf{r}-\mathbf{R}|$$

$$\mathcal{E}_{Ne,m}/N_{cell} = -\sum_{\mathbf{R}}\int d\mathbf{r}\bar{\mathcal{F}}_m(\mathbf{r})Z_{\mathbf{R}}/|\mathbf{r}-\mathbf{R}| \tag{14}$$

This too has an infinite limit if $\bar{A}_m \neq 0$. A combination of Eqs. (13) and 14 and a suitable norm solves the problem. Write

$$\frac{\mathcal{E}_{mn}}{N_{cell}} + \frac{\mathcal{E}_{Ne,m}}{N_{cell}} = \sum_{\mathbf{R}}\int d\mathbf{r}\bar{\mathcal{F}}_m(\mathbf{r})\left[\int d\mathbf{r}'\bar{\mathcal{F}}_n(\mathbf{r}')/|\mathbf{r}-\mathbf{r}'-\mathbf{R}| - Z_{\mathbf{R}}/|\mathbf{r}-\mathbf{R}|\right]$$

$$= \sum_{\mathbf{R}}\int d\mathbf{r}\bar{\mathcal{F}}_m(\mathbf{r}) \times \left\{\int d\mathbf{r}'\left[\bar{\mathcal{F}}_n(\mathbf{r}') - Z_{\mathbf{R}}\delta(\mathbf{r}')\right]/|\mathbf{r}-\mathbf{r}'-\mathbf{R}|\right\} \tag{15}$$

If the local function be normed such that

$$\int d\mathbf{r}'\left[\bar{\mathcal{F}}_n(\mathbf{r}') - Z_{\mathbf{R}}\delta(\mathbf{r}')\right] = 0 \tag{16}$$

then the sum in braces in Eq. (15) is the sum of Coulomb potentials of a neutral distribution which by the multipole expansion falls off as $\mathbf{R}^{-3}$ in a crystal (and also in a film with in-plane inversion symmetry). Since $\bar{\mathcal{F}}_m(\mathbf{r})$ is a bounded, well-localized, integrable function, the combination in Eq. (15) has a finite value.

Because of occasional confusion on the point, note that all the integrals in the foregoing discussion are over all space. Equivalent expressions in terms of integrals over unit cells sometimes are useful. For example if $\bar{\mathcal{F}}_i$ are net *neutral* localized charge densities, $\int d\mathbf{r}\bar{\mathcal{F}}_i(\mathbf{r}) = 0$, then so are the corresponding lattice

periodic distributions $\int d\mathbf{r}\mathcal{F}_i(\mathbf{r}) = \sum_{\mathbf{R}} \int d\mathbf{r}\bar{\mathcal{F}}_i(\mathbf{r}-\mathbf{R}) = 0$, whence

$$\begin{aligned}
\mathcal{E}_{ij} &= \int d\mathbf{r}_1 d\mathbf{r}_2 \mathcal{F}_i(\mathbf{r}_1)\mathcal{F}_j(\mathbf{r}_2)/r_{12} \\
&= \int d\mathbf{r}_1 \mathcal{F}_i(\mathbf{r}_1) \sum_{\mathbf{R}} \int_{cell} d\mathbf{r}_2 \mathcal{F}_j(\mathbf{r}_2+\mathbf{R})/|\mathbf{r}_1-\mathbf{r}_2-\mathbf{R}| \\
&= \int d\mathbf{r}_1 \mathcal{F}_i(\mathbf{r}_1) \sum_{\mathbf{R}} \int_{cell} d\mathbf{r}_2 \mathcal{F}_j(\mathbf{r}_2)/|\mathbf{r}_1-\mathbf{r}_2-\mathbf{R}| \\
&= \sum_{\mathbf{R}} \int d\mathbf{r}_1 \mathcal{F}_i(\mathbf{r}_1) \int_{cell,\mathbf{R}} d\mathbf{r}_2 \mathcal{F}_j(\mathbf{r}_2)/|\mathbf{r}_1-\mathbf{r}_2| \qquad (17)
\end{aligned}$$

where the notation in the last line indicates an integral over the cell at $\mathbf{R}$ from the origin and the next-to-last line occurs because of periodicity: $\mathcal{F}_j(\mathbf{r}+\mathbf{R}) = \mathcal{F}_j(\mathbf{r})$. By change of variables $\mathbf{r}_1 \rightarrow \mathbf{r}_1 + \mathbf{R}$ in the next-to-last line and periodicity of $\mathcal{F}_i(\mathbf{r})$ we have

$$\begin{aligned}
\mathcal{E}_{ij} &= \sum_{\mathbf{R}} \int d\mathbf{r}_1 \mathcal{F}_i(\mathbf{r}_1+\mathbf{R}) \int_{cell} d\mathbf{r}_2 \mathcal{F}_j(\mathbf{r}_2+\mathbf{R})/|\mathbf{r}_1-\mathbf{r}_2| \\
&= \sum_{\mathbf{R}} \int d\mathbf{r}_1 \mathcal{F}_i(\mathbf{r}_1) \int_{cell} d\mathbf{r}_2 \mathcal{F}_j(\mathbf{r}_2)/|\mathbf{r}_1-\mathbf{r}_2| \\
&= N_{cell} \int d\mathbf{r}_1 \mathcal{F}_i(\mathbf{r}_1) \int_{cell} d\mathbf{r}_2 \mathcal{F}_j(\mathbf{r}_2)/|\mathbf{r}_1-\mathbf{r}_2| \qquad (18)
\end{aligned}$$

1.4.2. Variational Coulomb Fitting without Charge Neutrality - Finite Systems

The density dependence of E_{ee} motivates variational Coulomb fitting. To understand the effect of charge neutrality requirements in periodic systems, it helps to summarize variational Coulomb fitting of the charge density in a molecule or cluster. They have a finite number of nuclei in a bounded region of space and vacuum boundary conditions and do not require charge neutrality. A careful introduction to the details for such systems is in Dunlap and Rösch [30].

To distinguish finite and infinite systems, denote the electron number density of the former by $\rho(\mathbf{r})$, with $\int d\mathbf{r}\rho(\mathbf{r}) = N_e$. Define the Coulomb bracket of any two densities (both corresponding to N_e) as

$$[\rho_1|\rho_2] \equiv \int d\mathbf{r}_1 d\mathbf{r}_2 \rho_1(\mathbf{r}_1)\rho_2(\mathbf{r}_2)/r_{12} \qquad (19)$$

and

$$E_{coul}[\rho] = \frac{1}{2}[\rho|\rho] \tag{20}$$

Introduce an approximation for ρ as a linear combination of fitting functions

$$\begin{aligned} \rho(\mathbf{r}) &= \tilde{\rho}(\mathbf{r}) + \Delta\rho(\mathbf{r}) \\ \tilde{\rho}(\mathbf{r}) &= \sum_{\ell}^{N_Q} q_\ell Q_\ell(\mathbf{r}) \end{aligned} \tag{21}$$

Substitution gives

$$\tilde{E}_{coul}[\tilde{\rho}] := [\rho|\tilde{\rho}] - \frac{1}{2}[\tilde{\rho}|\tilde{\rho}]$$

$$E_{coul}[\rho] - \tilde{E}_{coul}[\tilde{\rho}] = \frac{1}{2}[\Delta\rho|\Delta\rho] \tag{22}$$

The error in approximating E_{coul} by $\tilde{E}_{coul}[\tilde{\rho}]$ is $\frac{1}{2}[\Delta\rho|\Delta\rho] \geq 0$, so immediately there is a variation principle for optimization of $\tilde{\rho}$:

$$\frac{\delta(E_{coul}[\rho] - \tilde{E}_{coul}[\tilde{\rho}])}{\delta\tilde{\rho}} = -\frac{\delta\tilde{E}_{coul}[\tilde{\rho}]}{\delta\tilde{\rho}} = 0 \tag{23}$$

For $\tilde{\rho}$ that satisfy Eq. (23), it follows that

$$0 = \int d\mathbf{r}'\rho(\mathbf{r}')/|\mathbf{r}' - \mathbf{r}| - \int d\mathbf{r}'\tilde{\rho}(\mathbf{r}')/|\mathbf{r}' - \mathbf{r}| \Rightarrow$$

$$[\rho|\tilde{\rho}] = [\tilde{\rho}|\tilde{\rho}] \Rightarrow \tilde{E}[\tilde{\rho}] = \frac{1}{2}[\tilde{\rho}|\tilde{\rho}] \tag{24}$$

For the linear expansion Eq. (21), application of the variation principle Eq. (23)

gives

$$\sum_j q_j [Q_j|Q_i] = [\rho|Q_i] \tag{25}$$

Determination of the q_js at each iteration of an SCF cycle is efficient beause the contributions to Eq. 25 can be constructed directly from the molecular orbital coefficients $C^i_{j,\ell}$ (analogous with Eq. (5) for finite systems) and precomputed matrix elements.

Eq. (22) shows that the Coulomb fitting variation principle is a bound from *below*, so improving the fitting basis *raises* the total energy. This behavior is the reverse of what happens to the total energy as the orbital basis is augmented (because of the Rayleigh-Ritz variational principle). The difference can seem counter-intuitive to new users of the method.

1.4.3. Variational Coulomb Fitting with Charge Neutrality - Extended Systems

Because of the charge neutrality requirements for extended systems discussed above, literal transcription of variational Coulomb fitting for finite systems [by replacing $\rho(\mathbf{r})$ everywhere by $n_e(\mathbf{r})$] clearly will not work. The solution is to do the charge fitting with neutralized functions. Here it is useful to allow explicitly for multiple atoms per cell.

To exploit McMurchie-Davidson [68] recursion, GTOFF (and FILMS before it) uses Hermite gaussian functions [69] for its orbital basis $G^\ell_j(\mathbf{r})$ Eq. (4) and both the charge and XC fitting bases, $Q_s(\mathbf{r})$ Eq. (8) and $\Xi_s(\mathbf{r})$ Eq. (10). From here on the development is explicitly in terms of Hermite gaussians therefore. A general Hermite gaussian of order $\vec{\nu} := (\nu_1, \nu_2, \nu_3)$ and orbital exponent μ centered at position $\mathbf{A}$ is given by

$$\begin{aligned} f(\vec{\nu},\mu,\mathbf{A};\mathbf{r}) &:= \frac{\partial^{\nu_1}}{\partial A_x}\frac{\partial^{\nu_2}}{\partial A_y}\frac{\partial^{\nu_3}}{\partial A_z} f(\vec{0},\mu,\mathbf{A};\mathbf{r}) \\ &:= \partial^{\nu_1}_{A_x}\partial^{\nu_2}_{A_y}\partial^{\nu_3}_{A_z} f(\vec{0},\mu,\mathbf{A};\mathbf{r}) \\ &\equiv \partial^{\vec{\nu}}_{\mathbf{A}} f(\vec{0},\mu,\mathbf{A};\mathbf{r}) \\ f(\vec{0},\mu,\mathbf{A};\mathbf{r}) &:= \exp(-\mu|\mathbf{r}-\mathbf{A}|^2) \end{aligned} \tag{26}$$

The zeroth-order ("s-type") Hermite gaussians have non-zero norm (they are

"charged" or "charge carrying"); the rest have zero norm:

$$\int d\mathbf{r} f(\vec{\nu},\mu,\mathbf{A};\mathbf{r}) = (\pi/\mu)^{3/2}\delta_{\vec{\nu},0} \tag{27}$$

(In practice, we normalize the s-type functions to unity, but oddly enough it is easier to follow the development if the norm is kept explicit as just shown.)

Define a neutralized set of charge fitting functions as

$$Q(\vec{\nu},\mu,\mathbf{A};\mathbf{r}) := f(\vec{\nu},\mu,\mathbf{A};\mathbf{r}) - (\pi/\mu)^{3/2}\delta_{\vec{\nu},0} n_{nuc}(\mathbf{r}-\mathbf{A}) \tag{28}$$

where n_{nuc} is the charge density (actually number density) for the nuclear array in one unit cell. For N_{nuc} nuclei in each cell at positions $\mathbf{D}_\alpha$ with respect to the cell origin and charges (in units of electron magnitude) Z_α and with $Z_{tot} = \sum_\alpha Z_\alpha$ the total cellular nuclear charge, the nuclear array term is

$$n_{nuc}(\mathbf{r}) = \sum_\alpha \frac{Z_\alpha}{Z_{tot}} \delta(\mathbf{r}-\mathbf{D}_\alpha) \tag{29}$$

where the sum is over one cell. Use of the nuclear array guarantees cell-by-cell charge neutrality and preserves cellular symmetry irrespective of the basis, whereas using a charge at the s-type Hermite gaussian centers does not.

In terms of the $Q(\vec{\nu},\mu,\mathbf{A};\mathbf{r})$, the density fitting becomes

$$\begin{aligned} n_{neutral}(\mathbf{r}) &:= n_e(\mathbf{r}) - n_{ion}(\mathbf{r}) \\ &\approx \tilde{n}(\mathbf{r}) \\ \tilde{n}(\mathbf{r}) &\equiv \sum_{\vec{\nu},\mu,} q_{\vec{\nu},\mu} \sum_{\mathbf{R}} Q(\vec{\nu},\mu,\mathbf{R};\mathbf{r}) \end{aligned} \tag{30}$$

where n_{ion} is the nuclear charge distribution for the whole system

$$n_{ion}(\mathbf{r}) = \sum_{\mathbf{R},\alpha} Z_\alpha \delta(\mathbf{r}-\mathbf{D}_\alpha-\mathbf{R}) \tag{31}$$

("Ion" is used here simply because a different nuclear charge distribution already has been defined as n_{nuc}. No distinction between species is involved.)

Since all the densities now are neutral, Eq. (15) assures a finite result per unit cell for the Coulomb bracket Eq. (19):

$$\begin{aligned}\frac{1}{2}[n_{neutral}|n_{neutral}] &= \frac{1}{2}[n|n]-[n|n_{ion}]+\frac{1}{2}[n_{ion}|n_{ion}] \\ &= E_{ee}+E_{Ne}+E_{NN}\equiv E_{coul,tot}\end{aligned} \tag{32}$$

where $E_{coul,tot}$ is the total classical Coulomb energy for the extended system.

Analogous with the first line of Eq. (21), we have

$$n_{neutral}=\tilde{n}+\Delta n \tag{33}$$

Note that Δn is neutral by construction, In parallel with Eq. (22) we can write

$$\begin{aligned}E_{coul,tot}[n_{neutral}]-\tilde{E}_{coul,tot}[\tilde{n}] &= \frac{1}{2}[\Delta n|\Delta n] \\ \tilde{E}_{coul,tot}[\tilde{n}] &:= [n_{neutral}|\tilde{n}]-\frac{1}{2}[\tilde{n}|\tilde{n}]\end{aligned} \tag{34}$$

Since n_{ion} is unaffected by the fitting procedure, the decomposition $\tilde{n}=\tilde{n}_e-n_{ion}$ is unique. Using it in Eq. (34)gives

$$\begin{aligned}\tilde{E}_{coul,tot}[\tilde{n}] &= [n_e|\tilde{n}_e]-[n_e|n_{ion}]-[\tilde{n}_e|n_{ion}]+[n_{ion}|n_{ion}]-\frac{1}{2}[\tilde{n}_e|\tilde{n}_e] \\ &+ [\tilde{n}_e|n_{ion}]-\frac{1}{2}[n_{ion}|n_{ion}] \\ &= [n_e|\tilde{n}_e]-\frac{1}{2}[\tilde{n}_e|\tilde{n}_e]-[n_e|n_{ion}]+\frac{1}{2}[n_{ion}|n_{ion}]\end{aligned} \tag{35}$$

For the purposes of Eq. (38), this expression differs from Eq. (22) only by terms that are fixed, so Eq. (24) holds for $\tilde{n}$:

$$[n_{neut}|\tilde{n}]=[\tilde{n}|\tilde{n}]\Rightarrow\tilde{E}_{coul,tot}[\tilde{n}]=\frac{1}{2}[\tilde{n}|\tilde{n}] \tag{36}$$

The argument about the variation principle for optimization of $\tilde{n}$ goes through almost as in the non-neutral case, with one important exception. Thus far there is nothing explicit to force the electron density contribution to $\tilde{n}$ to integrate to

the right number of electrons, so a Lagrange multiplier λ for that constraint is required. Specifically, the constraint is

$$\begin{aligned} N_e &= \int d\mathbf{r} \sum_{\vec{\nu},\mu} q_{\vec{\nu},\mu} f(\vec{\nu},\mu,0,\mathbf{r}) \\ &:= \sum_{\vec{\nu},\mu} q_{\vec{\nu},\mu} \eta_{\vec{\nu},\mu} \end{aligned} \tag{37}$$

In terms, therefore, of the linear expansion Eq. (30), the extremum is determined by the condition

$$\partial\{\tilde{E}_{coul,tot}[\tilde{n}] + \lambda \int d\mathbf{r}(N_e - \sum_{\vec{\nu},\mu} q_{\vec{\nu},\mu}\eta_{\vec{\nu},\mu})\}/\partial q_{\vec{\nu}',\mu'} = 0 \tag{38}$$

This gives

$$\sum_{\vec{\nu},\mu} q_{\vec{\nu},\mu} \sum_{\mathbf{R},\mathbf{R}'} [Q(\vec{\nu},\mu,\mathbf{R})|Q(\vec{\nu}',\mu',\mathbf{R}')] = \sum_{\mathbf{R}} [n_{neut}|Q(\vec{\nu}',\mu',\mathbf{R})] + \lambda\eta_{\vec{\nu}',\mu'} \tag{39}$$

or

$$\mathrm{q}\mathbb{B} = \mathbb{A} + \lambda\eta \tag{40}$$

where the quantities in the latter equation are defined in order by those in Eq. (39). Immediately it follows that

$$\mathrm{q} = \mathbb{B}^{-1}(\mathbb{A} + \lambda\eta) \tag{41}$$

and the Lagrange parameter can be evaluated via the foregoing definition of $\eta_{\vec{\nu}\mu}$:

$$\eta^{\dagger}\mathrm{q} = \eta^{\dagger}\mathbb{B}^{-1}(\mathbb{A} + \lambda\eta) \;\Rightarrow$$

$$\lambda\eta^{\dagger}\mathbb{B}^{-1}\eta = N_e - \eta^{\dagger}\mathbb{B}^{-1}\mathbb{A}\lambda = \frac{N_e - \eta^{\dagger}\mathbb{B}^{-1}\mathbb{A}}{\eta^{\dagger}\mathbb{B}^{-1}\eta} \tag{42}$$

These equations are solved at each SCF iteration. Though the matrix $\mathbb{A}$ involves the electron density n_e associated with a given iteration (via n_{neut}), that contribution can be evaluated swiftly in terms of precomputed matrix elements with respect to the primitive basis functions for the orbitals and the charge fitting along with elements of the density matrix $\mathcal{P}$ with respect to the orbital basis. Eqs. 1 and 5 combined give

$$n_e(\mathbf{r}) = \sum_{i,\mathbf{k}} n_{i,\mathbf{k}} |\varphi_{i,\mathbf{k}}(\mathbf{r})|^2$$

$$= \frac{1}{N_{cell}} \sum_{i,\mathbf{k}} n_{i,\mathbf{k}} \sum_{\vec{\nu},\vec{\nu}',\mu,\mu'} c^{i,\mathbf{k}}_{\vec{\nu}\mu} c^{i,\mathbf{k}}_{\vec{\nu}'\mu'} * \sum_{\mathbf{R}\mathbf{R}'} \exp -i\mathbf{k}\cdot(\mathbf{R}-\mathbf{R}') f(\vec{\nu},\mu,\mathbf{R},\mathbf{r}) f(\vec{\nu}',\mu',\mathbf{R}',\mathbf{r})$$

$$:= \sum_{\vec{\nu},\vec{\nu}',\mu,\mu'} \sum_{\mathbf{R}\mathbf{R}'} \mathcal{P}_{\vec{\nu},\vec{\nu}',\mu,\mu'}(\mathbf{R}\mathbf{R}') f(\vec{\nu},\mu,\mathbf{R},\mathbf{r}) f(\vec{\nu}',\mu',\mathbf{R}',\mathbf{r}) \tag{43}$$

With this result, evaluation of the n_e contribution to $\mathbb{A}$ becomes a matter of precomputing the "orb-fit-orb" integrals, it i.e., Coulomb integrals with respect to products of the form $f(\vec{\nu},\mu,\mathbf{R},\mathbf{r})Q(\vec{\nu}'',\mu'',\mathbf{R},\mathbf{r})f(\vec{\nu}',\mu',\mathbf{R}',\mathbf{r})$ from the two primitive basis sets; compare Eq. (40).

1.5. Generalized Ewald Method for Coulombic Lattice Sums

Coulombic lattice sums occur in the charge fitting, Eq. (40), in the matrix elements of the KS Hamiltonian with respect to the orbital basis, and in the total energy. The charge neutral generalization of Eq. (7) is an example of the form when written in Hermite gaussian orbital and charge-fit basis sets:

$$\sum_{\mathcal{R},\mathcal{R}'} \exp(i\mathbf{k}\cdot\mathbf{R})[f(\vec{\nu}_1,\mu_1,\mathbf{R}+\mathbf{D}_\alpha) f(\vec{\nu}_2,\mu_2,\mathbf{D}_\beta)|Q(\vec{\nu}',\mu',\mathbf{R}'+\mathbf{D}_\gamma)] \tag{44}$$

This is precisely the sum of the "orb-fit-orb" matrix elements just mentioned. The product property, that two ordinary gaussians on two sites multiply to give a gaussian at a third site, carries over to Hermite GTOs by virtue of their partial derivative forms; see Eq. (26). Details are given in Appendix A. The relevant

result is

$$[f(\vec{\nu}_1,\mu_1,\mathbf{R}+\mathbf{A})f(\vec{\nu}_2,\mu_2,\mathbf{R}+\mathbf{B})|f(\vec{\nu}_3,\mu_3,\mathbf{R}+\mathbf{C})]$$

$$= \sum_{\vec{\zeta}=0}^{\vec{\nu}_1+\vec{\nu}_2} g(\vec{\nu}_1,\vec{\nu}_2,\vec{\zeta},\mu_1,\mu_2)f(\vec{\zeta},\frac{\mu_1\mu_2}{\mu_1+\mu_2},\mathbf{A}-\mathbf{B}-\mathbf{R})$$

$$\times[f(\vec{\nu}_1+\vec{\nu}_2-\vec{\zeta},\mu_1+\mu_2,\frac{\mu_1\mathbf{A}+\mu_2(\mathbf{B}+\mathbf{R}}{\mu_1+\mu_2})|f(\vec{\nu}_3,\mu_3,\mathbf{R}+\mathbf{C})] \tag{45}$$

irrespective, of course, of whether f belongs to the orbital basis (also denoted with f), the charge fit basis Q, or the XC fit basis Ξ. Eq. 44 then can be written in terms of an "inner" and an "outer" lattice sum, with the former sum expressed as

$$\sum_{\mathbf{R}',\mathbf{D}_\gamma} [f(\vec{\nu},\mu,\mathbf{A})|Q(\vec{\nu}',\mu',\mathbf{R}'+\mathbf{D}_\gamma)] \tag{46}$$

The challenge is to evaluate this sum accurately, robustly, and swiftly. As mentioned before, the customary approach is via some form of multipole expansion. FILMS had just such a procedure. Though usually adequate, it shared the conceptual problem of all multipolar schemes of which we are aware, namely, there was no systematic way to sum the entire series with controllable precision. A more practical criticism was that we found it difficult to diagnose when the technique was failing despite appearing to be successful.

Motivated by the fact that classical Ewald techniques allow one to sum the Coulomb potential of a cell-wise neutral set of point charges exactly, Birkenheuer [70] replaced the multipolar evaluation of $V_{ee,ij}$ Eq. (7) and the corresponding total energy in FILMS with a generalized Ewald procedure. Boettger extended the treatment to all the Coulomb sums (primarily the matrices $\mathbb{A}$ and $\mathbb{B}$) and to 3D lattices when GTOFF was introduced. Details never have been published and the working equations are not explicit even in ref. [70]. Hence the detail that follows. As an aside, there are some detailed differences between Eq. (46) and the expressions in $\mathbb{B}$, primarily from the point charge ion array contributions.

Recall first the classical argument. For a net-neutral array of charges Z_α in one

unit cell ($\sum_\alpha Z_\alpha = 0$), the Coulomb potential is

$$V(\mathbf{r}) = \sum_{\mathbf{R},\mathbf{D}_\alpha} \frac{Z_\alpha}{|\mathbf{r}-\mathbf{R}-\mathbf{D}_\alpha|} \tag{47}$$

Each term can be rewritten as

$$\frac{Z_\alpha}{|\mathbf{r}-\mathbf{R}-\mathbf{D}_\alpha|} = \frac{2Z_\alpha}{\pi^{1/2}} \int_0^\infty du \exp(-|\mathbf{r}-\mathbf{R}-\mathbf{D}_\alpha|^2 u^2)$$

$$= \frac{2Z_\alpha}{\pi^{1/2}} \left\{ \int_0^\eta du \exp(-|\mathbf{r}-\mathbf{R}-\mathbf{D}_\alpha|^2 u^2) + \int_\eta^\infty du \exp(-|\mathbf{r}-\mathbf{R}-\mathbf{D}_\alpha|^2 u^2) \right\} \tag{48}$$

$$\begin{aligned} V(\mathbf{r}) \;=\; & \sum_\alpha Z_\alpha \left\{ \frac{4\pi}{\Omega} \sum_{\mathbf{K}\neq 0} K^{-2} \exp(-K^2/4\eta) \exp[i\mathbf{K}\cdot(\mathbf{r}-\mathbf{D}_\alpha)] \right. \\ & \left. + \sum_{\mathbf{R}} \frac{\operatorname{erfc}(\eta|\mathbf{r}-\mathbf{R}-\mathbf{D}_\alpha|)}{|\mathbf{r}-\mathbf{R}-\mathbf{D}_\alpha|} \right\} \end{aligned} \tag{49}$$

The large R terms that converge slowly when summed directly thus are summed in reciprocal space, while the smaller R terms are summed straightforwardly. The $K = 0$ divergence vanishes because of charge neutrality.

To apply this approach to the sum of Coulomb energies Eq. (46), note first that the only neutral distribution is $Q(\vec{\nu}', \mu', \mathbf{R}' + \mathbf{D}_\gamma \mathbf{r})$ so it must be used as the charge source for the Coulomb potential analogous with Eq. (47). Shortly it will become apparent that it actually is beneficial to split Q into three offsetting ("compensating" is Birkenheuer's term) pieces. Define the "compensated" charge fitting function Q_{comp} in terms of a bare Hermite GTO as

$$Q_{comp}(\vec{\nu}, \mu, \mathbf{A}, \mathbf{r}) := \left[f(\vec{\nu}, \mu, \mathbf{A}, \mathbf{r}) - \left(\frac{\pi}{\mu}\right)^{3/2} \partial_{\mathbf{A}}^{\vec{\nu}} \delta(\mathbf{r}-\mathbf{A}) \right] \tag{50}$$

The second term is a point charge distribution of multipolar order $\vec{\nu}$ and unit multipolar moment [71], which means that both $f(\vec{\nu}, \mu, \mathbf{R}+\mathbf{D}, \mathbf{r})$ and the com-

pensating multipole have the same point group symmetry. The form of the compensation also preserves the derivative relationship of higher-order to lower-order Hermite gaussians. (Local monopole compensation was introduced by Boettger in FILMS to improve the behavior of the multipolar summations then in use. The all-order compensation was by Birkenheuer in the context of the generalized Ewald procedure.)

Substitute Eq. (50) in the definition of the neutralized fitting function Eq. (28), then add and subtract as shown:

$$Q(\vec{\nu},\mu,\mathbf{R}+\mathbf{A},\mathbf{r}) = Q_{comp}(\vec{\nu},\mu,\mathbf{R}+\mathbf{A},\mathbf{r})$$

$$+(\pi/\mu)^{3/2}\left[\partial^{\vec{\nu}}_{\mathbf{R}+\mathbf{A}}\delta(\mathbf{r}-\mathbf{R}-\mathbf{A}) - \delta_{\vec{\nu},0}\sum_{\alpha}\frac{Z_\alpha}{Z_{tot}}\delta(\mathbf{r}-\mathbf{R}-\mathbf{A}-\mathbf{D}_\alpha)\right] \tag{51}$$

$$= Q_{comp}(\vec{\nu},\mu,\mathbf{R}+\mathbf{A},\mathbf{r})$$

$$-(\eta/\mu)^{3/2}\left[f(\vec{\nu},\eta,\mathbf{R}+\mathbf{A},\mathbf{r}) - (\pi/\eta)^{3/2}\partial^{\vec{\nu}}_{\mathbf{R}+\mathbf{A}}\delta(\mathbf{r}-\mathbf{R}-\mathbf{A})\right]$$

$$+(\eta/\mu)^{3/2}\left[f(\vec{\nu},\eta,\mathbf{R}+\mathbf{A},\mathbf{r}) - \delta_{\vec{\nu},0}(\pi/\eta)^{3/2}\sum_{\alpha}\frac{Z_\alpha}{Z_{tot}}\delta(\mathbf{r}-\mathbf{R}-\mathbf{A}-\mathbf{D}_\alpha)\right] \tag{52}$$

$$= Q_{comp}(\vec{\nu},\mu,\mathbf{R}+\mathbf{A},\mathbf{r}) - (\eta/\mu)^{3/2}Q_{comp}(\vec{\nu},\eta,\mathbf{R}+\mathbf{A},\mathbf{r})$$

$$+(\eta/\mu)^{3/2}\left[f(\vec{\nu},\eta,\mathbf{R}+\mathbf{A},\mathbf{r}) - \delta_{\vec{\nu},0}(\pi/\eta)^{3/2}\sum_{\alpha}\frac{Z_\alpha}{Z_{tot}}\delta(\mathbf{r}-\mathbf{R}-\mathbf{A}-\mathbf{D}_\alpha)\right] \tag{53}$$

The definition of Q_{comp} Eq. (50) implies that

$$\sum_{\alpha}\frac{Z_\alpha}{Z_{tot}}\delta(\mathbf{r}-\mathbf{D}_\alpha) = \left(\frac{\eta}{\pi}\right)^{3/2}\sum_{\alpha}\frac{Z_\alpha}{Z_{tot}}\left[Q_{comp}(0,\eta,\mathbf{D}_\alpha,\mathbf{r}) - f(0,\eta,\mathbf{D}_\alpha,\mathbf{r})\right] \tag{54}$$

so

$$Q(\vec{\nu},\mu,\mathbf{R}+\mathbf{A},\mathbf{r}) = Q_{comp}(\vec{\nu},\mu,\mathbf{R}+\mathbf{A},\mathbf{r})$$

$$-(\eta/\mu)^{3/2}\left[Q_{comp}(\vec{\nu},\eta,\mathbf{R}+\mathbf{A},\mathbf{r})p-\delta_{\vec{\nu},0}\sum_{\alpha}\frac{Z_\alpha}{Z_{tot}}Q_{comp}(0,\eta,\mathbf{R}+\mathbf{A}+\mathbf{D}_\alpha,\mathbf{r})\right]$$

$$+(\eta/\mu)^{3/2}\left[f(\vec{\nu},\eta,\mathbf{R}+\mathbf{A},\mathbf{r})-\delta_{\vec{\nu},0}\sum_{\alpha}\frac{Z_\alpha}{Z_{tot}}f(0,\eta,\mathbf{R}+\mathbf{A}+\mathbf{D}_\alpha,\mathbf{r})\right] \tag{55}$$

The rationale for this somewhat intricate decomposition is that one can show [70] exactly what would be expected by analogy with the classical Ewald technique, namely exponential decay with increasing lattice separation

$$\lim_{R\to\infty}[f(\vec{\nu}_1,\mu_1,\mathbf{A})|Q_{comp}(\vec{\nu}_2,\mu_2,\mathbf{R}+\mathbf{B})]$$

$$=-\partial_{\mathbf{B}}^{\vec{\nu}_1}\partial_{\mathbf{C}}^{\vec{\nu}_2}\frac{\sqrt{\pi^5(\mu_1+\mu_2)}}{\mu_1^2\mu_2^2}\frac{\exp(-\frac{\mu_1\mu_2}{\mu_1+\mu_2}|\mathbf{A}-\mathbf{B}-\mathbf{R}|^2)}{|\mathbf{A}-\mathbf{B}-\mathbf{R}|^2} \tag{56}$$

As a result, the "inner lattice sum", Eq. (46) converges extremely rapidly for the more compact basis functions (larger μ_i).

The summations of matrix elements involving "Ewald" quantities, $Q_{comp}(\vec{\nu},\eta,\mathbf{R}+\mathbf{A},\mathbf{r})$, $Q_{comp}(0,\eta,\mathbf{R}+\mathbf{A},\mathbf{r})$, and $f(\vec{\nu},\eta,\mathbf{R}+\mathbf{A},\mathbf{r})$, are not, of course, so rapidly convergent in the direct lattice. The trick is to pick a value of η such that reciprocal lattice sums converge rapidly. The more significant point in that regard is shown by the formatting of Eq. (55). The inner lattice sum of the latter two sets of terms in Eq. (55) involves *only one* exponent η for each submanifold order $\vec{\nu}$ of Hermite gaussian fitting functions, so those lattice sums need be evaluated only once per submanifold, independent of the details of the fitting basis. The contribution involving $Q_{comp}(0,\eta,\mathbf{R}+\mathbf{A},\mathbf{r})$ can be done efficiently as a direct lattice sum, while the remaining contribution, in $f(\vec{\nu},\eta,\mathbf{R}+\mathbf{A},\mathbf{r})$, is done readily in reciprocal space.

A simple recipe for balancing between those two Ewald contributions comes from enforcing a requirement that the number of terms in each sum give equal exponential convergence. Specifically, let that number be N_{sum}, then the maximum radius cutoffs R_m and K_m in 2D would be roughly

$$\begin{aligned} N_{sum}\Omega_{cell} &= \pi R_m^2 \\ N_{sum}\Omega_{BZ} &= \pi K_m^2 \end{aligned} \tag{57}$$

where Ω_{cell} is the unit-cell area in 2D and correspondingly for the first Brillouin Zone. Assuming exponential decay, the criterion for equality of convergence becomes

$$\exp(-\eta R_m^2) = \exp(-K_m^2/4\eta) \tag{58}$$

so in 2D

$$\eta = \pi/\Omega_{cell} \tag{59}$$

A corresponding result for 3D is

$$\eta = \left(\frac{4\pi}{3\Omega_{cell}}\right)^{2/3} \tag{60}$$

A similar criterion can be used to determine whether, for a given orbital product, the Ewald technique will be more efficient than a straightforward reciprocal space summation analogous with Eq. (46). We compare the slowest rate of convergence, considering all charge and XC fitting functions, of the real and reciprocal space versions of Eq. (46), and ask which would require the smaller number of terms to obtain the same level of convergence. If the real space version is preferred, then there is room for improvement via the decomposition of Eq. (55). Otherwise, use of the reciprocal-space analogue of Eq. (46) is preferable.

1.6. Exchange-Correlation Fitting

1.6.1 Fit-to-Fit Strategy

Fitting function techniques originally were introduced [72–74] to deal with the non-linear dependence of V_{XC} upon n_e and quickly generalized to include the Coulombic contributions. The general approach was to fit *both* the electron density and the various XC quantities *directly* to the true density ("true" in the sense of corresponding to the KS orbitals that belong to the current SCF iteration) as reference. Unlike the charge fit, no variational principle for fitting the XC quantities has ever been derived to our knowledge. Therefore the XC fitting procedure always proceeds by what amounts to least-square-error minimization. For the XC

quantities of a periodic system, the straightforward version of this approach has a high computational cost which can be illustrated simply. We have

$$E_{XC} = \int d\mathbf{r} n_e(\mathbf{r}) \mathcal{E}_{XC}[n_e(\mathbf{r})]$$

$$V_{XC} = \frac{\delta E_{XC}}{\delta n_e} = \mathcal{E}_{XC} + n_e \frac{\delta \mathcal{E}_{XC}}{\delta n_e} \tag{61}$$

(with obvious generalizations for gradient-dependent functionals). To proceed by the most obvious least-squares procedure would require

$$\begin{aligned} \mathcal{E}_{XC} &\approx \sum_{\vec{\nu},\mu} x^{\mathcal{E}}_{\vec{\nu},\mu} \Xi(\vec{\nu},\mu,\mathbf{r}) \\ V_{XC} &\approx \sum_{\vec{\nu},\mu} x^{\delta}_{\vec{\nu},\mu} \Xi(\vec{\nu},\mu,\mathbf{r}) \end{aligned} \tag{62}$$

where a shorthand notation has been used;

$$\Xi(\vec{\nu},\mu,\mathbf{r}) := \sum_{\mathbf{R}} \Xi(\vec{\nu},\mu,\mathbf{R},\mathbf{r}) \tag{63}$$

The coefficients are determined by solution of a matrix equation that involves a vector with elements of the form

$$\int d\mathbf{r} \Xi(\vec{\nu},\mu,\mathbf{r}) \mathcal{E}_{XC}[n_e(\mathbf{r})] \tag{64}$$

The non-linear dependence of the integrand upon n_e means that such integrals must be done numerically, which means evaluating n_e on a quadrature mesh. Even in a molecule this is somewhat demanding, but the gaussian fitting functions are smooth enough that there is some advantage to XC fitting nevertheless. The added problem in a periodic system is that the evaluation of n_e on the quadrature mesh involves a sum over the BZ (more strictly, the irreducible wedge of the BZ) and a double sum over the real-space lattice *at every real-space quadrature mesh point*; see Eq. (43) for the density matrix $\mathcal{P}$ above.

A comparison of a simple crystal with one atom per cell, 25 primitive ba-

sis functions for the KS orbitals and a 19 point BZ sum for the crystal versus a five-atom molecule also with 25 basis functions per atom is instructive. For the molecule, the density matrix sum $\mathcal{P}$ involves $125 \times 125/2 \approx 9000$ terms, while for the solid it is $25 \times 25/2 \times 19 \approx 5{,}900$ terms *for each pair of lattice vectors* $\mathbf{R}$, $\mathbf{R}'$. The double sum over lattice vectors (and intra-cellular displacement vectors, here suppressed), even after exploiting symmetry, easily can multiply the foregoing number of terms by 250, giving roughly 1.4 million terms *at every real space mesh point.*

This disparity between extended systems and molecules motivates the approach used in GTOFF. As summarized in the introduction (recall Eq. (9)), GTOFF does exchange-correlation fitting to reference quantities evaluated with the fitted spin densities that are the output of the variational Coulomb fitting procedure, a procedure called "fit-to-fit". In that procedure, rather than use Eq. (62), we approximate further:

$$\begin{aligned} \mathcal{E}_{XC}[n_e] &\approx \mathcal{E}_{XC}[\tilde{n}_e] \approx \tilde{\mathcal{E}}_{XC} = \sum_{\vec{\nu},\mu} x_{\mathcal{E},\vec{\nu},\mu} \Xi(\vec{\nu},\mu,\mathbf{r}) \\ V_{XC}[n_e] &\approx V_{XC}[\tilde{n}_e] \approx \tilde{V}_{XC} = \sum_{\vec{\nu},\mu} x_{V,\vec{\nu},\mu} \Xi(\vec{\nu},\mu,\mathbf{r}) \end{aligned} \tag{65}$$

This procedure obviously is computationally efficient because $\tilde{n}_e$ can be recovered from the fitted neutral density $\tilde{n}$. In particular note Eq. (30) and the remark just below Eq. (34). By comparison with the task of evaluating n_e, evaluation of $\tilde{n}_e$ requires only a single lattice sum and no sum over the Brillouin zone. Moreover, even in systems that require extremely large orbital basis sets, *e.g.* light actinides, the fact that the density is a smooth, nodeless function means that the charge fitting basis will be at least somewhat smaller. In the case of Pu for example, a rich fitting basis is an order of magnitude smaller than the orbital basis.

The least-square-error criterion for the fit-to-fit procedure for V_{XC} is

$$\begin{aligned} 0 = \frac{\partial}{\partial x_{V,\vec{\nu}',\mu'}} \Bigg\{ & \int d\mathbf{r} \left(V_{XC}[\tilde{n}_e(\mathbf{r})] - \sum_{\vec{\nu},\mu} x_{V,\vec{\nu},\mu} \Xi(\vec{\nu},\mu,\mathbf{r}) \right)^2 \\ & + 2\gamma \int d\mathbf{r} \left(\tilde{n}_e(\mathbf{r}) V_{XC}[\tilde{n}_e(\mathbf{r})] - \int d\mathbf{r} \tilde{n}_e(\mathbf{r}) \tilde{V}_{XC}(\mathbf{r}) \right) \Bigg\} \end{aligned} \tag{66}$$

where the term pre-multiplied by the Lagrange parameter γ is the fit-to-fit version of the constraint introduced in Ref. [40]). There is an exact equivalent of Eq.

(66) for $\mathcal{E}_{XC}$. The fit criterion yields

$$\int d\mathbf{r} V_{XC}[\tilde{n}_e(\mathbf{r})]\Xi(\vec{\nu}',\mu',\mathbf{r}) + \gamma \int d\mathbf{r}\, \tilde{n}_e(\mathbf{r})\Xi(\vec{\nu}',\mu',\mathbf{r})$$

$$= \sum_{\vec{\nu},\mu} x_{V,\vec{\nu},\mu} \int d\mathbf{r}\, \Xi(\vec{\nu},\mu,\mathbf{r})\Xi(\vec{\nu}',\mu',\mathbf{r})$$

$$\mathbb{X} + \gamma \mathbb{Y} = \mathbf{x}_V \mathbb{G} \Rightarrow$$

$$\mathbf{x}_V = \mathbb{G}^{-1}[\mathbb{X} + \gamma \mathbb{Y}] \tag{67}$$

where the matrices and vectors in the second line are defined in order by the terms of the first line. The constraint equation corresponds to

$$\begin{aligned} \mathbb{Y}^\dagger \mathbf{x}_V &= \int d\mathbf{r}\, \tilde{n}_e(\mathbf{r}) V_{XC}[\tilde{n}_e(\mathbf{r})] \\ &:= N_V \end{aligned} \tag{68}$$

From Eq. (67) evaluated at $\gamma = 0$, we have

$$\mathbf{x}_{V,0} = \mathbb{G}^{-1}\mathbb{X} \tag{69}$$

while the corresponding effect on Eq. (68) is to generate an error term

$$\mathbb{Y}^\dagger \mathbf{x}_{V,0} - N_V = -\Delta N_V \tag{70}$$

(with the sign chosen for convenience). Define $\Delta \mathbf{x}_V := \mathbf{x}_V - \mathbf{x}_{V,0}$. Then Eqs. (68) and (70) combined yield

$$\mathbb{Y}^\dagger \Delta \mathbf{x}_V = \Delta N_V \tag{71}$$

However, Eqs. (67) and (69) combine to give

$$\Delta \mathbf{x}_V = \gamma \mathbb{G}^{-1}\mathbb{Y} \tag{72}$$

which with Eq. (71) gives

$$\gamma = \frac{\Delta N_V}{\mathbb{Y}^\dagger \mathbb{G}^{-1} \mathbb{Y}} \tag{73}$$

The solution then is to evaluate Eqs. (68), (69), (70), (73), and finally (67) in order. Doing so requires evaluation of three types of integrals that cannot be done analytically, namely those for $\mathbb{X}$, $\mathbb{Y}$, and N_V.

1.6.2. Quadrature Grid

The numerical quadrature meshes used in GTOFF differ slightly for UTFs and crystals. Because a UTF has both an atomic lattice and two vacuum regions, it is clear that the grid for the UTFs must be more complicated than for crystals.

In the UTF, the 2D unit cell is partitioned into three distinct types of regions:

1. A set of "muffin-tin-spheres" surrounding every atom and, if desired, other preselected high symmetry sites in the unit cell. Each sphere radius is defined to be half the distance to the nearest neighboring grid center. The radial integrals in each sphere are carried out on an exponential mesh using Simpson's rule. The smallest radial mesh point is selected by requiring that the most local s-type charge fitting function at that site should contain 0.02 electrons inside of that radius. (If there are no fitting functions at that site an exponent of unity is assumed.) The largest spacing of the mesh points (at the sphere boundary) is defined to be 5% of the sphere radius. These two constraints are sufficient to define the mesh fully, though a small adjustment is made to both defined spacings to ensure an integral number of mesh points. The angular mesh points and weights are chosen to provide a Gaussian quadrature using all spherical harmonics up to some user-selected maximum ℓ value, with default $\ell = 12$. Further details follow this list.

2. An interstitial region, defined as that portion of the unit cell that lies outside of the muffin-tin spheres but inside the two planes that are tangent to the outermost layers of muffin-tin spheres. The interstitial mesh is built by first generating a uniform mesh over that portion of the unit cell which is enclosed by the tangent planes and assigning a constant volume weight to each point. The mesh parallel to the tangent planes is obtained by dividing each primitive lattice vector by its own integer divisor (provided as input; on the order of 60 for a small unit cell). The divisors need not be identical, unless

required by symmetry. The number of mesh points (and the mesh spacing) in the perpendicular direction is obtained by dividing the separation of the tangent planes by the smaller spacing in the parallel directions and rounding to an integer value. The uniform mesh, so defined, is then reduced by excluding all points that lie inside any of the spheres. Finally, the weights of the mesh points adjacent to spheres are renormalized to ensure that the sum of weights for all of the interstitial mesh points equals the interstitial volume.

3. Two vacuum regions, each defined to lie outside one of the tangent planes mentioned above and inside a second, parallel plane placed a fixed distance beyond the first plane, with default distance of 25 a.u.. Integrals over the coordinate perpendicular to the bounding planes are again carried out on an exponential mesh using Simpson's rule. The minimum spacing is set equal to the smallest separation used for the interstitial mesh and the maximum spacing is set equal to the minimum spacing times e^4. Again, these two spacings are adjusted slightly to ensure an integral number of mesh points. The mesh parallel to the bounding planes is defined in the same manner as the parallel mesh for the interstitial region, but with integers that are notably smaller; typically on the order of 20. The integrals over this 2D mesh are carried out using areal weights.

In detail, the exponential grid is uniquely defined by a set of four parameters: R_{min}, R_{max}, α, and N_r. The parameter N_r is required to be an odd integer and the first grid point is R_{min}. All other odd-numbered grid points are given by

$$R(n) = C * [\exp(x) - 1] + R_{min}$$

$$C = \frac{R_{max} - R_{min}}{\exp(\alpha) - 1}$$

$$x = \frac{(n-1)\alpha}{N_r - 1} \tag{74}$$

Each even-numbered grid point is then defined to lie at the midpoint between its odd-numbered neighbors, thus simplifying the Simpson's rule form. It is possible to find α and N_r such that the minimum and maximum spacings between the odd

numbered points correspond to specified values (roughly twice the minimum and maximum spacings desired). The value of N_r obtained thus is not, however, an integer, hence it must be rounded to the nearest odd integer.

For the muffin-tin-sphere grids, the minimum and maximum spacings are defined as described. The vacuum regions also use the exponential grid, with the minimum spacing defined as described and but with $\alpha = 4$. This corresponds to the aforementioned maximum spacing that is e^4 times larger than the minimum.

The numerical integration meshes used for solids differ from those used for films in two ways: (1) Vacuum regions do not exist; and (2) the interstitial mesh is generated using the program GMESH (see Internal Structures, below) rather than in the integrals segment of the code.

Nearly all of the error in the numerical integrals comes from the interstitial region, hence the larger mesh density used for that integration. The numerical integration meshes are tested in the code segment IGTOFF by comparison of $\mathbb{G}$ matrix elements that are calculated analytically and numerically. If the calculated values differ too greatly, the various meshes can be enriched.

During the SCF cycle, GTOFF also reports (and the user should monitor) the size of

$$\int d\mathbf{r}\tilde{V}_{XC}\Delta n_e \equiv \int d\mathbf{r}\frac{\partial \tilde{E}_{XC}}{\partial \tilde{n}_e}\Delta n_e$$

$$\Delta n_e = n_e - \tilde{n}_e \tag{75}$$

Evidently this integral is the first order perturbation correction to E_{XC}. If it becomes significant in magnitude compared to $\tilde{E}_{XC}$ it is a sign that tightened tolerances need to be imposed. We typically aim for less than 1 mE_H per atom. Efforts to use this quantity to improve $\tilde{E}_{XC}$ have not been successful, perhaps because the reference value, as defined by Eq. (66), is constrained in a way that does not correspond to any simple DFT perturbation theory expression.

1.6.3. Spurious Negative Density

It is essential to address the issue of regions of negative fitted electron density. There is nothing in charge-neutralized variational Coulomb fitting that completely prevents such negative densities, particularly in regions far from any nuclei. Obviously such spurious contributions introduce improper signs in the KS

potential and the potential energy contributions to the total energy. We surmise that the problem is worse in finite system codes that do variational Coulomb fitting with charged rather than neutral densities, but have not studied the issue.

In any event, the amplitudes of negative fitted density typically are very small when they first occur in an SCF cycle. Therefore, the approach we have taken is to use a pragmatic algorithm to shift charge (from one SCF iteration to the next) into any deficient region. At each SCF iteration, GTOFF goes through the fitted density $\tilde{n}_e$ on the numerical grid and finds all points that have negative fitted density. At each such point, the fitted density in the exchange-correlation potential V_{XC} ONLY is reset to +1.0E-48 (*i.e.* just barely above machine zero). DESPITE being negative, the fitted density is left UNchanged in V_{ee}. The result at the next iteration is that the spatial domains that have negative density are more attractive than they should be because the Coulomb repulsion is artificially made attractive whereas the artificial repulsion from negative density in V_{xc} is changed to being very slightly attractive. This combination moves charge into the formerly deficient regions.

The approach works well but not perfectly. It certainly does not guarantee the absence of negative fitted density. In a crystal this usually does little harm but in a UTF or slab calculation, it can be a real problem. The issue is the work function ($-\varepsilon_F$). In a UTF it can be energetically favorable to put a very small amount of negative density very far out in the most diffuse fitting function. The result is a dipole reversed from the physical situation which ruins the calculated work function. We monitor calculations and when this behavior occurs (infrequently), we eliminate it by careful study of computed output to see how to improve the Q-fitting basis.

1.7. Relativistic Methodology

The details of implementation of scalar relativity in GTOFF were presented in [41] and reviewed in [75], so we summarize the essential assumptions and methodological features here. First, all practical DFT implementations of relativistic corrections of which we are aware assume the validity (either explicitly or implicitly) of an underlying Dirac-Kohn-Sham four-component equation. We do also. The Hamiltonian is therefore a relativistic free particle Hamiltonian augmented by the usual non-relativistic potentials

$$V_{eff} = V_{ee} + V_{Ne} + V_{XC} \tag{76}$$

Because the eigenspectrum of the DKS equation is unbounded below (both electron and positron solutions), simple variational approaches will fail unless constraints of some sort are imposed. The large energy gap between the solutions motivates development of unitary transformations that achieve an approximate decoupling into a pair of two-component subspaces. The most widely known version is the Foldy-Wouthuysen transformation sequence [76]. That procedure, however, produces transformed operators that are highly singular at the nuclear centers, hence cause problems for the kind of variational approach that is central to our strategy. Details are in Ref. [44]. Another approach, which is incompatible with our all-electron focus, is to use relativistic core potentials (thereby hiding the nuclei).

For basis sets derived from a cellular decomposition of space, *e.g.* the muffin-tin decomposition used in LAPW and LMTO methods, the difficulty can be sidestepped by constructing the basis in terms of fully relativistic atomic-like functions determined by the muffin-tin potential. By restricting the selection to the electron states, the desired decomposition is automatically enforced. This is the essence of the Koelling-Harmon scalar relativistic scheme widely used in cellular-based modified plane-wave basis methods [45].

Obviously this cellular approach cannot be used with linear combinations of GTOs. Instead, we have adopted the DKH methodology. It projects off the negative-energy free particle states via Hess' strategy of an intermediate transformation (with respect to the uncontracted GTO basis) to an approximate momentum space [43] for efficient implementation of the Douglas-Kroll transformation [42]. This strategy is effective because several of the operators in the transformed Hamiltonian have reasonably simple multiplicative form in the momentum-space representation. The result is a numerically stable two-component formalism that is quite convenient to handle with localized basis sets such as the GTOs. The formalism is second order in the total potential V_{eff} without producing singular operators.

However, these benefits come at a price. Both V_{ee} and V_{XC} and their contributions to the transformations obviously change at each self-consistent iteration so the net effect is that some very complicated operator products, involving both momentum and direct space representations, must be done at every iteration. What Rösch and co-workers noticed [44] was that the singular part of the Hamiltonian V_{Ne} of course does not change from iteration to iteration, so they attempted an "incomplete" DKH transformation which retained only V_{Ne} and incorporated, therefore, the bare electron-electron interactions in the transformed Hamiltonian.

This strategy had been tried successfully in relativistic Hartree-Fock calculations. They found, and Boettger verified independently [77], that the scheme also works well with a DFT Hamiltonian, even though the theoretical underpinnings are very different from Hartree-Fock.

The nuclear-only DKH (nDKH) approximation described above may be trivially extended to include spin-orbit coupling (SOC) effects. Unfortunately, the nDKH approximation systematically overestimates the spin-orbit splittings of the one-electron energies (in some cases by as much as 100%) due to the neglect of compensating two-electron SOC terms.[78] This error can be corrected through the use of the screened-nuclear-spin-orbit (SNSO) approximation, developed by Boettger [78]; see discussion below.

The one-electron equation associated with the fully-relativistic nDKH+SNSO approximation described as, and implemented in GTOFF, may be written as

$$[h_{KS} + \Delta h_{nDKH} + \Delta h_{SNSO}]\,\phi_i = \varepsilon_i \phi_i \tag{77}$$

In Eq. (77), the first term on the left-hand side is the ordinary, non-relativistic Kohn-Sham operator

$$h_{KS} = \frac{p^2}{2m} + V_{eff} \tag{78}$$

with V_{eff} as defined above. The second operator on the left-hand side of Eq. (77) is the nDKH approximate relativistic correction operator [42–44]

$$\Delta h_{nDKH} = \left[E_p - \frac{p^2}{2m}\right] + A_p\,[V_{Ne} + R_p V_{Ne} R_p]\,A_p \tag{79}$$

$$- \frac{1}{2}(E_p W^2 + W^2 E_p + 2W E_p W) - V_{Ne} \tag{80}$$

Here

$$E_p = c(p^2 + m^2 c^2)^{\frac{1}{2}} \tag{81}$$

$$A_p = \left[\frac{E_p + mc^2}{2E_p}\right]^{\frac{1}{2}} \tag{82}$$

$$R_p = K_p \sigma \cdot \mathbf{p}, \tag{83}$$

$$K_p = c/(E_p + mc^2), \tag{84}$$

and the momentum-space expression for W is

$$W_{p,p'} = A_p(R_p - R_{p'})A_{p'}\left[\frac{V_{Ne}(\mathbf{p},\mathbf{p}')}{E_p + E_{p'}}\right], \tag{85}$$

with $V_{Ne}(\mathbf{p},\mathbf{p}')$ the momentum-space representation of V_{Ne}. The final operator on the left-hand side of Eq. (77) is the two-electron spin-orbit correction ("SOC") operator obtained from the SNSO approximation

$$\Delta h_{SNSO}(i,j) = -\sqrt{\frac{Q(l_i)}{Z_i}} h_{nSO} \sqrt{\frac{Q(l_j)}{Z_j}} \tag{86}$$

Here i and j are generic basis function indices, Z_i is the nuclear charge associated with the center of basis function i, h_{nSO} is the nuclear-only SOC term embedded in Δh_{nDKH}, and $Q(l_i)$ is a basis function dependent operator given by;

$$Q(l_i = 0,1,2,3,\cdots) = 0,2,10,28,\cdots, \tag{87}$$

which corresponds to the total number of electrons contained in all filled shells with $n \leq l$. For large Z materials, the nDKH+SNSO approximation, expressed in Eq. (77), has been shown to produce reliable results that are more stable numerically than the results obtained using more conventional DFT electronic structure methods [78].

Very recently [79], GTOFF has been enhanced to support collinear spin-polarization in conjunction with SO corrections. The enhancement is straightforward. A spin polarization axis is stipulated. The collinearity with respect to that axis means that the off-diagonal spin-density $n_{\alpha,\beta}$ with respect to that axis is zero. The formulation is a straightforward analogy with the extension to spin-polarized treatment from non-spin-polarized ones, except that in the present case the KS orbitals no longer are pure spin but a mixture of α and β spins.

1.8. Internal Structures

The present version of GTOFF (and all prior versions of both it and FILMS) has its own integrals package, now called IGTOFF. The other two major packages are the scf segment, SGTOFF, and the relativistic corrections RGTOFF. IGTOFF generates matrix elements of the non-relativistic KS Hamiltonian over the primitive GTO basis. These include the overlap integrals for the orbital basis (hence also the KE integrals), the two-center Coulomb integrals (for both the orbital and charge-fit basis sets), and the orb-fit-orb Coulomb integrals discussed previously. The data structures for those integrals are a set of flat files with simple indexing that follows the indexing of the KS basis functions and the two sets of fitting basis functions. This structure has grown up through the various versions of GTOFF (and prior to that, FILMS). Though awkward to revise, it is adequate for serial operation. Because fitting-function methodology requires several classes of integrals that do not show up in wave-function-based quantum chemistry codes (they use only one basis set, not three) it is less straightforward than might be imagined to adapt GTOFF for interchangeable use of various integral packages.

By design GTOFF does not depend on an intrinsic lattice symmetry; low symmetry systems are handled with no more basic difficulty than high symmetry. They simply run more slowly. The cost in the present version is a somewhat arcane procedure for setting up the integrals input for a particular symmetry. Part of today's GTOFF package is a code GMESH that takes symmetry information (irreducible representation information) and generates a set of files that are a component of the input to IGTOFF. GMESH also generates the Brillouin Zone mesh for the SCF step. The process is somewhat awkward and is being replaced, see "Betterments and Enhancements" below.

The scf segment, SGTOFF, is fairly conventional with the exception of the implementation of the fitting function methodologies (discussed above) and the reciprocal lattice sum techniques used in the generalized Ewald method. The essential issues of reciprocal lattice summations are well-documented [80–82]. However, what we actually do is a bit different. An outline of the essential steps is given in Appendix B for the case of 2D periodicity. 3D periodicity is much simpler and 1D is more complicated. In addition, SGTOFF has two kinds of scf convergence stabilization algorithm, linear and Broyden-II [83]. Both are used to mix the charge fitting coefficients $q_{\vec{\nu},\mu}$, Eq.(30).

The relativistic segment, RGTOFF, is also straightforward, other than one conceptual complication. The incomplete DKH transformation discussed above involves evaluation of Coulomb matrix elements of the nuclear array without any

associated electrons, *i.e.*, a non-neutral charge distribution. In fact, this non-neutrality does not pose any particular problem. Inspection of the relativistic correction terms for the potentials reveals that any uniform potential (or charge distribution) will have zero effect on the relativistic matrix elements. This happens because the DKH transformation always involves products (scalar or vector) with factors pVp, so the effect of imposing charge neutrality via a uniform background is nil; see Eqs. (78) through (85). Charge neutrality of course results in the elimination of the $K = 0$ term in the reciprocal lattice summation of the potential. Thus we are able to use the matrix elements of the nuclear array calculated in reciprocal space as part of the generalized Ewald procedure described earlier for the nDKH transformation without modifcation.

1.9. Selection of Basis Sets

Conventional wisdom in the quantum chemistry community seems to be that DFT calculations require less-rich basis sets than wave function ("ab initio") methods. While this may be true with respect to some standard of precision (generally unstated) for molecules, experience does not support the claim in the case of periodic systems. In particular, we find that it is necessary to have a rich basis of tight functions in order that the DFT kinetic energy be really stable against basis set augmentation. Along more expected lines, for UTFs it also is necessary to have a rich basis perpendicular to the surface z, so it is not uncommon to have p_z functions in the orbital basis without their in-plane counterparts.

Our usual procedure for constructing the orbital basis is to begin with a rather rich published basis and decontract it into a list of simple primitives. A calculation for the isolated atom (with the code GATOM, part of the GTOFF suite) then gives contraction information, which we typically use to construct a few short contractions.

The fitting sets can be chosen in a variety of ways. One that usually works but is not terribly economical is simply to use the orbital basis. A more effective choice relies on the fact that the density and the XC quantities are relatively structureless functions. This means that a fitting basis rich in s functions and trimmed with a few "p^2" and/or d functions often is quite satisfactory. It also is the case that one often can use the same fitting basis for both the Q and XC fitting if the set is fairly rich.

A superficially appealing way to choose the fitting basis sets, sometimes called the "Dunlap rules", [32] actually should be avoided. Those rules state that the Q basis should be formed by doubling the exponents of the orbital basis and the XC

basis by multiplying the orbital exponents by two-thirds. For a single atom the guidelines are rational: n_e goes as the square of the orbitals and the XC quantities are dominated by $n_e^{1/3}$. But, with more than one center, and especially with well-separated centers, the guidelines do not work. In fact, they give rather poor fitting basis sets. One example suffices. Consider the contribution to the density from a product of a compact orbital basis function of *s*-symmetry on one site and a diffuse *s*-function on a site well away. A brief study of the gaussian product formula will convince one that there is no exponent in the Q-basis generated by the doubling guideline that will describe this contribution. Thus it is better generally to build a fitting basis empirically than to apply these guidelines.

1.10. Availability

GTOFF currently runs under three Unix variants, Solaris, AIX, and Linux. A non-commercial license for unsupported usage is available by contacting the first author.

2. APPLICATIONS

With these GTO-based fitting-function algorithms, GTOFF performs all-electron, full-potential DFT calculations on essentially any ordered system. It can treat films and slabs with two-dimensional periodicity and vacuum boundary conditions without an inversion symmetry plane (no 3D super cells needed), as well as any crystalline space group. Hooks were built in to handle infinite periodic polymers. Implementation of that capability is incomplete at this writing. Oddly the 1D periodicity is the most technically demanding for the generalized Ewald technique because reduction of dimensionality (which simplifies the Coulomb integrals) cannot be exploited as in 2D and 3D.

In addition to the α-quartz calculation mentioned earlier, examples of successful applications of GTOFF in its present state of development and its antecedents include

- Prediction of equations of state (including resolution of some anomalies) for UO_2, PuO_2, and light actinides [84–87]
- Prediction of derivative discontinuities in the magnetic moment versus strain curves of Fe monolayers [88] and other transition metals [89]
- Prediction of quantum size effects for UTFs [90]

- Treatment of metal adsorption at metal surfaces [91]
- Extremely accurate determination of the high- and ultra-high-pressure equation of state of bulk Al, including prediction of how close the most recent diamond anvil cell experiment came to achieving the fcc→hcp phase transition [23, 92]
- Analysis of the pressure-dependence of the crystalline phases of Mo [93]
- Interpretation of photoelectron spectroscopy in BN films [94]
- Prediction of proton stopping cross-sections in metal films[95] and crystals [49, 50]

This section gives highlights of these calculations in order.

2.1. α-Quartz

Six parameters determine the Wigner-Seitz unit cell geometry of α-quartz: the two hexagonal cell constants (a, c), the bond length and bond angle in one SiO_2 unit, the offset of an Si from a cell wall, and the dihedral angle of an SiO_2 unit with respect to the cell basal plane.

Most of the reported DFT calculations on α-quartz use plane-wave pseudopotential methods. Restricting consideration to the all-electron results, LDA calculations yield 9.1463 au $\leq a \leq$ 9.2899 au (vs. T= 13 K experiment 9.2634 au) and $1.0988 \leq c/a \leq 1.114$ (vs. T= 13 K experiment 1.1016). The corresponding range of cell volume per formula unit is 36.22 Å^3 $\leq \Omega \leq$ 37.64 Å^3 for the vs. T= 13 K experiment of 37.5 Å^3). Previously we remarked that Catti *et al.*[62] reported a double minimum at cell volumes of 36.5 Å^3 and 36.9 Å^3, separated in energy by only about 100 μE_H ($\approx$ 2.7 meV) per formula unit. For gradient-dependent DFT approximations less has been reported but the Perdew-Burke-Ernzerhof (PBE) GDA [96] gives $\Omega = 39.42$ Å^3 versus PW91 [97] $\Omega = 40.19$ Å^3. Catti *et al.* also report a double minimum for the empirical hybrid B3LYP [98] DFT model: $\Omega = 37.9$ Å^3 and 38.5 Å^3.

We [63] did large basis (Orbital: Si - 12*s*7*p*1*d*/6*s*4*p*1*d*, O - 12*s*7*p*1*d*/7*s*4*p*1*d*; Q-fit: Si and O - 9*s*2*p*^{2}; XC-fit: Si - 9*s*2*p*^{2}, O - 9*s*2*p*^{2}2*p*$_z$; details available from the first author), tight-tolerance GTOFF calculations on an extensive mesh of points with numerical gradients in the LDA [99] approximation. At and near the LDA minimum energy structure we also evaluated the PBE energies. We do not find the type of double minimum reported by Catti *et al.* Rather, we find a broad

well with two numerically indistinguishable minima with respect to the *internal* coordinates of the cell but at the *same* cell constants $a = 9.319$ au, $c/a = 1.0871$, or a cell volume per formula unit of 37.63 $Å^3$. The GTOFF results are consistent with experiment qualitatively as well: the internal motions are soft, while the crystal itself is brittle. A double minimum with respect to cell volume is not consistent with these characteristics.

2.2. PuO_2, UO_2, and Light Actinides

All standard DFT approximations that do not include either self-interaction corrections [100] or exact exchange (*i.e.* single-determinantal exchange of the same form as Hartree-Fock) mis-represent the transition-metal and actinide oxides as metals. The difficulty usually is stated in the language of Mott-Hubbard insulators and highly-correlated systems. An interesting issue is whether the artificial metallic character has any consequence for the structure and total energies predicted by such XC approximations, since the Kohn-Sham bands are artifacts of the KS variational procedure. UO_2 and PuO_2 are important examples because they also involve substantial relativistic corrections.

Prior to the work of Ref. [84], a series of LMTO calculations had studied UO_2. A full-potential, non-spin-polarized LMTO treatment with a gradient-corrected XC model gave a lattice constant (fluorite structure) of 9.81 au, well below the experimental 10.34 au (see [84] for references to the other literature). An approximate LMTO (LMTO-ASA) non-spin-polarized treatment with LDA XC gave 9.92 au and a bulk modulus of B = 291 GPa versus the experimental value 207 GPa. Spin-polarized LDA calculations did give anti-ferromagnetic ordering (found experimentally) at the experimental lattice constant but the moment vanished at the LDA equilibrium value. All the results were metallic.

There is a technical pecularity of the LMTO basis in regard to relativistic corrections, namely whether certain J states can be represented correctly [101]. More physically, none of the foregoing work included spin-orbit corrections. Though SO effects are small in elemental U, that is not a compelling argument that SO effects also should be small in UO_2. Ref. [84] therefore addressed the effects of (a) SO, (b) gradient-dependent contributions to XC, and (c) spin-polarization. Care was taken to use extremely rich basis sets (Orbital: U - 23*s*20*p*15*d*11*f*/17*s*14*p*11*d*7*f*, O - 12*s*7*p*1*d*/7*s*4*p*1*d*; Q-fit: U - 25*s*, O - 9*s*; XC-fit: U - 21*s*, O - 9*s*; details available from the third author). The outcome is that all three effects are about equally important in increasing the equilibrium lattice constant (to an estimated value of 10.35 au) and decreasing the bulk mod-

ulus (to a estimated value of 190 GPa) relative to the scalar relativistic, LDA, non-spin-polarized values, 9.99 au and 250 GPa respectively. Ferromagnetic ordering was found to be quite stable relative to both antiferromagnetic and paramagnetic order, in contrast with the prior LDA result and with experiment. The phrase "estimated value" is necessary because at the time of those calculations, GTOFF did not support the combination of SO corrections and spin-polarization, so extrapolation from the other possible combinations (scalar relativity versus SO, non-spin-polarized versus spin-polarized) was necessary.

Somewhat similar results emerged from a comparable study of PuO_2 [85]. Spin-orbit corrections, density gradient corrections, and spin-polarization each contribute a lattice parameter increase in the range 0.1 - 0.2 au and a decrease in B of order 15 - 30 GPa. The combined effect is to move the estimated lattice parameter to 10.30 au (experiment 10.20 au) and estimated B to 175 GPa (experiment 379 GPa) relative to scalar relativistic, LDA, non-spin-polarized values of 9.83 au and 246 GPa respectively.

The obvious disparity between the PuO_2 and UO_2 studies is the remarkable *underestimate* of B for PuO_2 compared to the 25% overestimate in UO_2. The disparity is even more striking in view of the fact that the same approach [86] gave B for metallic Pu between a factor of 2 and 3 *greater* than the observed value. Moreover, that study considered elemental Th, Pa, U, Np, and Pu with both full-potential LAPW methodology and GTOFF. Within reasonable tolerances, the two methods produce the same trends and both give unit cell volumes that are 3-10 % larger than those obtained from full-potential LMTO method [102].

In contrast, the scalar-relativistic, gradient-corrected GTOFF calculation of metallic α-U produces an atomic volume in almost perfect agreement with experiment, with the calculated B almost as good, whereas inclusion of the SO correction pushes the atomic volume slightly to the high side and B to a value 14 % too low. This behavior is rather similar with that found for UO_2.

It has proved useful to characterize the contrast between U and Pu in terms of a switch from delocalized 5*f* electrons to localized. ¿From that perspective, α-Pu, the ambient phase, is a reasonable 5*f* light actinide, while δ-Pu (high temperature phase) is intermediate in the sense of 5*f* localization. This switch is associated with the "volume upturn" and change in behavior that occurs in the vicinity of Z=94. However, there is evidence for non-zero ground state magnetic moment in δ-Pu. Introduction of collinear spin polarization in GTOFF in conjunction with SOC has enabled the calculation of a ferromagnetic state [spins aligned along (001)] and two anti-ferromagnetic states [spins aligned perpendicular to

each plane (001) or parallel (100)] [79]. With or without SO corrections, the antiferromagnetic configuration is favored. Inclusion of SO coupling favors the (001) antiferromagnetic ordering (2.0 μ_B per atom), which at zero-pressure is favored over the non-magnetic state by approximately 20 mE_H per atom. Most interesting, the resulting lattice constant is small by less than 2%, although the calculated bulk modulus is large by 53% . Since the ferromagnetic result gives a lattice constant that is large by only 1% and B off by only 11 %, it is plausible to speculate that some more complicated non-collinear spin arrangement is the physical reality.

2.3. Novel Phenomena in Ultra-thin Films

2.3.1. Spin-polarization Cusps in Strained Transition Metal

Unsupported, ordered ultra-thin films are, from the experimental perspective, almost pure abstractions because of the shear difficulty of fabrication. Nevertheless, such UTFs are the zero-coupling limit of overlayers on substrates as well as the objective of increasingly sophisticated fabrication techniques. Localization in ordered UTFs is distinctly different from that in the 5*f* solids just discussed, yet there is a certain commonality, especially for monolayers. Monolayers ("1Ls") have the peculiar property that the electrons must conform to atomic boundary conditions (*i.e.* vacuum boundary conditions) in the z direction but periodic boundary conditions in the x-y plane. In this sense, the electrons in a monolayer also are partially localized. This motivates study of the interplay of spin ordering with translational symmetry and strain.

In a pair of papers [88] the third author treated the hexagonal and square symmetry Fe 1Ls in the LDA [99]. Large basis sets were used as usual (Orbital: $14s10p1p_z5d/10s10p1p_z3d$; Q-fit and XC-fit: $11s3d$; note the only d symmetry compatible with 1L symmetry is $z^2-(1/2)(x^2+y^2)$). The total energy was converged to less than 5 μE_H iteration-to-iteration, with the resulting spin-magnetic moment convergence of 0.001 μ_B. Consistent with expectations from coordination number considerations, the hexagonal symmetry systems are energetically favored but the advantage for the spin-polarized (ferromagnetic) case is much larger than for the paramagnetic case, 0.38 eV/atom vs. 0.02 eV/atom.

Less expected and more interesting is the behavior of the system under in-plane compression. For comparison of the two symmetries a common geometrical parameter is useful, conveniently taken either to be the primitive unit cell area

Ω_{cell} or the 2D Wigner-Seitz radius $\pi r_{WS}^2 := \Omega_{cell}$. Beginning at r_{WS} above the equilibrium value, the spin-magnetic moment of the hexagonal system displays three clear changes in slope with decreasing r_{WS}. There are corresponding but somewhat less prominent cusps in the square system. The phenomenon is related to compressional band broadening, which drives a decrease from about 3.3 μ_B per atom at $r_{WS} = 3.1$ au down to the paramagnetic state below $r_{WS} = 1.8$ au. In the large lattice case, just one majority spin band crosses ε_F. As r_{WS} is decreased, three majority spin bands in succession are broadened and driven up. The cusps occur as those bands first touch ε_F, the point at which spin redistribution must begin. By the point at which compression has achieved paramagnetism, four bands cross ε_F. In the square symmetry system, three band touchings also are involved but the fall-off of magnetic moment as a function of *decreasing* r_{WS} is much steeper. Presumably this behavior results from the near degeneracy of the spin-polarized and non-spin-polarized ground states for the square 1Ls.

In contrast, there is essentially no trace of spin-dependent band-occupancy effects in the work function ($\phi = -\varepsilon_F$) as a function of r_{WS}. For both symmetries ϕ for the spin-ordered systems is strongly peaked at $r_{WS} \approx 2.20$ au and decreases rapidly as a function of r_{WS} in either direction. Both declines are attributable to reodering from a relatively diffuse 4*s* band to a more localized 3*d* band. Taken together, these results show that while the *total* density n_e is a rather smoothly varying function of r_{WS}, the spin densities are not.

Subsequently we found [89] that Ti behaves more or less the same but that V and Cr are different, in particular regarding the work function. Those calculations focused on the crossover from ferromagnetic to paramagnetic behavior, without considering larger r_{WS}. For Ti, the hexagonal system is favored by 0.25 eV/atom, with the magnetic-non-magnetic crossover at $r_{WS} \approx 2.75$ au in the hexagonal case versus a broad, smooth crossover between 2.85 and 3.00 au for the square symmetry. The equilibrium hexagonal system moment is 0.08 μ_B at $r_{WS} = 2.69$ au. There is a bare hint of a change in slope for ϕ_{square} at 2.85 au but nothing visible in ϕ_{hex}.

For V, there are cusps visible in the rather abrupt crossover (at about r_{WS} = 2.75 - 2.8 au) in both hexagonal (1 cusp) and square (2 cusps) cases. The former is favored energetically by only 0.16 eV/atom, with the equilibrium geometry at $r_{WS} = 2.38$ au. As with solid V, the equilibrium system is paramagnetic. For the hexagonal system, there is a clear jump of about 0.5 eV in $\phi(r_{WS})$ concurrent with the non-magnetic to magnetic transition. A smaller but discernible jump in ϕ occurs for the square V 1L.

In Cr we encountered 3 cusps in the magnetization curve above the transition to paramagnetic for the square 1L but only one for the hexagonal system. Both symmetries exhibit extremely sharp transitions between paramagnetic and non-magnetic states, and, to computational accuracy, they have the same cohesive energy (an interesting failure of the coordination number argument). Both also exhibit a sharp jump, again about 0.5 eV, in $\phi(r_{WS})$ concurrent with the non-magnetic to magnetic transition. with the cusps in μ above that transition also discernible in ϕ.

Since the magnetization is a physical observable, the outcome is of these calculations is that there is a physical meaning to the KS band edges when they are close to ε_F. This is consistent with the unique role that ε_F itself plays in KS theory and offers the prospect of being able to probe spin energetics near the Fermi surface directly. Harrison [103] has provided additional interpretive insight, via tight binding models, of the cusp phenomenon.

2.3.2. Static Quantum Size Effects in Ultra-thin Metal Films

Band crossing of the Fermi level is also supposed to be the essential physics of static quantum size effects (SQSE) in metal UTFs. Here the control parameter is UTF thickness rather than compression as in the transition metal 1Ls just discussed. JCB and SBT have published extensively on this problem, so we only summarize a few of the most interesting features here. Jellium models [104] predict thickness-dependent oscillations in the work-function ϕ caused by new bands touching the Fermi level as thickness is increased. Our calculations [90] on Li 1-5Ls showed only weak evidence for the oscillations. Note, in passing, that the surface energies in that paper are incorrect; see ref. [20, 21]. However, we did find very strong SQSE in $\mathcal{N}_E(\varepsilon_F)$, the density of states at the Fermi level. This is a direct consequence of two-dimensional periodicity. In the jellium model, a 2D periodic system has a step in $\mathcal{N}_E$ at the band edge. Though these Li UTFs are far from free-electron in many ways (as is also the metal, contrary to conventional wisdom [105, 106]), their density of states does add one step per layer, which is what drives the SQSE.

Somewhat stronger evidence for work function SQSE was found in a study of hexagonal Al 1-7Ls [107]. By virtue of large basis sets and a dense Brillouin zone scan, we found that ϕ for the 1L through 7L was 4.873 eV, 4.636 eV, 4.372 eV, 4.323 eV, 4.553 eV, and 4.482 eV. Thus one has a decrease for $\nu = 1 \rightarrow 4$, a jump up for $\nu = 5$, followed by another decrease. Essentially the same behavior is found with the surface energy, except that the minimum value is for $\nu = 3$ and

saturation appears to have set in by $v = 7$.

2.3.3. Na Adsorption on Hexagonal Al UTFs

Another way to modify the work function is by adsorption of a metal overlayer, a technique used at least since vacuum tube technologies. Ref. [91] examined the specifics of Na adsorption on Al(111) via a substitutional mechanism (in ordered surface vacancy sites) versus non-substitutional adsorption at sites of hcp symmetry. The issue was whether the pseudopotential calculations [108] that had found the somewhat unfamiliar substitutional mechanism to be favored were accurate enough to give reliable results. In the LCGTO fitting function calculations, the substitutional adsorption was treated by calculating the vacuum formation energy for a $(\sqrt{3} \times \sqrt{3})$R 30° vacancy array that was modeled by an hcp 4L with a third of its atoms removed on each surface and replaced with Na atoms. A one-step path equivalent to the previously proposed two-step substitional mechanism enabled the use of this substituted 4L. The non-substitutional model was an Al 3L with an Na atom adsorbed in one-third of the hcp sites adjacent to the two surfaces (that is, directly above and directly below the mid-layer Al atoms). In both cases the adsorbate height was optimized. The resulting vacuum formation energies confirmed the overall substitutional picture based on pseudopotential calculations. Indeed, the LCGTO results suggest that if anything, the substitutional overlayer is more stable relative to the hcp overlayer than previously predicted.

2.4. Other Examples of Crystalline Phase Stability Calculations

The discussion earlier of Pu, U, and α-quartz all point to one of the strong points of GTOFF and the methdology it implements: the capability of treating the equation of state (P vs. Ω) of a solid in all its symmetries on an even-handed, high-precision basis. We give two more examples, one non-relativistic, the other scalar relativistic. Another example is recent work on Ta [109].

2.4.1. Al at High Pressures

The sequence of crystalline phases as a function of P for Al was the subject of substantial theoretical interest in the early 1980s, with considerable divergence of prediction among methods and little experimental data to discipline the activity; see ref [53] for the other citations. That changed in 1994 with the publication of diamond-anvil-cell data through 219 GPa [110]. In two papers [23, 92], we did LDA calculations with GTOFF up to 1 TPa. The calculated isotherm lay

slightly and almost uniformly high to the measurements over their entire range. Our prediction is that the sequence of phases should be fcc → hcp → bcc with room temperature transitions at 205 ± 20 GPa (a volume compression relative to room temperature equilibrium of $\Omega/\Omega_{300} = 0.510$ and 565 ± 60 GPa ($\Omega/\Omega_{300} = 0.364$) respectively. The fcc → bcc transition is predicted to be at 340 ± 15 GPa ($\Omega/\Omega_{300} = 0.436$). On the basis of analysis of phonon contributions, we speculated that the experiment was close to the fcc → hcp transition when the diamonds shattered. It is tempting to speculate that perhaps the shattering was driven by the transition.

2.4.2. Phase Stability of Mo

Because of its position in the periodic table, molybdenum has been the object of myriad computational studies, both non-relativistic and with various relativistic approximations. GTOFF calculations [93] of the relative stabilities of fcc, bcc, and hcp Mo over a substantial volume range, with and without scalar-relativistic corrections, showed that relativity does contribute significantly to the bcc-fcc structural energy difference, but essentially negligibly to the hcp-fcc structural energy difference. Though the relativistic corrections to the lattice constants are modest, they are not ignorable: for bcc Mo, the relativistic lattice constant increment is -0.026 au. In contradistinction with an earlier FLMTO calculation [111], the GTOFF calculation found no region of hcp phase stability at T = 0 K. Instead, the bcc → fcc transition proceeds directly at $P \approx 6.6$ Mbar. It turned out that the discrepancy arose from the difference in basis sets. The GTOFF calculation included *s*-, *p*-, *d*-, and *f*- functions in the orbital basis, whereas the FLMTO did not employ *f*-functions. Because the hcp structure does not have atomic site inversion symmetry and the cubic structures do, that omission turns out to be decisive. A subsequent FLMTO test calculation with *f*-functions confirmed this analysis: no region of hcp stability was found. A small caveat to the entire discussion is that the hcp calculations were done at ideal c/a.

2.5. Spectroscopy and Response

We conclude this section with two brief examples of spectroscopic and response property treatments.

2.5.1. Interpretation of Photoelectron Spectroscopy in BN Films

On the basis of angle-resolved electron spectroscopy Nagashima *et al.* [112] concluded that the electronic structure of the hexagonal BN 1L "...is almost

independent of the substrate". If true, *h*-BN would be important as an example of a stable, weakly physisorbed overlayer. They also noted that the growth rate of subsequent BN layers is quite low, a finding suggestive of the possibility that the overlayer might be extremely similar to a weakly interacting 2-L.

We therefore did GTOFF calculations on the *h*-BN 1L and 2L [94] and compared our results both with experiment and with other calculations that were either supercell or bulk crystal treatments. The calculated 1L and 2L cohesive energies are -7.66 and -7.69 eV/atom, a result clearly consistent with the weak overlayer binding. The *a* lattice parameter was 4.7197 au for the 1L and 4.7220 au for the 2L, deviations from experimental bulk of less than 0.3% and 0.2% respectively. This may be misleading, since a more proper comparison would be to bulk crystal *a* calculated with the same E_{XC} and methodology.

Allowing for the usual underestimate of the band gap in bare KS bands [113], the calculated and experimental bands are quite consistent, again lending credence to the experimenter's claim that the *h*-BN overlayer is close to being a free 1L. Our calculation also showed that the so-called "interlayer" states, those with density maxima in between BN planes in a BN slab or crystal, in fact exist already in the 1L. Thus they have nothing intrinsically to do with interlayer confinement but are simply a part of the unoccupied KS manifold at the zone center. The 2L band structure clearly corresponds to a pair of weakly interacting 1Ls. Among other things that means that the 1L and 2L band structures are not just a clipped version of the bulk crystal band, as had been suggested. Finally, because GTOFF implements all-electron methodology, we can compute surface-core-level shifts that are inaccessible to pseudopotential codes. We find B 1*s* shifts of 5.7 and 6.0 eV relative to the spin-split KS $1s_\alpha$ and $1s_\beta$ states of the B atom respectively, compared to a measured value of 4 eV [114]. Given the errors in both the calculation and experiment, the comparison is acceptable.

2.5.2. Proton Stopping Cross-sections and Dielectric Functions

With colleagues, the first author has used GTOFF (and FILMS) to provide the charge densities and KS bands and orbitals needed as input to both approximate calculations (via the so-called orbital local plasma approximation) and rather precise calculations (via the RPA form of the dielectric function) of the proton stopping cross-sections in metal UTFs [49, 50, 95, 115–117]. Since those calculations rely on GTOFF outputs as inputs to other codes but do not use GTOFF otherwise, in the interest of space we do not review those results here but simply refer the reader to the references just cited.

3. BETTERMENTS AND ENHANCEMENTS

Obviously no code is perfect and GTOFF certainly is not. It was developed for research, not for distribution, with emphasis on getting the physics right in a robust and high-precision implementation. The code thus shows the traits of a research tool built over years by a handful of workers. At this writing, we are rebuilding the code to address the following issues:

1. A conventional Fortran structure (extensive common blocks, large arrays with multiple assignments, long argument lists, complicated calling sequences of cascaded subroutines and functions, and loops organized for vectorization) - This structure is a barrier to adding major new functionality, a bother for adding new XC functionals, and a burden on maintainability

2. Matrix element (integrals) indexing and data storage conventions that have developed incrementally rather than with a long-term design - This organization is a barrier to effective parallelization of the integrals step. It also is a barrier to adding the computation of new properties because of the intricacy of retrieving the needed subsets of integrals and/or indexing the storage and retrival of new integral types.

3. An SCF step that does not exploit obvious parallelism with respect to the Brillouin Zone (**k** vector) in the solution of Eq. (2).

4. Lack of analytic and/or automated numerical gradients for optimization of geometry (cell constants, intra-cell positional parameters, interlayer spacings). Only user-managed numerical gradients can be done with the present version.

5. An idiosyncratic user interface and input data structures.

We presently are engaged in a wholesale reworking of GTOFF to address these issues, starting with redesign of variational Coulomb fitting, fit-to-fit, and generalized Ewald algorithms to provide for modularity, support parallel implementation, and take advantage of modern programming practices. Part of the redesign of the integral indexing, storage, and retrieval is aimed at providing data structures that will support parallel integral evaluation, including pre-calculation of load balance information among the different types (n-center versus m-center, Coulomb repulsion versus XC, relativistic versus non-relativistic). More speculatively, we are investigating grid-based indexing, storage, and retrieval of multiple

sets of integrals for use during the SCF step to drive optimization of cell constants and intra-cell positional parameters. The SCF modules are being redesigned to support parallel execution over the Brillouin Zone grid and to include algorithms for fit-to-fit-based evaluation of energy gradients with respect to cell constants and other geometrical parameters of the system.

At this writing the plan is for implementation to be in C++, though some unresolved issues may change that. There are two primary motivations: (i) students no longer learn FORTRAN and lack motivation to do so; (ii) the performance premium that once was provided by Fortran compilers has largely vanished.

Despite these limitations, GTOFF has proven, as exemplified by the calculations reviewed here, to be a robust, highly precise implementation of DFT in a GTO basis for very general 2D and 3D periodic systems. We expect the enhanced and re-implemented version to be no less potent and much easier both to use and to enhance.

4. ACKNOWLEDGMENTS

We thank Uwe Birkenheuer, Notker Rösch, Jin-Zhong Wu, and Richard Mathar for their contributions to the evolution of GTOFF and FILMS. We also thank Steve Alexander, Norbert Flocke, Wuming Zhu, and Asok Ray plus his students for stress-testing the code in various versions, and Frank Harris, John Mintmire, Florian Müller-Plathe, and Max Seel for helpful discussions. SBT and JAA were supported in part by the U.S. National Science Foundation under ITR Award DMR-0218957 and SBT also was supported in part under NSF KDI Award DMR-9980015. JCB was supported by the U.S. Dept. of Energy under contract W-7405-ENG-36.

Appendix A - Products of Hermite GTOs

The product of two Hermite GTOs on two centers reduces to a sum of two-center products as follows:

$$f(\vec{v}_1,\mu_1,\mathbf{A});\mathbf{r})f(\vec{v}_2,\mu_2,\mathbf{B};\mathbf{r}) = \sum_{\vec{\zeta}=0}^{\vec{v}_1+\vec{v}_2} g(\vec{v}_1,\vec{v}_2,\vec{\zeta},\mu_1,\mu_2)f(\vec{\zeta},\frac{\mu_1\mu_2}{\mu_1+\mu_2},\mathbf{A}-\mathbf{B};\mathbf{0}) \times[f(\vec{v}_1+\vec{v}_2-\vec{\zeta},\mu_1+\mu_2,\frac{\mu_1\mathbf{A}+\mu_2\mathbf{B}}{\mu_1+\mu_2};\mathbf{r}) \quad (88)$$

$$g(\vec{v}_1,\vec{v}_2,\vec{\zeta},\mu_1,\mu_2) = \prod_{i=1}^{3} g_0(v_{1i},v_{2i},\zeta_i,\mu_1,\mu_2)$$

$$g_0(\alpha,\beta,\zeta,\mu_1,\mu_2) := \sum_{\ell=\max(0,\zeta-\alpha)}^{\min(\beta,\zeta)} (-1)^{\ell}\frac{\mu_1^{\alpha-\zeta+\ell}}{(\mu_1+\mu_2)^{\alpha+\beta-zeta)}}\binom{\alpha}{\zeta-\ell}\binom{\beta}{\ell} \quad (89)$$

Appendix B - Lattice Sums of Coulomb Integrals for 2D Periodicity

In this Appendix certain 2D vectors are used:

$$\mathbf{s} := (s_x,s_y,0)$$

$$\begin{aligned}\mathbf{R}_i &:= (R_{i,x},R_{i,y},0)\\ \mathbf{K}_i &:= (K_{i,x},K_{i,y},0)\end{aligned} \quad (90)$$

The latter two are the 2-D direct and reciprocal lattice translation vectors respectively. In contrast, the vectors **r**, **A**, **B**, **C**, are 3D vectors throughout.

Because variational Coulomb fitting with charge neutrality involves a combination of electron-electron repulsion and nuclear-electron attraction Coulomb integrals, we consider the following prototypical combination of those integrals

treated as a function of the probe vector **s**:

$$V_{ab}(\mathbf{s}) := \frac{1}{N_{cell}}\sum_{\mathbf{R}}\left\{\int d^3\mathbf{r}d^3\mathbf{r}'\frac{\exp(-a|\mathbf{r}-\mathbf{s}-\mathbf{A}-\mathbf{R}|^2)\exp(-b|\mathbf{r}'-\mathbf{B}|^2)}{|\mathbf{r}-\mathbf{r}'|}\right.$$
$$\left.-\left(\frac{\pi}{b}\right)^{3/2}Z_{tot}^{-1}\sum_{1}^{m}Z_m\int d^3\mathbf{r}\frac{\exp(-a|\mathbf{r}-\mathbf{s}-\mathbf{A}-\mathbf{R}|^2)}{|\mathbf{r}-\mathbf{C}_m|}\right\} \tag{91}$$

Two integrals apparently due to Boys [118] are needed. First

$$I_1(a,\mathbf{A},\mathbf{B}) := \int d^3r\exp[-a|\mathbf{r}-\mathbf{A}|^2]\frac{1}{|\mathbf{r}-\mathbf{B}|} = \frac{2\pi}{a}F_0(aT^2) \tag{92}$$

where $T = |\mathbf{T}| = |\mathbf{A}-\mathbf{B}|$ and the incomplete gamma function is

$$F_0(w) = \int_0^1 du\exp[-wu^2] \tag{93}$$

Second,

$$I_2(a,b,\mathbf{A},\mathbf{B}) := \int d^3r_1d^3r_2\exp[-a|\mathbf{r}_1-\mathbf{A}|^2]\exp[-b|\mathbf{r}_2-\mathbf{B}|^2]\frac{1}{|\mathbf{r}_1-\mathbf{r}_2|}$$
$$= \frac{2\pi^{5/2}}{ab(a+b)^{\frac{1}{2}}}F_0\left[\frac{ab}{a+b}T^2\right] \tag{94}$$

With these two expressions one can convert Eq. (91) into

$$V_{ab}(\mathbf{s}) = \frac{1}{N_{cell}}\sum_{\mathbf{R}}\sum_{m}\alpha_m\int_0^1 du\exp[-\beta_m|\mathbf{s}+\mathbf{r}_m+\mathbf{R}|^2u^2] \tag{95}$$

The values of α_m, β_m, and $\mathbf{r}_m$ for $m = 0$ and $m \neq 0$ terms are respectively

$$\alpha_0 = \frac{2\pi^{5/2}}{ab\sqrt{a}+b}$$
$$\beta_0 = \frac{ab}{a+b}$$
$$\mathbf{r}_0 = \mathbf{A}-\mathbf{B}$$

$$\begin{aligned}\alpha_m &= -\frac{2\pi^{5/2}Z_m}{Z_{tot}ab^{3/2}} \\ \beta_m &= a \\ \mathbf{r}_m &= \mathbf{A}-\mathbf{C}_m\end{aligned} \tag{96}$$

For a lattice periodic function

$$f(\mathbf{r}) = \sum_{\mathbf{R}} U(\mathbf{r}-\mathbf{R}) \tag{97}$$

the 2D lattice Fourier expansion is

$$f(\mathbf{r}) = f(\mathbf{s},z) = \sum_{\mathbf{K}} e^{i\mathbf{K}\cdot\mathbf{s}}\bar{f}(\mathbf{K},z) \tag{98}$$

with

$$\bar{f}(\mathbf{K},z) = \frac{1}{\Omega}\int d^2s e^{-i\mathbf{K}\cdot\mathbf{s}} f(\mathbf{s},z) \tag{99}$$

which reduces to

$$\bar{f}(\mathbf{K},z) = \frac{N_{cell}}{\Omega}\int d^2s e^{-i\mathbf{K}\cdot\mathbf{s}} U(\mathbf{s},z) \tag{100}$$

with Ω the cell area. Thus the Fourier coefficients for V_{ab} are

$$\bar{V}(\mathbf{K}) = \sum_m \alpha_m \frac{1}{\Omega}\int d^2s e^{-i\mathbf{K}\cdot\mathbf{s}} \int_0^1 du \exp[-\beta_m|\mathbf{s}+\mathbf{r}_m|^2 u^2] \tag{101}$$

To proceed requires distinguishing $\mathbf{K} \neq 0$ and $\mathbf{K} = 0$ terms, a well-known issue. For $\mathbf{K} \neq 0$, the order of integrations in Eq. (101) can be interchanged to yield

$$\bar{V}(\mathbf{K}) = \sum_m \alpha_m \frac{1}{\Omega}\int_0^1 du \int d^2s \exp[-\beta_m|\mathbf{s}+\mathbf{r}_m|^2 u^2 - i\mathbf{K}\cdot\mathbf{s}] \tag{102}$$

Change integration variables:

$$\begin{aligned} s_x &\rightarrow s_x - x_m \\ s_y &\rightarrow s_y - y_m \Rightarrow \mathbf{s} + \mathbf{r}_m \rightarrow (s_y s_y, z_m) \end{aligned} \tag{103}$$

Then straightforward manipulation and use of the identity

$$\int_{-\infty}^{\infty} dx \exp(-\gamma x^2 + \beta x) = \exp[\beta^2/4\gamma] \left(\frac{\pi}{\gamma}\right)^{\frac{1}{2}} \qquad \gamma > 0, \text{ a}ll\ \beta \tag{104}$$

gives

$$\begin{aligned} \bar{V}(\mathbf{K}) \;=\; & \\ & \frac{1}{\Omega} \sum_m \alpha_m \int_0^1 du \int d^2 s \exp[-\beta_m (s^2 + z_m^2) u^2 - i\mathbf{K} \cdot \mathbf{s} + i\mathbf{K} \cdot \mathbf{r}_m] \\ & = \frac{1}{\Omega} \sum_m \alpha_m e^{i\mathbf{K} \cdot \mathbf{r}_m} \int_0^1 du \exp[-\beta_m z_m^2) u^2] \int d^2 s \exp[-\beta_m s^2 u^2 - i\mathbf{K} \cdot \mathbf{s}] \\ & = \frac{1}{\Omega} \sum_m \alpha_m e^{i\mathbf{K} \cdot \mathbf{r}_m} \int_0^1 du \exp[-\beta_m z_m^2) u^2] \int_{-\infty}^{\infty} ds_x \exp[-\beta_m s_x^2 u^2 - iK_x s_x] \\ & \qquad \times \int_{-\infty}^{\infty} ds_y \exp[-\beta_m s_y^2 u^2 - iK_y s_y] \\ & = \frac{1}{\Omega} \sum_m \alpha_m e^{i\mathbf{K} \cdot \mathbf{r}_m} \int_0^1 du \exp[-\beta_m z_m^2) u^2] \left(\frac{\pi}{\beta_m u^2}\right)^{\frac{1}{2}} \exp[-K_x^2/(4\beta_m u^2)] \\ & \qquad \times \left(\frac{\pi}{\beta_m u^2}\right)^{\frac{1}{2}} \exp[-K_y^2/(4\beta_m u^2)] \\ & = \sum_m \frac{\pi \alpha_m}{\beta_m \Omega} e^{i\mathbf{K} \cdot \mathbf{r}_m} \int_0^1 du \frac{1}{u^2} \exp[-\beta_m z_m^2) u^2] \exp[-K^2/(4\beta_m u^2)] \end{aligned} \tag{105}$$

Evaluation of the zero-wavevector Fourier coefficient requires a long, intricate argument, so here we simply give the result:

$$\bar{V}(0) = -\frac{\pi}{\Omega} \sum_m \alpha_m [\beta_m^{-1} \exp(-\beta_m z_m^2) + 2 z_m^2 F_0(\beta_m z_m^2)] \tag{106}$$

REFERENCES

[1] P. Hohenberg and W. Kohn, Phys. Rev. 136, (1964) B864.

[2] W. Kohn and L.J. Sham, Phys. Rev. 140 (1965) A1133.

[3] R.O. Jones and O. Gunnarsson, Rev. Mod. Phys. 61, (1989) 689.

[4] R.G. Parr and W. Yang, Density Functional Theory of Atoms and Molecules, Oxford, NY, 1989.

[5] R.M. Dreizler and E.K.U. Gross, Density Functional Theory, Springer, Berlin, 1990.

[6] E.S. Kryachko and E.V. Lude˜na, Energy Density Functional Theory of Many-Electron Systems, Kluwer, Dordrecht, 1990.

[7] S.B. Trickey spec. ed., Density Functional Theory for Many-Fermion Systems, Adv. Quant. Chem. 21, Academic, San Diego, 1990.

[8] E.K.U. Gross and R.M. Dreizler (eds.) Density Functional Theory, Plenum, NY, 1995.

[9] J.M. Seminario and P. Politzer (eds.), Modern Density Functional Theory, Elsevier, Amsterdam, 1995.

[10] D.P. Chong (ed.) Recent Advances in Density Functional Methods, World Scientifi c, Singapore, 1995.

[11] W. Kohn, A.D. Becke, and R.G. Parr, J. Phys. Chem. 100 (1996) 12974.

[12] J.M. Seminario (ed.), Recent Developments and Applications of Modern Density Functional Theory, Elsevier, Amsterdam, 1996.

[13] R.F. Nalewajski (ed.) Density Functional Theory, Springer, Berlin, 1996.

[14] H. Eschrig, The Fundamentals of Density Functional Theory, Teubner Texte f˙ur Physik 32 Teubner, Stuttgart and Leipzig, 1996.

[15] A. G˙orling, S.B. Trickey, P. Gisdakis, and N. R˙osch, in Topics in Organometallic Chemistry 4, P. Hoffmann and J.M. Brown (eds.) Springer, Berlin, (1999) 109.

[16] W. Koch and M.C. Holthaussen, A Chemist's Guide to Density Functional Theory, Second Ed. Wiley VCH, Weinheim, 2001.

[17] M.T. Yin and M.L. Cohen, Phys. Rev. B 26 5668 and references therein.

[18] P. Blaha, K. Schwarz, P. Sorantin, and S.B. Trickey, Comput. Phys. Commun. 59 (1990) 399 and references therein.

[19] J.M. Wills and O. Eriksson, Phys. Rev. B 45 (1992) 13879 and references therein.

[20] J.C. Boettger, Phys. Rev. B 49 (1994) 16798.

[21] J.C. Boettger, John R. Smith, U. Birkenheuer, N. R¨osch, S.B. Trickey, J.R. Sabin, and S. Peter Apell, J. Phys.: Cond. Matt. 10 (1998) 893.

[22] J.C. Boettger and S.B. Trickey, J. Molec. Struct. (Theochem) 501-02 (2000) 285.

[23] J.C. Boettger and S.B. Trickey, Phys. Rev. B 53 (1996) 3007.

[24] J.C. Boettger, Internat. J. Quantum Chem. S-29 (1995) 197.

[25] J.W. Mintmire and J.R. Sabin, Internat. J. Quantum Chem. S 14 (1980) 707.

[26] J.W. Mintmire, 'An LCAO Local Density Functional Approach to Surface Electronic Structure Calculations, Ph.D. Thesis, University of Florida, 1980 (unpublished).

[27] J.W. Mintmire, J.R. Sabin, and S.B. Trickey, Phys. Rev. B 26 (1982) 1743 and references therein.

[28] J.C. Boettger and S.B. Trickey, Phys. Rev. B 32, (1985) 1356 (Rapid Communication).

[29] U. Birkenheuer, J. C. Boettger, and N. R¨osch: J. Chem. Phys. 100 (1994) 6826.

[30] B.I. Dunlap and N. R¨osch, in [7], pp. 317-39 and references therein.

[31] B.I. Dunlap, J.W.D. Connolly, and J.R. Sabin, Internat. J. Quantum Chem. S-11 (1997) 81.

[32] B.I. Dunlap, J.W.D. Connolly, and J.R. Sabin, J. Chem. Phys. 71 (1979) 3396.

[33] J.L. Whitten, J. Chem. Phys. 58 (1973) 4496.

[34] J.W. Mintmire and B.I. Dunlap, Phys. Rev. A 25 (1982) 88.

[35] N. R¨osch, S. Kr¨uger, T. Belling, F. N¨ortemann, M. Staufer, C. Zenger, and T. Grauschopf in HPSC97 — Status and Perspectives of Parallel High-Performance Supercomputing, Proceedings of Symposium organized by the German Ministry of Education, Science, Research and Technology (BMBF), held in Munich, Feb. 24-26, 1997, H. Wolf and R. Krahl (eds.), pp. 165-80.

[36] see http://www.sao.nrc.ca/sims/deMon/public_html/ for summary, history, and bibliography.

[37] G. Te Velde, F.M. Bickelhaupt, E.J. Baerends, C. Fonseca Guerra, S.J.A. Van Gisbergen, J.G. Snijders, and T. Ziegler J. Comput. Chem. 22 (2001) 931; also see http://www.chem.vu.nl/afdelingen/TC/index-en.html and http://www.scm.com/ for summary, history, and bibliography.

[38] M.v. Arnim and R. Ahlrichs J. Comput. Chem. 19 (1998) 1746; other references at http://www.chemie.uni-karlsruhe.de/PC/TheoChem/ .

[39] (a) G.H.F. Diercksen, and J.C. Boettger, Phys. Rev. B 45 (1992) 4460 ; (b) B.I. Dunlap and J.C. Boettger, J. Phys. B: At. Mol. Opt. Phys. 29 (1996) 4907.

[40] J. Andzelm, E. Radzio, and D.R. Salahub, J. Comput. Chem. 6F (1985) 520; see Eq. (13).

[41] J.C. Boettger, Phys. Rev. B 57 (1998) 8743.

[42] M. Douglas and N.M. Kroll, Ann. Phys. 82 (1974) 89.

[43] B.A. Hess, R.J. Buenker, and P. Chandra, Internat. J. Quantum Chem. 29 (1986) 737.

[44] N. R¨osch, S. Kr¨uger, M. Mayer, and V. A. Nasluzov, in Recent Developments and Applications of Modern Density Functional Theory, J. M. Seminario (ed.) Elsevier, Amsterdam, 1996, pp. 497 - 566.

[45] D.D. Koelling and B.N. Harmon, J. Phys. C 10 (1977) 3107.

[46] E. van Lenthe, J.G. Snijders, and E.J. Baerends J. Chem. Phys. 105 (1996) 6505; E.J. Baerends, and J.G. Snijders Internat. J. Quantum Chem. 57 (1996) 281.

[47] M. Mayer, O. D. H¨aberlen, and N. R¨osch Phys. Rev. A 54 (1996) 4775.

[48] J.C. Boettger, Phys. Rev. B 62 (2000) 7809.

[49] J. Wang, R.J. Mathar, S.B. Trickey, and J.R. Sabin, J. Phys. Cond. Matt. 11 (1999) 3973.

[50] R.J. Mathar, S.B. Trickey, and J.R. Sabin, Nucl. Inst. Meth. B 155 (1999) 249.

[51] C.S. Wang and J. Callaway, Computer Phys. Commun. 14 (1978) 327.

[52] J. Callaway, X. Zou, and D. Bagayoko, Phys. Rev. B 27 (1983) 631.

[53] J.C. Boettger and S.B. Trickey, Phys. Rev. B 29 (1984) 6425; J.C. Boettger and S.B. Trickey, Phys. Rev. B 29 (1984) 6434.

[54] D. Laurent, private communication to SBT

[55] J.A. Applebaum and D.R. Hamann, Solid State Commun 27 (1978) 881.

[56] P.J. Feibelman, J.A. Appelbaum, and D.R. Hamann, Phys. Rev. B 20 (1979) 1433.

[57] P.J. Feibelman and D.R. Hamann, Phys. Rev. B 21 (1980) 1385.

[58] P.J. Feibelman and F.J. Himpsel, Phys. Rev. B 21 (1980) 1394.

[59] D.R. Jennison, C. Verdozzi, P.A. Schultz, and M.P. Sears, Phys. Rev. B 50 (1999) R15605.

[60] Information about SeqQUEST and its capabilities is found at http://www.cs.sandia.gov/ paschul/Quest/

[61] M.D. Towler, A. Zupan, and M. Causà, Computer Phys. Commun. 98 (1996) 181.

[62] M. Catti, B. Civalleri, and P. Ugliengo J. Phys. Chem. B 104 (2000) 7259.

[63] Wuming Zhu, N. Flocke, and S.B. Trickey (submitted to Phys. Rev. B).

[64] J.E. Jaffe and A.C. Hess, J. Chem. Phys. 105 (1996) 10983.

[65] S. Hirata and S. Iwata, J. Chem. Phys. 107 (1997) 10075; see also M. Tobita, S. Hirata, and R J. Bartlett, J. Chem. Phys. 114 (2001) 9130 and refs. therein.

[66] K.N. Kudin and G.E. Scuseria, Phys. Rev. B 61 (2000) 16440.

[67] K.N. Kudin, G.E. Scuseria, and R.L. Martin Phys. Rev. Lett. 89 (2002) 266402.

[68] L.E. McMurchie and E.R. Davidson, J. Comp. Phys. 26 (1978) 218.

[69] T. Zivkovi´c and Z.B. Maksi´c, J. Chem. Phys. 49 (1968) 3083.

[70] U. Birkenheur, "Quantenmechanische Beshreibung von Oberflächen und gordeneten Adsorbatsystemen", PhD Thesis, Technische Universität München, 1994 (unpublished).

[71] Robert D. Richtmeyer Principles of Advanced Mathematical Physics,vol. 1, Springer-Verlag, New York, Heidelberg and Berlin, 1978, p. 27.

[72] E.J. Baerends, D.E. Ellis, and P. Ros, Chem. Phys. 2 (1973) 41.

[73] H. Sambe and R.H. Felton, J. Chem. Phys. 62 (1975) 1122.

[74] J. Koller, M. Zaucer, and A. Azman, Z. Naturforsch. 31a (1976) 1022.

[75] J.C. Boettger and S.B. Trickey, J. Molec. Struct. (Theochem) 501-02 (2000) 285.

[76] L.L. Foldy and S.A. Wouthuysen, Phys. Rev. 78 (1500) 29.

[77] J.C. Boettger, Internat. J. Quantum Chem. 65 (1997) 565.

[78] J.C. Boettger, Phys. Rev. B 62 (2000) 7809.

[79] J.C. Boettger, Internat. J. Quantum Chemistry [accepted]

[80] F.E. Harris and H.J. Monkhorst, Phys. Rev. B 2 (1973), 4400; erratum Phys. Rev. B 9 (1974) 3946.

[81] F.E. Harris, L. Kumar, and H.J. Monkhorst, Phys. Rev. B 7 (1973) 2850.

[82] H.J. Monkhorst and W.A. Schwalm, Phys. Rev. B 23 (1981) 1729.

[83] G.P. Srivastava, J. Phys. A: Math. Gen. 17 (1984) L317.

[84] J.C. Boettger and A.K. Ray, Internat. J. Quantum Chem. 80 824 (2000).

[85] J.C. Boettger and A.K. Ray, AIP Conf. Proc. 532 (2000) 422.

[86] M.D. Jones, J.C. Boettger, R.C. Albers, and D.J. Singh, Phys. Rev. B 61 (1999) 4644.

[87] J.C. Boettger, M.D. Jones, and R.C. Albers, Internat. J. Quantum Chem. 75 (1999).

[88] J.C. Boettger, Phys. Rev. B 48 (1993) 10247; J.C. Boettger, Phys. Rev. B 47 (1993) 1138 (Rapid Communication).

[89] S.B. Trickey and J.C. Boettger, Invited lecture, Fifth Chemical Congress of North American, Cancún, México, 15 Nov. 1997 (unpublished).

[90] J.C. Boettger and S.B. Trickey, Phys. Rev. B 45 (1992) 1363.

[91] J. C. Boettger, U. Birkenheuer, S. Kr¨uger, N. R¨osch, and S. B. Trickey Phys. Rev. B 52 (1995) 2025.

[92] J.C. Boettger and S.B. Trickey, Phys. Rev B 51 (1995) 15623 (Rapid Communications).

[93] J.C. Boettger, Internat. J. Quantum Chem. 70 (1998) 825.

[94] S.B. Trickey, R.J. Mathar, and J.C. Boettger, in Proc. Third UNAM-Cray Supercomputing Conference: Computational Chemistry, G. Cisneros, J.A. Cogordan, M. Castro, and C. Wang (eds.), World Scientifi c, Singapore, 1997, pp. 239-54.

[95] J.Z. Wu, S.B. Trickey, and J.R. Sabin, Nucl. Instr. and Meth. B 79 (1993) 206.

[96] J.P. Perdew, K. Burke, and M. Ernzerhof, Phys. Rev. Lett. 77 (1996) 3865; erratum Phys. Rev. Lett. 78 (1997) 1396.

[97] J.P. Perdew, J.A. Chevary, S.H. Vosko, K.A. Jackson, M.R. Pederson, D.J. Singh, and C. Fiolhais, Phys. Rev. B 46 (1992) 6671; erratum Phys. Rev. B 48 (1993) 4978 and references therein.

[98] P.J. Stephens, F.J. Devlin, C.F. Chabalowski, and M.J. Frisch J. Phys. Chem. 98 (1994) 11623.

[99] L. Hedin and B.I. Lundqvist, J. Phys. C 4 (1971) 2064.

[100] J.P. Perdew and A. Zunger, Phys. Rev. B 23 (1981) 5048.

[101] L. Nordstr¨om, J.M. Wills, P.H. Andersson, P. S¨oderlind, and O. Eriksson, Phys. Rev. B 63 (2000) 035103.

[102] P. S¨oderlind, O. Eriksson, B. Johansson, and J.M. Wills, Phys. Rev. B 50, (1994) 7291.

[103] W.A. Harrison, Phys. Rev. B 49 (1994) 3584.

[104] F.K. Schulte, Surf. Sci. 55 (1976) 427.

[105] J.C. Boettger and S.B. Trickey, Phys. Rev. B 32 (1985) 3391; W.G. Zittel , J. Meyer-ter-Vehn, J.C. Boettger, and S.B. Trickey, J. Phys. F: Met. Phys. 15 (1985) L247.

[106] J.B. Neaton and N.W. Ashcroft, Nature 400 (1999) 141.

[107] J.C. Boettger, U. Birkenheuer, N. R¨osch, and S.B. Trickey, Internat. J. Quantum Chem. S-28 (1994) 675.

[108] J. Neugebauer and M. Scheffler, Phys. Rev. B 46 (1992) 16067.

[109] J.C. Boettger, Phys. Rev. B 64 (2001) 035103.

[110] R.G. Greene, H. Luo, and A.L. Ruoff Phys. Rev. Lett. 73 (1994) 2075.

[111] P. S¨oderlind, R. Ahuja, O. Eriksson, B. Johansson, and J.M. Wills, Phys. Rev. B 49 (1994) 9365.

[112] A. Nagashima, N. Tejima, Y. Gamou, T. Kawai, and C. Oshima, Phys. Rev. B 51 (1995) 4606; A. Nagashima, N. Tejima, Y. Gamou, T. Kawai, and C. Oshima, Phys. Rev. Lett. 75 (1995) 3918.

[113] S.B. Trickey, F.R. Green, Jr., and F.W. Averill, Phys. Rev. B 8 (1973) 4822.

[114] G. Hanke, M. Kramer, and K. M¨uller in Synthesis and Properties of Boron Nitride, J.J. Pouch and S.A. Alterovitz (eds.), Materials Science Forum 54 & 55, (1990) pp. 207-28.

[115] S. Peter Apell, J.R. Sabin, and S.B. Trickey, in Applications of Accelerators, Research and Industry: Proc. 14th International Conference, J.L. Duggan and I.L. Morgan (eds.), American Physical Society, NY, 1997 AIP Conf. Proc. 392, vol. 1, p. 1369.

[116] S.P. Apell, J.R. Sabin, and S.B. Trickey, Internat. J. Quantum Chem. S-29 (1995) 153.

[117] Jin Zhong Wu, S.B. Trickey, J.R. Sabin, and J.A. Nobel, Internat. J. Quantum Chem. S-28 (1994) 299.

[118] S.F. Boys, Proc. Roy. Soc. A 200 (1950) 542.

J. Leszczynski (Editor)
Computational Materials Science
Theoretical and Computational Chemistry, Vol. 15

Chapter 7

Many-body luminescence from highly excited quantum-confined structures

T. V. Shahbazyan[a] and M. E. Raikh[b]

[a]Department of Physics, Jackson State University, Jackson, MS 39217

[b]Department of Physics, University of Utah, Salt Lake City, UT 84112

We review recent results on many-body effects in the luminescence from semiconductor nanostructures. Many-body luminescence from highly excited quantum-confined structures is *conceptually* important topic since a new parameter, a level spacing, plays a crucial role. This spacing is *not* merely a discretization of the bulk luminescence spectrum, as it could seem. The *interplay* of finite spacing with interactions (even weak) results in a highly nontrivial sequence of emission lines, their heights revealing the many-body correlations in the system. Here the complex structure of the emission spectrum, resulting from the shakeup processes in many-particle (but finite) system, is demonstrated for a confined electron-hole system of a particular geometry, in which the interacting carriers are confined to a ring. For this geometry, the Luttinger liquid theory allows one to exactly calculate the *intensities* of all many-body spectral lines. The *positions* of the lines are governed by the relation of the level spacings for electrons and holes. While close to the emission threshold the interactions cause only weak shakeup satellites of the single-particle lines, away from the threshold the discrete luminescence spectrum is completely dominated by the many-body transitions. We describe the Luttinger liquid approach for calculations of optical spectra in finite one-dimensional systems. The calculations are preceded by a detailed review of experimental and theoretical work on many-body luminescence from various infinite systems. We also review the current status of the experimental and theoretical research on quantum nanorings.

1 INTRODUCTION

Luminescence from zero-dimensional objects (quantum dots) is one of the highlights in physics of nanostructures which emerged during the last decade. Early papers (see, e.g., Refs. [1,2], and the review article Ref. [3]) reported the PL spectra consisting of "zero-width" luminescence lines.

High surface density of quantum dots caused an ambiguity in assigning of these lines. In the later studies the emission from a *single* dot was resolved. This progress [4] has permitted the luminescence spectroscopy of individual dots with controllable exciton population determined by the excitation intensity.

Since many-body optical transitions in zero-dimensional objects was demonstrated experimentally, it is important to assess this phenomenon from the perspective of the well established field of many-body luminescence. This is accomplished in the present chapter. Below we review the many-body luminescence in various systems studied to date experimentally and theoretically. We then demonstrate that many-body luminescence from highly excited zero-dimensional objects has unique features due to *large* number of *discrete* lines. This discreteness *unravels* the many-body correlations that are otherwise masked in the continuous spectrum of luminescence from infinite systems. We describe in detail the emergence of such correlations for a particular nanostructure geometry – semiconductor nanorings – using the Luttinger liquid approach for quasi-one-dimensional finite-size systems.

2 SPECTROSCOPY OF MANY-BODY PROCESSES

2.1 Shakeup effects in optical spectra of many-electron systems

Shakeup represents a fundamental many-body effect that takes place in optical transitions in many-electron systems. In such systems, an absorption or emission of light is accompanied by electronic excitations in the final state of the transition. The most notable shakeup effect is the Anderson orthogonality catastrophe [5] in the electron gas when the initial and final states of the transition have very small overlap due to the readjustment of the Fermi sea electrons in order to screen the Coulomb potential of photoexcited core hole. Shakeup is especially efficient when the optical hole is immobilized, and therefore it was widely studied in conjunction with the Fermi edge singularity (FES) in metals [6–8] and doped semiconductor quantum wells [9–15]. Comprehensive reviews of FES and related issues can be found in Refs. [16, 17].

2.1.1 Shakeup processes in electron gas

The long-time dynamical Fermi sea response to a sudden appearance of the optical hole Coulomb potential can be viewed as a dressing of that hole by the low-energy Fermi sea excitations. This leads to the power-law infrared divergence in the hole density of state [16, 17]. In three-dimensional (3D) electron gas, the only low-energy excitations are the Fermi sea electron-hole pairs, and, therefore, close to the absorption onset, the electron-electron interactions are usually neglected. Incorporation of electron-electron interactions gives rise to the plasmon satellites [8, 18], which are somewhat similar to the low-energy phonon replicas. Each of these satellites also represents a power-law divergence at the energy $n\omega_p$, where ω_p is the bulk plasmon frequency (we set $\hbar = 1$) and n is an integer. In contrast, in low-dimensional electron systems, the plasmon is gapless, so the shakeup of single-particle and collective excitations must be treated on equal footing. In 2D electron gas, where the plasmon dispersion is $\omega_q \propto \sqrt{q}$ for Small q, the plasmon shakeup leads to a narrowing of the main singularity and to an additional structure at energies corresponding to the plasmon bandwidth [19]. Note, however, that plasmon effect is negligible near the Fermi edge because of a much smaller 2D plasmon density of states at low energies as compared to that of electron-hole pairs. In contrast, the role of plasmon shakeup is much more important in 1D electron systems, where the plasmon dispersion is linear. Since the electron dispersion in the vicinity of the Fermi level is also linear, single-particle and collective excitations are intertwined, forming a strongly correlated electron liquid. The exact solution of the 1D FES in the long time limit, which was carried out using the Luttinger model [20], revealed that the power-law exponent is determined by both electron-hole and electron-electron interactions [21–23].

2.1.2 Magnetoplasmon shakeup in semiconductor quantum wells

Shakeup processes are quite pronounced in luminescence from a 2D electron gas in a perpendicular magnetic field. In such systems, the single-particle energy spectrum represents a staircase of equidistant Landau levels (LLs) separated by the cyclotron energy ω_c. Here, a recombination of an interband electron-hole pair is accompanied by electronic transitions across the cyclotron gap. Shakeup satellites, corresponding to excitation of magnetoplasmons as well as to inter-LL Auger transitions, were observed in a number of experiments [24–32], in agreement with earlier theoretical pre-

dictions [33–35]. The general expression for the ground state luminescence intensity has the form [16]

$$I(\omega) \propto \sum_f C_f \, \delta(\omega + E_f - E_i), \tag{1}$$

where E_i and E_f are initial (ground) and final state energies and the oscillator strengths C_f are given by the square of the dipole matrix element. In the absence of interactions, the recombination act does not perturb the system and so the initial and final state energy difference is simply $E_g + (\omega_c^e + \omega_c^h)/2$, where both electron and hole belong to the lowest LL [36]. In the presence interaction, the inter-LL magnetoplasmon satellites appear in the lower tail of the spectrum at frequencies that are multiples of the electron cyclotron energy, ω_c^e. Note that in doped quantum wells, the actual separation between LLs is less than ω_c^e due to exchange effects, so the magnetoplasmon energy lies above that of single-particle transitions. Magnetic-filed dependence of oscillator strengths C_f is determined by several factors. For even integer filling factors, $\nu = 2\pi l^2 n_e$ (n_e is electron concentration and l is the magnetic length), the screening of Coulomb interaction by the electron gas is strongly suppressed, resulting in the enhancement of satellite amplitudes [30, 33]. Another widely-observed feature was a suppression of satellite peaks for filling factor $\nu < 2$, i.e., when only the lowest LL is occupied. Such a suppression originates from the electron-hole symmetry in the lowest LL [37], which results in a cancellation of the electron and hole final state Coulomb matrix element contributions to C_f [36]. In the valence band, similar inter-LL shakeup processes were observed in p-doped [38, 39] GaAs quantum wells.

2.1.3 Spin wave shakeup in quantum Hall ferromagnets

In one-side modulation-doped quantum wells, the aforementioned electron-hole symmetry is violated due to the spatial separation between the electron and valence hole planes that is caused by the interface potential. In such samples, polarization-dependent spectral redshifts were reported as the filling factor was swept through integer values [28, 29, 31, 40–43]. These redshifts were attributed to the competition between interband Coulomb binding and electron self-energies in the final state [44, 45]. For example, for $\nu = 1^-$, the initial state represents a valence hole and a full spin-polarized LL in conduction band which is negatively charged in order to compensate the positive hole charge. A recombination leaves a hole in the

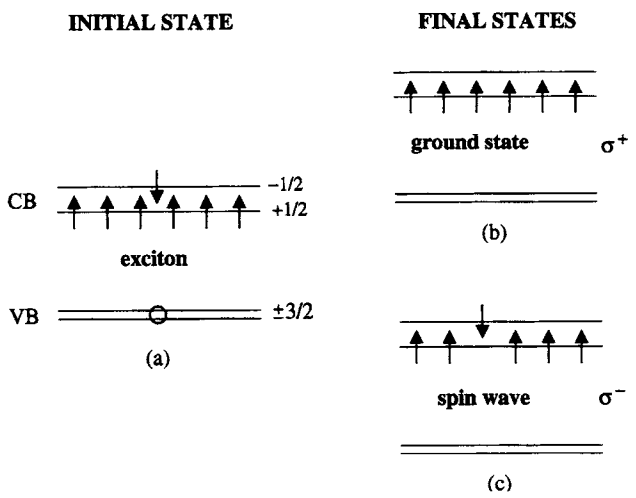

Figure 1: Luminescence from $n = 0$ LL at filling factor $\nu = 1$. Recombination of initial interband exciton (a) can result either in ground state for σ^+ polarization (b), or spin wave shake up for σ^- polarization (c).

conduction band LL with exchange energy $E_{ex} = \sqrt{\pi/2}\, e^2/\kappa l$ (κ is the dielectric constant). For $\nu = 1^+$, the initial state consists of an interband magnetoexciton made up from a valence hole and an electron in the upper (spin-up) polarized LL, with a binding energy E_0. Then the removal of an electron from the lower (spin-down) polarized LL leaves a *spin wave* in the final state of the transition with just the Zeeman energy (see Fig. 1). The difference between below and above $\nu = 1$ final state energies is thus $E_{ex} - E_0 > 0$ in such asymmetric structures, which accounts for the redshift. A similar analysis was applied to the redshifts observed near $\nu = 2$ filling factor [28,29,31,40,43]. In single heterojunctions, systematic studies of the electron-hole separation as a function of carrier concentration were carried out in Ref. [46].

The shakeup of spin waves, mentioned above, has been observed prominently in the magnetoluminescence spectra at filling factors close to 1, 3, and 5 [31,40–43,47]. At $\nu = 1$, an asymmetric broadening of the luminescence peak with additional spectral weight on low energy side was observed for σ_--polarized light [47]. The origin of this broadening was explained as follows [44]. For σ_+ polarization, the recombination of an exciton, made up from a valence hole and an $n = 1$ LL electron, leaves the 2DEG in the ground state, resulting in narrow emission peak (see Fig. 1). For σ_- polarization, the final state is a spin-wave with momentum q equal to that

of the exciton before the recombination, so the lineshape at low energies is determined by the difference between the dispersions of a spin wave and an exciton. Furthermore, for filling factors $\nu = 3$ and 5, a splitting of the ground state luminescence peak was observed for σ_- polarization [31,40]. This splitting, greatly enhanced at low temperatures, was attributed to the Anderson-Fano resonance in the final state that originated from the destructive interference between the hole, left in the conduction band LL after recombination, and the continuous spectrum of the spin wave [45].

2.2 Shakeup of electron excitations in few-particle systems

2.2.1 Shakeup satellites in atoms

In atoms and molecules, shakeup satellites, corresponding to internal electronic transitions, are routinely observed using photoelectron and resonant Raman spectroscopy. In particular, shakeup satellites can be observed in the two particle spectrum, i.e., when two holes are left in the final state of an atom after electron emission. Satellite's strength can be strongly enhanced in the presence of a resonant intermediate state. For example, in copper atoms, the incident photon can first excite the core 3p electron to the 4s shell; the core hole then decays to the 3d shell through the Auger process (with electron ejected from 3d shell) leaving two 3d holes in the final state [48]. For recent reviews of extensive literature the reader is referred to Refs. [49,50]).

2.2.2 Many-body luminescence lines in single quantum dots

In semiconductors, multiple emission lines have been recently observed in the luminescence from single self-assembled quantum dots [51–64]. At low excitation intensities, the luminescence from a dot is dominated by the ground state single-exciton recombination (i.e., from lowest size-quantization levels in conduction and valence bands). Upon increasing the excitation intensity, as the number of excited carriers increases, new emission lines appear in the luminescence spectrum. These lines were interpreted in terms of recombination within many-exciton complexes. One reason for the emergence of additional lines is that the carriers, constituting a complex, occupy higher size-quantization levels. Another reason, is that the interactions between strongly confined photoexcited carriers lift the *degeneracies* within the final many-body states. The latter mechanism was

addressed in Refs. [55, 56, 63–65] for the situations with [63–65] and without [55, 56] orbital degeneracy of single-particle states. The calculations carried out in Refs. [55, 56, 64, 65] predicted the splittings of luminescence lines, originating from different many-body final states, to be of the order of matrix element of the interaction potential. The actual positions of these lines, corresponding to interband transitions between states with the *same* size-quantization quantum numbers, reproduce quite accurately the experimental PL spectra of Refs. [55–57, 60] (for up to $N = 16$) and of Ref. [59,64] (for $1 \leq N \leq 6$). The third type of additional lines were identified with the transition energies corresponding to *different* size-quantization levels [55, 56]. Such transition energies point to shakeup processes in a *confined electron-hole system*, when the recombination of an electron-hole pair is accompanied by internal excitations within the exciton multiplex.

2.2.3 Density dependence of optical spectra

The evolution of optical spectra with increasing electron gas density was studied both in metals [66] and in semiconductor quantum wells [67–70]. In the absence of conduction electrons, the absorption spectrum is characterized by two peaks – a sharp exciton line well separated from a step-like onset of continuum states. In metals, the presence of conduction band electrons asymmetrically broadens the exciton peak according to $(\omega - \omega_1)^{-\alpha}$ with α decreasing in the (0,1) interval as the electron concentration increases, while the step-like continuum edge also acquires a power-law shape, $(\omega - \omega_2)^{\beta}$ with β increasing with concentration in the (0,3) interval [66]. In contrast, in semiconductor quantum wells with low electron concentration, the ground state represents a negatively charged exciton, X^-, formed as a result of the binding of an additional conduction electron by a photoexcited interband electron-hole pair [71–73]. This leads to an emergence of the exciton peak (X), corresponding to ionized X^-, located between the ground state X^- peak and the absorption onset at the Fermi energy E_F [67]. The evolution of absorption/emission spectra with increasing 2D electron gas concentration was traced in Refs. [68–70]. As the electron concentration increases, so does the separation between X^- and X peaks; at the same time, the oscillator strength of X is reduced as the exciton binding energy becomes smaller than E_F. The lineshape undergoes a qualitative change from exciton-like to continuum-like as concentration exceeds some characteristic value [68–70]. In particular, above that value, the absorption

spectrum develops higher-energy tail corresponding to the shakeup transitions. It was also noted [70] that, in a weak magnetic field, the character of shakeup satellites in the low-energy tail of luminescence spectrum changes: for higher electron concentrations, the magnetic field dependence of satellite peak separation indicates excitation of magnetoplasmons, as opposed to single-particle transitions for lower concentrations [74, 75].

2.3 Shakeup effects in highly excited nanostructures

All the above studies of the optical spectra evolution from few- to many-particle cases were carried out for *infinite* systems, i.e., those with *continuous* excitation spectrum (at zero field). In such systems, the shakeup processes play increasingly important role, as indicated by the emergence of the power-law behavior at higher electron concentrations. However, these studies provide no insight into the structure of many body states at the onset of transition from discrete to continuous spectrum. In *finite-size* systems with *discrete* excitation spectrum, the oscillator strengths of satellite peaks characterize the amplitudes of corresponding shakeup transitions which, in turn, are determined by the interaction matrix elements as well as by statistical weights of the contributing many-body processes. With increasing system size (at constant carrier concentration) new shakeup satellites should emerge due to an increase in the number of many-body states available for non-radiative transitions. In fact, the positions and magnitudes of shakeup satellites represent the *fingerprint* of the system many-body excitation spectrum. With further increase in the system size, the satellite peaks should eventually merge; the energy dependence of their peaks *envelope* should then follow the power-law lineshape of the continuous spectrum for the corresponding infinite system.

In the following, we consider in some detail the transition from discrete to continuum spectra for the case of luminescence from highly excited semiconductor nanostructures. We will restrict ourselves to undoped semiconductors so that all carriers in conduction and valence band are optically excited. The luminescence is preceded by a fast carrier relaxation [76], so the recombination takes place when the electron and hole gases are in their respective ground states. In quantum wells, luminescence from high-density optically created electron-hole gases was studied in Refs. [77–79]. In confined structures, such as quantum dots, electrons and holes fill size-quantization energy states up to their respective Fermi

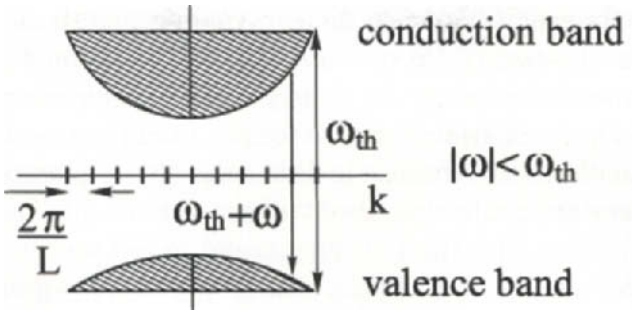

Figure 2: In highly-excited quantum-confined structures, photoexcited carriers form electron and hole Fermi seas in conduction and valence bands, respectively; ω_{th} is the energy distance between the corresponding Fermi levels. Recombination of electron-hole pairs, belonging to space-quantization energy levels, gives rise to discrete lines in the luminescence spectrum.

levels in conduction and valence bands (see Fig. 2). We will only consider the higher-frequency domain of the emission spectrum corresponding to frequencies not far from the electron and hole Fermi edge's separation. For a noninteracting system, the emission lines would correspond to the transitions between size-quantization levels in conduction and valence bands which obey the selection rules, so the the general expression (1) becomes

$$I(\omega) \propto \sum_n C_n \delta[\omega + (\Delta_1 + \Delta_2)n], \tag{2}$$

where Δ_1 and Δ_2 are level spacings for electrons and holes; C_n are the oscillator strength which depend on n only *weakly* ($\omega < 0$ is measured from the Fermi edge).

As discussed above, the many-body transitions due to the interactions between carriers change qualitatively the form of the spectrum. Namely, a removal of an electron-hole pair shakes up the respective Fermi seas by causing them to emit Fermi sea excitations. Since in a *finite-size* system, the energies of excitations are *quantized*, such a shakeup would lead to the following spectrum,

$$I(\omega) \propto \sum_{mn} C_{mn} \delta(\omega + m\tilde{\Delta}_1 + n\tilde{\Delta}_2), \tag{3}$$

rather than Eq. (2). Here $\tilde{\Delta}_1$ and $\tilde{\Delta}_2$ are the level spacings renormalized by interactions. The emission lines with $m \neq n$ are, thus, shakeup satellites. All the information about many-body correlations in the system is encoded in the oscillator strengths C_{mn}. In fact, C_{mn}, being governed by interactions, are *strong* functions of m and n.

In general, the evaluation of coefficients C_{mn} presents a major challenge. Remarkably, in the case of 1D systems, C_{mn} can be calculated *analytically* when the number of carriers, N, is large, but the emission spectrum is still discrete [80]. Such systems have recently been manufactured and will be reviewed in the next section. In this case, the luminescence from 1D electron-hole system can be described within the finite-size Luttinger-liquid formalism [20]. Note that the Luttinger liquid model was employed earlier for calculations of the Fermi-edge optical properties of *infinite* 1D systems (with and without defects) in Refs. [21–23, 81, 82].

2.4 Semiconductor nanorings

Properties of electron systems confined to a ring have been a subject of a lot of studies during the last decade (see Ref. [83] for review). Conceptually, the distinctive feature of the ring geometry is that it is nonsimply connected. As a result, the orbital magnetism of electrons on a ring depends periodically on the magnetic flux, Φ, threading the ring. Also, as a consequence of nonsilmply connectedness, the many-electron ground state on a ring becomes chiral even in a weak magnetic field, when $\Phi \ll \Phi_0$, where $\Phi_0 = hc/e$ is the flux quantum. Nontrivial magnetic and transport properties of electrons in the ring geometry become observable when the ring is small enough, so that the electron coherence length exceeds the perimeter. This condition is met at low enough temperatures. On the other hand, since the sensitivity to the flux originates from the ring geometry, it persists even if the electron elastic mean free path is smaller than the perimeter, so that the overall character of the electron transport is diffusive. The actual sizes of such rings, that were studied experimentally [83], were $\sim 10^3$ nm and more, so that the discreteness of the quantum states in these zero-dimensional objects could not be resolved.

Recently, a new technique for fabrication of the rings has been introduced [84–87]. In contrast to lithography [83], this technique is based on the phenomenon of self-assembly. The rings are formed in two steps. The first step is the conventional epitaxial growth of the array of narrow gap (InAs) quantum dots on the surface of the wide-gap (GaAs) substrate. Epitaxial islands are formed spontaneously in course of this growth in order to minimize the elastic energy, caused by the 7% mismatch of the lattice constants of InAs and GaAs. These islands are then made into dots by covering them with another GaAs layer. The shape of the dots is lens (or

pyramid)-like with $\sim$ 20 nm in diameter and $\sim$ 7 nm in height. The second step is conversion of the dots into volcano-shape rings [84–87], which is achieved by annealing at the growth temperature. The rings have the height of $\sim$ 2 nm and the outer diameter between 60 nm and 140 nm [88]. The center hole of $\sim$ 20 nm diameter is responsible for nonsimply connectedness of the confining potential for electrons and holes.

To demonstrate that this topology indeed dramatically changes the response of electronic states in the rings to the magnetic flux, two complementary spectroscopic techniques, capacitance-voltage spectroscopy and far-infrared spectroscopy, were employed in Ref. [88]. First technique measures the magnetic-field dispersion of the ground state energy, whereas the second technique provides information about the magnetic-field dependence of the excitations. The measurements [88, 89] have revealed a cusps in charging energy and in positions of the minima in far-infrared transmission as a function of magnetic field at $\Phi \approx \Phi_0$. These cusps were identified with the change in the angular momentum of the ground state. This conclusion was supported by numerical calculations of Ref. [90], which reproduce the evolution of the peak positions in the far-infrared absorption with magnetic field.

Experimental findings of Ref. [88] have triggered theoretical studies of the single-electron states in quantum rings [91,92]. In particular, the effect of external electric filed [91] and impurity states in the ring geometry [92] were addressed. Most interesting, however, are the many-body effects in the ring geometry.

First experimental study of the many-body effects in quantum rings was carried out in Ref. [93], where the optical emission from a charge-tunable ring was measured. Similar to [88] the tunability of the number of electrons on the ring was achieved due to the presence of a gate electrode separated from a self-assembled ring by a tunnel barrier. Changing the gate voltage allowed to add electrons to the ring one-by-one. Addition of each new electron manifested itself as a step in the capacitance-voltage characteristics. The prime observation of Ref. [93] is that all lines in the emission spectrum from the ring change abruptly upon addition of an extra electron. Photoluminescence in Ref. [93] was measured in the weak-excitation limit, which corresponds to the "classical" shakeup situation (a single hole plus degenerate electron gas). Rearrangement of the entire emission spectrum with addition of a single electron is a clear manifestation of the many-body character of the luminescence from a ring.

Lithographically fabricated [83] and self-assembled rings differ by more than an order of magnitude in diameter. Characteristic level spacing in self-assembled rings is rather large, $\sim$ 10 meV. This fact, and the finite bandgap offsets at GaAs/InAs boundaries, restricts the maximal number of photoexcited electron-hole pairs as well as the number of electrons, injected from the gate electrode into the dot, to $\sim$ 10. Taking into account the spin degeneracy, the description of such a limited number of carriers in terms of a Fermi sea is hardly adequate. Therefore, in Ref. [93] the language used to interpret the many-body emission spectrum was not a shakeup (as in infinite system), but rather the electron-hole recombination in the presence of "spectators".

Photoluminescence from quantum rings in external magnetic field is an issue of conceptual interest for the following reason. Photoexcited electron and hole form an exciton, which is a neutral entity. Neutral particle does not accumulate the Aharonov-Bohm phase in magnetic field. Therefore, it might seem that, in contrast to the infrared absorption, photoluminescence from the ring should not exhibit oscillations with period $\Phi = \Phi_0$. This is, however, not the case. The reason is that the exciton is a composite object. Therefore, even bound electron and hole can tunnel in the opposite directions and "meet" each other on the "opposite" side of the ring. This process gives rise to the flux sensitivity of the exciton. Theoretical studies of magneto-optical properties of the neutral and charged quantum ring excitons were reported in Refs. [94–104]. Moreover, the mechanism [94,96] of the flux sensitivity of the exciton in a ring geometry was extended in Refs. [106,107] to other neutral excitations (plasmons).

In the experimental paper Ref. [105], a weak anomaly in the luminescence spectrum of a neutral exciton in a self-assembled ring was interpreted as a possible manifestation of the Aharonov-Bohm effect.

3 LUTTINGER LIQUID THEORY OF LUMINESCENCE FROM HIGHLY EXCITED NANORINGS

3.1 General expression for emission rate

Here we outline the general formulas for recombination of an electron-hole pair belonging to Luttinger liquid rings in conduction and valence bands. (see Fig. 3). We start with the two-component Luttinger liquid model on a ring [108] with Hamiltonian $H_1 + H_2 + H_{int}$, where H_j describe noninter-

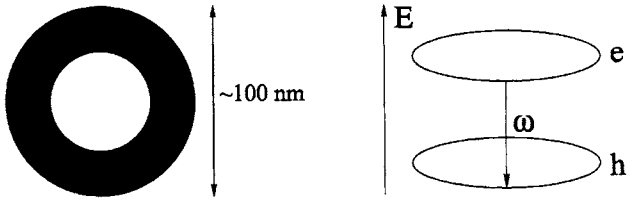

Figure 3: Schematic representation of an electron-hole pair recombination in highly-excited Luttinger liquid ring

acting electrons ($j = 1$) and holes ($j = 2$) with linearized dispersions (the slopes are determined by the Fermi velocities v_j); H_{int} describes the interactions between carriers via screened potential $U(x)$. The electron-hole recombination rate is given by the Golden rule [16] [compare Eq. (1)]

$$W(\omega) = \frac{2\pi}{L}\sum_f |\langle f|T|i\rangle|^2 \delta(E_i - E_f - \omega) = \frac{1}{L}\int_{-\infty}^{\infty} dt e^{-i\omega t}\langle i|T^\dagger(t)T(0)|i\rangle, \quad (4)$$

where E_i and E_f are the energies of initial (ground) and final (with electron-hole pair removed) states, and

$$T = T_+ + T_- \quad T_\pm = d\int_0^L dx \psi_{2\mp}(x)\psi_{1\pm}(x) \quad (5)$$

is the dipole transition operator. Here $\psi_{i\pm}$ are annihilation operators for left $(-)$ and right $(+)$ moving carriers, d is the interband dipole matrix element, and L is the ring circumference. Note that recombination occurs between left (right) electrons and right (left) holes. The recombination rate is then expressed via a four-particle Green function,

$$W(\omega) = d^2\int_0^L dx \int_{-\infty}^{\infty} dt e^{-i\omega t}[D_+(x,t) + D_-(x,t)] = d^2[D_+(\omega) + D_-(\omega)], \quad (6)$$

where

$$D_\pm(x,t) = \langle \psi^\dagger_{2\mp}(x,t)\psi^\dagger_{1\pm}(x,t)\psi_{1\pm}(0)\psi_{2\mp}(0)\rangle. \quad (7)$$

3.2 Bosonisation of electron-hole Hamiltonian

In order to evaluate $D_\pm(x,t)$ for a two-component Luttinger liquid [109–111], we use the bosonization technique on a ring [20, 108]. The right/left fermion fields are presented as

$$\psi_{j\alpha}(x) = L^{-1/2} : e^{i\varphi_{j\alpha}(x)} := (2\pi\epsilon)^{-1/2} e^{i\varphi_{j\alpha}(x) + i\alpha\pi x/L}, \quad (8)$$

where ϵ is a cutoff, while right/left ($\alpha = \pm$) bosonic fields $\varphi_{j\alpha}(x)$ are related to the corresponding densities as

$$\rho_{j\alpha}(x) = \frac{\alpha}{2\pi}\frac{\partial\varphi_{j\alpha}(x)}{\partial x}. \tag{9}$$

The bosonic field has a decomposition

$$\varphi_{j\alpha}(x) = \varphi^0_{j\alpha} + \alpha N_{j\alpha} 2\pi x/L + \bar{\varphi}_{j\alpha}(x), \tag{10}$$

where the number operator $N_{j\alpha}$ and its conjugate $\varphi^0_{j\alpha}$ satisfy the commutation relations

$$[N_{j\alpha}, \varphi^0_{k\beta}] = i\delta_{kj}\delta_{\alpha\beta}, \tag{11}$$

and the periodic field $\bar{\varphi}_{j\alpha}(x) = \bar{\varphi}_{j\alpha}(x + L)$ has a standard form,

$$\bar{\varphi}_{j\alpha}(x) = \sum_k \theta(k\alpha)\sqrt{\frac{2\pi}{L|k|}}e^{-|k|\epsilon/2}\Big(e^{ikx}a_{kj} + e^{-ikx}a^\dagger_{kj}\Big), \tag{12}$$

with a_{kj} and $a^\dagger_{kj}$ satisfying boson commutation relations [$\theta(x)$ is the step function]. The boundary condition for the fermion fields, $\psi_{j\alpha}(x + L) = (-1)^{N_j}\psi_{j\alpha}(x)$, depends on the parity of the number of particles, $N_j = 2N_{j\alpha}$, and follows from the factorization

$$\psi_{j\alpha}(x) = L^{-1/2} : e^{\bar{\varphi}_{j\alpha}(x)} : e^{\varphi^0_{j\alpha}} e^{\alpha N_{j\alpha} 2\pi i x/L}. \tag{13}$$

The Hamiltonian $H = H_0 + H_{int}$ is quadratic in boson fields:

$$H_0 = \sum_{j\alpha}\frac{v_j}{4\pi}\int_0^L dx\Big[\frac{\partial\varphi_{j\alpha}(x)}{\partial x}\Big]^2, \tag{14}$$

and

$$H_{int} = \frac{1}{2}\sum_{jl}\int_0^L dx\int_0^L dy\Big[\sum_\alpha \frac{\alpha}{2\pi}\frac{\partial\varphi_{j\alpha}(x)}{\partial x}\Big]U_{jl}(x-y)\Big[\sum_\beta \frac{\beta}{2\pi}\frac{\partial\varphi_{l\beta}(y)}{\partial y}\Big], \tag{15}$$

where $U_{jl}(x)$ is the screened potential. Using Eqs. (10) and (12), the zero-modes can be separated from the bosonic part. The total Hamiltonian is then just a sum, $H = H_0 + \bar{H}$, of the zero-modes contribution,

$$H_0 = \frac{\pi}{L}\sum_{jl\alpha\beta} N_{j\alpha}\Big(v_j\delta_{jl}\delta_{\alpha\beta} + \frac{u_{jl}}{2}\Big)N_{l\beta}, \tag{16}$$

and periodic bosonic fields contribution

$$\bar{H} = \sum_{qjl} e^{-|q|\epsilon}|q|\Big[v_j\delta_{jl}a^\dagger_{qj}a_{qj} + \frac{u_{jl}}{4}(a^\dagger_{qj} + a_{-qj})(a^\dagger_{-ql} + a_{ql})\Big], \qquad (17)$$

where $u_{jl} = \pi^{-1}\int dx U_{jl}(x)$.

In order to calculate the correlation functions, the Hamiltonian $\bar{H}$ has to be brought to the canonical form. This is done in two steps. First, we perform a two-component Bogolubov transformation in order to eliminate the cross-terms with opposite momenta,

$$a_{qj} = \sum_l (X_{jl}b_{ql} + Y_{jl}b^\dagger_{-ql}), \quad \sum_l (X_{jl}X^\dagger_{ln} - Y_{jl}Y^\dagger_{ln}) = \delta_{jn}. \qquad (18)$$

We then obtain

$$\bar{H} = \sum_{qjl} e^{-|q|\epsilon}|q| b^\dagger_{qj}(X^\dagger - Y^\dagger)_{jl}v_l(X - Y)_{ln}b_{qn}, \qquad (19)$$

where the matrices X and Y must satisfy

$$\sum_{lm}(X^\dagger + Y^\dagger)_{jl}(u_{lm} + v_l\delta_{lm})(X + Y)_{mn} = \sum_l (X^\dagger - Y^\dagger)_{jl}v_l(X - Y)_{ln}. \qquad (20)$$

Second, we diagonalize the Hamiltonian (19) by first presenting the matrices X and Y as

$$X = \cosh\lambda\, O, \quad Y = \sinh\lambda\, O, \qquad (21)$$

where $\lambda_{jl} = \lambda_j\delta_{jl}$ is the diagonal matrix of Bogolubov angles λ_j and O is an orthogonal matrix, and then by introducing new boson operators

$$c_{qj} = \sum_l O_{jl}b_{ql}. \qquad (22)$$

The Hamiltonian $\bar{H}$ then takes the form

$$\bar{H} = \sum_{qj} e^{-|q|\epsilon}|q|\tilde{v}_j c^\dagger_{qj}c_{qj}, \qquad (23)$$

with renormalized Fermi velocities

$$\tilde{v}_j = e^{-2\lambda_j}v_j. \qquad (24)$$

Note that old and new boson operators are related as

$$a_{qj} = \cosh\lambda_j\, c_{qj} + \sinh\lambda_j\, c^\dagger_{-qj}. \qquad (25)$$

Using the decomposition (21), Eq. (20) takes the form $\tilde{O}AO = 0$, where $\tilde{O}$ is the transposed matrix, and the matrix A is given by

$$A_{jl} = u_{jl}e^{\lambda_j+\lambda_l} + \delta_{jl}v_j(e^{2\lambda_j} - e^{-2\lambda_j}). \tag{26}$$

The Bogolubov angles λ_j are found from the condition that all the eigenvalues of A_{jl} vanish. In a two-component case, this yields

$$e^{-2\lambda_1} = \sqrt{Q\frac{v_1 + u_{11} - v_2 Q}{v_1 Q - v_2 - u_{22}}}, \quad e^{-2\lambda_2} = Q/e^{-2\lambda_1},$$
$$Q = \sqrt{\left(1 + \frac{u_{11}}{v_1}\right)\left(1 + \frac{u_{22}}{v_2}\right) - \frac{u_{12}^2}{v_1 v_2}}. \tag{27}$$

Correspondingly, the level spacings are now $\tilde{\Delta}_j = 2\pi\tilde{v}_j/L$.

3.3 Calculation of the Green function

With the Hamiltonian (23), the time-dependence of new operators is standard,

$$c_{kj}(t) = e^{-i\tilde{v}_j|k|t}c_{kj}. \tag{28}$$

Using the relation (25), the periodic fields take the form

$$\bar{\varphi}_{j\alpha}(x,t) = \sum_k \sqrt{\frac{2\pi}{L|k|}}e^{-|k|\epsilon/2}[\theta(k\alpha)\cosh\lambda_j + \theta(-k\alpha)\sinh\lambda_j]$$
$$\times(e^{ikx - i\tilde{v}_j|k|t}c_{kj} + e^{-ikx + i\tilde{v}_j|k|t}c_{kj}^\dagger). \tag{29}$$

The time-dependence of zero-modes can be easily obtained using equation of motion,

$$i\partial\varphi_{j\alpha}^0/\partial t = [\varphi_{j\alpha}^0, H_0], \tag{30}$$

with the zero-mode Hamiltonian (16). The final expression for the total time-dependent bosonic field reads

$$\varphi_{j\alpha}(x,t) = \varphi_{j\alpha}^0 + \alpha N_{j\alpha}2\pi(x - \alpha v_j t)/L - \sum_{l\beta} u_{jl}N_{l\beta}\,\pi t/L + \bar{\varphi}_{j\alpha}(x,t). \tag{31}$$

We are now in position to calculate the Green functions. For this, we separate out annihilation and creation parts of the periodic field (29),

$$\bar{\varphi}_{j\alpha}(x,t) = \bar{\varphi}_{j\alpha}^-(x,t) + \bar{\varphi}_{j\alpha}^+(x,t), \tag{32}$$

which satisfy the following commutation relations

$$[\bar{\varphi}^{-}_{j\alpha}(x,t),\bar{\varphi}^{+}_{j\alpha}(x',t')] = \ln f_\alpha(z_{j\alpha}-z'_{j\alpha})+\mu_i \ln[f_\alpha(z_{j\alpha}-z'_{j\alpha})f_{-\alpha}(z_{j,-\alpha}-z'_{j,-\alpha})], \tag{33}$$

with

$$z_{j\alpha} = x - \alpha\tilde{v}_j t. \tag{34}$$

Then we present the fermion operator (8) in the normal-ordered form,

$$\begin{aligned}
\psi_{j\alpha}(x,t) &= \psi^0_{j\alpha}(x,t)\bar{\psi}_{j\alpha}(x,t),\\
\psi^0_{j\alpha}(x,t) &= e^{iv_j(1+u_{jj}/2)\pi t/L}e^{i\varphi^0_{j\alpha}}e^{i\alpha N_{j\alpha}2\pi z_{j\alpha}/L - i\sum_{l\beta}u_{jl}N_{l\beta}\pi t/L},\\
\bar{\psi}_{j\alpha}(x,t) &= L^{-1/2}(2\pi\epsilon/L)^{\mu_j}e^{i\bar{\varphi}^{+}_{j\alpha}(x,t)}e^{i\bar{\varphi}^{-}_{j\alpha}(x,t)},
\end{aligned} \tag{35}$$

where we again separated out zero-mode and periodic parts. Using Eq. (35) together with commutators (11) and (33), the correlation functions can be straightforwardly calculated. For the Green function (7), we obtain

$$\begin{aligned}
D_\alpha(x,t) = \left(\frac{2\pi\epsilon}{L}\right)^{2(\mu_2+\mu_2)}\frac{e^{-it\delta_P - it\delta_u}}{L^2}&[f_\alpha(z_{1\alpha})]^{1+\mu_1}[f_{-\alpha}(z_{1,-\alpha})]^{\mu_1}\\
&\times[f_{-\alpha}(z_{2,-\alpha})]^{1+\mu_2}[f_\alpha(z_{2\alpha})]^{\mu_2},
\end{aligned} \tag{36}$$

where

$$\mu_i = \sinh^2\lambda_i \tag{37}$$

is the Luttinger liquid interaction parameter, while $\delta_P = \pi(v_1+v_2)/L$ and $\delta_u = \pi(u_{11}+u_{22}+2u_{12})/2$ are energy shifts due the changes in the parity of electron and hole numbers and in the Coulomb energy, caused by a removal of an electron-hole pair. The coordinate dependence of $D_\alpha(x,t)$ is determined by (with $\alpha = \pm$)

$$f_\alpha(z_{j\alpha}) = \frac{1}{1-e^{i\alpha(2\pi z_{j\alpha}/L+\alpha i\bar{\epsilon})}}, \tag{38}$$

where $\bar{\epsilon} = 2\pi\epsilon/L$ is the dimensionless cutoff. We assume that the screened interaction is the same for electrons and holes, $u_{11} = u_{22} = -u_{12} = u$, so that $\delta_u = 0$. After neglecting the parity phase δ_P (which can be absorbed into the frequency), we finally write

$$D_\pm(x,t) = \frac{\bar{\epsilon}^{2(\mu_2+\mu_2)}}{L^2}[f_\pm(z_{1\pm})]^{1+\mu_1}[f_\mp(z_{1\mp})]^{\mu_1}[f_\mp(z_{2\mp})]^{1+\mu_2}[f_\pm(z_{2\pm})]^{\mu_2}. \tag{39}$$

The interaction strength is characterized by the ratio u/v_j, where

$$u = \frac{1}{\pi}\int dx U(x) \tag{40}$$

is the Fourier of screened potential; this ratio represents the average (screened) interaction in units of the (bare) level spacing near the Fermi energy. For weak interactions, $u/v_j \ll 1$, we have

$$\mu_j \simeq \left(\frac{u}{4v_j}\right)^2, \quad \tilde{\Delta}_j \simeq \Delta_j \left(1 + \frac{u}{2v_j}\right). \tag{41}$$

Note finally that the above calculation is easily generalized if the ring is penetrated by a magnetic flux ϕ. In this case, the electron and hole number operators should be shifted by flux-dependent constants, $N_{1\alpha} \to N_{1\alpha} + \alpha\phi/\phi_0$ and $N_{2\alpha} \to N_{2\alpha} - \alpha\phi/\phi_0$, where ϕ_0 is the flux quantum. This results in the replacement $\delta_P \to \delta_P(1 - 2\alpha\phi/\phi_0)$ in Eq. (36).

3.4 Derivation of oscillator strengths

The correlator $D_\alpha(x,t)$ is periodic in variables $z_{j\alpha}$. In order to carry out the integration in Eq. (6) we first perform the Fourier expansion of $[f_\alpha(z_{j\alpha})]^\nu$ as

$$[f_\alpha(z_{j\alpha})]^\nu = \sum_n b_\nu(n) e^{i\alpha 2\pi n z_{j\alpha}/L}, \quad b_\nu(n) = \frac{\sin \pi\nu}{\pi} B(n+\nu, 1-\nu), \tag{42}$$

Substituting this Fourier expansion into Eq. (39), the Green function $D_\alpha(\omega)$ takes the form

$$D_\pm(\omega) = \bar{\epsilon}^{2(\mu_1+\mu_2)} \sum_{\{n\}} b_{1+\mu_1}(n_1) b_{\mu_1}(n_1') b_{1+\mu_2}(n_2) b_{\mu_2}(n_2') \Lambda_\pm(\omega, \{n\}), \tag{43}$$

with

$$\begin{aligned}\Lambda_\pm(\omega,\{n\}) &= \frac{1}{L^2}\int dt \int_0^L dx \exp\Big[-i\omega t \pm i\frac{2\pi}{L}(n_1 z_{1\pm} - n_1' z_{1\mp} - n_2 z_{2\mp} \\ &\qquad + n_2' z_{2\pm})\Big] \\ &= \frac{2\pi}{L}\delta_{n_1-n_1',n_2-n_2'}\delta\Big[\omega + \frac{2\pi\tilde{v}_1}{L}(n_1+n_1') + \frac{2\pi\tilde{v}_2}{L}(n_2+n_2')\Big],\end{aligned} \tag{44}$$

where we absorbed the parity shift δ_P into ω. The Kronecker delta and the delta-function reflect the conservation of momentum and energy, respectively. Thus, we obtain

$$D_\alpha(\omega) = \frac{2\pi}{L}\sum_{mn} C_{mn}\delta(\omega + \tilde{\Delta}_1 m + \tilde{\Delta}_2 n), \tag{45}$$

with

$$C_{mn} = \bar{\epsilon}^{2(\mu_1+\mu_2)} \sum_l b_{1+\mu_1}[(m+n)/2 - l] b_{1+\mu_2}(n-l) b_{\mu_1}[(m-n)/2 + l] b_{\mu_2}(l). \tag{46}$$

From Eq. (45), the emission spectrum (3) follows. Finally, using integral representation for the Beta-function in Eq. (42) we arrive at

$$C_{mn} = \int_{-\pi}^{\pi} \frac{d\phi_1 d\phi_2 d\phi_3 \, \bar{\epsilon}^{2(\mu_1+\mu_2)} \, e^{-\frac{i}{2}(\phi_1+\phi_2)(m+n)+\frac{i}{2}\phi_3(m-n)}}{(2\pi)^3 (1-e^{i\phi_1})^{1+\mu_1} (1-e^{i\phi_2})^{1+\mu_2} (1-e^{i(\phi_2-\phi_3)})^{\mu_1} (1-e^{i(\phi_1+\phi_3)})^{\mu_2}}. \tag{47}$$

Note, that the sum in Eq. (3) is constrained by the selection rule that m and n are of the same parity, i.e., the combinations

$$N = (m+n)/2, \quad M = (m-n)/2, \tag{48}$$

which enter into the rhs of Eq. (47), are integers, as can be seen from Eq. (44). This is the result of the linear dispersion of electrons and holes near the Fermi levels.

It is easy to see that Eq. (47) correctly reproduces the non-interacting limit. Indeed, upon setting $\mu_i = 0$, the integral over ϕ_3 yields $C_{mn} = \delta_{mn}$. Another important limiting case $m, n \gg 1$ corresponds to the transitions well away from the Fermi edge. In this case, the main contribution to the integral (47) comes from the domain $\phi_1 + \phi_2 \sim (m+n)^{-1} \ll 1$. Within this domain, one can neglect the difference between ϕ_1 and $-\phi_2$ in the last two factors in the denominator. Then the integrals over ϕ_1, ϕ_2 factorize, yielding

$$C_{mn} = \frac{\Gamma(N+1+\mu_1)\Gamma(N+1+\mu_2)}{\Gamma(1+\mu_1)\Gamma(1+\mu_2)[\Gamma(N+1)]^2} K(M), \tag{49}$$

with

$$K(M) = \int_{-\pi}^{\pi} \frac{d\phi}{2\pi} \frac{\bar{\epsilon}^{2(\mu_1+\mu_2)} \, e^{iM\phi}}{(1-e^{-i\phi})^{\mu_1} (1-e^{i\phi})^{\mu_2}} = \frac{\epsilon^{2(\mu_1+\mu_2)} (-1)^M \Gamma(1-\mu_1-\mu_2)}{\Gamma(1-M-\mu_1)\Gamma(1+M-\mu_2)}, \tag{50}$$

where $\Gamma(x)$ is the Gamma-function. It can be seen from Eq. (50) that, for a given N, the oscillator strengths, C_{mn}, fall off as $C_{mn} \propto |M|^{\mu_1+\mu_2-1}$ with increasing $|M| = \frac{1}{2}|m-n|$. This slow power-law decay reveals strong correlations within electron-hole system on a ring. Finally, using the large x asymptotics of $\Gamma(x)$, we obtain the expression for the oscillator strengths

valid for $|m-n| \gg 1$,

$$C_{mn} = \frac{\bar{\epsilon}^{2\mu}\Gamma(1-\mu)}{\Gamma(1+\mu_1)\Gamma(1+\mu_2)} \frac{\sin \pi\tilde{\mu}}{\pi} \left(\frac{m+n}{2}\right)^{\mu} \left|\frac{m-n}{2}\right|^{\mu-1}, \qquad (51)$$

where

$$\mu = \mu_1 + \mu_2, \quad \tilde{\mu} = \frac{1}{2}\mu + \frac{1}{2}(\mu_1 - \mu_2)\mathrm{sgn}(m-n). \qquad (52)$$

4 FINE STRUCTURE OF THE EMISSION SPECTRUM

The general expression (47) determines the heights of the emission peaks, while the *order* of the peaks with different $\{m,n\}$ is governed by the δ-functions in Eq. (3), which ensure the energy conservation. Therefore, this order depends crucially on the relation between $\tilde{\Delta}_1$ and $\tilde{\Delta}_2$. Moreover, a *commensurability* between $\tilde{\Delta}_1$ and $\tilde{\Delta}_2$ leads to accidental degeneracies in the positions of the emission lines. However, in order to establish the general properties of the spectrum, it is instructive to consider first several cases of commensurate $\tilde{\Delta}_1$ and $\tilde{\Delta}_2$.

4.1 Symmetric case

We start with the symmetric case $\tilde{\Delta}_i = \tilde{\Delta}/2$ (and, hence, $\mu_i = \mu/2$). The peak positions, as determined by Eq. (3), coincide with those for single-particle transitions, $|\omega| = N\tilde{\Delta}$. The corresponding oscillator strengths can be straightforwardly evaluated from Eq. (47) as

$$c_N = \sum_M C_{N+M,N-M} = \left[\int_{-\pi}^{\pi} \frac{d\phi}{2\pi} \frac{\bar{\epsilon}^{\mu} e^{-iN\phi}}{(1-e^{i\phi})^{1+2\mu}}\right]^2. \qquad (53)$$

For $N \gg 1$, the denominator of the integrand can be expanded, yielding

$$c_N \simeq (\bar{\epsilon}N)^{2\mu} = \left|\frac{\bar{\epsilon}\omega}{\tilde{\Delta}}\right|^{2\mu}. \qquad (54)$$

Note that single-particle oscillator strengths correspond to $c_N = 1$. We thus conclude that interactions affect strongly the peak heights for $|\omega/\tilde{\Delta}|^{2\mu} \gg 1$, i.e., in the high frequency domain. In fact, even for an arbitrary relation between $\tilde{\Delta}_1$ and $\tilde{\Delta}_2$, the crossover between "single-particle" and "many-body" domains of the spectrum is governed by the dimensionless parameter

$$\xi = \mu \ln \frac{|\omega|}{\tilde{\Delta}_1 + \tilde{\Delta}_2}. \qquad (55)$$

4.2 Commensurate case

Now consider the case when the level spacings in the conduction and valence band are commensurate:

$$\frac{\tilde{\Delta}_1}{\tilde{\Delta}_2} = \frac{p}{q}, \tag{56}$$

where p and q are integers. Introducing a notation

$$\tilde{\Delta} = \tilde{\Delta}_1 + \tilde{\Delta}_2, \tag{57}$$

the Green function (45) takes the form

$$D_\alpha(\omega) = \frac{2\pi}{L}\sum_{mn} C_{mn}\delta\Big(\omega + \tilde{\Delta}\frac{mp+nq}{p+q}\Big) = \frac{2\pi}{L}\sum_k C_k\delta(\omega + \tilde{\Delta}k/Q), \tag{58}$$

where $Q = p+q$, $P = p-q$, and

$$\begin{aligned} C_k &= \sum_{mn}\delta_{k,mp+nq}C_{mn} = \sum_{MN}\delta_{k,MP+NQ}C_{N+M,N-M} \\ &= \sum_{MN}\delta_{k-MP,NQ}C_{\frac{k}{Q}+M\left(1-\frac{P}{Q}\right),\frac{k}{Q}-M\left(1+\frac{P}{Q}\right)}. \end{aligned} \tag{59}$$

Using the relation

$$\sum_N \delta_{k,NQ} = \frac{1}{Q}\sum_{l=0}^{Q-1} e^{-i2\pi lk/Q}, \tag{60}$$

the oscillator strengths can be presented as

$$C_k = \frac{1}{Q}\sum_{l=0}^{Q-1} e^{-i2\pi lk/Q} f_l(k), \tag{61}$$

with

$$f_l(k) = \sum_M e^{i2\pi lMP/Q} C_{\frac{k}{Q}+M\left(1-\frac{P}{Q}\right),\frac{k}{Q}-M\left(1+\frac{P}{Q}\right)}. \tag{62}$$

Using integral representation (47), the sum over M can be explicitly performed. For $k/Q = |\omega|/\tilde{\Delta} \gg 1$, the resulting expression for coefficients f_l takes the form

$$\begin{aligned} f_l(k) = \int_{-\infty}^{\infty} &\frac{d\phi_1 d\phi_2\, i^{2+\mu_1+\mu_2}\,\bar{\epsilon}^{2(\mu_1+\mu_2)}\, e^{-i(\phi_1+\phi_2)k/Q}}{(2\pi)^2(\phi_1)^{1+\mu_1}(\phi_2)^{1+\mu_2}(1-s_l-is_l[\phi_2+(\phi_1+\phi_2)P/Q])^{\mu_1}} \\ &\times \frac{1}{(1-s_l^*-is_l^*[\phi_1-(\phi_1+\phi_2)P/Q])^{\mu_2}}, \end{aligned} \tag{63}$$

where $s_l = e^{i2\pi lP/Q}$. The l-dependence of $f_l(k)$ is determined by the relative magnitude of Q/k and $|1 - s_l|$:

$$f_l(k) \simeq \left|\frac{\bar{\epsilon}k}{Q}\right|^{2(\mu_1+\mu_2)} \tag{64}$$

for $k/Q \ll |1 - s_l|^{-1}$, and

$$f_l(k) \simeq \left(\frac{\bar{\epsilon}^2 k/Q}{1 - s_l}\right)^{\mu_1} \left(\frac{\bar{\epsilon}^2 k/Q}{1 - s_l^*}\right)^{\mu_2} \tag{65}$$

for $k/Q \gg |1 - s_l|^{-1}$, with the two estimates matching at $k/Q \sim |1 - s_l|^{-1}$.

Summarising, each "parent" single-particle peak, corresponding to $k = nQ$ in Eq. (58), acquires $Q - 1$ shakeup satellites separated in energy by $\tilde{\Delta}/Q$. Such equidistant distribution of satellite positions is due to periodicity in the excitation spectrum caused by commensurate level spacings in conduction and valence band. The oscillator strengths depends strongly on frequency, $\omega/\tilde{\Delta} = k/Q$, as indicated by Eqs. (61,64,65). The emergence of satellite peaks with increasing $\omega/\tilde{\Delta}$ is demonstated below for the simplest case when each single-particle peak acquires just one satellite.

4.3 Case $\tilde{\Delta}_1 = 3\tilde{\Delta}_2$

Consider now the case $\tilde{\Delta}_1 = 3\tilde{\Delta}_2$ (and thus $\mu_2 \simeq 9\mu_1$) which corresponds to the doubling of luminescence peaks number as compared to noninteracting case. Indeed, as follows from Eq. (3), here the peak spectral positions are given by

$$\frac{|\omega|}{\tilde{\Delta}} = \frac{n}{2}. \tag{66}$$

For $P = 2$ and $Q = 4$, so that $s_l = (-1)^l$, the coefficients f_l take two different values depending on the parity of l [see Eqs. (64,65)],

$$f_{even}(k) \simeq \left|\frac{\bar{\epsilon}k}{4}\right|^{2\mu} = \left|\frac{\bar{\epsilon}\omega}{\tilde{\Delta}}\right|^{2\mu}, \tag{67}$$

$$f_{odd}(k) \simeq \left|\frac{\bar{\epsilon}^2 k}{8}\right|^{\mu} = \left|\frac{\bar{\epsilon}^2\omega}{2\tilde{\Delta}}\right|^{\mu}, \tag{68}$$

yielding [see Eq. (61)],

$$C_k = \left|\frac{\bar{\epsilon}\omega}{\tilde{\Delta}}\right|^{2\mu} \frac{1 + (-1)^k}{2} \frac{1 + e^{i\pi k/2}|\frac{\tilde{\Delta}}{2\omega}|^{\mu}}{2}, \tag{69}$$

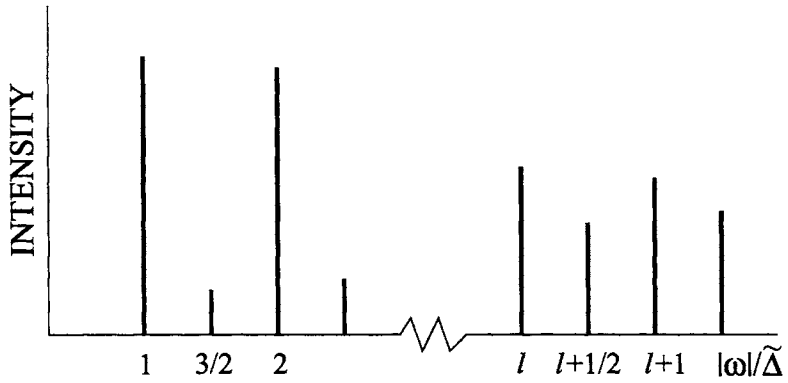

Figure 4: Emission spectrum for $\tilde{\Delta}_1 = 3\tilde{\Delta}_2$. In low-frequency domain, the single-particle peaks acquire weak many-body shakeup satellites. In high-frequency domain, the heights of the parent ($|\omega|/\tilde{\Delta} = l$) and satellite ($|\omega|/\tilde{\Delta} = l + 1/2$) peaks are close to each other.

with $\mu = \mu_1 + \mu_2$. Obviously, $C_k = 0$ for k odd. For k even, we have

$$C_{4l} \simeq \left|\frac{\bar{\epsilon}\omega}{\tilde{\Delta}}\right|^{2\mu} \frac{1 + |\frac{\tilde{\Delta}}{2\omega}|^{\mu}}{2}, \tag{70}$$

$$C_{4l+2} \simeq \left|\frac{\bar{\epsilon}\omega}{\tilde{\Delta}}\right|^{2\mu} \frac{1 - |\frac{\tilde{\Delta}}{2\omega}|^{\mu}}{2}, \tag{71}$$

and we finally obtain

$$D_{\pm}(\omega) = \frac{2\pi}{L}\left|\frac{\bar{\epsilon}\omega}{\tilde{\Delta}}\right|^{2\mu} \sum_l \left[\frac{1 + |\frac{\tilde{\Delta}}{2\omega}|^{\mu}}{2}\,\delta(\omega + \tilde{\Delta}l) + \frac{1 - |\frac{\tilde{\Delta}}{2\omega}|^{\mu}}{2}\,\delta\Big[\omega + \tilde{\Delta}\Big(l + \frac{1}{2}\Big)\Big]\right], \tag{72}$$

with $\mu = \mu_1 + \mu_2 \simeq 10\mu_1$ and $\tilde{\Delta} = \tilde{\Delta}_1 + \tilde{\Delta}_2 = 4\tilde{\Delta}_1$.

The above result illustrates how the structure of the spectrum evolves as the frequency departs from the Fermi edge. For $\xi = \mu \ln|\frac{\omega}{\tilde{\Delta}}| \ll 1$, each single-particle peak, $|\omega| = l\tilde{\Delta}$ acquires a weak shakeup satellite at $|\omega| = (l + \frac{1}{2})\tilde{\Delta}$. In the opposite limit, $\xi \gg 1$, the oscillator strength of an "integer" peak is equally redistributed between the doublet components. The crossover frequency, separating the "single-particle" and the developed many-body domains of the spectrum is determined by the condition $\xi \sim 1$, or, $\omega \sim \tilde{\Delta}e^{1/\mu}$. The spectrum (72) is schematically depicted in Fig. 4.

4.4 General structure of the smission spectrum

Let us turn to the structure of the spectrum in the general case of incommensurate $\tilde{\Delta}_1$ and $\tilde{\Delta}_2$. We start from the observation that the peak posi-

tions can be classified by "generations". Namely, once a peak $\{m,0\}$ (or $\{0,n\}$) emerges at $\omega=\omega_m=-m\tilde{\Delta}_1$ (or $\omega=\omega_n=-n\tilde{\Delta}_2$), it is followed by next generations of peaks $\omega_m^{(k)}=\omega_m-k(\tilde{\Delta}_1+\tilde{\Delta}_2)$ or $\omega_n^{(k)}=\omega_n-k(\tilde{\Delta}_1+\tilde{\Delta}_2)$ repeating with a period $\tilde{\Delta}=\tilde{\Delta}_1+\tilde{\Delta}_2$. Thus, for a crude description of the spectrum away from the Fermi edge it is convenient to divide the frequency region $\omega<0$ into the intervals of width $\tilde{\Delta}$.

The number of peaks within the spectral interval $\{-|\omega|,-|\omega|-\tilde{\Delta}\}$ is the number of integers satisfying the conditions

$$|\omega|<m\tilde{\Delta}_1+n\tilde{\Delta}_2<|\omega|+\tilde{\Delta}. \tag{73}$$

This number is equal to

$$\mathcal{N}_\omega=\frac{|\omega|\tilde{\Delta}}{2\tilde{\Delta}_1\tilde{\Delta}_2}, \tag{74}$$

where we assumed $|\omega|\gg\tilde{\Delta}$ and took into account the parity restriction. From Eq. (74) we find the peak density

$$g_\omega=\frac{\mathcal{N}_\omega}{\tilde{\Delta}}=\frac{|\omega|}{2\tilde{\Delta}_1\tilde{\Delta}_2}. \tag{75}$$

It also follows from Eq. (74) that

$$\delta\mathcal{N}=\mathcal{N}_{\omega-\tilde{\Delta}}-\mathcal{N}_\omega=\frac{\tilde{\Delta}^2}{2\tilde{\Delta}_1\tilde{\Delta}_2} \tag{76}$$

generations start within each interval independently of frequency. Since the heights of consecutive peaks within the interval $\tilde{\Delta}$ vary non-monotonically, it is natural to characterize these heights by the distribution function

$$F(\mathcal{C})=\frac{1}{2g_\omega}\int_0^\infty dm\,dn\,\delta(\omega+m\tilde{\Delta}_1+n\tilde{\Delta}_2)\,\delta(C_{mn}-\mathcal{C}), \tag{77}$$

where C_{mn} is given by Eq. (51). Here we made use of the fact that $\mathcal{N}_\omega\gg 1$ by treating m and n as continuous variables. The prefactor in Eq. (77) ensures the normalization ($\int_0^\infty d\mathcal{C}F(\mathcal{C})=1$). It is easy to see that $F(\mathcal{C})$ is nonzero in the interval $(\mathcal{C}_{min},\mathcal{C}_{max})$, where (hereafter we omit the cutoff)

$$\begin{aligned}\mathcal{C}_{min} &= \min\{2\mu_{1,2}|\frac{\tilde{\Delta}_{1,2}}{\omega}|^{1-2\mu}\},\\ \mathcal{C}_{max} &= 2|\frac{\omega}{\tilde{\Delta}}|^{\mu}\max\{\mu_{1,2}\}.\end{aligned} \tag{78}$$

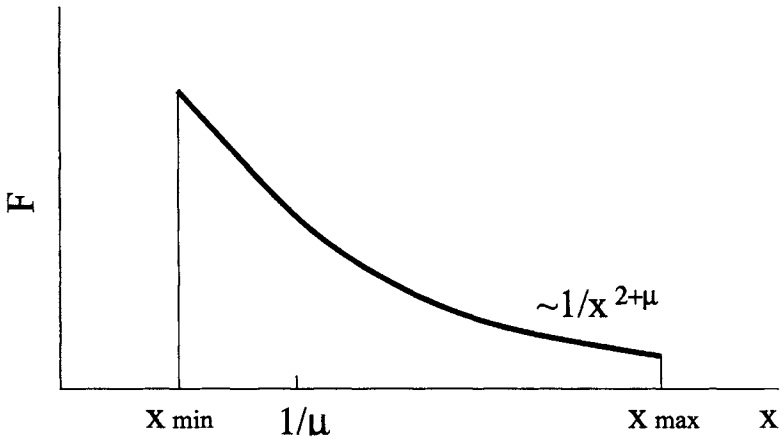

Figure 5: The distribution function (77) of the peak heights within the interval $\tilde{\Delta}$ is plotted schematically versus $x = \mathcal{C}/\mathcal{C}_*$. The minimal value of x is $x_{min} \sim 1$, while $x_{max} \sim |\omega/\tilde{\Delta}|^{1-\mu} \gg 1$. The point $x = \mu^{-1}$ corresponds to the average oscillator strength.

Within this wide interval, the distribution function falls off as

$$F(\mathcal{C}) \sim \left(\frac{\mathcal{C}_0}{\mathcal{C}}\right)^{2+\mu}, \quad \mathcal{C}_0 = \mu\left|\frac{\omega}{4}\left(\frac{1}{\tilde{\Delta}_1} + \frac{1}{\tilde{\Delta}_2}\right)\right|^{2\mu-1} \tag{79}$$

where $\mathcal{C}_0$ is the *typical* value of the oscillator strength. On the other hand, the *average* oscillator strength, which can be easily calculated from Eq. (77), is equal to $\overline{\mathcal{C}} = \mu^{-1}\mathcal{C}_0 \gg \mathcal{C}_0$. The distribution function $F(\mathcal{C})$ is schematically depicted in Fig. 5. The fact that $\overline{\mathcal{C}}$ *decreases* with $|\omega|$ can be understood in the following way. As it is seen from Eq. (54), in the symmetric case, with only a single peak per interval $\tilde{\Delta}$, the peak heights increase with $|\omega|$ as $|\frac{\omega}{\tilde{\Delta}}|^{2\mu}$. In the general case, this spectral intensity gets redistributed between $\mathcal{N}_\omega$ different peaks. Thus,

$$\overline{\mathcal{C}} \sim \mathcal{N}_\omega^{-1}\left|\frac{\omega}{\tilde{\Delta}}\right|^{2\mu} \propto |\omega|^{2\mu-1}. \tag{80}$$

5 CONCLUDING REMARKS

The underlying origin of the multitude of many-body lines in the emission spectrum from quantum-confined systems is that a recombination is accompanied by shakeup processes whose number increases as the frequency deviates from the Fermi edge. The theoretical value of the dimensionless

interaction parameter μ is determined by the ratio of screened interaction U to the level spacings $\tilde{\Delta}_1, \tilde{\Delta}_2$ at the corresponding Fermi levels. Both quantities depend on the number of excited carriers, N, which in turn is determined by the excitation intensity. This, and the sensitivity of the screening to the details of experimental setup, lead to a common ambiguity in the theoretical determination of μ. For example, in quantum wires, the value of μ measured in resonant tunneling experiments, [112, 113] was significantly larger then theoretical estimates. Concerning the estimates for $\tilde{\Delta}_1$ and $\tilde{\Delta}_2$, in the experimental paper Ref. [93] on luminescence from ring-shape dots the total energy separation $\tilde{\Delta}$ between the lowest levels was approximately $5mev$. This value comes almost exclusively from the conduction band, due to the large ratio of the electron and hole effective masses. Both $\tilde{\Delta}_1$ and $\tilde{\Delta}_2$ increase linearly with increasing N. This implies that the shake-up processes within the hole system are experimentally much more relevant than those for electrons.

T.V.S. was supported by the Army High Performance Computing Research Center under the auspices of the Department of the Army, Army Research Laboratory under Cooperative Agreement No DAAD19-01-2-0014, and by the National Science Foundation under Grant Nos DMR-0304036 and DMR-0305557. M.E.R. was supported by the National Science Foundation under Grant No. DMR-0202790 and by Petroleum Research Fund under Grant No. 37890-AC6.

REFERENCES

[1] K. Brunner, U. Bockelmann, G. Abstreiter, M. Walter, G. Bohm, G. Trankle, and G. Weimann Phys. Rev. Lett., 69 (1992) 3216.
[2] J.-Y. Marzin, J.-M. Jérard, A. Israël, D. Barrier, and G. Bastard, Phys. Rev. Lett., 73 (1994) 716.
[3] A. Zrenner, J. Chem. Phys., 112 (2000) 7790.
[4] D. Gammon, Nature, 405 (2000) 899.
[5] P. W. Anderson, Phys. Rev. Lett., 18 (1967) 1049.
[6] G. D. Mahan, Phys. Rev., 153 (1967) 882.
[7] P. Nozieres and C. T. de Dominicis, Phys. Rev., 178 (1969) 1097.
[8] D. C. Langreth, Phys. Rev. B, 1 (1970) 471.
[9] R. Sooryakumar, A. Pinczuk, A. C. Gossard, D. S. Chemla, and L. J. Sham, Phys. Rev. Lett., 58 (1987) 1150.

[10] A. E. Ruckenstein, S. Schmitt-Rink and R. C. Miller, Phys. Rev. Lett., 56 (1986) 504.
[11] A. E. Ruckenstein and S. Schmitt-Rink, Phys. Rev. B, 35 (1987) 7551.
[12] M. S. Skolnick, J. M. Rorison, K. J. Nash, D. J. Mowbray, P. R. Tapster, S. J. Bass, and A. D. Pitt, Phys. Rev. Lett., 58 (1987) 2130.
[13] G. Livescu, D. A. B. Miller, D. S. Chemla, M. Ramaswamy, T. Y. Chang, N. Sauer, A. C. Gossard and J. H. English, IEEE J. Quantum Electron., 24 (1988) 1677.
[14] S. Schmitt-Rink, D. S. Chemla, and D. A. B. Miller, Adv. Phys., 38 (1989) 89.
[15] H. Kalt, K. Leo, R. Cingolani, and K. Ploog Phys. Rev. B, 40 (1989) 12017.
[16] G. D. Mahan, *Many-Particle Physics* (Plenum, New York, 1990).
[17] K. Ohtaka and Y. Tanabe, Rev. Mod. Phys., 62 (1990) 929.
[18] P. Livins and S. E. Schnatterly, Phys. Rev. B, 37 (1988) 6742.
[19] P. Hawrylak, Phys. Rev. B, 42 (1990) 8986.
[20] F. D. M. Haldane, J. Phys. C, 14 (1981) 2585.
[21] A. Gogolin, Phys. Rev. Lett., 71 (1993) 2995.
[22] N. V. Prokof'ev, Phys. Rev. B, 49 (1994) 2148.
[23] C. L. Kane, K. A. Matveev, and L. I. Glazman, Phys. Rev. B, 49 (1994) 2253.
[24] M. Potemski, R. Stepniewski, J. C. Maan, G. Martinez, P. Wyder, and B. Etienne, Phys. Rev. Lett., 66 (1991) 2239.
[25] L. V. Butov, V. I. Grinev, V. D. Kulakovskii, and T. G. Andersson Phys. Rev. B, 46 (1992) 13627.
[26] K. J. Nash, M. S. Skolnick, M. K. Saker, and S. J. Bass, Phys. Rev. Lett., 70 (1993) 3115.
[27] M. S. Skolnick, D. J. Mowbray, D. M. Whittaker, and R. S. Smith, Phys. Rev. B, 47 (1993) 6823.
[28] M. S. Skolnick, K. J. Nash, M. K. Saker, and S. J. Bass, Phys. Rev. B, 50 (1994) 11771.
[29] G. Finkelstein, H. Shtrikman, and I. Bar-Joseph Phys. Rev. B, 56 (1997) 10326.
[30] J. Rubio, H. P. van der Meulen, J. M. Calleja, V. Härle, R. Bergmann, and F. Scholz, Phys. Rev. B, 55 (1997) 16390.
[31] M. J. Manfra, B. B. Goldberg, L. Pfeiffer, and K. West, Phys. Rev. B, 57 (1998) 9467.

[32] K. Asano and T. Ando, Phys. Rev. B, 65 (2002) 115330.
[33] T. Uenoyama and L. J. Sham, Phys. Rev. B,39 (1989) 11044.
[34] S. Katayama, T. Ando, Solid State Commun., 70 (1989) 97.
[35] P. Hawrylak, Phys. Rev. B, 44 (1991) 11236.
[36] In strong magnetic field, valence band mixing can give rise to interband transitions with different Landau levels, see S.-R. E. Yang and L. J. Sham, Phys. Rev. Lett., 58 (1987) 2598.
[37] I. V. Lerner and Yu. E. Lozovik, Zh. Exp. Teor. Fiz., 80 (1981) 1488 [Sov. Phys.-JETP, 53 (1981) 763].
[38] S. Glasberg, H. Shtrikman, and I. Bar-Joseph, Phys. Rev. B, 63 (2001) 201308.
[39] M. Kubisa, L. Bryja, K. Ryczko, J. Misiewicz, C. Bardot, M. Potemski, G. Ortner, M. Bayer, A. Forchel, and C. B. Srensen, Phys. Rev. B, 67 (2003) 035305.
[40] L. Gravier, M. Potemski, P. Hawrylak, and B. Etienne, Phys. Rev. Lett., 80 (1998) 3344.
[41] L. Osborne, A. J. Shield M. Y. Simmons, N. R. Cooper, D. A. Ritchie, and M. Pepper, Phys. Rev. B, 58 (1998) 4427.
[42] S. Takeyama, G. Karczewski, T. Wojtowicz, J. Kossut, H. Kunimatsu, K. Uchida, and N. Miura, Phys. Rev. B, 59 (1999) 7327.
[43] F. M. Munteanu, Y. Kim, C. H. Perry, D. Heiman, D. G. Rickel, M. Sundaram, and A. C. Gossard, Phys. Rev. B, 62 (2000) 4249.
[44] N. R. Cooper and D. B. Chklovskii, Phys. Rev. B, 55 (1997) 2436.
[45] P. Hawrylak and M. Potemski, Phys. Rev. B, 56 12 (1997) 386.
[46] Y. Kim, F. M. Munteanu, C. H. Perry, D. G. Rickel, J. A. Simmons, L. N. Pfeiffer, and K. W. West, Phys. Rev. B, 64 (2001) 195302.
[47] F. Plentz, D. Heiman, L. N. Pfeiffer, and K. W. West, Phys. Rev. B, 57 (1998) 1370.
[48] A. Zangwill and P. Soven, Phys. Rev. B, 24 (1981) 4121.
[49] F. Gel'mukhanov and H. Agren, Phys. Rep., 312 (1999) 87.
[50] G. B. Armen, H. Aksela, T. Aberg, S. Aksela, J. Phys. B, 33 (2000) R49.
[51] M. Ikezawa, Y. Masumoto, T. Takagahara, and S. V. Nair, Phys. Rev. Lett., 79, (1997) 3522.
[52] L. Landin M. S. Miller, M.-E. Pistol, C. E. Pryor, and L. Samuelson, Science, 280 (1998) 262.
[53] M. Bayer, T. Gutbrod, A. Forchel, V. D. Kulakovskii, A. Gorbunov, M. Michel, R. Steffen, and K. H. Wang, Phys. Rev. B, 58 (1998) 4740.

[54] V. D. Kulakovskii, G. Bacher, R. Weigand, T. Kummell, A. Forchel, E. Borovitskaya, K. Leonardi, and D. Hommel, Phys. Rev. Lett., 82 (1999) 1780.
[55] E. Dekel, D. Gershoni, E. Ehrenfreund, D. Spector, J. M. Garcia, and P. M. Petroff, Phys. Rev. Lett., 80 (1998) 4991.
[56] E. Dekel, D. Gershoni, E. Ehrenfreund, J. M. Garcia, and P. M. Petroff, Phys. Rev. B, 61 (2000) 11009.
[57] E. Dekel, D. V. Regelman, D. Gershoni, E. Ehrenfreund, W. V. Schoenfeld, and P. M. Petroff, Phys. Rev. B, 62 (2000) 11038.
[58] F. Findeis, A. Zrenner, G. Bohm, and G. Abstreiter, Solid State Commun., 114 (2000) 227.
[59] M. Bayer, O. Stern, P. Hawrylak, S. Fafard, and A. Forchel, Nature, 405 (2000) 923.
[60] E. Dekel, D. V. Regelman, D. Gershoni, E. Ehrenfreund, W. V. Schoenfeld, and P. M. Petroff, Solid State Commun., 117 (2001) 395.
[61] D. V. Regelman, U. Mizrahi, D. Gershoni, E. Ehrenfreund, W. V. Schoenfeld, and P. M. Petroff, Phys. Rev. Lett., 87 (2001) 257401.
[62] D. V. Regelman, E. Dekel, D. Gershoni, E. Ehrenfreund, A. J. Williamson, J. Shumway, A. Zunger, W. V. Schoenfeld, and P. M. Petroff, Phys. Rev. B, 64 (2001) 165301.
[63] K. Hinzer, P. Hawrylak, M. Korkusinski, S. Fafard, M. Bayer, O. Stern, A. Gorbunov, and A. Forchel, Phys. Rev. B, 63 (2001) 075314.
[64] M. Bayer, G. Ortner, O. Stern, A. Kuther, A. A. Gorbunov, A. Forchel, P. Hawrylak, S. Fafard, K. Hinzer, T. L. Reinecke, S. N. Walck, J. P. Reithmaier, F. Klopf, and F. Schfer, Phys. Rev. B, 65 (2002) 195315.
[65] P. Hawrylak, Phys. Rev. B, 60 (1999) 5597.
[66] M. Combescot and P. Nozieres, J. Phys (Paris), 32 (1971) 913.
[67] P. Hawrylak, Phys. Rev. B, 44 (1991) 3821.
[68] S. A. Brown, J. F. Young, J. A. Brum, P. Hawrylak, and Z. Wasilewski, Phys. Rev. B, 54 (1996) 11082; 56 (1997) 1637.
[69] V. Huard, R. T. Cox, K. Saminadayar, A. Arnoult and S. Tatarenko, Phys. Rev. Lett., 84 (2000) 187.
[70] G. Yusa, H. Shtrikman, and I. Bar-Joseph, Phys. Rev. B, 62 (2000) 15390.
[71] K. Kheng, R. T. Cox, Merle Y. d' Aubignè, Franck Bassani, K. Saminadayar, and S. Tatarenko, Phys. Rev. Lett., 71 (1993) 1752.
[72] G. Finkelstein, H. Shtrikman, and I. Bar-Joseph Phys. Rev. Lett., 74 (1995) 976.

[73] A. J. Shields, M. Pepper, M. Y. Simmons, and D. A. Ritchie, Phys. Rev. B, 52 (1995) 7841.
[74] G. Finkelstein, H. Shtrikman, and I. Bar-Joseph, Phys. Rev. B, 53 (1996) 12593.
[75] J. R. Chapman, N. F. Johnson, and V. N. Nicopoulos Phys. Rev. B, 57 (1998) 1762.
[76] Y. Toda, O. Moriwaki, M. Nishioka, and Y. Arakawa, Phys. Rev. Lett., 82 (1999) 4114.
[77] L. V. Butov, V. D. Kulakovskii, E. Lach, A. Forchel, and D. Grtzmacher, Phys. Rev. B, 44 (1991) 10680.
[78] L. V. Butov, V. D. Egorov, V. D. Kulakovskii, and T. G. Andersson, Phys. Rev. B, 46, (1992) 15156.
[79] S. Glasberg, H. Shtrikman, and I. Bar-Joseph, Phys. Rev. B, 63 (2001) 113302.
[80] T. V. Shahbazyan, I. E. Perakis, and M. E. Raikh, Phys. Rev. B, 64 (2001) 115317.
[81] M. Sassetti and B. Kramer, Phys. Phys. Lett., 80, (1998) 1485.
[82] B. Kramer and M. Sassetti, Phys. Phys. B, 62 (2000) 4238.
[83] C. Chapelier, D. Mailly, and A. Benoit, Adv. Solid State Phys., 34 (1995) 163.
[84] J. M. Garcia, G. Medeiros-Ribeiro, K. Schmidt, T. Ngo, J. L. Feng, A. Lorke, J. Kotthaus, and P. M. Petroff, Appl. Phys. Lett., 71 (1997) 2014.
[85] A. Lorke and R. J. Luyken, Physica B, 256 (1998) 424.
[86] A. Lorke, R. J. Luyken, M. Fricke, J. P. Kotthaus, G. Medeiros-Ribeiro, J. M. Garcia, and P. M. Petroff, Microelectron. Eng., 47 (1999) 95.
[87] H. Pettersson, R. J. Warburton, A. Lorke, K. Karrai, J. P. Kotthaus, J. M. Garcia, and P. M. Petroff, Physica E (Amsterdam), 6 (2000) 510.
[88] A. Lorke, R. J. Luyken, A. O. Govorov, J. P. Kotthaus, J. M. Garcia, and P. M. Petroff, Phys. Rev. Lett., 84 (2000) 2223.
[89] P. M. Petroff, A. Lorke, and A. Imamoglu, Physics Today, 54 (2001) 46.
[90] A. Emperador, M. Pi, M. Barranco, and A. Lorke, Phys. Rev. B, 62 (2000) 4573.
[91] Z. Barticevic, G. Fuster, and M. Pacheco, Phys. Rev. B, 65 (2002) 193307.

[92] B. S. Monozon and P. Schmelcher, Phys. Rev. B, 67 (2003) 045203.
[93] R. J. Warburton, C. Schflein, D. Haft, F. Bickel, A. Lorke, K. Karrai, J. M. Garcia, W. Schoenfeld, and P. M. Petroff, Nature (London), 405 (2000) 926.
[94] A. V. Chaplik JETP Lett., 62 (1995) 900.
[95] A. V. Chaplik and A. O. Govorov, Physica B, 256/258 (1998) 477.
[96] R. A. Römer and M. E. Raikh, Phys. Rev. B, 62 (2000) 7045.
[97] R. A. Römer and M. E. Raikh, Phys. Status Solidi (b), 221 (2000) 535.
[98] H. Hu, D.-J. Li, J.-L. Zhu and J.-J. Xiong, J. Phys.: Condens. Matter, 12 (2000) 9145.
[99] H. Hu, G.-M. Zhang, J.-L. Zhu, and J. J. Xiong, Phys. Rev. B, 63 (2001) 045320.
[100] R. A. Römer and M. E. Raikh, Phys. Status Solidi (b), 227 (2001) 381.
[101] T. Meier, P. Thomas, and S. W. Koch, Eur. Phys. J. B, 22 (2001) 249.
[102] J. Song and S. E. Ulloa, Phys. Rev. B, 63 (2001) 125302.
[103] H. Hu, J.-L. Zhu, D.-J. Li, and J.-J. Xiong, Phys. Rev. B, 63 (2001) 195307.
[104] A. O. Govorov, S. E. Ulloa, K. Karrai, R. J. Warburton, Phys. Rev. B, 66 (2002) 081309(R).
[105] D. Haft, C. Schulhauser, A. O. Govorov, R. J. Warburton, K. Karrai, J. M. Garcia, W. Schoenfeld, P. M. Petroff, Physica E, 13 (2002) 165.
[106] A. I. Vedernikov, A. O. Govorov, and A. V. Chaplik, JETP, 93 (2001) 853.
[107] A. V. Chaplik, JETP Lett., 75 (2002) 292.
[108] T. V. Shahbazyan and S. E. Ulloa, Phys. Rev. B, 55 (1997) 13702.
[109] I. E. Dzyaloshinsky and A. I. Larkin, JETP, 38 (1974) 202.
[110] K. A. Matveev and L. I. Glazman, Phys. Rev. Lett., 70 (1993) 990.
[111] K. Penc and J. Sólyom, Phys. Rev. B, 47 (1993) 6273.
[112] O. M. Auslaender, A. Yacoby, R. de Picciotto, K. W. Baldwin, L. N. Pfeiffer, K. W. West, Phys. Rev. Lett., 84 (2000) 1764.
[113] T. Kleimann, M. Sassetti, B. Kramer, and A. Yacoby, Phys. Rev. B, 62 (2000) 8144.

J. Leszczynski (Editor)
Computational Materials Science
Theoretical and Computational Chemistry, Vol. 15

Chapter 8

Spin-polarised surfaces: Current state of Density Functional Theory investigations

S.J. Jenkins

Department of Chemistry, University of Cambridge, Lensfield Road, Cambridge CB2 1EW, United Kingdom

1. INTRODUCTION

The importance of electronic structure in determining the static and dynamic properties of materials can hardly be over-emphasised. The interplay between the spatial arrangement of atomic nuclei and the orbital interactions of their associated electrons forms the basis of all modern physical and chemical theories of the solid and molecular states. The role of first-principles calculations in elucidating the details of this nuclear-electronic dialogue has been one of central importance in contextualising and explaining an ever-growing range of experimentally observed phenomena. Amongst the most challenging and exciting of fields into which first-principles theory is currently expanding must rank the study of magnetic surfaces and adsorption thereon. Here, the long-range metallic interactions of condensed matter physics and the short-range covalent interactions of quantum chemistry come into conflict to determine the spin-polarisation of the surface atoms. This is the story of that struggle.

1.1. Density Functional Theory

In the realm of quantum chemistry, the key to understanding molecular structure has traditionally been assumed to be the electronic wavefunction. In Hartree-Fock theory, for instance, the many-body wavefunction is taken to be a determinant formed from a set of one-electron wavefunctions. Within this framework, the exchange interaction is derived exactly, and the concepts of Pauli exclusion and electronic spin are included in a natural manner. As the system size increases, however, dynamic correlations between electrons gradually become more important, and it is necessary to go beyond the Hartree-Fock theory if reasonable results are to be obtained.

As one moves towards the realm of condensed matter physics, the hope of a wavefunction-based theory involving an exact treatment of spin-polarisation and exchange fades. Most modern work in this field is carried out within the density functional theory (DFT) introduced by Hohenberg, Kohn and Sham [1,2], in which the electron density takes on the role of the primary variable. This allows scope for any number of approximate treatments of electronic exchange and correlation, so that calculations for even the largest systems become tractable. Insofar as spin-polarisation is included, it is treated in a parametric manner, making use of exact results obtained for the homogeneous electron gas.

The happy conjunction of (seemingly) ever-increasing computational resources and substantial theoretical/algorithmic improvements has brought about a revolution in magnetic surface theory over the last few years. In particular, small-scale cluster models of surface structure, with all their inherent uncertainties regarding finite-size effects, have largely given way to slab-supercell or semi-infinite geometries in which 2D periodicity is invoked to describe a formally boundless surface. Where once such studies were relatively rare, today we see the literature on the subject expanding rapidly. This review is intended selectively to summarise the findings of recent periodic DFT calculations on spin-polarised surfaces, and to place these in the context of what are often limited and inconclusive experimental observations

1.2. Long-range magnetic order and the Stoner Criterion

The origin of long-range magnetic order in the *d*-block elements and their alloys is reasonably well understood, at least in outline. A brief summary at this stage will not be inappropriate. The essential pre-requisite for the phenomenon to occur is that localised *d* states overlap spatially and energetically with delocalised *s/p* states in the vicinity of the metallic Fermi level. The *s/p* states constitute a medium capable of supporting spin density waves over several lattice spacings, with wavelengths related to the shape of the Fermi surface. An isolated *d* state embedded in such a medium would generate such a wave by virtue of its exchange interaction with the *s/p* states; an array of *d* states, such as one would find in a crystal, will necessarily generate a complex interference pattern in the *s/p* spin-structure. In the case when the crystal structure happens to be commensurate with the natural wavelength of these spin-density waves, the system *may* exhibit an instability towards forming a definite pattern of permanent spin moments, localised on the spatially separated *d* states by virtue of their exchange interaction with the *s/p* continuum. In this way, both ferromagnetism and antiferromagnetism may be explained within the same so-called "itinerant" picture, although the details of the relative importance of direct *d-d* coupling and the indirect *s/p-d* coupling remain to be fully elucidated (see, for example, Petit *et al* [3], for a recent discussion of some of these issues).

Such qualitative arguments surrounding magnetic instability were first quantitatively formalised by Stoner [4], and his scheme was subsequently

adapted to a density functional paradigm by Vosko and Perdew [5]. The key is to understand that the magnetic energy of a system is proportional to m^2/χ, where m is the magnetisation (i.e. ρ_α-ρ_β) and χ the magnetic susceptibility. Within a uniform model, one can obtain a lower bound for χ of the form

$$\chi = \frac{N(E_F)}{(1 - N(E_F) I_{xc})} \quad , \tag{1}$$

in which $N(E_F)$ is the density of states (DOS) at the Fermi level [5]. The parameter I_{xc} is an exchange-correlation integral defined as:

$$I_{xc} = \int \gamma^2(r) K(r) d^3r \, . \tag{2}$$

Here, $K(r)$ is related to the functional derivative of the exchange-correlation energy, E_{xc}, with respect to the magnetisation,

$$2K(r)\delta(r - r') = \left. \frac{\delta^2 E_{xc}[\rho, m]}{\delta m(r) \delta m(r')} \right|_{m=0} \tag{3}$$

and $\gamma(r)$ is a normalised local density of states (LDOS) at the Fermi level:

$$\gamma(r) = \frac{1}{N(E_F)} \sum_i \delta(E_F - E_i) |\psi_i(r)|^2 \, . \tag{4}$$

Clearly, the critical parameter that must be evaluated is simply the "Modified Stoner Factor" $N(E_F)I_{xc}$: if this exceeds unity then the magnetic energy will become negative and spontaneous magnetisation will become favourable. This is the so-called "Stoner Criterion". Janak [6] has calculated I_{xc} for several elements, providing an insightful commentary on trends in this quantity across the periodic table.

Kim *et al* [7] have pointed out that the bulk value of I_{xc} is rather similar across a range of pure transition metals and their alloys; it is therefore the Fermi level DOS that should be seen as the primary factor in determining whether long-range magnetic ordering will occur in the bulk. This explains, for example, why it is those elements on the right-hand side of the *d*-block which tend to be either intrinsically ferromagnetic or to show a propensity for induced magnetic ordering. The *d*-band DOS in transition metals tends to be somewhat weighted towards higher energies, and these later elements are simply those for which the Fermi level cuts across the densest part.

The dependence of long-range magnetic order upon the Fermi level DOS is of fundamental importance in understanding the nature of magnetism at

surfaces. The broadening of isolated atomic *d* orbitals into a crystalline *d*-band is, of course, due to the interactions between neighbouring atoms. Cutting an infinite crystal to form a surface, however, significantly reduces the interactions experienced by those atoms in the surface layer, causing a localised narrowing of the *d*-band, and a consequent increase in $N(E_F)$ at the surface. The Stoner Criterion thus leads us to two related predictions: (i) that magnetic moments in magnetically-ordered materials may be enhanced at the surface, and (ii) that magnetic ordering may occur at surfaces, even when it does not occur in the bulk. Furthermore, any changes to the surface that might reduce the Fermi level DOS can be expected to reduce, or even entirely to quench, the magnetisation of the surface layer. These simple conclusions will be examined in relation to the case studies that follow in sections 2-4.

1.3. State of the Art for spin-polarised systems

A detailed treatment of the many subtleties of the DFT technique may be found elsewhere, notably in the seminal book by Parr and Yang [8]. We therefore merely highlight a few key aspects of particular relevance for the discussion to follow.

1.3.1. Spin-polarised exchange-correlation functional

The choice of exchange-correlation functional is one of the most problematic issues in modern DFT studies. The original local density approximation (LDA), introduced by Kohn and Sham in 1965 [2] performed admirably in the vast majority of uses to which it was put, with only a few notable exceptions. Those exceptions typically involve cases where electrons are highly localised, so that the assumption of a slowly varying electron density no longer holds true. Transition metals and molecular adsorbates are therefore two particularly sore points for the surface theorist; the LDA generally overbinds the adsorbed species considerably. In such cases, a generalised gradient approximation (GGA), which takes into account not only the magnitude of the electron density but also its gradient, can lead to a considerable improvement. The problem is that flexibility in the manner in which gradient corrections are included has produced a plethora of different GGA functionals, each with its own strengths and weaknesses. Thus, for example, the Perdew-Wang [9] form (PW91) can accurately reproduce surface geometry in close agreement with low energy electron diffraction (LEED) results, and reproduces relative energy differences between different molecular adsorption sites rather better than the LDA [10]. Nevertheless, although improved [11] over the LDA, absolute adsorption energies are still often overestimated by the PW91 functional, and indeed by the simplified Perdew-Burke-Ernzerhof [12] functional (PBE). The revised PBE functional (revPBE) proposed by Zhang and Yang [13], on the other hand, tends to bring adsorption energies more into line with experimental results (albeit with some considerable scatter), as does the alternative revised

form (RPBE) proposed by Hammer *et al* [14]. If anything, though, these latter two functionals tend to be less satisfactory in their results for atomic geometry than PW91 or PBE.

In relation to magnetic systems specifically, the main effect of GGA functionals tends to be to increase the lattice constant of the bulk relative to the (usually underestimated) value generated by the LDA. Magnetic moments calculated within GGA tend therefore to be somewhat larger than those from LDA, due to a narrowing of the *d*-band concomitant with the increased interatomic distances. Thus, for example, Kresse and Joubert [15] report increases in the spin-polarisation of bulk Fe, Co and Ni of up to 12% when changing from LDA to PW91 functionals. Where possible, the discussion of surface-specific changes in magnetic polarisation in this chapter makes reference to percentage changes relative to bulk values, in an effort to ameliorate some of the discrepancy between LDA and GGA calculations. Regardless of arguments concerning which gives the better representation of surface magnetism, however, it is worth stating that some form of GGA is absolutely necessary whenever either molecular or atomic adsorption is involved.

1.3.2. Pseudopotential vs. all-electron methods

The very earliest significant contributions to the study of magnetic surfaces through DFT were made by Freeman and co-workers, starting in the early 1980s [16-18]. Using a full-potential linearised augmented plane-wave (FLAPW) technique, they investigated a range of mono- and bi-metallic clean and adsorbate-covered systems, obtaining remarkable results of lasting worth in an era when available computer resources were negligible by modern standards. Nevertheless, the FLAPW method remains an expensive approach to DFT calculations, by virtue of the fact that it aims to describe explicitly the contribution of all the electrons within the systems studied.

In contrast, the pseudopotential method describes explicitly only the valence electrons, whilst implicitly parametrising the influence of the "frozen" core electrons through their contributions to an effective electron-ion potential. This pseudopotential can be made significantly "softer" than the true electron-ion potential, thus enabling calculations to utilise a relatively small basis set in the expansion of the valence electronic wavefunctions; the softer the pseudopotential, the fewer the basis functions (e.g. plane-waves) necessary to achieve convergence, and hence the cheaper the calculation. The pseudopotentials themselves are generated from first-principles (i.e. *ab initio*) according to well-defined rules which should ensure that the calculated results can be made compatible with those obtained by all-electron methods such as FLAPW. Nevertheless, there is always a compromise to be made between the quality of the results and the speed of the calculation. The pseudopotential is typically constructed to match precisely the true potential beyond some core radius, and it is the value of this key parameter that largely dictates the balance

between softness and accuracy: too large and the core encroaches into regions important for chemical bonding and physical properties, too small and the expense of the calculation rapidly increases.

Certainly the most significant step forward in pseudopotential theory since the introduction of *ab initio* generation schemes in the early 1980s, has been the introduction of so-called ultrasoft pseudopotentials (USPP). Traditional pseudopotentials are constructed to satisfy the "norm-conservation" requirement, which is to say that particle numbers are conserved in electron scattering from these potentials. The USPP scheme proposed by Vanderbilt [19] relaxes this constraint, allowing far greater freedom in the precise form of the potential, which may then be adjusted to be much softer than an otherwise equivalent norm-conserving pseudopotential (NCPP). The relaxation of the norm-conservation constraint is not without consequence, of course, since a correction must now be calculated by solution of a generalised eigenvalue equation [19], but this additional expense is typically rather less than the savings made through employing a smaller basis set.

Ultrasoft pseudopotentials were applied increasingly frequently through the second half of the 1990s to a variety of systems, latterly including magnetically ordered solids and their surfaces. Moroni *et al* [20] devoted considerable attention to the question of their reliability in such cases, concluding that use of the USPP approach for magnetic systems was justified, with a few caveats. First, they stressed the importance of including non-linear core corrections (NLCC), as described by Louie *et al* [21], in order to correct for the fact that the non-linear exchange-correlation interaction between valence and core states cannot be completely described by a linear interaction between the valence density and an inert pseudopotential. Secondly, they pointed out that it may be necessary in certain cases (notably for elements on the left hand side of the *d*-block) to include semi-core states explicitly within the valence complex, rather than freezing them within the core.

Furthermore, Kresse and Joubert [15] noted that although magnetic moments calculated within the USPP scheme were generally accurate, the calculated magnetisation energies were overestimated by as much as 0.06 eV/μ_B for bulk Fe, in comparison with a frozen-core all-electron projector augmented wave (PAW) scheme [22]. This is more than double the discrepancy found by the same authors for traditional NCPP calculations, and if similar errors were to occur in other systems one might therefore expect the USPP technique to show a tendency towards predicting magnetic order when no such order should occur. One should be careful, however, before taking this as a general rule, remembering that much is likely to depend upon the precise parameters employed in constructing the USPP. In *most* cases, the USPP approach is capable of providing perfectly reliable results for magnetic systems, so long as non-linear core corrections are applied, and semi-core electrons are included in the valence complex where appropriate. As always, careful testing of the

pseudopotential on well-understood systems is essential before endeavouring to tackle the unknown. For the purposes of this review, however, we will operate under the reasonable assumption that NCPP, USPP, PAW and FLAPW methods should be of comparable accuracy, and omit specific mention of which particular technique has been employed in any given work, *except* in the few cases where it has a bearing on controversial discrepancies between the results from different groups.

1.3.3. Extraction of localised information

Whether one uses an all-electron or a pseudopotential technique, the fundamental aims of a DFT calculation are to calculate the total energy and the charge/spin density of a given configuration of atoms. The Kohn-Sham equation [2] provides an efficient methodology for achieving this, by way of a set of effective one-electron eigenvalues and eigenfunctions. Notwithstanding the famous "band gap problem" that arises for the Kohn-Sham eigenvalues of insulating systems [23,24], the Kohn-Sham eigenfunctions may generally be considered more or less equivalent to the physical eigenfunctions of the system [25]. Note that within an itinerant magnetic crystal, the *s*- and *p*-derived eigenfunctions (and to a lesser extent the *d*-derived also) are typically delocalised throughout the material. Ideally, however, we would like to partition the charge and spin of the system between the individual atoms. How can this be achieved?

For calculations carried out in a localised basis set, the question of charge and spin partition may appear clear. Each eigensolution is naturally expressed as a linear combination of localised functions, each of which is unequivocally assigned to one atom or another. The charge and spin associated with each band can therefore be notionally distributed between atoms according to the weight of each basis function appearing in its description. Even for calculations carried out within a plane-wave basis set, it is possible to *project* the calculated eigenfunctions onto a localised basis set *after* self-consistency has been achieved. This form of Mulliken population analysis [26] can provide not only atom-localised information, but also information regarding overlap integrals between neighbouring atoms. One way or another, it represents a common approach to extracting localised information from DFT calculations on magnetic surfaces and in many other fields.

One objection to the Mulliken approach, however, is that the results of the analysis depend (sometimes quite strongly) upon the particular localised basis set chosen as the reference. There is no *a priori* reason why atomic orbitals, for instance, should be a better basis set into which to decompose the system eigenfunctions than, say, a set of Muffin-tin orbitals, or a set of Gaussian orbitals. Once the atoms in a system are brought together to form a molecule or a solid, the localised orbitals of the isolated atoms cease to have any special meaning except as a convenient localised basis set, and we should not interpret a

Mulliken analysis based on such a set as if it provided a unique result. Furthermore, one should recall that the one-electron DFT eigenfunctions are only a good *approximation* to the true many-body eigenfunctions of the system, and to this extent the Mulliken approach is only ever an approximate treatment.

An alternative approach to the partitioning of charge and spin is simply to integrate the corresponding densities within appropriately-chosen regions of real-space. Atom-centred close-packed spheres, or muffin-tin spheres, are two common choices. A less arbitrary partitioning of space can, however, be found in the topological theory advocated by Bader [27] and used extensively to characterise spin-polarised surfaces by Jenkins and co-workers [28-36]. In this scheme, the surfaces of zero normal flux in the charge density gradient field are identified as interatomic boundaries, within which quantum observables can have well-defined expectation values [27]. The partitioning of space in this way is conceptually appealing for two reasons: (i) it relies only upon the charge density of the system, which DFT in principle provides exactly; and (ii) it does not rely upon any external and/or arbitrary reference system. It is therefore a unique and accurate decomposition. Once the interatomic boundaries have been defined, any real-space observable, such as charge or spin, may simply be integrated within the individual atomic regions. Although the Mulliken, Bader and sphere-integrated approaches sometimes differ significantly in their estimates for atomic charges, one should recall that this is not in itself surprising as they are based upon such radically different philosophies. Nevertheless, the magnetic moments obtained by the topological and spherical methods generally appear to be in remarkably close agreement with those obtained by Mulliken analyses.

1.3.4. Practical considerations

For the working theorist, magnetic ordering raises immediate and challenging practical difficulties beyond those theoretical issues discussed above. Not only must the chosen theoretical approach be capable of including the effects of spin-polarisation, but in addition one must expect the spin degree of freedom to lead to rather more subtle electronic interactions than might be found in non-magnetic materials. For instance, two or more different spin-states of the system may be separated by only relatively small magnetic energies, and a self-consistent calculation might conceivably oscillate between these local electronic energy minima and either fail to converge or become trapped in a metastable state. The additional cost of a magnetic DFT calculation is therefore not limited to a factor of two (due to dealing with each spin species separately) but will typically include delayed convergence due to the exploration of electronically similar but magnetically distinct configurations. Furthermore, one may also need to incur the cost of performing multiple calculations with differing starting spin-states as a defence against finding only local minima.

2. IRON, COBALT, NICKEL

The late 3*d* transition metals Fe, Co and Ni, form an intriguing subset of the periodic table. Not only do they represent the three major types of metallic crystal structure (*bcc*, *hcp* and *fcc* respectively) but they are also important catalysts for the Haber process (Fe), the Fischer-Tropsch process (Fe, Co, Ni) and for olefin hydrogenation (Ni). They also happen to be ferromagnetic, and the computational expense associated with this simple fact has meant that DFT studies of these important catalysts have been conspicuously rare when viewed in the context of the literature on paramagnetic metals such as Pt, Pd or Ir. That state of affairs is now beginning to change, prompted in part by the advent of USPP codes and in part by advances in computer resources. We take this opportunity to review the current position regarding DFT calculations on these systems, paying particular attention to issues of substrate and adsorbate spin-polarisations.

2.1. Clean surfaces

A reasonable number of calculations have now been carried out on the clean surfaces of the elemental 3*d* ferromagnets, and these therefore constitute the best opportunity for observing any general trends in surface spin-polarisation that one might hope to extract. We therefore choose to group the clean surfaces according to similarities in their geometric structure, in the hope that this will help to reveal aspects of the magnetic behaviour most clearly. Calculated values of the magnetic moments in surface and sub-surface layers are collected in Tables 1-3, and deviations from reported bulk values are plotted against co-ordination number in Fig. 1. Note that these and all other magnetic moments quoted in this chapter are *spin* magnetic moments; orbital magnetic moments have been computed only rarely for surface systems, and are anyway usually of secondary importance.

2.1.1. Close-packed surfaces: fcc{111}, hcp{0001} and bcc{110}

The close-packed surfaces of Fe, Co and Ni might reasonably be expected to show the smallest degree of deviation from bulk behaviour of all the clean magnetic surfaces, and this does indeed seem essentially to be the case. The Co{0001} surface, in particular, displays calculated magnetic moments of around 1.70-1.75 μ_B/atom [37-39] in the outermost surface layer, to be compared with bulk values calculated by the same groups in the region of 1.58-1.64 μ_B/atom. On Ni{111}, the outermost surface atoms are slightly more perturbed, with the surface layer predicted to have a polarisation in the region of 0.62-0.68 μ_B/atom [36,37,40,41], compared with bulk values from the same groups in the range 0.58-0.64 μ_B/atom. By far the greatest effect, however, is seen for Fe{110}, where polarisations in the range 2.35-2.65 μ_B/atom have been

Table 1
Spin Magnetic Moments at Clean Fe surfaces (μ_B/atom)

	Coordination Number							
Fe{111}	4	5	6	7	7	8	8'	Bulk
Ref. 56[a]	2.62			2.25		2.34	2.15	2.15[43]
Ref. 57[a]	2.73			2.20		2.32	2.15	2.15[43]
Ave. Δ%	+24%			+3%		+8%	+0%	
Fe{110}	4	5	6	7	7	8	8'	Bulk
Ref. 37[b§]			2.57			2.35	2.25	2.24
Ref. 42[c]			2.35					2.06
Ref. 43[a§]			2.65			2.37	2.28	2.15
Ref. 44[d]			2.59			2.35	2.26	2.20
Ref. 45[e]			2.47			2.29	2.32	2.20†
Ave. Δ%			+16%			+7%	+4%	
Fe{001}	4	5	6	7	7	8	8'	Bulk
Ref. 16[a§]	2.98					2.35	2.39	2.15[43]
Ref. 37[b§]	2.97					2.30	2.37	2.24
Ref. 46[h]	2.87					2.43		2.31
Ref. 48[a§]	3.01					2.36	2.42	2.20†
Ref. 49[b§]	2.87					2.34	2.33	2.18
Ave. Δ%	+33%					+6%	+9%	
Fe{310}	4	5	6	7	7	8	8'	Bulk
Ref. 54[f]	2.85		2.65			2.33	2.43	2.23
Ave. Δ%	+28%		+19%			+4%	+9%	
Fe{211}	4	5	6	7	7	8	8'	Bulk
Ref. 31[g]		3.01		2.52		2.39	2.38	2.24
Ave. Δ%		+34%		+13%		+7%	+6%	
Fe{111}‡	6	7	8	9	10	11	12	Bulk
Ref. 47[h]				2.51				2.20†
Ave. Δ%				+14%				

(a) FLAPW/LDA; (b) LMTO/LDA; (c) FLAPW; (d) PAW/PW91; (e) FLAPW/PBE; (f) FLAPW/PW91; (g) USPP/RPBE; (h) USPP/PW91

N.B. If bulk moments have not been explicitly stated in the cited work, values calculated by the same group using similar methods have been inserted and referenced where possible. When not possible, a nominal "mean" value of 2.20 μ_B/atom has been assumed, and marked as †.

‡ Surface of *fcc* Fe.

predicted for the surface layer [37,42-45], compared with bulk values of the order of 2.06-2.24 μ_B/atom.

We thus observe that the well-known phenomenon of magnetic enhancement at 3*d* ferromagnetic surfaces is, in percentage terms, weakest for Co (around +6% on average) and strongest for Fe (around +16% on average). The case of Ni is somewhat intermediate, with an enhancement of around +10% (+7%) on average if we exclude (include) the somewhat anomalous result of Aldén *et al* [37], which had shown no enhancement for the surface layer but a clear enhancement of the immediate sub-surface layer. Note that this latter calculation was performed without structural relaxation of the surface.

The reason for the general enhancement in surface magnetic moment is rather clear, as the narrowing of the *d*-band due to removal of the nearest neighbours from the surface-layer atoms increases the Fermi level DOS and locally pushes the system further beyond the critical limit of the Stoner Criterion. The effect is presumably larger for *bcc* Fe *in part* because the reduction in nearest neighbours from eight to four is a more radical perturbation than from twelve to nine in both *hcp* Co and *fcc* Ni.

In addition to these results for the surfaces of *bcc* Fe, *hcp* Co and *fcc* Ni, however, a smaller number of studies have also been carried out for the close-packed surfaces of metastable crystal structures. So, for example, the {111} surface of *fcc* Fe has been calculated to possess a surface-layer polarisation of 2.51 μ_B/atom [47], while the {111} surface of *fcc* Co is predicted to have a surface-layer polarisation of 1.72 μ_B/atom [37]. It is noteworthy that the surface-induced enhancement of the magnetic moment in the case of Fe is still a rather greater percentage of the nominal bulk value (+14%) than for either Co (+5%) or Ni (+7/10%) in the same structure. This difference must presumably arise from differences in the shapes of the DOS for the three metals, and from the position of the *d*-band relative to the Fermi level.

2.1.2. Square-symmetric surfaces: fcc{001} and bcc{001}

Somewhat more open than the close-packed surfaces considered in the preceding sub-section, the square-symmetric surfaces of the *fcc* and *bcc* crystal structures are expected to display even greater enhancement in the magnetic moments of surface-layer atoms. In the case of Fe{001}, several groups [16,37,46,48,49] have calculated surface-layer polarisations in the range 2.87-3.01 μ_B/atom, an average increase of +33% from their bulk values of 2.15-2.31 μ_B/atom. Similarly for Ni{001}, a number of groups have calculated surface-layer polarisations in the range 0.59-0.76 μ_B/atom [18,37,38,40], compared with bulk values from the same groups in the range 0.55-0.64 μ_B/atom (an average increase of around +12%). It is interesting to note, however, that the only calculation to allow for substrate relaxation resulted in a substantially larger enhancement of around +25% [40], while the other three resulted in much

Table 2
Spin Magnetic Moments at Clean Co surfaces (μ_B/atom)

	Coordination Number							
Co{0001}	6	7	8	9	10	11	12	Bulk
Ref. 37[a§]				1.70			1.65	1.64
Ref. 38[a§]				1.75			1.67	1.58
Ref. 39[a§]				1.70			1.62	1.64†
Ave. Δ%				+6%			+2%	
Co{10$\bar{1}$0}	6	7	8	9	10	11	12	Bulk
Ref. 33[b]			1.84					1.71
Ref. 53[b]			1.87		1.64		1.62	1.71
Ave. Δ%			+9%		-4%		-5%	
Co{111}‡	6	7	8	9	10	11	12	
Ref. 37[a§]				1.72			1.67	1.64
Ave. Δ%				+5%			+2%	
Co{001}‡	6	7	8	9	10	11	12	Bulk
Ref. 37[a§]			1.84				1.63	1.64
Ref. 50[c§]			1.86				1.64	1.64†
Ref. 51[a]			1.78					1.63
Ave. Δ%			+12%				+0%	

(a) LMTO/LDA; (b) NCPP/PW91; (c) FLAPW/LDA
N.B. If bulk moments have not been explicitly stated in the cited work, a nominal "mean" value of 1.64 μ_B/atom has been assumed, and marked as †.
‡ Surfaces of *fcc* Co.
§ Geometry not relaxed.

smaller enhancements of just around +8% [37,38] or up to +17% [18]. Further calculations to clarify the situation would be welcome, but on balance the higher figure may well be the more reliable. In addition, several groups have considered the {001} surface of *fcc* Co, finding magnetic moments in the outermost layer of 1.78-1.86 μ_B/atom [37,50,51], increased by an average of +12% relative to bulk values from the same groups in the range 1.63-1.64 μ_B/atom.

2.1.3. Ridge and furrow surfaces: fcc{110}, hcp{10$\bar{1}$0} and bcc{211}

The {110} surfaces of *fcc* metals consist of parallel ridges running in the {1$\bar{1}$0} direction, separated by shallow trenches. The *hcp*{10$\bar{1}$0} and *bcc*{211} surfaces are closely analogous, and the three surfaces together afford an ideal

Table 3
Spin Magnetic Moments at Clean Ni surfaces (μ_B/atom)

	Coordination Number							
Ni{111}	6	7	8	9	10	11	12	Bulk
Ref. 36[a]				0.68				0.62
Ref. 37[b§]				0.62			0.67	0.64
Ref. 40[a]				0.68			0.65	0.61
Ref. 41[c§]				0.63			0.64	0.58
Ave. Δ%				+7%			+8%	
Ni{110}	6	7	8	9	10	11	12	Bulk
Ref. 17[c§]		0.63				0.54		0.56
Ref. 28[a]		0.76				0.58	0.65	0.62
Ref. 40[a]		0.76				0.66	0.64	0.61
Ref. 52[d]		0.72				0.59	0.60	0.60
Ref. 52[e]		0.75				0.63	0.62	0.63
Ave. Δ%		+20%				-1%	+2%	
Ni{001}	6	7	8	9	10	11	12	Bulk
Ref. 18[c§]			0.68				0.60	0.58[41]
Ref. 37[b§]			0.69				0.64	0.64
Ref. 38[b§]			0.59				0.58	0.55
Ref. 40[a]			0.76				0.68	0.61
Ave. Δ%			+14%				+4%	
Ni{210}	6	7	8	9	10	11	12	Bulk
Ref. 55[f]	0.78			0.71		0.64	0.62	0.62
Ave. Δ%	+26%			+15%		+3%	+0%	
Ni{211}	6	7	8	9	10	11	12	Bulk
Ref. 34[a]		0.72		0.69	0.63			0.62
Ave. Δ%		+16%		+11%	+2%			

(a) USPP/PW91; (b) LMTO/LDA; (c) FLAPW/LDA; (d) USPP/LDA; (e) USPP/PBE; (f) FLAPW/PBE
N.B. If bulk moments have not been explicitly stated in the cited work, values calculated by the same group using similar methods have been inserted and referenced.
§ Geometry not relaxed.

opportunity for cross-comparison of the different elements in similar structural environments. By far the most widely studied of this group is Ni{110}, for which ridge-atom magnetic moments in the range 0.63-0.76 μ_B/atom have been

calculated [17,28,40,52], as against bulk values quoted by the same groups in the range 0.56-0.63 μ_B/atom. The average enhancement of +20% is certainly the largest of the three low-index surfaces of Ni. In addition, however, this surface differs from the close-packed and square-symmetric surfaces by virtue of the fact that second-layer trough-atoms are also exposed to the vacuum. The calculations of Mittendorfer *et al* [40] suggest that these atoms too should display enhanced magnetic moments of 0.66 μ_B/atom, but others [17,28,52] in fact predict unchanged or, if anything, slightly decreased moments for these atoms, in the range 0.54-0.63 μ_B/atom. Averaged over all of these calculations, the consensus would be a small decrease amounting to around -1% of the bulk value, but clearly some further work to clarify this point would be beneficial.

The Co$\{10\bar{1}0\}$ surface has been investigated by Jenkins and King [53], who reported ridge-atom polarisation of 1.87 μ_B/atom and trough-atom polarisation of 1.64 μ_B/atom (based upon a Mulliken analysis). In a later publication [33], they reanalysed the same raw data within the topological approach introduced by Bader [27], obtaining a value of 1.84 μ_B/atom for the ridge-atoms, and values for the remainder essentially unchanged from the Mulliken result. The average increase in magnetic moment for the ridge-atoms (+9%) is once again the highest amongst the low-index surfaces of Co, and we once again note a decrease (-4%) in the polarisation of the trough atoms.

On Fe{211}, the ridge-atom polarisation has been calculated by Jenkins [31] to be 3.01 μ_B/atom, while the polarisation of the trough atoms amounts to 2.52 μ_B/atom. Both of these exceed the magnetic moment of bulk Fe, which is calculated by the same author as 2.24 μ_B/atom. The rather large +34% increase found for the ridge-atoms exceeds the average enhancement found on Fe{001} [16,37,46,48,49] and thus may be the greatest of any clean Fe surface. The +13% enhancement for trough-atoms is, in contrast, relatively modest for undercoordinated Fe atoms at a clean surface. The Fe{211}, Co$\{10\bar{1}0\}$ and Ni{110} surfaces can all, therefore, be characterised as displaying particularly high ridge-atom polarisation, and notably smaller trough-atom polarisation.

2.1.4. Stepped surfaces: bcc{310}, fcc{211} and fcc{210}

Despite the best efforts of experimentalists, even the nominally flat single-crystal samples prepared for use in the laboratory will feature occasional steps in the structure due to imperfect alignment during cleavage or growth. Surfaces in the real world will typically feature a considerably higher density of such defects. Indeed, the concept of employing single-crystals as model systems for catalytic studies has often been criticised precisely for this reason; industrial catalysts are typically oxide-supported nanoparticles, which could be described as possessing more step than surface. The step sites have often been postulated to be the active sites for molecular adsorption and/or reaction, so there is an urgent need to study surface steps in a controlled and systematic manner. In view of the requirement of plane-wave DFT that the systems studied must be

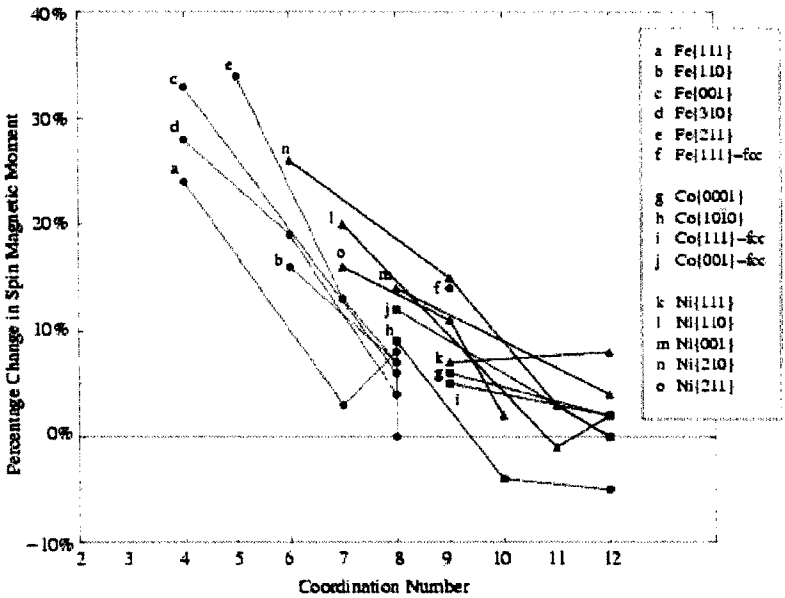

Fig. 1. Percentage changes in spin magnetic moments as a function of coordination number. Notwithstanding considerable scatter, the change for an atom of coordination number n may be reasonably well approximated as $\Delta\% = 150\exp(-7n/20) \pm 10\%$.

periodic, high-index stepped surfaces such as *fcc*{211}, *fcc*{210} and *fcc*{531} have lately come under scrutiny; such surfaces feature a high density of steps, regularly arranged in relatively small surface unit cells, and thus present reasonable *and* tractable models for real-world surfaces. From the point of view of surface magnetism, the tendency for these surfaces to feature low-coordination atoms will be of particular interest. The expectation that low-coordination atoms at stepped surfaces must necessarily feature conspicuously high magnetic moments is, however, only partly supported by the available data. On Fe{310}, for example, Geng *et al* [54] report polarisation of the four-fold coordinated step-edge atoms as 2.85 μ_B/atom. Whilst representing a considerable +28% enhancement over their bulk value of 2.23 μ_B/atom, it is nevertheless lower than the 2.87-3.01 μ_B/atom (average +33%) enhancements reported by various groups [16,37,46,48,49] for the similarly four-fold coordinated surface atoms of Fe{001}, and indeed lower also than the value of 3.01 μ_B/atom (+34%) found by Jenkins [31] for the *five*-fold coordinated ridge-atoms of Fe{211}.

In the same vein, consider the seven-fold coordinated step-edge atoms of Ni{211}, which are reported by Karmazyn *et al* [34] to display polarisations of 0.72 μ_B/atom, representing a +16% increase over the bulk value of 0.62 μ_B/atom

quoted by the same group. This sizeable increase is nevertheless exceeded by the enhancements reported by several groups for the similarly seven-fold coordinated ridge-atoms of the Ni{110} surface, which average at +20% [17,28,40,52], and nearly matched by the +15% enhancement reported for the *nine*-fold coordinated surface atoms of the Ni{210} surface [55]. Nevertheless, the six-fold coordinated step-edge atoms at the Ni{210} surface do display the highest magnetic moment enhancement of all Ni surfaces studied thus far, at +26% [55]. Clearly, the low-coordination atoms on stepped surfaces can indeed possess rather high magnetic moments, but by no means *necessarily* surpassing atoms with the same (or even slightly higher) coordination numbers on the square-symmetric or ridge-and-furrow surfaces. Much must depend upon interactions at the level of next-nearest neighbours or beyond.

One interesting phenomenon, noted both by Geng *et al* [54] and by Karmazyn *et al* [34], is the Smoluchowski smoothing of step-edges by the delocalised *s/p* electrons, seen rather clearly in Fig. 2. The localised *d* electrons, meanwhile, remain at the step-edge, so that the overall effect is to accentuate the apparent spin-imbalance when viewed from the vacuum. The polarisation of step-edge atoms may not necessarily be unduly strong, but it *is* likely to be distributed in a less isotropic manner than for atoms on flatter surfaces.

2.2. Atomic and molecular adsorption

It has long been known that molecular adsorbates and non-metallic adatoms tend to quench the spin of magnetic surfaces, but it is only recently that a sufficiently large body of theoretical work has built up to enable general features to be recognised. Here we attempt to summarise the calculations that have thus far been carried out for adsorption on the surfaces of the elemental 3*d* ferromagnets.

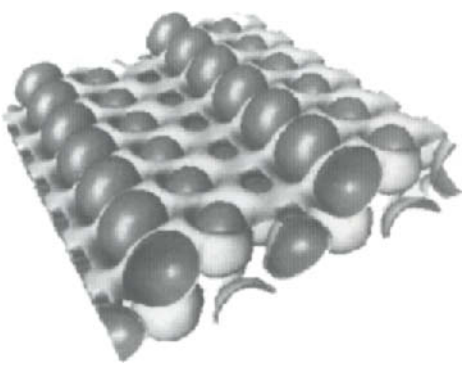

Fig. 2. Residual spin density at the Ni{211} surface. Dark isosurfaces represent regions of net majority spin; light isosurfaces show regions of net minority spin. Image taken from Karmazyn *et al* [34].

2.2.1. Atomic adsorbates: C, N and O

Non-metallic adatom adsorption on magnetic substrates has been addressed within DFT for C, N and O on Co{0001} [39] and Fe{211} [31]; adsorption of O on Ni{111} [32,58] and of N on the low index surfaces of Fe [46,59] have also been considered. Pick and Dreyssé [39] in particular contributed the useful observation that C and N couple in an antiferromagnetic spin alignment with respect to the Co{0001} substrate, while O couples ferromagnetically in all but one (high coverage) adsorption model. Polarisation of the adatom can amount to as much as 0.22 μ_B/atom. Magnetic moments on the Co atoms directly bonded to the adatom show significant reductions from the clean surface value of 1.70 μ_B/atom, amounting to as much as 46% in the case of C adsorption, 52% for N, and 16% for O (all at 0.25 ML adatom coverage). Reductions for 1 ML adatom coverage range up to 96% in the case of C adsorption, 78% for N, and 66% for O. The calculations of Pick and Dreyssé [39] do not, however, allow for geometric relaxation of either the substrate or the adatom (although they do consider two different fixed adsorption heights and several different adsorption sites). It is therefore not clear to what extent their systematics would hold true if this constraint were removed.

Fully-relaxed calculations by Yamagishi *et al* [32] for O adsorbed on Ni{111} do, however, show agreement with the prediction of ferromagnetic coupling to the substrate suggested by Pick and Dreyssé [39]. The adatom is found to adsorb preferentially in the *fcc* hollow site, with structural parameters in close agreement with experimental and other theoretical [58] results. The polarisation of a p($\sqrt{3}$ x $\sqrt{3}$) adlayer is reported as 0.16 μ_B/atom [32]. Eichler *et al* [58] report the polarisation of a p(2x2) adlayer to be 0.09 μ_B/atom, but unfortunately do not explicitly specify whether this is ferromagnetic or antiferromagnetic with respect to the substrate, although the former is perhaps implied by omission. In addition, Mortensen *et al* [46] have reported a nearly-vanishing magnetic moment for N on Fe{001}, again without specifying the sense of the spin relative to the surface.

Interestingly, however, recent results for adatom adsorption on Fe{211} [31] support the notion of Pick and Dreyssé [39] that adatom-substrate coupling follows a trend from antiferromagnetism towards ferromagnetism when progressing from C to N to O. Adsorption of C and N is found to occur preferentially in a trough site that could be described as long-bridge with respect to the Fe ridge-atoms and short-bridge with respect to the trough-atoms. The adsorbed C atoms couple antiferromagnetically with the surface, gaining a moment of 0.25 μ_B/atom in the opposite sense to the substrate. The ridge-atoms nearest to the adatom suffer a reduction in their magnetic moments, from 2.94 μ_B/atom on the clean surface down to 2.44 μ_B/atom; the other ridge-atoms actually show a further enhanced polarisation of 3.12 μ_B/atom. The trough-atoms display reduced magnetic moments of 1.89-2.00 μ_B/atom, which may be compared with 2.44 μ_B/atom for the clean surface [31].

Adsorbed N atoms also couple antiferromagnetically to the substrate, but with magnetic moments of only 0.08 μ_B/atom [31]. Once again, the ridge-atoms closest to the adatoms display quenched magnetic moments, although the effect is less strong than for C as they retain a polarisation of 2.57 μ_B/atom; the other ridge-atoms are again strongly polarised at 3.05 μ_B/atom. Trough-atom polarisations are quenched to 1.82-2.00 μ_B/atom in the presence of the N overlayer.

In contrast, O adatoms at the same adsorption site are ferromagnetically coupled to the substrate, with a calculated polarisation of 0.12 μ_B/atom [31]. The polarisation of the ridge-atoms is either slightly quenched down to 2.77 μ_B/atom (those closest to the adatoms) or slightly enhanced at 2.99 μ_B/atom (those furthest from the adatoms). Trough-atoms are also only mildly influenced by the presence of the O adatoms, with moments of 2.26-2.31 μ_B/atom. When O is placed in its preferred three-fold adsorption site, however, the magnetic moment on the adatom drops to 0.06 μ_B/atom, although it remains ferromagnetic with respect to the substrate; the ridge-atom polarisations drop dramatically to a bulk-like range of 2.22-2.35 μ_B/atom, and the trough-atoms actually exceed them in their polarisation of 2.46-2.54 μ_B/atom. What is clear, however, is that the trend observed by Pick and Dreyssé [39] does indeed appear to be correct, even when adatom and substrate relaxations are taken fully into account.

2.2.2. Diatomic adsorbates: CO, NO and N_2

The nature of molecule-induced demagnetisation at elemental ferromagnetic surfaces has been of interest for decades, but theoretical calculations have only seriously addressed the matter in the last few years. To our knowledge, the first DFT work specifically to discuss the effect in detail within a slab model of such a surface was that of Ge *et al* [28], in which CO adsorption on Ni{110} was tackled at 0.5 ML and 1.0 ML coverage. Favot *et al* [52] subsequently reported results for the same two cases and also included a 0.25 ML model. The conclusion of both groups was that CO induced a reduction in the magnetic moments of surface atoms that was essentially localised to just those atoms that were directly involved in bonding with the molecule. Thus, for example, adsorption into the energetically preferred short-bridge site at 0.5 ML coverage was found to result in the magnetic moments of the ridge-atoms being quenched to 0.26 μ_B/atom, from a value on the clean surface of 0.76 μ_B/atom, while the trough-atoms displayed moments of 0.46-0.57 μ_B/atom, quenched only slightly from 0.58 μ_B/atom [28]. Even more striking was the effect of atop adsorption on the ridge-atoms (the second most stable adsorption site), whereupon the atom directly beneath the molecule showed a magnetic moment of only 0.19 μ_B/atom, whilst the other ridge-atom retained a moment of 0.68 μ_B/atom [28]. The molecule itself was found to gain a very small net minority spin, reported by Favot *et al* [52] as 0.01 μ_B/atom in the monolayer case, and by Ge *et al* [28] as 0.03-0.04 μ_B/atom in all cases. The residual spin density (i.e. ρ_α-ρ_β) associated

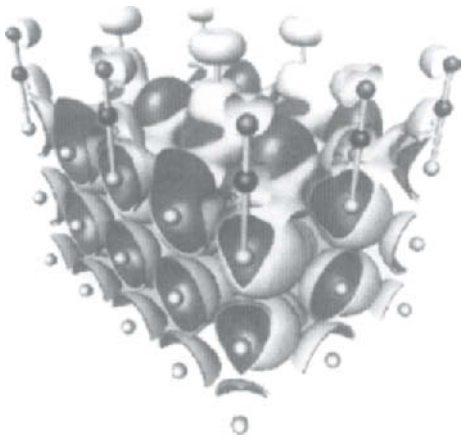

Fig. 3. Residual spin density for CO on Ni{110} in the atop site. Dark isosurfaces represent regions of net majority spin; light isosurfaces show regions of net minority spin. Image after Ge *et al* [28].

with this net imbalance was distributed (see Fig. 3) in a region strongly resembling linear combinations of the molecular LUMOs (i.e. the two orthogonal $2\pi^*$ orbitals). Both groups [28,52] concluded that the short-range quenching of magnetisation was indicative of a covalent interaction, and the discussion was taken further by Jenkins *et al* [35], who also extended the database to include NO adsorption on the same substrate. The extra electron of NO appears to enhance the ability of the molecule to quench surface spin-polarisation, with ridge-atom moments as low as 0.12 μ_B/atom in the case of short-bridge adsorption [35].

Various calculations for CO adsorption have since been reported on a number of different ferromagnetic substrates, including an exhaustive study of several coverages and overlayer symmetries on Ni{111} by Eichler [60], a comparative survey of adsorption on a range of flat, stepped and step-kinked surfaces by Shah *et al* [61], and a joint experimental/theoretical investigation of adsorbate geometry on Ni{001} by Sayago *et al* [62]. Sadly, none of these works focussed specifically upon the detailed nature of spin-polarisation at these surfaces. Similarly, Stibor *et al* [44] have reported results for CO adsorption on Fe{110}, as have Sorescu *et al* [63] for Fe{001}, while Jenkins and King have considered adsorption of CO [64,65] and NO [65] on Co{10$\bar{1}$0} - all without a detailed analysis of adsorbate-induced spin quenching. Karmazyn *et al* [34], however, have reported calculations for the atom-resolved spin-polarisation of Ni{211}/CO, in which the energetically-favoured step-edge bridge-site model features extremely localised quenching of the step-edge Ni atoms down to 0.34 μ_B/atom (from 0.72 μ_B/atom), whilst the terrace atoms are almost entirely unperturbed relative to the clean surface.

Very recent calculations by Jenkins [31] for CO adsorption on Fe{211} reveal a highly tilted and stretched molecular geometry in which the C end of the molecule occupies a three-fold site on the side of one surface ridge, while the O end bonds in a two-fold manner with the adjacent ridge. The molecule couples antiferromagnetically with the surface, gaining an extraordinarily large magnetic moment of 0.22 μ_B. In the overlayer studied, all ridge-atoms are involved in molecular bonding, and their magnetic moments are quenched to 2.63-2.82 μ_B/atom, from a clean-surface value of 3.01 μ_B/atom. Trough-atoms involved in molecular bonding suffer a reduction in polarisation from 2.52 μ_B/atom to 1.95 μ_B/atom, while those not involved in bonding retain a magnetic moment of 2.30 μ_B/atom [31].

For completeness, we note that Nørskov and co-workers have published extensive calculations concerning the adsorption of N_2 on Fe{111} [66], Fe{110} [47,67] and Fe{001}[59]. Detailed comparison of their calculations against experimental work underlines the ability of modern DFT calculations to provide valuable insight into real catalytic problems (in this case the energetics and kinetics of the rate-determining-step for ammonia synthesis), but no details of the influence of adsorption on surface magnetism are reported.

2.2.3. Polyatomic adsorbates: C_6H_6, C_5H_5N and CH_n

In addition to the studies of diatomic molecules on ferromagnetic surfaces described in the previous sub-section, a small number of calculations for rather more complex adsorbates have also been undertaken. Notably, these have included benzene on Ni{111} [36,68], Ni{110} and Ni{001} [68]. The same effects as for diatomic adsorbates are once again apparent, with the benzene molecule in each case gaining a net minority spin and the surface magnetic moments being quenched for just those atoms that form bonds with the molecule. For instance, Yamagishi *et al* [36] reported moments of 0.28-0.29 μ_B/atom for those atoms of the Ni{111} surface that bond to two C atoms of the benzene ring, 0.28-0.30 μ_B/atom for those that bond to a single C atom, and 0.56-0.64 μ_B/atom for those that do not bond to the molecule at all. They found also that the benzene molecule gains a net minority spin varying with adsorption site in the range 0.03-0.08 μ_B/atom. Just as for CO and NO, the residual minority spin was found to reside in regions suggestive of linear combinations of the molecular LUMO orbitals appropriate to the symmetry of the local adsorption geometry [36]. Subsequent work by Mittendorfer and Hafner has extended the study of aromatic molecules on magnetic substrates to include hydrogenation of benzene on Ni{111} [69] and the adsorption of thiophene on Ni{001} [70], although it is fair to say that the chemistry of these systems has been the focus of the work, rather than the surface magnetic properties. Similarly, Michaelides and Hu [71-73], discussing methane dissociation on Ni{111}, mention a localised quenching of surface magnetism due to adsorbed CH_n moieties, but provide few details of this aspect of their work.

3. THIN FILM MAGNETISM

With confidence in the ability of DFT correctly to describe the properties of pure ferromagnetic materials, comes a natural desire to extend the methodology to encompass more complex and challenging situations. In recent years, therefore, a number of theoretical studies have been undertaken on surfaces at which two metallic species are present, one or both of which may maintain a permanent magnetic moment.

3.1. Ferromagnetic substrates

Theoretical studies of thin overlayers on ferromagnetic substrates are remarkably few in number, considering the possibilities for induced magnetisation that one might expect. Nevertheless, a number of calculations have been carried out, and we review some examples here.

Wu and Freeman [74] were the first to perform calculations for Fe monolayers on Ni{111}, reporting an interesting preference for epitaxy in the *hcp* hollow sites of the surface. Thus a naturally *bcc* overlayer material (i.e. Fe) and a naturally *fcc* substrate material (i.e. Ni) combine to produce an interface structure more akin to the intervening *hcp* material (i.e. Co). The calculated magnetic moment of the Fe monolayer on Ni{111} amounts to 2.33 μ_B/atom, which is only slightly higher than the bulk value, while the polarisation of the uppermost Ni layer was reportedly enhanced to 0.67 μ_B/atom.

Considering a somewhat complementary system, Lee *et al* [75] carried out calculations for monolayer and bilayer *bcc* Ni on the Fe{001} substrate. For the monolayer, they reported a magnetic moment of 0.86 μ_B/atom, enhanced by a massive 54% from the bulk value of 0.56 μ_B/atom calculated previously by the same authors. This they attributed to the effect of interfacial hybridisation, noting that the moments of the surface atoms in the bilayer case had already dropped to 0.69 μ_B/atom. Similarly, the magnetic moment of the uppermost Fe layer was found to rise from a bulk value of 2.22 μ_B/atom [43] to 2.65 μ_B/atom in the monolayer case, and to remain at 2.59 μ_B/atom in the bilayer case (although both of these values are less than that of 2.98 μ_B/atom calculated for the clean surface [16]). The sub-surface Ni atoms in the bilayer case also retained a substantially enhanced magnetisation of 0.69 μ_B/atom. Lee *et al* [75] therefore concluded that magnetic enhancement was an intrinsic property of the Fe/Ni interface that would likely survive to the thick-overlayer regime.

These results for Fe/Ni systems were expanded upon by Mirbt *et al* [76], who considered several 3*d* overlayers on the Fe{001} surface. Exploring only intralayer-ferromagnetic configurations, they found that monolayers of Ti, V, and Cr preferred to couple antiferromagnetically with respect to the substrate, while monolayers of Mn, Fe, Co, and Ni coupled in the ferromagnetic sense. Wu and Freeman [77], however, subsequently demonstrated that an intralayer-

antiferromagnetic state, associated with a marked c(2x2) structural buckling, was energetically favoured in the case of the Mn monolayer – a result later confirmed by the calculations of Elmouhssine *et al* [78]. In fact, Blügel and co-workers [79-81] have concluded that intralayer-ferromagnetic and intralayer-antiferromagnetic spin-structures are competing metastable configurations for almost all of the 3*d* overlayers on Fe{001}; Mn simply falls at the boundary between the stability of layered antiferromagnetism for Ti, V and Cr, and of ferromagnetism for Fe, Co and Ni.

3.2. Paramagnetic substrates

Relatively few calculations have been undertaken for magnetic overlayers on paramagnetic substrates, in part presumably because in many cases the magnetic ordering of bulk ferro- and antiferro-magnets is strongly quenched due to interaction between the *d*-bands of the overlayer and a transition metal substrate (as noted in an early review article by Freeman and Wu [82]). There are, nevertheless, notable exceptions to this rule, for instance the case of Co monolayers on both Pd{111} and Pt{111}, where Wu *et al* [83] have calculated substantial induced spin-polarisation of the underlying material. Both Pd and Pt have rather high paramagnetic susceptibilities (see e.g. Janak [6]) and so are always on the brink of magnetic order. Furthermore, Blügel *et al* [84] have reported enhanced magnetic moments in 3*d* overlayers on Pd{001}, including a small antiferromagnetic moment on V, which one would normally expect to be paramagnetic. This may presumably be attributed to an unusually small overlayer-substrate interaction, and a consequent narrowing of the overlayer *d*-band. Such issues will be considered rather more closely in the next sub-section.

In a particularly interesting case, Wu and Freeman [85] have studied an Fe monolayer on the Ru{0001} substrate within the FLAPW/LDA approach. They find a preference for *hcp* epitaxial stacking over *fcc*, and report an intralayer-antiferromagnetic spin-ordering to be favoured over the ferromagnetic by 0.08 eV/adatom, and over the paramagnetic by around 0.20 eV/adatom. This, they note, runs counter to the results for a free-standing Fe{111} monolayer, and indeed for pure Fe surfaces, in which the ferromagnetic ordering is clearly favoured. The magnetic moments of the monolayer on Ru{0001} were found to be 2.24 μ_B/atom for the ferromagnetic case, and 2.23 μ_B/atom for the antiferromagnetic case [85], and the authors remark upon a significant magnetic pressure effect that forces both magnetically-ordered monolayers some 0.16 Å further from the substrate than would be the case for a paramagnetic monolayer. Nørskov and co-workers [47,67] have subsequently reported USPP/GGA calculations for N_2 adsorption and dissociation upon the Ru{0001}/Fe surface, with a view towards efficient ammonia synthesis. Their findings [47] confirm the preference for *hcp* epitaxial stacking (by a margin of 0.15 eV/adatom) and antiferromagnetic ordering (by a margin of 0.05 eV/adatom) first observed by Wu and Freeman [85].

3.3. Diamagnetic substrates

The attribution of overlayer-specific magnetic ordering to the phenomenon of *d*-band narrowing, alluded to in sub-section 3.2 above, raises the intriguing possibility that materials that are paramagnetic in three dimensions might become ferromagnetic in two, even without the influence of a ferromagnetic substrate. To achieve the necessary effect, it is crucial that the bonding between the overlayer and the substrate be sufficiently weak that a substantial narrowing can occur. To this end, the (diamagnetic) coinage metals Cu, Ag and Au are expected to be suitable substrate materials, in view of the fact that their filled *d*-bands lie some way below the Fermi level and should not couple strongly with that of a transition metal overlayer.

3.3.1. 3d monolayers

The first theoretical predictions for induced magnetic order in an overlayer at a diamagnetic surface were made by Fu *et al* [86], who reported calculated moments of 1.75 μ_B/atom for a ferromagnetic monolayer of V on Au{001} and 1.98 μ_B/atom for the same monolayer on Ag{001}. Blügel and Dederichs [87,88] report moments of around 2.0 μ_B/atom for V on Ag{001} in both a metastable ferromagnetic state *and* a stable intralayer-antiferromagnetic state. Blügel [89] has also reported a very small magnetic moment for ferromagnetic Ti on Ag{001}, but emphasised that this may be highly sensitive to experimental conditions.

In addition to these cases of induced ordering, the 3*d* elements that show permanent magnetisation in the bulk are predicted to display enhanced magnetic moments as overlayers on diamagnetic surfaces. The bulk antiferromagnets Cr and Mn can support metastable ferromagnetic ordering on Ag{001} and possess moments of 3.70 μ_B/atom [86] and around 4.0 μ_B/atom [89] respectively. On Cu{001}, there is no ferromagnetic phase for Cr, and that of Mn features magnetic moments of only around 3.0 μ_B/atom [81,87]. Once again, however, it is the antiferromagnetic ordering which is, in fact, energetically favoured on both Ag{001}[88] and Cu{001} [89], with similar magnetic moments to those of the ferromagnetic phases. Eder *et al* [90] also report an antiferromagnetic preference for a monolayer of Mn on Cu{001}, but with a rather larger overlayer magnetic moment of 3.75 μ_B/atom.

The bulk ferromagnets Fe, Co and Ni all favour ferromagnetic ordering on Cu{001} [88], Ag{001} [87] and Au{001} [43]. In fact, the magnetic moment of ferromagnetic Fe is enhanced from a bulk value typically calculated in the vicinity of 2.2 μ_B/atom, to monolayer values of between 2.74 μ_B/atom [91] and 2.85 μ_B/atom [86] on Cu{001}, and of 2.96 μ_B/atom on Ag{001} [86]. Similarly, the magnetic moment of a Co monolayer on Ag{001} is predicted as 2.0 μ_B/atom [88], whilst on Cu{001} it is variously calculated as 1.85 μ_B/atom [38], 1.78 μ_B/atom [92,93] or 1.71 μ_B/atom [94]; these figures may be compared with

bulk values calculated in the range 1.63-1.71 μ_B/atom for *hcp* Co [37,51,53]. Such monolayer enhancements typically equal or exceed those found for the low index surfaces of elemental *bcc* Fe and *hcp* Co. Only Ni monolayers seem consistently to show relatively little enhancement over the bulk polarisation [87].

3.3.2. 4d and 5d monolayers

As Blügel [89] points out, the exchange-correlation integral I_{xc} decreases in going from the 3*d* to 4*d* to 5*d* transition metals, as does the Fermi level DOS. It therefore becomes progressively more difficult to satisfy the Stoner Criterion, and thereby to induce a magnetic instability, as one descends the *d*-block of the periodic table. Nevertheless, numerous DFT predictions of two-dimensional ferromagnetic ordering have been made for 4*d* monolayers of Tc on Ag{001} [89], and for Ru [89,95,96] and Rh [89,95-97] on both Ag{001} *and* Au{001}. A somewhat smaller magnetic moment for Rh has also been calculated on Cu{001} [98], but the ferromagnetic state is reported to be only marginally more stable than the paramagnetic state on this substrate. Of the 5*d* metals, only Os and Ir have been predicted to display monolayer-induced magnetic ordering [89]; Os is calculated to possess a magnetic moment of 0.34 μ_B/atom on Ag{001} only, while for Ir the values are 0.91 μ_B/atom on Ag{001} and 0.94 μ_B/atom on Au{001} [89]. Redinger *et al* [99] have further extended such calculations to the Ag{111} substrate, finding substantial magnetic moments for Ru and Rh (1.23 and 0.67 μ_B/atom, respectively), and a very small moment for Ir (0.05 μ_B/atom). In very recent calculations, Liu *et al* [100] have found a much higher magnetic moment (1.27 μ_B/atom) for an Ir monolayer on Au{111}.

Interestingly, despite the multitude of theoretical predictions for induced magnetisation of overlayers at coinage metal surfaces, conclusive experimental verification of this supposed phenomenon has been somewhat elusive. A variety of techniques have been deployed [101-107], but with contradictory results. For instance, Rau *et al* [105,106] reported electron-capture experiments that indicated ferromagnetic ordering of monolayer V on Ag{001}, in contrast to the negative conclusions drawn from the Kerr-effect measurements of Fink *et al* [107] on the same system. Similar Kerr-effect measurements also failed to detect magnetic moments for Rh on Ag{001} [101] and for Rh and Pd on Au{001} [102]. In contrast, Li *et al* [103] performed photoemission experiments and reported that the 4*s* level of a Rh monolayer on Ag{001} showed a measurable splitting, although similar results on Au{001} could not be observed due to the proximity of the Au 4*f* levels. Splitting of the 4*s* level in these spin-unpolarised photoemission experiments could, of course, arise from non-magnetic origins, such as the occupation by Rh of more than one adsorption site, and indeed Beckmann and Bergmann [104] adduce weak localisation and anomalous Hall effect data to argue that both Rh and Ru overlayers are non-magnetic on both Ag and Au substrates. Their case is weakened, however, by the fact that they

worked with disordered films rather than single-crystals. The induced magnetisation is likely to be highly dependent upon the overlayer structure, which in turn will be strongly modulated by the particular geometry (and quality) of the surface facet (or indeed facets) examined. Furthermore, the possibility of interdiffusion between the overlayer and substrate materials is an additional ever-present consideration. Clearly theoretical predictions of thin-film magnetism are of little value if the thin-films in question cannot be realised in practice.

In fact, of course, the range of possible surface structures is not limited to monolayers and randomised alloy diffusion. It is expected [108] that several combinations of metals may result in segregation of entire monolayers, so that the deposited material may exclusively occupy one or more complete subsurface layers, while the substrate material provides a capping layer. In their calculations for monolayer Ir on Au{111}, for example, Liu *et al* [100] have determined an energetic preference of 0.47 eV/adatom for Ir to occupy the second layer rather than the first, and a further 0.13 eV/adatom for Ir to occupy the third layer rather than the second. The spin-polarisation of the Ir monolayer drops from 1.27 μ_B/atom at the surface to 0.78 μ_B/atom in the second layer, but then rises again to 1.07 μ_B/atom in the third.

3.3.3. Sub- and super-monolayer films

The question of whether magnetic ordering is, in fact, present in these monolayer systems remains open. It also remains to be seen whether surface facets other than {001} and {111} are conducive to the same effect or not. An interesting recent contribution to this matter is the work of Bellini *et al* [109] on 4*d* transition metal nanowires at the {711}, {410} and {221} surfaces of Ag. The stepped facets constitute, in effect, a template for the growth of such one-dimensional structures, with the overlayer species preferentially adsorbing in the lee of the step-edges. They calculated magnetic moments for nanowires of Nb, Mo, Tc, Ru and Rh that were neatly intermediate between the monolayer results of Blügel [89] and results for isolated adatoms calculated by Lang *et al* [110]. Notably, they found that the Nb and Mo nanowires displayed antiferromagnetic interwire ordering, as opposed to the ferromagnetic ordering characteristic of the Tc, Ru and Rh wires [109]. Further nanowire calculations on a coinage metal substrate have recently been reported by Spišák and Hafner [111], who discuss Fe adsorbed on various Cu{11n} surfaces. Their results indicate ferromagnetically coupled wires in all cases, with magnetic moments in the range 2.79-3.01 μ_B/atom.

In addition to the study of 1D nanowires at sub-monolayer coverages, a small number of calculations have also addressed changes in the nature of magnetism as one builds up towards 3D films at super-monolayer coverages. Kraft *et al* [112], for instance, considered a paramagnetic four-layer *fcc* Fe film on Cu{001}, concluding that the interface interaction plays a minimal role apart

from the imposition of a metastable overlayer structure and of a substrate-determined lateral lattice parameter. Subsequently considering an appropriately constrained spin-polarised 11-layer *fcc* Fe slab *without* a Cu substrate, they determined ferromagnetic intralayer coupling in all layers [112]. Furthermore, they reported ferromagnetic interlayer coupling for the outer two layers on each side of the slab, with antiferromagnetic interlayer coupling for all deeper layers (i.e. the spin directions alternated as uududududuu, where u=up and d=down). The surface-layer magnetic moments were found to be substantially enhanced, relative to the bulk value. This simple picture was later extended by Moroni *et al* [113,114], who considered *fcc* Fe films on Cu{001} at coverages up to 9 ML. For coverages of 3 ML and below, they determined that the overlayer was entirely ferromagnetic, but beyond this critical thickness some rather subtle behaviour ensued (although note that ferromagnetic intralayer coupling was assumed in all cases). For even numbers of Fe layers, bilayer antiferromagnetism was favoured (i.e. uudd/Cu; uudduu/Cu; uudduudd/Cu), with magnetic moments of the surface-layer *and* interface-adjacent Fe atoms typically somewhat enhanced. For odd numbers of Fe layers, ferromagnetic coupling within the outermost bilayer and within the substrate-adjacent bilayer was again the rule, but no *general* pattern could be discerned for the remaining layers (i.e. uuddd/Cu; uuudduu/Cu; uudududuu/Cu). Surface-layer and interface-adjacent magnetic moments were again somewhat enhanced, and it is easy to imagine the result of Kraft *et al* [112] for an isolated 11-layer *fcc* Fe slab forming the next step in the sequence.

For the 4*d* and 5*d* overlayers, Blügel [115] has reported a significant reduction in calculated ferromagnetic moments for bilayer Ru, Rh and Ir on Ag{001}, compared to the monolayers. Clearly, the bulk-like paramagnetism of these adlayer materials is reasserted very rapidly with increasing thickness. Interestingly, bilayers of Pd and Pt were reported to show ferromagnetism, even though the monolayers did not; the authors attribute this to the onset of bulk ferromagnetism in the artificially lattice-expanded overlayers [115].

3.4. The mysterious case of V{001}

As a final offering in this section, we briefly note a long-standing controversy that rumbles on to this day, namely the existence (or otherwise) of magnetic ordering at the V{001} surface. The first hint that something unusual might occur on this surface could be gleaned from the FLAPW/LDA calculations of Fu *et al* [86] for a bilayer of V on Ag{001}; they reported a magnetic moment of 1.15 μ_B/atom for the surface layer, and less than 0.05 μ_B/atom for the layer in contact with the substrate. The observation that the surface layer could become magnetically ordered, even when sitting on top of a paramagnetic second layer, would seem to suggest the possibility that the surface layer of V{001} might also become magnetically ordered, even though the bulk is paramagnetic. The first calculations directly to address the issue,

however, indicated that no such ordering occurred on the pure V{001} surface (Ohnishi *et al* [116], within FLAPW/LDA). Indeed, there the matter might have rested, were it not for the subsequent electron-capture measurements of Rau *et al* [105,106] that indicated ferromagnetic ordering of the surface *did* in fact occur.

Prompted by these conflicting findings, Bryk *et al* [117] recently carried out calculations using NCPP and the PW91 [9] form of the GGA, reporting that a seven-layer V{001} slab did indeed become magnetic, with moments of 1.45 μ_B/atom in the surface layer, and oppositely-aligned moments of -0.70, -0.35 and -0.15 μ_B/atom in the second, third and fourth sub-surface layers respectively. Subsequently, Robles *et al* [118] showed that a combination of NCPP and the PBE [12] functional supported surface-layer magnetic moments of 1.70 μ_B/atom for slabs up to 15 layers thick, but found that these vanished for the thicker slabs within an all-electron linear muffin-tin orbital (LMTO) scheme. Batyrev *et al* [119] have confirmed robustly magnetic results within PW91 NCPP calculations for nine-layer slabs, but again obtained almost vanishing moments within an all-electron FLAPW scheme once slab relaxation was allowed. Bihlmayer *et al* [120] had earlier reported that they too could reproduce only a rather negligible surface magnetic moment within their FLAPW/PW91 calculations, and then only for very thin slabs. Meanwhile, recent LDA calculations [121] within the all-electron LMTO scheme continue to support the original non-magnetic conclusion reached in the all-electron FLAPW/LDA studies of Ohnishi *et al* [116].

If there are any general messages to be drawn from the preceding results, they are (i) that there may be a tendency for GGA functionals to favour magnetic ordering, when compared with LDA; (ii) that there may be a tendency for NCPP methods to favour magnetic ordering, when compared with all-electron techniques; and (iii) that there may be a tendency for thin slabs to favour magnetic ordering in all-electron calculations, when compared with thicker slabs. At the time of writing, the (current) last word on the subject appears to be the contribution of Kresse *et al* [122], who have carried out tests, within a single computational package, of several norm-conserving and ultrasoft pseudopotentials, comparing the results with those obtained using the frozen-core all-electron PAW scheme [15,22]. Their conclusion is that both NCPP and USPP calculations should be capable of matching results from all-electron methods only if rather small core radii are applied; this of course renders NCPP calculations prohibitively expensive, but USPP approaches would still be feasible. Kresse *et al* [122] therefore emphasise the need for care to be taken in the generation and convergence testing of pseudopotentials for use in such situations, while promoting the PAW technique as the more robustly reliable methodology.

4. MAGNETIC ALLOY SURFACES

Moving beyond the realm of thin-film magnetism, one arrives in the kingdom of the magnetic alloys. Strictly-speaking, we should at the outset recognise two distinct kinds of alloy which may exist at the surface: the first is simply the surface of a bulk alloy (an "alloy surface"), while the second is an alloy that is formed only in the surface layer or the selvedge of an otherwise compositionally dissimilar bulk material (a "surface alloy"). For reasons of brevity, we shall restrict ourselves here to the former situation, and furthermore examine just two particularly instructive cases: the first chosen because it illustrates how exotic magnetic behaviour in bulk alloys may be radically altered at the surface, and the second because it shows how surface chemistry can be radically altered by the magnetic properties of the bulk alloy.

4.1. The surface of a half-metallic semi-Heusler alloy: NiMnSb{001}

Amongst the magnetic alloys, two groups in particular have been subjected to considerable attention in recent years: the so-called Heusler and semi-Heusler alloys. These materials were first described in two short papers [123,124] published in 1903, and take the general compositional formulae X_2MnY and XMnY respectively, where X represents an element from the *d*-block of the periodic table, and Y an element from the *p*-block. For a wide range of combinations of X and Y, these alloys crystallise in well-ordered structures based upon the *fcc* lattice.

Despite their long pedigree, however, the current interest in the Heusler and semi-Heusler alloys was only sparked in 1983 upon the publication of a theoretical paper by de Groot *et al* [125] in which the prototypical semi-Heusler alloy NiMnSb was predicted to display half-metallic properties. The concept of a half-metal needs to be carefully distinguished from the similar-sounding but entirely different concepts of the semi-metal and the semiconductor. The property of half-metallicity is inextricably linked with the permanent magnetic polarisation of a material, and refers to the case when the electrons at the Fermi level display 100% spin-polarisation. In other words, while the electronic bands of one spin-species cross the Fermi level, those of the other spin-species do not. In the case of half-metallic semi-Heusler alloys, the majority-spin electrons behave as if the material were a good metal, while the minority-spin electrons behave as if the material were an insulator or semiconductor.

Subsequent to the initial work of de Groot *et al* [125] on NiMnSb, a number of other semi-Heusler alloys have also been predicted to be half-metallic. Their potential in spintronic applications cannot be overstressed. In effect, semi-Heusler alloys could one day be employed as perfect spin-valves, for injection of polarised charge carriers into semiconductor devices. Before such potential can be realised, however, it will be necessary to understand in detail the electronic

behaviour of the surfaces and interfaces of these half-metallic materials; exotic bulk properties are of very limited use if one cannot introduce or extract electrons in a controlled and reproducible manner.

It is fair to say that the surface science of the half-metal semi-Heusler alloys is in its infancy. The majority of studies on these materials have focussed upon the bulk properties, and surface effects have been viewed largely as unwanted complications. Nevertheless, a small amount of experimental data on the electronic nature of the NiMnSb surface is now available, and DFT calculations have a considerable role to play, both in interpreting the results and in suggesting routes for further investigation.

One of the most troublesome aspects of semi-Heusler alloy surfaces is that they are prone to segregation, so that the surface stoichiometry may differ radically from that of the bulk. Clearly such an occurrence would likely upset the fine balance which leads to the desired half-metallicity, so the first challenge to experimentalists in this field must be the production of well-ordered surfaces with a well-defined stoichiometry. The first to achieve this goal were Dowben and co-workers [126], who showed that segregation at a NiMnSb{001} surface could be suppressed by the growth of a thick capping-layer of Sb immediately following the co-deposition of the alloy components. The capping-layer could then be removed by flash annealing, leaving a well-ordered (1x1) surface. Characterisation of the surface composition, by means of photoemission spectroscopy, demonstrated a near-perfect surface stoichiometry with MnSb-termination. Both the clean MnSb-terminated surface and the interface with the Sb capping-layer have been studied within DFT by Jenkins and King [29,30] and by de Wijs and de Groot [127].

The DFT studies of the clean NiMnSb{001} surface [29,127] revealed that the half-metallicity of the alloy is lost, even when the stoichiometry is perfect. Two surface-localised minority-spin states exist within the bulk minority-spin band gap, exhibiting unusual dispersion curves and cutting the Fermi level around a highly elliptical contour in reciprocal space [29]. The states are robust against lateral displacements of the surface atoms, which accounts for the lack of driving force towards surface reconstruction, although the relatively small energy changes involved may be taken to imply a rather mechanically soft surface. In contrast, however, the two minority-spin surface states were found to be significantly disrupted by the addition of 0.5 ML of Sb to the surface [30]. Calculations showed that the adatoms preferred adsorption site was in the hollows of the uppermost MnSb layer, directly above the vacant sites of the sub-surface Ni layer. In this location, the adatom coupling was found to drive one surface state entirely out of the minority-spin band gap, and to perturb the other so strongly as to be almost unrecognisable from the clean surface case.

The picture revealed by DFT changed dramatically, however, when a further 0.5 ML of Sb was added [30]. The preferred site for the adatoms at 1.0 ML coverage was found to switch to the atop position, and recognisable versions of

both surface states were found to reappear within the minority-spin band gap. The only major change in electronic structure was the appearance of overlayer-localised minority-spin states within the bulk minority-spin band gap, but these were confined to the edges of the Brillouin zone. Indeed, upon adding further layers of Sb to the surface, the electronic structure was found to alter very little from the 1.0 ML case; the erstwhile surface states remained as distinct interface states, while the overlayer states at the zone edge became more dense but only gradually encroached upon the zone centre. Despite being semi-metallic, the low density of states exhibited by Sb in the region of the zone centre makes it a good model for an insulating or semiconducting overlayer. The two key messages of the DFT calculations are therefore clear: (i) that even stoichiometric semi-Heusler surfaces may not necessarily be half-metallic [29,127], and (ii) that minority-spin surface states may persist as interface states upon formation of an insulating, semiconducting or semi-metallic overlayer [30]. Finding interfaces for which these surface states are saturated will be a major step towards their development as components in spintronic devices. The calculations of de Wijs and de Groot [127] have shown how DFT can be of use in such work, demonstrating that an idealised CdS/NiMnSb{111} interface can indeed remain half-metallic. Realising such a structure in practice may, of course, turn out to be less than straightforward.

4.2. Adsorption on an alloy surface: CO and NO on Pd_3Mn

Citing Pd/Mn alloys as efficient catalysts for NO reduction by CO, Delbecq and Sautet [128-130] have carried out a series of calculations for adsorption of these two molecules on Pd{001} and on two possible surface terminations of Pd_3Mn{001}. Their results highlight an intriguing interplay between chemical and magnetic driving forces that can lead to remarkable and subtle effects when both low-spin and high-spin species are present at the same surface.

For CO adsorption on Pd{001}, Delbecq and Sautet [128] report a marginal preference for bonding at the hollow site rather than the bridge site, with the atop site distinctly unfavoured. The same is true of NO adsorption [129]. Interestingly, these authors report a non-vanishing magnetic moment on the clean Pd{001} surface-slab [128], but this must be viewed in light of the controversy surrounding similar reports for V{001} (see sub-section 3.4 above). For the record, the authors note that their frozen-core all-electron LDA calculations show a significant reduction in the magnetic moment as the slab size increases [128], so spin-polarisation is probably not a feature of the real surface.

Moving to the Pd_3Mn{001} surface, two different terminations are possible: one features only Pd atoms (A), the other a mixture of Pd and Mn atoms (B). Both CO and NO are reported to bind on the "A" surface with the same site preferences as on the Pd{001} surface [128,129]. Remarkably, however, when both Pd and Mn are exposed, on the "B" surface, CO shows a marked preference

for atop binding on the Pd atoms, and NO shows an equally marked preference for atop binding on the Mn atoms [128-130]. Adsorption of CO on this surface was found to lead to a reduction of the small top-layer Pd moment down to 0.01 μ_B/atom from 0.14 μ_B/atom on clean $Pd_3Mn\{001\}$, but left that of the top-layer Mn atom almost unchanged at 4.50 μ_B/atom, compared with 4.56 μ_B/atom on the clean surface; the CO molecule gained only a very small magnetic moment of 0.02 μ_B/atom, antiferromagnetically coupled with the substrate [128]. Adsorption of NO, on the other hand, was found to lead to a strong quenching of the magnetic moment for the top-layer Mn atom, down to 2.96 μ_B/atom, with very little effect on the top-layer Pd atom (0.10 μ_B/atom) and a large antiferromagnetically-coupled moment on the adsorbate amounting to 0.64 μ_B/atom [129]. The conclusion of Delbecq and Sautet [130] was that spin-polarisation dominated the nature of bonding at this surface, with the affinity of the diamagnetic CO molecule for the low-spin site, and of the paramagnetic NO molecule for the high-spin site, overcoming the "chemical" preference of both molecules for high-coordination sites. If such a mechanism is borne out in future work on magnetic alloy surfaces, then the implications for bimetallic catalyst design could be quite profound.

5. CONCLUDING REMARKS

The field of theoretical density functional studies on magnetic surfaces is a rapidly expanding and developing one. No review of this size could hope to cover all aspects of the current situation in any kind of depth. Indeed, the author is aware of some notable omissions, particularly in relation to first-principles modelling of scanning probe microscopy at spin-polarised surfaces [42,131-134], non-collinearity [81,135], and spin-orbit effects [136,137]. These somewhat specialised areas are deserving of separate attention, and a general review such as this could not do them justice.

The key points that this review should nevertheless serve to highlight include: (i) the generally high level of agreement between all-electron and ultrasoft pseudopotential techniques; (ii) the inability of a simple coordination number picture to fully explain the details of magnetic enhancement at surfaces; (iii) the localised nature of adsorbate-induced demagnetisation; (iv) the possibility of spin-polarisation in reduced dimensions, even when the bulk material is non-magnetic; (v) the sensitivity of exotic magnetic alloy materials to the presence of even a stoichiometric surface; and (vi) the potential for the magnetic properties of alloys to influence the chemistry of adsorbates. The open questions implicit in several of the above points should continue to provide opportunities for fruitful research for many years to come.

6. ACKNOWLEDGEMENTS

The author wishes to thank his colleagues at Cambridge, past and present, for useful discussions and/or critical comments on this review. The author is also grateful to The Royal Society for a University Research Fellowship.

REFERENCES

[1] P. Hohenberg and W. Kohn, Phys. Rev., 136 (1964) B864.
[2] W. Kohn and L.J. Sham, Phys. Rev., 140 (1965) A1133.
[3] L. Petit, S.V. Beiden, W.M. Temmerman, Z. Szotek, G.M. Stocks and G.A. Gehring, J. Phys. Condens. Matter., 12 (2002) 8439.
[4] E.C. Stoner, Proc. R. Soc. Lond., A169 (1939) 339.
[5] S.H.Vosko and J.P. Perdew, Can. J. Phys., 53 (1975) 1385.
[6] J.F. Janak, Phys. Rev. B, 16 (1977) 255.
[7] I.J. Kim, J.I. Lee and A.J. Freeman, Phys. Rev. B, 65 (2002) 064525.
[8] R.G. Parr and W.Yang, Density Functional Theory of Atoms and Molecules, Oxford, Oxford, 1994.
[9] J.P. Perdew, J.A. Chevary, S.H. Vosko, K.A. Jackson, M.R. Pederson, D.J. Singh and C. Fiolhais, Phys. Rev. B 46 (1992) 6671.
[10] P. Hu, D.A. King, S. Crampin, M.-H. Lee and M.C. Payne, Chem. Phys. Lett., 230 (1994) 501.
[11] Q. Ge, R. Kose and D.A. King, Adv. Catal., 45 (2000) 207.
[12] J.P. Perdew, K. Burke and M. Ernzerhof, Phys. Rev. Lett., 77 (1996) 3865.
[13] Y. Zhang and W. Yang, Phys. Rev. Lett., 80 (1998) 890.
[14] B. Hammer, L.B. Hansen and J.K. Nørskov, Phys. Rev. B, 59 (1999) 7413.
[15] G. Kresse and D. Joubert, Phys. Rev. B, 59 (1999) 1758.
[16] S. Ohnishi, A.J. Freeman and M. Weinert, Phys. Rev. B, 28 (1983) 6741.
[17] H. Krakauer, A.J. Freeman and E. Wimmer, Phys. Rev. B, 28 (1983) 610.
[18] E. Wimmer, A.J. Freeman and H. Krakauer, Phys. Rev. B, 30 (1984) 3113.
[19] D. Vanderbilt, Phys. Rev. B, 41 (1990) 7892.
[20] E.G. Moroni, G. Kresse, J. Hafner and J. Furthmüller, Phys. Rev. B, 56 (1997) 15629.
[21] S.G. Louie, S. Froyen and M.L. Cohen, Phys. Rev. B, 26 (1982) 1738.
[22] P.E. Blöchl, Phys. Rev. B, 50 (1994) 17953.
[23] L.J. Sham and M. Schlüter, Phys. Rev. Lett., 51 (1983) 1888.
[24] J.P. Perdew and M. Levy, Phys. Rev. Lett., 51 (1983) 1884.
[25] M.S. Hybertsen and S.G. Louie, Phys. Rev. B, 34 (1986) 5390.
[26] R.S. Mulliken, J. Chem. Phys., 23 (1955) 1833.
[27] R.F.W. Bader, Atoms in Molecules: A Quantum Theory, Clarendon, Oxford, 1990.
[28] Q. Ge, S.J. Jenkins and D.A. King, Chem. Phys. Lett. 327 (2000) 125.
[29] S.J. Jenkins and D.A. King, Surf. Sci. Lett., 494 (2001) L793.
[30] S.J. Jenkins and D.A. King, Surf. Sci. Lett., 501 (2002) L185.
[31] S.J. Jenkins (unpublished).
[32] S. Yamagishi, S.J. Jenkins and D.A. King, Surf. Sci. (submitted).
[33] S.J. Jenkins and D.A. King, Chem. Phys. Lett., 317 (2000) 372.
[34] A.D. Karmazyn, V. Fiorin, S.J. Jenkins and D.A. King, Surf. Sci., 538 (2003) 171.
[35] S.J. Jenkins, Q. Ge and D.A. King, Phys. Rev. B, 64 (2001) 014213.
[36] S. Yamagishi, S.J. Jenkins and D.A. King, J. Chem. Phys., 114 (2001) 5765.

[37] M. Aldén, S. Mirbt, H.L. Skriver, N.M. Rosengaard and B. Johansson, Phys. Rev. B, 46 (1992) 6303.
[38] O. Eriksson, A.M. Boring, R.C. Albers, G.W. Fernando and B.R. Cooper, Phys. Rev. B, 45 (1992) 2868.
[39] Š. Pick and H. Dreyssé, Surf. Sci., 474 (2001) 64.
[40] F. Mittendorfer, A. Eichler and J. Hafner, Surf. Sci., 423 (1999) 1.
[41] C.L. Fu and A.J. Freeman, J. Phys. C, 49 (1988) C8.
[42] S. Heinze, S. Blügel, R. Pascal, M. Bode and R. Wiesendanger, Phys. Rev. B, 58 (1998) 16432.
[43] A.J. Freeman and C.L. Fu, J. Appl. Phys., 61 (1987) 3356.
[44] A. Stibor, G. Kresse, A. Eichler and J. Hafner, Surf. Sci., 507 (2002) 99.
[45] J. Braun, C. Math, A. Postnikov and M. Donath, Phys. Rev. B, 65 (2002) 184412.
[46] J.J. Mortensen, M.V. Ganduglia-Pirovani, L.B. Hansen, B. Hammer and J.K. Nørskov, Surf. Sci., 442 (1999) 1.
[47] A. Logadottir and J.K. Nørskov, Surf. Sci., 489 (2001) 135.
[48] A.A. Ostroukhov, V.M. Floka and V.T. Cherepin, Surf. Sci., 333 (1995) 1388.
[49] O. Eriksson, G.W. Fernando and R.C. Albers, Solid State Commun., 78 (1991) 801.
[50] C. Li and A.J. Freeman, J. Magn. Magn. Mater., 75 (1988) 53.
[51] S. Meza-Aguilar, O. Elmouhssine, H. Dreyssé and C. Demangeat, Surf. Sci., 454 (2000) 900.
[52] F. Favot, A. Dal Corso and A. Baldereschi, Phys. Rev. B, 63 (2001) 115416.
[53] S.J. Jenkins and D.A. King, Chem. Phys. Lett., 309 (1999) 434.
[54] W.T. Geng, M. Kim and A.J. Freeman, Phys. Rev. B 63 (2001) 245401.
[55] W.T. Geng, A.J. Freeman and R. Wu, Phys. Rev. B, 63 (2001) 064427.
[56] R. Wu and A.J. Freeman, Phys. Rev. B, 47 (1993) 3904.
[57] R. Wu, A.J. Freeman and G.B. Olsen, Phys. Rev. B, 53 (1996) 7504.
[58] A. Eichler, F. Mittendorfer and J. Hafner, Phys. Rev. B, 62 (2000) 4744.
[59] M.Ø. Pedersen, L. Österlund, J.J. Mortensen, M. Mavrikakis, L.B. Hansen, I. Stensgaard, E. Lægsgaard, J.K. Nørskov and F. Besenbacher, Phys. Rev. Lett., 84 (2000) 4898.
[60] A. Eichler, Surf. Sci., 526 (2003) 332.
[61] V. Shah, T. Li, K.L. Baumert, H. Cheng and D.S. Sholl, Surf. Sci., 537 (2003) 217.
[62] D.I. Sayago, J.T. Hoeft, M. Polcik, M. Kittel, R.L. Toomes, J. Robinson, D.P. Woodruff, M. Pascal, C.L.A. Lamont and G. Nisbet, Phys. Rev. Lett., 90 (2003) 116104.
[63] D.C. Sorescu, D.L. Thompson, M.M. Hurley and C.F. Chabalowski, Phys. Rev. B, 66 (2002) 035416.
[64] S.J. Jenkins and D.A. King, Surf. Sci., 504 (2002) 138.
[65] S.J. Jenkins and D.A. King, Surf. Sci., 529 (2003) 312.
[66] J.J. Mortensen, L.B. Hansen, B. Hammer and J.K. Nørskov, J. Catal., 182 (1999) 479.
[67] R.C. Egeberg, S. Dahl, A. Logadottir, J.H. Larsen, J.K. Nørskov and I. Chorkendoff, Surf. Sci., 491 (2001) 183.
[68] F. Mittendorfer and J. Hafner, Surf. Sci., 472 (2001) 133.
[69] F. Mittendorfer and J. Hafner, J. Phys. Chem. B, 106 (2002) 13299.
[70] F. Mittendorfer and J. Hafner, Surf. Sci., 492 (2001) 27.
[71] A. Michaelides and P. Hu, Surf. Sci., 437 (1999) 362.
[72] A. Michaelides and P. Hu, J. Chem. Phys., 112 (2000) 6006.
[73] A. Michaelides and P. Hu, J. Chem. Phys., 114 (2001) 2523.
[74] R. Wu and A.J. Freeman, Phys. Rev. B, 45 (1992) 7205.
[75] J.I. Lee, S.C. Hong, A.J. Freeman and C.L. Fu, Phys. Rev. B, 47 (1993) 810.
[76] S. Mirbt, O. Eriksson, B. Johansson and H.L. Skriver, Phys. Rev. B, 52 (1995) 15070.
[77] R. Wu and A.J. Freeman, Phys. Rev. B, 51 (1995) 17131.

[78] O. Elmouhssine, G. Moraitis, C. Demangeat and J.C. Parlebas, Phys. Rev. B 55 (1997) R7410.
[79] S. Handschuh and S. Blügel, Solid State Commun., 105 (1998) 633.
[80] T. Asada, S. Blügel, G. Bihlmayer, S. Handschuh and R. Abt, J. Appl. Phys., 87 (2000) 5935.
[81] T. Asada, G. Bihlmayer, S. Handschuh, S. Heinze, Ph. Kurz and S. Blügel, J. Phys. Condens. Matter, 11 (1999) 9347.
[82] A.J. Freeman and R. Wu, J. Magn. Magn. Mater., 100 (1991) 497.
[83] R. Wu, C. Li and A.J. Freeman, J. Magn. Magn. Mater., 99 (1991) 71.
[84] S. Blügel, M. Weinert and P.H. Dederichs, Phys. Rev. Lett., 60, (1988) 1077.
[85] R. Wu and A.J. Freeman, Phys. Rev. B, 44 (1991) 4449.
[86] C.L. Fu, A.J. Freeman and T. Oguchi, Phys. Rev. Lett., 54 (1985) 2700.
[87] S. Blügel, Appl. Phys. A, 63 (1996) 595.
[88] S. Blügel and P.H. Dederichs, Europhys. Lett., 7 (1988) 743.
[89] S. Blügel, Phys. Rev. Lett., 68 (1992) 851.
[90] M. Eder, J. Hafner and E.G. Moroni, Phys. Rev. B, 61 (2000) 11492.
[91] T. Anderson and W. Hübner, Phys. Rev. B, 65 (2002) 174409.
[92] R. Wu and A.J. Freeman, J. Magn. Magn. Mater., 116 (1992) 202.
[93] R. Wu and A.J. Freeman, J. Appl. Phys., 79 (1996) 6500.
[94] R. Pentcheva and M. Scheffler, Phys. Rev. B, 61 (2000) 2211.
[95] O. Eriksson, R.C. Albers and A.M. Boring, Phys. Rev. Lett., 66 (1991) 1350.
[96] R. Wu and A.J. Freeman, Phys. Rev. B, 45 (1992) 7222.
[97] M.J. Zhu, D.M. Bylander and L. Kleinman, Phys. Rev. B, 43 (1991) 4007.
[98] C.S. Chang, L.H. Cho, J.I. Lee, S.C. Hong, R. Wu and A.J. Freeman, J. Magn. Magn. Mater., 177 (1998) 1255.
[99] J. Redinger, S. Blügel and R. Podloucky, Phys. Rev. B, 51 (1995) 13852.
[100] Z. Liu, S.J. Jenkins and D.A. King (unpublished).
[101] G.A. Mulhollan, R.L. Fink and J.L. Erskine, Phys. Rev. B, 44 (1991) 2393.
[102] C. Liu and S.D. Bader, Phys. Rev. B, 44 (1991) 12062.
[103] H. Li, S.C. Wu, D. Tian, Y.S. Li, J. Quinn and F. Jona, Phys. Rev. B, 44 (1991) 1438.
[104] H. Beckmann and G. Bergmann, Phys. Rev. B, 55 (1997) 14350.
[105] C. Rau, C. Liu, A. Schmalzbauer and G. Xing, Phys. Rev. Lett., 57 (1986) 2311.
[106] C. Rau, G. Xing and M. Robert, J. Vac. Sci. Technol. A, 6 (1988) 579.
[107] R.L. Fink, C.A. Ballentine, J.L. Erskine and J.A. Araya-Pochet, Phys. Rev. B, 41 (1990) 10175.
[108] A. Christensen, A.V. Ruban, P. Stoltze, K.W. Jacobsen, H.L. Skriver, J.K. Nørskov and F. Besenbacher, Phys. Rev. B, 56 (1997) 5822.
[109] V. Bellini, N. Papanikolaou, R. Zeller and P.H. Dederichs, Phys. Rev. B, 64 (2001) 094403.
[110] P. Lang, V.S. Stepanyuk, K. Wildberger, R. Zeller and P.H. Dederichs, Solid State Commun., 92 (1994) 755.
[111] D. Spišák and J. Hafner, Phys. Rev. B, 65 (2002) 235405.
[112] T. Kraft, P.M. Marcus and M. Scheffler, Phys. Rev. B, 49 (1994) 11511.
[113] E.G. Moroni, G. Kresse and J. Hafner, J. Phys. Cond. Matter, 11 (1999) L35.
[114] E.G. Moroni, G. Kresse and J. Hafner, J. Magn. Magn. Mater., 199 (1999) 551.
[115] S. Blügel, Phys. Rev. B, 51 (1995) 2025.
[116] S. Ohnishi, C.L. Fu and A.J. Freeman, J. Magn. Magn. Mater., 50 (1985) 161.
[117] T. Bryk, D.M. Bylander and L. Kleinman, Phys. Rev. B, 61 (2000) R3780.
[118] R. Robles, J. Izquierdo, A. Vega and L.C. Balbás, Phys. Rev. B, 63 (2001) 172406.
[119] I.G. Batyrev, J.-H. Cho and L. Kleinman, Phys. Rev. B, 63 (2001) 172420.

[120] G. Bihlmayer, T. Asada and S. Blügel, Phys. Rev. B 62 (2000) R11937.
[121] I. Turek, S. Blügel and J. Kudrnovský, Phys. Rev. B, 57 (1998) R11065.
[122] G. Kresse, W. Bergermayer and R. Podloucky, Phys. Rev. B, 66 (2002) 146401.
[123] F. Heusler, Verhandl. Deuts. Phys. Ges., 5 (1903) 219.
[124] F. Heusler, W. Stark and E. Haupt, Verhandl. Deuts. Phys. Ges., 5 (1903) 220.
[125] R.A. de Groot, F.M. Mueller, P.G. van Engen, K.H.J. Buschow, Phys. Rev. Lett., 50 (1983) 2024.
[126] D. Ristoiu, J.P. Nozieres, C.N. Borca, T. Komesu, H.-K. Jeong and P.A. Dowben, Europhys. Lett., 49 (2000) 624.
[127] G.A. de Wijs and R.A. de Groot, Phys. Rev. B, 64 (2001) 020402.
[128] F. Delbecq and P. Sautet, Phys. Rev. B, 59 (1999) 5142.
[129] F. Delbecq and P. Sautet, Surf. Sci., 442 (1999) 338.
[130] F. Delbecq and P. Sautet, Chem. Phys. Lett., 302 (1999) 91.
[131] W.A. Hofer and A.J. Fisher, Surf. Sci., 515 (2002) L487.
[132] W.A. Hofer and A.J. Fisher, Surf. Sci., 498 (2002) L65.
[133] W.A. Hofer, J. Redinger, A. Biedermann and P. Varga, Surf. Sci., 482 (2001) 1113.
[134] W.A. Hofer, J. Redinger, A. Biedermann and P. Varga, Surf. Sci., 466 (2000) L795.
[135] Ph. Kurz, G. Bihlmayer, K. Hirai and S. Blügel, Phase Transitions, 75 (2002) 101.
[136] R. Wu, Z.X. Yang and J.S. Hong, J. Phys. Condens. Matter, 15 (2003) S587.
[137] R. Wu and A.J. Freeman, J. Magn. Magn. Mater., 200 (1999) 498.

J. Leszczynski (Editor)
Computational Materials Science
Theoretical and Computational Chemistry, Vol. 15

Chapter 9

Simulating the structure and reactivity of oxide surfaces from first principles

Simon P. Bates[a] & Simon D. Elliott[b]*

[a]School of Physics, University of Edinburgh, Edinburgh EH9 3JZ, UK; S.P.Bates@ed.ac.uk.

[b]NMRC, University College Cork, Lee Maltings, Prospect Row, Cork, Ireland; Simon.Elliott@nmrc.ucc.ie.

A review of First Principles simulation of oxide surfaces is presented, focussing on the interplay between atomic-scale structure and reactivity. Practical aspects of the First Principles method are outlined: choice of functional, role of pseudopotential, size of basis, estimation of bulk and surface energies and inclusion of the chemical potential of an ambient. The suitability of various surface models is discussed in terms of planarity, polarity, lateral reconstruction and vertical thickness. These density functional calculations can aid in the interpretation of STM images, as the simulated images for the rutile (1 1 0) surface illustrate. Non-stoichiometric reconstructions of this titanium oxide surface are discussed, as well as those of ruthenium oxide, vanadium oxide, silver oxide and alumina (corundum). This demonstrates the link between structure and reactivity in vacuum versus an oxygen-rich atmosphere. This link is also evident for interaction with water, where a survey of relevant *ab initio* computational work on the reactivity of oxide surfaces is presented.

Keywords : Oxide surfaces, First Principles, Surface energy, Structure of clean surfaces, Reconstructions, Solid-gas/vacuum interfaces, Density functional theory, Crystal stoichiometry, Adsorption

1. INTRODUCTION

Every real condensed phase is bounded by surfaces. The surface is where the liquid or solid interacts with its surroundings. Surface structure and reactivity are thus intimately linked, at least at the atomic scale, which is the subject of this review. In particular, we consider results obtained from electronic structure

* corresponding author

calculations, which are now established as important probes of atomic-scale behaviour.

As the computational tools mature and become standardised, electronic structure theory is increasingly being applied to the study of complex materials, such as metal oxides rather than pure metals, surfaces rather than bulk phases, and reacting rather than stable systems. Oxide surfaces and their interactions with an ambient are the active elements for many current and emerging technologies - in energy conversion (sensors, solar and fuel cells), manufacturing industry (catalysis) and information technology (DRAM, CMOS). In many of these contexts, it is recognised that valuable insights into fundamental behaviour at the atomic-scale can be obtained from electronic structure calculations. We aim to highlight the growing interaction between theory and experiment in surface science, and show both how to simulate measured data and what questions from experiment can motivate computational studies.

As this review is intended to illustrate, the interplay between metal and oxygen leads to a richness of reactivity that is reflected in the surface structure of oxides. Much of this richness can be rationalised as varying proportions of ionic and covalent character in the metal-oxygen bonding, and is manifest in a variety of non-stoichiometric surfaces. We therefore focus on the prototypical transition metal oxide surface: rutile TiO_2 (1 1 0). This is contrasted with computational results for one of the most widely-studied p-block oxide surfaces - corundum Al_2O_3-(0 0 0 1) - and we refer also to computational surface studies on oxides of ruthenium, iron, vanadium, tin and silver, as well as ternary oxides.

The only heteroatom which we consider is H (via adsorption of H_2O). As our subject is periodic calculations, amorphous films are outside the scope of this review. The large body of work on adsorption onto titanium oxide of organic molecules or metal nanoparticles is reviewed in Ref. [1]. Metals on oxide supports are covered in the chapter by N. Roesch (in this volume). Two related reviews consider the computation of thin films [2] and polar surfaces, especially their reconstruction [3]. Useful overviews of surface science techniques and terminology, as well as historical views of work on metal surfaces, are given in Refs. [4,5].

This article is organised as follows. We begin with a deliberately brief presentation of the more practical aspects of the methodology of First Principles (FP) calculations. This is followed by a discussion of the connection to thermodynamics from the simulations, particularly focussing on practical ways to calculate the surface free energy. In Section 4, we return to the slab model used to simulate the surface and highlight the requirements of the slab to

accurately model, in an unbiased way, the `real' surface. We then compare relaxed, rumpled and reconstructed surfaces from FP calculations to experimental data. Section 5.1 investigates the simulation of Scanning Tunnelling Microscope (STM) topographs and Section 5.2 looks at their relation to experimental images, exemplified by recent studies of rutile surfaces. Section 6 deals with non-stoichiometric surfaces and their reactivity towards oxygen, while Section 7 looks at the adsorption of water on surfaces, particularly rutile. We offer some general conclusions in Section 8.

2. METHODOLOGY

This section is not intended to be a fully comprehensive presentation of all the theoretical and technical aspects of the calculation metholdology that has come to be known under the umbrella term of `First Principles' (FP). There are such reviews available and we direct the interested reader towards these throughout this Section; this is not a wheel we need reinvent. It is, instead, a selective look at some of the more important aspects of the methodology, a prescription for the practitioner. We try and highlight the general features employed by almost all studies cited in this review and briefly examine strengths and weaknesses.

By restricting this article to FP calculations, we exclude the large body of *ab initio* computational work based on the cluster as a surface model. Other reviews compare both approaches [2]. We likewise do not consider semi-empirical methodologies or pair-potential methods. A very recent comprehensive look at FP calculations in theory and in practice is that of Lindan et al. [6]. Equally, Ref. [7] is a review aimed somewhat at the geological community, discussing atomistic and *ab initio* methods for modelling minerals.

The term First Principles applied to atomistic simulation has, over the last few years, become synonymous with a calculation strategy that embodies the following methodology: it employs Density Functional Theory (DFT); it describes the system under consideration using a 3-D periodic supercell; it utilises a plane-wave basis set and it incorporates pseudopotentials to replace the atomic cores and core electrons by an effective potential. We take a look at each of these ingredients in turn. We do not distinguish between static and dynamic calculations (though the majority of the literature cited pertains to static calculations). Rather, we recognise both as valuable and complementary tools. Equally, we do not discuss (but do highlight) the distinction between different approaches to dynamic FP calculations. The seminal paper by Car and Parrinello [8] employed 'ficticious' electron dynamics and simulated annealing to minimise the energy. Other implementations explicitly minimise the total energy

of the system at every timestep and move the atoms according to forces calculated via the Hellmann-Feynman theorem.

Unlike wavefunction methods, DFT does not attempt the daunting task of constructing (and finding a solution for) the many-body wavefunction. This is in contrast to the collection of techniques which one might collect under the familial umbrella of `quantum chemical methods'. Rather, it starts from the premise that it is the electron density that determines the ground-state energy of the system. This results in a formalism that is, in principle, exact and practical as well (via the one-particle Kohn-Sham equations [9]).

The single biggest problem in the practical implementation of the theory is to find a functional for the exchange-correlation energy, denoted $E_{xc}[\rho(r)]$. One of the most surprising aspects about this entire field is that a very simple approximation to the form of the exchange-correlation functional actually works for a wide variety of systems. This simple approximation is that the exchange-correlation energy is that of a uniform electron gas (the so-called Local Density Approximation (LDA) [9]). The electron density around atoms or ions in a system is clearly markedly different from that of a uniform electron gas, so one might suggest that the LDA has no right to work at all. Yet it does,and in a surprisingly wide variety of systems, accurately predicts a variety of physical properties.

More recently, functionals have been proposed to include a dependence on the gradient of the electron density at a given point as well. These 'gradient corrections' have been found to improve the accuracy of calculated quantites for molecules (e.g. bond energies, dissociation energies), despite a slight tendency to increase the calculated lattice parameters of oxides by about 3%, typical of other materials too [10]. Practically all FP calculations use the LDA with / without gradient corrections in some form.

The employment of a 3-dimensional periodic supercell to model a particular surface of a system is equally ubiquitous. However, the starting point for all simulations is the bulk material, with the calculation of lattice parameters and the fitting of a curve of energy against lattice parameter to an equation of state. Care and attention here to get the most accurate predictions can pay dividends in later considerations of the surface, as small errors in bulk lattice parameters can be magnified to larger errors in, for example, surface relaxations. Most codes and implementations offer their own recipes for how to achieve the best accuracy in terms of selecting a suitable Fast Fourier Transform (FFT) mesh and reciprocal space sampling strategy. From an accurate bulk material description, one is able to progress to the construction of the surface model.

Here, a quasi-2D system (a surface) is modelled (most frequently) as a 3D periodic system, via a method of approximating a surface as a slab of finite thickness separated from periodic neighbour slabs by a layer of vacuum. The latter is most easily dealt with: on top of the surface (plus, if relevant, adsorbate) system there should be at least 5 Å of vacuum. However, a more difficult issue is how thick a slab is necessary for a given surface? The answer is a suitably cautious one: as thick as is necessary but no more. As thick as is necessary to make the upper layer(s) of surface atoms (and adsorbates that interact with them) behave as if there was a bulk solid structure beneath them; no more than is necessary on the usual grounds of computational expediency. In general, increasing slab thicknesses should be tested for convergence against calculated properties, such as surface atomic displacements or adsorption energies, and a compromise should be struck between accuracy and efficiency.

In the case of the TiO_2 (1 1 0) surface, the structure exhibits oscillating displacements of surface-layer Ti atoms [11] as a function of increasing slab thickness suggesting that at least 5 'layers' (where here a layer comprises adjacent O-Ti_2O_2-O planes) is needed. This is reinforced by recent calculations by Lindan and Zhang [12], who have noted a significant slab thickness dependence (up to 40%) on the adsorption energy of a single water molecule, and actually use 7 layer slabs for calculation of adsorption energies. In general a slab model generates two surfaces, and in practice this reduces an N layer slab to an effective thickness of $N/2$ (if N is even, $(N-1)/2$ if N is odd). We return to slab models in Section 4, from the point of view of what constitutes a realistic atomistic model of the surface.

In FP calculations, the single electron wavefunctions are expanded in a plane-wave basis. Such a basis has the advantages of being able to perform an exact variational calculation based on a discrete numerical grid, and that most operators can be made diagonal by the use of FFTs, facilitating frequent toggling between real and reciprocal space. (Indeed, the favourable scaling of FFTs with system size facilitates the application of the FP method to larger systems; Ref. [6] contains a fuller discussion). An infinite series expansion of plane waves is made practicable by truncation of the sum to only include plane waves up to a certain kinetic energy.

As attractive as it appears, a plane-wave basis also carries with it its own disadvantages. Generally, we are interested in the behaviour of the valence electrons of a material; it is these electrons that form chemical bonds which break and reform during the process of chemical reactions. However, near the atomic cores, the valence electron wavefunctions undergo rapid oscillations, due

to the strong Coloumb potential and the requirement to be orthogonal to the core wavefunctions. And although chemically-uninteresting, these core electrons present problems too; an impractically large number of plane-waves would be required to describe these core electrons. The solution is a pseudopotential; the replacement of the potential of the atomic core region with another that, if viewed from the environment of the atom, acts (practically) identically. The core states are replaced and the core regions of the valence wavefunctions are smoothed out. The generation and testing of pseudoptentials, together with the criteria for norm-conservation and transferability have received a great deal of attention and other articles document this development [6]. Here, we note that most implementations of the FP method now utilise so-called 'ultra-soft' pseudopotentials [13] which relax the norm-conserving criteria (permitting a lower plane wave cutoff energy to be used) by adding 'augmentation' charges into the core region.

3. FIRST PRINCIPLES THERMODYNAMICS

3.1. Surface free energy

It is a defining characteristic of a surface that it is an open system, the interface between two chemical reservoirs - often an ambient gas (A, say) and a bulk solid (B). Atoms may enter/leave the surface from/to these reservoirs. This variation in number of atoms (N_A, N_B) at the surface presents a challenge for total energy calculations, where it is more usual for systems with the same number of atoms to be compared. The grand canonical ensemble provides the appropriate framework for computing energetics of an open system [14]: the surface Gibbs free energy $G_{surf}(p,T,N_A,N_B)$ quantifies stability under given conditions of pressure p, temperature T and chemical potential μ, where the latter is defined

$$\mu_A=\partial G/\partial N_A \text{ at constant } T, p, N_B \qquad (1)$$

How accurately systems with various numbers of atoms can be simulated depends therefore on the accuracy of the chosen values for chemical potential. From a numerical point of view, values should be chosen that maximise favourable cancellation of systematic errors. From the modelling point of view, we seek to link μ reliably to physical reality. In the next sections we assess a number of approaches to determining μ and relating it to experimental conditions.

We first of all establish the link between total energies of slabs calculated by First Principles (E_{slab}) and the thermodynamic state variables. Changes in the internal energy $U(V,S,N_A,N_B)$ due to differences in atomic structure at zero temperature (or modelled by molecular dynamics (MD) [8,15,16] at finite

temperature) are well-accounted for by changes in the computed electronic energy: $\Delta U_{surf} \approx \Delta E_{slab}$. Then, changes in the Gibbs' free energy of a surface containing chemical species A and B at a given temperature and pressure are given by [14]:

$$\Delta G_{surf} = \Delta U_{surf} + p\Delta V - T\Delta S + \mu_A \Delta N_A + \mu_B \Delta N_B. \quad (2)$$

Changes with negative ΔG are thermodynamically favoured. Eq. (2) permits the effects of finite temperature and pressure to be introduced by estimating changes in volume ΔV and entropy ΔS, or from the choice of chemical potential, since $\mu = \mu(T,p)$. These contributions are discussed for a sample surface in Ref. [17]. At equilibrium with reservoirs of A and B, μ_A and μ_B of the surface are equal to those of the reservoirs, and so it is often convenient to use the reservoirs as the $\Delta G = 0$ reference. These chemical potentials may be calculated from First Principles or from calorimetric measurements and this is the focus of our discussion.

Surface free energies are usually normalised by expressing them independently of surface area A:

$$\gamma_{surf} = \Delta G_{surf} / A \quad (3)$$

(The units J m^{-2} are equivalent to the N m^{-1} of surface tension). Clearly, for a slab with two identical faces, the total area A is twice the area of one face.

3.2. Bulk chemical potential and stoichiometric surfaces

The most straightforward application of Eq. (2) is to a single component system - such as an oxide surface in equilibrium with the bulk oxide. Both bulk and surface are therefore stoichiometric, meaning that, for the example of rutile, both bulk and surface have the chemical formula TiO_2. Thus, the computed bulk energy per TiO_2 unit is used in Eq. (1) to give the chemical potential $\mu = E_{bulk}(TiO_2)$, and Eqs. (2) and (3) give a surface energy relative to the bulk of

$$\gamma_{surf} = \lim_{N \to \infty} [E_{slab} - N E_{bulk}] / A. \quad (4)$$

In practice, the limit is approximated by the finite thickess of a $(TiO_2)_N$ slab. In other words, the slab energy is the sum of bulk and surface contributions.

The most convenient way to obtain E_{bulk} is by computing a bulk cell by First Principles [11,18]. However, as shown in Refs. [19,20,21,22], the unavoidable discrepancies between bulk and slab calculations cause γ_{surf} to diverge with

increasing slab thickness (N). This is at odds with the idea of the slab model, namely that surface properties should converge as N is increased.

Instead, it is more accurate to estimate both E_{bulk} and γ_{surf} by calculating slabs across a range of N. By Eq. (4), a straight line of slope E_{bulk} and intercept $A\gamma_{surf}$ may be fitted to a plot of E_{slab} *vs* N. Errors are minimised by using the same technical parameters for all of the slabs and by favouring large N in the extrapolation. This procedure was tested in Ref. [23] for (1 1 0)-oriented slabs of $(TiO_2)_N$, $1 \leq N \leq 8$ and the sensitivity of γ_{surf} was demonstrated to be about 10% (± 0.1 J m^{-2}) to variations in E_{bulk} of ± 0.05 eV. The best γ_{surf} value was accurate to ± 0.04 J m^{-2} at N=8. Another benefit of the extrapolation is the averaging out of oscillations in E_{slab} *vs* N that are a result of the alternating (1 1 0) layers of this oxide.

Eq. (4) is the standard expression used to assess the stability of computed surfaces - the lower γ_{surf}, the more thermodynamically favoured [24]. Most surface energies are positive, reflecting the greater cohesion of the bulk relative to the surface. However, Eq. (4) neglects entirely the influence of an ambient (see section 6).

Once γ_{surf} has been determined for a range of surfaces of a given system, some aspects of the macroscopic morphology may be predicted. Facetting may occur if the increase in surface area is compensated by a lowering in surface energy, as illustrated for {0 1 1} facets on TiO_2 (0 0 1) in Ref. [18]. The Wulff construction may be used to estimate the overall shape of a crystal, surfaces contributing to the total surface area according to their relative stability [18,25].

4. GENERATING SLAB MODELS

The challenge facing any simulation is to build an idealised model, that is nevertheless sufficiently realistic to describe the properties of interest. Surfaces are particularly challenging in this regard, as shown by the examples from the recent literature in this article.

For instance, what model should be assumed for the atomic structure of a surface? The simplest picture of a surface is a planar terrace, a static array of passive adsorption sites. For a crystal, such terraces are slices through the bulk stacking sequence, a cleavage of the bulk. Is the planar terrace a reasonable model? Some unrelaxed bulk terminations are polar and thus inherently unstable (see below). But for non-polar surfaces, planarity is often favoured in order to minimise the surface energy (Section 3). Thus on the timescales of diffraction techniques, such as LEED and XAFS, many surfaces are indeed observed to be

static arrays of ions [26] and this justifies the use of periodic, planar slabs in the corresponding FP simulations.

However it must be borne in mind that many examples of more complex surfaces are known. Clays and zeolites show huge internal surface area, with a variety of layers and pore sizes. The whole field of heterogeneous catalysis depends on nano-structured surfaces of massive area, which certainly can not be thought of as planar. Grain boundaries may be thought of as internal surfaces or homo-interfaces [27] and are perhaps similar to the solid-liquid interface during melting.

The first step in building a planar model of a surface is cleaving the carefully-optimised bulk crystal to produce a slab with two exposed faces. Both surface orientation and cleavage plane must be selected. Low-index orientations ($h\ k\ l$) are parallel to close-packed layers of ions and so can be expected to show little corrugation and minimal surface area. As a result, low-index orientations are often those of lowest surface energy and predominate in experiment.

The more complex the crystal structure, the greater the number of inequivalent cleavage planes that are all oriented parallel to ($h\ k\ l$). Care should be taken when cleaving the crystal to avoid the inadvertent generation of polar surfaces. As detailed in Ref. [3], a polar surface is one where each repeat unit along [$h\ k\ l$] bears a non-zero dipole moment. The classical electrostatic argument is that the dipole contributions sum to give an energy which diverges with the size of crystal. This is easy to assess in most cases by assigning formal charges to the ions and checking for cancellation across the layers of the slab [28]. Indeed, an unrelaxed polar surface is unstable, and relieves the massive electrostatic energy by major rearrangment of the ionic and/or electronic structure, often manifest as surface reconstructions. This may explain why the surfaces of oxides are more prone to reconstruction than metals [29].

A surface reconstruction is a change in unit cell size due to atomic distortion parallel to the surface. Thus, rather than the (1×1) cell of the bulk termination, a reconstructed surface shows the lower symmetry of an $(n \times m)$ cell. An example is the (1×2) surface of rutile (1 1 0) (section 5.2).

As a tool for atomic-scale characterisation, FP calculations show the unique capacity to quantitatively assess the stability of any structural model for a reconstruction. It is advantageous that the $(n \times m)$ periodicity of the reconstruction is known (*e.g.* from LEED), as this fixes the size of cell which should be used in simulation. A geometry optimisation (possibly followed by a short MD run at low temperature) can be used to check whether any proposed

models do in fact represent local minima. For the same number of atoms in the cell, a simple comparison of total computed energies reveals which model is the most stable. Candidate reconstructions of differing composition may be assessed via the surface energy (Section 3), but to lower precision.

Rather than a few *ad hoc* models motivated by experiment and intuition, a truly *ab initio* prediction would systematically consider all arrangements of surface atoms that are consistent with the $(n \times m)$ periodicity. This remains a formidable challenge, particularly for complex materials like oxides. The combinatorial problem is magnified in size by both the range of possible oxide stoichiometries (see Section 6) and the uncertainty in the thickness of the selvedge (see below). Differences in surface energy can be slight, necessitating a high level of computational accuracy - that is, FP calculations on thick slabs. The availability of computer time is therefore the primary limit on this type of study. Compromises must be made in terms of the scope and accuracy of calculations and reliable findings from experiment should be exploited.

One strategy to avoid bias is the use of simulated annealing to generate novel, but reasonable, surface structures, such as the 50 or more V_xO_y ($\sqrt{3} \times \sqrt{3}$) and (2×2) reconstructions of Ref. [30]. The authors have confidence in this set of models based on their understanding of the vanadium oxide chemistry, from calculating the various bulk phases, more complex unsupported thin films and finally the complete system of oxide layers on a metal support.

A pseudo-combinatorial method has been developed in Refs. [23,31] to determine the most stable (1×2) reconstruction of rutile (1 1 0). Even for this small cell (3×13 Å, Ti_4O_8 per bulk-like layer), there are many possible structures and so a screening strategy was adopted. 'Thin films' of just 2 cation layers per slab were computed for a near-exhaustive list (>60 stoichiometric, >100 reduced structures), primarily to obtain local minima. As the accuracy of 2-layer γ_{surf} was estimated at ca. 0.4 J m^{-2}, it was safe to discard those less stable by >1 J m^{-2}. The remaining structures (over 100 in all) were computed in 4-layer slabs, yielding reasonable energetics (±0.1 J m^{-2}) and allowing further screening. Surface energies of the most stable 20-30 isomers in each class were determined from 6-layer slabs, to an estimated precision of ±0.04 J m^{-2}, which is a reasonable limit for FP γ_{surf} [23]. The need for this approach was confirmed by the small energy differences distinguishing candidate reconstructions from one another: considering only (1×1) and (1×2) patterns on the (1 1 0) stoichiometric surface, 36 distinct reconstructions are calculated to have γ_{surf} within just 1.0 J m^{-2} of the global minimum [23].

As noted above, uncertainties in the thickness of the reconstructing surface zone adds complexity to FP simulations. In a mathematical sense, a surface is the two-dimensional interface between two otherwise three-dimensional and continuous phases, such as a bulk solid and a gaseous ambient. For the discrete atoms of the physical system however, the partitioning between solid, surface and gas is rather arbitrary. While at its minimum the surface may be thought of as just 1-2 atomic layers thick, its influence may in fact be felt many nanometres into the solid and gas phases. The 'thickness' of the surface thus depends on the property under consideration. Some authors refer to the surface zone as the 'selvedge', a term normally describing the lengthwise edge of a piece of cloth.

The many successes of the slab model demonstrate that, often, surface structure and energetics are well described by a thin selvedge atop a thin segment of the bulk. For example, γ_{surf} of stoichiometric (1 × 1) rutile (1 1 0) is converged to ±0.04 [23] by 6-layer (20 Å) slabs, consisting of a sandwich of repeat units - just one surface bilayer (6.6 Å) atop and beneath a bulk bilayer. Surprisingly then, quantitatively correct energetics were obtained by comparing reconstructions on a single bilayer (2-layer slab) to a bulk-terminated 3-layer slab [32], as confirmed by later 6-layer calculations [31]. Such thin films can not be used for detailed structural analysis: anomalous relaxations of bridging O are found in calculations on 3-layer slabs (see section 5.2). The cross-linked (N × 2) reconstructions, which feature in the redox growth of reduced rutile, are highly-corrugated, measured by STM to be 4 Å deep [33]. The corresponding surface model must therefore consider rearrangement of the entire 6.6 Å bilayer, unlike most of the candidates calculated in Ref. [31].

Another complex case is (0 0 1) $SrTiO_3$ - many reconstructions are found in oxidising conditions [34]. A combination of fitting to diffraction patterns and optimisation by FP has yielded a SrO-deficient reconstructed surface [35]. The first layer of Sr ions thus occurs below two Ti layers, so that the surface zone must be at least this deep. It would be interesting to see this structure tested against the simpler, bulk-like SrO and TiO_2 terminations of earlier FP studies [36,37].

Finally, if heteroatoms are present at the surface, building a reliable surface model becomes challenging. The most devious heteroatom in this regard is hydrogen, because it is hard to detect experimentally and yet is almost ubiquitous, the product of water adsorption (see section 7). The (0 0 0 1) plane of α-Al_2O_3 provides an example: inclusion of H in the surface model seems to clarify the long-standing puzzle surrounding this structure [38,39], although some authors suggest that vibrational anisotropy can explain the discrepancy between theory and experiment [40]. All levels of theory agree that Al-

termination of the bare surface is most stable, but this disagrees with the experimental finding that O is topmost. In fact, by calculating various H coverages in Ref. [38], it is shown that a fully hydroxylated surface is favoured and consistent with experimental data for 'O-terminated' alumina.

5. RELAXATION, RUMPLING AND RECONSTRUCTION

Relaxation refers generally to the structural distortions perpendicular to the surface, atoms in the first layer generally moving inwards relative to bulk positions. Rumpling is where different atoms relax with different magnitudes, giving a corrugated structure relative to the bulk [2,5]. A surface reconstruction is a change in unit cell size due to atomic distortion parallel to the surface, as discussed in section 4. Relaxed, rumpled and reconstructed surfaces obtained from FP calculations are compared in this section to the corresponding structural data from experiment, in particular from scanning tunneling microscopy (STM). Rutile (1 1 0) is used as a sample surface [41].

5.1. Simulating Scanning Tunnelling Microscopy

A conducting sample is essential in STM, which means that it is hard to apply this technique to insulating oxides. A number of approaches have however been developed and have successfully yielded atomic resolution of oxide surfaces, as reviewed in Refs. [41,42]. These STM advances are largely responsible for the recent increase in research activity on oxide surfaces.

Strictly, STM does not image atoms, but rather, the surface topography of electronic bands of the sample, modulated by the tip. In highly ionic oxides, the valence band is spatially localised on O^{2-} and the conduction band on M^{n+}, so that assigment of atomically-resolved STM signals is straightforward. For iono-covalent bonding however, such intuitive arguments about electronic structure can not be relied upon, especially with the partially-occupied conduction band of a non-stoichiometric surface [43,44].

As an example, we detail below the debate surrounding STM assignments in a surface as simple as (1 × 1) rutile (1 1 0). Even more contentious is the (1 × 2) reconstruction of this surface, and contributions from computational studies to this debate are discussed as well.

FP calculations are found to accurately account for iono-covalent bonding [45] and can thus be used to complement STM experiments by indicating which bands are localised on which atoms. Some caution is however appropriate, as current DFT functionals suffer from systematic over-delocalisation of electrons.

STM images may be simulated from FP calculations using the Tersoff and Hamann model [46] as follows. An isotropic point-like tip is assumed, so that a first order approximation to the tunneling current at r is given by $\rho(r)$, the spatially-resolved density of states of the oxide sample summed over the energy range relevant for tunneling. A negatively-biased sample raises the band energy in the sample relative to the tip, so that tunneling is from occupied sample states into virtual tip states. For a positively-biased sample (as in most rutile studies), a range of virtual sample states is imaged. This range of electronic energies is assumed to correspond to the sample bias, but not exactly, because band energies from density functional theory differ from physical excitation energies - DFT is a ground state theory. It is therefore important to check that the simulated image is robust with respect to the range of virtual states which are summed. A related issue is the systematic underestimation of the electronic band gap that is a well-known failing of DFT [47].

In experiment, the tip height z is varied so as to keep the tunneling current constant and the variation in z is displayed as the STM image (constant-ρ / variable-z. Constant current mode may be simulated by choosing one isosurface of $\rho(r)$ and plotting image brightness proportional to z-protrusions of this isosurface [48]. Alternatively, the variation in calculated $\rho(r)$ at constant z may be presented [32,44,49,50,51]. More advanced simulations explicitly consider tip-surface overlap, allowing an estimation of the tunneling current [50,52], while others use a Green's function based scattering approach [53]. By using the optimised ionic positions, no account is made of thermal vibration nor of response to the applied electric field.

5.2. Structure of Rutile Surfaces

Optimised geometric parameters for calculated for the bulk (1 1 0) termination of TiO_2 rutile (Fig. 1) match those of the experimental (1 × 1) surface to the <5% level expected of DFT, with one exception. Surface X-ray diffraction (SXRD) finds substantial relaxation of the supra-surface bridging O, Δz=-0.27±0.08 Å [54]. Calculations of thick slabs find little relaxation (Δz=-0.06 Å [18], -0.02 Å [11] and 0.00±0.02 Å [23] for 6, 7 and 8-layer slabs respectively), in disagreement with SXRD and with less reliable theoretical results (Δz=-0.09 Å [55], -0.14 Å [56], -0.16 Å [57] all from 3-layer slabs). Direct comparison with data from impact-collision ion-scattering spectroscopy [58] is difficult: the finding of negligible O relaxation supports the thick slab results, while the 18% interlayer contraction is closer to SXRD (30%). Further experimental data is discussed in this context in Ref. [1]. No explanation is advanced in Ref. [54] for the unusual Ti-O distances, 13% shorter/longer than usual, that result from the

SXRD fitting. Maximum deviations in Ti-O of 8% were found in 100 surface structures computed by DFT in Ref. [31].

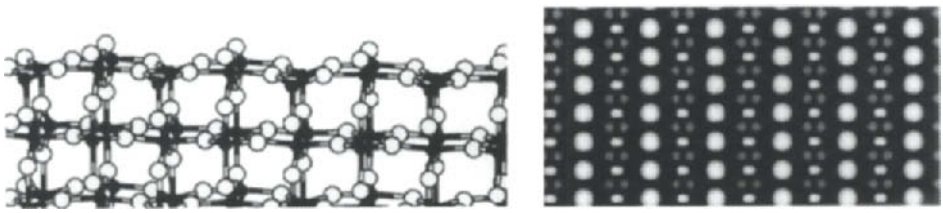

Figure 1: Bulk-terminated stoichiometric rutile (1 1 0): ball-and-stick geometry (side view, black=Ti, white=O) and simulated constant-ρ/variable-*z* STM image reproduced from [48].

One possible explanation is that the surface models (both for the fitting of SXRD and for FP calculations) are too simple. The range of data for vacuum-annealed and (1 × 3)-reconstructed TiO_2 (1 0 0) highlights the difficulties of fitting SXRD patterns to a limited set of over-simplified structural models [59]. However, an FP survey of over 60 stoichiometric surfaces of rutile (1 1 0) confirmed that the unreconstructed (1 × 1) bulk-termination is the most stable, with a computed surface energy of γ_{surf}=0.80±0.04 Jm^{-2} [23].

Bulk rutile shows a high dielectric constant and low-frequency ('soft') phonons, but how is this manifest at the surface? An FP study finds a soft, anisotropic and anharmonic surface mode (0.15 Å ionic displacements at room temperature), which could account for some of the discrepancy between SXRD and zero-temperature FP structures [60]. More generally, this illustrates that many oxide surfaces can be expected to show vibrational anisotropy [40], complicating the use of FP to provide quantitative predictions of structure at a given temperature.

STM of (1 × 1) rutile also supports the bulk-terminated structure. The STM topograph seems simple - one isotropic bright spot is imaged per cell - but interpretation is not straightforward [1,42]. Some authors assign the spot to the diffuse virtual states of exposed 5-coordinate Ti, while others suggest that O contributes sufficiently to the conduction band via covalency to allow the *ca.* 1 Å protruding bridging O to be imaged. FP simulations support the imaging of Ti [43,44,48,61], but also reveal the unusual flatness of the density of virtual states above this surface (Fig. 1). Indeed, occasionally STM detects both Ti and O signals [6]. Further support for assignment to Ti comes from formate adsorption STM [62]. Most measured corrugations along (1 $\bar{1}$ 0) are also consistent with the bulk-terminated model [63,64].

The removal of oxygen from rutile by sputtering and vacuum-annealing produces a TiO_{2-x} crystal that is reduced due to the presence of bulk interstitial Ti [65]. As a result, [0 0 1] line defects occur on the (1 1 0) surface [33,63] and accumulate to give a (1 × 2) pattern as observed in LEED, STM [33,63,64,66-69] and AFM [70,71]. This has become the prototypical non-stoichiometric oxide surface, and the large body of recent research has revealed a rich surface morphology, with the observation of rosettes, various [0 0 1] strands and a cross-linked, reactive ($N \times 2$) pattern [1].

We focus here on the most widely observed and clearly measured (1 × 2) reconstruction. This pattern is resolved by AFM and STM into bright double rows, mirror-symmetric about (1 -1 0) and growing along [0 0 1] on top of (1 × 1) sub-terraces. Three structural models have been proposed for this (1 × 2) reconstruction, as will now be discussed.

In the simplest model, alternating rows of bridging O from the bulk-termination are missing (Fig. 2(b)). This model contradicts most experimental findings; in particular, the STM image would be dominated by a single row of under-coordinated Ti, as FP simulations show [44,48]. Nevertheless, loss of bridging O remains a popular candidate for simulations of reduced rutile: TiO_2 [43,49,51,61], as well as SnO_2 [72,73] and RuO_2 [74,75]. The argument that such a surface is representative of isolated O vacancies has yet to be tested. It is likewise an open question whether O_2 desorption proceeds such simple vacancies or whether the complex process of O--O aggregation and electron transfer to Ti would lead to a more complex reorganisation of the reduced surface.

With the missing-O model discounted, debate has centred on the two competing `added-row' models, which may be described as $+Ti_2O_3$ [63] (Fig. 2(a)) and Ti_3O_5 (Fig. 2(b)). Both of these plausibly fit LEED and ion desorption data, with differences in STM images. Both simulated images show a double row of bright spots, with fainter out-of-phase central X's. However the $+Ti_2O_3$ reconstruction gives better agreement with AFM for the z corrugation and (1 $\bar{1}$ 0) width of the double row structure [31]. In addition, the $+Ti_2O_3$ reconstruction is computed to be the lowest energy reduced surface under vacuum conditions (see section 6.2).

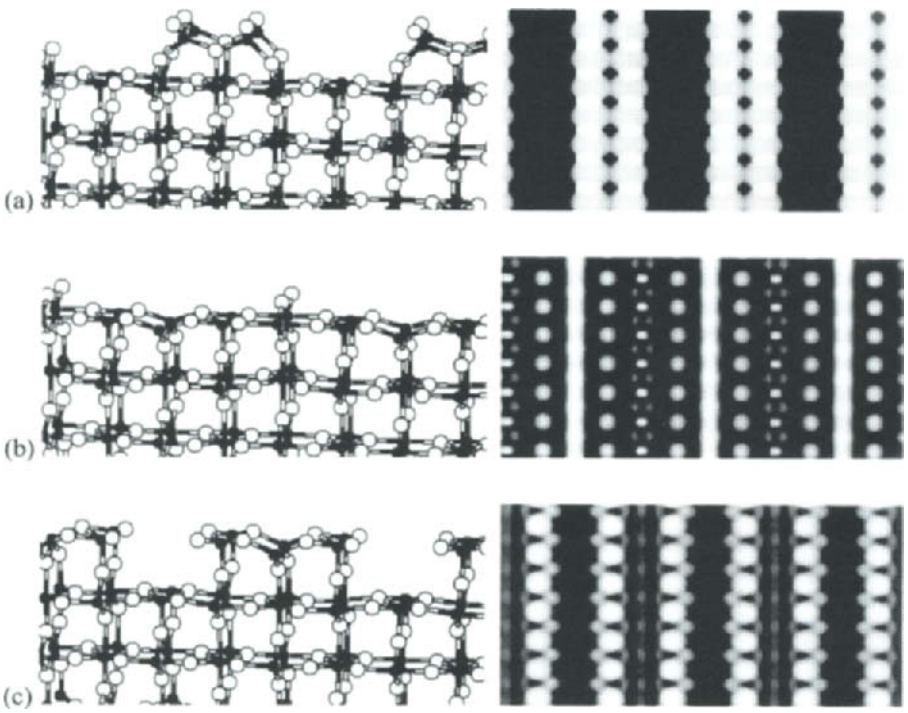

Figure 2: Reduced (1 × 2) surface reconstructions: (a) $+Ti_2O_3$, (b) missing-O, (c) $+Ti_3O_5$. Ball-and-stick geometry (side view, black=Ti, white=O) and simulated constant-ρ/variable-*z* STM image reproduced from [48].

6. NON-STOICHIOMETRY AND OXYGEN REACTIVITY

Even the simplest oxide is a binary compound, and so perpetually in dynamic equilibrium with non-stoichiometric species, *i.e.* those that are more oxidised (peroxide or molecular dioxygen) and more reduced (metal or suboxide):

$$M+MO_2 \leftrightarrow 2MO \leftrightarrow 2M+O_2. \qquad (5)$$

At the gas-solid surface, this equilibrium is mediated by the gain/loss of O_2, since the oxygen vapour pressure is generally lower than that of gaseous metal. It can therefore be too simplistic to think of an oxide surface as an inert termination of the bulk, as implied by Eq. (4) for γ_{surf}. The simple view is justified under conditions where the rate of O_2 exchange is low or when the oxidation/reduction energies in Eq. (5) are prohibitively high, as for oxides of the main group metals. On the other hand, transition metal ions are more easily reduced and oxidised, and varying stoichiometry is an important feature of their

oxide chemistry. In ultra-high vacuum and elevated temperature, O_2 will desorb, as the cohesive energy of the oxide competes with the entropy of the free oxygen molecule. An accurate description of the transition metal oxide surface thus requires consideration of the O_2 ambient.

By 'stoichiometric' we mean that the chemical formula matches a well-defined formal oxidation state. For the example of titanium(IV) oxide, TiO_2 is stoichiometric because all Ti may be assigned the +4 state and all O the -2 state. Pure oxides of different stoichiometry are either more oxidised (*e.g.* a metal peroxide with $[O_2]^{2-}$) or more reduced, such as the Ti(III) oxide Ti_2O_3. Typically, in non-stoichiometric oxides, no single oxidation state can be formally assigned: thus in the range of Magnéli phases TiO_{2-x}, $0<x<0.5$, the average Ti has an oxidation states between III and IV.

6.1. Energetics of non-stoichiometric surfaces

Subject to kinetic limitations, equilibrium can always be established between the oxygen of the bulk (usually O^{2-}) and of the gas-phase (O_2) and this equilibrium will fix μ_O for any conditions of temperature and pressure. Using this μ_O, Eq. (2) (section 3) allows us to compare the stability of oxide surfaces of various stoichiometries, albeit with neglect of slab volume and entropy changes [76]. For the example of a rutile surface with a deficiency of m O atoms per cell (*i.e.* a Ti_nO_{2n-m} surface):

$$\gamma_{surf}=[E_{slab}-nE_{bulk}(TiO_2)-m\mu_O]/A. \quad (6)$$

If equilibrium is established with a reservoir of gaseous O_2 then one could use the calculated energy of an isolated $^3\Sigma_g^-$ molecule of O_2 as the reference chemical potential:

$$\mu_O^{max}=\mu(O_2)/2=E(O_2)/2. \quad (7)$$

This is in fact the high-pressure limit and a reasonable maximum for μ_O, since at higher μ_O there would be condensation of O_2 on the surface. Some studies therefore assume a slightly lower μ_O [77]. Problems with the FP calculation of $E(O_2)$ are discussed below. Notwithstanding these, this μ_O is for example appropriate for estimating γ_{surf} of the oxygen-healed (1 × 1) rutile surface (section 5).

We note that for any adsorbate, the adsorption/desorption energy and γ_{surf} of the corresponding adsorbate-covered surface are related by γ_{surf} of the bare surface in the high pressure limit [53].

The dominant pressure and temperature corrections to γ_{surf} come from the vapour contribution [53]. μ_O at some ambient pressure may be obtained from ideal gas behaviour [14]:

$$\mu(p)=\mu^{ref}+RT\ln(p/p^{ref}) \quad (8)$$

Deviations in μ_O from ideality (as at low temperature or high pressure) may be obtained from thermochemical tables [78]. Eq. (8) means that p is very sensitive to small errors in μ_O and absolute pressures estimated from μ could be wrong by many orders of magnitude. As pointed out in Ref. [30], an error of just 1 eV in μ_O leads to pressure changes of 10^{10} at 1000 K, or 10^{20} at 500 K. It is more prudent therefore to concentrate on trends in surface stability, rather than trying to predict specific behaviour at specific pressures.

As an alternative to Eq. (8), the low pressure limit of μ_O may be found by exploiting the fixed redox relationship between metal, oxygen and oxide. At very low oxygen pressures all surface oxygen desorbs to leave metal crystallites on the oxide surface [17,79,38]. This fixes the maximum of the metal chemical potential at that of a bulk metal atom, *e.g.* for rutile $\mu(Ti)^{max}=E_{bulk}(Ti)$. Since the surface is still in contact with a reservoir of bulk rutile, the overall oxide potential is constant $\mu(TiO_2)=E_{bulk}(TiO_2)$, and so at equilibrium the oxygen chemical potential must be at its minimum:

$$\mu_O^{min}=[\mu(TiO_2)-\mu(Ti)^{max}]/2=[E_{bulk}(TiO_2)-E_{bulk}(Ti)]/2. \quad (9)$$

While the underlying assumption of complete chemical equilibrium may not be correct at the surface during reaction, the aim is simply to establish approximate physical bounds on μ_O. A popular approach for non-stoichiometric surfaces is then to treat μ_O as an extrinsic degree of freedom and to compute the variation in stability $\gamma_{surf}(\mu_O)$ across the range of physical μ_O. Examples of this approach are discussed below.

Because the formation of non-stoichiometric surfaces in this scheme is governed by the balanced chemical equation between metal, oxygen and oxide, the allowed range of chemical potential ($\mu_O^{max}-\mu_O^{min}$) is given by the formation energy of the oxide (ΔG_f). For example, since

$\Delta G_f(TiO_2) = G(TiO_2) - G(Ti) - G(O_2)$,
Eq. (9) may be rewritten

$$\mu_O^{min}= [E(O_2)+\Delta G_f(TiO_2)]/2$$

The high-pressure limit is $\mu_O^{max}=E(O_2)/2$, so that the range of μ_O is given by $\Delta G_f(TiO_2)$. Note that ΔG_f is both temperature and pressure dependent.

A computed ΔG_f may be used, as in Refs. [79] and [17], where respectively $\Delta G_f(RuO_2)$ and $\Delta G_f(Al_2O_3)$ values from FP differ from experiment by just 5%. If the computed value is unreliable the formation energy may be read from thermochemical tables [78].

One major source of error in Eq. (7) or ΔG_f is the calculation of the O_2 molecule using single determinant theories of electronic structure (such as DFT and Hartree-Fock) [80,81]. In general, gradient-corrected DFT functionals overestimate formation and binding energies and it is estimated that these are accurate for O_2 to less than ±0.5 eV [48]. It is fortunate however that many studies of surface stability are not sensitive even to this magnitude of discrepancy in μ_O, as is clear in the examples discussed below.

Apart from these fundamental obstacles, care should be taken with technical aspects of the FP calculation of isolated O_2. Sufficient separation is needed between neighbouring molecules, which is achieved by using large supercells. A tetragonal rather than cubic supercell is necessary in order to allow symmetry breaking to the $^3\Sigma_g^-$ state. Harder ultrasoft pseudopotentials and a larger plane wave basis are needed (*e.g.* 500 eV cutoff gives adsorption energies to ±0.02 eV [30]). This is so that the tightly-bound molecule is described properly, as opposed to the usual case of widely separated O anions in a solid (300 eV cutoff is adequate).

6.2. Non-stoichiometric surface phases

The scheme described above has been applied to FP calculations of TiO_2 (1 1 0) under various O_2 partial pressures. This has confirmed that the $+Ti_2O_3$ added-row reconstruction [63] (Fig. 2(a)) is the most thermodynamically favoured in vacuum, while the bulk termination (Fig. 1) is more stable in air [48]. Structural analysis of these surfaces is reviewed in section 5.2.

Relative to rocksalt, half of the octahedral cation sites in rutile are vacant. Occupation of these interstices where they occur at the surface gives a wide range of possible reconstructions and decorations. A single adsorbed TiO or TiO_2 would be a point defect; a [0 0 1] line of such interstitial Ti can be thought of as the surface analogue of a dislocation; while an entire surface of occupied interstices resembles the shear planes of the Magnéli phases [82]. Computational studies have predicted that this motif occurs at the step edges

between rutile ribbons and is thus responsible for many rutile reconstructions (stoichiometric (1 1 0) and (2 1 0), reduced (1 × 3)-(1 0 0) and (1 × 2)-(1 1 0)) [83]. The particular stability of Ti at interstitial surface sites is due in part to the stabilising contribution from the reversion of layers beneath the reconstruction to their bulk-like coordinates. The bonding is analysed in more detail in Ref. [31]. Occupation of interstices allows an increase in the Ti:O ratio without disrupting the O sub-lattice through the creation of O vacancies. This is therefore favoured in a polarisable transition metal oxide like TiO_2.

FP studies have provided important insights into the catalytic properties of ruthenium. The metal has long been used to catalyse the oxidation of organic molecules, without completely understanding how the organic adsorbate can be so reactive as to abstract O from Ru metal. A series of studies, including FP calculations, have shown that the catalytic species is in fact a non-stoichiometric RuO_2 surface, so that the Mars-von-Krevelen mechanism can operate [75,84]. Islands of oxide are found to be preferred at the surface, rather than a smooth suboxide overlayer or diffusion of O into the bulk metal [85]. RuO_2 is also computed to show a stable O-rich termination, again underlining the richness of possible interactions with O_2. An O-rich termination is also found in an iron oxide surface, hematite-(0 0 0 1), with large atomic rearrangements to alleviate surface polarity [86].

The link between structure and reactivity is again demonstrated by the complicated succession of vanadium oxide surface phases predicted by FP [77]. At certain O_2 partial pressures, the metal substrate is computed to stabilise thin film phases that are not known in equivalent bulk form. The implication is that STM studies of thin insulator films on conducting substrates may have to contend with the complex, and sometimes novel, chemistry of thin films [2]. A phase diagram of non-stoichiometric surfaces is also generated by FP in Ref. [53], this time for silver oxidation. The aim is to bridge the 'pressure gap' between ultra-high-vacuum research and the industrial reality of high-pressure reactors.

The thermodynamic formalism detailed above is used to establish that the stoichiometric Al-termination of bare α-Al_2O_3-(0 0 0 1) is the most stable surface over a wide range of O_2-rich conditions [53]. In a highly-reducing environment however, the same surface undergoes a ($\sqrt{31} \times \sqrt{31}$) reconstruction and there is consensus from grazing incidence X-ray scattering and LEED that a bilayer coating of Al is responsible. Direct computation of the ($\sqrt{31} \times \sqrt{31}$) surface is unrealistic at current levels of computing power.

Considering instead the (1 × 1) surface it is demonstrated by FP that a metallic 'wetting-layer' of fcc-like Al is preferred to a surface of Al-rich suboxide [79]. This illustrates that non-stoichiometry is manifest as segregation of metal layers in this p-block oxide, in clear contrast to the d-block oxides of Ti, Ru and V discussed above. Of course, segregation leads to more complexity, by introducing a metal/oxide interface at the surface: whether this interface oxide is stoichiometric or Al-rich is computed to depend sensitively on μ_O [79]. A later FP simulation [87] used a (1 × 1) surface cell and removed oxygen layers to generate the Al-rich reconstruction.The Al overlayer was found to be metallic, in conflict with experiment, and it is hard to know whether this reflects the limitations of the model or provides a genuine insight into the surface conductivity.

7. HYDROXIDES AND REACTIVITY WITH WATER

As previously mentioned, hydrogen (as a elemental component of water) is the only heteroatom we consider in this review. The adorption and subsequent chemical behaviour of moecules on surfaces is certainly one of the most active areas of both experimental and computational surface science studies. For such a small and seemingly simple adorbate, the many types of possible interactions of water on oxide surfaces lead to richly complex chemistry. Water may be physisorbed intact, chemisorbed molecularly or dissociatively. In the last case, surface hydroxyls are formed, with the oxygen constituent of the hydroxyl originating either from the dissociated water molecule or the surface oxygen atoms. The H atom in the hydroxyls may be considered to be acidic (added to or abstracted from oxide anions as H^+) or basic (as part of OH^- added to or removed from metal cations). For all adsorbed species, molecular or dissociated, water or hydroxyl, there is the capability of strong hydrogen bond formation between other H, OH or O surface species.

A complete consideration of hydroxides is beyond our scope, but the interaction with water inevitably is the first/last step from oxide to hydroxide. As an example, we here highlight some simulations on corundum or sapphire, α-Al_2O_3. The bulk hydroxides AlO(OH) and $Al(OH)_3$ show 6-coordinate Al, in common with anhydrous α-Al_2O_3, but are structurally closer to the transition aluminas that show mixed 4-/6-coordination (*e.g.* γ-Al_2O_3) as shown by MD calculation of their interconversion [88]. It is therefore no surprise that the most stable bare surface of α-Al_2O_3 is highly reactive to water. Static and dynamic FP simulations of this surface, the basal or (0 0 0 1) plane, concur that a fully-hydroxylated surface is most stable in a water ambient, with 3H replacing a capping Al and so forming 3 hydroxyl groups per (1 × 1) cell, reminiscent of the laminar structure of $Al(OH)_3$ hydroxide [38,79,89,90] . Further H_2O adsorption

is possible at low temperatures, with the diffusion of H into subsurface layers indicating a mechanism for oxide-to-hydroxide conversion [89]. Other studies of water adsorption onto metal sesquioxides (Cr, Fe and V) are reviewed in Ref. [91].

We note that MD is a useful method for sampling the many nearly-isoenergetic hydrogen-bonded networks that occur at a water/oxide interface [89]. On the other hand, extended hydroxo-polymers and gels may be formed when water reacts with an oxide (*e.g.* alumina), and in this case the standard computation of bulk and surface energies from small FP simulation cells will be of little use [92].

7.1. Water on rutile surfaces

As well as being a widely studied model system, the chemistry of water on rutile surfaces also underpins many of the diverse uses of oxide materials, as first illustrated with the photoelectroysis of water on rutile [93]. Almost all photocatalytic applications take place in an aqueous environment. Even in UHV systems, water is a principal component of the residual gas. The recent applications of FP techniques to study this system illustrate the efficacy of using FP simulations as a complementary investigative tool alongside experimental techniques. However, the story also highlights clear requirements regarding the accuracy and flexibility of the surface model.

Experimentally, the most widely studied low-index surface is (1 1 0), the most stable bare surface. The general consensus from a large number of experimental studies (see Table 8 in Ref. [1] for a comprehensive list) is that water does not dissociate on the surface, except at defect sites. Support for the assertion that water adsorbs dissociatively at defect sites has recently been presented by Schaub and co-workers [61] on the basis of STM experiments.

In contrast to this general consensus, most theoretical calculations predict that dissociation of the water molecules is energetically most favourable on the perfect surface. Initial FP calculations on the system were limited by available computational power [94] both from the point of view of thin slabs and the periodicity imposed by small surface units cells. This did not permit flexibility for anything other than either all-molecularly or all-dissociately adsorbed molecules on a simple (1×1) surface unit cell.

Larger surface unit cells [(1×2) and larger] allowed for lower coverages and also the possibility of higher coverages with the individual molecules in different and independent configurations. Low coverage calculations (typically

0.5 ML) [12,95,96,97,98] show that the dissociated form is still predicted to be more favourable. For full coverage calculations, *ab initio* MD simulations offer conflicting predcitions: Lindan *et al.* [98] have found that a mixed adsorption state containing molecular water is stabilised by intermolecular hydrogen bonding (with a small relative stabilisation over either purely molecular or purely dissociative states). Conversely, Car-Parrinello MD simulations [99] have suggested that perfect (1 1 0) surfaces adsorb water molecularly, with no spontaneous dissociation found even at O vacancies (though hydroxylated configurations were found to be stable). This last finding is in itself contradictory to recent predictions on the basis of DFT calculations made by Schaub *et al.* [61].

Despite the apparent morass of conflicting predictions, a clear(er) picture of the interaction between water and the surface is emerging from the body of theoretical work, but only by careful and realistic reconciliation of the predictions from the simulations and those from the experiments. It is important to not lose sight of the reliability limits of the simulations, and apply tentative energy 'error bars' (estimated at no more than 0.1 eV for this system [97]), derived from eqivualent calculations using our 'best' models for the system, in terms of slab thickness, pseudopotential reliability etc. Zhang and Lindan [12] have recently demonstrated once again that the thickness of the slab used to model the oxide remains the Achilles' Heel; they have found large deviations of adsorption energy as a function of slab thickness, by as much as 40% for the 3-layer slabs used in the calculations of Schaub *et al.* [61] recently. Use of such thin slabs must be discouraged; they muddy still further already murky water.

It is clear that this system involves competing states that are separated by a narrow energy window. Although an absolute, definitive assingment may be beyond the resolution limits of current calculation methods, there are general valid conclusions that are enabling us to build a clearer picture of what is occuring on the surface. It is clear that inter-molecular interactions do stabilise the molecular species. Reconciliation with experimental data is possible since even at low total surface coverages the water molecules might be expected to cluster and there would be local higher coverage allowing for mixed states to form. It seems only a matter of time before ($n \times m$) simulations probe the full picture.

In recent studies on this system, the gap between the 'real' surface and the computational model used is closing further: recent studies have begun the investigations of interaction with defective surfaces and coverages greater than one ML of water. Real surfaces are not perfect; the paper by Schaub *et al.* [61] looks at adsorption on the oxygen vacancies on the reduced (1 1 0) surface. This

investigation concludes that dissociative adsorption is highly favoured at oxygen vacancy sites, based on their own FP calculations and STM measurements, in agreement with other STM studies [100].

In the first application of FP methods to study multilayer adsorption of water on rutile [12], the adsorption energy of H_2O on (2×1) cells of unreconstructed TiO_2 is calculated to be more or less constant as coverage increases - about 0.4 eV/H_2O for 0.5ML on the bare surface, rising to an average of 0.5 eV/H_2O at 1ML, possibly due to cooperative effects within the layer, dropping to 0.4 eV/H_2O for 1.5ML. Interestingly, molecular and dissociative adsorption are practically isoenergetic on the bare surface, but (partial) dissociation is favoured in the H-bonding networks at >1ML. Thus, this estimates a constant desorption energy of 0.5 eV for TPD at 0-1ML.

In summary, this system provides an excellent exemplification of what Lindan *et al.* [6] have called the 'virtuous circle' of combining computational and experimental evidence to produce an insight that is greater than the sum of the constituent parts.

8. CONCLUSION

We have reviewed some of the recent simulations of oxide surfaces by First Principles methods. Our emphasis throughout is on the reliability of simulation - how suitable are the models which are built and how accurate are the quantities calculated? Practical aspects of the calculation are outlined, but also the thermodynamic framework in which energies can be interpreted and linked to experiment. Computational studies of surface relaxation and reconstruction are surveyed and compared against experiment. The link between surface structure and dynamics is illustrated for the cases of reactivity with oxygen and water.

Increasingly, simulations are being designed so as to take the complexity of surface structure into account and relate it to actual experimental conditions - ranging from that within laboratory vacuum equipment to that of the industrial reactor. As the surface is the contact zone between bulk and ambient (*e.g.* between solid and gas), the reactivity of these two components dictates its atomic-scale structure. We can safely predict therefore that familiar surfaces will behave in surprising new ways when subjected to new ambients at different temperatures and pressures. However, it is still useful to identify the general trends emerging in oxide surface science.

For instance, it is clear that all surfaces show unsaturated coordination spheres (ionic picture) or dangling bonds (if covalent) relative to the bulk. Does this

mean that surface ions rearrange so as to maximise their coordination number? In the case of many TiO_2 surfaces, the answer is no: some reconstructions with 4-coordinate Ti are favoured, but these are recognisable as bulk-like segments. Many examples show that relaxations and reconstructions lead to bulk-like structural motifs at the surface, but that these are rarely so simple as to show maximum coordination number.

Another common theme in FP studies is the richness of possible surface phases - in some cases, dozens of structural isomers are computed to be thermodynamically accessible at room temperature. This has led to speculation that many oxide surfaces are more dynamic than previously thought, but definitive conclusions will only be possible once the processes of surface diffusion are identified and their activation energies are computed. This is perhaps the next frontier in FP oxide simulation. Meanwhile, the 'flexible surface' model for active sites on metals [5] is finding some application in explaining the apparently facile diffusion of interstitial ions in non-stoichiometric oxides, despite the rigidity of the oxide lattice [26].

It is a little over 10 years since the first FP calculations of oxide surfaces began to be published. The methodology has matured, matched by concomitant advances in software (for the implementation of the methodology) and hardware (for the implementation of the software). This has brought us to the point where FP calculations can inform and aid interpretation of experimental studies, direct future ones and also stand alone as predictive tools in the vigorous area of the physics and chemistry of oxide surfaces.

REFERENCES

[1] U. Diebold, Surf. Sci. Rep., 48 (2003) 53.
[2] C. Noguera, Surf. Rev. Lett., 8 (2001) 121.
[3] C. Noguera, J. Phys.: Condens. Matter, 12 (2000) R367.
[4] G. A. Somorjai, Chem. Rev., 96 (1996) 1221.
[5] G. A. Somorjai and G. Rupprechter, J. Chem. Ed., 75 (1998) 161.
[6] M. D. Segall, P. J. D. Lindan, M. J. Probert, C. J. Pickard, P. J. Hasnip, S. J. Clark, M. C. Payne, J. Phys.: Condens. Mattter 14 (2002) 2717.
[7] R. T. Cygan and J. D. Kubicki (eds.), Rev. Min. Geochem., 42 (2001) 1.
[8] R. Car and M. Parrinello, Phys. Rev. Lett., 55 (1985) 2471.
[9] W. Kohn, L.J. Sham, Phys. Rev., 140 (1965) A1133.
[10] J. Goniakowski, J. M. Holender, L. N. Kantorovich and M. J. Gillan, Phys. Rev. B, 53 (1996) 957.
[11] S. P. Bates, G. Kresse ad M. J. Gillan, Surf. Sci. 385 (1997) 386.
[12] C. Zhang and P. J. D. Lindan, J. Chem. Phys., 118 (2003) 4620.
[13] D. Vanderbilt, Phys. Rev. B, 50 (1990) 4316.
[14] P. W. Atkins, Physical Chemistry, Oxford University Press, 4th ed. 1990.

[15] M. R. Radeke and E. A. Carter, Annu. Rev. Phys. Chem., 48 (1997) 243.
[16] G. Kresse and J. Hafner, Phys. Rev. B, 48 (1993) 13115.
[17] K. Reuter and M. Scheffler, Phys. Rev. B, 65 (2001) 035406.
[18] M. Ramamoorthy and D. Vanderbilt, Phys. Rev. B, 49 (1994) 16721.
[19] J. C. Boettger, Phys. Rev. B 49 (1994) 16798.
[20] J. C. Boettger, J. R. Smith, U. Birkenheuer, N. Rösch, S. B. Trickey, J. R. Sabin and S. P. Apell, J. Phys. Condens. Matter 10 (1996) 893.
[21] V. Fiorentini and M. Methfessel, J. Phys. Condens. Matter 8 (1996) 6525.
[22] V. Fiorentini and M. Methfessel, J. Phys. Condens. Matter 10 (1996) 895.
[23] S. D. Elliott and S. P. Bates, Surf. Sci., 495 (2001) 211.
[24] H. Lüth, Solid surfaces, interfaces and thin films, Springer, Berlin, 2001.
[25] P. Raybaud, M. Digne, R. Iftimie, W. Wellens, P. Euzen and H. Toulhoat, J. Catal., 201 (2001) 236.
[26] M. Bowker and R. A. Bennett, Top. Catal., 14 (2001) 85.
[27] W. Lojkowski and H.-J. Fecht, Prog. Mater. Sci., 45 (2000) 339.
[28] P. W. Tasker, J. Phys. C: Solid State Phys., 19 (1979) 291.
[29] M. A. Barteau, Chem. Rev., 96 (1996) 1413.
[30] G. Kresse, S. Surnev, M. G. Ramsey and F. P. Netzer, Surf. Sci., 492 (2001) 329.
[31] S. D. Elliott and S. P. Bates, Phys. Rev. B, 65 (2002) 245415.
[32] K. -O. Ng and D. Vanderbilt, Phys. Rev. B, 56 (1997) 10544.
[33] R. A. Bennett, P. Stone, N. J. Price and M. Bowker, Phys. Rev. Lett., 82 (1999) 3831.
[34] N. Erdman and L. D. Marks, Surf. Sci., 526 (2003) 107.
[35] N. Erdman, K. R. Poeppelmeier, M. Asta, O. Warschkow, D. E. Ellis and L. D. Marks, Nature, 419 (2002) 55.
[36] J. Padilla and D. Vanderbilt, Surf. Sci., 418 (1998) 64.
[37] Z. Fang and K. Terakura, Surf. Sci., 470 (2000) L75.
[38] X.-G. Wang, A. Chaka and M. Scheffler, Phys. Rev. Lett., 84 (2000) 3650.
[39] M. A. Nygren, D. H. Gay and C. R. A. Catlow, Surf. Sci., 380 (1997) 113.
[40] E. A. Soares, M. A. Van Hove, C. F. Walters and K. F. McCarty, Phys. Rev. B, 65 (2002) 195405.
[41] H.-J. Freund, J. Chem. Soc. Faraday Discuss., 114 (1999) 1.
[42] R. G. Egdell and F. H. Jones, J. Mater. Chem., 8 (1998) 469.
[43] U. Diebold, J. F. Anderson, K. -O. Ng and D. Vanderbilt, Phys. Rev. Lett., 77 (1996) 1322.
[44] O. Gülseren, R. James and D. W. Bullett, Surf. Sci., 377-379 (1997) 150.
[45] M. J. Gillan, Contemp. Phys., 38 (1997) 115.
[46] J. Tersoff and D. R. Hamann, Phys. Rev. B, 31 (1985) 805.
[47] R. H. French, J. Am. Ceram. Soc., 73 (1990) 477.
[48] S. D. Elliott and S. P. Bates, Phys. Rev. B, 67 (2003) 035421.
[49] J. Smith and D. A. Bonnell, Phys. Rev. B, 62 (2000) 4720.
[50] W. A. Hofer and A. J. Fisher, Surf. Sci., 498 (2002) L65.
[51] D. Jung, H. -J. Koo, D. Dai and M. -H. Whangbo, Surf. Sci., 473 (2001) 193.
[52] M. Di Ventra and S. T. Pantelides, Phys. Rev. B, 59 (1999) R5320.
[53] A. Michaelides, M.-L.Bocquet, P.Sautet, A.Alavi and D.A.King, Chem. Phys. Lett., 367 (2003) 344.
[54] G. Charlton, P. B. Howes, C. L. Nicklin, P. Steadman, J. S. G. Taylor, C. A. Muryn, S. P. Harte, J. Mercer, R. McGrath, D. Norman, T. S. Turner and G. Thornton, Phys. Rev. Lett., 73 (1994) 1825.

[55] P. J. D. Lindan, N. M. Harrison, M. J. Gillan and J. A. White, Phys. Rev. B, 55 (1997) 15919.
[56] P. Reinhardt and B. A. Heß, Phys. Rev. B, 50 (1994) 12015.
[57] D. Vogtenhuber, R. Podloucky, A. Neckel, S. G. Steinemann and A. J. Freeman, Phys. Rev. B, 49 (1994) 2099.
[58] E. Asari, T. Suzuki, H. Kawanowa, J. Ahn, W. Hayami, T. Aizawa and R. Souda, Phys. Rev. B, 61 (2000) 5679.
[59] P. J. D. Lindan and N. M. Harrison, Surf. Sci., 479 (2001) L375.
[60] N. M. Harrison, X. G. Wang, J. Muscat and M. Scheffler, J. Chem. Soc. Faraday Discuss., 114 (1999) 305.
[61] R. Schaub, P. Thostrup, N. Lopez, E. L{ae}gsgaard, I. Stensgaard, J. K. Nørskov and F. Besenbacher, Phys. Rev. Lett., 87 (2001) 266104.
[62] H. Onishi and Y. Iwasawa, Surf. Sci., 357-358 (1996) 773.
[63] H. Onishi and Y. Iwasawa, Surf. Sci., 313 (1994) L783.
[64] P. W. Murray, N. G. Condon and G. Thornton, Phys. Rev. B, 51 (1995) 10989.
[65] M. A. Henderson, Surf. Sci., 419 (1999) 174.
[66] A. Szabo and T. Engel, Surf. Sci., 329 (1995) 241.
[67] R. E. Tanner, M. R. Castell and G. A. D. Briggs, Surf. Sci., 412/413 (1998) 672.
[68] M. Li, W. Hebenstreit and U. Diebold, Phys. Rev. B, 61 (2000) 4926.
[69] C. L. Pang, S. A. Haycock, H. Raza, P. W. Murray, G. Thornton, O. Gülseren, R. James and D. W. Bullett, Phys. Rev. B, 58 (1998) 1586.
[70] K. Fukui, H. Onishi and Y. Iwasawa, Phys. Rev. Lett., 79 (1997) 4202.
[71] M. Ashino, T. Uchihashi, K. Yokoyama, Y. Sugawara, S. Morita and M. Ishikawa, Phys. Rev. B, 61 (2000) 13955.
[72] J. Oviedo and M. J. Gillan, Surf. Sci., 513 (2002) 26.
[73] M. A. Maki-Jaskari and T. T. Rantala, Phys. Rev. B, 65 (2002) 245428.
[74] B. Slater, C. R. A. Catlow, D. E. Williams and A. M. Stoneham, Chem. Commun., 2000 (2000) 1235.
[75] S. Wendt, A. P. Seitsonen, Y. D. Kim, M. Knapp, H. Idriss and H. Over, Surf. Sci., 505 (2002) 137.
[76] I. Batyrev, A. Alavi and M. W. Finnis, J. Chem. Soc. Faraday Discuss., 114 (1999) 33.
[77] S. Surnev, G. Kresse, M. G. Ramsey and F. P. Netzer, Phys. Rev. Lett., 87 (2001) 086102.
[78] CRC handbook of chemistry and physics, 75th ed., ed. R. C. Weast, CRC, Boca Raton Fla., 1994.
[79] R. di Felice and J. E. Northrup, Phys. Rev. B, 60 (1999) R16288.
[80] P. Stampfuß and W. Wenzel, Chem. Phys. Lett., 370 (2003) 478.
[81] C. Stampfl and M. Scheffler, Phys. Rev. B, 54 (1996) 2868.
[82] O. T. Sørensen (ed.), Nonstoichiometric Oxides, Academic Press, New York, 1981.
[83] S. D. Elliott and S. P. Bates, Phys. Chem. Chem. Phys., 3 (2001) 1954.
[84] H. Over, Y. D. Kim, A. P. Seitsonen, S. Wendt, E. Lundgren, M. Schmid, P. Varga, A. Morgante and G. Ertl, Science, 287 (2000) 1474.
[85] K. Reuter, C. Stampfl, M. Veròmica Ganduglia-Pirovano and M. Scheffler, Chem. Phys. Lett., 352 (2002) 311.
[86] X.-G. Wang, W. Weiss, Sh. K. Shaikhutdinov, M. Ritter, M. Petersen, F. Wagner, R. Schl{\"o}gl and M. Scheffler Phys. Rev. Lett., 81 (1998) 1038.
[87] E. A. A. Jarvis and E. A. Carter, J. Phys. Chem. B, 105 (2001) 4045.
[88] X. Krokidis, P. Raybaud, A.-E. Gobichon, B. Rebours, P. Euzen and H. Toulhoat, J. Phys. Chem. B, 105 (2001) 5121.

[89] K. C. Hass, W. F. Schneider, A. Curioni and W. Andreoni, J. Phys. Chem. B, 104 (2000) 5527.
[90] K. C. Hass, W. F. Schneider, A. Curioni and W. Andreoni, Science, 282 (1998) 265.
[91] M. A. Henderson, Surf. Sci. Rep., 46 (2002) 5.
[92] K. M. Rosso and J. R. Rustad, Amer. Miner., 86 (2001) 312.
[93] A. Fujishima, K. Honda, Nature, 238 (1972) 37.
[94] J. Goniakowski,M. J. Gillan, Surf. Sci., 350 (1996) 145.
[95] P. J. D. Lindan, J. Muscat, S. P. Bates, N. M Harrison, M. J. Gillan, J. Chem. Soc. Faraday Discuss., 106 (1998) 135.
[96] M. J. Gillan, P. J. D. Lindan, L. N. Kantorovich and S. P. Bates, Min. Mag., 62 (1998) 669.
[97] S. P. Bates, G. Kresse, M. J. Gillan, Surf. Sci., 409 (1998) 336.
[98] P. J. D. Lindan, N. M. Harrison, M. J. Gillan, Phys. Rev. Lett., 80 (1998) 762.
[99] W. Langel, Surf Sci., 496 (2002) 141.
[100] I. M. Brookes, C. A. Muryn and G. Thornton, Phys. Rev. Lett., 87 (2001) 266103.

J. Leszczynski (Editor)
Computational Materials Science
Theoretical and Computational Chemistry, Vol. 15

Chapter 10

A theory-guided design of bimetallic nanoparticle catalysts for fuel cell applications

Yasuyuki Ishikawa, Meng-Sheng Liao and Carlos R. Cabrera

Department of Chemistry, University of Puerto Rico,
P.O. Box 23346, San Juan, PR 00931-3346, USA

1. INTRODUCTION

The dynamics of metal particle surface reactions depend on the properties of the cluster surface as well as those of the adsorbed reactants, intermediates and products. Systematic exploration of catalytic systems must be based on an understanding of the fundamental processes taking place on the cluster surfaces. Progress in instrumentation and in techniques of molecular-level modeling is accelerating the understanding of surface phenomena. New development of sophisticated experimental techniques has provided substantial insight into the details of the dynamical processes occurring on supported and unsupported metal clusters, monolayers, and bulk surfaces. Recent experiments on the nonreactive scattering of molecular beams from surfaces have produced considerable information on interactions of the beam molecules with surfaces.

Modern experimental techniques that have dramatically improved our understanding of molecules in monolayers are low energy electron diffraction (LEED), neutron diffraction and X-ray methods, e.g., NEXAFS and SEXAFS. Other modern experimental techniques are employed to locate adsorbed molecules when the adsorbate has short-range order, e.g., on heterogeneous surfaces. Scanning tunneling microscopy (STM) and atomic force microscopy (AFM) possess a resolving power in the sub-Angstrom range, and the systems that can be studied using these techniques are virtually unlimited. These experimental results have stimulated the development of more sophisticated models that describe the underlying surface processes.

With recent developments in *ab initio* methodologies and rapid developments in computer hardware and software, numerical simulations on modern computers are beginning to provide predictive capability for the study of the dynamics of many-body systems. Computer simulations of dissociative chemisorption and catalytic activities based on *ab initio* electronic structure and first-principles molecular dynamics methods can produce dynamical properties not readily accessible to experiment. A key to finding the right metal and its cluster size for use as catalyst in, e.g., the direct methanol-air fuel cell is to understand the electrophilic character of the metal cluster. By varying cluster size, surface morphology and composition, one can change electronic properties to adjust the chemistry of catalytic processes occurring on cluster surfaces.

Fuel cells have the potential to serve as the power systems for a new generation of "green" vehicles and power plants that operate with increased fuel efficiency and reduced emissions. The most attractive fuel cell for transportation and/or power plant applications is the direct methanol-air cell. Methanol, the most electroactive of the alcohol and hydrocarbon fuels, is also the most economical liquid fuel generated on an industrial scale from the primary energy resources, natural gas and coal. However, development of the methanol cell has been slow. The major barrier to practical use of direct methanol-air fuel cells lies in the low energy efficiencies and power densities currently attainable. These drawbacks arise from the high irreversibility of methanol oxidation, slow kinetics of cathodic oxygen reduction at low temperature, and CO poisoning of the anode surface [1-5]. Several studies have addressed the problems of low electrocatalytic activities and CO poisoning by examining the catalytic oxidation of methanol [6-9], dehydrogenation of adsorbed H_2O (H_2O_{ads}) [10] and oxidation of CO_{ads} with novel mixed metal cluster surface [10].

Supported and unsupported metal nanoclusters are becoming the building blocks of a host of new catalytic materials, but their structures and activities, which may vary dramatically with cluster size, must be well understood. Only a few theoretical studies have been reported on the important subject of the energetics of methanol oxidation, CO adsorption and H_2O dissociation on mixed metal particles. In this chapter, we review our relativistic density-functional study of the energetics of methanol oxidation [7], the spectroscopic properties of adsorbed carbon monoxide $CO_{ads(Pt)}$ on platinum and the energetics of methanol and $H_2O_{ads(M)}$ dissociation and combination reactions of $CO_{ads(Pt)}$ with $OH_{ads(M)}$ on Pt-M mixed metal clusters [10]. The effects of a number of alloying metals M are examined with M = Ru, Sn, Mo, W, Re, Os, Rh, Ir, Cu, Zn, Ge, Pb, and Zr. From the trends in adsorption and activation energies we discuss their use in identifying catalytic compositions that enhance CO tolerance. Experimentally, many Pt-M systems have been tested and displayed a greater activity than pure Pt for electro-oxidation

of $CO_{ads(Pt)}$. Comparison of the effects of different alloying metals is important from the standpoint of catalyst design. The purpose of the review is to provide insight into the mechanism of methanol and CO_{ads} electro-oxidation on Pt-based bi-functional catalysts and to aid in designing surface morphology and composition of highly CO-tolerant bimetallic nanoparticle catalysts for fuel cell applications. Microscopic details of arrangement of and the effects on the cluster electronic structure in metal nanoparticles are assessed.

2. THE ADSORPTION OF CO ON PURE Pt AND ON MIXED Pt-M METAL SURFACES

2.1. Carbon monoxide poisoning of Pt electrode surface

The interest in surface chemistry of CO on Pt-M mixed metals stems from the adverse poisoning role of CO in fuel cell applications. The direct oxidation of organic compounds in a fuel cell is an attractive way to convert chemical energy into electrical energy. Methanol is a primary fuel and platinum is the catalyst of choice for the anode. However, the electro-oxidation of methanol (EOM) at Pt electrode gives rise to strongly adsorbed CO species that poison the electrode surface by blocking reactive sites [11], a major problem in the development of direct methanol fuel cells. $CO_{ads(Pt)}$ is formed by the initial dehydrogenation of the organic molecule. In the case of methanol, the overall dehydrogenation may be written as

$$CH_3OH_{ads(Pt)} \rightarrow CH_2OH_{ads(Pt)} + H^+ + e^-. \quad (1)$$
$$CH_2OH_{ads(Pt)} \rightarrow CHOH_{ads(Pt)} + H^+ + e^-. \quad (2)$$
$$CHOH_{ads(Pt)} \rightarrow HCO_{ads(Pt)} + H^+ + e^-. \quad (3)$$
$$HCO_{ads(Pt)} \rightarrow CO_{ads(Pt)} + H^+ + e^-. \quad (4)$$

It is thought to be the result of consecutive dissociation steps. The catalytic activity of Pt for EOM, however, may be enhanced by introducing a secondary metal M such as Ru [12], Sn [13], Mo [14], or Rh [15]. Thus far, Ru and Sn have been shown to be the most effective promoters. Oxidation of $CO_{ads(Pt)}$ to CO_2 on a bimetallic Pt-M surface proceeds via a 2-step mechanism [2,5,16], $OH_{ads(M)}$ formation on a secondary metal M followed by $CO_{ads(Pt)}$ elimination:

$$H_2O_{ads(M)} \rightarrow OH_{ads(M)} + H^+ + e^- \quad (5)$$
$$CO_{ads(Pt)} + OH_{ads(M)} \rightarrow CO_2 + H^+ + e^- \quad (6)$$

On a pure Pt electrode, $H_2O_{ads(Pt)}$ dissociation is difficult [6,7] and relatively high positive electrode potentials are needed to "activate" H_2O. Nanoscale binary Pt-M catalysts are often employed to increase the efficiency of CO electro-oxidation to combine the catalytic effects of both metals. The binary catalysts may be alloys or segregated metal particles. Pt-Ru and Pt-Sn alloys have received considerable attention as promising catalysts for the direct electro-oxidation of methanol (EOM); it has been shown that the catalytic activity of Pt for EOM can be enhanced by alloying with Ru or Sn. Other metals, e.g. Mo [17-21], Re [22], and Rh [23], have also been used as alloying metals.

The promoting effect of M in nanoscale binary Pt-M catalysts is attributed to a bi-functional mechanism suggested by Watanabe and Motoo [24]. Pt sites serve to adsorb and dehydrogenate methanol, and M provides nucleation sites for OH_{ads} formation (Eq. 5). The reaction between $CO_{ads(Pt)}$ and $OH_{ads(M)}$ facilitates methanol oxidation by removing the poisoning carbon monoxide. This mechanism has now generally been accepted [2,5,25-27]. An alternative explanation is the so-called "ligand effect" [28] of M influencing Pt-CO binding by affecting the electronic structure of the binding site. The latter mechanism is also supported by some electrochemical experiments [29,30], and it has been asserted that the bi-functional mechanism should be modified to account for electronic effects [30].

2.2. Adsorption of CO on pure Pt clusters

Chemisorption of CO on Pt(111) surface has been an active subject for theoretical research [31-35] because of the importance of the system in the field of catalysis and the large amount of experimental data. Carbon monoxide poisoning of the platinum anode has been the major impediment to development of the direct methanol and hydrogen fuel cells. Adsorption properties for CO on Pt(111) have been well characterized under ultra high vacuum (UHV). It has been demonstrated that CO is adsorbed mainly at an on-top site at low coverages. Stretching vibrational frequencies (ω) of CO/Pt(111) have been measured by means of various spectroscopy methods [36-39]. The spectra reveal two bands at 467 and 2100 cm^{-1}, which are assigned to the Pt-C and C-O stretching vibrations, respectively. The ω values are of course sensitive to coverage and temperature conditions. Although experimental Pt-C and C-O bond lengths are determined to be 1.85±0.05 and 1.15±0.05 Å, respectively [40], the adsorption energy (E_{ads}) is not firmly established. In early LEED [41,42], LEMS [43], modulation molecular beam [44], and surface temperature modulation [45] studies, the E_{ads} were measured to be 1.34, 1.43, 1.40, 1.53 and 1.55 eV, respectively. More recently, King et al. [46], using a micro calorimetric technique, measured a value of 1.90±0.07 eV for the low-coverage adsorption of CO on Pt(110). Although this

value refers to a different metal surface, it was found that adsorption energies of CO and other small molecules do not vary much with crystal facial structure [47].

Recent theoretical studies of CO adsorption on Pt surfaces are reported in Refs. [32-35]. Illas et al. [32] gave a detailed discussion on the origin of the frequency shift of adsorbed CO. They did not provide any calculated adsorption energy. Ohnishi and Watari [33] reported a local density-functional study for CO on a Pt_{13} model of bulk Pt(111) surface; their Pt-C bond length is 0.2 Å too long and their C-O frequency grossly underestimated (by ~290 cm^{-1}) compared with experiment; no adsorption energy was calculated.

2.2.1. Metal nanoparticle surface modeling for relativistic density-functional calculations

In our relativistic density-functional study of mixed Pt-M nanoparticle surfaces is represented by a two-layer cluster with seven surface and three second-layer atoms, $Pt_{10-n}M_n(7,3)$ [6]. The subnano cluster model does not simulate bulk surface properties because of its limited size and undercoordinated metal atoms. However, the model is suitable for simulating the properties of nanoscale particle catalysts, e.g., Pt-Ru alloy nanoparticles with an fcc surface. Catalytically much more active than bulk metal surfaces, these nanocrystals exhibit a transition from metallic to insulator properties [48]. The cluster model is also suitable for rough Pt-M electrode surfaces that exhibit a high surface density of reactive Pt-M sites [49].

The geometrical structures of the different clusters are shown in Fig. 1. In pure Pt_{10}, the first layer consists of one Pt atom surrounded by a hexagon of six more. In the case of Pt-M mixed metal, the Pt_{10} template was used with some Pt atoms substituted by M-atoms. According to the bi-functional mechanism, Pt are sites for CO_{ads}, and M for H_2O_{ads}. For CO_{ads}, we have considered $(Pt_3)(M_2Pt_5)$, $(Pt_3)(M_4Pt_3)$, $(M_3)(Pt_7)$ and $(M_3)(M_2Pt_5)$ cluster models. The cluster designated by the form $(Pt_3)(M_nPt_{7-n})$ implies that *n* M- and *7-n* Pt-atoms are in the first layer, *3* Pt-atoms in the second layer, and that CO_{ads} is attached in an on-top position to the central Pt-atom with C down. For H_2O dissociation, a $(Pt_3)(Pt_6M)$ cluster model was employed. We have shown that the H_2O dissociation on Pt-M is insensitive to cluster composition [6]. All nearest neighbor distances (R_{N-N}) were kept the same in the calculations, but the distance varied with cluster composition. Experimental values were used where available [50,51]. Others were estimated from known atomic radii, $R_{N-N} = (R_M/R_{Pt})^{1/3} \times 2.77$ Å [52]. The R_{N-N} data for the various Pt-M mixed metals are given in Table 1.

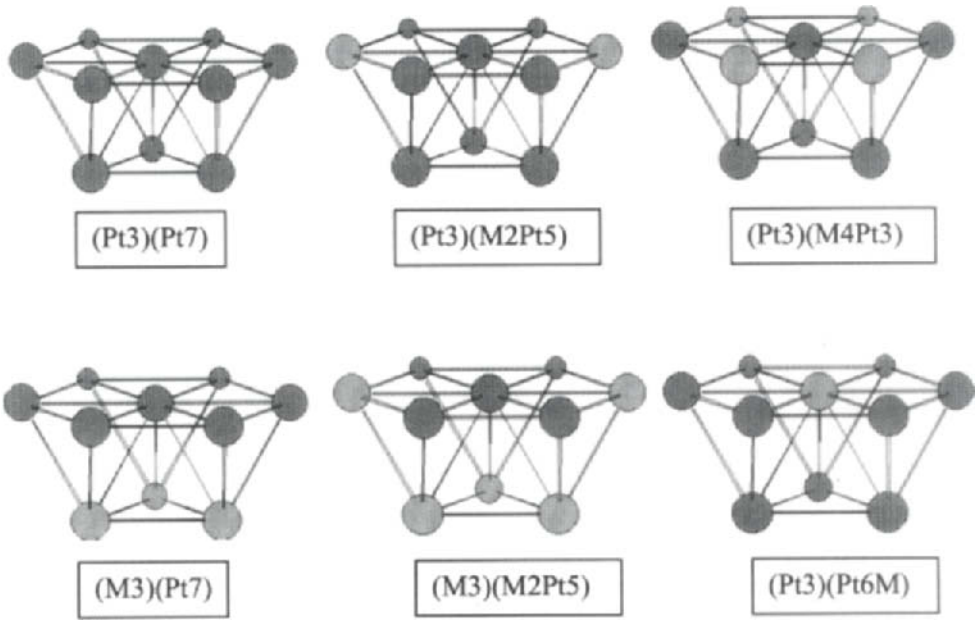

Fig. 1. Arrangement of metal atoms in the two-layer 10-atm clusters.

Table 1
Pt-Pt bond distances R_{PtPt} estimated for Pt-M metals

Metal	R_M[a] (Å)	R_{PtPt} (Å)	Metal	R_M[a] (Å)	R_{PtPt}(Å)
Pt (pure)	1.39	2.774[b]	Pt-Rh	1.34	2.74
Pt-Ru	1.34	2.74[b]	Pt-Ir	1.36	2.75
Pt-Sn	1.61	2.83[b]	Pt-Cu	1.28	2.70
Pt-Mo	1.39	2.774[b]	Pt-Zn	1.38	2.77
Pt-W	1.41	2.78	Pt-Ge	1.37	2.76
Pt-Re	1.37	2.76	Pt-Pb	1.75	2.99
Pt-Os	1.35	2.75	Pt-Zr	1.60	2.82

[a]Atomic (metallic) radii from Ref. 49. [b]Experimental value (Refs. 50,51)

2.2.2. CO adsorption on pure Pt_{10} cluster

The relativistic density-functional calculations were carried out using the Amsterdam density-functional (ADF) program package developed by Baerends and co-workers [53]. The main features of the ADF method are the use of the linear combination of Slater-type functions (LC-STF) expansion technique and frozen-core approximation. The bond energy is evaluated by the so-called "transition state method" [54], an important advantage of the ADF program package. Scalar relativistic corrections are accounted for by a quasi-relativistic method [55].

Triple-zeta STF basis sets were used for the valence shells, extended by single-zeta STF to accurately represent the nodal structure of the core. For the transition metals, *(n-1)d* and *ns* were considered as valence shells and one *np* polarization function was added. For C and O, *2s* and *2p* were the valence shells and a *3d* polarization function was added. For H one *2p* polarization function was added. Core shells were frozen.

In a large metal cluster, a number of low-lying (unoccupied) orbitals lie energetically very close (~0.1 eV). In our calculations, the fractional occupation number (FON) technique [56] was employed, where electrons are 'smeared' by an energy width of 0.15 eV over the orbitals around the Fermi energy. The resulting total energy may be viewed as an average over configurations lying energetically close to the ground state of the cluster. The FON technique is useful in suppressing the finite size effect of discrete level spacings in small metal clusters, and in achieving convergence of the self-consistent field (SCF).

A number of exchange-correlation potential functionals are available. Our experience with heavy-atom systems has been that the simple Xα potential (α=0.7) performs very well in comparative studies [6,7]. We have therefore employed it in these calculations. According to our calculations on CO/Pt(111) [6], there is little improvement by gradient corrections and the simple Xα potential performed very well for the heavy-metal surface-CO interaction. There are many examples [57] where the Xα method gives a satisfactory picture of molecular properties such bond lengths, bond energies, vibrational frequencies, etc. The reason has been discussed by Cook and Karplus [58]. They pointed out that although the Xα potential does not correct for correlation as usually defined, it does not force dissociating fragments toward ionic limits. Therefore the Xα method is able to produce the physically correct dissociation to a sum of neutral atom (or fragment) energies. This feature is demonstrated in our SCF-Xα calculations on CO/Pt.

Pure Pt nanoclusters occurs in an fcc crystal structure. We chose Pt(111) as the surface for adsorption. Pt(111) is simulated by a Pt_{10} cluster. The CO molecule is placed at an on-top site with C ending down on the surface and with

the C-O axis perpendicular to it. Fig. 1 shows the geometric structure of $(Pt_3)(Pt_7)$ used here.

The Pt-CO system contains two types of bonds, Pt-C and C-O. For the determination of bond lengths R_{Pt-C}, R_{C-O} and stretching force constants k_{Pt-C}, k_{C-O}, an internal coordinate approach has been employed. The Pt-C and C-O bond lengths were optimized separately. For C-O vibration, the position of the ligand center of mass is fixed and the C-O distance is varied. For the Pt-C vibration, the C-O distance is fixed and the Pt-C distance is varied. The force constants k_{Pt-C} and k_{C-O} were obtained from an nth degree polynomial fit to m energy points ($m > n$) around the equilibrium. A secular equation was then solved to determine the stretching frequencies ω_{Pt-C} and ω_{C-O}. The calculated frequencies are called the normal-mode frequencies, which involve a mixture of the internal Pt-C and C-O modes. The internal coordinate approach neglects the coupling force constant of the two internal modes, which is expected to be small. The adsorption energy of CO on the metal is defined as

$$E_{ads} = E_{CO} + E_{cluster} - E_{(cluster-CO)} \qquad (7)$$

where $E_{(cluster-CO)}$, $E_{cluster}$, and E_{CO} are the total energies of the complex (cluster-CO), cluster, and CO, respectively.

The calculated results (R_{Pt-C}, R_{C-O}, E_{ads}, k_{Pt-C}, k_{C-O}, ω_{Pt-C}, ω_{C-O}) for CO on the Pt_{10} cluster are collected in Table 2. The calculated results for free CO are also given for comparative purpose. Fig. 2 displays the binding energy (E_{bind}) of CO to Pt_{10} as a function of Pt-C distance in a large R_{Pt-C} range. The potential curve clearly shows that $Pt_{10}CO$ dissociates correctly into neutral Pt_{10} and CO fragments with CO binding energy 1.92 eV unlike other, more sophisticated methods that tend to dissociate $Pt_{10}CO$ into ionic fragments, e.g., $Pt_{10}^{\delta+}$ and $CO^{\delta-}$. The net charge on CO (Q_{CO}) goes to zero at large R_{Pt-C}, as shown in Fig. 3. These results also provide some support for the argument [58] that the Xα method includes some effects of static correlation empirically.

Table 2
Calculated properties of CO adsorbed on Pt_{10}.

		R_{Pt-C}	R_{C-O}	E_{ads}	k_{Pt-C}	k_{C-O}	ω_{Pt-C}	ω_{C-O}
CO(gas)			1.130			18.78		2150
	Expt		1.128					2143
(Pt3)(Pt7)CO		1.862	1.144	1.92	3.58	17.11	449	2124
	Expt	1.85±0.05	1.15±0.05	1.43–1.90			467	2093

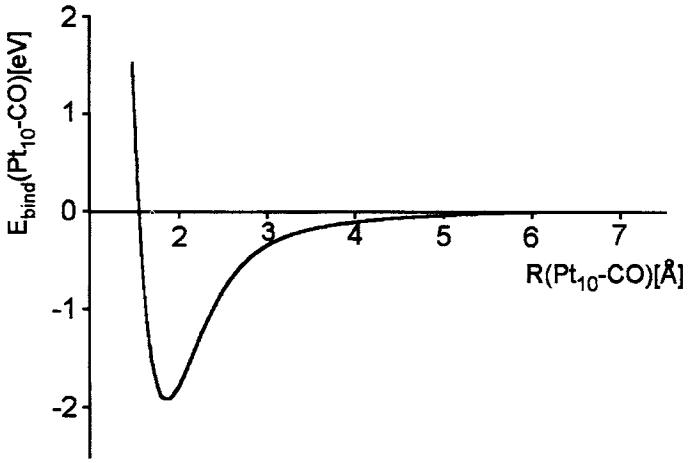

Fig. 2. Binding energy (E_{bind}) curve for adsorption of CO on Pt_{10} in the SCF-Xα calculation [$E_{bind} = E(Pt_{10}CO) - E(Pt_{10}) - E(CO)$].

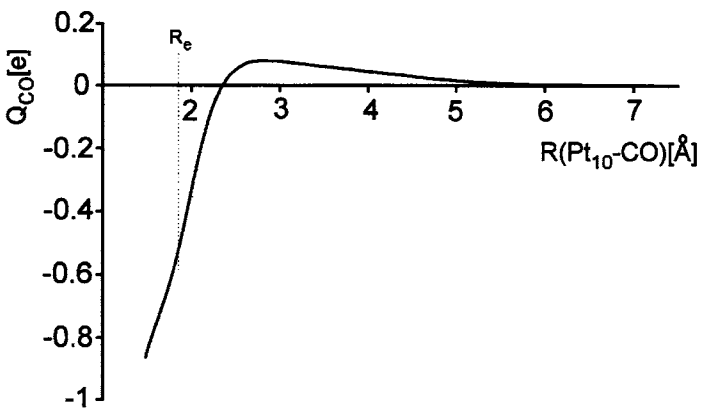

Fig. 3. Variation of charge distribution (Q_{CO}) for CO on Pt_{10} with Pt-C distance

We again point out that there are a number of experimental values of E_{ads} for CO atop bulk Pt(111) surface. Early studies measured the E_{ads} to be 1.43 eV [42], 1.40 [43] and 1.55 eV [45]. King et al. [46], by single crystal adsorption microcalorimetry, have recently measured a value of 1.90±0.07 eV for the low-coverage adsorption of CO on Pt(110) surface. Although this value refers to a different metal bulk surface, adsorption energies of many small molecules on Pt do not vary much with facial structure. The calculated E_{ads} (= 1.92 eV) of CO on Pt_{10} cluster is closer to the most recent experimental value [46].

Table 3 presents relativistic effects on several properties calculated as the difference (Δ) obtained in calculations which included the quasirelativistic correction, and corresponding calculations that excluded the correction, and used Hartree-Fock-Slater core orbitals rather than Dirac-Slater. The method finds significant relativistic Pt–C bond shortening, and little effect on the CO bond. The effect on adsorption energy is dramatic. E_{ads} increases by about 50% when relativity is included. There is also an increase in the Pt-C force constant and frequency. The shortened Pt–C bond results in an increase in CO frequency through a 'wall effect', a Pauli repulsion effect. Ref. 34 ascribed the anomalously small shift in CO frequency from gas phase to adsorbed on Pt to the relativistic effect.

We also have examined two groups of Pt_n cluster: [(Pt_7), $(Pt_3)(Pt_7)$, $(Pt_6)(Pt_7)$, $(Pt_3)(Pt_6)(Pt_7)$, $(Pt_6)(Pt_6)(Pt_7)$] where the first layer contains 7 platinum atoms, and [$(Pt_3)(Pt_{13})$, $(Pt_6)(Pt_{13})$, $(Pt_3)(Pt_6)(Pt_{13})$] where 13 platinum atoms are included in the first layer. The results of calculated bond lengths, CO adsorption energy, stretching force constants and harmonic vibrational frequencies for CO_{ads} are present in Table 4. The calculated adsorption energies (E_{ads}) on (Pt_7), $(Pt_3)(Pt_7)$, and $(Pt_6)(Pt_7)$ are very close, 1.9 – 2.0 eV. As the cluster size is increased from $(Pt_6)(Pt_7)$ to $(Pt_3)(Pt_6)(Pt_7)$, there is a decrease of 0.4 eV in E_{ads}, indicating a strong dependence of CO adsorption energy on the number of cluster layers. The E_{ads} is further decreased by ~0.1 eV when additional three Pt-atoms are included in the third layer of $(Pt_3)(Pt_6)(Pt_7)$. The results indicate that one- and two-layer nanocluster Pt catalysts bind CO much more strongly, and thus, are more susceptible to CO poisoning. The adsorption energy seems to converge fast with the cluster size to the experimental value measured on a bulk metal surface [46].

The calculation on the one-layer (Pt_7) cluster gives shorter Pt-C bond length by about 0.06 Å than the experimental Pt-C bond length on a bulk metal surface. Although the experimental Pt-C bond length has an uncertainty of ±0.05 Å, the fact that the calculated Pt-C frequency in $(Pt_7)CO$ is larger by ~80 cm^{-1} indicates that the Pt-C bond length calculated on (Pt_7) is notably shorter and the Pt-C bond stronger than on bulk Pt surface. The calculated $\omega_{C\text{-}O}$ on (Pt_7) is also substantially (~70 cm^{-1}) higher than the experimental value.

Table 3
Relativistic effects on properties of CO adsorbed on Pt_{10}

	ΔR (Å)		ΔE_{ads} (eV)	Δk (N cm^{-1})		Δω (cm^{-1})	
	Pt-C	C-O		Pt-C	C-O	Pt-C	C-O
(Pt3)(Pt7)CO	-0.122	0.001	0.58	1.24	0.34	84	45

Table 4
Calculated properties[a] of CO adsorbed on various Pt clusters

System	R_{Pt-C}	R_{C-O}	E_{ads}	k_{Pt-C}	k_{C-O}	ω_{Pt-C}	ω_{C-O}
CO		1.130			18.78		2150
(Expt)[b]		1.128					2143
$(Pt_7)CO$	1.792	1.145	2.01	5.56	17.17	548	2169
$(Pt_3)(Pt_7)CO$	1.862	1.144	1.92	3.58	17.11	449	2124
$(Pt_6)(Pt_7)CO$	1.861	1.144	2.01	3.57	17.08	448	2122
$(Pt_3)(Pt_6)(Pt_7)CO$	1.857	1.144	1.64	3.65	17.02	453	2121
$(Pt_{13})CO$	1.827	1.141	1.98	4.23	17.50	485	2160
$(Pt_3)(Pt_{13})CO$	1.873	1.141	1.76	3.30	17.37	432	2133
$(Pt_6)(Pt_{13})CO$	1.852	1.143	1.87	3.73	17.17	457	2131
$(Pt_3)(Pt_6)(Pt_{13})CO$	1.845	1.142	1.81	3.92	17.26	468	2140
Bulk Pt (Expt)[c]	1.85±0.05	1.15±0.05	1.43 - 1.90			467	2100

[a]Bond length R in Å, adsorption energy E in eV, stretching force constant k in N/cm, stretching vibrational frequency ω in cm^{-1}. [b]K. P. Huber and G. Herzberg, *Molecular Spectra and Molecular Structure, Vol. 4, Constants of Diatomic Molecules* (Van Nostrand-Reinhold, NY, 1979). [c]Bond lengths are from [40], adsorption energies from [42,46], frequencies from [36].

When a two-layer $(Pt_3)(Pt_7)$ cluster is employed, the results show significant Pt-C bond elongation and large reduction in k_{Pt-C}. Both R_{Pt-C} and ω_{Pt-C} calculated on $(Pt_3)(Pt_7)$ are in good agreement with the experimental data. We see that although the calculated k_{C-O} values on (Pt_7) and $(Pt_3)(Pt_7)$ are very close, the C-O frequency on $(Pt_3)(Pt_7)$ is in fact significantly lower than on (Pt_7). This is ascribed to a contribution from the coupling between the Pt-C and C-O internal modes. From $(Pt_3)(Pt_7)$ to $(Pt_6)(Pt_6)(Pt_7)$, there is no longer dependence of R_{Pt-C} and k_{Pt-C} on the cluster size, indicating a very rapid cluster convergence for these properties; the R_{C-O} and k_{C-O} do nearly not change with the cluster size.

Upon adding six Pt-atoms in the same layer of (Pt_7), the E_{ads} remains almost unchanged. The Pt-C bond length is shown to increase by ~0.04 Å from (Pt_7) to (Pt_{13}). Corresponding to a longer Pt-C bond length in (Pt_{13}), there is a decrease of 1.3 Ncm^{-1} in k_{Pt-C}. Nevertheless, the (Pt_{13}) cluster still yields somewhat shorter Pt-C bond length and larger Pt-C force constant as compared to experiment.

Significant differences are also found between the one-layer and the two-layer results for the second group clusters. Adding three Pt-atoms to (Pt_{13}) as the second layer leads to a decrease of ~0.2 eV in E_{ads}, an increase of ~0.05 Å in R_{Pt-C}, and a reduction of ~1 Ncm^{-1} in k_{Pt-C}. Then, the E_{ads} exhibits a very slight decrease (0.07 eV) from the two-layer cluster to the three-layer one. The variation of E_{ads}

here is much weaker than that found on $(Pt_6)(Pt_7)$ to $(Pt_3)(Pt_6)(Pt_7)$. The calculated adsorption energies on $(Pt_3)(Pt_{13})$, $(Pt_6)(Pt_{13})$, and $(Pt_3)(Pt_6)(Pt_{13})$ are in fact fairly close, 1.8 – 1.9 eV. From $(Pt_3)(Pt_{13})$ to $(Pt_3)(Pt_6)(Pt_{13})$, there is weak trend in the Pt-C distance: $R_{Pt\text{-}C}$ decreases from 1.873 to 1.845 Å with increasing cluster size. Correspondingly, the $k_{Pt\text{-}C}$ increases from 3.30 to 3.92 Ncm^{-1}. The calculated $R_{C\text{-}O}$ and $k_{C\text{-}O}$ are always insensitive to the cluster size. The results strongly indicate that one can exploit the observed trends to custom-design CO-tolerant nanoscale catalysts by controlling the size.

The adsorption of CO on the metal leads to longer C-O bond length and smaller C-O force constant with respect to free CO. The origin of the $R_{C\text{-}O}$ or $k_{C\text{-}O}$ shift for adsorbed CO is explained in terms of π--back donation mechanism [59]. However, this mechanism does not hold strictly here because in many cases, a shorter $R_{Pt\text{-}C}$ does not correspond to a longer $R_{C\text{-}O}$, and there is almost no correlation between E_{ads} and shifts in $k_{C\text{-}O}$. According to the calculations, the bond length shift for the adsorbed CO is 0.011 – 0.014 Å.

2.3. Adsorption of CO on mixed Pt-M clusters

Calculated Pt-C and C-O bond lengths ($R_{Pt\text{-}C}$, $R_{C\text{-}O}$), force constants ($k_{Pt\text{-}C}$, $k_{C\text{-}O}$), stretching vibrational frequencies ($\omega_{Pt\text{-}C}$, $\omega_{C\text{-}O}$), and adsorption energies (E_{ads}) for CO attached to pure Pt and Pt-M are presented in Table 5. A comparison of E_{ads} for CO adsorbed on pure Pt and mixed Pt-M metals is schematically shown in Fig. 4. $Pt_{10}CO$ is our reference in evaluating the effect of M on Pt.

2.3.1. Adsorption of CO on $(Pt_3)(Ru_nPt_{7-n})$ and $(Pt_3)(Sn_nPt_{7-n})$

Ru and Sn are the alloying metals most commonly employed to enhance the activity of Pt for EOM. A number of experimental studies of CO adsorbed on mixed Pt-Ru and Pt-Sn metals have been reported. The adsorption energy of $CO_{ads(Pt)}$ on Pt-Ru is 0.3 – 0.4 eV less than E_{ads} on Pt_{10} (Table 2). The calculated E_{ads} is relatively insensitive to cluster composition. Ru weakens the C-O bond and lowers the C-O stretching frequency. This lowering is in agreement with several experimental observations [26,27,60], but counter to observations by Iwasita et al.[61] noted above. The calculated C-O stretching frequencies on $(Pt_3)(Ru_2Pt_5)$ and $(Pt_3)(Ru_4Pt_3)$ differ from each other by only 5 cm^{-1}. The calculated properties are in accord with *in situ* FTIR results for CO_{ads} on $Pt_{0.5}Ru_{0.5}$ and $Pt_{0.7}Ru_{0.3}$ surface alloys [27], where no significant difference in $\omega_{C\text{-}O}$ between allloys was found. The calculated Pt-C bond lengths of $CO_{ads(Pt)}$ on Pt-Ru clusters are slightly (0.01 – 0.02 Å) longer than on pure Pt_{10}. Ru reduces Pt-C harmonic frequency by a relatively greater amount than it does C-O.

Table 5
Calculated properties[a] of CO adsorbed on pure Pt_{10} and mixed $(Pt_3)(M_nPt_{7-n})$ metal clusters (n = 2, 4)

		R_{Pt-C}	R_{C-O}	E_{ads}	k_{Pt-C}	k_{C-O}	ω_{Pt-C}	ω_{C-O}
CO			1.130			18.78		2150
	Expt[b]		1.128					2143
(Pt3)(Pt7)		1.862	1.144	1.92	3.58	17.11	449	2124
Bulk (111)	Expt[c]	1.85	1.15	1.43- 1.90			467	2093
$(Pt_3)(Ru_2Pt_5)$		1.877	1.145	1.62	3.17	16.88	420	2101
$(Pt_3)(Sn_2Pt_5)$		1.874	1.147	1.69	3.32	16.73	433	2099
$(Pt_3)(Mo_2Pt_5)$		1.883	1.147	1.34	3.08	16.72	418	2091
$(Pt_3)(W_2Pt_5)$		1.892	1.145	1.28	2.92	16.86	408	2096
$(Pt_3)(Re_2Pt_5)$		1.885	1.145	1.48	3.02	16.93	414	2102
$(Pt_3)(Os_2Pt_5)$		1.882	1.144	1.57	3.10	17.03	420	2110
$(Pt_3)(Rh_2Pt_5)$		1.870	1.145	1.70	3.31	16.92	432	2107
$(Pt_3)(Ir_2Pt_5)$		1.876	1.144	1.70	3.24	17.11	428	2117
$(Pt_3)(Cu_2Pt_5)$		1.873	1.146	1.93	3.46	16.93	441	2111
$(Pt_3)(Zn_2Pt_5)$		1.870	1.146	1.83	3.51	16.88	444	2109
$(Pt_3)(Ge_2Pt_5)$		1.878	1.147	1.71	3.28	16.75	430	2097
$(Pt_3)(Pb_2Pt_5)$		1.862	1.147	1.92	3.66	16.71	453	2103
$(Pt_3)(Zr_2Pt_5)$		1.891	1.150	0.91	2.90	16.26	405	2060
$(Pt_3)(Ru_4Pt_3)$		1.870	1.147	1.60	3.38	16.70	436	2096
$(Pt_3)(Sn_4Pt_3)$		1.880	1.147	1.63	3.25	16.68	429	2092
$(Pt_3)(Mo_4Pt_3)$		1.852	1.149	1.22	3.43	16.45	439	2083
$(Pt_3)(W_4Pt_3)$		1.873	1.146	1.04	3.42	16.71	439	2098
$(Pt_3)(Re_4Pt_3)$		1.872	1.145	1.22	3.36	16.94	435	2110
$(Pt_3)(Os_4Pt_3)$		1.878	1.144	1.38	3.27	17.04	430	2114
$(Pt_3)(Rh_4Pt_3)$		1.866	1.147	1.79	3.40	16.77	438	2101

[a]Bond lengths R in Å, adsorption energies E_{ads} in eV, force constants k in N/cm, and vibrational frequencies ω in cm^{-1}. [b]Ref. 45. [c]Bond lengths are from Ref. 46, adsorption energies from Refs. 42-46, Pt-C frequency from Ref. 51, C-O frequency for low coverage and low temperature (see text).

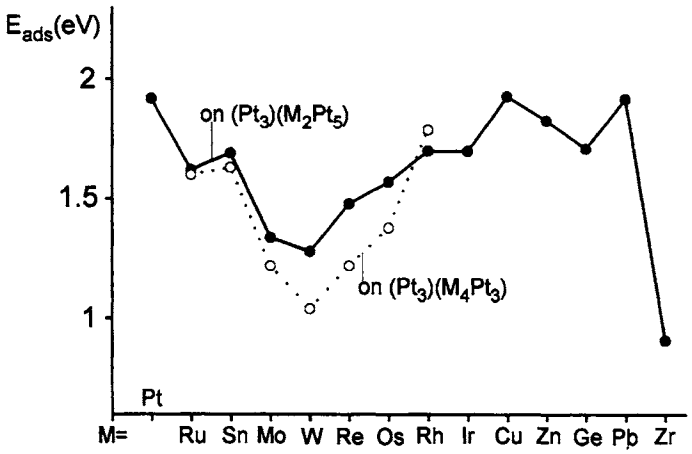

Fig. 4. Schematic illustration of the calculated CO adsorption energies on Pt and Pt-M metal clusters

The calculated adsorption energies of $CO_{ads(Pt)}$ on Pt-Sn clusters are 0.2 – 0.3 eV lower than that on Pt_{10}, an effect observed in gas-phase experiments for CO adsorbed on a Pt(111)-Sn alloy [62]. The C-O stretching frequencies on the Pt-Sn clusters are also 25 – 32 cm^{-1} below those for CO on Pt_{10}. The gas-phase experiments [62] indicated that alloying with Sn decreases ω_{C-O} by about 20 cm^{-1}, independent of surface CO concentration.

Variations in the vibrational frequencies of $CO_{ads(Pt)}$ have been related to variations in the environment of surface Pt atoms. How the C-O stretching frequency varies from Pt-M to pure Pt is not a settled question. The infrared (IR) spectroscopy experiments by Gasteiger et al.[26], Ianniello et al. [27], and Fan et al. [60] have shown decreases in the frequency of $CO_{ads(Pt)}$ on Pt-Ru. These results have been interpreted as indicating that the Pt-C bond is stronger in the alloy than in pure Pt. However, Iwasita et al. [61] detected a higher frequency for the C-O stretch on Pt-Ru than on pure Pt, which they took to indicate a weaker adsorption bond. So far, there have been no experimental measurements for adsorption energy of $CO_{ads(Pt)}$ on Pt-M, and it is unknown whether there is a correlation between C-O frequency and Pt-C bond strength. The gas-phase experiments for $CO_{ads(Pt)}$ on Pt(111)-Sn [62] and Pt(111)-Ge [63] under ultra high vacuum (UHV) suggest that binding energies of CO are lower on the alloy than on pure Pt(111). Frelink et al. [64] have tried to obtain evidence for either a bi-functional mechanism or a ligand effect through combined experiments; they concluded that the promoting action of M in Pt-M involves both water activation and platinum modification. This viewpoint is supported by our recent calculations [6,7]. To

interpret the effect of alloying M on EOM, theoretical study on the adsorption properties of CO on Pt-M would be valuable [65]. Our recent calculations [6] based on cluster models yielded several striking features of the bonding of CO on Pt-M metals, and provided insight into factors important in constructing electrode surface.

2.3.2. Adsorption of CO on Pt-M mixed metals with M=Mo, W, Os, Re, Rh, Ir, Zn, Ge, Zr, Cu and Pb

The presence of Mo, W, or Re significantly lowers CO adsorption energy, by 0.4 – 0.6 eV. E_{ads} is decreased by more than 1 eV by the presence of Zr. On the other hand, Rh, Ir, Zn, or Ge induces a weakening of only 0.1 – 0.2 eV. The E_{ads} of CO on $(Pt_3)(Ge_2Pt_5)$ is similar to that on $(Pt_3)(Sn_2Pt_5)$. The $(Pt_3)(Os_2Pt_5)$ and $(Pt_3)(Ru_2Pt_5)$ clusters also show similar adsorption energies. The E_{ads} of CO attached to Pt is essentially unaffected by the presence of Cu or Pb.

In some cases E_{ads} is affected by changes in the fraction of M present. For M = Mo, W, Re, and Os, E_{ads} on the M-richer $(Pt_3)(M_4Pt_3)$ clusters are about 0.2 eV below the values obtained with $(Pt_3)(M_2Pt_5)$, whereas for M = Rh, the adsorption energy on $(Pt_3)(M_4Pt_3)$ is higher than on $(Pt_3)(M_2Pt_5)$.

The C-O stretching frequencies on the Pt-M clusters are again lower than on Pt_{10}. The frequency decrease ranges from 10 cm^{-1} to 60 cm^{-1}. Although there is equally strong adsorption of CO on pure Pt, Pt-Cu, and Pt-Pb, the C-O stretching frequencies on the mixed metals are lower than on pure Pt, indicating a weakening of C-O bond strength. There is a good negative correlation between R_{Pt-C} and k_{Pt-C} — a shorter Pt-C bond length correlates with a larger Pt-C force constant. There seems to be no correlation between R_{Pt-C} and k_{C-O}. Although the Pt-C bond length on the Pt-Zr cluster is long, the C-O force constant and frequency on Pt-Zr are comparatively small.

The CO stretching frequency decreases substantially in going from the free molecule to the adsorbed species [66,36], and the calculated frequencies confirm the decrease. The frequency shift is attributed in the Blyholder donation-backbonding model to a weakening of the C–O bond when charge flows out of the bonding 5σ orbital onto the metal atom and to charge migration back from the metal atom into the lowest-lying antibonding $2\pi^*$ orbital. The frequency shifts observed when the surface composition around the Pt–CO bond changes, however, are not explained by the model. Our calculated frequencies, as well as experimental studies [60] of vibration of CO adsorbed on Pt-M, generally find small decreases in the CO stretching frequency for CO attached to Pt on the alloy surfaces. Since the Pt–C bond is weaker in these systems, relative to CO on pure platinum, the donation-backbonding model would predict frequency increases. We do not notice any significant charge migration onto or away from the highest

occupied or lowest unoccupied CO orbitals in the mixed clusters, and the electronic effects that cause the frequency shifts are more subtle than the model is able to account for. The CO frequency, according to our results, is neither sensitive to surface composition nor to the strength of the Pt–C bond. The Pt-C frequency more reliably monitors the strength of the bond.

2.3.3. Adsorption of CO on $(M_3)(Pt_7)$ and $(M_3)(M_2Pt_5)$

Calculations were done on the clusters, $(M_3)(Pt_7)CO$ and $(M_3)(M_2Pt_5)CO$, in which secondary metal M comprised the second layer and CO was attached to a central Pt. The calculated properties of CO on these clusters are given in Table 3.

For both $(M_3)(Pt_7)CO$ and $(M_3)(M_2Pt_5)CO$ with M = Ru, the reduction in E_{ads} is as much as 0.6 eV compared to Pt_{10}. The reduction in E_{ads} is even more pronounced for M = Sn, Mo, W, or Ge, where the adsorption energies are more than 1 eV lower. With the exception of M = Os, the CO adsorption energies on $(M_3)(Pt_7)$ lie below those for $(Pt_3)(M_nPt_{7-n})$ clusters. CO adsorption energy on $(M_3)(M_2Pt_5)$ can be even smaller than on $(M_3)(Pt_7)$. Therefore, placing M-atoms in both the first and second layers of the cluster has a large effect on E_{ads}. For $CO_{ads(Pt)}$ on $(Sn_3)(Mo_2Pt_5)$ and $(Sn_3)(Ru_2Pt_5)$, E_{ads} is small, 0.22 eV and 0.62 eV, respectively, implying high CO-tolerance for the ternary metal systems.

Os is an exception: the adsorption energy of $CO_{ads(Pt)}$ on $(Os_3)(Pt_7)$ is larger than that on $(Pt_3)(Os_nPt_{7-n})$. The adsorption energy of $CO_{ads(Pt)}$ on $(Os_3)(Os_2Pt_5)$ is also comparatively high. In the case of M = Zr, both $(M_3)(Pt_7)$ and $(Pt_3)(M_2Pt_5)$ clusters show comparable E_{ads} values.

3. ADSORPTION ENERGIES OF METHANOL INTERMEDIATE FRAGMENTS AND THE ENERGETICS OF METHANOL AND H_2O DEHYDROGENATION

Three decades ago, Bockris et al. reported enhancement of the efficiency of methanol oxidation with a platinum-ruthenium alloy electrocatalyst. Two decades ago, another promising approach to electrocatalysis of methanol oxidation was presented. That was the platinum-ruthenium oxide electrocatalyst proposed by Watanabe and Motoo [24].

The effect of Pt particle size on oxidation of methanol has been studied by several researchers. Machida et al. [67] introduced several platinum-cluster-attached graphite electrodes and reported enhanced electrocatalytic activity in anodic methanol oxidation with Pt clusters ranging in size from Pt_9 to Pt_{15} [67]. The catalytic activity of supported Pt clusters is significantly higher than that of conventional Pt electrodes. They used platinum carbonyl clusters of the type $Pt_{3n},(CO)_{6n}^{2-}$ (n= 3,5) as well as $HRu_3(CO)_{11}^-$. Modification of the graphite surface

was done by an anoin exchange method. In a related study, Yates and coworkers have recently achieved the first adsorbate desorption measurements from size-selected metal particles deposited on carefully prepared, clean surfaces [68]. The reported results of CO desorption from size-selected Pt_n (n=1-3) clusters on clean SiO_2 film clearly indicate the CO desorption process to be a unique feature of highly dispersed Pt atoms on SiO_2. Supported (and unsupported) metal clusters have received attention because they are finite systems that differ a great deal physically and chemically from bulk metals. Cox et al. have investigated size dependent variations in electronic structure of supported metal clusters and demonstrated that the clusters exhibit pronounced variations in electronic and chemical properties as the number of metal atoms in the cluster is varied [69]. These recent studies strongly indicate that size-selected metal clusters would exhibit much higher catalytic activity than bulk metals toward methanol oxidation. Thus, one key class of active electrocatalysts for methanol oxidation may well be size-selected metal or bimetallic clusters on an appropriate support material.

Besides the promoting effects of mixed Pt-M clusters, a number of mechanistic details in EOM need to be investigated to identify cluster compositions that enhance dissociation of methanol and water and CO oxidation. Such compositions are a prerequisite to improving activity by the subnanostructuring of catalysts for EOM. Three important questions were addressed in our earlier study [7] : First, what is the relative importance of a ligand effect vs. a bifunctional mechanism? Second, what are the possible reactive intermediates and their adsorption energies in methanol decomposition? The problem of intermediates in EOM has been addressed by *in situ* IR spectroscopy [4,61,70-76], but controversy exists as to the nature of the 'reactive' intermediates. Because of the similarity in stretching frequencies in many of the postulated intermediates, IR spectroscopy may not be able to give an unequivocal answer. Last, which reaction step is the rate-determining step (RDS)? We examine theoretically several alternative RDSs that experimental studies have postulated. The principal aim of the study in this section is to examine the energetics of methanol decomposition, Pt-C bond length, OH formation, and CO oxidation on Pt, Ru, and mixed Pt-M (M = Ru, Sn) metals, and attempt to provide broader understanding of the catalysis of EOM.

3.1. Metal Surface Modeling

Pt(111) was chosen again as the surface for adsorption of methanol intermediate species. The Pt(111) surface was simulated by a two-layer $(Pt_3)(Pt_7)$ cluster model, containing seven platinum atoms in the first layer and three in the second. In the case of mixed Pt-M metal (M = Ru, Sn), the cluster model of Pt(111) was used with some Pt-atoms being substituted by M atoms. Fig. 1 shows

the geometrical structures of the different clusters. Experimentally, EOM on Pt-M alloys with several M:Pt atom ratios have been examined [26,27,61]. However, the microstructures of these alloys are unknown. In our calculations, Pt_nM_{10-n} clusters with different *n* were used and compared. We have considered the following cluster models, $(Pt_3)(M_2Pt_5)$, $(Pt_3)(M_4Pt_3)$, $(Pt_3)(Pt_4M_3)$, and $(M_3)(Pt_7)$. A cluster denoted $(A_m)(B_nA_{10-m-n})$ comprises n B- and 10-m-n A-atoms in the first layer, m A-atoms in the second layer, and the adsorbate species attached to the central A-atom (for an on-top site model). For pure Ru, a (001) plane was selected as the adsorption surface and was modeled by a $(Ru_3)(Ru_7)$ cluster. Because the cluster model of Ru(001) is two layers thick, it is in fact equivalent to the cluster model of Pt(111).

The geometries of the possible intermediate fragments adsorbed on the metal surface are shown in Fig. 5. The structures of the adsorbed species on the cluster surface were fully optimized under certain symmetries. The Pt_nM_{10-n} cluster geometries were held fixed in the calculations and nearest neighbor metal-metal distances were based on bulk crystal data; they are 2.77, 2.74, 2.83, and 2.68 Å for Pt, Pt-Ru [50], Pt-Sn [51], and Ru, respectively. The alloying of Pt with Ru decreases Pt-Pt bond length. The opposite is the case for M = Sn.

3.2. Adsorption energies of methanol intermediate fragments

The adsorption energies (E_{ads}) of the various species in reactions (1) – (4) are essential information for understanding methanol oxidation. The results are collected in Table 6, together with available experimental data. Calculations were done for two types of sites, on-top (t) and threefold hollow (h). Excepting H and OH, the species treated prefer the on-top site in both pure and mixed clusters.

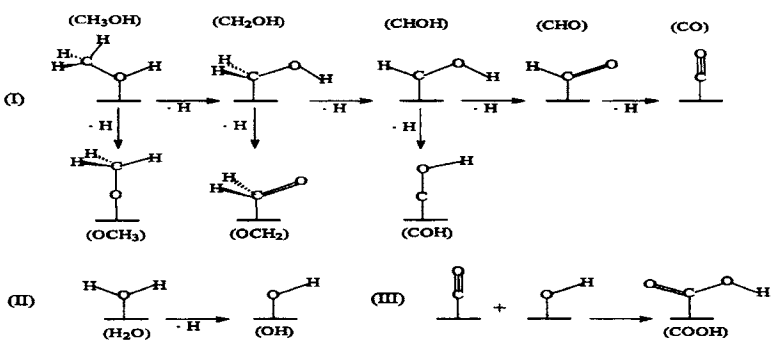

Fig. 5. Geometries of the possible intermediate fragments involved in methanol dehydrogenation on metal surface: intermediates for (I) methanol dehydrogenation, (II) water dissociation, and (III) CO oxidation

3.2.1. Adsorbed CH_3OH

X_α calculations show that the molecule attaches at the oxygen atom (Fig. 5). The adsorption structure has been derived experimentally from spectroscopic data [77]. Both theory and experiment indicate that the on-top site is more favorable for adsorption of CH_3OH. This is in agreement with the general observation that, for a saturated molecule, one can assume on-top coordination [78]. On Pt_{10} and Ru_{10} clusters, the calculated E_{ads} are as large as 0.7 eV, indicating some degree of chemical bonding. Sexton and Hughes assumed that the principal bonding orbital of CH_3OH or H_2O on a metal surface is that of oxygen lone pair[77]. Mulliken population analysis indicates some charge transfer from the molecule to the surface, supporting their assumption.

The calculated E_{ads} of 0.66 eV on pure Pt overestimates the experimental value (0.49 eV). The presence of secondary metal M in the cluster weakens the platinum-methanol bond. The same is true for other adsorbates. The decrease in charge transfer indicated by the Mulliken population analysis and the increase in the calculated heights above the metal surface also indicate weakening. On the $(Pt_3)(Sn_4Pt_3)$ cluster, with the highest Sn:Pt ratio, the adsorption energy is decreased dramatically in comparison to adsorption on pure Pt. Similar trends are found in other mixed cluster species. CH_3OH is adsorbed more strongly on Ru than on Pt. Sn is a poor electron acceptor; the Sn site in $(Pt_3)(Pt_4Sn_3)$ does not adsorb CH_3OH ($E_{ads} = 0$).

3.2.2. Adsorbed CH_2OH, CHOH, and CHO

DFT results indicate that the coordination via C is more favorable than via O (Fig. 5 (I)). The three intermediates, CHOH in particular, are strongly adsorbed on pure and mixed metal surfaces, and the on-top site is preferred. CH_2OH and CHO are monovalent radicals. Unsaturated C in these species seems to have a tendency to bond, in agreement with the extended Hückel band calculations by Hoffmann et al. [79] Because CHOH is divalent, it might be expected to prefer a bridging site to either of those considered here. The fact that E_{ads} differs little from on-top to hollow, and that on-top is the preferred position, lead toward the conclusion that any preference for a bridge site is small. No experimental E_{ads} data are available for these species. The calculated adsorption energies on pure Pt and Ru are similar. The adsorption energies at a Sn site are comparatively small.

3.2.3. Adsorbed OCH_3, OCH_2, and COH

Successive dehydrogenation of CH_3OH may also produce OCH_3, OCH_2, and COH (see Fig. 5 (I)). We have evaluated adsorption energies of these species only on pure Pt. An examination of the energetics shows that the formation of these species is less favorable than formation of CH_2OH, CHOH and CHO. OCH_2 is a saturated

molecule and can only weakly bond to the metal surface; the calculated E_{ads} (hollow site) is 0.31 eV. A hollow site is clearly preferred for adsorption of OCH_3 and COH. The differences in E_{ads} between the on-top and hollow sites for the two species are large. COH is a tri-valent radical possessing a large adsorption energy (4.86 eV).

Table 6
Calculated adsorption energies (eV)

		CH_3OH	CH_2OH	CHOH	CHO	CO	H	H_2O	OH	COOH
$(Pt_3)(Pt_7)$	(t)	0.66	2.51	3.79	2.84	1.92	2.36	0.46	2.29	2.75
	(h)	0.33	1.55	3.29	2.57		2.61	0.31	2.54	2.15
	Expt	(0.49)[a]				(1.43)[b] (1.90)[c]	(2.64)[d]	(0.44)[a]	(2.65)[e]	
$(Ru_3)(Ru_7)$	(t)	0.75	2.44	3.63	2.74	2.30	2.32	0.69	3.43	2.72
	(h)	0.49	2.15	3.51			2.56		3.81	
$(Pt_3)(Ru_2Pt_5)$	(t)	0.46	2.28	3.47	2.54	1.62	2.36	0.37	2.23	2.55
	(h)		1.12	2.92	1.96		2.38			
$(Pt_3)(Ru_4Pt_3)$	(t)	0.32	2.37	3.33	2.64	1.60	2.35	0.19	2.28	2.57
	(h)			3.03	2.52		2.64			
$(Pt_3)(Sn_2Pt_5)$	(t)	0.43	2.41	3.26	2.43	1.69	2.52	0.29	2.25	2.37
	(h)			2.57	2.04		2.50			
$(Pt_3)(Sn_4Pt_3)$	(t)	0.02	1.53	2.16	2.06	1.63	2.23	0.04	2.13	1.03
	(h)						1.20			
$(Pt_3)(Pt_4Ru_3)$	(t)	0.91	2.37	3.89	2.65	2.41	2.26	0.73	3.31	2.11
	(h)						2.28			
$(Pt_3)(Pt_4Sn_3)$	(t)	0.0	1.24	1.34	0.92	0.0	0.58	0.29	2.43	—
	(h)						1.46			
$(Ru_3)(Pt_7)$	(t)	0.42	2.11	3.27	2.52	1.37	2.12	0.38	2.26	2.38
	(h)						2.36		2.41	
$(Sn_3)(Pt_7)$	(t)	0.20	1.86	2.40	1.95	0.85	1.60	0.10	1.85	2.01
	(h)						2.29		2.09	

3.2.4. Adsorbed H

H favors the hollow site on pure Pt, Ru, and most Pt-M clusters. The $(Pt_3)(Sn_4Pt_3)$ cluster is an exception, where the on-top site is preferred. On $(Pt_3)(Ru_2Pt_5)$, $(Pt_3)(Sn_2Pt_5)$, and $(Pt_3)(Pt_5Ru_3)$, there is but a small difference (0.02 eV) in E_{ads} between on-top and hollow sites. The H adsorption energy at substituted Ru is smaller than at Pt. The calculated E_{ads} of 2.61 eV on Pt_{10} is in excellent agreement with experimental value of 2.64 eV for H on Pt(111) [80].

3.2.5. Adsorbed H_2O and OH

Like CH_3OH, H_2O is bound to the surface via O and prefers the on-top site. H_2O is more strongly adsorbed on Ru than on Pt, while Sn adsorbs H_2O more weakly than Pt. The OH radical is strongly adsorbed on the metal surface, whether Pt, Ru, or Sn. The M-OH bond lengths are smaller than those of M-OH_2. On pure Pt and Ru clusters, OH favors the hollow site. However, there is no significant difference in E_{ads} between the on-top and hollow sites ($\Delta^{hol\text{-}top}$ ~0.3 eV). Because H_2O is adsorbed at an on-top site, it is reasonable to assume that when an O-H bond in H_2O_{ads} breaks, OH will remain at the original site to react with CO_{ads} (reaction 6). Therefore we consider only the on-top site for OH_{ads}. The OH adsorption energy, $E_{ads}(OH)$, to Ru is considerably larger, by more than 1 eV, than that to Pt. The $E_{ads}(OH)$ to the secondary Sn is slightly larger than that to Pt. The calculated adsorption energies on pure Pt agree well with experiment [77,81] for these adsorbates.

3.2.6. Adsorbed COOH

Reaction of CO_{ads} with OH_{ads} results in formation of COOH. *In situ* IR spectroscopy [61] has demonstrated the presence of COOH, suggesting that the reaction involves a COOH intermediate. COOH is a monovalent species that binds more stably at an on-top site. The surface-C distance is longer for $COOH_{ads}$ than for CO_{ads} in each cluster, whereas on most clusters, the adsorption energy of COOH is larger than that of CO.

3.3. The Methanol Oxidation Mechanism

The EOM on a metal surface is known to proceed via a 3-step mechanism, namely CH_3OH dissociation (reactions 1-4), OH formation (reaction 5), and CO oxidative removal (reaction 6). The calculated adsorption energies given in Table 6 together with the calculated C-H or O-H bond energy in gas phase CH_xOH_g can be used to determine the dissociation energy $D_{e,ads}$ of CH_xOH_{ads}. The scheme is

$$\begin{array}{ccccc} & & D_{e,ads} & & \\ CH_xOH_{ads} & \rightarrow & CH_{x-1}OH_{ads} & + & H_{ads} \\ \uparrow -E_1 & & \uparrow -E_2 & & \uparrow -E_H \\ CH_xOH_g & \rightarrow & CH_{x-1}OH_g & + & H_g \\ & & D_{e,g} & & \end{array} \qquad (8)$$

Thus

$$D_{e,ads} = D_{e,g} + E_1 - E_2 - E_H \qquad (9)$$

where E_1, E_2, and E_H are, respectively, the adsorption energies of CH_xOH, $CH_{x-1}OH$, and H. The term $D_{e,g}$ represents the dissociation energy of CH_xOH in the gas phase. For H_2O_{ads} dissociation (reaction 5) and CO_{ads} + OH_{ads} combination (reaction 6), similar schemes (See Section 3.4) can be used to determine $D_{e,ads}$ and the energy of combination, $C_{e,ads}$.

In addition to reaction energies, activation barriers are also important in interpreting reaction processes. It is, of course, difficult to locate transition states for surface reactions. In order to circumvent the problem, Shustorovich [78] and Shustorovich and Sellers [82] have developed the bond order conservation-Morse potential (BOC-MP) and UBI-QEP methods, respectively, to predict accurately activation energies for dissociations or combinations of adsorbates on metal surfaces. For the dissociation reaction of CH_xOH_{ads} or H_2O, the activation energy is given by

$$E^* = \frac{1}{2}\left(D_{e,g} + \frac{E_2E_H}{E_2+E_H} + E_1 - E_2 - E_H\right)$$

$$= \frac{1}{2}\left(\frac{E_2E_H}{E_2+E_H} + D_{e,ads}\right) \qquad (10)$$

Here the energy terms are shown in scheme 8. The UBI-QEP method [82] employs experimental atomic adsorption energies to evaluate the energy terms of Eq. 10. The adsorption and activation energies evaluated with the UBI-QEP method are typically accurate to within 1-3 kcal/mol [82] if accurate experimental atomic adsortion energies are used. In the present study, the X_α method is employed to calculate the energy terms in Eq. 10. For combination reaction 6, the appropriate equation is

$$E^* = \frac{1}{2}\left(\frac{E_{CO}E_{OH}}{E_{CO}+E_{OH}} + C_{e,ads}\right). \qquad (11)$$

Here E_{CO} and E_{OH} are, respectively, the adsorption energies of CO and OH computed by X_α. $C_{e,ads}$ is the combination energy of CO_{ads} + OH_{ads} $\rightarrow$ $COOH_{ads}$. According to Eqs. 10 and 11, the formula reveals a correlation between the activation energy (E*) and dissociation energy ($D_{e,ads}$) or combination energy ($C_{e,ads}$) for the reaction. The X_α-calculated $D_{e,ads}$ or $C_{e,ads}$, and E* on the various clusters are given in Tables 7-9 [7].

3.3.1. CH_3OH Oxidation on Pure Pt

Dehydrogenations of CH_xOH to $CH_{x-1}OH$ are highly endothermic in the gas phase (Table 7). The calculated dehydrogenation energies of CH_3OH, for both $CH_3OH_g \rightarrow CH_2OH_g + H_g$ and $CH_3OH_g \rightarrow OCH_{3,g} + H_g$, and of H_2O in the gas phase are in good agreement with the available experimental data [52]. On metal surface [61], there is a considerable reduction in the dehydrogenation energies $D_{e,ads}$ due to the formation of strong metal-adsorbate bonds.

Table 7

Calculated dissociation (or combination) energies ($D_{e,ads}$ in eV) and activation barriers (E* in eV) on pure Pt_{10} and Ru_{10}

		$(Pt_3)(Pt_7)$		$(Ru_3)(Ru_7)$	
	$D_{e,g}$	$D_{e,s}$	E*	$D_{e,s}$	E*
$CH_3OH_s \rightarrow CH_2OH_s + H_s$	4.03 (4.16)[a]	-0.43	0.42	-0.22	0.51
$\rightarrow OCH_{3,s} + H_s$	4.41 (4.52)[a]	0.39	0.77		
$CH_2OH_s \rightarrow CHOH_s + H_s$	3.44	-0.45	0.55	-0.31	0.60
$\rightarrow OCH_{2,s} + H_s$	1.09	0.68	0.56		
$CHOH_s \rightarrow CHO_s + H_s$	1.17	-0.49	0.44	-0.50	0.41
$\rightarrow COH_s + H_s$	3.05	-0.56	0.53		
$CHO_s \rightarrow CO_s + H_s$	0.90	-0.79	0.16	-1.22	0.0[c]
$H_2O_s \rightarrow OH_s + H_s$	5.25 (5.18)[a]	0.81	1.02	-0.05	0.71
$CO_s + OH_s \rightarrow COOH_s$	-2.65[b]	-1.19[b]	0.0[c]	0.36	0.87
$COOH_s \rightarrow CO_{2,s} + H_s$	0.06	-0.01	0.09	-0.03	0.10

Note. g, gas; s, surface adsorbed. [a]Experimental data (ref 36). [b]These are combination energies C_e. [c]Negative values are obtained by using the BOC-MP formula, and so they are set as zero.

On pure Pt, two alternative elementary reaction steps that may be involved in methanol dissociation were examined. The dehydrogenation of CH_3OH_{ads} may produce CH_2OH_s or $OCH_{3,ads}$. The reaction to yield $OCH_{3,ads}$ is endothermic, while that for producing CH_2OH_s is exothermic. A lower dissociation energy in general corresponds to a lower activation energy according to Eq. 10 (E*=0.42 eV and 0.77 eV, respectively, for formation of CH_2OH_{ads} and $OCH_{3,ads}$). Therefore, the formation of CH_2OH_s should be the preferred process. Similarly, the dehydrogenation of CH_2OH_s may produce either $CHOH_{ads}$ or $OCH_{2,ads}$, the former being preferred. It has been shown that in the gas phase OCH_2 is more stable than

CHOH. However, the calculated adsorption energy of $CHOH_{ads}$ is lower than that of $OCH_{2,ads}$ (Table 7). *In situ* FTIR studies have identified $CHOH_{ads}$ as an intermediate [76].

Table 8
Calculated $D_{e,ads}$ and E* on $(Pt_3)(Ru_2Pt_5)$, $(Pt_3)(Ru_4Pt_3)$, $(Pt_3)(Sn_2Pt_5)$, and $(Pt_3)(Sn_4Pt_3)$ (see legend of Table 7)

	$(Pt_3)(Ru_2Pt_5)$		$(Pt_3)(Ru_4Pt_3)$		$(Pt_3)(Sn_2Pt_5)$		$(Pt_3)(Sn_4Pt_3)$	
	$D_{e,s}$	E*	$D_{e,s}$	E*	$D_{e,s}$	E*	$D_{e,s}$	E*
$CH_3OH_s \rightarrow CH_2OH_s + H_s$	-0.17	0.50	-0.66	0.29	-0.47	0.38	0.29	0.60
$CH_2OH_s \rightarrow CHOH_s + H_s$	-0.13	0.64	-0.16	0.66	0.07	0.75	0.58	0.84
$CHOH_s \rightarrow CHO_s + H_s$	-0.28	0.47	-0.78	0.27	-0.52	0.36	-0.96	0.06
$CHO_s \rightarrow CO_s + H_s$	-0.56	0.20	-0.70	0.15	-0.88	0.07	-0.90	0.02
$H_2O_s \rightarrow OH_s + H_s$	1.01	1.08	0.52	0.87	0.77	0.98	0.93	1.01
$CO_s + OH_s \rightarrow COOH_s$	-1.35	0.0	-1.34	0.0	-1.08	0.0	0.08	0.50
$COOH_s \rightarrow CO_{2,s} + H_s$	0.07	0.11	-0.16	0.0	-0.27	0.0	-1.25	0.0

Note. g, gas; s, surface adsorbed.

Table 9
Calculated $D_{e,s}$ and E* on $(Pt_3)(Pt_4Ru_3)$, $(Pt_3)(Pt_4Sn_3)$, $(Ru_3)(Pt_7)$, and $(Sn_3)(Pt_7)$ (see legend of Table 7)

	$(Pt_3)(Pt_4Ru_3)$		$(Pt_3)(Pt_4Sn_3)$		$(Ru_3)(Pt_7)$		$(Sn_3)(Pt_7)$	
	$D_{e,s}$	E*	$D_{e,s}$	E*	$D_{e,s}$	E*	$D_{e,s}$	E*
$CH_3OH_s \rightarrow CH_2OH_s + H_s$	0.21	0.70	0.27	0.55	-0.02	0.55	0.08	0.55
$CH_2OH_s \rightarrow CHOH_s + H_s$	-0.44	0.51	0.82	0.85	-0.08	0.65	0.61	0.89
$CHOH_s \rightarrow CHO_s + H_s$	0.05	0.65	-0.93	0.0	-0.44	0.39	-0.67	0.19
$CHO_s \rightarrow CO_s + H_s$	-1.22	0.0	-0.70	0.0	-0.31	0.28	-0.29	0.12
$H_2O_s \rightarrow OH_s + H_s$	0.31	0.84	0.59	0.91	1.01	1.08	1.21	1.21
$CO_s + OH_s \rightarrow COOH_s$	0.96	1.18	—	—	-1.40	0.0	-1.96	0.0
$CO_{Pt} + OH_M \rightarrow COOH_{Pt}$	-0.27	0.41	-0.90	0.05				
$COOH_{Pt} \rightarrow CO_{2,Pt} + H_s$	0.07	0.11	-0.27	0.0	-0.02	0.04	-0.23	0.0

Note. g, gas; s, surface adsorbed.

Dehydrogenation of $CHOH_{ads}$ can produce CHO_{ads} and COH_{ads}. The formation of COH_{ads} is slightly more exothermic (by ~0.1 eV) than that of CHO_{ads}, but the formation of COH_{ads} requires a slightly higher activation energy (by ~0.1 eV). Experimentally, controversy exists about the nature of the adsorbates. *In situ* EMIR investigations claim evidence for CHO_{ads} [70,74] while the adsorbate is suggested to be COH_{ads} according to *in situ* FTIR studies [71,72]. The present study indicates that the formations of both CHO_{ads} and COH_{ads} are energetically feasible, and likely. The preferred species depends on the experimental conditions.

Shustorovich and Bell [83] employed the BOC-MP method to examine the energetics of the elementary steps in mthanol synthesis by hydrogenation of CO on copper and palladium. Sellers and coworkers [84] examined the elementary steps in methanol synthesis from CH_4 on platinum. These studies have identified some of the same intermediate fragments discussed in the present study. For the reaction, CH_3OH_{ads} $CH_2OH_{ads} + H_{ads}$ on Pt(111), the activation energy computed with the BOC-MP method is 14.4 kcal/mol (0.63 eV), 0.2 eV higher than our X calculated value.

Table 7 shows that the dehydrogenation steps of CH_3OH on pure Pt are all exothermic processes with low activation energies. The dehydrogenation of CHO_{ads} is exothermic, and CHO_{ads} can rapidly decompose ($E^*=0$) to form CO_s and H_s in agreement with earlier BOC-MP calculations [83]. Previous studies have suggested that adsorbed CHO [73] and COH [85] were poisoning species. Others have thought it more likely that they are short-lived reaction intermediates [70]. Our calculations support the latter view.

The dissociation reaction of H_2O_{ads} is endothermic by 0.8 eV, and its activation energy is estimated to be 1 eV. The combination reaction, $CO_{ads} + OH_{ads} \rightarrow COOH_{ads}$, should be rapid; it is exothermic by -1.2 eV and there is no activation barrier. $COOH_{ads}$ should decompose readily to $CO_{2,ads}$ and H_{ads}. No energy is required to break the COO-H bond on the metal surface; The estimated dissociation and activation energies are, respectively, -0.01 eV and 0.09 eV. Among the dehydrogenation processes, the X_α calculations clearly indicate that the H_2O_{ads} dissociation to generate OH_{ads} is the rate-determining step (RDS) for the methanol oxidation on pure Pt. The X_α study supports the conjecture made earlier by Anderson and Grantscharova [86].

3.3.2. CH_3OH Oxidation on Pure Ru

In the electrochemical environment, pure Ru is found to be inactive for methanol dissociation at low voltages [72,30]. This situation is ascribed to the fact that adsorbed H_2O and OH block the Ru surface and inhibit the adsorption of CH_3OH. In section 3.2.5 it has been shown that Ru adsorbs H_2O and OH more

strongly than does Pt (see Table 6). There have been a few experimental studies for electro-oxidation of CO on pure Ru-electrode [72,25,30,87], where CO and COOH were found to form adsorbates on the Ru surface. In ultra high vacuum (UHV), methanol is found to decompose on Ru(001), $CH_3OH_{ads} \rightarrow CO_{ads} + 4H_{ads}$, at temperatures of 220 – 280 K [88]. In this subsection we examine the energetics of CH_3OH oxidation on pure Ru.

The dehydrogenation steps of CH_xOH are exothermic on both Pt and Ru and have relatively low activation energies (Table 7). Pt and Ru under UHV behave similarly for CH_3OH decomposition [88,89], and the calculated results are consistent with the experimental observations. The greatest differences occur in the first (methanol dissociation) and last ($CHO_{ads} \rightarrow CO_{ads} + H_{ads}$, Reaction 4) steps.

The H_2O_{ads} dissociation ($H_2O_{ads} \rightarrow OH_{ads} + H_{ads}$) on Ru is slightly exothermic ($D_{e,ads}$=-0.05 eV), in contrast with dissociation on pure Pt, which is quite endothermic ($D_{e,ads}$=0.81 eV). E* is also notably smaller on Ru than on Pt. Thus H_2O dissociation on Ru is more favorable than on Pt. The $CO_{ads} + OH_{ads}$ combination reaction on Ru is endothermic and requires a high activation energy (0.87 eV), again in contrast to the situation on Pt, where the activation energy is zero. E* for this reaction is the highest among the dehydrogenation steps. Thus the combination reaction is the RDS for CH_3OH oxidation on pure Ru.

3.3.3. CH_3OH Oxidation at Pt on Mixed Pt-Ru Surfaces

Two clusters, $(Pt_3)(Ru_2Pt_5)$ and $(Pt_3)(Ru_4Pt_3)$, were used to simulate the Pt site on mixed Pt-Ru clusters. The dehydrogenation energies of CH_xOH on $(Pt_3)(Ru_2Pt_5)$ are slightly less exothermic than on pure Pt. H_2O_s dissociation on $(Pt_3)(Ru_2Pt_5)$ is also slightly more endothermic and has slightly higher activation energy than on $(Pt_3)(Pt_7)$. On $(Pt_3)(Ru_4Pt_3)$, the dehydrogenation energies of CH_3OH and CHOH become significantly more exothermic than they are on $(Pt_3)(Ru_2Pt_5)$. $D_{e,ads}$ and E* for H_2O_{ads} dissociation on $(Pt_3)(Ru_4Pt_3)$ are also lower, by 0.5 eV and 0.2 eV, respectively, than on $(Pt_3)(Ru_2Pt_5)$. In general then, the mixed Pt-Ru cluster with the higher Ru percentage exhibits the greater activity in EOM. Experimental studies have indicated that optimum Pt/Ru composition lies between 10 and 50 atom % [26]. Figure 6 compares the $D_{e,ads}$ and E* for CH_xOH dehydrogenation on pure Pt with those on $(Pt_3)(Ru_4Pt_3)$. The dehydrogenation of CH_xOH on $(Pt_3)(Ru_4Pt_3)$ is more favorable than on pure Pt.

3.3.4. CH_3OH Oxidation at Pt on Pt-Sn clusters

We have also examined $(Pt_3)(Sn_2Pt_5)$ and $(Pt_3)(Sn_4Pt_3)$ cluster models. The dehydrogenation of CH_2OH on $(Pt_3)(Sn_2Pt_5)$ has an activation energy of 0.75 eV, 0.2 eV higher than that, but all other calculated $D_{e,ads}$ and E* are comparable to those, on pure Pt. On $(Pt_3)(Sn_4Pt_3)$, the dehydrogenation of CH_2OH has even higher

activation energy (0.84 eV). The dehydrogenation energies of CH_3OH and CH_2OH on the cluster also become endothermic. The results indicate that a Pt-Sn surface with high atomic Sn percentage is not conducive to CH_3OH dissociation. Hence in EOM, the optimal Sn surface coverage must be low. At a surface with a high Sn:Pt ratio of (3:4), catalytic activity for methanol oxidation was found to be lower than on pure Pt [99]. The $D_{e,ads}$ and E* values for H_2O_{ads} dissociation on $(Pt_3)(Sn_2Pt_5)$ and $(Pt_3)(Sn_4Pt_3)$ are similar to those on Pt_{10}. The combination reaction of $CO_{ads} + OH_{ads}$ on $(Pt_3)(Sn_4Pt_3)$ has an activation energy of 0.5 eV, while the corresponding E* is zero on $(Pt_3)(Sn_2Pt_5)$.

3.3.5. CH_3OH Oxidation at M on Pt-M (M = Ru, Sn)

A $(Pt_3)(Pt_4M_3)$ cluster was used to simulate adsorption at the M site in a Pt-M mixed metal surface. It is shown in Table 6 that the adsorption energy of H on the hollow site of $(Pt_3)(Pt_4M_3)$ is lower than on the Pt site of $(Pt_3)(M_2Pt_5)$ or $(Pt_3)(M_4Pt_3)$. Therefore H species should adsorb preferentially at Pt. Dissociation of H_2O on M would lead to M-OH and Pt-H bond formations. The adsorption energy of H (E_H) at the on-top site of $(Pt_3)(M_2Pt_5)$ was employed in calculating $D_{e,ads}$ and E* on $(Pt_3)(Pt_4M_3)$.

The calculations show that the substitutional Ru should be active for CH_3OH dissociation. As mentioned earlier experimentally methanol does not bind at Ru because the sites are preferentially covered by H_2O and OH. The Ru atoms in the surface provide nucleation sites only for OH_{ads} formation. Like pure Ru_{10}, substituted Ru shows smaller $D_{e,ads}$ and E* for H_2O dissociation than does Pt. The calculated $D_{e,ads}$ of H_2O on $(Pt_3)(Pt_4Ru_3)$ is 0.31 eV, 0.5 eV less endothermic than on pure Pt (Fig. 6). The activation energy for H_2O dissociation on $(Pt_3)(Pt_4Ru_3)$ is also smaller by 0.18 eV than on pure Pt, in agreement with earlier work of Anderson et al. [86]. Assuming that the pre-exponential factors A in the Arrhenius equation, $k=A\ \exp(-E^*/RT)$, are approximately the same for both pure Pt and mixed Pt-Ru clusters, a decrease of 0.18 eV in E* would increase the rate of H_2O dissociation reaction by a factor of 1000.

The combination reaction $CO_{ads} + OH_{ads} \rightarrow COOH_{ads}$ on the secondary Ru is endothermic with high E*, again similar to the case with pure Ru_{10}. On a Pt-Ru electrode, however, the initial dehydrogenation of methanol yielding CO, proceeds only through Pt sites and Ru provides sites solely for OH_{ads}. Reaction 6 is the process of interest, and we find that $CO_{ads(Pt)} + OH_{ads(Ru)} \rightarrow COOH_{ads(Pt)}$ is exothermic with low E*, and should proceed readily.

On substituted Sn, the dehydrogenation of CH_2OH is endothermic and has a high E*, indicating that the Sn atoms in mixed Pt-Sn metal do not facilitate CH_3OH dissociation. Because CO is not adsorbed at the Sn site ($E_{ads} = 0$), no $COOH_s$ will form on Sn in Pt-Sn. H_2O_{ads} dissociation on alloyed Sn is 0.3 eV less endothermic

and has a smaller E* (by 0.1 eV) than does the process on pure Pt_{10}. This implies that Sn in Pt-Sn is more active than pure Pt, but less so than Ru in Pt-Ru. The combination reaction $CO_{ads(Pt)} + OH_{ads(Sn)} \rightarrow COOH_{ads(Pt)}$ is strongly exothermic with a low activation energy.

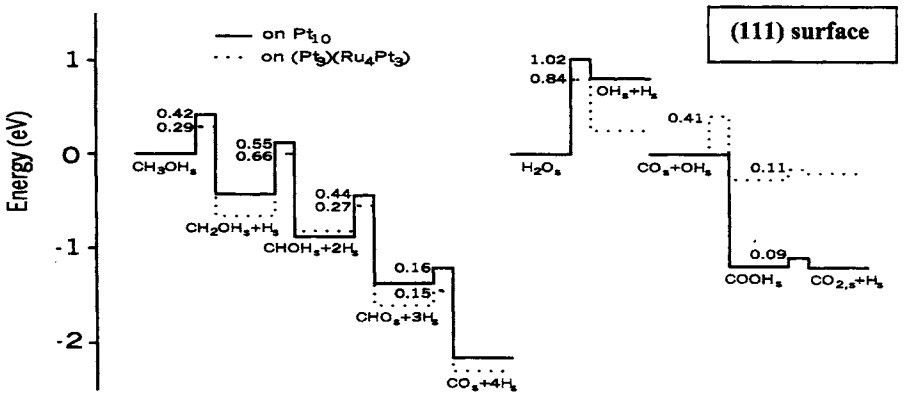

Fig. 6. Potential energy diagrams for the methanol dehydrogenation, water dissociation and CO_s + OH_s combination reactions on pure platinum and mixed Pt-Ru surfaces.

3.3.6. CH_3OH Oxidation on $(M_3)(Pt_7)$ Clusters

It has been shown [6] that when the atoms substituted for Pt are placed in the second cluster layer, the adsorption of CO to Pt can be weakened, especially when M = Sn. We therefore examined CH_3OH and H_2O dissociations on $(M_3)(Pt_7)$ clusters. For M = Ru the dissociation of CH_3OH on the cluster can proceed readily, but each step in the dehydrogenation of CH_xOH is less exothermic than on pure Pt_{10}. On the other hand, the dissociation of H_2O is more difficult on $(Ru_3)(Pt_7)$ than on pure Pt_{10}. For M = Sn, both CH_3OH and H_2O dissociations on the cluster are energetically unfavorable. So, although M_3 in the second layer greatly reduces the adsorption energy of CO, it is not conducive to CH_3OH and H_2O dissociations.

3.3.7. Ligand Effect vs. Bifunctional Mechanism

There has been a longstanding controversy in EOM studies over whether the effect of alloys on electrode performance is due solely to the bifunctionality provided by the substituted metal, or whether these are extra electronic effects that need to be considered [75,25,91]. From the calculated dissociation and activation energies of reactions 5 and 6, we are able to conjecture as to the relative

importance of a ligand electronic effect vs. the bifunctional mechanism. On pure Pt_{10}, the dissociation of H_2O is the RDS, while the formation of $COOH_{ads(Pt)}$ from $CO_{ads(Pt)} + OH_{ads(Pt)}$ is exothermic. So, once OH_{ads} is generated, the poison CO_{ads} is easily removed from the surface despite the fact that CO is strongly adsorbed on Pt. The calculated results for $(Pt_3)(Ru_2Pt_5)$ show that a reduction in E_{ads} for CO on Pt gives a more negative $D_{e,ads}$ for the $CO_{ads} + OH_{ads}$ combination reaction, but reduction in E_{ads} should not affect the rate of reaction. For a mixed Pt-M metal the effect of M is to promote the activation of water. There are decreases in $D_{e,ads}$ and E^* for the generation of OH_{ads} from H_2O on M site as compared to a Pt site. Nevertheless, H_2O dissociation at M is still the RDS for CH_3OH oxidation on Pt-M. For M = Ru, the combination reaction $CO_{ads(Pt)} + OH_{ads(Ru)} \rightarrow COOH_{ads(Pt)}$ is slightly exothermic (~ −0.3 eV) and has an activation energy of ~0.4 eV. Were not E_{ads} for CO on Pt reduced, this reaction would have an E^* of 0.62 eV. Thus the ligand effect does play some role in CO oxidation. In the case of M = Sn, the reaction $CO_{ads(Pt)} + OH_{ads(Sn)} \rightarrow COOH_{ads(Pt)}$ is exothermic, and electronic effects on the Pt-CO bond should not affect the rate of oxidation. Our theoretical study provides insights into the energetics of the elementary steps of CH_3OH oxidation on pure Pt, Ru, and mixed Pt-M (M = Ru, Sn) metals. The following conclusions may be drawn from the computational study.

(1) On pure Pt, the dissociation of CH_3OH to form CO_s occurs easily, in agreement with experiment [88]. CH_2OH, CHOH, and CHO (or COH) are intermediates in methanol decomposition. The formations of $OCH_{3,ads}$ and $OCH_{2,ads}$ are much less favorable than the formations of CH_2OH_s and $CHOH_s$. The highest activation energy for the stepwise dehydrogenation of CH_3OH is that for the second step $CH_2OH_{ads} \rightarrow CHOH_{ads} + H_{ads}$, while the last step, CHO_{ads} (or COH_{ads}) $\rightarrow CO_{ads} + H_{ads}$, has the lowest activation energy. The dissociation reaction of H_2O_{ads} is endothermic by 0.8 eV, and its activation energy is estimated to be 1 eV. The dissociation of H_2O to form OH_{ads} is rate-determining.

(2) Theoretically, the dissociation of CH_3OH on pure Ru is as favorable as on pure Pt. This is in agreement with experimental results on methanol dissociation in UHV on both Pt and Ru single crystal surfaces [88,89]. In the electrochemical environment, Ru atoms can be blocked by strong H_2O and OH adsorptions. This may be the reason why methanol does not undergo oxidation on Ru electrodes at low voltage. The RDS on Ru is the formation of $COOH_{ads}$. H_2O dissociation on Ru is significantly more favorable than on Pt.

(3) Energetically there is not much difference between single Ru atoms in Pt/Ru and in pure Ru for H_2O dissociation. Ru in Pt-Ru promotes the dissociation of CH_3OH and formation of OH_{ads} from adsorbed H_2O (Fig. 6). The dissociation of H_2O at a Sn site in Pt-Sn is only slightly more favorable than at a Pt. The

presence of M atoms reduces the Pt-CO bond strength substantially, indicating the existence of a "ligand effect". Because H_2O dissociation is the RDS and the combination reaction $CO_{ads(Pt)} + OH_{ads(M)} \rightarrow COOH_{ads(Pt)}$ can proceed readily on Pt-M, a ligand effect is not to be expected to play a significant role in the rate of CO oxidation. However, a ligand effect may reduce the accumulation of surface CO.

(4) The activity of a Pt site in mixed Pt-M for CH_3OH dissociation should vary somewhat with atomic M:Pt ratio. With more Sn, the activity at Pt becomes less. Because another effect of Sn is to impede methanol adsorption, the optimal Sn surface composition must be low. In contrast, the CH_3OH dissociation on a Ru-rich surface can proceed effectively. A metal with relatively high Ru:Pt ratio should benefit for CH_3OH oxidation.

3.4. Dissociation of H_2O on the M site in mixed Pt-M (M=Mo, W, Ru, Re, Os, etc.) metals

The assumption underlying the bi-functional mechanism toward CO oxidation is that the alloying metal provides sites for dissociation of $H_2O_{ads(M)}$ to OH_{ads}. Therefore the effects of M on the energetics of $H_2O_{ads(M)}$ dissociation is of interest. In the previous section we have examined the adsorption energies of $H_2O_{ads(M)}$, $OH_{ads(M)}$, and $H_{ads(M)}$ where M=Pt, Ru and Sn. In this section we examine the adsorption energies of $H_2O_{ads(M)}$, $OH_{ads(M)}$, and $H_{ads(M)}$, and the energetics of $H_2O_{ads(M)}$ dissociation on the alloying metal M where M= Re, W, Mo, Os, Ru, Ir, Sn, Cu, Zn, Ge, Zr, Rh. A $(Pt_3)(Pt_6M)$ cluster simulates the M site in a Pt-M mixed metal. $H_2O_{ads(M)}$ and $OH_{ads(M)}$ were attached at M by O. For H the hollow site of the cluster was used because it is preferred [78]. The calculated E_{ads} of $H_2O_{ads(M)}$, $OH_{ads(M)}$, and $H_{ads(M)}$ are collected in Table 10.

Pure Pt metal binds H_2O weakly. The calculated $E_{ads}(H_2O)$ of 0.46 eV on Pt_{10} agrees with the experimental adsorption energy of 0.42 eV for H_2O on Pt(111) [77]. Sn, Ge, and Pb show comparable E_{ads}. H_2O binds more strongly to Mo, W, Re, and Zr. E_{ads} is more than 1 eV for binding to these metals. The H_2O adsorption energies with Ru, Os, Rh, Ir, Cu, and Zn are slightly greater than with Pt. OH is strongly adsorbed on either Pt or M. The metal-OH bond lengths are all considerably smaller than for metal-OH_2. The calculated E_{ads} of OH adsorbed on pure Pt is about 2.3 eV, in reasonable agreement with experiment (2.6 eV) [92]. OH adsorption energies for Mo, W, and Re are over 4.2 eV. Adsorption on Ru, Os, and Ir is also stronger than on Pt while Cu, Zn, and Pb adsorb OH more weakly than Pt.

The calculations also show large adsorption energies for H on Pt and Pt-M. Again the calculated E_{ads} of H, 2.61 eV, on pure Pt agrees with experiment, 2.64 eV, for H on Pt(111) [93]. The adsorption energy of H on $(Pt_3)(Pt_6M)$ is reduced in all cases, compared with Pt_{10}, by 0.1 - 1 eV.

The calculated adsorption energies of H_2O, OH, and H and the calculated O-H bond energy for free H_2O provide enough information to calculate the dissociation (dehydrogenation) energy ($D_{e,ads}$) of $H_2O_{ads(M)}$ by the thermodynamic cycle employed in Section 3.2.

$$\begin{array}{ccccc} & & D_{e,ads} & & \\ H_2O_{ads(M)} & \rightarrow & OH_{ads(M)} & + & H_{ads} \\ \uparrow -E_{H2O} & & \uparrow -E_{OH} & & \uparrow -E_H \\ H_2O_g & \rightarrow & OH_g & + & H_g \\ & & D_{e,g} & & \end{array} \qquad (12)$$

Thus $$D_{e,ads} = D_{e,g} + E_{H2O} - E_{OH} - E_H \qquad (13)$$

where E_{H2O}, E_{OH}, and E_H are the calculated adsorption energies of H_2O, OH, and H, respectively, $D_{e,g}$ is the dissociation energy of H_2O and (ads) indicates surface adsorption.

To estimate the activation energy (E*) for dissociation of H_2O_{ads}, the UBI-QEP approach of Shustorovich and Seller [78,82] is employed again. This method has proven to be accurate to within 1-3 kcal/mol in treating energetics of molecular adsorbates on transition metals [94,95]. For the surface dissociation, $H_2O_{ads(M)} \rightarrow OH_{ads(M)} + H_{ads}$, the activation energy is related to the reactant and product adsorption energies by the UBI-QEP formula [78,82],

$$E^* = \frac{1}{2}\left(\frac{E_{OH}E_H}{E_{OH}+E_H} + D_{e,s}\right). \qquad (14)$$

The energy terms are those shown in Eq. 12 and relate the activation and dissociation energies for the reaction. The calculated results for $D_{e,ads}$ and E* for different M are collected in Table 10 and schematically illustrated in Fig. 7.

The calculated dissociation energy of free H_2O, $D_{e,g}$, of 5.25 eV, agrees well with the experimental gas phase energy of 5.18 eV [52]. The strong metal-OH and metal-H bonds significantly lower surface $D_{e,ads}$ compared to $D_{e,g}$. On pure Pt, H_2O dissociation is endothermic by 0.8 eV, and E* estimated to be 1.02 eV. On $(Pt_3)(Pt_6Ru)$, the $D_{e,ads}$ for $H_2O_{ads(Ru)}$, 0.27 eV, is less endothermic, and estimated E* is lower by 0.18 eV than on pure Pt. We also examined H_2O dissociation on a Ru-rich cluster, $(Pt_3)(Pt_4Ru_3)$; the calculated $D_{e,ads}$ and E* on $(Pt_3)(Pt_6Ru)$ and $(Pt_3)(Pt_4Ru_3)$ are quite close. A simple transition state argument would predict that a decrease of 0.18 eV in E* should increase the reaction rate by a factor of about a thousand. The $H_2O_{ads(M)}$ dissociation on Sn is $\approx$ 0.3 eV less endothermic, and E* lower by 0.1 eV, than on Pt. Thus Sn in Pt-Sn is more active than pure Pt, but less

so than Ru in Pt-Ru. According to the ASED-MO calculations of Anderson et al. [96], however, Sn in Pt-Sn does not promote $H_2O_{ads(M)}$ dissociation.

Table 10
Calculated adsorption energies E_{ads} (eV) for H_2O, OH, and H and dissociation energies $D_{e,ads}$ (eV) (for $H_2O_{ads} \rightarrow OH_{ads} + H_{ads}$) on Pt site in pure Pt_{10} and on M site in mixed $(Pt_3)(Pt_6M)$ and $(M_3)(Pt_6M)$ clusters. The activation energies E* (eV) for the dissociation reaction are estimated by Eq. 14.

	E_{ads}			$D_{e,ads}$	E*
	H_2O	OH	H (hol)		
$(Pt_3)(Pt_7)$	0.46	2.29	2.61	0.81	1.02
$(Pt_3)(Pt_6Ru)$	0.85	3.41	2.42	0.27	0.84
$(Pt_3)(Pt_4Ru_3)$	0.73	3.31	2.38	0.29	0.84
$(Pt_3)(Pt_6Sn)$	0.39	2.55	2.52	0.57	0.92
$(Pt_3)(Pt_6Mo)$	1.20	4.23	2.11	0.11	0.76
$(Pt_3)(Pt_6W)$	1.18	4.32	2.02	0.09	0.73
$(Pt_3)(Pt_6Re)$	1.13	4.30	2.23	-0.15	0.66
$(Pt_3)(Pt_6Os)$	0.86	3.66	2.34	0.11	0.77
$(Pt_3)(Pt_6Rh)$	0.81	2.86	2.54	0.66	1.00
$(Pt_3)(Pt_6Ir)$	0.66	3.01	2.46	0.44	0.90
$(Pt_3)(Pt_6Cu)$	0.66	2.02	2.51	1.38	1.38
$(Pt_3)(Pt_6Zn)$	0.65	2.11	2.28	1.51	1.51
$(Pt_3)(Pt_6Ge)$	0.42	2.57	2.02	1.08	1.11
$(Pt_3)(Pt_6Pb)$	0.42	1.93	1.69	2.05	2.05
$(Pt_3)(Pt_6Zr)$	1.25	3.75	1.91	0.84	1.05
$(Ru_3)(Pt_6Ru)$	0.58	3.24	2.21	0.38	0.85
$(Sn_3)(Pt_6Sn)$	0.56	2.71	1.51	1.59	1.59
$(Mo_3)(Pt_6Mo)$	0.94	3.62	1.97	0.60	0.94
$(W_3)(Pt_6W)$	0.85	3.44	1.98	0.68	0.97
$(Os_3)(Pt_6Os)$	0.94	3.77	2.11	0.31	0.83
$(Sn_3)(Pt_6Ru)$	0.58	2.22	2.21	1.40	1.40
$(Sn_3)(Pt_6Mo)$	0.71	3.17	2.25	0.54	0.93

Among the transition metals considered here, Re is predicted to have the highest activity in dissociating H_2O, while Mo, W, and Os are also more active than Ru. The estimated E* with Cu, Zn, and Pb are rather high, and these would not be expected to show much activity for $H_2O_{ads(M)}$ dissociation. Ir is comparable to Sn in activity, and Rh and Ge are comparable to Pt. Table 5 shows that the mixing with Zr significantly reduces the adsorption energy of CO. However, Zr is less active than Pt for H_2O dissociation, and without $OH_{ads(M)}$, CO is not removed, even though E_{ads} is quite low. In fact Pt-Zr alloys do not seem to display enhanced activity in the electro-oxidation of $CO_{ads(Pt)}$ [14]. E* for H_2O dissociation varies in the order Re < W < Mo ≈ Os < Ru < Sn ≈ Ir < Rh ≈ Pt < Zr < Ge << Cu < Zn << Pb.

Second layer M-atoms show significant effects on CO adsorption, and we examined the effect on H_2O dissociation as well on $(M_3)(Pt_6M)$ (M = Ru, Sn, Mo, W, Os), $(Sn_3)(Pt_6Ru)$ and $(Sn_3)(Pt_6Mo)$. Table 10 displays the calculated $D_{e,ads}$ and E* for these. In general dissociation of $H_2O_{ads(M)}$ on $(M_3)(Pt_6M)$ is more endothermic and has higher E* than on $(Pt_3)(Pt_6M)$. The increase in $D_{e,ads}$ or E* for M = Mo is more pronounced than for M = Ru. Sn_3 as the second layer causes the dissociation reaction to become strongly endothermic. So, although Sn_3 as an underlayer greatly reduces the adsorption energy of CO, it is not beneficial for H_2O dissociation.

4. REACTION OF $CO_{ads(Pt)}$ WITH $OH_{ads(M)}$

H_2O dissociation on pure Pt and on the Pt site in mixed Pt-Ru clusters is difficult. Ru sites more actively dissociate H_2O [6,7]. In the present study we also find that Mo, W, and Re activate H_2O more effectively than does Ru, partly because these metals (Mo, W, Re) adsorb OH strongly. $CO_{ads(Pt)}$ is removed by $OH_{ads(M)}$, the principal oxidizing agent. However, strong OH adsorption introduces a barrier to CO oxidation. In this section, we examine the energetics of the surface reaction of $CO_{ads(Pt)}$ with $OH_{ads(M)}$. The scheme for calculating the combination energy ($C_{e,ads}$) is

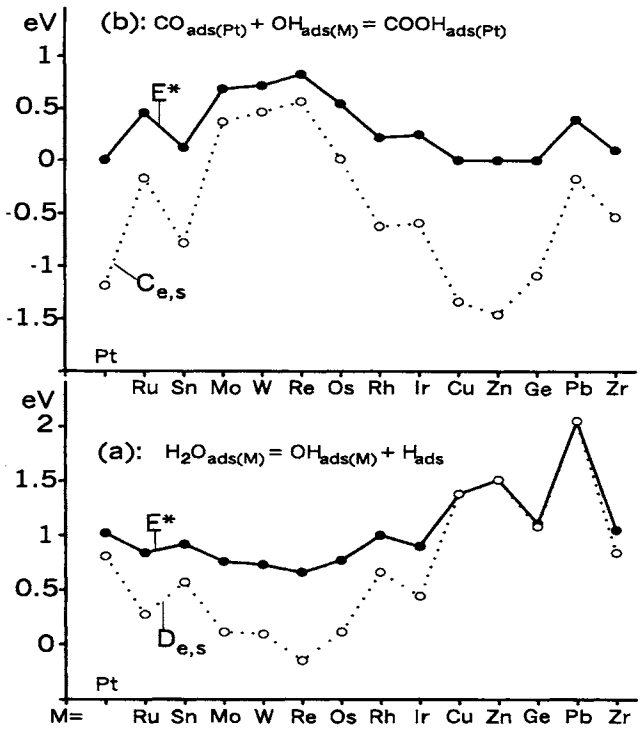

Fig. 7. Schematic illustration of the calculated: (a) H_2O dissociation and activation energies at Pt and M sites, (b) $CO_{ads(Pt)} + OH_{ads(M)}$ combination and activation energies.

$$\begin{array}{ccccc} & & & C_{e,ads} & \\ CO_{ads(Pt)} & + & OH_{ads(M)} & \rightarrow & COOH_{ads(Pt)} \\ \uparrow -E_{CO} & & \uparrow -E_{OH} & & \uparrow -E_{COOH} \\ CO_g & + & OH_g & \rightarrow & COOH_g \\ & & & C_{e,g} & \end{array} \qquad (15)$$

Thus $$C_{e,ads} = C_{e,g} + E_{CO} + E_{OH} - E_{COOH} \qquad (16)$$

Here E_{CO} and E_{COOH} are the adsorption energies of CO and COOH on $(Pt_3)(M_2Pt_5)$; E_{OH} is the adsorption energy of OH on $(Pt_3)(Pt_6M)$; $C_{e,g}$ is the combination energy of the CO + OH reaction in the gas phase, the calculated value being –2.65 eV. To

estimate E* for the reverse reaction of the combination, we employ the formula in Eq. 11. The calculated $C_{e,ads}$ and E* for the Pt-M metals are collected in Table 11 and schematically illustrated in Fig. 7.

On pure Pt, the combination reaction is exothermic (-1.2 eV) and proceeds readily despite the inability of Pt to dissociate water and produce OH. Eq. 11 produces a negative E*, indicating that the combination reaction on pure Pt is barrierless. The same holds true for M = Cu, Zn, and Ge while $C_{e,ads}$ for M = Ru is only slightly exothermic (-0.2 eV). Therefore the combination reaction on Pt-Ru should proceed readily. $C_{e,ads}$ for M = Sn, -0.8 eV, is more exothermic than for M = Ru. Rh and Ir are comparable to Sn. However, the combination reactions for M = Mo, W, and Re are endothermic. For M = Re, the estimated E* of 0.83 eV is significantly higher than that for the $H_2O_{ads(Re)}$ dissociation. Although the Re site on the Pt-Re surface is most efficient in generating active $OH_{ads(Re)}$, the very large E_{ads}(OH) to Re does not favor the formation of $COOH_{ads}$, limiting the overall rate. In the case of M = Mo and W, the estimated E* values for this reaction are also high, but smaller than those for the $H_2O_{ads(M)}$ dissociation. Thus, the H_2O dissociation reaction on Pt-Mo or Pt-W is the rate-determining step. According to section 4.5, Mo and W are more active toward H_2O dissociation than Ru and Mo or W should be better catalysts. Experiments by Ross et al. [18] show that Pt-Mo alloy catalysts do provide better CO tolerance than Pt-Ru. As far as we know no experimental results on the activity of Pt-W alloys in CO electro-oxidation have appeared.

The combination reaction of $CO_{ads(Pt)} + OH_{ads(M)}$ was also examined on clusters with M_3 in the second layer. Because CO and OH on such clusters have relatively low adsorption energies (except for M = Os), their combination reaction is quite exothermic, even for M = Mo or W (see Table 11). From the results given in Tables 10 and 11, it is possible to examine the relative importance of a "ligand effect" vs. a bi-functional mechanism. $CO_{ads} + OH_{ads} \rightarrow COOH_{ads}$ on pure Pt proceeds readily despite strong CO adsorption, so the promoting effect of the alloying metal mainly involves H_2O activation. According to Eqs. 11 and 16, a ligand effect can play an important role when the OH binding to M is strong as is the case with M = Mo, W, and Re. A reduction in E_{ads} for CO on Pt will give a less endothermic $C_{e,ads}$ and lower E*. From the results presented in Section 2.3, E_{ads} for $(Pt_3)(M_4Pt_3)$ is lower than for $(Pt_3)(M_2Pt_5)$ for the three. Thus, a somewhat higher M:Pt ratio should benefit CO electro-oxidation.

Table 11
Calculated combination reaction energies $C_{e,ads}$ (eV) for $CO_{Pt} + OH_M \rightarrow COOH_{Pt}$. The activation energies E* (eV) are estimated by Eq. 11.

		$-E_{COOH}$	E_{CO}	E_{OH}	$C_{e,ads}$	E*
$CO_{Pt} + OH_M \rightarrow COOH_{Pt}$[a]	M=Pt	-2.75	1.92	2.29	-1.19	0.0[b]
	=Ru	-2.55	1.62	3.41	-0.17	0.46
	=Sn	-2.37	1.69	2.55	-0.78	0.12
	=Mo	-2.55	1.34	4.23	0.37	0.69
	=W	-2.48	1.28	4.32	0.47	0.72
	=Re	-2.56	1.48	4.30	0.57	0.83
	=Os	-2.57	1.57	3.66	0.01	0.55
	=Rh	-2.53	1.70	2.86	-0.62	0.22
	=Ir	-2.65	1.70	3.01	-0.59	0.25
	=Cu	-2.64	1.93	2.02	-1.34	0.0[b]
	=Zn	-2.75	1.83	2.11	-1.46	0.0[b]
	=Ge	-2.72	1.71	2.57	-1.09	0.0[b]
	=Pb	-1.37	1.92	1.93	-0.17	0.40
	=Zr	-2.54	0.91	3.75	-0.53	0.10
$(Ru_3)(Ru_2Pt_5)CO + (Ru_3)(Pt_6Ru)OH$		-2.29	1.31	3.24	-0.39	0.27
$(Sn_3)(Sn_2Pt_5)CO + (Sn_3)(Pt_6Sn)OH$		-2.05	0.70	2.71	-1.29	0.0[b]
$(Mo_3)(Mo_2Pt_5)CO + (Mo_3)(Pt_6Mo)OH$		-2.10	0.72	3.62	-0.41	0.10
$(W_3)(W_2Pt_5)CO + (W_3)(Pt_6W)OH$		-2.08	0.57	3.44	-0.72	0.0[b]
$(Os_3)(Os_2Pt_5)CO + (Os_3)(Pt_6Os)OH$		-2.50	1.43	3.77	0.05	0.54
$(Sn_3)(Ru_2Pt_5)CO + (Sn_3)(Pt_6Ru)OH$		-1.90	0.62	2.22	-1.71	0.0[b]
$(Sn_3)(Mo_2Pt_5)CO + (Sn_3)(Pt_6Mo)OH$		-1.74	0.22	3.17	-1.00	0.0[b]

[a]COOH and CO adsorption energies are calculated on $(Pt_3)(M_2Pt_5)$; OH adsorption energy is calculated on $(Pt_3)(Pt_6M)$. [b]Negative values are obtained by the UBI-QEP formula, and are set to zero.

5. SUMMARY

The theoretical study of CO adsorption and H_2O dissociation on a series of mixed Pt-M surfaces [6,7,10] has provided a broad array of information necessary to understand the required characteristics of CO-tolerant binary catalysts. In

addition some understanding of important steps in electrocatalytic reactions of small molecules has been gained. The growing awareness that enhanced catalytic activity is to be sought at the nanoscale level, rather than in bulk alloys, renders theoretical studies of reactions on small metal clusters especially significant.

With the exceptions of Cu and Pb, the adsorption strength of CO on binary Pt-M is substantially reduced compared with pure Pt. Thus a "ligand effect" appears to be important in CO electro-oxidation on Pt-M electrodes. Although Zr reduces the binding energy of CO to Pt by about 1 eV, CO still adsorbs too strongly to be removed without oxidants. Reductions in E_{ads} are more pronounced, especially for M = Sn, Mo, W, and Ge, when these metals appear in the second cluster layer. The effect is in part due to the fact that second layer is a terminal layer, but still points up the significant fact that adsorption properties strongly depend on the micro-structure of adsorption site in nanoparticle catalysts.

The present computational study has clearly shown that poor performance of pure Pt for methanol oxidation results from both the strong adsorption shown by CO and the difficulty of dissociating H_2O and forming OH on the metal site. Thus a secondary metal (M) capable of activating H_2O and producing OH is necessary. Ru is better able to dissociate H_2O into OH than is Pt, whereas dissociation on Sn is only slightly more favorable than on Pt. Mo, W, and Re are more active than Ru in adsorbing and dissociating H_2O. These metals not only weaken CO adsorption, but also promote H_2O dissociation.

For the secondary metals examined in this study, the ability to dehydrogenate water to OH follows the order,

$$Re > W > Mo > Os > Ru > Ir > Sn >> (Cu, Zn, Ge, Zr, Rh).$$

Cu, Zn, Ge, Zr, and Rh have high $D_{e,ads}$ and E* for water dissociation, and thus are unsuitable as secondary metals. The enhanced promoting effect of Re, W, or Mo toward H_2O dissociation are due to strong M-OH adsorption, and large $E_{ads}(OH)$ does not promote oxidative removal of CO. For M = Re, the activation energy for the $CO_{ads} + OH_{ads}$ combination reaction is the highest of all, and thus the reaction becomes the rate-determining step in CO removal.

The computed activation energies for the combination reaction suggest the following order in which the metals facilitate the reaction,

$$(Cu, Zn, Ge, Zr, Rh, Ir, Sn) >> Ru > Os > Mo > W > Re$$

resulting in a reversal of order obtained for water dissociation. The activation energies in M= Cu, Zn, Ge, Zr, Rh, Ir, and Sn for $CO_{ads} + OH_{ads}$ reaction are zero or nearly zero as in pure platinum.

The best alloying metals are those that possess low activation energies for H_2O dissociation and for $CO_{ads} + OH_{ads} \rightarrow COOH_{ads}$. Based on the energetics, with more emphasis on water activation and oxidant OH formation, we predict the most suitable alloying metals in CO electro-oxidation to be Mo, W, and Os, with Ru close behind.

Because the surface electronic processes play a fundamental role in catalytic activities, heterogeneous catalytic activity is determined primarily by the surface morphology and composition of the nanoparticle catalyst. The structure and composition of a few atomic layers below the surface play a secondary role, while the bulk of the catalyst remains a spectator of the catalytic activity. At the same time, cost considerations necessitate the optimization of dispersion and homogeneity of the catalytic sites, particularly when expensive noble metals are involved. Consequently, research towards the improvement of existing catalysts and the design of new ones focuses on two aspects: tailoring of the surface structure, and minimizing the mass of the catalytically inert material. Therefore, catalyst fabrication techniques that allow control over those factors are desirable.

By tailoring the surface structure and composition of a nanocatalyst, one can in principle vary the surface electronic properties to ultimately design an appropriate catalyst. Consequently, it is necessary to understand their electronic structure if one is to understand the synergism of heterometallic catalysts. Since experimental information on the structural and dynamic properties of supported and unsupported metal clusters is limited, a computational/modelling study is a useful complement to experimental studies.

Metal nanoparticles are new promising materials that display high catalytic activities. Size constraints in metal nanoclusters strongly affect their physical and chemical properties. Metal atoms in nanoclusters are undercoordinated compared to those in bulk and display enhanced catalytic reactivities. Thus microscopic control or subnanostructuring of metal nanoparticles leads to catalysts with customized properties. Goodman et al. [48] recently reported that monodispersed Au_{55} nanoclusters (size 1.4 nm) display a pronounced maximum of catalytic efficiency, with unusual catalytic properties, e.g., for CO oxidation, while gold in bulk does not. Although supported and unsupported metal nanoparticles are becoming the building blocks of a host of new catalytic materials, their structures and activities, which may vary dramatically with cluster size, must be well understood to design surface morphology and composition of higly active nanoparticle catalysts.

ACKNOWLEDGEMENTS

This work was supported by DOD-EPSCoR grant DAAD19-00-1-0092, ARL Collaborative Technology Alliance in Power and Energy (Cooperative Agreement No. DAAD19-01-2-0010) and NASA-URC grant No. NCC3-1034.

REFERENCES

[1] C. Lamy, J.-M. Leger, J. Clavilier and R. Parsons, J. Electroanal. Chem. 150 (1983) 71.
[2] H. A. Gasteiger, N. M. Markovic, P. N. Ross, Jr., E. J. Cairns, J. Phys. Chem. 98 (1994) 617.
[3] B. Beden, C. Lamy, N. R. de Tacconi and A. Arvia, J. Electrochim. Acta 35 (1990) 691.
[4] V. S. Bagotzky, Yu. B. Vassil'en and O. A. Khazova, J. Electroanal. Chem. 81 (1977) 229.
[5] E. Ticanell, J. G. Beery, M. T. Paffett, S. Gottesfeld, J. Electroanal. Chem. 258 (1989) 61.
[6] M.-S. Liao, C. R. Cabrera and Y. Ishikawa, Surf. Sci. 445 (2000) 267.
[7] Y. Ishikawa, M.-S. Liao and C. R. Cabrera, Surf. Sci., 463 (2000) 66.
[8] J. Greeley and M. Mavrikakis, J. Am. Chem. Soc. 124 (2002) 7193.
[9] S. K. Desai, M. Neurock and K. Kourtakis, J. Phys. Chem. B 106 (2002) 2559.
[10] Y. Ishikawa, M.-S. Liao and C. R. Cabrera, 513 (2002) 98.
[11] B. Beden, C. Lamy, A. Bewick, and K. Kunimatsu, J. Electroanal. Chem. 121 (1981) 343.
[12] M. Krausa and W.Vielstich, J. Electroanal. Chem. 379 (1994) 307.
[13] T. Frelink, W. Visscher, and J. A. R. van Veen, Electrochim. Acta **39**, 1871 (1994).
[14] B. N. Grgur, N. M. Markovic, and P. N. Ross, Jr. J. Phys. Chem. B **102**, 2494 (1998).
[15] A. Aramata, I. Toyoshima, and M. Enyo, Electrochim. Acta **37**, 1317 (1992).
[16] D. A. Hickman, L. D. Schmidt, Science 25 (1993) 343.
[17] S. Mukerjee, S. J. Lee, E. A. Ticianelli, J. McBreen, B. N. Grgur, N. M. Markovic, P. N. Ross, J. R. Giallombardo, E. S. De Castro, Electrochem. Solid-State Lett. 2 (1999) 12.
[18] B. N. Grgur, N. M. Markovic, P. N. Ross, Jr., J. Electrochem. Soc. 416 (1999) 1613.
[19] B. N. Grgur, G. Zhuang, N. M. Markovic, P. N. Ross, Jr., J. Phys. Chem. B 101 (1997) 3910.
[20] B. N. Grgur, N. M. Markovic, P. N. Ross, Jr., J. Phys. Chem. B 102 (1998) 2494.
[21] Y. Wang, E. Rosim Fachini, G. Cruz, Y. Ishikawa, J. Colucci and C. Cabrera, J. Electrochem. Soc. 148 (2001) c222.
[22] B. N. Grgur, N. M. Markovic, P. N. Ross, Jr., Electrochim. Acta 43 (1998) 3631.
[23] A. Aramata, I. Toyoshima, M. Enyo, Electrochim. Acta 37 (1992) 1317.
[24] M. Watanabe, S. Motoo, J. Electroanal. Chem. 60 (1975) 275.
[25] H. A. Gasteiger, N. M. Markovic, P. N. Ross, Jr., E. J. Cairns, J. Phys. Chem. 97 (1993) 12020.
[26] H. A. Gasteiger, N. M. Markovic, P. N. Ross, Jr., J. Phys. Chem. 99 (1995) 16757.
[27] R. Ianniello, V. M. Schmidt, U. Stimming, J. Stumper, A. Wallau, Electrochim. Acta 39 (1994) 1863.
[28] M. M. P. Janssen, J. Moolhuysen, J. Catal. 46 (1977) 289.
[29] A. Wieckowski, J. Electroanal. Chem. 78 (1977) 229.
[30] M. Krausa, W. Vielstich, J. Electroanal. Chem. 379 (1994) 307.
[31] A. Gavezzotti, G. F. Tantardini, and H. Miessner, J. Phys. Chem. 92 (1988) 872.
[32] F. Illas, S. Zurita, J. Rubio, and A. M. Marquez, Phys. Rev. B 52 (1995) 12372; F. Illas,

S. Zurita, A. M. Marquez, and J. Rubio, Surf. Sci. 376 (1997) 279.
[33] S. Ohnishi and N. Watari, Phys. Rev. B 49 (1994) 14619.
[34] G. Pacchioni, S.-C. Chung, S. Krüger, and N. Rösch, Surf. Sci. 392 (1977) 173.
[35] H. Aizawa and S. Tsuneyaki, Surf. Sci. 399 (1988) L364.
[36] R. G. Tobin and P. L. Richards, Surf. Sci. 179 (1987) 387.
[37] E. Schweizer, B. N. J. Persson, M. Tushaus, D. Hoge, and A. M. Bradshaw, Surf. Sci. 213 (1989) 49.
[38] S. Hong and H. H. Richardson, J. Phys. Chem. 97 (1992) 1258.
[39] C. Klünker, M. Balden, S. Lehwald, and W. Daum, Surf. Sci. 360 (1996) 104.
[40] D. F. Ogletree, M. A. van Hove, and G. A. Somorjai, Surf. Sci. 173 (1987) 251.
[41] C. M. Comrie and R. M. Lambert, Faraday Trans. I 72 (1976) 1659.
[42] G. Ertl, M. Neumann and K. M. Streit, Surf. Sci. 64 (1977) 393.
[43] D. H. Winicur, J. Hurst, C. A. Becker, and L. Wharton, Surf. Sc. 109 (1981) 263.
[44] J. Fair and R. J. Madix, J. Chem. Phys. 73 (1980) 3480.
[45] J. R. Engstrom and W. H. Weinberg, Surf. Sci. 201 (1988) 145.
[46] C. E. Wartnaby, A. Stuck, Y. Y. Yeo, and D. A. King, J. Phys. Chem. 100 (1996) 12483.
[47] W. T. Lee, L. Ford, P. Blowers, H. L. Nigg, and R. I. Masel, Surf. Sci. 416 (1998) 141.
[48] M. Valden, X. Lai, D. W. Goodman, Science 281 (1998) 1647.
[49] H. Hoster, T. Iwasita, H. Baumgärtner, and W. Vielstich, Phys. Chem. Chem. Phys. 3 (2001) 337.
[50] A. J. Aldykiewicz, Jr., D. Zurawski, S. Baxter, R. Kumar, M. Krumpelt, G. Bunker, C. Segre (unpublished results).
[51] S. Mukerjee, J. J. McBreen, Electochem Soc. 146 (1999) 600.
[52] D. Lide (Ed.), CRC Handbook of Chemistry and Physics, 75th Ed., CRC Press, Boca Raton, FL, 1994 – 1995.
[53] ADF program package, version 2.0.1: G. te Velde, E. J. Baerends, J. Comp. Phys. 99 (1992) 84.
[54] T. Ziegler, A. Rauk, Theoret. Chim. Acta 46 (1977) 1.
[55] T. Ziegler, V. Tschinke, E. J. Baerends, J. G. Snijders, W. Ravenek, J. Phys. Chem. 93 (1989) 3050.
[56] B. I. Dunlap, N. Rösch, Adv. Quantum Chem. 21 (1990) 317.
[57] S.-G. Wang, *Ph.D. Thesis* (Verlag Shaker, Aachen, Germany, 1994).
[58] M. Cook and M. Karplus, J. Phys. Chem. 91 (1987) 31.
[59] G. Blyholder, J. Phys. Chem. 68 (1964) 2772.
[60] Q. Fan, C. Pu, E. S. Smotkin, J. Electrochem. Soc. 143 (1996) 3053.
[61] T. Iwasita, F. C. Nart, W. Vielstich, Ber. Bunsenges. Phys. Chem. 94 (1990) 1030.
[62] M. T. Paffett, S. C. Gebhard, R. G. Windham, B. E. Koel, J. Phys. Chem. 94 (1990) 6831.
[63] K. Fututani, T. T. Magkoev, Y. Murata, K. Terakura, Surf. Sci. 363 (1996) 185.
[64] T. Frelink, W. Visscher, J. A. R. van Veen, Surf. Sci. 335 (1995) 353.
[65] P. Shiller, A. B. Anderson, Surf. Sci. 236 (1990) 225.
[66] K. P. Huber, G. Herzberg, Molecular Spectra and Molecular Structure, Vol. IV, Constants of Diatomic Molecules, Van Nostrand Reinhold: New York, 1979.
[67] K.-I. Machida, A. Fukuoka, M. Ichikawa, M. Enyo, J. Electrochem. Soc. 138 (1991) 1958.
[68] U. Heiz, R. Sherwood, D. M. Cox, A. Kaldor, J. T. Yates, Jr., J. Phys. Chem. 99 (1995) 8730
[69] D. M. Cox, B. Kessler, P. Fayet, W. Eberhardt, Z. Fu, D. Sondericher, R. D. Sherwood,

A. Kaldor, NanoStruct. Mater. 1 (1992) 161.
[70] J.-M. Leger, C. Lamy, Ber. Bunsenges. Phys. Chem. 94 (1990) 1021.
[71] P. A. Christensen, A.Hamnett, S. A. Weeks, J. Electroanal. Chem. 250 (1988) 127.
[72] T. Iwasita, W. Vielstich, J. Electroanal. Chem. 250 (1988) 451.
[73] J. Willsan, J. Heitbaum, Electrochim. Acta 31 (1986) 943.
[74] B. Beden, F. Hahn, S. Juanto, C. Lamy, J.-M. Leger, J. Electroanal. Chem. 225 (1987) 215.
[75] T. Iwasita, W. Vielstich, E. Santo, J. Electroanal. Chem. 229 (1987) 367.
[76] T. Iwasita, F. C. Nart, J. Electroanal. Chem. 317 (1991) 291.
[77] B. A. Sexton, A. E. Hughes, Surf. Sci. 140 (1984) 227.
[78] E. Shustorovich, Adv. Catal. 37 (1990) 101.
[79] C. Zheng, Y. Apeloig, R. Hoffmann, J. Am. Chem. Soc. 110 (1988) 749.
[80] G. E. Gdowski, J. A. Fair, R. J. Madix, Surf. Sci. 127 (1983) 541.
[81] A. B. Anton, D. C. Cadogan, Surf. Sci. 239 (1990) L548.
[82] E. Shustorovich, H. Sellers, Surf. Sci. Rep. 31 (1998) 1.
[83] E. Shustorovich, A. T. Bell, Surf. Sci. 253 (1991) 386.
[84] P. Paredes-Olivera, E. M. Pattrito, H. Sellers, Surf. Sci. 327 (1995) 330.
[85] W. Vielstich, P. A. Christensen, S. A. Weeks, A. Hamnett, J. Electroanal. Chem. 242 (1987) 327.
[86] A. B. Anderson, E. Grantscharova, J. Phys. Chem. 99 (1995) 9149.
[87] W. F. Lin, M. S. Zei, M. Eiswirth, G. Ertl, T. Iwasita, W. Vielstich, J. Phys. Chem. *B* 103 (1999) 6968.
[88] A. A. Deckert, J. L. Brand, C. H. Mak, B. G. Koehler, S. M. George, J. Chem. Phys. 87 (1987) 1936.
[89] B. A. Sexton, Surf. Sci. 102 (1981) 271.
[90] T. Frelink, W. Visscher, J. A. R. van Veen, *Electrochim. Acta* 39 (1994) 1871
[91] (a) M. M. P. Janssen, J. Moolhuysen, *Electrochim. Acta* 1976, *21*, 861. (b) M. M. P. Janssen, J. Moolhuysen, *J. Catal.* 46 (1977) 289.
[92] A. B. Anton, D. C. Cadogan, Surf. Sci. 239 (1990) L548.
[93] G. E. Gdowski, J. A. Fair, R. J. Madix, Surf. Sci. 127 (1983) 541.
[94] H. Sellers, E. M. Pattrito, P. Paredes-Olivera, Surf. Sci. 380 (1997) 264.
[95] H. Sellers, E. M. Pattrito, P. Paredes-Olivera, Surf. Sci. 418 (1998) 376.
[96] A. B. Anderson, E. Grantscharova, S. Seong, J. Electrochem. Soc. 143 (1996) 2075.

J. Leszczynski (Editor)
Computational Materials Science
Theoretical and Computational Chemistry, Vol. 15

Chapter 11

Supported metal species and adsorption complexes on metal oxides and in zeolites: Density functional cluster model studies

Notker Rösch,[a] Vladimir A. Nasluzov,[b] Konstantin M. Neyman,[a] Gianfranco Pacchioni[c] and Georgi N. Vayssilov[d]

[a]Institut für Physikalische und Theoretische Chemie, Technische Universität München, Lichtenbergstr. 4, 85747 Garching, Germany

[b]Institute of Chemistry and Chemical Technology, Russian Academy of Sciences, ul. K. Marx 42, 660049 Krasnoyarsk, Russian Federation

[c]Dipartimento di Scienza dei Materiali, Università di Milano-Bicocca, via R. Cozzi 53, 20125 Milano, Italy

[d]Faculty of Chemistry, University of Sofia, Blvd. J. Bouchier 1, 1126 Sofia, Bulgaria

This review describes high-level computational activities concerning adsorption complexes and metal species supported on ionic metal oxides and in zeolite cages. We focus on applications carried out by the authors with the help of density functional codes developed at the Technische Universität München, in particular, with the new powerful parallel code PARAGAUSS. The following topics are covered: (i) computational method and details of the calculations; (ii) pertinent aspects of method development; (iii) adsorption complexes of small probe molecules, such as CO, N_2, CH_4, C_2H_2, CH_3OH, on surfaces of the ionic metal oxides MgO and α-Al_2O_3 as well as in zeolites; (iv) deposited transition metal particles, e.g. of Cr, Co, Ni, Cu, Mo, Rh, Pd, Ag, W, Re, Os, Ir, Pt, and Au, on metal oxide surfaces and in zeolite cavities and complexes with these metal species; (v) complexes of CO molecules adsorbed on palladium nano-clusters.

1. INTRODUCTION

Supported metal clusters play an important role in nanoscience and nanotechnology for a variety of reasons [1-6]. Yet, the most immediate applications are related to catalysis. The heterogeneous catalyst, installed in automobiles to reduce the amount of harmful car exhaust, is quite typical: it consists of a monolithic backbone covered internally with a porous ceramic material like alumina. Small particles of noble metals such as palladium, platinum, and rhodium are deposited on the surface of the ceramic. Other pertinent examples are transition metal clusters and atomic species in zeolites which may react even with such inert compounds as saturated hydrocarbons activating their catalytic transformations [7-9]. Dehydrogenation of alkanes to the alkenes is an important initial step in the transformation of ethane or propane to aromatics [8-11]. This conversion via nonoxidative routes augments the type of feedstocks available for the synthesis of these valuable products.

To act as efficient catalysts, metal particles must have a size of a few nanometers. Controlling the size distribution of the particles is a very important issue for preparing good catalysts. Despite strong efforts to unravel relationships between surface morphology, size, and shape of metal particles, deeper understanding of catalytic mechanisms often is still lacking. Recently, new deposition techniques have been developed which allow a controlled nucleation and growth of nano-clusters in ultrahigh vacuum (UHV) on well-defined faces of crystalline oxides and thin films [12-14]. These supported nano-clusters often show specific chemical behavior, which is characteristic of the small dimension of the particles; they represent new model systems of more complex industrial catalysts [15-17].

Transition metal clusters in zeolite cages form another important class of supported species. Zeolites are very suitable supports/hosts for small metal particles because the dimensions of their cavities affect the formation of encaged moieties of nanometer and sub-nanometer scale, thus stabilizing clusters of desired sizes and shapes. Experimental investigations in this direction resulted in preparation procedures that yield nearly uniform small encapsulated metal moieties in zeolites [18-20].

The nature of the bonding at the interface between metal species and oxide support is known only very approximately. Ideally, one would like to be able to prepare monodispersed catalyst particles, all with the same and, if possible, very small number of atoms. In fact, the active part of the catalyst is its surface where low-coordinated atoms are responsible for most of the specific chemistry [20]. However, surface atoms form only a small fraction of the total number of atoms of the particle. Because heterogeneous catalysis often deals with precious metals, reducing the size of the particle immediately results in reduced cost due to a better surface-to-volume ratio: with a given quantity of material, it is

possible to produce many more active sites and to increase the efficiency of the catalyst.

A further appealing consequence of good control of particle size and shape is that the selectivity of the catalyst can improve. The selectivity is the capability to produce a large fraction of just one product over the many products that can be obtained in a chemical reaction. Supported metal particles exhibit atoms with different coordination, hence different reactivity, and in this way give rise to a mixture of products. Thus, the preparation of small well-ordered metal species supported on an oxide substrate is at the heart of the research on supported metal catalysts.

Supported metal clusters will also play a role in microelectronic technologies, in particular, the production of sensors. Sensors are often defined as "artificial noses". Their function is to detect the presence of molecules in the atmosphere by means of their chemical reaction with a metal particle which is part of a metal oxide semiconductor field effect transistor (MOSFET). In such a device a thin metal film is separated from a semiconducting silicium crystal by a very thin layer of an insulating oxide, SiO_2. The conductivity of the semiconductor can be modulated by applying an electric field perpendicular to the semiconductor surface because charge separation across the metal-semiconductor interface affects the lateral conductivity of the semiconductor. This charge separation may depend on several factors, e.g. film thickness and film morphology. It is also affected by adsorbed molecules on its surface and thus changes in the charging of the film can provide a direct measure of the amount of gas adsorbed. Performance, durability and sensitivity of such devices very critically depend on the structure of the metal overlayer which can be modified based on our understanding of the mechanisms of nucleation and growth of metal particles forming the film. Cluster formation is a crucial step in the preparation of such a device, and better control of size and shape of the metal islands would considerably improve the possibility for monitoring the gas adsorption on these systems.

Another area of potential use of supported clusters and nanoparticles is in magnetic recording. The magnetic properties of atoms are quite well understood, but the development of magnetic order on a macroscopic scale in a solid is a rather complex problem. Long-range magnetic order is not simply the sum of the effects of the individual components (i.e. the isolated atoms). Rather, it is a collective effect of atoms which can result in the well known ferromagnetic or anti-ferromagnetic orderings or in more complicated alignments. Magnetic clusters provide a link between the magnetism at the atomic level and in the condensed state [21]. A target of the present hard disk technology is to reduce the size of the magnetic particles down to 50 nm. In this context the capability to produce small particles of good quality is essential for exploiting the permanent magnetization of the material.

One last example of potential application of clusters is in the field of materials with tailored optical properties. A spherical metal particle exhibits a special collective (plasmon) excitation of its surface electrons which was discovered and described by A. Mie in 1908 [22]. This absorption can fall in the visible part of the spectrum, thus giving rise to a colored cluster sample. Indeed, the red color of old stained glass windows in medieval cathedrals is due to tiny gold particles in a glass matrix. However, as the size of the metal particles decreases, the optical properties become size-dependent and do not obey Mie theory anymore, but follow the laws of quantum mechanics (QM) and in particular of confined electrons in an external potential. For small clusters the energy levels are discrete with energy splittings depending on the size and the shape of the cluster, which can lead to specific optical properties.

It is no surprise that the contribution of quantum theory is extremely useful for the study of all the problems just outlined. This chapter aims at accounting for recent high-level computational activities in the area of supported metal species and adsorption complexes on ionic metal oxides, such as MgO and Al_2O_3, and in zeolite cages. This review will focus mainly on applications carried out by the authors with the help of density functional (DF) codes developed at the Technische Universität München. Pertinent features of the method development will also be briefly discussed.

In the following sections, we shall begin our presentation with a discussion of the computational method, method developments and details of the calculations. Sections 3 and 4 are devoted to adsorption complexes of small probe molecules on ionic metal oxide MgO and α-Al_2O_3 surfaces as well as in zeolites, respectively. Deposited transition metal particles on metal oxide surfaces and in zeolite cavities and complexes with them are addressed in Sections 5 and 6. Complexes of molecules adsorbed on nanoclusters of transition metals are considered in Section 7. The chapter will close with a summary and our outlook.

2. COMPUTATIONAL METHOD, TOOLS AND MODELS

2.1. Basic details and tools

Most of the calculated model cluster results discussed below were obtained at the all-electron level using the linear combination of Gaussian-type orbitals fitting-functions density functional (LCGTO-FF-DF) method [23]. Some earlier DF calculations were carried out with the help of a code developed by Dunlap [24,25] and extended at TU München in the group of Rösch [26,27]. Later on, the novel powerful parallel code PARAGAUSS [28,29], developed at TU München, was employed. The scalar relativistic variant of the LCGTO-FF-DF method [30] was used for systems where pronounced relativistic effects were expected, e.g., in the presence of 4*d*- and 5*d*-metal atoms. This scalar relativistic approach employs a second-order Douglas-Kroll transformation [31] to

decouple electronic and positronic degrees of freedom of the Dirac-Kohn-Sham equation [32].

The computationally economic local density approximation (LDA) to the exchange-correlation (xc) functional was successfully used in chemical applications since the seventies. This approach, e.g. in the VWN parameterization [33], has been demonstrated to describe accurately such properties of adsorption complexes and other molecular species as bond lengths and vibrational parameters. Unfortunately, calculated LDA binding energies often were notably overestimated [27]. Soon it became obvious that density gradient corrections to an LDA xc functional considerably improve the calculated molecular energetics [34]. Several "nonlocal" xc functionals of the generalized gradient approximation (GGA) type were used in our calculations. The gradient-corrected expressions suggested by Becke [35] or, alternatively, by Perdew and Wang [36,37] were utilized to calculate density gradient corrections to the exchange energy functional. The correlation contribution was computed following Perdew et al. [36,38], Lee Yang, and Parr [39,40] or Perdew, Burke and Ernzerhof [41]. The GGA functionals used in the applications addressed below include Becke-Lee-Yang-Parr (BLYP) [35,39,40], Becke-Perdew (BP86) [35,38], Perdew-Wang (PW91) [36,37], Perdew-Burke-Ernzerhof as revised by Nørskov et al. (PBEN) [41,42] as well as the hybrid approach B3LYP [39,43,44].

Energies of weak bonds may be underestimated by standard DF approximations because very small dispersion contributions are not taken into account even if gradient-corrected xc functionals are employed [45-48]. On the other hand, it is well documented that GGA DF methods adequately describe structure and energetics of weakly (but not merely dispersively) bound systems and, in general, those where electrostatics dominates [49,50]. DF binding energies of such systems are usually at least as accurate as results of Møller-Plesset perturbation theory to second order (MP2) and often comparable in precision to benchmark data calculated at highly correlated configuration interaction levels [49-52]. Thus, the choice of DF methods to describe even weakly bound adsorption complexes with primarily electrostatic interactions is justified [53].

Extended orbital Gaussian basis sets of triple-zeta quality or better were used in the LCGTO-FF-DF calculations discussed below. The two auxiliary bases sets employed in the LCGTO-FF-DF method to represent the electron charge density and, in some cases, the xc potential were constructed from the orbital exponents in a standard fashion [23]. For weakly bound molecular systems the "counterpoise" technique [54] was applied to correct interaction energies for the estimated basis set superposition error (BSSE). Vibrational frequencies were obtained either by diagonalizing the mass-weighted force constant matrix which had been computed from finite differences of total energy gradients or by using a polynomial fit to a point-by-point representation of a potential energy hypersurface. In the latter case, both harmonic and anharmonic

frequencies can be calculated by assuming negligible coupling of the vibrational modes under consideration. Absolute intensities of the infrared (IR) bands (integrated absorption coefficients) were calculated in the double-harmonic approach [55] where the IR intensity is proportional to the square of the dynamic dipole moment of the normal mode.

2.2. Embedded cluster models of oxide materials

Currently, two types of computational models are used for QM calculations of solid surfaces and surface complexes. The "supercell" method represents the surface in terms of a unit cell, periodically repeated in two or three dimensions, and then imposes translation symmetry constraints. In such a periodic approach, unit cells containing a rather small number of atoms usually suffice to describe perfect surfaces of single crystal solids. However, any distortion of the surface periodicity, by a defect or an adsorbate, requires significantly larger unit cells and thus results in a notably higher computational cost. Otherwise, such surface irregularities repeated periodically would be spuriously too close to each other, leading to exaggerated interactions between them. This periodic approach is very well suited for modeling physical properties of ordered materials.

The model cluster approach [56], as an alternative to the "supercell" scheme, focuses on a particular part on the surface under consideration. This method can be applied even when periodicity is absent. The modeled surface site (or a group of them) in the cluster method is represented by a finite number of atoms or ions of the material. Such a cluster may (or may not) be embedded in an environment medium mimicking the rest of the extended system. The environment is commonly treated at a less sophisticated level than the most interesting central part of the model. By construction, results of cluster model calculations depend on the size and shape of the most rigorously described "active" part of the model as well as on the accuracy of how adequately the environment is represented. Cluster models offer several advantages, provided they are validated to furnish "converged" calculated observables with respect to the sufficiently large size and accurately imposed boundary conditions. Namely, cluster models are perfectly suited for describing the most general situation without translation symmetry, e.g., adsorption complexes or surface defects at infinitely low concentration without any mutual interaction between the species. Furthermore, cluster models treat complexes on solid surfaces in terms of localized states, using the conventional chemical language of molecular orbitals (MO), exactly as if one merely considers a chemical compound formed by two moieties. Thus, the vast arsenal of quantum chemical codes, schemes and tools is readily applicable. This is particularly useful when dealing with surface reactivity.

2.2.1. Cluster embedding for ionic systems in a rigid environment

Systems with strongly ionic bonding, like alkali halides and alkaline-earth oxides, are among those favorably simulated with cluster models. Here, an adequate description of the long-range contributions to the electrostatic potential (Madelung field) is important. To account for such effects of the crystal surrounding, it is customary to embed a model cluster in an array of point charges (PCs). To first approximation, the values of the PCs may be formal charges of ions of a purely ionic bonding model or they can be reduced to account for covalent bonding contributions [57,58]. In the latter case, stoichiometric clusters have to be used to arrive at the proper ordering and occupation of the one-electron levels. Together with others, we began using explicit PC embedding for models of MgO in the early nineties [57,59]. In particular, embedding increases the energy gap between occupied and vacant levels. A drawback of such simple PC embedding is that PCs can artificially distort the electron density of ions at the cluster edges. Clearly, boundary anions with their diffuse electron shells will be distorted much stronger by neighboring positive PCs than the compact and less polarizable cations by negative PCs. Calculated properties of the "chemically interesting" central region of the cluster depend on such boundary artifacts and these spurious anion-PC effects on calculated observables have to be rectified. For instance, in a DF study [60], it was possible to trace a strong dependence of the electrostatic potential above the MgO(001) surface back to the artificial polarization of anions at the cluster borders [61]. To obtain results converged with increasing cluster size with this simple embedding strategy, one may have to employ extended (and rather expensive) cluster models with boundaries far from the chemically active region.

Artifacts due to immediate contacts of frontier cluster anions with positive PCs of the surrounding can be reduced if one substitutes these PCs with bare model potential cations (pseudopotential, PP), taken without basis functions. This helps to restore the repulsion between electron shells of anions of the cluster and cations of the environment, an interaction that is missing in a cluster embedding based in merely a PC array. Less efficient from the computational viewpoint is the "brute force" alternative where positive PCs at the cluster borders are replaced by all-electron (AE) cations; in the latter case, one is forced to use formal (nominal) charges of the environmental ions and, as a rule, the QM cluster model is non-stoichiometric.

Early applications of pseudopotentials in cluster models [62,63], which dealt with impurities in alkali halide crystals, used Hartree-Fock (HF) based model potentials [64] and complete-cation norm-conserving pseudopotentials [65]. A similar technique was found valuable to describe bulk properties of alkaline-earth oxides [66-68]. A general procedure for calculating embedded clusters under the assumption of a "frozen" environment and orthogonality requirements for the wave function of the cluster and the environment was also discussed

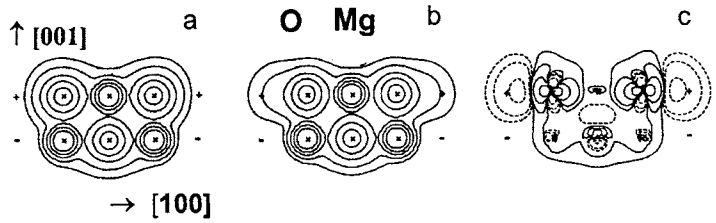

Fig. 2.1. Electron density contour maps for the model Mg_9O_9 of the MgO(001) surface in the plane containing the fourfold symmetry axis and the moiety O–Mg–O: a) Mgpp*+PC embedding; b) PC only embedding; c) electron density difference $\Delta\rho = \rho(Mg_9O_9, Mg^{pp*}+PC) - \rho(Mg_9O_9,PC)$ with negative values indicated by dashed lines.

[69,70]. Ab initio cluster model schemes for alkaline-earth oxides, based on model potentials and repairing the deficiency of spurious interactions between ions at the cluster boundary and nearby PCs, have been used since the middle of the nineties [60,71,72]. PC only as well as bare pseudopotential embedding DF schemes were used to compute such properties as the electron density distribution, core level splittings, the electron affinity (EA), and the electrostatic potential of cluster models of an MgO(001) substrate [60]. Fig. 2.1 compares the charge density of Mg^{pp*}+PC (Mg^{pp*} refers to bare Mg^{2+} core PP) and PC only embedded Mg_9O_9 cluster models of MgO(001) surface, along with the corresponding electron density difference.

All oxygen anions in the Mg^{pp*}+PC embedded model (Fig. 2.1a) exhibit a regular spherical shape, whereas in the PC embedded model (Fig. 2.1b) the anions at the cluster border are notably distorted as the electron density extends toward neighboring positive PCs. The electron density difference (Fig. 2.1c) exhibits nonzero values around the nearest-neighbor positive charges in the PC embedded model. In other words, electron density is spuriously transferred from the nearby anion because the attraction of the bare positive charge is not balanced by a repulsion from core electrons of those Mg^{2+} cations.

Charge density artifacts affect calculated observables. For instance, in the PC embedded models, the occupied one-electron levels lie 4 eV lower than those in models with Mg^{pp*}+PC embedding because the attractive potential due to the surrounding positive PCs is overestimated. Ideally, ions of one sort belonging to the same layer of a regular MgO(001) surface should have identical core level energies. The large splitting of O1s and Mg1s core level manifolds in PC embedded models, e.g., 0.8 and 2.2 eV in Mg_9O_9, manifests differences in the description of atoms of the same kind, located at different cluster positions. Mg^{pp*}+PC embedding reduces this level splitting to less than 0.1 eV.

A comment is due concerning the electrostatic potential above the (001) plane of MgO cluster models. This is a region where adsorbates can be located. Many of them form rather weak bonds with the oxide surface, governed mainly by electrostatics. For Mg^{pp*}+PC embedded cluster models, the electrostatic

potential above the central Mg^{2+} cations in the adsorbate region is notably weaker than in models with simple PC embedding [60]. Hence, the adsorbate-substrate interactions on MgO(001) should be calculated weaker; this effect has to be account for when one analyzes results for adsorption complexes treated with the PC embedding approach. Finally, we note that observables calculated according to the Mg^{pp*}+PC embedding procedure closely agree with results obtained in the scheme which employs all-electron Mg^{2+} ions for embedding instead of bare pseudopotential ions Mg^{pp*}.

2.2.2. Cluster embedding for ionic systems in an elastic polarizable environment

PP*+PC embedded cluster models just discussed may become insufficient for an adequate description of surface sites in cases of strong long-range relaxation that usually accompanies the formation of polar surfaces or charged defects. To this end, an advanced logically complete embedding scheme is required that allows a variational treatment of the entire system under consideration, cluster plus its environment. Such a scheme, where a cluster treated at a QM level is embedded in a molecular-mechanical (MM) elastic polarizable environment (EPE) of ionic metal oxides, has been developed and implemented [73,74] in the code PARAGAUSS. A similar approach was also utilized recently elsewhere [75,76]. This description of the environment incorporates features of the shell model [77], widely used in studies of solids. Applications of the EPE embedding scheme will be described in Sections 3 and 5.

The basic features of the EPE cluster embedding approach are as follows: (i) the structure of a regular (unperturbed) surface is defined by a classical atomic simulation of a periodic slab model of the surface; (ii) an unperturbed surface site is described by a QM cluster, embedded in such a slab represented as an elastic polarizable environment; (iii) the surface site under investigation (e.g. an adsorption complex or a defect center) is treated as a defect of the regular periodic structure; (iv) both long-range Coulomb coupling and short-range interactions of the QM and classical regions are explicitly taken into account and the structure of the whole system is determined variationally by minimizing the total energy. The EPE embedding avoids pitfalls of the cluster approach that can arise from somewhat arbitrary constraints of the adsorption induced relaxation.

A system under study in the EPE embedding scheme is partitioned into the active area, Region I, and its environment, Region II (Fig. 2.2). Region II is described classically: the mechanic and electric relaxation of the environment is taken into account by a shell-model description combined with the Mott-Littleton approach [77,78]; Region I comprises the QM cluster model including, if present, an adsorbate and PP centers representing atoms at boundary region. In the EPE method, the total energy, E_{tot}, of the system is a sum of three contributions describing the interaction in the QM cluster, E_{cl}, the coupling of the QM cluster and the environment, E_{int}, and the interactions within the lattice, E_{lat}.

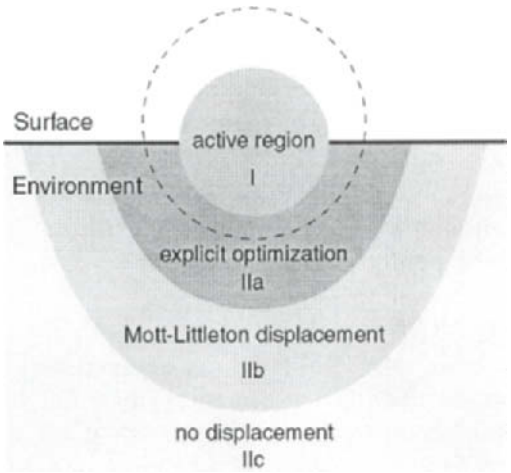

Fig. 2.2. Space partitioning in EPE embedded cluster calculations. I – internal region treated at a QM level; II – shell model environment of the QM cluster subdivided into regions of explicit optimization (IIa), of the effective (Mott-Littleton) polarization (IIb) and of the external area (IIc). The sphere indicates an auxiliary surface charge distribution which represents the Madelung field acting on the QM cluster (dashed line).

The effect of the surrounding on the QM cluster is represented by its Madelung field and by the short-range forces of the MM model at the cluster boundary. Parameters of the short-range interactions with terminal bare PP centers and across the boundary are adjusted to yield an optimal (with a given ansatz) representation of structural and bonding characteristics in the frontier region of the cluster model of the clean regular surface. Furthermore, in the EPE scheme, a special QM/MM interface is constructed such that the forces are balanced relative to the situation at a regular site [73,74]. By this construction, the environment is assured to retain its MM equilibrium structure if a cluster representing a regular site is embedded. In general, both the cluster and its environment undergo a relaxation due to changes caused, for instance, by an adsorbate.

Two preparatory computational Steps 1 and 2 need to be performed once, before an active region, modified by the presence of an adsorbate, a defect or both, can finally be described in Step 3, the QM/EPE calculations. In Step 1, a straightforward MM treatment of the regular (unperturbed) surface is performed. The structure of the surface is calculated by minimizing the total energy of an arrangement of repeated slabs using the shell-model scheme. Step 2 provides the QM reference of the unperturbed cluster (Region I; geometry optimized without an adsorbate or defect) embedded in the regular environment of the frozen lattice configuration.

The consistent embedding of the QM/EPE approach enables one to build multifunctional models of isolated sites by means of unconstrained geometry optimization, where the polarization of the cluster surrounding is completely

accounted for. With this strategy, also complex systems, e.g. those formed by reconstruction of polar surfaces [79], can be studied using a cluster model approach. As one target of the EPE approach, the equilibrium geometry of a cluster simulating a regular crystal has to be close enough to the geometry of the corresponding fragment of an infinite lattice, e.g. as described by a QM calculation of the unperturbed system. Therefore, it is a prerequisite for the success of the EPE procedure that the structure of the unperturbed substrate as determined by the MM treatment (i.e. the regular structure; Step 1) is close to the reference, furnished by either experiment or high-level calculations.

2.2.3. Extension of EPE cluster embedding for polar covalent oxide systems

Embedding schemes for polar covalent oxides with directional bonds have to face substantial complications that arise due to the necessity that the QM cluster is cut from a covalent framework of the material under study. Consequently, artificial unsaturated bonds appear for atoms at the boundary of the QM cluster. Therefore, special capping atoms terminating these dangling bonds are introduced in the interface region. For such terminations, H atoms are often used and referred to as "link atoms", with special restrictions for the length and orientation of the saturating bond [80-82]. Because these link atoms are absent in the real system, their energy contributions have to be eliminated [80,81], e.g., by a subtraction scheme as suggested by Morokuma and co-workers for organic compounds and complexes [83]. That approach correctly represents the steric constraints of the framework. Usually in such procedures, e.g. in the QM-potential scheme [80,81], the QM Hamiltonian does not depend on the charge distribution of the environment and thus effects of the environmental long-range Coulomb potential are accounted for only at the MM level. The approach of Sherwood et al. [82] attempts to overcome this deficiency similarly to method of Thiel and co-workers [84]. Both procedures account for mechanical as well as electrostatic coupling between the QM and MM systems, but they include the contribution of the link atoms in the energy of the system. The electrostatic potential of the MM region contributes to the electronic Hamiltonian of the cluster; also the polarization of the classical region due to variations of the charge density in the QM cluster is accounted for. However, the presence of link atoms in artificial positions of the structure of the framework (too close to some of the "real" atoms) requires a special rearrangement of the charges on those atoms of the MM part which are close to link atoms. As a result, the electrostatic potential near the border between QM and MM regions is strongly perturbed and likely influences both the QM cluster and the guest species in an undesirable fashion.

To improve this situation, the EPE embedding scheme [73,74] was extended for the case of oxides with directional polar covalent bonds [85]. Whereas in the EPE scheme for ionic systems, the QM cluster is terminated by atoms represen-

ted by effective core potentials without basis functions, the QM cluster in the covalent elastic polarizable environment (covEPE) is saturated by specially constructed monovalent "pseudoatoms". These capping atoms are constructed in analogy to the pseudobond embedding approach suggested for hydrocarbons [86]. To represent properly the electronic and geometry structure of the border region, pseudopotential parameters are optimized to reproduce the characterristics of an analogous fragment inside of a suitable cluster treated with the selected QM method. In the covEPE scheme [85] for different frameworks constituted by SiO_2, bond capping border centers are located (Fig. 2.3) at anionic (oxygen) positions of the silicate framework.

An important function of the border atoms is to maintain charge balance; therefore, one has to assign to them an incremental point charge, Δq_{pp}, which is half of the charge of O atoms inside the MM region where these centers participate in two Si-O bonds. Unlike in link atom schemes [80-82], the covEPE QM cluster is in general charged. The covEPE approach aims at an adequate reproduction of the mutual polarization of the QM cluster and environment. Therefore, without perturbation, charges of ions in the environment and inside the cluster should be internally consistent. The covEPE approach [85] offers such a consistent treatment based on PCs values of the environmental centers chosen to reproduce, at a distance, the electrostatic potential of the corresponding fragment of the crystal when described quantum chemically. For this purpose, we generated a special shell-model type force field employing these potential derived charges (1.2 e for Si atoms and -0.6 e for O atoms) [85].

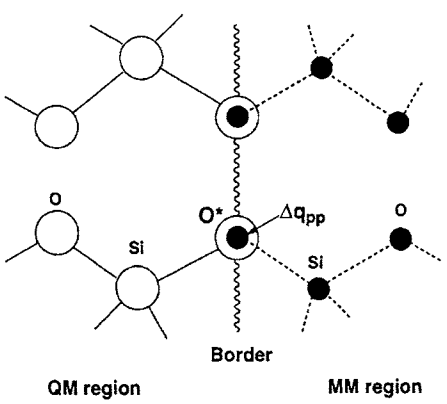

Fig. 2.3. Construction of the border region between a QM cluster and its MM environment. The atoms participating in the QM part are shown as open circles, and the centers of the MM part are depicted as filled circles. Solid and dashed lines denote bonding between atoms in the QM cluster and the MM part, respectively.

3. PROBE MOLECULES ON SURFACES OF IONIC METAL OXIDES

Solid MgO is not only a textbook example of a typical ionic material with a very simple structure, of rock salt type, but it also represents an important class of metal oxides relevant for catalysis [87]. Composed of light atoms with only few electrons, MgO is a system computationally tractable at a rather high level. These and other reasons make MgO itself and adsorption complexes on it attractive touchstones for quantum chemical studies. Despite the seemingly simple nature of the bonds within MgO, that are often referred to as purely ionic, a number of questions concerning the bonding mechanism and electronic properties of the MgO substrate remained unsolved until a few years ago. For another important ionic substrate, Al_2O_3, the situation is much less clear until today, especially concerning γ-Al_2O_3 and other transition modifications. However, even the properties of corundum, α-Al_2O_3, the best studied common modification of alumina, continue to be debated, e.g. the structure of its most stable but strongly relaxed polar (0001) surface [88].

In this section we review our DF studies of adsorption complexes of such probes as CO and C_1-C_2 hydrocarbons on MgO(001) and α-Al_2O_3(0001) surfaces. We address the role of both regular sites and various defects. We begin with the structure and properties of the oxide surfaces without an adsorbate. The results outlined in the following complement the data presented in our previous review article [89].

3.1. Clean MgO(001) and α-Al_2O_3(0001) surfaces

3.1.1. Regular MgO(001) surface

One of the questions frequently asked when investigating adsorption at surfaces of ionic metal oxides concerns the quantification of the amount of charge separation between the anions and cations of the oxide substrate [89]. Very recently [90] we examined the charge distribution in our EPE embedded models of the regular MgO(001) [73] surface employing a new tool to analyze atomic charges based on the criterion of best reproduction of the external electrostatic field generated by the system under study. At the LDA VWN level, the potential-derived charges of Mg and O ions in the cluster models are around $\pm$(1.80–1.85) e, in agreement with Xα results for slabs, $\pm$1.80 e [91]. We found only a very slight increase of the Mg-O bond ionicity in the cluster models, by less than 1 %, when the GGA functionals BP86 or PBEN were used instead of LDA. These data demonstrate the strongly ionic character of the bonding in MgO; furthermore, they show only a minor difference between LDA and GGA electron densities.

One-electron properties also are key subjects for analysis. The band gap of 4.3 and 3.8 eV, as determined by the HOMO-LUMO splitting $\Delta\varepsilon$ of the models

$Mg_9O_9PP^*$+PC and $Mg_{25}O_{25}PP^*$+PC, respectively [60], agrees reasonably well with the result (3.0 eV at the Γ point) of Xα calculations on a two-layer MgO slab [91]. However, due to the well-known overestimation of the electron self-interaction [92], LDA results for the gap are smaller than the measured value of 6.0-6.2 eV at the surface MgO(001) [93]. The energy of the LUMO in the two cluster models (-1.2 and -1.5 eV, respectively) is also close to the corresponding value of the slab model, -1.5 eV [91]. The energy of the LUMO, related to the electron affinity, EA = *E*(neutral) – *E*(anion), is only slightly positive, 0.2 eV, for the largest model $Mg_{25}O_{25}PP^*$+PC of MgO(001). Therefore, this idealized regular (001) surface is expected to exhibit essentially no oxidative power, which is corroborated in Sections 3.2 and 3.3 by very weak interactions in adsorption complexes.

Structural relaxation of the regular MgO(001) surface with respect to the positions of ions in the MgO bulk is generally considered to be very small [87]. Therefore, in PP*+PC embedded cluster models, the clean MgO(001) surface can be treated, in a good approximation, at the bulk-terminated geometry with the nearest-neighbor distance *r*(Mg-O) = 210 pm. The more sophisticated EPE embedding technique enabled a straightforward inspection of the validity of this bulk-terminated approach and, not unexpectedly, it confirmed the assumption [73]. For instance, the optimized BP86 distance *r*(Mg-O) is 213 pm and the rumpling (buckling) of the MgO(001) surface in the EPE embedded model is 5 pm, to be compared with recent result of GIXS experiments, 2±1 pm [94].

3.1.2. Vacancies on MgO(001)

Notably stronger structural relaxation should accompany the formation of sites on the MgO(001) surface that are characterized by a reduced coordination number of ions, such as point (vacancy) or extended (step, edge, corner, etc.) defects [87]. This new situation is adequately reproduced by DF cluster models. For instance, for the edge formed by the intersection of (001) and (100) surfaces of MgO, a notable inward (into the substrate) displacement of Mg and O ions from the bulk-terminated position was computed in the [101] direction, by 15 and 12 pm, respectively [95]. Corner three-coordinated Mg_{3c} cations are predicted to move even further, 32 pm, along the [111] direction, "down" to the three O anion neighbors [60]. Opposite displacements of the Mg and O ions, to partly restore the bulk-terminated geometry, take place when an adsorbate effectively repairs the reduction of coordination numbers at these defects on clean MgO surface, e.g. Refs. 60 and 95.

We studied the relaxation and the electronic properties of the MgO(001) surface with oxygen vacancy sites, F_s, F_s^+ and F_s^{2+}, using Mg^{pp^*}+PC [96] and EPE [73] embedded models. These two approaches furnish similar, although quantitatively somewhat different results. Briefly [73], in terms of displacements of the atoms closest to the vacancy, the relaxation is moderate for F_s and F_s^+

centers ($\Delta r_i \leq 10$ pm), but becomes stronger for F_s^{2+} centers (which are probably formed very rarely, if at all), $\Delta r_i \sim 10 - 20$ pm. The relaxation energies ΔE_r of the vacancy models, calculated as differences between total energies of the equilibrium structure of the regular site and the relaxed structure, are 11, 189 and 704 kJ/mol for F_s, F_s^+ and F_s^{2+}, respectively. Importantly, the relaxation significantly decreases the EA value: from 4.41 to 2.56 eV and from 9.86 to 4.52 eV for F_s^+ and F_s^{2+} centers, respectively. The EA value of unrelaxed F_s^{2+} would suffice to oxidize even such a noble metal atom as Pd [73]; however, the EA value of a relaxed F_s^{2+} center renders oxidation very unlikely. When relaxation is accounted for, *only* F_s^{2+} centers are expected to show a notable propensity for attracting electron density from adsorbates on the MgO(001) surface [73].

3.1.3. Regular α-Al_2O_3(0001) surface

α-alumina exhibits a crystal structure with a hexagonal unit cell containing 12 Al and 18 O atoms [97]. Ions are grouped along the *c* axis in an alternating stacking of two Al^{3+} and one O^{2-} planes. The cations occupy two-third of the octahedral sites of the hexagonal close-packed O sub-lattice and are situated slightly closer to one of the two oxygen planes. This structure features three Al1-O1 distances at 186 pm and three Al2-O1 distances at 197 pm. Geometric relaxation is crucial for the formation of the most stable (0001) surface of α-Al_2O_3 (Fig. 3.1). Both experiment [5,98] and calculations [99] show a strong distance reduction, by 50–90%, between the first (upper) and the second surface layers with respect to the interplane spacing of the bulk. Two major changes of the truncated-bulk surface are observed in the relaxed structure [5]: the distance between the first, O1, and the second, O2, oxygen layers is increased and oxygen triangles alter their size in a non-uniform fashion.

For our DF calculations of adsorption complexes on an α-Al_2O_3(0001) surface, discussed below, it is important to inspect how accurately the structure of the clean surface is described in the EPE embedding scheme. We demonstrated [74] that the force field [100], employed to model the environment of QM clusters, is able to reproduce fairly well the structure of both α-Al_2O_3 bulk and the strongly relaxed (0001) surface. This agreement between the results

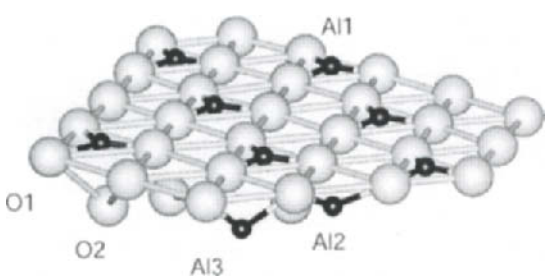

Fig. 3.1. Sketch of the α-Al_2O_3(0001) surface terminated by Al1 cations.

of the classical simulations and experiment [5] implies that the driving force for relaxation and reconstruction of the ionic system α-Al_2O_3(0001) is electrostatics.

Bond distances and angles of the equilibrium geometry of the QM cluster embedded in the above mentioned MM environment is somewhat different from those parameters of equilibrium MM model of the surface [74], similar to differences in α-Al_2O_3(0001) slab model results calculated at the DF and MM levels. In the embedded cluster calculations the distances Al1-O1, ~170 pm, are longer than the MM value of 163 pm, but still shorter than the (experimental) GIXS value of 177 pm [5]. The DF distances O1-Al2, ~178 pm, are only slightly longer than the MM and GIXS values, 174 pm. The contraction of the interplane distance Δz(O1-Al1), usually taken as a measure of relaxation for the α-Al_2O_3(0001) surface, is calculated at 20 pm, shorter than the MM and GIXS values, 29 and 41 pm, respectively. Δz(O1-Al1) slightly increases, $\leq$5 pm, with growing size of the QM cluster. A Δz value of 14 pm obtained in a periodic GGA DF calculation on an 18-layer slab model [99], agrees with our EPE embedded cluster result [74], indicating that the GIXS value may be overestimated [5]. Time-of-flight scattering and recoiling spectrometry as well as classical ion trajectory simulations yield Δz values of 30±10 pm [98]. The other inter-plane distances calculated with the EPE approach, Δz(Al2-O1) = 73 pm and Δz(Al3-O1) = 113 pm, are in closer agreement with the corresponding MM distances of 69 pm and 104 pm whereas the values obtained in DF band structure calculations are 83 and 110 pm, respectively [99]. Thus, the computational approaches discussed for the relaxed structure of the surface α-Al_2O_3(0001) exhibit acceptable agreement, among each other and with available experimental data [98,99].

3.2. Bonding and vibrations of adsorbed CO molecules

3.2.1. CO/MgO

CO molecules adsorbed on MgO are representative systems of surface complexes on metal oxides. Notwithstanding their seeming simplicity, strong efforts of experimentalists and theoreticians in the best research groups around the world for about two decades were required to elucidate the picture of CO bonding on single crystal and polycrystalline MgO samples. This long and intriguing story of the CO bonding on MgO, that resulted in several dozens of papers, was thoroughly reconstructed by one of us in a recent review [101]. DF model cluster studies [57,60,102-105] also contributed to create an adequate picture of bonding and vibrations of CO on MgO, that only very recently unified viewpoints based on first-principles calculations and precise surface science experiments.

In the following, we focus on the impact of the gradually improved accuracy of xc functionals and embedded cluster models on the DF observables calculated for single CO molecules on the regular MgO(001) surface. As just mentioned,

various aspects of the adsorption system CO/MgO were under debate until very recently, among them energy and nature of the MgO-CO interaction as well as the size and the mechanism of the adsorption-induced alterations of vibrational parameters of a CO probe. Earlier DF data on CO/MgO(001) complexes were calculated at the LDA level for cluster models embedded in an array of PCs [57,102,103]. They should be compared with more recent GGA BLYP and BP86 results [60,104].

The first issue to address is how the computed MgO(001)-CO binding energy depends on the size of the substrate cluster model [60,104]. This problem is of particular importance for judging the reliability of model cluster results. Compared to other observables, like structural and vibrational data, the model cluster adsorption energy is known to be significantly more sensitive to cluster size and shape [106]. Earlier LDA values of the CO adsorption energy D_e for extended stoichiometric cluster models of MgO(001) with PC embedding, 36 kJ/mol [102], furnished an upper estimate, in line with the overestimation of the binding typical for LDA [45,53]. At the GGA BLYP level, the CO adsorption energy varies still noticeably for two-layer clusters, ranging from Mg_5O_5 to $Mg_{25}O_{25}$, from 19 to 9 kJ/mol; the corresponding BP86 values are ~50% larger [104]. This energy lowering should be ascribed to the artificial influence of nearest-neighbor PCs on the boundary atoms of the clusters. The number of such distorting interactions increases with the cluster size and, despite the cluster boundaries are displaced farther from the adsorption site, the latter effect is incapable to completely balance the former one. Obviously, any unphysical exposure to neighboring PCs is more dramatic for the highly polarizable O anions affected by positive charges than for the "hard" Mg cations in the presence of negative PCs. This deficiency can be amended by means of a more accurate embedding with the nearest positive PCs substituted by either AE Mg^{2+} cations or pseudopotentials Mg^{pp*}, AE Mg^{2+}+PC and Mg^{pp*}+PC embedding schemes, respectively (see Subsection 2.2.1). For cluster models of MgO(001) designed in such a way [60], the calculated CO adsorption energy showed essentially no dependence on the cluster size and it was extremely weak at the BLYP level. Another GGA xc functional, BP86, yielded binding energy values of 5–7 kJ/mol for representative cluster models [60]. This notable weakening of the interaction of CO with a MgO substrate occurs for two reasons. First, the electrostatic potential above MgO(001) where the CO molecules are located, becomes very small in AE Mg^{2+}+PC and Mg^{pp*}+PC embedding schemes. Therefore, the polarization attraction of the CO molecule to the surface is reduced compared to that in PC-only embedded models. Second, in AE Mg^{2+}+PC and Mg^{pp*}+PC models, the substrate anions are more extended in the direction of the adsorbate. This leads to a stronger repulsion between the CO molecule and the closed shells of the O^{2-} anions. In the end, electrostatic attraction and Pauli repulsion cancel each other, resulting in an almost vanishing adsorption energy.

Structural defects of various kinds are usually thought to determine the surface reactivity of MgO [87], at variance with the relatively inert regular sites of MgO(001) surface considered so far. Among such irregularities, low-coordinated cationic sites on edges (Mg_{4c}) and corners (Mg_{3c}) of the (001) terraces of crystalline MgO are most relevant for CO adsorption. The Mg^{pp*}+PC embedding technique was applied to model Mg_{3c}-CO species using GGA xc functionals [60]. On the unrelaxed site (the substrate structure kept "frozen" at bulk termination), the BLYP energy of CO adsorption is 45–46 kJ/mol, very close to that computed with the MCPF method [72], despite that the C-O frequency shift of 26 – 27 cm^{-1} at BLYP level is significantly smaller than the MCPF value of 56 cm^{-1} [72]. The relaxation of the top magnesium atom was also considered [60]: the cation moves down toward the O^{2-} anions by 32 pm in line with the HF result, 26 pm [107]. At a relaxed corner site, the energy of CO adsorption with both BLYP and BP86 xc functionals is calculated at 36 kJ/mol, about 10 kJ/mol smaller than at the unrelaxed site [60].

DF results for the relaxed Mg_{3c} site are very similar to experimental data for CO adsorption on MgO films grown over a Mo(100) surface [108]. In the latter work, an IR absorption peak, blue-shifted by 35 cm^{-1} with respect to gas-phase CO, was observed at 90 K. The adsorption energy was determined from isothermal adsorption and temperature-programmed desorption to 41 and 44 kJ/mol, respectively [108]. It was argued [108] that the supported MgO film exhibits a low concentration of surface defects, but no direct information followed from experiment which type of sites are being probed by CO adsorbates. DF data [60] support the proposition [72] that only CO bonding at low-coordinated defect sites of MgO(001), but not at regular Mg_{5c} sites, yields an adsorption energy exceeding 40 kJ/mol as measured by Goodman et al. [108].

In summary, experimental and computational data on the adsorption energy of CO on regular sites of MgO(001) were in contradiction at the end of nineties [101,105]: the most recent experimental estimations were above 40 kJ/mol [108,109] whereas the most accurate quantum chemical investigations [105] (including DF studies, neglecting a dispersion energy contribution of ~7 kJ/mol [110]) furnished values lower than 10 kJ/mol. A plausible explanation of this disagreement was given by Pettersson et al. [70] and finally confirmed by a conclusive experiment [111,112]: the adsorption energy of CO on regular sites of the MgO(001) surface at low coverage is as small as 14 kJ/mol. This implies that the experimental adsorption energy around 40 kJ/mol [108,109] manifests bonding with surface defects [101,105].

3.2.2. CO/Al_2O_3

The acidity of dehydroxylated alumina is commonly ascribed to Lewis acid sites (LAS) of either strong or medium power. These two kinds of LAS can be identified using vibrational spectra of adsorption complexes with probe CO

molecules [113-116]. Based on the spinel structure of γ-Al_2O_3, strong LAS were assigned to three-coordinated cations, Al_{3c}^{3+}, that originate from Al ions located in the tetrahedral spinel positions. The LAS of medium strength were ascribed to five-coordinated Al ions, Al_{5c}^{3+}, derived from Al species at octahedral sites. Only few theoretical works using molecular cluster models [116-118] aimed at rationalizing the difference in acid strength of Al_{3c}^{3+} and Al_{5c}^{3+} LAS with the help of calculated vibrational parameters of an adsorbed CO probe. The molecular cluster models are, however, rather indirectly related to the specific structure of the oxide surface under consideration. For instance, these models do not distinguish between surface centers of the same coordination on different types of alumina.

To overcome this limitation, embedded cluster models of LAS were designed to take the long-range order of the oxides into account. For alumina this is a particularly complicated task because only α- and κ-modifications of Al_2O_3 exhibit an ordered structure whereas other known modifications feature a random distribution of the Al cations over partially occupied crystal positions. Accurate experimental structural information on the surface sites of transition aluminas, required for designing adequate models of such surfaces, is still lacking. Thus, as an important step in the direction of surface complexes on transition aluminas, our EPE embedding technique was applied to describe CO adsorption on the most thoroughly studied alumina surface, the polar α-Al_2O_3(0001) surface [74]. One of the goals of that study was to establish a relationship between calculated adsorption properties of low-coordinated cations on the (0001) surface with the experimentally characterized Lewis acidity of α-Al_2O_3.

The interaction of CO with LAS of the surface α-Al_2O_3(0001) is local. Therefore, size limitations of the QM cluster part should not be crucial as long as the perturbation of the adsorption site due to the cluster borders is small.

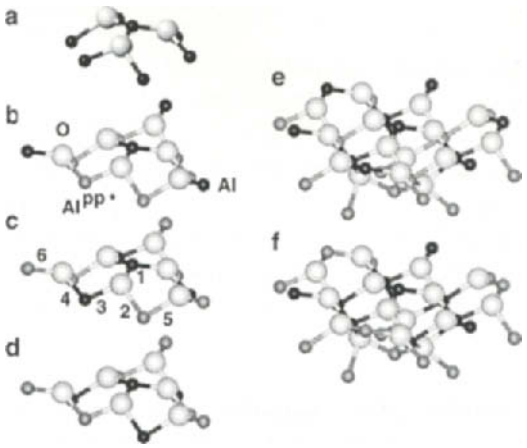

Fig.3.2. Cluster models a) $[Al_7O_3]^{15+}$, b – d $[Al_4O_6]Al_6^{pp*}$ and e, f – $[Al_{10}O_{15}]Al_{13}^{pp*}$ for representing LAS on α-Al_2O_3(0001) surface.

Note, that the use of regular Al atoms with basis functions to represent Al^{3+} centers in the frontier region of (usually non-stoichiometric) clusters may result in a biased description when the bonding within the substrate comprises a covalent contribution. In such a case, the central region of the QM cluster would acquire an artificial electron-deficient character due to electron transfer to the frontier cations included in the cluster in excess of its stoichiometry. In calculations of the model $[Al_7O_3]^{15+}$ (Fig. 3.2) with such an embedding using only regular Al centers on the cluster border (an alternative to employing bare Al^{3+} ion pseudopotentials Al^{pp*} without basis functions), the blue shift of the CO vibrational frequency is as large as 42 cm^{-1} [74]. This frequency shift and the corresponding binding energy value of 47 kJ/mol are probably upper limits for these observables calculated for a series of clusters which differ in the representtation of their boundaries. However, for other clusters studied, the calculated vibrational and binding characteristics of CO adsorption complexes fall in a narrow interval of $\Delta\omega$(C-O) = 35±7 cm^{-1} and D_e = 39±3 kJ/mol [74]. This lends credibility to the quality of our EPE embedding procedure employed.

A moderate experimental blue frequency shift, ~20 cm^{-1}, was reported for CO interacting with LAS of α-alumina [114]. The IR band measured at 77 K and a CO pressure of 40 Torr was assigned to CO interacting with Al^{3+} ions via a weak σ bond. No significant shift of the frequency was observed with decreasing CO coverage. At variance with this finding, another experimental group observed a notable coverage dependence of the C-O vibrational frequency, connected to CO adsorption at extended terraces; these alternative measurements on CO adsorbed on powder α-A_2O_3 crystallites yielded a shift $\Delta\omega$(C-O) = 39 cm^{-1} in the low pressure limit [115]. The CO frequency shift is a very sensitive indicator of delicate adsorbate-substrate interactions. Hence, it is satisfying that calculations on the most realistic cluster models $[Al_{10}O_{15}]/Al_{13}^{pp*}$ (Fig. 3.2) yielded frequency shifts of 38–42 cm^{-1}, in excellent agreement with experiment [115].

3.3. Adsorbed hydrocarbon molecules

3.3.1. CH_4/MgO

Adsorption complexes of methane at MgO are interesting because they relate to the conversion of methane to ethylene and methanol. In particular, oxidative coupling of methane on metal-oxide catalysts attracted great attention [119]. Usage of methane as a probe to identify and characterize adsorption sites of different acid strength on oxide catalysts is another important aspect. Because CH_4 is not easily captured by surfaces of metal oxides, the nature of the interaction of methane with surface sites was little understood until recently. A FTIR spectroscopy investigation of methane on MgO at 173 K revealed adsorbed molecular species preferentially bound at Lewis basic sites; CH_4 adsorption on a Lewis acid-base pair has also been proposed [120].

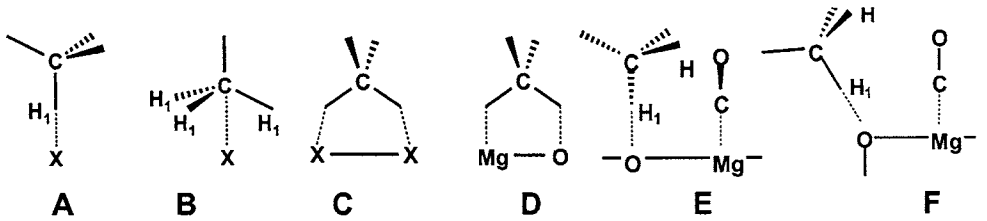

Fig. 3.3. Conceivable configurations for CH_4 adsorption (A – D) and co-adsorption with CO (E, F) on an MgO surface (X = Mg or O). E displays planar and edge sites, F represents corner sites.

To gain more information about adsorption sites on MgO surfaces and on the configuration of methane molecularly adsorbed at low temperatures, the interaction of CH_4 with MgO was investigated by combining FTIR experiments and DF cluster model calculations [121]. The following open questions pertaining to CH_4 adsorption on an MgO surface were clarified: (i) which adsorption sites are favorable? (ii) which configurations of the adsorbed molecules are energetically preferred? (iii) what is the role of low-coordinated surface sites in methane adsorption? (iv) what are the IR spectroscopic features of adsorbed methane? (v) how can CO and CH_4 co-adsorption on MgO be rationalized?

Methane adsorption on a MgO surface and co-adsorption with CO were computationally investigated for different adsorbate configurations (Fig. 3.3), including interaction with both Mg^{2+} and O^{2-} surface sites. Because MgO usually exhibits a large amount of morphological defects (edges, steps, corners, kinks) with lower coordinated surface ions, various MgO sites were considered: regular planar (100) surface sites formed by five-coordinated ions; edge sites where the surface ions are four-coordinated and corner sites characterized by three-coordinated ions. The model clusters were embedded in large arrays of PCs (±2 e); positive PCs at the cluster borders were substituted by bare pseudopotential Mg^{2+} cations. The xc functional BP86 was employed.

According to these DF results, CH_4 is weakly bound on Mg^{2+} and O^{2-} corner sites with energies of 6-15 kJ mol^{-1}; the interaction is calculated to occur preferentially with Lewis acid sites Mg^{2+}. At cationic sites, CH_4 interacts in a threefold way whereas one-fold coordination is favored at anionic sites. Disproving previous assumptions [120], no binding of methane on a regular, planar MgO(100) surface was found. Spectroscopic and computed data revealed that the IR symmetric stretching mode of methane is activated by adsorption, accompanied by red shifts of both the symmetric and antisymmetric C-H stretching peaks. The measured half width of the C-H bands is large enough (10 –30 cm^{-1}) to account for the presence of different complexes of adsorbed methane which display a calculated splitting of at most 30 cm^{-1}.

The finding that methane does not adsorb on the (100) MgO planar surface was also corroborated by experimental results for CH_4 and CO co-adsorption [121]. The integral IR intensity of the antisymmetric C-H stretching vibration

was found to be reduced, showing that only about a third of the preadsorbed methane molecules are displaced by CO. Because CO is more strongly bound on LAS than methane, it would displace methane from these Mg^{2+} sites under thermodynamic equilibrium conditions. At variance with previously proposed models [120], CO co-adsorption also was found to affect methane molecules interacting with Lewis basic sites O^{2-} due to the strong repulsion calculated between the co-adsorbates when located at adjacent O^{2-} and Mg^{2+} centers on a planar surface. This repulsion was shown to be significantly reduced if methane is adsorbed on Lewis basic defect sites (low-coordinated O^{2-}). Thus, only methane molecules on these lower coordinated sites (corner and edge) should remain unaffected by CO co-adsorption. On the other hand, if CH_4 were bound to regular (100) MgO terraces, a much more pronounced reduction of the IR integral intensity of the antisymmetric C-H stretching mode would have been observed due to CO co-adsorption, because the (100) planar surface accounts for the majority of available adsorption sites. The picture emerging from the experimental and calculated results is consistent: CH_4 is adsorbed only at low-coordinated sites.

Apparently, CH_4 molecules cannot discriminate between Lewis basic and Lewis acid sites of MgO, at variance with adsorbed CO which is a well-established probe for acid centers. However, due to the exclusive adsorption affinity of methane for low-coordinated sites, these molecules can be employed to probe the relative amount of morphological defects of MgO samples obtained under different experimental conditions.

3.3.2. C_2H_2/MgO

The same computational approach as just discussed was applied to study structural, energetic and vibrational features of acetylene molecules adsorbed on terraces as well as edge and corner sites of the MgO(001) surface [95]. That investigation focused on low-coverage adsorption complexes formed on MgO polycrystalline materials with a relatively small surface area. This situation corresponds to the experimental conditions of IR measurements [122] of single adsorbed C_2H_2 molecules. Conceivable structures of adsorption complexes were discussed not only based on adsorption energies, very low in some cases, but also by comparing reliably calculated vibrational frequency shifts and IR intensity alterations with experimental data.

According to the calculated results, C_2H_2 can adsorb very weakly at the regular O^{2-} sites of a (001) surface, $D_e \sim 10$ kJ/mol. The bonding is somewhat stronger at edge sites, $D_e = 20$ kJ/mol, and notably stronger at corner O^{2-} and Mg^{2+} sites of MgO, $D_e = 40$–60 kJ/mol. Dissociation was found to occur only in the case of a relaxed corner O^{2-} site. At low-coordinated sites, the interaction is more favorable due to a higher electrostatic field; adsorption induces only small changes in the geometry of C_2H_2. The calculations revealed that the symmetric

stretching C-H and C-C vibrations (modes ν_1 and ν_2) are IR activated and all bands ν_1, ν_2, and ν_3 are red shifted, in agreement with experiment [122].

The detected C-H (ν_3) band shift of -137 cm^{-1} in C_2H_2/MgO most probably arises from upright adsorption at planar (001) terraces via H-bonds; the latter are manifested by the large width of the ν_1 mode. All other calculated adsorption schemes led to either too large or too small frequency red shifts. However, as the C-H band is asymmetric and quite broad and the C-C band is rather weak, the other bands with frequency red shifts up to about -400 cm^{-1} (estimated from the IR spectra [122]) may well be hidden. Thus, adsorption complexes at edge and corner sites should also be formed under appropriate experimental conditions. IR measurements for gradually increasing temperatures corroborated this suggestion.

As the calculated adsorption energy of acetylene on regular O^{2-} sites of (001) terraces is notably lower than that on edge and corner defects, adsorbates at terraces should desorb already at lower temperature. Therefore, IR bands related to C_2H_2 at edge and corner sites can be observed if the concentration of the latter sites in an MgO sample is sufficiently high.

Acetylene adsorbed on nano-sized MgO polycrystallites had been suggested to undergo dissociation [123]. At 323 K and with removal of the excess of physisorbed C_2H_2 at 298 K, the IR spectrum of C_2H_2 adsorbed on such MgO samples is rather different from the spectra reported in Ref. 122 where MgO samples of larger polycrystallites with more extended (001) terraces and thus with smaller specific surface area were employed. For nano-sized polycrystalline samples, many sharp peaks in the range 1800–3400 cm^{-1} were observed and assigned to C-C and C-H vibrations [123]. Sufficiently large binding energies were calculated for complexes of molecularly adsorbed acetylene at edge and corner sites so that some stable adsorption complexes at defect sites are supposed to remain under evacuation at room temperature (unlike findings of Ref. 122). Therefore, some bands in the IR spectrum of Ref. 123 may be caused by molecularly adsorbed C_2H_2. For example, the strong peak at 2966 cm^{-1} likely corresponds to the mode ν_3 of upright adsorption complexes at edge sites, whereas the peak at 3301 cm^{-1} may well be due to the mode ν_3 of an adsorption complex where the triple bond of C_2H_2 interacts with corner Mg^{2+} sites. Both peaks probably became stronger owing to more abundant edge and corner sites in the nano-sized MgO samples used in Ref. 123.

According to our calculations, C_2H_2 adsorption on MgO is qualitatively different from methane adsorption [121]. CH_4 was shown not to bind at sites of the regular MgO(001) surface. Therefore, the adsorption-induced red shift of IR frequencies of CH_4 relative to the free molecule was assigned to adsorption complexes at low-coordinated edge and corner sites. However, adsorption of C_2H_2 at MgO(001) terraces is bound. In MgO samples of low surface area, adsorption sites on regular (001) terraces likely dominate the number of populated

edge and corner sites. Also, the IR bands of C_2H_2/MgO(001) are quite broad [122]. Therefore, the bands resulting from edge and corner adsorption (if present) probably cannot be resolved.

4. ADSORPTION COMPLEXES IN ZEOLITES

Complexes of guest species with active sites in zeolite pores are formed during various processes such as characterization of the material, catalytic transformation, selective sorption, and separation [124,125]. A guest molecule adsorbed in a zeolite can in general be involved in several types of interactions:

i) van der Waals interactions with the zeolite pore walls;
ii) Coulomb interactions with the Madelung field of the zeolite framework;
iii) interactions with the active centers of the zeolite;
iv) intermolecular interactions with other adsorbed species.

The model cluster studies reviewed here account for the third type of interactions which are assumed to be most important for the catalytic behavior of zeolite materials. Guest-guest interactions can also be estimated with such a cluster approach using suitable models. The recently developed covEPE method (see Section 2.2) enables an adequate evaluation of all four energy contributions and will be utilized in future studies of complexes in zeolites.

Generally, zeolites exhibit three types of active centers:

i) Bridging OH groups (next to Al atoms of the framework) that act as Brønsted acid centers. Such groups exist in protonic and mixed forms of zeolites.
ii) Extra-framework metal cations that compensate the negative charge of the framework around Al centers. Usually such charge compensation is accomplished by alkaline or alkaline-earth cations in the corresponding forms of the zeolites. Lately, also various transition metal cations have been introduced as charge-compensating cations, thus opening new opportunities for zeolite-based catalysis [125].
iii) Basic oxygen centers of the framework close to Al centers. Such centers exist both in protonic and alkali (or other cationic) forms of zeolites; their strength depends on the type of the charge-compensating cation.

In this section we will consider the factors influencing the properties of these three types of active sites and discuss some examples of complexes of extra-framework metal cations with small probe or reactant molecules.

4.1. Brønsted acid sites

The strength of the interaction of a guest molecules (probe, reactant, product, adsorbate) with a Brønsted acid site is mainly determined by the acidity of the OH group and its accessibility. The acidity of zeolite OH groups can be affected by various factors, most of them studied both experimentally and computationally [126,127]: (i) the aluminum content of the zeolite framework;

(ii) the type of three-valent T atoms connected to the bridging OH group (e.g. Al, Ga, Fe); (iii) the structure of the framework; (iv) the crystallographic position of the OH group; (v) the presence of other charge-compensating cations in the vicinity of the OH group.

We studied the influence of the aluminum content and the location of the OH group in zeolites with model six-rings containing one (Al-1), two (Al-2) or three (Al-3) aluminum atoms [128,129]. For the cluster Al-2, both possible relative positions of the two Al atoms in the rings allowed by the Loewenstein rule [130] were considered, *para* (Al-2p) and *meta* (Al-2m). The initial positions of the T and O atoms in the ring were taken from mean crystallographic values [131]; the structures of the cluster models were partially optimized keeping the atoms T fixed. As a measure of the Brønsted acidity of the bridging OH groups, we calculated their deprotonation energies (DE), namely the energy difference between the initial neutral cluster and the deprotonated cluster [126,128]. The lower the DE value of an OH group, the higher is its Brønsted acidity.

The calculated DE values of some model clusters are collected in Table 4.1. The DE value of the cluster H–Al–2p (Fig. 4.1a) has been taken as reference because it is the lowest among the proton compensated clusters. Not unexpectedly, the DE values of OH groups between two Al centers in *meta* position (in next-nearest neighbor framework positions), as found in the clusters H–Al–2m and H–Al–3, are about 65–80 kJ/mol larger than the DE of OH groups where the Al centers are farther from each other, as in the clusters H–Al–2p and H–Al–2m

Table 4.1

Pertinent properties of bridging OH groups in different zeolite clusters

Cluster	r(OH)[a]	ω(OH)[b]	DE[c]	ΔDE[d]
H-Al-1	98.3		1203	31
H-Al-2p[e]	98.4, 98.4	3651, 3648	1172	0
H-Al-3[f]	98.2, 98.2, 98.3		1244	72
Li-Al-2p	98.3	3659	1133	-39
Na-Al-2p	98.5	3651	1116	-56
K-Al-2p	98.6	3635	1130	-42
Na-Al-2m	98.5	3648	1122	-50
Na-Al-3[e]	98.5, 98.6		1173, 1177	-11, -7
Mg-Al-3	98.5	3645	1146	-26
Ca-Al-3	98.8	3600	1090	-82

a) O-H distance r (in pm). b) Vibrational frequency ω (in cm^{-1}). c) Deprotonation energy DE (in kJ/mol). d) Change of DE (in kJ/mol) with respect to the deprotonation energy of the cluster H-Al-2p. e) The model cluster contains two bridging OH groups in equivalent positions. f) The model cluster contains three bridging OH groups in equivalent positions.

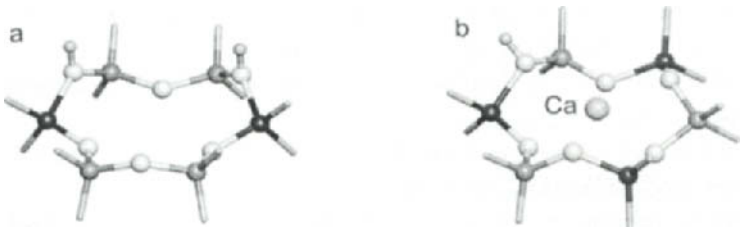

Fig. 4.1. Model clusters H-Al-2p (a) and Ca-Al-3 (b).

which are deprotonated at oxygen centers not between next-nearest neighbor Al atoms (Table 4.1) [128]. This trend in the DE values of the clusters compensated only by protons agrees with the conclusions of recent QM-Pot calculations [132]. The DE value of the cluster H–Al–2p is 31 kJ/mol lower than that of the cluster with one Al center, H–Al–1. This is due to a stabilization of the anionic form of the six-ring H–Al–2p, in which the remaining second proton moves toward the center of the ring and thus partly compensates the loss of the proton of the deprotonated hydroxyl group.

The effect of an additional metal cation on the Brønsted acidity of bridging OH groups in zeolites was studied for the three smaller alkali cations as well as Mg^{2+} and Ca^{2+}. The bond length r(O-H) changes only very slightly with the type of the cation located near the bridging OH group. In the model clusters, the O-H vibrational frequency decreases, as expected, with $r(O\text{-}H)^{-2}$, taken as a rough measure of the local electric field. Along the series K-Al-2p, Na-Al-2p, and Li-Al-2p, the calculated frequency increases by 24 cm^{-1} together with a reduction of the O-H distance by 0.3 pm. The presence of an alkali or alkali-earth cation leads to a decrease of the DE of the bridging OH group; thus, mixed clusters containing both protons and metal cations for charge compensation, are more acidic than purely protonic forms. The lowest DE value was calculated for the bridging OH group of the cluster Ca-Al-3 which contains three Al and three Si T-atoms in the six-ring [128] (Fig. 4.1b). It is 154 kJ/mol lower than the DE value of the corresponding protonic cluster H-Al-3; also, the difference ΔDE with respect to the most acidic cluster compensated only by protons, H-Al-2p, is -82 in kJ/mol. This suggests that zeolites containing Ca^{2+} and H^+ close to each other, e.g. HCaX, are the most acidic among the systems studied. In order of decreasing acidity, they are followed by the zeolites HNaY and HNaX, represented by the models Na-Al-2p and Na-Al-2m with ΔDE from -50 to -56 kJ/mol.

The DE depends both on the effect of the charge-compensating cation on the initial state of the OH group and on the stabilization of the final anionic form of the cluster. The trend that longer OH bonds and lower OH frequencies correspond to lower DE values is rather poor [128]. The DE values of bridging OH groups of the alkali-compensated clusters Al-2p clearly deviate from this trend, the DE goes through a minimum for Li, Na and K derivatives; the ΔDE values relative to the reference cluster H-Al-2p are -39, -56, and -42 kJ/mol, respec-

tively. Because the initial-state characteristics r(OH) and ω(OH) of the bridging OH group change synchronously with the ionic radii of the cation, the broken trend in ΔDE should be attributed to the stabilization of the deprotonated form of these clusters.

In fact, the lack of a good correlation between DE values on the one hand and bond lengths r(OH) as well as O-H vibrational frequencies ω(OH) on the other, suggests that these initial-state characteristics are not representative for the acidity of these hydroxyl groups in zeolites as evaluated by their DE values. Other theoretical studies of zeolite acidity reported similar trends. Studying various bridging OH groups of protonic forms of zeolites, Sierka et al. [132] noted that calculated O-H frequencies correlated with ^{1}H-NMR chemical shifts, but DE values did not correlate with either. Using chain-like isolated clusters models of a zeolite framework, Gonzales et al. [133] also excluded interactions with weakly basic probe molecules as measure of DE.

4.2 Complexes with charge-compensating metal cations

Computational modeling was successfully used to identify the locations of cations in zeolites and to clarify their interaction with zeolite hosts: Cu^+ and Cu^{2+} in ZSM-5 (MFI), ferrierite (FER), and faujasite (FAU) zeolites [134-136]; alkali and alkaline-earth cations in MFI [133]; Zn^{2+} in FAU and MFI [137,138]; also some divalent cations in MFI [139]. Yet, these investigations represent only first steps in the exploration of the large variety of both metal cations (especially of transition metals) and zeolite structures. Moreover, the interaction of cations in zeolites with probe molecules or reagents [137,140,141] is much less investigated computationally, despite the fact that these interactions are crucial for interpreting results of spectroscopic methods used to characterize the cations as well as for rationalizing specific catalytic, adsorption, sensor, or other properties of the materials.

4.2.1 Interaction of CO and N_2 with alkali metal cations

The influence of the local structure and the Al content of a zeolite on the coordination of alkali cations was investigated for alkali-exchanged faujasites (Y and X zeolites) [124,129]. The FAU framework is constructed from four- and six-rings. In both four- and six-rings, T-atoms lie in one plane whereas the oxygen atoms are above or below that plane, oriented toward the inside, O_{in}, or outside, O_{out}, the ring. These variations determine changes in the cation-oxygen distances and the properties of the framework O atoms [129]. The main feature of the FAU structure are the "supercages" with a diameter of ~1.3 nm connected by windows of a diameter of 0.74 nm. These cavities and windows are interesting for catalytic or adsorption processes because they are large enough to accommodate small to medium-size molecules. Crystallographic studies suggest five types of cationic sites in FAU. Sites SI, SI', SII and SII' are located at six-

rings while in the site SIII the cation is coordinated to four-rings. However, only site SII of the first group of cationic positions is accessible to guest molecules because it is located in the supercage whereas the other three sites are blocked by the zeolite framework. Site SIII is also in the supercage; however, it is occupied by cations only in zeolites with high Al content (and thus with a large number of alkali cations, as in X zeolites). In EMT zeolites, the local interaction of cations with four- and six-rings is similar to that in faujasites [142].

We modeled the interaction of a Na cation with FAU six-rings with one to three Al atoms as described for protonated clusters in Section 4.1. The negative charge due to second or third Al atom in the model ring was compensated by additional protons. The optimized structures show that Na^+ prefers positions near oxygen centers bonded to Al atoms rather than those of Si-O-Si bridges. Na^+ species interact stronger with oxygen centers O_{in} oriented toward the inside the zeolite ring. Also, the cation is far from oxygen centers which are connected to compensating cations, additional protons in our models [129].

The sodium cation in the cluster with one Al atom, Na-Al-1, is located almost in the plane of the ring, near the oxygen atoms of the Al-O-Si bridges. Note that these two O centers are oriented toward different sides of the six-ring. The geometry optimization of the clusters with two Al atoms was performed for rings whose negative charge excess is compensated by a proton. For the other six-rings, Na-Al-2m, Na-Al-2p, and Na-Al-3, two possible positions of the Na^+ ion were found, one at each side of the ring. The positions are denoted as *anti* or *syn*, referring to the centers O_{in} [129]. The *anti* cation position is located almost in the plane of the oxygen atoms O_{out} which are directed toward the outside of the ring. The *syn* position of Na^+ is on the same side as the centers O_{in}. The two Na^+ positions yield almost the same energy of the cluster models. The potential energy barrier for the transfer of a Na^+ cation between the two local minima, *anti* and *syn*, for cluster Na-Al-2p is only ~10 kJ/mol. Comparing calculated distances with crystallographic data as well as calculated vibrational frequencies of CO probe molecules with IR spectra of CO on NaY zeolite, we proposed that the crystallographic sites SII of FAU actually represent two cation positions. The mean Na-O distances for the *anti* position of Na^+ are closer to the crystallographic values; this implies that most of the cations at SII sites of zeolite samples are located in this way.

Li^+ cations at Al-2p rings are located near the plane of T-atoms of the six-ring, shifted somewhat toward the plane of the oxygen centers O_{in} [124,128]. The shortest Li-O distances are 190 pm (Table 4.2). Geometry optimization with different starting positions of Li^+ at the six-ring Al-2p lead to the optimized structure described above, i.e. *anti* and *syn* position was not observed for this cation. The specific location of Li^+ cation inside the zeolite ring allows only one probe molecule to approach it and the cation cannot be displaced enough in order to be accessible from a second probe, as in the cases of larger cations.

Table 4.2

Pertinent properties of the metal cations at model six-rings

Cluster	r(M-O)[a]	r<(M-O)>[b]	z(M)[c]	q(M)[d]
Na-Al-1	234	235	13	0.51
Li-Al-2p	190	249	15	0.49
Na-Al-2p	223	254	59	0.53
K-Al-2p	270	293	171	0.62
Na-Al-2m	220	232	80	0.54
Na-Al-3	225	252	33	0.51
Mg-Al-3	203	240	8	1.12
Ca-Al-3	229	245	30	1.62

a) Shortest M-O distances (in pm). b) Average M-O distance of the oxygen centers of the Al-O-Si bridges. c) Distance of the metal cations to the plane of the T-atoms (in pm). d) Mulliken charge of the cation (in e).

Such peculiarity of Li^+ at variance with other alkali cations was experimentally observed for CO and N_2 molecules [143,144].

Two local minima were found for K^+ at the six-ring Al-2p, similar to the *syn* and *anti* positions of Na^+, but compared to sodium farther away from the plane of T-atoms. At the *syn* position, i.e. at the side of the O_{in} oxygen atoms, the K^+ equilibrium is located 203 pm from the plane of the ring, and in *anti* position it is 171 pm from the plane. At variance with Na^+, both positions of K^+ were also observed at the six-ring Al-1 because K^+ is too large to move through the center of the ring as does Na^+. The shortest K-O distance of the *anti* position at the six-ring Al-2p is 270 pm [128,145] (Table 4.2).

Two alkaline-earth cations, Mg^{2+} and Ca^{2+}, were studied at the Al-3 ring. The alkaline-earth cations show trends like alkali cations with similar ionic radius; the location of Mg^{2+} is similar to Li^+ and that of Ca^{2+} similar to Na^+ [128]. Mg^{2+} is close to the plane of T-atoms of the six-ring Al-3, with 203 pm as the shortest Mg-O distance. The position of Ca^{2+} at the six-ring Al-3 is at 30 pm above the plane of T-atoms of the ring, with 229 pm as shortest Ca-O distance. Such a location of the cation allows simultaneous coordination of more than one probe molecule (CO or N_2). IR spectra suggest that even three CO molecules can be coordinated to a single Ca^{2+} cation [146], likely due to its stronger electrostatic field compared to Na^+.

The vibrational frequency of a CO molecule increases when adsorbed at an alkali cation [124,125,147,148]. Earlier computational studies of this interaction, performed on bare alkali cations, gave correct trends for the variation of the C-O frequency but the calculated frequency shifts were considerably overestimated [147]. In order to better describe experimental frequency shifts of CO adsorbed

Table 4.3

Calculated frequency shifts (in cm^{-1}) for CO adsorption on Na^+ cations at different six-rings and assignment of the experimental bands for CO adsorption on NaY zeolite at low temperature

Calculated shift[a]	Six-rings	Experimental shift[b]
37-38	Al-2m, Al-2p, and Al-3; *syn*-Na^+	40
32-33	Al-2m and Al-2p; *anti*-Na^+	29
28	Al-3 with *anti*-Na^+	23
24	Al-1	14

a) Ref. 129. b) Proposed assignment of measured vibrational frequency shifts from Ref. 152

on a series of alkali metal ions in zeolite cavities, we embedded the cations in a simple zeolite model, a negatively charged cluster with C_{3v} symmetry consisting of one Al atom, three OH or $OSiH_3$ groups, and one saturating H atom [148]. The alkali cations interact with the three O centers at distances depending on their ionic radii. Computational results agreed well with experimental frequency shifts of a CO adsorbate on a series of alkali cations; the calculated C-O frequency shift varies from 45 to 21 cm^{-1} from Li^+ to Cs^+, close to the experimental interval of 45 to 14-12 cm^{-1} for alkali exchanged mordenite (MOR) and MFI zeolites [149,150]. Following an earlier hypothesis [151], we also modeled CO bound via the O atom to an alkali cation at a zeolite cluster. The calculated negative shifts of the C-O frequency, from -17 cm^{-1} to -23 cm^{-1}, were similar to the experimental red-shift, ranging from -20 cm^{-1} to -24 cm^{-1}. As established in IR studies [149,150], the calculated adsorption energies of the two modes for the series of alkali cations show that the fraction of O-bound CO molecules increases with the cation radius.

In a further DF study, we aimed at elucidating the effect of the Al content of the ring on the Lewis acidity of the cation as measured by the vibrational frequency of adsorbed CO [129]. Assuming such dependence, Huber and Knözinger [152] had suggested CO adsorption as a tool to determine experimentally the distribution of zeolite six-rings with different Al content. Modeling a zeolite fragment by a sodium cation at a zeolite six-ring, we determined adsorption energies, D_e = 13-20 kJ/mol, in line with the experimental values, 21-24 kJ/mol [153,154]. The calculated C-O frequency shifts varied between 24 and 38 cm^{-1} whereas the observed values for the stretching vibrational shift of CO on NaY zeolites at low temperature are ~30 cm^{-1}. Deconvolution of the experimental spectrum at low CO pressure yielded four bands at 2183, 2172, 2166, and 2157 cm^{-1} with shifts of 40, 29, 23, and 14 cm^{-1}, respectively, relative to free CO. The strongest peak features a shift of 29 cm^{-1}. Because six-rings with two Al atoms are expected to dominate in Y zeolites [155], this band can be assigned to CO molecules adsorbed on sodium at the SII position of such a ring. The

experimental shift fits well the value calculated for the clusters Al-2p and Al-2m with Na^+ in *anti* position, 32-33 cm^{-1}. Table 4.3 provides a tentative assignment of the other bands of the experimental spectrum, assuming that the calculations represent the proper cause of this inhomogeneous line broadening.

The calculations help also in the interpretation of the IR peaks of CO on NaX zeolite [152]. In this spectrum, two main bands of almost equal intensity are observed at 2175 and 2165 cm^{-1} with shifts of 32 and 22 cm^{-1} [156]; the lines were assigned to sodium cations in SIII and in SII sites, respectively [129].

N_2 is an alternative to CO as IR probe; its convenient feature is the linear correlation of the frequency shifts $\Delta\omega$(N-N) and intensities I(N-N) of the N-N stretching mode on the series of alkali cations [157]. We studied the adsorption of one or two probe molecules, on both bare alkali cations and cations embedded in a zeolite fragment, and we confirmed the experimental observation [144] concerning the simultaneous adsorption of two N_2 molecules at one alkali cation. In all considered cases the linear configuration M-N-N of the adsorption complexes was found most favorable; no stable configuration was calculated for N_2 molecule adsorbed in side-on fashion on cations at the zeolite ring models. In linear complexes, the stretching mode ω(N-N) is blue-shifted by 10-25 cm^{-1} compared to the value calculated for a N_2 molecule in the gas phase. The blue-shift of the N-N stretching band for monomolecular adsorption is 21 and 15 cm^{-1} for the clusters Na-Al-2p and K-Al-2p, respectively [157]. The mean blue-shift of the two N-N bands for bimolecular adsorption at the cluster Na-Al-2p, 17 cm^{-1}, both for $^{14}N_2$ and $^{15}N_2$, is 4 cm^{-1} smaller than the shift for monomolecular adsorption, whereas for the cluster K-Al-2p the mean shift of bimolecular adsorption is essentially the same as for monomolecular adsorption. This is in line with experimental observations where the frequency of the N-N band decreases by 2.0-3.5 cm^{-1} upon adsorption of a second probe molecule to a Na^+ center in zeolites NaY, NaEMT, and NaETS [143,144,158], whereas the frequency for a bis-dinitrogen complex on K-containing zeolites is only by 0.5 cm^{-1} lower than for the corresponding monomolecular adsorption.

4.2.2. CH_4 adsorption on alkali and alkaline-earth metal cations

Methane has been proposed as an alternative probe for cationic forms of zeolites [159,160]. As with probes of metal oxides (Section 3.3), the low adsorption affinity of CH_4 and its similarity to other hydrocarbon molecules involved in catalytic reactions are considered particularly advantageous. We studied adsorption complexes of CH_4 with cationic sites of alkali (Li, Na, K, Rb, Cs) and alkaline-earth (Mg, Ca, Sr, Ba) forms of zeolites [161]. The goal was to rationalize structure and bonding of methane complexes with metal forms of high-silica zeolites as well as their measured vibrational features. We aimed also at clarifying the origin of opposite trends observed in the adsorption-induced alteration of the vibrational frequency and the IR intensity of the symmetric stretching mode

ν_1 of CH_4 for cation-exchanged zeolites with different metal loading: for ion-exchanged high-silica zeolites (MOR, MFI) the radii of alkali [159] and alkaline-earth [160] metal cations (related to their polarizing power) were found to correlate with vibrational parameters whereas in Na-Y and Cs-Y zeolites with higher metal loading the frequency shift and IR intensity of adsorbed CH_4 were found to be independent of the polarizing power of the metal cation [162].

Our calculations [161] suggested that, on both alkali- and alkaline-earth cations in zeolites, CH_4 is bound in a three-fold configuration M-H_3CH. Other conceivable structures, two-fold M-H_2CH_2 and one-fold M-HCH_3, are only slightly less stable transition states. The most important adsorption-induced effects are the activation of the ν_1 vibrational mode, IR forbidden in free CH_4, and a red-shift of ν_1 and other bands that decreases from Li^+ to Cs^+ and from Mg^{2+} to Ba^{2+}. These trends, consistent with experiments for CH_4 in metal-exchanged high-silica zeolites [159,160], were rationalized in terms of the electrostatic perturbation of the adsorbate as measured by the size and the charge changes of the cations. The trends remained unchanged for extended cluster models that included part of the zeolite framework. Thus, the observations that both the frequency red-shift and the IR intensity of the ν_1 band of adsorbed methane are larger in Cs-Y than in Na-Y zeolites [162] can hardly be explained by models where CH_4 interacts exclusively with cations; based on the stronger polarizing power of Na^+ cation compared to the Cs^+ congener, one expects changes of opposite direction. Therefore, we proposed a simple bifunctional model $H_2O/Cs^+/CH_4$ [161] where CH_4 can interact *simultaneously* with a cation and an O center representing a zeolite framework oxygen. This model yielded notably enhanced values for the frequency shift $\Delta\nu_1$ and the IR intensity compared to Cs^+/CH_4, improving the agreement with experiment [162]. Hence, the experimental findings for methane in M-Y zeolites can be rationalized by a bifunctional coordination of CH_4 to both a Lewis acidic site M^+ and a basic O site.

4.2.3. Interaction with methanol

CH_3OH molecules can interact both with acidic and basic sites of zeolite. With bridging OH group, methanol forms a hydrogen bond via the O atom. Similarly, the O atom of methanol forms a coordination bond with metal cationic centers. The interaction with a basic zeolite oxygen center occurs via a hydrogen bond of the methanol OH group. In addition, formation of guest-guest H-bonds is also possible at higher adsorbate concentration. This complexity of the interaction of CH_3OH within cation-exchanged zeolites complicates the interpretation of the IR spectra of adsorbed methanol [163,164]. The position and intensity of the IR band depend on (i) the type of the alkali cation, (ii) the Al content (which is connected to the basicity) of the zeolite, and (iii) the methanol loading. To clarify the adsorption modes of methanol on alkali zeolites, we studied its adsorption on three model clusters Na-Al-1, Na-Al-2m, and K-Al-1

[164]. Comparison of CH_3OH adsorption on the first two models allows one to evaluate the effect of the Al content and of the zeolite basicity on the adsorption mode. The third model was used to analyze the influence of the type of the alkali cation that also affects the basicity of the zeolite O atoms [145].

The first type of adsorption on the zeolite cluster models represents O-bound methanol forming only a coordination bond of its O atom to the alkali cation. The second adsorption mode comprises O,H-bound species forming in addition an H-bond of the methanol OH group to a zeolite O center. For O-bound and O,H-bound adsorbates, the coordination bond between the methanol O atom and the metal cation furnishes the main contribution to the adsorption interaction with Na- or K-exchanged zeolites. Species bound only by a coordination bond exhibit adsorption energies of 41–56 kJ/mol, whereas an H-bond contributes in addition 12–18 kJ/mol. The energy increases with the Lewis acidity of the cation for both types of adsorption. On the other hand, the strength of the hydrogen bond increases with the proton affinity (PA) [145] of the basic O center of the zeolite model. Following these observations, one would expect that methanol will adsorb at available Na^+ or K^+ cations in the zeolites and will form an H-bond with a nearby basic zeolite O atom [164]. The dominant role of the coordination bond to the cation influences also the chemical reactivity of adsorbed methanol species on Na-exchanged zeolites. This bond activates CH_3OH by weakening the C-O bond, but it stabilizes the C-H bonds. Thus, Na-exchanged zeolites act similar to weak acidic catalysts rather than basic ones. The decrease of the Lewis acidity of the cation and the simultaneous increase of the basicity of the zeolite O centers when going from Li- to Cs-exchanged zeolites alters the relative contribution of the coordination and the H-bonds to the adsorption energy. In this way, the catalytic activity of zeolites exchanged with alkali cations varies with the atomic number of the cation.

Although the formation of an H-bond between the methanol OH group and a zeolite O atom contributes only about a quarter to the adsorption energy, it notably affects the IR O-H stretching band of the adsorbate. The calculated red-shift of the methanol OH mode upon formation of an H-bond depends strongly on the PA value of the zeolite O center. Similarly, the measured frequency shifts for CH_3OH adsorbed on NaX, KX, and NaY zeolites also correlate with the calculated PA of the most basic O atom in the corresponding six-rings, this can be used to estimate the PA of zeolite oxygen centers [164]. The frequency shift $\Delta\delta$(OH) of the OH deformation vibration of bifunctionally adsorbed methanol also depends on the PA of the zeolite O centers to which the guest molecule is coordinated. This shift $\Delta\delta$(OH) was found to correlate with the red-shift of the corresponding O-H stretching frequency. Deviations from this correlation can be used as indication of additional interactions of the methanol methyl group.

Since PA values of zeolite O centers cannot be measured directly, we tried to clarify its connection with experimentally measurable quantities. To this end

we inspected a correlation of the calculated PA values of the basic centers with two experimental characteristics: (i) the O-H frequency shift in adsorbed methanol molecule [165] and (ii) the shifts of the O1s core level in zeolites with respect to a reference value, ΔE_b(O1s), measured by XPS [145]. In both cases we found good linear correlations between the calculated PA values and measurable quantities. To render these correlations directly applicable to experiment without the detour to calculations, we calibrated the calculated PA against experimental gas phase PA values [166] of a series of O-containing organic molecules and water. The calibration suggested that the calculated PA values of zeolite O atoms should be adjusted by -27 kJ/mol to fit measured PA values [165]. Using corrected PA values, experimental PA values of zeolite oxygen centers can be estimated from *measured* IR frequency shifts [163] of the O-H stretching and deformation bands of methanol adsorbed on alkali-exchanged zeolites [165]:

$$PA(\omega) / \text{kJ/mol} = 776 - 0.282\ \Delta\omega(\text{OH}) / \text{cm}^{-1} \quad (4.1)$$

$$PA(\delta) / \text{kJ/mol} = 767 + 1.52\ \ \Delta\delta(\text{OH}) / \text{cm}^{-1} \quad (4.2)$$

As an advantage, this approach permits experimental estimates of the PA value of one and the same O center by means of two different criteria, Eqs. (4.1) and (4.2). Both frequency shifts are zero at PA = 772±5 kJ/mol.

The connection of the PA with O1s core level shifts was also justified. Calculated PA values of O atoms in the six-rings studied show a clear linear correlation with the corresponding calculated core level shifts ΔE_b(O1s). From the corresponding slope we concluded that a negative shift of the O1s binding energy by 1 eV (less stable O1s level) implies an increase of the PA by 82 kJ/mol. Such a linear correlation has been observed for PA and E_b(1s) values of a series of O- and N-containing gas-phase molecules [166]. The correlation of PA and ΔE_b values underlines the close connection between the PA and the energy of other orbitals located on the O center, in particular the HOMO (lone pair) at that center. However, the accuracy of XPS does not allow one to discriminate different O centers in a zeolite; rather, the measured O1s binding energy (shift) is an average value over all types of O atoms of the material. Thus, E_b(O1s) is useful as a basicity measure only for materials with uniform O centers, e.g. zeolites with Si only as T-atoms or with an Al/Si ratio close to one.

Using calculated PA values of the O centers in Na^+-containing zeolite clusters, we analyzed how the environment of an O atom affects its basicity [145]. For the *anti* position of Na^+, the most basic O atoms are located between the two Al atoms in *meta* position and far from the charge-compensating cations in the six-rings Al-2m and Al-3; the corrected PA values are 886 and 859 kJ/mol, respectively. These O centers, located between two Al atoms as next-nearest T-atom neighbors, are even more basic for Na^+ in *syn* position (by about

20 kJ/mol) because the distance to the cation is larger. The PA values of the most basic O centers in the other two Na^+ containing clusters, Na-Al-1 and Na-Al-2p, are by 40-50 kJ/mol smaller, i.e. the O centers in these rings are less basic. Least basic are the O centers of the cluster Na-Al-1 participating in Si-O-Si bridges, PA = 671 kJ/mol. The PA of the O atoms of the six-ring Si-6, containing only Si T-atoms, is 744 kJ/mol, 31 kJ/mol smaller than the PA of methanol, 775 kJ/mol, and notably less basic than O centers in clusters with Al centers [165]. To gauge the strength of basic sites in zeolites, note that the PA of ammonia, calculated in the same way at 885 kJ/mol, is somewhat smaller than the largest PA of basic sites in zeolite rings, whereas the PA of water is 724 kJ/mol, close to that of less basic zeolite O atoms. The calculated PA values of O atoms of the K^+ cluster model is 23-29 kJ/mol larger than PA values of the corresponding Na^+ model, in line with the observed higher basicity of K^+ exchanged zeolites compared to their Na^+ congeners.

5. SUPPORTED d-METAL SPECIES ON IONIC METAL OXIDES

Important questions of metal adsorption at ionic metal oxides are: (i) preferred adsorption sites; (ii) strength and nature of metal-support interactions on regular and defect-rich surfaces; (iii) charge redistribution between deposits and supports; (iv) geometric and electronic structure as well as magnetism of small metal particles and deposition-induced alteration of these features; (v) implications for the reactivity. We will also discuss accuracy improvements due to more precise xc functionals as well as more realistic cluster models of oxide supports.

As mentioned in Section 3, the MgO(001) surface is a prototype substrate. We systematically investigated a series of single *d*-metal atoms on regular sites of this representative support [73,96,167-170] and lately also on α-Al_2O_3(0001) [171]. We studied deposited dimers and tetramers of Co, Ni, Pd, Ag, Os and W on MgO [172-180] as well as larger clusters of Ni, Pd and Os [176,178-180]. Very recently, we investigated Pd_3 and Pt_3 moieties adsorbed on α-Al_2O_3(0001) surface without defects [181]. We considered the interactions with defect sites of MgO for single metal atoms [96,182], Os [180] and Ni clusters [178,179] as well as for an organometallic species $Re(CO)_3$ [183].

5.1. Interaction with regular MgO(001) and α-Al_2O_3(0001) surfaces

5.1.1. Single atoms on MgO(001)

As the initial step of forming a metallic overlayer, single metal atoms impinging on an oxide substrate can either be reflected from the surface or stick to it. In the latter case, atom diffusion with subsequent condensation or, alternatively, re-evaporation can take place. Of course, the strength of the bonding with the surface is crucial for forming an overlayer. There is enough experimental evi-

dence that nucleation occurs preferentially at low-coordinated sites and defects, rather than on well-ordered regular terraces of the substrate surface. However, structural and energetic details of the interaction of single metal atoms with regular sites at oxides are essential for understanding nucleation and growth of supported metal species at the microscopic level. Metal atoms on defect-free oxide surfaces constitute important elementary building blocks of such complex materials as supported metal particles and films.

We systematically studied the bonding of transition metal atoms to O ions of a regular, defect-free MgO(001) surface and we obtained results from nonrelativistic (3*d*-, 4*d*-atoms) and scalar relativistic (4*d*-, 5*d*-atoms) GGA DF calculations [167]. The investigation comprised nine atoms of three triads of the periodic system: Cr, Mo, W; Ni, Pd, Pt; Cu, Ag and Au. The substrate was represented by stoichiometric clusters embedded *only* in rigid PC arrays (see Section 2.2). Two conceivable adsorption sites were considered: on-top adsorption on O anion and bridge positions over two adjacent O anions.

On-top complexes were found to be energetically favored. Based on the strength of the bonding with the oxide substrate, the metal atom adsorbates under consideration were divided in two groups. With the BLYP xc functional, Cu, Ag, Au, Cr and Mo atoms exhibited weak or very weak bonds, less than 30 kJ/mol; their interaction is mainly due to polarization in the surface electrostatic field with only little mixing of adatom and substrate orbitals. At variance, Ni, Pd, Pt and W atoms form notably stronger bonds, of the order of 100 kJ/mol, with the O anions of MgO(001). These bonds are of a covalent polar nature with only limited charge transfer between metal and oxide, as indicated by the dynamic dipole moments $\partial\mu/\partial z$. The latter result reflects the properties of an MgO crystal as a wide band gap insulator with almost no propensity to oxidize. The higher "specificity" of the stronger M-O^{2-} bonds in the second group of the surface complexes is also manifest in the calculated enhanced corrugation of the potential energy surface for adsorbed W atoms and those of the Ni subgroup. Indeed, for instance, the adsorption interaction with a Ni atom at the bridge site of MgO(001) almost vanishes or is about 80 kJ/mol weaker than on the favorable on-top O^{2-} site; the corresponding reduction of the BLYP adsorption energy for a Cu atom is considerably less pronounced, from 30 to 20 kJ/mol.

The latter findings were corroborated by our further BLYP study of PC-only embedded cluster models [168] that considered three adsorption positions of the regular MgO(001) surface for Cu, Ni and Pd single atom adsorbates: on-top O^{2-}, bridge over two adjacent O^{2-} anions, and on-top Mg^{2+}. Calculated binding energies of the metal atoms at all three adsorption sites varied by more that 100 kJ/mol for the most strongly bound Ni atom, whereas for a Cu atom, with the weakest interaction with the oxide surface, this variation was only 15 kJ/mol, i.e. without a clear preference for either on-top O^{2-} or on-top Mg^{2+} positions.

Relativistic contributions to the strength of M-O^{2-} bonds are important for adsorbed 4*d*-metal atoms. For chemical bonds of these atoms, relativistic effects are only rarely considered to be crucial (but see [184]), at variance with the bonds involving 5*d*-metal atoms. In our BLYP calculations of the M-O^{2-} species on MgO, relativistic effects for the most strongly bound 4*d*-atom Pd were as large as 40% or 30 kJ/mol [167].

Experimental data on the bond energies of single transition metal atoms on regular sites of MgO are still very limited. The initial sticking probability of Cu atoms on a clean MgO(001) surface at 300 K was measured at ~0.5, which translates into a desorption energy of 20–50 kJ/mol [185]. Recently, nucleation and growth of Pd on MgO were studied by variable-temperature atomic force microscopy [186]. From these experiments, the adsorption energy of a single Pd atom at regular sites of the (001) terraces was estimated to 116±19 kJ/mol. Calculated adsorption energies of Cu and Pd atoms, 29 and 78 kJ/mol, respectively [167], are in a qualitative agreement with experiment; some energy underestimation can be ascribed to the GGA BLYP xc functional employed.

To quantify the accuracy of our DF data, two computational aspects have to be kept in mind. First, it is well known that calculated observables can depend notably on the xc potential [187]; this aspect will be discussed later in this section. Second, the cluster modeling issue, in particular, the embedding scheme chosen is also important (see Ref. [60] and Section 2.2). We examined [169] how improving the cluster embedding from a PC-only variant to a combined PC+Mg^{pp*} strategy [60] affects the calculated adsorption energies of single metal atoms on O^{2-} and Mg^{2+} sites of MgO. As exemplified for Pd atoms [169], the latter improved embedding furnishes more corrugated potential energy surface of Pd_1/MgO: the preference for the O^{2-} site is enhanced by ~20 kJ/mol, whereas the Mg^{2+} site is further destabilized, by ~30 kJ/mol, thus resulting in the notable difference of the adsorption energies for these two sites of 70 kJ/mol.

By employing another GGA (BP86) in combination with the PC+Mg^{pp*} embedding strategy [96,168], we assessed how calculated adsorption parameters of M_1/MgO surface complexes with Cu, Ag, Ni and Pd atoms depend on the xc functional. With the BP86 functional, somewhat larger adsorption energies were calculated compared to the BLYP functional for all four atoms under consideration [167-169]. Taking Pd_1/MgO as example, the BP86 adsorption energy of 130 kJ/mol [96,175] (to be compared with the experimental estimate of 116±19 kJ/mol [186]) is ~30 kJ/mol larger than the BLYP value obtained with the same cluster embedding. The energy difference between adsorption on-top O^{2-} and on-top Mg^{2+} is larger in the BP86 approach: for a Pd atom the former site is favored over the latter by about 90 kJ/mol [175]. However, it is essential to note that *no qualitative changes* of the nature of adsorbate-substrate interactions were found in Refs. 96 and 175 compared with the earlier studies [167-169]. The results calculated with the PC+Mg^{pp*} embedding are stable with

respect to the cluster size increase. For instance, for Pd on-top O^{2-}, the relativistic BP86 observables for an extended cluster $O_{13}Mg_{13}(13,13)$, D_e = 128 kJ/mol, z(MgO-Pd) = 211 pm, ω(MgO-Pd) = 178 cm^{-1}, compare well with the corresponding data for the smaller *standard* model $O_9Mg_9(9,9)$, 130 kJ/mol, 211 pm and 183 cm^{-1}, respectively [175].

Recently, with the introduction of EPE embedding, we proposed an improved model cluster strategy for surface complexes on ionic oxides [73] (Section 2.2). In line with the small relaxation of the stable stoichiometric MgO(001) surface, this improved BP86 embedded cluster description resulted in rather limited alterations of the adsorption parameters for M_1/MgO moieties compared the values just discussed, both calculated with the same GGA [96]. For instance, when surface relaxation was accounted for, the adsorption energy of Pd_1/MgO [73] increased by less than 10 kJ/mol compared to the value computed with a bulk-terminated substrate geometry [96]. Recently, results for Cu, Ag and Ni atoms on O^{2-} site of MgO(001) similar to those of Ref. 96 were calculated in an EPE-embedded GGA study [182] where we systematically explored the adsorption of 17 different single transition metal atoms from the subgroups of Cr, Mn, Fe, Co, Ni and Cu. We also calculated adsorption energies with two xc functionals, BP86 and PBEN. For all 17 atoms, the PBEN adsorption energies were computed by 20–30 kJ/mol smaller than the corresponding BP86 values. For metal species deposited on oxide substrates, the PBEN functional is expected to furnish more accurate adsorption energies; however, to corroborate this hypothesis, more experimental reference values are needed.

A further remark is in order on the accuracy of xc potentials to describe interactions with oxide supports. In recent calculations of the adhesion of Pd(111) and α-Al_2O_3(0001) slabs [188], where polarization interactions dominate, the relative contribution of electron self-interaction to the GGA value of the work of adhesion was estimated to be particularly large. Without a self-interaction correction, the calculated GGA PW91 energy amounts to less than 60% of the experimental adhesion energy [189]. It remains to be clarified which consequences this finding has for DF adsorption energies of finite metal species on oxides which exhibit more covalent bonding.

5.1.2. Single atoms on the polar α-Al_2O_3(0001) surface

For metal particles on ionic substrates one can differentiate between interactions with *non-polar* (stoichiometric) and *polar* surfaces. The former surfaces are represented by essentially unrelaxed (001) facets of oxides with rock-salt structure, such as MgO(001) which is widely utilized as metal support and was addressed in the previous subsection. Oxide supports exhibiting polar surfaces are also common. Clean polar surfaces are unstable and thus difficult to prepare unreconstructed, dehydroxylated, and free of defects [88]. Corundum, α-Al_2O_3, is a prototype of such metal oxides. Its most stable Al-terminated (0001) surface

was extensively studied experimentally [190]. We have already seen that this surface undergoes strong relaxation and hence shows decreased charge separation (polarity) effects [88] and reduced chemical activity. As a surface of a wide gap insulator, α-Al_2O_3(0001) is expected to feature adsorption properties that are quite similar to those of MgO(001).

For touchstone complexes of metal atoms on MgO(001), results of DF cluster [96,167] and periodic [191-193] calculations agree. In particular, (i) adsorption sites on-top of O are preferred, (ii) bonding can be rationalized by a polarization of metal atoms in the electrostatic field of the support with modest covalent and only very minor ionic contributions, (iii) adsorption energies are close in these model cluster and periodic slab computational approaches, provided the same xc functional is used. Embedded cluster GGA BP86 calculations on representative systems of Pd and Pt atoms on MgO(001) yielded binding energies of 135 kJ/mol [73] and 232 kJ/mol [170], respectively.

For low coverage of Pd atoms on the Al-terminated surface α-Al_2O_3(0001), a plane-wave periodic approach identified adsorption sites on-top of O^{2-} anions as preferred [194,195]. Despite a non-negligible ionic contribution to the Pd-Al_2O_3 bond, no ionization of adsorbed Pd atoms was found. A binding energy of ~135 kJ/mol with a strong contribution of substrate relaxation was calculated using the PW91 functional. Embedded cluster calculations with the same functional resulted in a smaller adsorption energy of 83 kJ/mol due to neglected substrate relaxation, but revealed a similar binding nature [195]. At variance, pseudopotential Gaussian-type orbital periodic calculations of single Pt atoms on α-Al_2O_3(0001) led to the conclusion that the interaction with the substrate induces ionization of atomic Pt adsorbates [196]. This finding implies a very different binding of Pt atoms on non-polar and polar oxides: minor ionic contribution on the one hand, and essentially ionic bonding on the other. Apparently, not such a strong difference was found for adsorbed isolated Pd atoms: the ionic part of the adsorption interaction prevailed with neither the stoichiometric surface MgO (001) nor the polar surface α-Al_2O_3(0001). Whereas Pd and Pt atoms bind in similar fashion to MgO(001), they seemed to behave quite differently on the non-stoichiometric surface α-Al_2O_3(0001) [196]. This issue required closer inspection.

We applied the EPE cluster embedding method and used the BP86 xc functional to study adsorption of single Pd and Pt atoms on the relaxed polar Al-terminated surface α-Al_2O_3(0001) [171]. In line with our results for metal species on MgO(001), outlined in Subsection 5.1.1, the most favorable adsorption complexes of atomic Pd and Pt on α-Al_2O_3(0001) were calculated at the site on-top O^{2-}. The adsorption energies of Pd and Pt (110 and 165 kJ/mol, respectively) are close to those of the corresponding periodic calculations [195,196]. Unlike the MgO(001) surface, a trend of the adatoms at on-top O sites of α-Al_2O_3(0001) to interact simultaneously with an O anion and a nearby Al cation of the top

layer is manifest. Strong adsorbate-induced relaxation results in an increase of the adsorption energy by almost 30 kJ/mol for Pd and 60 kJ/mol for Pt. This relaxation provides a contact of ~240 pm between the metal adatom and a nearby Al cation. Bonding in these stable stationary complexes is only moderately ionic, with adsorbed Pd and Pt atoms far from an ionized M^+ state, which was predicted in the periodic calculations for $Pt_1/\alpha\text{-}Al_2O_3(0001)$ moieties [196].

The binding energies in other conceivable positions above the centers of equilateral surface oxygen triangles of $\alpha\text{-}Al_2O_3(0001)$ are at least 40 kJ/mol (Pd) and 125 kJ/mol (Pt) smaller than for adsorption on-top O^{2-}. These triangular structures are not local minima of the energy hypersurfaces. Rather, they characterize barriers for the diffusion of adatoms. The calculated binding energies are similar for complexes with a metal adatom on-top Al, over oxygen triangles covering Al cations in octahedral positions and at triangles covering empty tetrahedral positions. Of the two metal atoms under study, adsorption of Pt causes a larger distortion of the substrate, and a concomitantly larger relaxation than adsorption of Pd. Also, a Pt atom is stronger bound to the $\alpha\text{-}Al_2O_3(0001)$ substrate and has a notably smaller propensity to migrate on the surface.

5.1.3. Dimers and small clusters of Co, Ni, Cu, Pd, Ag and W on MgO(001)

The interaction between Pd_2 and the surface was extensively investigated to localize preferential adsorption sites [173]. The preferred orientation of Pd_2 on the surface is in the proximity of O^{2-} ions with the adsorbate axis parallel to the surface. The dimer is considerably elongated compared to its equilibrium distance in the gas phase to adjust for improved interaction with surface anions. The computed adsorption energy D_e = 160 kJ/mol results from an interplay of the energy gain due to bonds at the interface and the cost of stretching the Pd-Pd bond with a partial loss of metal-metal bonding. In the most stable adsorption configuration, the adhesion energy of Pd_2 is almost the same as the stability of two isolated Pd atoms bound at separate surface O centers. This suggests that Pd_2 once deposited on the surface may cleave to form isolated Pd atoms.

An Ag dimer is calculated to be very weakly bound at the regular MgO(001) surface D_e = 55 kJ/mol [173]. Its geometry is virtually unperturbed by the interaction with the substrate; the preferred orientation is upright. This can be rationalized by the weak Ag-MgO interaction and the necessity to reduce Pauli repulsion. The structure of the adsorbed species is governed by repulsive interactions rather than by the bonding to the substrate.

Our earlier computational investigation dealt with model clusters Cu_4, Ag_4, Ni_4 and Pd_4 on MgO(001) considered in C_{4v} symmetry [172]. To complement that work we studied the adsorption properties of Ag and Pd tetramers (C_{2v} symmetry constraints) deposited at the regular (001) surface of MgO [173]. The calculations of cluster models embedded in arrays of PCs and AE Mg^{2+} cations were carried out with the BP86 GGA at the scalar relativistic level.

For a palladium tetramer, the adsorption energy D_e = 149 kJ/mol is somewhat smaller than for the dimer. Supported Pd_4 clusters are only slightly deformed relative to the gas phase structure because the cost for the deformation exceeds the energy gain of the interface bond. The tetrahedral form of Pd_4, which is the most stable gas phase isomer, is the preferred one also when adsorbed on the MgO surface.

Unlike Pd_4, an Ag tetramer is very weakly bound on MgO(001). As for adsorbed Ag_2, the geometry of supported Ag_4 cluster remains almost the same as for the free Ag_4 moiety. The preferred shape and orientation of the Ag_4 species is that of a rhombic particle with the adsorbate plane perpendicular to the surface. The most stable gas phase cluster Ag_4, a rhombic isomer, was the only one found at the surface; other structures, like tetrahedral Ag_4, undergo spontaneous transformations into the rhombic form.

To summarize, the calculations indicated [173] that when low-nuclearity Ag and Pd clusters are deposited on the surface in low concentrations and at low kinetic energy to avoid coalescence, the clusters do not tend to "wet" the surface, in line with the results of GIXS experiments [5]. Instead, the clusters retain structures close to those in the gas phase. This behavior can be rationalized by the competition between metal-metal and metal-oxide bonding. Pd clusters interact moderately strong with the substrate, but the relatively strong Pd-Pd bonds in the cluster disfavor any major deformation of the cluster framework. Ag moieties, on the other hand, interact weakly with the MgO surface and, irrespective of their size, the metal-metal interaction prevails over the interface bonds. Pd_2 is an exception: once deposited on the surface, it shows a propensity to dissociate into Pd_1/MgO complexes. This peculiar behavior is due to the relatively weak metal-metal bond in Pd_2. Note that the stronger adsorption bonding in Pd/MgO than in Ag/MgO is consistent with experimentally observed distances in the initial stage of the deposition [5].

Despite a large number of experiments on metal species deposited on the MgO surface, to the best of our knowledge the adsorption system W/MgO(001) was studied experimentally only by high resolution electron microscopy [197]. Single atoms and clusters composed of four and five atoms were detected on the MgO(001) surface. By analogy with other supported metal systems, the sites on-top O^{2-} were assumed to be preferred also by W_n species [197]. Notwithstanding the limited sensitivity of electron microscopy data to the (vertical) W-MgO distance, the experimental results were discussed as manifesting two-dimensional W_4 and W_5 clusters, formed parallel to the (001) surface of MgO. Such a picture implies that W-substrate bonds are quite strong compared with W-W bonds. Our studies of single metal atoms on MgO(001) indeed showed that, along with the bonds of atoms of the nickel subgroup, the W-MgO bond belongs to the strongest M-MgO bonds considered in the series M = Cr, Mo, W; Ni, Pd, Pt; Cu, Ag, Au [167]. Nevertheless, even for Pd_4 clusters with moderately strong metal-

metal bonds, the strength of the Pd-MgO interactions was found insufficient to deform the most stable gas phase structure, a tetrahedron, into a planar adsorbate due to formation of adsorption bonds at MgO(001) [173]. Therefore, the hypothesis of a potentially planar cluster W_4 on MgO(001) [197] seemed questionable. To clarify this issue and the question of preferable sites for adsorbed W atoms and clusters on MgO(001), we studied computationally (DF, BP86) the geometric and electronic structures as well as the bond strengths and nature of the adsorption complexes of the species W_1, W_2, W_3 and W_4 interacting with various sites of the ideal MgO(001) surface [174].

In line with previous studies of deposited metal species, O^{2-} anions rather than Mg^{2+} cations were found to form the preferred adsorption sites on the MgO surface. Adsorption of W_2 induces an elongation of the W-W bond by ~10 pm; with this distortion, the interaction of the W atoms with the surface O centers is maximized within the constraint of a W-W bond. Like for Pd clusters, the adhesion energy results from a competition between the energy gain due to bonds at the interface and the cost of stretching the strong W-W bond with a partial loss of metal-metal interaction. When the nuclearity of the adsorbate cluster increases, the cluster cohesive energy increases as well: from 222 kJ/mol/atom for the dimer to 338 kJ/mol/atom for the trimer and to 347–386 kJ/mol/atom for the tetramer, whereas the adsorption energy per atom tends to decrease due to the enhanced number of the W-W bonds which restrict the atom displacement to achieve the most favorable adsorption positions on-top O^{2-}. As before, also supported W_n clusters are only slightly distorted with respect to their ground-state gas phase congeners because the deformation cost exceeds the energy gain of the W-MgO bonds. The configuration of W_3 with two W atoms close to two nearest-neighbor O anions is favored over a structure where two W atoms are close to next-nearest-neighbor anions. In both cases, the adsorbed W_3 cluster tilts from an upright orientation. The slightly Jahn-Teller distorted tetrahedral form of W_4, which is the most stable isomer in the gas phase, is also preferred at the MgO surface. As the adsorption energy of square-planar W_4 is ~100 kJ/mol smaller than that of the tetrahedral cluster, a square-planar adsorbed configuration may be only possible if the W-O bonds become strong enough to compensate the loss of W-W interactions. This can happen when defect sites are present on the MgO(001) surface (see Section 5.2). Such adsorption sites may be the reason that a planar structure of the $W_4 - W_5$ clusters adsorbed on MgO(001) surfaces was derived from time-resolved high resolution electron microscopy studies [197]. However, results of our calculations definitely did not support the formation of very small *planar* adsorbed tungsten clusters on *defect-free* MgO(001) terraces.

Calculated results on the structure and stability of the supported clusters W_4, Pd_4 and Ag_4 [173,174] are summarized in Fig. 5.1.

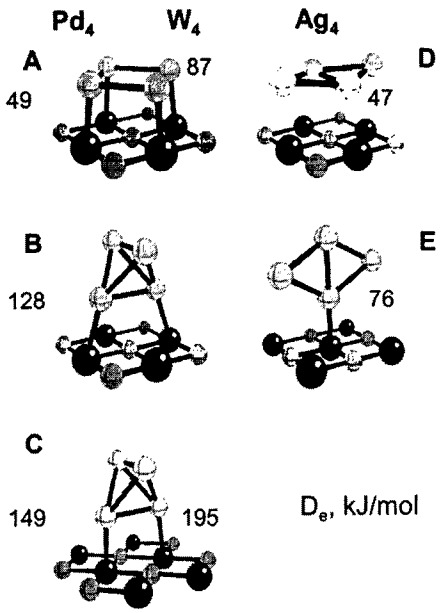

Fig. 5.1. Calculated structures and adsorption energies of W_4, Pd_4 and Ag_4 clusters deposited on the MgO(001) substrate.

Due to the particular importance of supported palladium catalysts [198-200], we performed additional studies of the model clusters Pd_4 and Pd_5 on MgO(001) [175,176] and of CO molecule adsorption on these deposited *model systems* [176]. These studies aimed at a more thorough elucidation of the changes in the electronic structure and reactivity of the clusters induced by interactions with the MgO(001) substrate.

The interaction of a Pd_4 (C_{4v}) cluster with the oxide surface was analyzed in more detail with the help of electron density difference plots and other theoretical tools, such as population analysis, core level shifts as well as induced and dynamic dipole moments [175]. Three interaction mechanisms were found to contribute to different extent: metal polarization with the subsequent electrostatic attraction, Pauli repulsion, and covalent orbital interactions. Electrostatic interactions make up a sizeable fraction of the adhesion energy: the polarization of the metal adsorbate by the surface electric field provides an important bonding mechanism. For the adsorption of Pd on-top or in the vicinity of the surface Mg^{2+} cations this electrostatic interaction accounts for almost the entire adsorption energy, albeit counteracted by Pauli repulsion. For adsorption on-top O^{2-}, on the other hand, mixing of adsorbate and substrate orbitals becomes noticeable. This hybridization or covalent bonding at the interface with the oxide anions is complemented by electrostatic polarization. Further work is required to establish in a more quantitative way the relative importance of electrostatic and chemical bonding contributions. However, in line with our other studies of

supported metal particles on regular sites of oxides, no or very little charge transfer occurs across the metal/oxide interface, consistent with the very low oxidizing and reducing ability of the regular MgO(001) surface.

As already mentioned for other surface systems, an indirect but efficient way to monitor changes in the electronic structure of a supported metal particle with respect to the free species is to analyze variations of properties of an adsorbed probe molecule. This is similar to the experimental approach to examine the acidity or basicity of a given adsorption site by measuring indirectly the flow of charge between the adsorbate and the substrate [201] (see Section 4). Comparison of spectral signatures of adsorbed CO molecules (e.g., the frequency of the C-O vibration) offers valuable information on the electronic state of the substrate. We analyzed computationally the properties of CO molecules adsorbed on free and supported model Pd_4 and Pd_5 clusters [176].

Adsorption of CO molecules on *supported* Pd species induces changes in the adsorption geometry and vibrational properties relative to unsupported metal particles of the same structure [176]. The small changes calculated could be due to minor modifications in the back-bonding ability of the Pd particle as well as to a modified surface charge density, hence differences in Pauli repulsion. The latter mechanism is consistent with computed charge density plots [176]. No significant Pd-MgO charge transfer was found. The largest changes in CO properties on Pd clusters caused by the oxide support occur in the adsorption energies which are larger on the supported than on the free cluster.

For the special case of a model Pd_4 cluster situated in pseudomorphic fashion on MgO(001), we considered two adsorption sites for CO, on-top and in the four-fold hollow. The interaction with the support reverses the order of stability of the sites, with CO being more stable on the hollow site of the free cluster (262 vs. 130 kJ/mol) and on the on-top site of the MgO supported cluster (192 vs. 159 kJ/mol). This very important result shows that relatively small perturbations due to the metal-oxide interface can suffice to change the order of stability of adsorption sites of a metal particle even when there is no large electron density transfer from or to the support. This implies that the catalytic activity and selectivity of a deposited metal particle can be modified compared to the free particle even by a relatively inert support.

Thus far, the vast majority of theoretical studies on supported metal clusters dealt with non-magnetic metals like Cu, Ag, Pd, Pt. An investigation of Fe on MgO [202] represents a rare exception; there, the magnetic properties of an epitaxial monolayer of Fe on MgO(001) substrate were found remarkably close to those of a free Fe monolayer. Comparison of the cluster magnetism of species in the gas-phase and deposited on an oxide surface can provide very important information on the changes in the cluster electronic structure due to the bonding at the interface [177]. In the same way, the study of the effect of the ligand shell on the magnetic properties of medium to large Ni clusters has provided valuable

information on the nature of metal-ligand bonding and on the appearance of metallic properties in ligand stabilized metal clusters [203,204]. On the other hand, the magnetic behavior of metal nanoparticles on oxides is of interest in the field of magnetic recording and even spintronics.

Small bare metal clusters exhibit several electronic states in a small energy range, but often high spin states are preferred. For instance, tetrahedral Co_4 has a magnetic ground state state (N_s = 10) [177], which is only 6 kJ/mol/atom less stable than the planar rhombus also with N_s = 10. (N_s is defined as the number of unpaired electrons of a cluster, i.e. the difference of the numbers of electrons occupying the majority and minority spin orbital manifolds.) One can relate the (average) magnetic moment per atom in Bohr magnetons, μ_B, to N_s/atom. Thus, the ground state of Co_4 is highly magnetic with a magnetic moment of 2.5 μ_B/atom; this value is to be compared with the moment of bulk hcp Co, 1.76 μ_B/atom. The cluster result is in line with the experimental study of Bloomfield et al. [205] who, with a beam technique, measured magnetic moments of Co clusters to be about 20% enhanced compared to the bulk [205]. In a similar way, tetrahedral Ni_4 exhibits a quintet ground state which corresponds to a magnetization of 1 μ_B per atom, larger than the (experimental) magnetization of the bulk, 0.606 μ_B/atom.

As mentioned above, small clusters do not tend to adhere to the regular MgO surface with the largest possible number of metal atoms. When the metal-oxygen bond is relatively strong, adhesion of the cluster occurs at the expense of metal-metal bonds within the cluster and the energy gain due to the formation of new bonds at the interface is compensated by an energy loss resulting from the distortion of the metal structure. For the same reason the magnetization on the cluster is largely unchanged also in the supported species. In some cases, however, there is a partial quenching of the magnetic moment which is generally restricted to the metal atoms in direct contact with the oxide anions [177]. Thus, despite of relatively strong M_4/MgO bonds (Co_4 is bound by 193 kJ/mol, Ni_4 by 232 kJ/mol), the electronic structure of supported transition metal moieties is only moderately perturbed. These conclusions are valid for an ideal defect-free surface; of course, investigations of the interaction of metal clusters with surface defects may lead to quite different conclusions.

5.1.4. Pd_3 and Pt_3 on α-Al_2O_3(0001)

Very recently, we studied EPE embedded cluster models of adsorption complexes of Pd_3 and Pt_3 on Al-terminated surface α-Al_2O_3(0001) [181]. Free Pd_3 and Pt_3 species of equilateral triangle shape were calculated to be most stable as singlets in the ground state. The lowest-lying triplet state is only ~20 kJ/mol higher in energy for both species; transition to the triplet is accompanied by a slight elongation of the M-M bonds. The calculated atomization energy of Pt_3, 691 kJ/mol (reference Pt d^9s^1), is significantly larger than that of Pd_3, 350

kJ/mol (reference Pd d^{10}). The energy of a Pd-Pd bond in Pd_3, 116 kJ/mol, is close to that of the adsorption bond of single Pd atoms on α-Al_2O_3(0001), 110 kJ/mol, calculated with the same approach [171]. At variance, the energy of Pt-Pt bond in Pt_3, 230 kJ/mol, notably exceeds the adsorption energy on a Pt atom on α-Al_2O_3(0001), 165 kJ/mol [171].

We also compared the bonding of the adsorption complexes formed at various conceivable surface sites with the M_3 plane oriented parallel to or (essentially) upright on the (0001) surface. The surface α-Al_2O_3(0001) is well suited for building interfaces to hexagonal metal surfaces, where each surface anion interacts with one metal atom. Relevant thin Al_2O_3 films are known to promote the growth of supported metal nanoclusters at such interfaces [189, 206,207]. M_3 species adsorbed parallel to the α-Al_2O_3(0001) plane represent the simplest model of the interaction mode that maximizes the number of contacts of metal atoms with surface anions. However, the surface anions do not necessarily occupy optimal positions to serve as ligands of M_3 fragments in such adsorption complexes. Alternatively, an adsorption complex can be favored with an M_3 species adsorbed (almost) upright. Whether a structural arrangement of adsorbed M_3 moieties "lying down" or "upright" is ultimately favored depends on the ability of the adsorbed particle and the α-Al_2O_3(0001) substrate to mutually adjust their geometries so that contacts are optimized for a strong adsorbate-

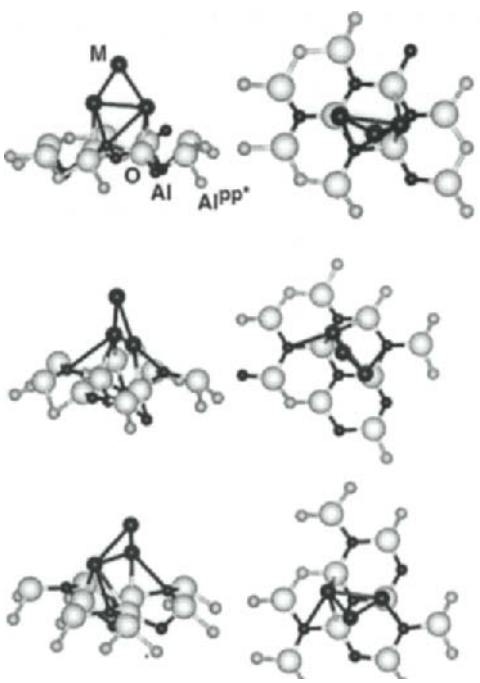

Fig. 5.2. Calculated adsorption complexes of Pd_3 adsorbed in upright fashion at different sites of the Al-terminated surface α-Al_2O_3(0001). Left-hand panels – side view, right-hand panels – top view.

substrate interaction. Complexes with upright orientation were calculated more stable [181]. In such complexes (Fig. 5.2) one of the metal atoms in the base of the M_3 triangle is bound to one of the surface anions whereas the second base atom M interacts with two other nearby anions. Structurally, the most stable complexes of upright Pd_3 and Pt_3 species are rather similar, despite notably larger adsorption energies of Pt_3 particles, 210–250 kJ/mol, compared to their Pd_3 congeners, 105–145 kJ/mol. The substrate structure in the vicinity of the adsorbed M_3 particles is strongly distorted such that cations of the top layer are displaced away from the "bulk" by 30–40 pm; anions typically move ~10 pm in the opposite of the bulk. Relaxation also affects the energetics in a major way and cannot be neglected.

5.2. Interaction with surface defects on MgO

5.2.1. Single atoms on anionic vacancies F_s, F_s^+ and F_s^{2+}

As next step, atomic adsorption of selected transition metals, Cu, Ni, Ag, and Pd, was studied on F_s and F_s^+ oxygen vacancies of the MgO(001) surface in comparison to that on regular O^{2-} centers [96]. Gradient-corrected BP86 DF calculations using Mg_9O_{13} and Mg_9O_{12} cluster models embedded in a matrix of model potentials and point charges (rigid embedding) were carried out. Scalar relativistic effects were taken into account for adsorbed Ag and Pd species.

On F_s sites, adsorption of all atoms under study was found to be stronger by 100–230 kJ/mol than that on regular O^{2-} sites, with Pd and Ni forming the most stable complexes. On the F_s^+ site, the single valence electron of Cu and Ag atoms couples with the unpaired electron of the vacancy forming a covalent bond. As a result, the adsorption energy of these atoms at F_s^+ sites is more than 100 kJ/mol stronger than on F_s sites. On the other hand, the adsorption energies of Ni and Pd are reduced on F_s^+ by 50 and 125 kJ/mol, respectively. The whole

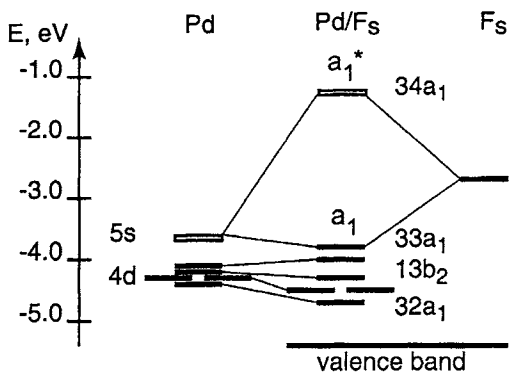

Fig. 5.3. Simplified orbital interaction diagram of the adsorption complex Pd/F_s (C_{4v} symmetry) [96]. Solid bars designate occupied KS levels.

Table 5.1
Binding energies (kJ/mol) of single atoms on the regular adsorption sites O^{2-} and on the defects F_s, F_s^+ and F_s^{2+} of MgO(001) calculated at the BP86 level with EPE embedding [73,182]. In parentheses is the contribution of the adsorption induced relaxation relative to the energies of Ref. 96, calculated for vacancy geometries fixed as optimized without an adsorbate.

Atom	O^{2-}	F_s	F_s^+	F_s^{2+}
Cu	93 (15)	189 (14)	242 (13)	61
Ag	46 (7)	178 (16)	229 (18)	210
Ni	154 (19)	297 (35)	223 (1)	91
Pd	137 (7)	387 (24)	255 (2)	123

series of M/F_s^+ complexes is characterized by rather uniform values of adsorbate-substrate distances, 150–170 pm, and adsorption energies, 210–250 kJ/mol.

The trend in the binding energies of metal atoms M at F_s and F_s^+ sites can be rationalized with an orbital interaction diagram, shown in Fig. 5.3 for the example of Pd/F_s. The empty Pd 5s KS orbital interacts with the doubly-occupied orbital of the F_s vacancy, forming a pair of bonding a_1 ($33a_1$) and antibonding a_1* ($34a_1$) MOs. In Pd/F_s, the bonding MO contains 2 electrons, whereas the antibonding MO is empty. The complex Pd/F_s^+ has one electron less, which is removed from the bonding MO $33a_1$, resulting in bond weakening. The bonding picture for the most stable systems Cu/F_s^+ and Ag/F_s^+ is very similar to that for Pd/F_s species. The (relative) destabilization of adsorption bonds in the complexes Cu/F_s and Ag/F_s can be attributed to the presence of an extra electron in the antibonding MO analogous to $34a_1$. Clearly, the closed-shell electron configuration $(a_1)^2(a_1*)^0$ is most stable.

Table 5.1 shows selected results of our most recent calculations with EPE embedding, where relaxation of both the vacancy sites and the adsorption complexes was accounted for [96,182]. The general trends in the adsorption energies and the binding mechanisms found with the rigid embedded models remain unchanged. However, as expected, the energy contributions of the adsorption induced relaxation are significant, in some systems up to 20%. If the PBEN xc potential is used instead of BP86, all adsorption energies listed in Table 5.1 are reduced by up to 50 kJ/mol. One of the most important, albeit not unexpected results of these studies is that defects bind metal atoms considerably stronger than the most favorable regular O^{2-} sites on the ideal (defect-free) MgO(001) surface. Thus, at low concentration of metal atoms on an oxide surface not completely free of defects (a common situation), cluster nucleation starts heterogeneously (on defects) rather than homogeneously on regular sites, provided diffusion barriers are sufficiently low for the temperature of the experiment.

5.2.2. Osmium clusters on regular sites and cationic vacancies

As an example of cluster adsorption at defect sites, we discuss the interactions of four- and five-atom osmium clusters with an MgO substrate, investigated at the AE scalar relativistic GGA BP86 DF level [180]. These systems were chosen because small clusters on MgO formed by decarbonylation of supported $[Os_5C(CO)_{14}]^{2-}$ are among the most stable known supported metal clusters. Their EXAFS (extended X-ray absorption fine structure) coordination numbers [208] show the retention of the metal frame, including a carbido C atom, after complete decarbonylation. Thus, on the basis of available structural information, these decarbonylated clusters were represented as Os_5C. We addressed several questions crucial to the characterization of supported osmium particles: (i) How are the structural parameters of supported C_{4v} model clusters Os_4, Os_5, and Os_5C on the most common sites (including defects) of MgO(001) modified relative to those of the free clusters and known osmium carbonyl clusters? (ii) How does the MgO substrate affect the electronic properties of these supported clusters? (iii) How strong are the adsorption bonds and what are the preferred positions of the clusters on MgO(001)? (iv) Do the results of these model calculations provide insight into the structure and bonding of clusters formed by decarbonylation of $[Os_5C(CO)_{14}]^{2-}$ supported on MgO powder and characterized by EXAFS spectroscopy?

We studied supported Os_4, Os_5, and Os_5C clusters centered above a Mg^{2+} cation and the Os atoms oriented either to the nearest surface O anions (A) or between them (B). The influence of surface V_s and V_s^{2-} defects (Mg vacancies) on the adsorption structure and energy of the clusters was also investigated. The calculations showed that Os_5 and Os_4 have very similar binding energies on the same adsorption sites (except for the regular site A). Both Os_4 and Os_5 moieties are more strongly bound to the ideal surface than Os_5C. All three osmium model clusters are bound stronger at surface V_s point defect sites of MgO(001) than on the ideal surface. Adsorption at such defects perturbs the Os_5C cluster most and the Os_5 clusters least. Computed interaction strengths of the Os clusters with the MgO(001) support range from non-bonding (defect-free site B when the basal Os atoms are aligned between the nearest O anions), to very weak (~60 kJ/mol, Os_5C at defect-free site A when the basal Os atoms are aligned with the nearest O anions), to weak (~190 kJ/mol for pure Os clusters at defect-free site A), to rather strong (~870 kJ/mol for V_s defect site A). Consistent with the calculations of other MgO-supported metal clusters (see Subsection 5.1.3), for Os_5C orienttation A with the Os atoms directed toward the surface O atoms was found to be preferred over orientation B with the Os atoms directed toward O-O bridge sites.

The EXAFS coordination numbers for MgO powder-supported clusters formed by decarbonylation of $[Os_5C(CO)_{14}]^{2-}$ agree with those of Os_5C chosen in our investigation, but the Os-Os bond distances are calculated to be about 30–50 pm shorter than the values measured by EXAFS spectroscopy. For such

rather strong bonds, this difference is far outside the bounds of the generally accepted inaccuracy of DF methods. Thus, our results [180] indicate that the MgO-powder-supported Os_5C clusters are likely not entirely ligand free and we suggest that this holds also for other small supported metal clusters formed by decarbonylation of metal carbonyl cluster precursors (see Sections 6.3 and 6.4). The most plausible model of the MgO-powder-supported clusters includes light-atom ligands, formed during decarbonylation and virtually undetectable with EXAFS and other spectroscopic techniques.

Our DF data also indicate that models of metal clusters on the ideal MgO(001) surface are too simple for an accurate representation of clusters on powder MgO. More realistic adsorption site models may be needed that account for structural features such as kinks and steps and surface hydroxyl groups.

5.2.3. $Re(CO)_3$/MgO: The support as a polydentate ligand

As seen in Subsection 5.2.1, bonds of ultrafine metal particles with oxide supports may become as strong as metal-ligand bonds in common coordination compounds. This happens, in particular, when the support exhibits defect surface sites that are notably more active than the sites on regular, defect-free parts of the surface. Then the question arises if one really can invoke the analogy of metal-ligand and metal-surface interactions. In other words, is the concept of a surface site as a polydentate ligand justified? We addressed this noteworthy issue for an organometallic surface complex [183].

Many supported organometallic species are important as industrial catalysts [198]. However, most of them are not uniform mixtures, with only a few being well characterized at the atomic level. Rhenium subcarbonyls on MgO comprise one of the examples of nearly uniform surface species and they are among the best-studied organometallic complexes on oxides [209,210]. EXAFS [209] and IR [210] investigations showed that decomposition of precursors on MgO powder results in fragments, assigned as $Re(CO)_3^{n+}$, coordinated to the surface. Depending on the degree of MgO surface hydroxylation, structural models of the supported complexes ranging from $Re(CO)_3\{OMg\}_3$ (three oxygen anions of MgO as ligands) to $Re(CO)_3\{HOMg\}_3$ (three surface hydroxyl groups of MgO as ligands) had been invoked [209,210]. Weakening of the adsorbate-substrate interactions with increasing surface hydroxylation was manifested by the C-O vibrational frequency shift [210]. From the sensitivity of IR band positions in the C-O stretch region, an approximate average number of surface oxide and hydroxide moieties coordinated to a Re atom of the supported complexes had been inferred [210]. Based on typical ω(C-O) features, C_{3v} symmetry was assigned to two limiting complexes [210], implying a surface site with three O atoms involved.

With the help of BP86 DF calculations using PC embedding, we examined various structural models of $Re(CO)_3$/MgO complexes: $Re(CO)_3$ and $Re(CO)_3^+$

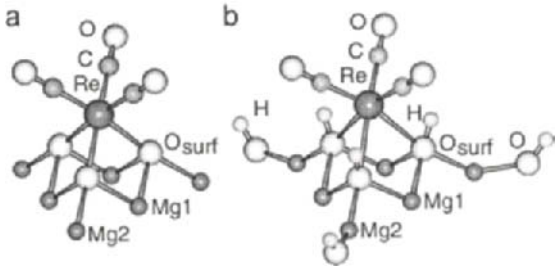

Fig. 5.4. Adsorption complexes of rhenium subcarbonyl on dehydroxylated $Re(CO)_3\{OMg\}_3$ (a) and hydroxylated $Re(CO)_3\{HOMg\}_3$ (b) cationic defects of MgO.

on cationic defects as well as V_s centers of dehydroxylated and hydrohylated MgO surfaces (Fig. 5.4). Our aim was (i) to justify the possibility of forming $Re(CO)_3$/MgO complexes, (ii) to determine their structural and spectroscopic parameters and (iii) to investigate whether the Re-O_{surf} bonds are similar in strength and nature to common coordination bonds. To the best of our knowledge, that work [183] was the first high-level computational study to assess quantitatively structure and bonding parameters of oxide-supported organometallic species.

The supported complexes $Re(CO)_3\{OMg\}_3$ and $Re(CO)_3\{HOMg\}_3$, proposed on the basis of experimental results, were shown to correspond indeed to stable configurations of our cluster models; calculated geometric and vibrational parameters agree quantitatively with experiment. The Re-O_{surf} bonds were computed as strong as M-O bonds in Re oxo complexes [211], thus justifying the concept that surface sites as polydentate ligands are able to anchor organometallic fragments to a support. Surface hydroxylation can dramatically reduce the strength of such adsorption bonds. This conclusion implies possibilities for tuning adsorptive and catalytic properties of supported organometallic species by modifying the surface stoichiometry of even such an inert support as MgO.

5.2.4. Larger Ni clusters on MgO

For small clusters with up to 10–20 atoms, the interaction with the support can play a direct role on the geometrical or electronic structure of the cluster, thus notably affecting its reactivity [212]. In this respect, point defects or morphological irregularities on the oxide surface can influence the chemical properties of the particle, hence its catalytic activity [16,213,214].

The interaction of very small clusters with point defects was addressed in a recent BP86 study of Ni species deposited on regular and defective sites of the MgO(001) surface, using models with Mg^{pp*}+PC embedding [178]. As defects, neutral F_s centers and paramagnetic F_s^+ centers with only one electron in the cavity were considered. The stability of two- and three-dimensional Ni clusters adsorbed on MgO was compared, allowing a discussion of the role of point defects at the surface in nucleation and growth of supported metal particles.

Small Ni clusters (up to Ni_9) were found to be weakly bound to the surface with adsorption energies of less than 100–200 kJ/mol per cluster. This result was obtained for moieties which all have four Ni atoms at the interface, so that the same number of oxide-Ni bonds is formed. A moderate increase of adsorption energy with cluster size was attributed to the enhanced polarizability of the cluster electrons. The metal polarizability is in fact an important ingredient of the interaction of metals on MgO. Weak binding and presumably small diffusion barriers suggest that not only isolated Ni atoms, but also (small) Ni clusters can easily diffuse on the surface at room temperature. Diffusion is terminated when a (small) cluster encounters a point defect like an oxygen vacancy, either neutral or charged. In that case, the adhesion energy becomes definitely larger, about 300 kJ/mol per cluster, and diffusion is expected to occur only at much higher temperatures.

In this respect, the cluster size, from which on the defect-induced perturbation on the electronic structure disappears, is a key quantity. The calculations showed [178] that effect of the surface defects on the adhesion energy decreases rapidly with cluster size. Thus, for particles of nanometer size, differences in the bonding to the substrate tend to vanish as the larger polarizability of the particle screens the effect of the defect and the relative effect of defect-related bonds become less important due to the larger number of metal-oxide bonds at the interface. However, because point defects are the most likely sites for the initial steps of nucleation, one has to expect that also large metal particles are still located at these sites unless the temperature is sufficiently high to permit diffusion of particles.

The mechanisms of nucleation and growth remain, to a large extent, unclear. The addition of one atom to a pre-existing cluster results in an energy gain which depends more on the size of the cluster than on the site where the cluster is grown. The energy released when one or more metal atoms are added to supported cluster depends only little on the site, a regular terrace site or an F_s center. The calculations on the Ni clusters showed that the energy released by adding a Ni atom to a supported cluster is much larger than the binding energy of the same single Ni atom to the MgO substrate. Therefore, atomic diffusion should stop when an atom encounters a cluster. Because both metal atoms and small clusters bind much more strongly at defects, these are the sites where cluster growth takes place.

Surface defects affect the growth mode of Ni clusters. On the regular MgO(001) surface, a two-layer structure of Ni_{12} (eight atoms in the first layer and four atoms in the second) is only slightly preferred over a three-layer isomer (four atoms in each layer), whereas preference for two-layer growth is more pronounced on F_s centers. This is a specific interface property because in the gas-phase the two Ni_{12} structures considered are almost iso-energetic, with the three-layer structure slightly more stable. Our results [178] show that surface

irregularities can play an important role in the stabilization of uncommon cluster shapes, with consequences on the chemical reactivity of the particles.

The latter point brings us to an important question in the field of catalysis by supported metal particles: to which extent is the chemical reactivity of a (sub-) nanocluster affected by the interaction with the substrate? Very few theoretical studies were dedicated to this problem, and most of them are related to the surface of MgO, an oxide which interacts weakly with the supported particle, as shown above. Still, the knowledge accumulated in the course of the years on the structure of surface defects and morphology of the MgO surface allows one to analyze some of the mechanisms which can modify the chemical properties of a supported cluster as a function of the site where nucleation has occurred.

In a recent study employing the same methodological approach, the reactivity of Ni clusters deposited on regular sites and oxygen vacancies (F_s centers) of MgO(001) was investigated [179]. Two-dimensional (2D) and three-dimensional (3D) metal deposits as well as the interaction of two single atoms, O and Na, with the Ni particles were considered. O and Na probes were chosen because they are representative of electronegative and electropositive adsorbed species, respectively. The calculations were performed for free and supported metal clusters, thus allowing a direct comparison of the electronic effects induced by the substrate on the cluster electronic structure.

In these calculations the O atom was placed at the center of the Ni_4 top layer (four-fold hollow position) because usually O adsorbs on open sites of metal surfaces [215]. On gas-phase square Ni_4 species, the adsorption of one O atom results in a strongly bound complex, D_e = 442 kJ/mol, with partial spin quenching. (On Ni surfaces, the heat of adsorption of atomic oxygen is experimentally determined to ~480 kJ/mol [215].) O adsorption is accompanied by a moderate expansion of the Ni-Ni distances, by 5 pm. When the O atom is adsorbed on the surface complex Ni_4/MgO, further elongation of the Ni-Ni bonds, additional spin quenching, and an increase of the adsorption energy (to 513 kJ/mol) result. This bond strengthening can be rationalized by the fact that the oxide anions at the surface provide an additional source of electrons for the supported cluster, favoring an increased electron charge transfer to the electronegative adsorbed oxygen atom. In fact, the interaction of O with metal surfaces and metal clusters is dominated by electron charge transfer toward the O atom. The change in the O/Ni_4 adsorption energy is even more pronounced when the Ni_4 cluster is deposited on F_s or F_s^+ centers with adsorption energies of 557 and 592 kJ/mol, respectively. The increase in the interaction energy for Ni_4/F_s is connected to the fact that two electrons trapped in the vacancy represent an additional source of electronic charge to compensate for the electron transfer from the Ni atoms to oxygen. In the case of Ni_4/F_s^+, the electrostatic interaction of the negatively charged O atom, $O^{\delta-}$, with the positively charged vacancy, F_s^+, increases the interaction energy even further. Thus, a 2D Ni cluster shows significant changes

in O adsorption properties depending on the site where the nucleation has occurred.

Now, we turn to the question whether substrate effects on adsorption properties can be observed also for 3D Ni clusters that consist of at least two layers of metal atoms. To this end the properties of O on a 3D Ni_8 cluster were analyzed [179]. For the isolated cluster, the binding energy and bond distances are very close to those found for O/Ni_4. When Ni_8 is deposited on the regular MgO surface, on F_s or F_s^+ centers, the chemisorption features are similar, with binding energies of 396–425 kJ/mol; distances between the adsorbed O and the Ni atoms do not depend on the MgO surface site where the cluster is placed. Also the effect of O adsorption on the total magnetic moment of the Ni_8 cluster is almost independent of the MgO nucleation site. Upon O adsorption, the distance of the Ni_8 cluster from the oxide surface increases only slightly for all sites, by 2 pm. This suggests that, at least for the case of O adsorption, the modifications in the electronic structure introduced by the bonding at the interface are largely restricted to the metal layer in direct contact with the oxide. In particular, the extension of the cluster-substrate distance is indicative of a reduced interface bond strength upon O adsorption.

Adsorption of an electropositive probe such as a Na atom provides another test of how the metal/oxide interface affects the properties of a deposited metal cluster. On metal surfaces the deposition of alkali metals at low coverage results in a net electron charge transfer to the metal surface [216]. For coverages below 0.1-0.2 monolayers, each Na atom transfers one electron to the substrate and becomes Na^+ [216]. The same effect is expected also on sufficiently large Ni clusters. As a direct measure of the charge transfer one can consider the dipole moment curve $\mu(z)$ for the vertical displacement z of Na with respect to the plane of the (top) Ni atoms. The shape of the dipole moment curve provides direct information about the ionic character of the bonding [217]. An ionic bond is characterized by a linear shape of the curve with a sufficiently large slope, $d\mu/dz$. Small values of the slope and/or deviations from linearity are expected for covalent bonds [217]. On a free Ni_4 cluster, the dipole moment curve for an adsorbed Na atom indicates the full cation character of the Na adsorbate. A similar slope is found for $Na/Ni_4/MgO$. On the other hand, a much smaller slope and a deviation from linearity of the dipole moment curve $\mu(z)$ was calculated for $Na/Ni_4/F_s$, i.e. for the same Ni_4 cluster adsorbed near an oxygen vacancy [179]. Hence, only a partial electron charge transfer occurs from Na to the cluster bound to an F center because the two electrons, trapped in the defect cavity, are partially transferred to the Ni cluster which becomes negatively charged. This, in turn, reduces the propensity of Na to transfer its valence s electron to the Ni cluster and results in an increase of the covalent character of the Na-Ni bond. Thus, the interaction with the substrate strongly modifies the electronic structure of the adsorbed cluster. Things change when one goes from

a 2D Ni_4 to a 3D Ni_8 cluster. In fact, adsorption of Na on free and supported Ni_8 moieties is similar, implying that the effect of the metal-oxide substrate is largely restricted to the metal atoms in direct contact with the substrate [179].

In summary, point defects at oxide surfaces are centers where nucleation and growth of metal clusters and small particles occur. Whereas no effect of the support is expected on the electronic properties of a supported metal particle of 1 nm size or larger, very small metal aggregates may interact strongly with these defects and exhibit modified activity due to the interface bond. The example of the interaction of Ni_4 and Ni_8 clusters with the regular and defective surface of MgO and of the adsorption of O and Na atoms shows that very small, two-dimensional clusters are strongly perturbed by surface defect sites (F_s centers) where nucleation had occurred; the effect of the bonding on regular sites of the MgO(001) surface is much smaller. On the other hand, small three-dimensional clusters containing less than 10 atoms already show a notable screening of the electronic perturbation at the interface due to the presence of delocalized metal electrons. Nevertheless, significant differences in the adsorption properties are found also for these 3D clusters. A more detailed analysis of the bonding characteristics of the various metal atoms of the cluster, e.g. of the metal atoms in the first layer of the cluster which are at direct contact with the oxide, can provide a better understanding of the induced changes in electronic structure of the supported particle.

5.3. Reactivity of ultrafine supported Pd species on MgO

The role of point defects at the surface of MgO in promoting or modifying the catalytic activity of isolated metal atoms and clusters deposited on this substrate was investigated in recent years by considering the cyclization reaction of acetylene to form benzene, $3C_2H_2 \rightarrow C_6H_6$. This process has been widely studied on single crystal surfaces from UHV conditions (10^{-12}–10^{-8} atm) to atmospheric pressure (10^{-1}–1 atm) [218-221]. On the most reactive surface Pd(111) [222,223], the reaction proceeds via a stable intermediate C_4H_4, resulting from the addition of two acetylene molecules [224]. This intermediate has been characterized experimentally [225-227] and theoretically [228] and its structure is now well established. Once the C_4H_4 intermediate is formed, it can incorporate a third acetylene molecule to form benzene that then desorbs from the surface at a temperature of about 500 K [218,219].

The same reaction has been studied on size selected Pd clusters deposited on a MgO surface using a new experimental setup specifically designed to study the chemical properties of size selected metal clusters deposited on oxide substrates [229]. In this experiment neutral and charged Pd clusters are produced by a laser evaporation source, then guided by ion optics through differentially pumped vacuum chambers and finally size-selected by a quadrupole mass spectrometer. The monodispersed clusters are deposited with low kinetic energy (0.1-2 eV)

onto a MgO thin film surface. The cluster-assembled materials obtained in this way exhibit a peculiar activity and selectivity in the polymerization of acetylene to form benzene and aliphatic hydrocarbons [229]. Temperature programmed reaction (TPR) spectra for the cyclotrimerization of acetylene on supported Pd_n ($1 \leq n \leq 30$) clusters show that Pd_1, Pd_2, and Pd_3 species form exclusively benzene at temperatures around 300 K. For Pd_7, an additional desorption peak of benzene is clearly observed at about 430 K. For Pd_8 this second feature becomes as important as the peak at 300 K and for Pd_{30} particles benzene mainly desorbs around 430 K. On a clean MgO(100) surface, no benzene is produced at the same experimental conditions. This size-dependent behavior is related to the distinct electronic and geometric properties of the metal clusters, making this new class of materials extremely interesting for understanding structure-property relationships. The results show that even a single Pd atom can produce benzene [16]. This has stimulated the study of the activity of the Pd atoms as function of the support where it is deposited or of the sites where it is bound [214,230].

In the following we briefly review crucial aspects of the cyclization reaction over supported Pd atoms, looking in particular at the role of various types of morphological defects present on the MgO surface, and we analyze the electronic effects involved in the metal-support interaction.

The possibility to catalyze the acetylene trimerization depends crucially on the ability of the metal center to coordinate and activate two C_2H_2 molecules and then bind the C_4H_4 intermediate according to reaction:

$$Pd + 2C_2H_2 \rightarrow Pd(C_2H_2)_2 \rightarrow Pd(C_4H_4) \qquad (5.1)$$

The activation of the acetylene molecules is easily monitored, for instance, by the deviation from linearity of the HCC angle due to a change of hybridization of the C atoms from *sp* to sp^2, or by the elongation of the C-C distance as a consequence of the electron charge transfer from the metal 4*d* orbitals to an empty π^* orbital of acetylene. This process can be followed by optimizing the geometry of one and two acetylene molecules coordinated to an isolated Pd atom, and of the corresponding $Pd(C_4H_4)$ complex. One acetylene is strongly bound to Pd, by almost 200 kJ/mol (BP86 results [16]); the second acetylene molecule is bound by 96 kJ/mol. Also the C_4H_4 intermediate is quite strongly bound to the Pd atom and is more stable than two adsorbed acetylene molecules. Similar results were obtained for the Pd(111) surface [228]. A single C_2H_2 adsorbate is more strongly activated, consistent with the idea that the electron density on the metal is essential for promoting the molecular activation. However, it should be kept in mind that stronger bonding may imply a larger barrier for conversion of two C_2H_2 moieties into C_4H_4. The following step, $C_4H_4 + C_2H_2 \rightarrow C_6H_6$, requires that the metal center is capable of coordinating and activating a third acetylene molecule according to reaction:

$$Pd(C_4H_4) + C_2H_2 \rightarrow Pd(C_4H_4)(C_2H_2) \rightarrow Pd(C_6H_6) \qquad (5.2)$$

However, the third C_2H_2 molecule interacts very weakly with $Pd(C_4H_4)$ with a binding energy less that 30 kJ/mol. The structure of the third molecule is not deformed compared to the gas-phase. The molecule is bound to the $Pd(C_4H_4)$ complex by dispersion forces only and its distance from the Pd atom is therefore very long, ~260 pm. This result indicates that *an isolated Pd atom is not* a catalyst for the cyclization process, at variance with the experimental observation for Pd_1/MgO.

The role played by the support becomes therefore a critical aspect of the interaction. As we have seen in Subsection 5.1.1, the Pd-MgO bonding is not characterized by a pronounced charge transfer and is better described as covalent polar. In this respect one can put forward two hypotheses. One states that the surface O anions of the MgO surface still have some oxidizing power to deplete charge from the metal atom. The other possibility is that the O anions are fully reduced, O^{2-}, and donate charge to the metal atom, thus leading to electron enriched species (the surface acts as a Lewis base). In the two cases, one would end up with positively or negatively charged supported Pd atoms, respectively. In principle, both situations can lead to an activation of the supported metal. In fact, the bonding of unsaturated hydrocarbons to metal complexes and metal surfaces is classically described in terms of σ donation from a filled bonding level on acetylene to empty states on the metal and π back-donation from the occupied *d* orbitals on the metal to empty antibonding π^* orbitals of the ligand [231,232]. Both mechanisms result in a weakening of the C-C bond and a distortion of the molecule. A simple model study where the charge on Pd was artificially augmented showed that charge on Pd center, either positive or negative, reinforces the bonding of acetylene to the complex $Pd(C_4H_4)$; however, a substantial activation of the third acetylene molecule was found only for negatively charged (electron-rich) Pd atoms [16]. Thus, increase of the electron density on Pd is a key mechanism to augment the catalytic properties of the metal center; the substrate increases the required "basic" character of the Pd atoms (or clusters).

When Pd is deposited on MgO, the activation of C_2H_2 is much more efficient than for an isolated Pd atom. The structural distortion of adsorbed C_2H_2 follows the trend corner > edge > terrace > free atom. The contribution of the electron charge transfer from acetylene to Pd or Pd_1/MgO, the σ donation in the Dewar-Chatt-Duncanson model [231,232], is similar in the four cases, and is much smaller than the charge transfer in the other direction, i.e. from Pd or Pd_1/MgO to acetylene. This corroborates the finding that the interaction with the MgO substrate increases the basic character of the Pd atom. The donor capability of Pd increases as a function of the adsorption site on MgO in the order terrace < edge < corner, the same order found for the deformation of the acety-

lene molecule. Therefore, one can conclude that (i) the substrate plays a direct role in modifying the properties of supported Pd atoms, and (ii) low-coordinated sites are more active than regular terraces. This is consistent with the idea that the degree of surface basicity in MgO is larger for the low-coordinated anions because of the lower Madelung potential at these sites.

In principle there are several defect sites which can be active in promoting the catalytic activity of a deposited Pd atom. The surface of polycrystalline MgO presents in fact a great variety of irregularities like morphological defects, anion and cation vacancies, divacancies, impurity atoms, etc. Recent studies concluded that even MgO thin films deposited on a conducting substrate are not completely defect free, as shown by the different adsorption properties of CO on MgO thin films and single crystal surfaces [111]. Therefore, it is difficult to determine which defect sites of an MgO surface are most likely involved in the acetylene trimerization. To contribute to a clarification of the role of defects, the structure and stability of Pd atoms, $Pd(C_2H_2)$, $Pd(C_2H_2)_2$, $Pd(C_4H_4)$ and $Pd(C_2H_2)(C_4H_4)$ complexes formed on various regular and defect sites at the MgO surface was investigated [230]. In particular, Pd-hydrocarbon complexes were studied on O sites as well as on neutral (F) and charged (F^+) oxygen vacancies.

Let us consider the reactivity of the supported Pd atoms. A Pd atom bound at terrace sites is able to add and activate one or two acetylene molecules and to form a stable $Pd(C_4H_4)/O_{5c}$ complex. However, a third acetylene molecule is not activated. The situation is reminiscent of that of an isolated Pd atom where the third acetylene is weakly bound by dispersion forces. Therefore, the complex is unstable and acetylene does not bind to $Pd_1(C_4H_4)/O_{5c}$. The situation is only slightly better on low-coordinated O sites. Formation of $Pd(C_4H_4)$ on four- and three-coordinated O anions and subsequent addition of a third acetylene molecule results in surface complexes $Pd(C_2H_2)(C_4H_4)/O_{4c}$ or $Pd(C_2H_2)(C_4H_4)/O_{3c}$ which are very weakly bound or even unbound. Thus, also O anions at low-coordinated defects are not good candidates for increasing the catalytic activity of supported Pd atoms.

Things are different on F and F^+ centers located on various sites. They all show a similar activity, forming a stable $Pd(C_4H_4)$ complex and substantially stabilizing a third acetylene molecule; the strength of the bonding of C_2H_2 to the supported $Pd(C_4H_4)$ complex is larger than for the morphological defects and becomes quite substantial, 200 kJ/mol, for a neutral F_{3C} center. The degree of activation is comparable in the three cases, with C-C distances of ~131 pm and HCC angles of ~140 degrees. Thus, F centers are promoting the catalytic activity of the deposited Pd atoms.

The study of the cyclization reaction of acetylene to benzene on Pd atoms supported on MgO allows one to clarify some of the experimental aspects and to draw some general conclusions about the role of defects on oxide surfaces. The results show that *only in the presence of surface defects a single Pd atom*

becomes an active catalyst for the reaction. In fact, an isolated Pd atom is not capable to add and activate three acetylene molecules, an essential step for the process. The change in the electronic structure of supported Pd is connected to the electron donor ability of the substrate, which does not simply act as an inert substrate. The oxide surface acts much in the same way as a ligand in coordination chemistry and provides an additional source of electron density, which increases the capability of the Pd atom to back donate charge to the adsorbed hydrocarbon. In this respect it is remarkable that on transition metal complexes the acetylene trimerization reaction follows a very similar mechanism as on heterogeneous supported catalysts [233]. Oxide anions of the MgO(001) surface, located either on terraces, steps, or corners, do not change significantly the catalytic activity of supported Pd. The Lewis basicity of these sites is not sufficient to significantly increase the electron density on the metal. The situation is completely different on oxygen vacancies, F or F^+ centers. Due to the electron(s) trapped in the cavity left by the missing O, these centers are good basic sites and promote the activity of an adsorbed Pd atom.

6. TRANSITION METAL PARTICLES IN ZEOLITE CAVITIES

6.1. Supported mononuclear Rh species in zeolites

As an example of *d*-metal cations in zeolites we studied monatomic Rh^I moieties in FAU [234,235]. Three different locations of the cationic species typical for this kind of zeolites were considered – a four-ring (T4), a six-ring (T6), and a three-fold hollow position (T5) next to an Al center (modeled as a four-membered ring with an additional $OSiH_3$ group attached at the Al atom [234]). The calculations showed that at four- and six-rings, a Rh^I ion is bound to the two O centers of the ring connected to the Al center, as a consequence of their high basicity. At the four-ring, Rh^I interacts with those two O atoms that are on the same side of the ring, whereas at the six-ring the cation is exactly in the plane of the T-atoms because this is the only position that allows interaction with the O centers of both Al-O-Si bridges in the ring. At the cluster T5, Rh^I is bound to the O atom of the Al-O-Si bridge and the two closest O centers of the four-ring.

$Rh^I(CO)_2$ complexes in zeolites and on metal oxide surfaces are stable and well characterized [234,236,237]. We tried to elucidate the structure of the complex based on a comparison of computational results with experimentally derived properties. Stable structures for $Rh^I(CO)_2$ species were found at four-rings, T4 and T5 model clusters, but not at the six-ring Al-1. In the optimized structure of the $Rh^I(CO)_2$ complex at the four-rings, T4 and T5, both CO groups are located opposite to O_z-Rh bonds and pointing in the same direction. The whole system including the Rh^I cation, both zeolite O centers bound to it, and two CO ligands, forms an essentially planar, four-ligand pseudo-square complex, similar to classical inorganic and organometallic complexes of Rh^I cations.

EXAFS experiments of the $Rh^{I}(CO)_2$ complex in DAY zeolite [234] provided an excellent opportunity to compare the interatomic distances derived from EXAFS spectra with the calculated structural data. Good agreement between the EXAFS parameters and the optimized structure of the $Rh^{I}(CO)_2$ complex on a zeolite four-ring support the hypothesis that the system $Rh^{I}(CO)_2$/DAY is correctly modeled by the calculated T4 structure (Table 4.4). Also the computed C-O vibrational frequencies of this system are close to those from IR spectra [234,236,237], with deviations below 12 cm^{-1} (Table 4.4).

Whereas dicarbonyl complexes $Rh^{I}(CO)_2$ are very stable surface species, monocarbonyls could be formed only after a special treatment of the dicarbonyls [237]. Therefore, the identification of the complex $Rh^{I}(CO)_2$ in DAY zeolite were useful in the assignment of the IR bands corresponding to $Rh^{I}(CO)$ monocarbonyl complex in this type of zeolites [235]. Earlier, an IR mode with a frequency value $\omega(CO)$ = 2093 cm^{-1} on DAY between those of the symmetric and antisymmetric CO modes of the corresponding $Rh^{I}(CO)_2$ dicarbonyls was suggested to originate from monocarbonyls [237]. However, our modeling and the analysis of experimental data suggested that the C-O frequency of the monocarbonyl complex $Rh^{I}CO$ supported on DAY is 2014 cm^{-1}, i.e. smaller than the frequencies of both symmetric and antisymmetric CO modes of the corresponding stable Rh^{I} dicarbonyls [235]. We assigned the experimental band at

Table 4.4

Comparison between calculated interatomic distances (in pm) and frequencies (in cm^{-1}) for the model rhodium dicarbonyl T4 complex and experimental EXAFS parameters and IR spectra of supported $Rh^{I}(CO)_2$ on zeolite DAY.

Interatomic	Calc.		EXAFS[a]	
distances	Number	*r*	Number	*r*
Rh-C	2	188	2.2	186
Rh-O(CO)	2	303	2.3	296
Rh-O(Zeo)	2	219-220	1.9	215
Rh-Al	1	280	1.1	273
Rh-X	1	324-333	1.0	331
Vibrational	Calc.[b]		IR spectroscopy[c]	
frequencies	Symm.	Antisymm.	Symm.	Antisymm.
$Rh^{+}(^{12}CO)_2$	2114	2060	2118-2115	2053-2049
$Rh^{+}(^{12}CO)(^{13}CO)$	2100	2025	2108-2100	2021-2018

a) Experimental data derived from EXAFS measurements [234]. b) C-O stretching mode corrected by 32 cm^{-1} according to the difference between calculated 2111 cm^{-1} and experimental 2143 cm^{-1} C-O frequencies [234]. c) Experimental data derived from IR spectra [234,236,237]

Table 4.5

Assignment of the IR bands of supported Rh^I carbonyl complexes based on calculations and comparison with experiment.

	System	$Rh^I(CO)_2$		Rh^ICO		$Rh^I(H)_2(CO)$[a]	$Rh^IH_2(CO)$[a]
				new[a]	*old*[b]		
Calc.	$Rh^I(CO)_2$/zeo[c]	2114	2060	2046		2076	2096
Exp.	On DAY[d]	2118	2053	2014	2093	2093	2093
	On Al_2O_3[e]	2099	2028	1984	2061	2061	2061
	On TiO_2[f]	2104	2028			2078	2078
	In n-hexane[g]	2084	2015	2001			
	In cyclohexane[g]	2082	2013	1996			
	In THF[g]	2081	2010	1970			

a) Our assignment, Ref. 235. b) Earlier assignment of Refs. 237,240. c) Ref. 234,235. d) Ref. 237. e) Ref. 240. f) Ref. 238. g) Experimental data for $[Rh^I(CO)_2(acac)]$ complex in the corresponding solvent, according to Ref. 239.

2093 cm^{-1} on DAY to mixed complexes $Rh^IH_2(CO)$ or $Rh^I(H)_2(CO)$, containing either a dissociated or an molecular H_2 species as an additional ligand (Table 4.5) [235]. Following the similarity of Rh^I carbonyl complexes on DAY zeolite and alumina, we extended our argument also on alumina-supported species [240] where the correct assignment of the C-O bands is 1984 cm^{-1} for the Rh^ICO complex and 2061 cm^{-1} for its hydrogen containing derivatives.

6.2. CO adsorption on electronically modified Pt_4 models

As platinum is especially important in catalysis, strong experimental efforts have been made to characterize small Pt particles entrapped in zeolite cages, using the whole arsenal of spectroscopic, structural and chemical methods (e.g. Refs. 200, 241, 242 and references therein). However, the interpretation of experimental data often remained ambiguous because the measured values commonly reflect more than one effect: as a rule, when the electronic state of an encapsulated metal species changes due to interactions with the zeolite host, so do its size and shape. Model calculations enable to separate these effects.

With a scalar relativistic DF study [243] we aimed at analyzing adsorption properties (binding, geometric and electronic structure, vibrations) of CO probe molecules bound to small platinum clusters; we focused on how these properties depend on the cluster charge and the adsorption site. To mimic encapsulated metal species that become (partially) charged due to interactions with the zeolite framework, we employed bare neutral cluster Pt_4 as well as singly charged Pt_4^+ and Pt_4^- moieties and considered monocarbonyl complexes of them. We also investigated the systems XPt_4CO (X = Na, Na^+) to validate electronically

modified clusters as models of moieties interacting with electron donor (Na) or slight acceptor (Na^+) centers in zeolites which induce chemical effects on the electronic structure and the adsorption properties of the cluster Pt_4.

Calculated observables of adsorbed CO probes were found to be rather sensitive to the electronic state and the adsorption site of the Pt_4 particles [243], in line with experiment. We established a linear correlation between the effective charge of the metal cluster and the adsorption-induced vibrational frequency shift $\Delta\omega$(CO) for CO at on-top position, the energetically preferred adsorption geometry. With this correlation, we estimated the effective charge of metal particles that results from their interaction with the surrounding. Accordingly, the calculated properties of CO adsorbed on Na/Pt_4 and Na^+/Pt_4 are very close to those for CO bound to the appropriately charged clusters Pt_4^q with q = -0.35 e and 0.68 e, respectively. These electronically modified clusters, indeed, constitute useful models for describing electron-enriched and electron-deficient states of small platinum particles as induced by metal-support interaction. CO molecules were found to probe the charge of the metal clusters by means of the frequency ω(CO), irrespective of how this particular state was generated: either by directly modifying the (partial) charge of the cluster or by charge exchange resulting from metal-ligand or metal-support interaction.

Lately, an IR band with very low C-O frequency, $\Delta\omega$(CO) = -186 cm^{-1}, was measured for terminal CO molecules on Pt_n species, formed by decomposition of the Chini complex $[Pt_3(CO)_3(\mu\text{-}CO)_3]_3^{2-}$ in NaX zeolite [242]. That frequency shift was attributed to a negative charge of the encapsulated platinum cluster, in good agreement with our correlation [243].

6.3. Clusters Ir_4 in faujasites

EXAFS spectroscopy is the method of choice for structural characterization of very small supported clusters [244,245]. Because a large fraction of the metal species is in contact with the support, a notable part of the EXAFS signals is due to metal-support contributions, thus providing information about the metal-support interface. Conventional preparation techniques result in non-uniform supported metal species which are difficult to characterize in detail. Thus, Gates developed a strategy [244,246] to prepare nearly uniform encapsulated metal clusters by synthesis of zeolite-supported metal carbonyl cluster precursors and subsequent removal of the carbonyl ligands with minimal disruption of the metal frame. However, decarbonylation commonly leads to fragmentation or aggregation of metal clusters. Supported iridium clusters on metal oxides and zeolites (KLTL, NaX, and NaY) were comprehensively investigated [246] because these clusters feature rather stable metal frames such as Ir_4. Despite the substantial work on such samples, questions remained, associated with limitations of EXAFS spectroscopy and the lack of other suitable experimental techniques for investigating metal species dispersed in porous solids. To shed light on these

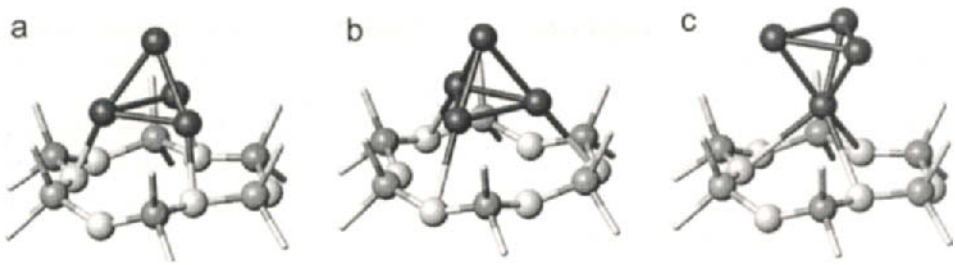

Fig. 6.1. Ir_4 cluster supported on a zeolite six-ring fragment $Al_3Si_3O_6H_{12}^{3-}$ in three conceivable configurations a, b, and c.

open questions, and in particular to clarify how the interaction with a zeolite framework can modify the structural and electronic properties of small supported metal particles, we carried out a DF study of the interaction between Ir_4 clusters and a zeolite fragment, using a cluster model of a FAU framework six-ring (Fig. 6.1) [247].

Two models were used to describe a T6 ring: the charged model Z, $Al_3Si_3O_6H_{12}^{3-}$, and the neutral model Z-Na, $Al_3Si_3O_6H_{12}Na_3$, where the negative charge induced by the presence of the three Al centers is compensated by three Na^+ cations, just as in alkali-exchanged zeolites. As to structure and energetics, the two models yield similar descriptions of the main features of the metal-support interaction. The resulting most stable structures, Ir_4(A)/Z and Ir_4(A)/Z-Na (Fig. 6.1 A), feature quite strong GGA BP86 binding energies, 357 kJ/mol and 260 kJ/mol, respectively. The shortest metal-oxygen distance r(Ir-O_1) was computed at ~220 pm. This value, in good agreement with EXAFS results [247], shows a close approach of the metal to the zeolite fragment. The computed Ir-Ir distances are slightly elongated, up to 6 pm, in comparison with the value r(Ir-Ir) = 244 pm calculated for a free tetrahedral metal cluster. This finding is at variance with EXAFS simulations which indicate an inter-metal distance r(Ir-Ir) $\cong$ 270 pm, very close to the corresponding values for $Ir_4(CO)_{12}$ (269 pm) and bulk iridium, 271.5 pm. This unusually large discrepancy (~20 pm) between calculated inter-metal distances of the bare Ir_4 cluster and the EXAFS result falls far outside the accuracy of relativistic AE DF calculations, in particular for M-M distances [247]. We analyzed possible reasons for this discrepancy [247]. For instance, a residuum at a supported cluster is conceivable as a result of the decarbonylation treatment during cluster preparation. Indeed, one C atom as extra ligand, at a two-fold bridge or a three-fold hollow site of the Ir_4 cluster, leads to an elongation of the Ir-Ir distance by as much as 20 pm. Therefore, further experimental investigation of possible undetected ligands of zeolite-supported clusters were initiated [248].

Furthermore, we employed a CO molecule adsorbed at the on-top site of the cluster Ir_4 to probe changes in its electronic structure induced by the support. When the zeolite substrate is described by the most realistic Z-Na model, the

interaction is accompanied by a small electron donation to the cluster, notable through a somewhat enhanced red shift of the C-O frequency.

The structural interpretation based on EXAFS data could be extended and improved by invoking our theoretical results [247] as follows. Zeolite-supported Ir_4 clusters bear only a small negative charge, if any. This statement may hold in general for noble metal clusters supported on metal oxides and zeolites. It is in line with the hypothesis of small, electron-rich Pt clusters formed in basic zeolites as a result of electron transfer from highly negatively charged framework O atoms [241]. Supported Ir_4 clusters are characterized by a moderate charge rearrangement in the bonding region between Ir and O atoms, accompanied by a polarization of the electron density toward the "top" site of the cluster. Such polarization might be responsible for some of the substrate effects observed in catalysis by supported metal clusters.

The EXAFS Ir-Ir distances manifest metal clusters that likely are not entirely ligand-free, even after decarbonylation and evacuation under mild conditions. EXAFS data are not sensitive enough to provide evidence of small numbers of ligands (in particular of light atoms) present in addition to the O atoms of the support. Computational models evidently provide a convincing method for establishing their likely presence, possibly in combination with IR spectra. Such experiments are expected to be challenging because the metal loading needs to be low and treatment under only moderately severe conditions to remove possible ligands (e.g., C that has been computed to bind strongly to Ir_4) readily induces restructuring of the metal frame.

6.4. Hydrogenation of Rh_6 clusters

Similarly to Ir_4 clusters just described, we found that the experimental metal-metal distances of Rh_6 clusters supported on Y zeolite [249], 267-269 pm, are than 8 to 20 pm longer than the optimized distances of ligand-free Rh_6 clusters in the gas-phase, 248-259 pm [250,251]. Just as with Ir_4 [247], variation of the cluster charge did not substantially affect the Rh-Rh distances. Similarly, our calculations also showed that adsorption of a ligand-free Rh_6 cluster on a zeolite fragment does not cause an elongation of the Rh-Rh bonds, sufficient for bringing them in agreement with experiment [250]. The adsorption energy (at the BP86 level) of the cluster Rh_6 on a neutral zeolite fragment containing three Si and three Al T-atoms compensated by three protons is estimated to 77 kJ/mol, i.e. only 26 kJ/mol per Rh-substrate bond. The latter value is notably smaller than that of tetrahedral Co_4 and Ni_4 clusters adsorbed on the regular sites of the MgO(001) surface, 64 and 75 kJ/mol, respectively [177] (see Subsection 5.2.4).

To inspect the influence of additional atomic "ligands" H, C, or O on the structure of Rh_6 species we modeled various structures of such complexes [250]. This study revealed that structures with impurity atoms inside the metal cluster are less stable than those with ligands coordinated at the cluster surface.

Accounting for relativistic effects on the cluster geometry resulted in shorter bonds, by 1 to 5 pm, for both Rh-Rh and Rh-ligand distances; also, the binding energy of the ligand atoms to the Rh_6 moiety increased, especially in the positions outside the cluster. Rh_6 clusters in C_3 symmetry with C or O atoms adsorbed at three-fold hollow sites featured two different types of Rh-Rh distances: 257-260 pm (similar to the ligand-free octahedral clusters) and a rather long one, 307-308 pm. When these clusters were supported on a zeolite fragment, the first type of Rh-Rh bonds became shorter, whereas the second type of distances elongated. Owing to the rather large difference between nearest and farthest neighbor Rh-Rh distances, $\Delta r \sim 50$ pm, of the optimized clusters containing C or O ligands, it is unlikely that such species correspond to the clusters described in the experiment [249].

H atoms at a three-fold hollow position outside the metal cluster lead to a shortening of the Rh-Rh bonds compared to the corresponding ligand-free clusters. An increase of Rh-Rh distance (by 10-30 pm) due to adsorption of H atoms was calculated for a bridging position; furthermore, among the structures studied, this bonding situation was identified as the most stable coordination of H ligands to the cluster Rh_6. Almost none of the studied structures of H-containing Rh_6 clusters fit the experimentally observed structural parameters of the cluster: either the average Rh-Rh distance was too short or the dispersion Δr between shortest and longest Rh-Rh distances was more than 20 pm. The structure, whose pertinent characteristics agreed best with available experimental data, was the model with three H atoms bound to Rh-Rh bonds on the sides of a twisted triangular prism with an average Rh-Rh distance of 264 pm and $\Delta r = 18$ pm. The relatively large value of Δr was substantially reduced to an acceptable value of 7 pm when the cluster was supported on zeolite, in the model $Rh_6(3H)/Z$ (Fig. 6.2). The latter cluster model represented best the experimental characteristics: the calculated average Rh-Rh distance was 262 pm, only 2 pm below the target interval defined by the EXAFS analysis and the corresponding experimental error [249,252]. In addition, the Rh-O_z distance of this structure, 218-220 pm, agrees well with the experimental values of 210-217 pm.

By analyzing the charge distribution of neutral and ionic clusters, we found that C and O ligands (impurity atoms) affect the electron density distribution on Rh atoms of the cluster in a different way [250]. In a cluster with a C impurity atom, the variation of the overall cluster charge influences mainly Rh atoms far from the ligand, whereas Rh atoms close to the ligand are affected in an O-ligated cluster. More importantly, we noted a polarization of the electron density of a bare Rh_6 cluster adsorbed on a neutral zeolite fragment (see Section 6.2); in that system, two types of Rh atoms occurred, carrying positive and negative charges $|q| \approx 0.3$ e. The charge distribution of supported clusters can be crucial for the catalytic activity because one type of Rh centers behaves as cations, whereas the reactivity of the other type of Rh atoms should be similar to that of

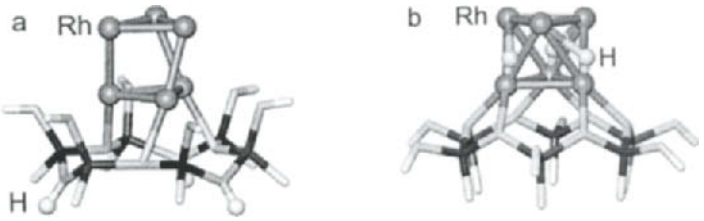

Fig. 6.2. Optimized structures of non-reactive, $Rh_6/Z(3H)$ (a), and reactive, $Rh_6(3H)/Z$ (b), adsorption of Rh_6 cluster on zeolite fragment.

electron-rich metallic species. Impurity atoms can cause a strong charge redistribution in supported clusters. After coordination of an impurity atom (H, C or O), only neutral or positively charged Rh atoms are present, resulting in a modified reactivity of the metal clusters. All impurity atoms studied, both in gas-phase and supported clusters, carry a negative charge and likely are also reactive.

To help clarify metal-support interactions and spillover effects, we compared two model systems that account for the interaction of bridging OH groups of zeolites with a supported cluster Rh_6 [251]. In the first model $Rh_6/Z(3H)$, the cluster is adsorbed on a model zeolite fragment with three bridging OH groups (Fig. 6.2a); this model represents "non-reactive" adsorption of Rh_6 on the zeolite. The structural data of the second model $Rh_6(3H)/Z$ (Fig. 6.2b) were found to agree [251] with EXAFS-derived geometric parameters of zeolite-supported Rh_6 species [249]. This structure can be considered as formed by reverse spillover from Rh_6/Z, where the protons of zeolite OH groups move to the Rh_6 cluster. The reactive structure with three H atoms on the cluster is by 370 kJ mol^{-1} more stable than the non-reactive model Rh_6/Z, i.e. about 120 kJ/mol per reacting OH group [251]. Based on the above structural comparison and the higher stability of the "reactive" structure $Rh_6(3H)/Z$, we concluded that zeolite-supported Rh_6 clusters prepared experimentally actually were not bare Rh_6, but were clusters decorated by H atoms, formed by migration of protons of zeolite OH groups onto the cluster by reverse hydrogen spillover.

In addition to the structural and energetic aspects of the interaction of Rh_6 with the support, our results indicated significant chemical changes in the supported cluster as diagnosed by an analysis of the charge distribution in the model systems, combining a Mulliken population analysis and core level binding energy shifts $\Delta E(\mathrm{Rh}3d)$. At variance with the polarization of the electron density of Rh_6 on a Z(3H) fragment mentioned before, the charge distribution in the reactive model $Rh_6(3H)/Z$ clearly showed oxidation of the "lower" layer of Rh atoms, likely to Rh^{I}. The charge of these Rh_z centers (in contact with framework oxygen atoms) was 0.76 e, and $\Delta E(\mathrm{Rh}3d) = 2.1$ eV. The charges of the "top" Rh_t atoms were close to zero, $q(Rh_t) = -0.04$ e, but their core levels are also strongly stabilized compared to those of the neutral gas-phase Rh_6 cluster, $\Delta E(\mathrm{Rh}3d) = 1.7$ eV. This high positive value of $\Delta E(\mathrm{Rh}3d)$ of Rh_t atoms was ascribed to the

presence of adsorbed protons and the resulting large positive formal charge on the cluster. An additional argument for the oxidation of Rh_z atoms as a result of the interaction with surface OH groups was based on a comparison of Rh_z-O distances. Measured (210-217 pm) and calculated (218-220 pm) Rh_z-O distances for zeolite-supported Rh_6 clusters are close to the corresponding experimental and calculated values of the cationic dicarbonyl complex $Rh^I(CO)_2$ supported on a zeolite, 216 pm and 219-220 pm, respectively (see Section 6.1). This observation suggests that the nature of the Rh atoms in the two types of supported species is similar, namely, the Rh_z centers bound to O atoms of zeolite in the supported Rh_6 cluster are oxidized and the resulting effective charge is similar to that of Rh^I in the supported dicarbonyl species.

Freund and co-workers [253,254] showed by XPS and IR spectroscopy that deposition of Rh particles on hydroxylated alumina entailed a consumption of surface OH groups. Simultaneously, XPS showed a stabilization of the Rh3*d* level by 0.3 eV (relative to the value of Rh particles on a OH-free surface). This finding can be rationalized by a direct chemical interaction of the metal particles with surface OH groups, including oxidation of some of the atoms to Rh^I, in line with trends of our computational models.

In general, our calculations showed that the interaction of small Rh clusters with support OH groups leads to oxidation of metal atoms in close contact with the support. Such redox processes of spillover may be quite general for small supported transition metal clusters, but it remains to be determined how these effects depend quantitatively on the metal, support, and metal cluster size.

The result of Sections 6.3 and 6.4 demonstrated how theory, used in concert with experiment, is helping to define opportunities for progress in research with supported metal clusters. Powerful computational tools will soon be able to routinely help identify reaction intermediates on supported heavy metal catalysts. Because reaction intermediates are inherently unstable, they are beyond the reach of current experimental methods such as *in-situ* EXAFS spectroscopy, which is likely to give evidence only of stable species.

7. TRANSITION METAL NANOCLUSTERS

Besides the obvious computational challenge, we would like to point out two aspects of transition metal particles of nanoscale size. First, such nanoclusters offer an excellent opportunity for mimicking so-called model supported metal catalysts which are characterized by a notably reduced complexity compared to the corresponding real metal catalysts on oxides [2,206]. Thus, such supported metal nanoclusters represent the limiting case of supported metal species opposite to metal atoms and dimers considered in Section 5. At variance with these smallest metal species on oxides, the electronic properties of metal nanoclusters are supposed to be essentially independent of the support in most of

the practical applications. In this section we describe our very recent DF results for supported model catalysts consisting of palladium nanoparticles [255,256].

The second aspect of nanosize meal clusters concerns the representation of single-crystal metal surfaces by cluster models [6,106], an approach which is able to compete successfully with the computational alternative that relies on slab models with periodic boundary conditions. The question to which extent cluster models of surface complexes are adequate for a problem under study represents a central issue for metal substrates where electrons are highly polarizable and localized bonds, common in chemical compounds, are absent. Fortunately, many parameters of adsorption complexes on metals, e.g., structural and vibrational features, are hardly sensitive to the size (and shape) of a sufficiently large substrate cluster model. This allows one to reliably estimate a variety of observables required for rationalizing experimental data on adsorption complexes at transition metals, employing moderately large cluster models. However, it is a well-known problem to achieve an accurate description of the *adsorption energy* on metals in the model cluster approach due to the very slow cluster size convergence of this property [257-260]. Recently, we proposed an advanced cluster model strategy [255] employing symmetric three-dimensional nanoparticles that helps to overcome this difficulty and improves the precision of calculated adsorption energies; we will outline this approach in the following using the surface Pd(111) and the adsorbate CO as an example.

7.1. Nanocluster models of single crystal metal surfaces: CO/Pd(111)

Adsorption energies on metals calculated in a cluster approach often show considerable oscillations with size and shape of the cluster models because such (finite) clusters describe the surface electronic structure insufficiently [257-260]. These models may yield rather different results for the Pauli repulsion between adsorbate and substrate, depending on whether pertinent cluster orbitals localized at the adsorption site are occupied or empty. The discrete density of states is an inherent feature of clusters that may prevent a correct description of the polarizability of a metal surface and thus hinders cluster size convergence of adsorption energies [257]. Even embedding of metal clusters does not offer an easy way out of this dilemma [260,261]. Anyway, the form of conventional moderately large cluster models may be particularly crucial. Such models are inherently "two-dimensional" with substrate atoms from two or three crystal layers usually taken into account; thus, a large fraction of atoms at the cluster boundaries lacks proper coordination.

Size *and shape* requirements of metal cluster models for reaching convergence of the chemisorption energy constituted the main topic of our study [255]. To reach convergence, we proposed to use symmetric models that can be accurately treated for clusters comprising of up to more than hundred atoms. A series of octahedral and cuboctahedral palladium clusters was considered, from Pd_{55} to

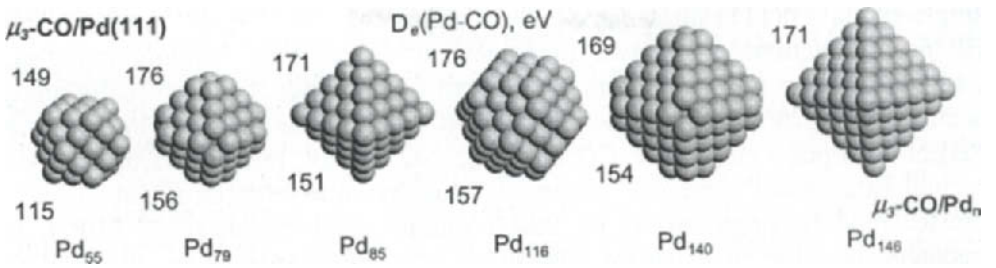

Fig. 7.1. Summary of the calculated BP86 adsorption energies D_e,(Pd-CO), kJ/mol, of CO molecules on three-fold hollow sites of the (111) facets of the cluster models Pd_{55} – Pd_{146} for fixed bulk-terminated (upper numbers) and optimized (low numbers) geometries [255].

Pd_{146} (Fig. 7.1.), in the geometry fixed as in Pd bulk with r(Pd-Pd) = 275 pm. These metal species exhibit eight hexagonal (111) facets with an fcc or hcp hollow site in the center, where an adsorbate can be placed in a symmetric fashion. The code PARAGAUSS allows full exploitation of the high symmetry and thus makes such large heavy-metal particles computationally tractable, even at accurate the AE scalar relativistic level, which we adopted for studying the adsorption of single CO molecules on the (111) facets of these clusters. In particular, we focused on the interaction of CO (one molecule per facet) with the three-fold hollow sites and inspected how calculated adsorption parameters vary with cluster size. We also considered how computed observables for that adsorption position on cluster facets relate to adsorption properties of the same site at the single crystal surface Pd(111). Based on results of slab model calculations [262,263] we neglected the very small difference in CO adsorption energy at the fcc and hcp hollows of a Pd(111) surface in our analysis.

The calculations [255] yielded not only rather uniform interatomic distances and C-O vibrational frequencies but also adequate *adsorption energies* for the substrate models starting from Pd_{79}: the adsorption energy per CO molecule varied in a very narrow range of 7 kJ/mol only, showing almost no size effects already for models of about 80 Pd atoms. This is a very important finding, which demonstrates that convergence of adsorption energies on a *d*-metal surface can be reached for moderately large cluster models. For that purpose, these models should feature a compact form terminated by low-index crystal facets. Such models, with shapes close to spherical, eliminate the effect of too low coordination of metal atoms at the boundaries of conventional cluster models and they appear to enable a sufficiently accurate representation of the polarizability of a metal surface.

The "converged" cluster model adsorption energy of CO *agreed quantitatively* with the values obtained for periodic slab models. Note that only results obtained with the same xc functional can be directly compared [187]. At the BP86 level, the adsorption energy of CO at the hollow position of cluster models, ~174 kJ/mol, is by ~30 kJ/mol larger than the experimental value for the

single-crystal Pd(111) surface at a low coverage, 142–149 kJ/mol [264,265]. The BP86 xc functional is known to somewhat overestimate binding energies, whereas energies calculated with the modern PBEN functional are usually more accurate [263,266]. Our results [255] also support this finding: indeed, the PBEN adsorption energy for CO on Pd_{140}, 142 kJ/mol, reproduces the experimental value with "chemical" accuracy. Thus, by combining three-dimensional cluster models, proposed by us, and accurate xc potentials, e.g., PBEN, it becomes possible to calculate adsorption energies on metals in *quantitative agreement* with experiment.

The calculated harmonic vibrational frequency ω(C-O) ~ 1755 cm^{-1} is by a factor 1.04 smaller than the value 1825 cm^{-1} measured at very low CO coverage on Pd(111) [267]. Such a frequency underestimation in gradient-corrected DF calculations is a general feature of common GGA xc functionals, in particular for bonds involving transition and other heavy atoms [34,53]. In cases of stronger interactions, LDA geometric parameters and vibrational frequencies are often more accurate than GGA values; gradient-corrected functionals appear to "improve" *only* the energetics [53]. For systems such as CO/Pd with bonds between heavy *d*-metal atoms and metal-molecule bonds, an xc functional for a sufficiently precise representation of *both* geometric observables *and* binding energies is still a desideratum.

7.2. Pd nanoclusters to represent supported model catalysts

We just saw that nanoclusters with Pd-Pd distances fixed as in Pd bulk enable an adequate description of adsorption complexes at the single-crystal (111) surface. An obvious next question explores how adsorption and other parameters of such clusters change when cluster relaxation is allowed. It is also related to the issue to which extent "real" metal clusters with a diameter of ~2 nm are able to model characteristics of notably larger metal particles and bulk materials. We examined these issues by fully relaxing (within O_h symmetry) the structure of the clusters Pd_{55} – Pd_{140} and by probing subsequently the propensity of these relaxed clusters to bind CO molecules, based on GGA BP86 calculations [255].

The variation of the average Pd-Pd distance in a series of Pd_n clusters, ~2 pm, is only a fraction of the difference between the average Pd-Pd distance in the largest system Pd_{140} and the ~5 pm longer extrapolated value for Pd bulk. Therefore, the average bond length of clusters with about hundred Pd atoms still differs significantly from the extrapolated value. This manifests the relatively slow cluster size convergence of the average bond length and implies some difference in the adsorption properties of the "infinite" surface planes of bulk materials and the corresponding facets of the smallest nanoparticles. More results on the scaling of metal cluster properties can be found elsewhere [268, 269 and references therein].

Results calculated for CO adsorption complexes on Pd_n nanoclusters ($79 \leq n \leq 140$) with the fully optimized structures showed a minor influence of the cluster geometry optimization on the bond lengths Pd-C and C-O, ~1 pm only. The C-O vibrational frequency on optimized Pd clusters is somewhat larger, by 10–20 cm^{-1}, than that for the Pd_n congeners with fixed geometry. The CO adsorption energy is reduced by ~10% (or 2 kJ/mol at most) compared to the fixed-cluster value. This modest energy alteration as well as rather small changes of other adsorption parameters provide a measure of the difference between cluster and bulk properties. Based on these data we concluded [255] that ordered Pd clusters with diameters as small as ~1 nm (nuclearity ~80) are able to reproduce structural features and vibrational frequencies of adsorption complexes on the corresponding sites of the infinite Pd substrate almost with the inherent accuracy of the employed DF computational method. This conclusion is in line with experimental findings that ordered Pd clusters with nuclearity ≥300 on alumina films exhibit a reactivity which differs from that of extended metal surfaces *mainly* due to an enhanced concentration of specific defects, e.g., edge or step sites [2,206,270].

The issue of various adsorption sites featured by supported Pd nanoparticles was also dealt with in our work [256]. There, the adsorption of CO on nanosize Pd particles was studied theoretically by a DF method (BP86) and spectroscopically by means of IR reflection absorption spectroscopy (IRAS) and sum frequency generation (SFG). Three-dimensional crystallites of about 140 atoms (chosen as fragments of fcc Pd bulk as justified above), that exhibit (111) and (001) facets, were studied in GGA BP86 calculations. Various types of adsorption sites were inspected: three-fold hollow, bridge, and on-top positions at (111) facets; four-fold hollow and on-top sites at (001) facets; bridge positions at cluster edges; on-top positions at cluster corners and on single Pd atoms deposited at regular (111) facets. To correlate the theoretical results with experiment, CO adsorbed on supported Pd nanocrystallites of different size and structure (well-faceted and defect-rich) were also studied with IRAS and SFG spectroscopies.

Selected DF results are summarized in Fig. 7.2. We showed that adsorption properties of rather small (111) and (001) cluster facets are similar to those of the corresponding ideal (infinite) Pd surfaces. In particular, on regular (111) facets of Pd clusters, CO adsorption at three-fold hollow positions is energetically preferred compared to bridge and on top sites, just as at the ideal Pd(111) surface [264,265]. This conclusion is also valid for adsorption sites in the vicinity of cluster edges and corners; they are characterized by even *lower* calculated adsorption energies. The strongest CO bonding was computed at bridge positions of cluster edges where the adsorbate binds to low-coordinated Pd centers. Consequently, at low CO pressures, such adsorption sites at cluster edges were predicted to be occupied first, in line with the experimental finding

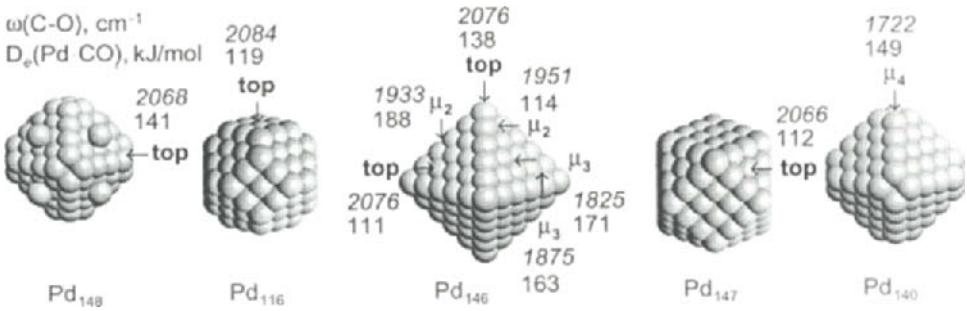

Fig. 7.2. Summary of the calculated BP86 adsorption energies D_e,(Pd-CO), kJ/mol, and vibrational frequencies ω(C-O), cm^{-1}, of CO molecules adsorbed on various sites of palladium nanoclusters [256].

that the signal from bridge bonded CO (at ~1975 cm^{-1}) is observed for supported Pd clusters already at very low pressure [271-273]. On-top adsorption on low-coordinated Pd centers (cluster corners and surface kinks) was calculated stronger than at on-top positions of regular (111) and (100) facets. This rationalizes the experimental observation that occupation of on-top positions on smaller and defect-rich supported Pd nanoparticles starts at much lower CO pressures than on larger well-faceted particles [272,273]. Comparing theoretical results with vibrational spectra of CO on different types of Pd nanoparticles, supported on a well-ordered Al_2O_3 film, it became clear that a dominating absorption band observed in the frequency region between 1955 cm^{-1} and 1970 cm^{-1} has to be assigned to CO adsorbed in a bridge-bonded fashion at particle edges and at edge-like defect sites.

These results for a specific systems demonstrate convincingly that studies of nanosize cluster present a challenging subject, worthwhile for both experimental and theoretical efforts.

8. SUMMARY AND OUTLOOK

In this chapter, we reviewed DF cluster model studies of surface complexes on ionic metal oxides (MgO, α-Al_2O_3) and in zeolites. We considered a wide range of adsorbed or deposited species: molecules (CO, N_2, CH_4, CH_3OH, C_2H_2, C_6H_6), main group (alkali and alkaline-earth ions) and *d*-metal atoms (Ni, Pd, Pt; Cu, Ag, Au; Cr, Mo, W; Re), small transition metal clusters (Co, Ni, Pd, Pt, Rh, Ag, W, Ir, Os), and finally models of supported palladium nanoclusters. A major part of these studies was devoted to clarifying structural and bonding features of surface systems as well as to rationalizing or predicting results of spectroscopic and chemical experiments. We also addressed method-oriented investigations on the applicability and accuracy of the employed computational methods and models. In particular, we discussed (i) advanced approaches of cluster embed-

ding in an elastic polarizable environment to improve the description of long-range electrostatic effects and interactions at strongly relaxed surfaces of oxide materials and we presented (ii) a strategy to describe adsorption properties (and the reactivity) of metal surfaces and supported metal nanoparticles by means of symmetric three-dimensional cluster models of nanometer size.

For the touchstone adsorbate CO on the ideal MgO(001) surface we demonstrated how increasingly sophisticated cluster embedding and more accurate xc potentials gradually lead to theoretical description based on a very weak adsorption bond with the energy of ~10 kJ/mol only, recently corroborated by experiment. On the other hand, the binding of CO molecules at the regular α-Al_2O_3(0001) surface is computed notably stronger, concomitant with a larger adsorption-induced C-O vibrational frequency shift; the bonding is reminiscent to that of CO adsorbed at corner cations of MgO. CH_4 and C_2H_2 molecules were calculated to be bound on MgO even weaker than CO. Thus, a dependable structural assignment of these complexes required, beyond energetic arguments, a comparison of reliably calculated and accurately measured vibrational spectroscopy "signatures".

In zeolites, we examined properties of three kinds of active sites: (i) bridging OH groups (Brønsted acid centers); (ii) charge-balancing extra-framework metal cations; (iii) basic oxygen centers close to Al atoms. We analyzed factors that affect the Brønsted acidity of the bridging OH groups. To rationalize IR spectroscopy findings for methane in Cs-Y zeolites, we proposed bifunctional coordination of CH_4 to both a Lewis acidic site (Cs^+) and a basic framework O site. Modeling of adsorption complexes with methanol molecules, that can interact with both acidic and basic sites of zeolites, lead to a correlation of the proton affinity of substrate O atoms with the IR frequencies of an adjacent CH_3OH adsorbate.

Our systematic investigation of single *d*-metal atoms adsorbed on the ideal surface MgO(001) showed that many of them interact weakly with surface O^{2-} anions, mainly due to polarization; notably stronger bonds, of covalent polar origin, but almost without any metal/oxide charge transfer, were calculated for Ni, Pd, Pt, and W atoms. Pd and Pt atoms interact with the regular α-Al_2O_3(0001) surface in a rather similar manner as with MgO(001). Like the monatomic adsorbates, very small supported *d*-metal species on oxides also tend to occupy positions where their atoms are in the vicinity of O^{2-} anions. Due to the competition between metal-metal bonds and (weaker) metal-oxide bonds, adsorbed *d*-metal moieties prefer structures similar to their gas phase structure. Metal particles can interact with an oxide substrate notably stronger when surface defects are exposed. For instance, the adsorption bonds of a $Re(CO)_3$ fragment at a corner Mg vacancy on MgO are as strong as bonds in common oxo coordination compounds; the surface adsorption site acts a polydentate ligand. Especially spectacular substrate effect on the activation of supported

metal species were found and rationalized for the system Pd_1/MgO: in the presence of surface defects, a single Pd atom becomes, due to extra electron density donated by the support, an active catalyst of acetylene trimerization.

Model studies of Ir_4 and Rh_6 moieties in zeolite cavities led to a revision of the original interpretation of EXAFS results: measured metal-metal distances are indicative for supported clusters which are not entirely ligand-free; likely, these cluster interact with light atoms in addition to the O centers of the support. In line with the results for metal species on regular MgO and α-$Al_2O_3(0001)$ substrates, the interaction of small *d*-metal clusters with a zeolite fragment was found to induce hardly any charge redistribution between the metal species and the substrate; a slight accumulation of electron density was noticeable for various transition metal moieties.

The well-known challenge to describe adsorption energies on metals with a model cluster approach was overcome with our proposition to employ a cluster model strategy based on symmetric three-dimensional nanoparticles. On such Pd nanoclusters, starting already from about 80 metal atoms, the adsorption energy of CO molecules is essentially converged. Furthermore, this novel strategy of three-dimensional nanosize models is particularly fruitful for studying surface complexes on supported model metal catalysts that are otherwise hardly accessible to high-level electronic structure calculations.

The state and the nearest future of the reviewed area of quantum chemistry of oxide-related materials can be summarized as follows:
(i) accurate modeling of regular surfaces of simple ionic metal oxides has become possible and should soon become a standard for more complex, reducible and disordered oxide substrates;
(ii) beyond the currently addressed isolated defect sites, one anticipates large-scale investigations of the interplay of various defects and metal-support interface sites, aiming at establishing a data base of accurate calculated parameters for building blocks of complex supported metal systems;
(iii) realistic models of bi- (and poly-) metallic nanoclusters will be as easily tractable as are nowadays idealized models of transition metal nanoparticles;
(iv) computational studies of pertinent reactions (kinetics) on all kinds of materials mentioned above will routinely supplement the investigations of stable surface complexes (thermodynamics).

Acknowledgment. We thank U. Birkenheuer, S. Cai, C. Di Valentin, A.M. Ferrari, L. Giordano, J.F. Goellner, A. Hu, F. Illas, C. Inntam, E.A. Ivanova, S. Krüger, A.V. Matveev, V.V. Rivanenkov, R. Sahnoun, A.M. Shor, S. Vent, C. Xiao, and I.V. Yudanov for their contributions to the research reviewed here. The authors enjoyed collaborations with the experimentally working colleagues H.-J. Freund, B.C. Gates, U. Heiz, H. Knözinger, J.A. Lercher, J. Libuda, and G. Rupprechter. The members of the PARAGAUSS team T. Belling, T. Grauschopf,

S. Krüger, F. Nörtemann, M. Staufer, M. Mayer, U. Birkenheuer, A. Hu, A.V. Matveev, A.M. Shor, M.S.K. Fuchs-Rohr, D.I. Ganyushin, T. Kerdcharoen, A. Woiterski, and A.B. Gordienko deserve particular recognition; they helped develop an efficient computational tool with unique features. The research had been supported by Deutsche Forschungsgemeinschaft (via SFB 338 and several Priority Programs), Alexander von Humboldt Foundation, Volkswagen-Stiftung, INTAS, and Fonds der Chemischen Industrie (Germany).

LIST OF ABBREVIATIONS AND NOTATIONS

AE	all-electron (calculation)
B3LYP	Becke (three-parameter)-Lee-Yang-Parr (functional)
BP86	Becke-Perdew (functional)
BLYP	Becke-Lee-Yang-Parr (functional)
BSSE	basis set superposition error
Calc.	calculated
covEPE	covalent elastic polarizable environment (method)
D_e	binding (adsorption) energy
DAY	dealuminated Y zeolite
DE	deprotonation energy
DF, DFT	density functional (theory)
E	total energy
EA	electron affinity
EPE	elastic polarizable environment
EXAFS	extended X-ray absorption fine structure
fcc	face-centered cubic
FF	fitting function
FTIR	Fourier-transform infrared (spectroscopy)
GGA	generalized gradient approximation (of xc functional)
GIXS	grazing incidence X-ray scattering
hcp	hexagonal closed packed
HF	Hartree-Fock (method)
HOMO	highest occupied molecular (Kohn-Sham) orbital
I	(absolute) infrared intensity of a vibrational mode
IR	infrared
IRAS	infrared reflection adsorption spectroscopy
KS	Kohn-Sham (method, orbital)
LAS	Lewis acid sites
LCGTO	linear combination of Gaussian-type orbitals
LDA	local density approximation
LUMO	lowest unoccupied molecular (Kohn-Sham) orbital
MM	molecular mechanics, molecular mechanical

MO	molecular (Kohn-Sham) orbital
MP2	Møller-Plesset perturbation theory of second order
N_s	the number of unpaired electrons
PA	proton affinity
PBEN	Perdew-Burke-Ernzerhof (functional), modified by Norskøv et al.
PC	point charge
PP	pseudopotential, effective core potential (ECP)
pp*	label of bare pseudopotential centers without basis functions
PW91	Perdew-Wang (functional)
q	atomic charge
QM	quantum mechanics, quantum mechanical
r	interatomic distance
SFG	sum frequency generation (spectroscopy)
TPR	temperature programmed reaction
VWN	Vosko-Wilk-Nusair (functional)
UHV	ultrahigh vacuum
xc	exchange-correlation (functional, potential)
XPS	X-ray photoelectron spectroscopy
Z	zeolite
z	height of adsorbate above the upper substrate plane
μ	dipole moment
μ_B	Bohr magneton
ρ	electron density
ω	vibrational frequency (stretching)

REFERENCES

[1] G. Schmid, M. Bäumle, M. Geerkens, I. Heim, C. Osemann, and T. Sawitowski, Chem. Soc. Rev., 28 (1999) 179.
[2] H.-J. Freund, Surf. Sci., 500 (2002) 271.
[3] C.T. Campbell, Surf. Sci. Rep., 27 (1997) 1.
[4] C. Henry, Surf. Sci. Rep., 31 (1998) 231.
[5] G. Renaud, Surf. Sci. Rep., 32 (1998) 1.
[6] R.M. Lambert and G. Pacchioni (eds.), Chemisorption and Reactivity of Supported Clusters and Thin Films, NATO ASI Series E, Vol. 331, Kluwer, Dordrecht, 1997.
[7] M.A. Uddin, T. Komatsu, and T. Yashima, J. Catal., 150 (1994) 439.
[8] B.S. Kwak, W.M.H. Sachtler, and W.O. Haag, J. Catal., 149 (1994) 465.
[9] J. Biscardi and E. Iglesia, J. Catal., 182 (1999) 117.
[10 G. Ertl, H. Knözinger, and J. Weitkamp (eds.), Handbook of Heterogeneous Catalysis, Wiley-VCH, Weinheim 1997.
[11] T. Mole, J. R. Anderson, and G. Creer, Appl. Catal., 17 (1985) 187.
[12] H.-J. Freund, Faraday Discuss., 114 (1999) 1.
[13] H.-J. Freund, H. Kuhlenbeck, and V. Staemmler, Rep. Prog. Phys., 59 (1996) 283.
[14] J.T. Ranney, D.E. Starr, J.E. Musgrove, D.J. Bald, and C.T. Campbell, Faraday Discuss., 114 (1999) 195.

[15] U. Heiz, F. Vanolli, A. Sanchez, and W.D. Schneider, J. Am. Chem. Soc., 120 (1998) 9668.
[16] S. Abbet, A. Sanchez, U. Heiz, W.D. Schneider, A.M. Ferrari, G. Pacchioni, and N. Rösch, J. Am. Chem. Soc., 122 (2000) 3453.
[17] M. Frank and M. Bäumer, Phys. Chem. Chem. Phys., 2 (2000) 3723.
[18] W.M.H. Sachter and Z. Zhang, Adv. Catal., 39 (1993) 129.
[19] G.C. Shen, A.M. Liu, T. Shido, and M. Ichikawa, Top. Catal., 2 (1995) 141.
[20] B.C. Gates, Chem. Rev., 95 (1995) 511.
[21] J. Shi, S. Gider, K. Babcock, and D.D. Awschalom, Science, 271, 937 (1996).
[22] A. Mie, Ann. Phys. 25 (1908) 377.
[23] B.I. Dunlup and N. Rösch, Adv. Quant. Chem., 21 (1990) 317.
[24] B.I. Dunlap, Adv. Chem. Phys., 69 (1987) 287.
[25] B.I. Dunlap, in Density Functional Methods in Chemistry. Eds. J.K. Labanowski and J.W. Andzelm, Springer, New York, 1991, p. 49.
[26] N. Rösch, P. Knappe, P. Sandl, A. Görling, and B.I. Dunlap, in The Challenge of d and f Electrons. Theory and Computation. Eds. D.R. Salahub, M. Zerner, ACS Symposium Series No 394, Am. Chem. Soc., Washington, DC, 1989, p. 180.
[27] N. Rösch, in Cluster Models for Surface and Bulk Phenomena, Eds. G. Pacchioni, P.S. Bagus, F. Parmigiani, NATO ASI Series B, Plenum Press, New York, 1992, p. 251.
[28] T. Belling, T. Grauschopf, S. Krüger, M. Mayer, F. Nörtemann, M. Staufer, C. Zenger, and N. Rösch, in High Performance Scientific and Engineering Computing, Eds. H.-J. Bungartz, F. Durst, and C. Zenger, Lecture Notes in Computational Science and Engineering, Vol. 8, Springer, Heidelberg, 1999; p. 439.
[29] T. Belling, T. Grauschopf, S. Krüger, F. Nörtemann, M. Staufer, M. Mayer, V.A. Nasluzov, U. Birkenheuer, A. Hu, A.V. Matveev, A.M. Shor, M.S.K. Fuchs-Rohr, K.M. Neyman, D.I. Ganyushin, T. Kerdcharoen, A. Woiterski, and N. Rösch, ParaGauss, Version 2.2, Technische Universität München, Munich, 2001.
[30] O.D. Häberlen and N. Rösch, Chem. Phys. Lett., 199 (1992) 491.
[31] B.A. Hess, R.J. Buenker, and P. Chandra, Int. J. Quantum Chem., 29 (1986) 737.
[32] N. Rösch, S. Krüger, M. Mayer, and V.A. Nasluzov, in Recent Developments and Applications of Modern Density Functional Theory, Ed. J.M. Seminario, Elsevier, Amsterdam, 1996, p. 497.
[33] S.H. Vosko, L. Wilk, and M. Nusair, Can. J. Phys., 58 (1980) 1200.
[34] T. Ziegler, Chem. Rev., 91 (1991) 651.
[35] A.D. Becke, Phys. Rev., A 38 (1988) 3098.
[36] J.P. Perdew, J.A. Chevary, S.H. Vosko, K.A. Jackson, M.R. Pederson, D.J. Singh, and C. Fiolhais, Phys. Rev. B, 46 (1992) 6671.
[37] J.P. Perdew and Y. Wang, Phys. Rev. B, 45 (1992) 13244.
[38] J.P. Perdew, Phys. Rev. B, 33 (1986) 8622; 34 (1986) 7406.
[39] C. Lee, W. Yang, and R.G. Parr, Phys. Rev. B, 37 (1988) 785.
[40] B. Miehlich, A. Savin, H. Stoll, H. Preuss, Chem. Phys. Lett., 157 (1989) 200.
[41] J.P. Perdew, K. Burke, and M. Ernzerhof, Phys. Rev. Lett., 77 (1996) 3865.
[42] B. Hammer, L.B. Hansen, J.K. Nørskov, Phys. Rev. B, 59 (1999) 7413.
[43] A.D. Becke, J. Chem. Phys., 98 (1993) 5648.
[44] P.J. Stevens, J.F. Devlin, C.F. Chabalowski, and M.J. Frisch, J. Phys. Chem., 98 (1994) 11623.
[45] W. Koch and M.C. Holthausen, A Chemist's Guide to Density Functional Theory, Wiley-VCH, Weinheim, 2000.
[46] J.M. Pérez-Jordá and A. D. Becke, Chem. Phys. Lett., 233 (1995) 134.

[47] B.J. Lundqvist, Y. Andersson, H. Shao, S. Chan, and D.C. Langreth, Int. J. Quantum Chem., 56 (1995) 247.
[48] S. Kristyán and P. Pulay, Chem. Phys. Lett., 229 (1994) 175.
[49] B. Civalleri, E. Garrone, and P. Ugliengo, J. Mol. Struct. (Theochem), 419 (1997) 227 and references therein.
[50] A.M. Ferrari, P. Ugliengo, and E. Garrone, J. Chem. Phys., 105 (1996) 4129 and references therein.
[51] J.J. Novoa and C. Sosa, J. Phys. Chem., 99 (1995) 15837.
[52] F. Sim, A. St-Amant, I. Papai, and D. R. Salahub, J. Am. Chem. Soc., 114 (1992) 4391.
[53] A. Görling, S.B. Trickey, P. Gisdakis, and N. Rösch, in Topics in Organometallic Chemistry, eds. P. Hofmann and J.M. Brown, Vol. 3, Springer, Berlin, Heidelberg, 1999, p. 109.
[54] S.F. Boys and F. Bernardi, Mol. Phys., 19 (1970) 553.
[55] R.D. Amos, Adv. Chem. Phys., 67 (1987) 99.
[56] G. Pacchioni, P.S. Bagus, and F. Parmigiani (eds.), Cluster Models for Surface and Bulk Phenomena, NATO ASI Series B, Vol. 283, Plenum, New York, 1992.
[57] K.M. Neyman and N. Rösch, Chem. Phys., 168 (1992) 267.
[58] U. Birkenheuer, J.C. Boettger, N. Rösch, J. Chem. Phys., 100 (1994) 6826.
[59] G. Pacchioni, G. Cogliandro, and P.S. Bagus, Surf. Sci., 225 (1991) 344.
[60] I.V. Yudanov, V.A. Nasluzov, K.M. Neyman, and N. Rösch, Int. J. Quantum Chem., 65 (1997) 975.
[61] A.M. Ferrari and G. Pacchioni, Int. J. Quantum Chem., 58 (1996) 241.
[62] N.W. Winter, R.M. Pitzer, and D.K. Temple, J. Chem. Phys., 86 (1987) 3549.
[63] Z. Barandiarán and L. Seijo, J. Chem. Phys., 89 (1988) 5739.
[64] S. Huzinaga, L. Seijo, Z. Barandiarán, and M. Klobukowski, J. Chem. Phys., 86 (1987) 2132.
[65] P.A. Christiansen, Y.S. Lee, and K.S. Pitzer, J. Chem. Phys., 71 (1979) 4445.
[66] J.M. Vail, J. Phys. Chem. Solids, 51 (1990) 589.
[67] V.A. Nasluzov, G.L. Gutsev, V.V. Rivanenkov, K.M. Neyman, and A.G. Anshits, Zh. Strukt. Khim. (Soviet J. Struct. Chem.), 33 (1992) 3.
[68] A.G. Anshits, E.N. Voskresenskaya, V.V. Rivanenkov, V.A. Nasluzov, and K.M. Neyman, React. Kinet. Catal. Lett., 46 (1992) 285.
[69] J.A. Mejias and J.F. Sanz, J. Chem. Phys., 102 (1995) 327.
[70] L.G.M. Pettersson, M. Nyberg, J.-L. Pascual, and M.A. Nygren, in Chemisorption and Reactivity on Supported Clusters and Thin Films: Towards an Understanding of Microscopic Processes in Catalysis, Eds. R. M. Lambert, G. Pacchioni, NATO ASI Series E, Vol. 331, Kluwer, Dordrecht, 1997, p. 425.
[71] M.A. Nygren, L.G.M. Pettersson, and Z. Barandiarán, L. Seijo, J. Chem. Phys., 100 (1994) 2010.
[72] M.A. Nygren and L.G.M. Pettersson, J. Chem. Phys., 105 (1996) 9339.
[73] V.A. Nasluzov, V.V. Rivanenkov, A.B. Gordienko, K.M. Neyman, U. Birkenheuer, and N. Rösch, J. Chem. Phys., 115 (2001) 8157.
[74] V.A. Nasluzov, V.V. Rivanenkov, A.M. Shor, K.M. Neyman, U. Birkenheuer, and N. Rösch, Int. J. Quantum Chem., 90 (2002) 386.
[75] P.V. Sushko, A.L. Shluger, and C.R.A. Catlow, Surf. Sci., 450 (2000) 153.
[76] V.B. Sulimov, P.V. Sushko, A.H. Edwards, A.L. Shluger, and A.M. Stoneham, Phys. Rev. B, 2002, 66, 024108.

[77] C.R.A. Catlow and W.C. Mackrodt, in Computer Simulation of Solids, Eds. C.R.A. Catlow and W. C. Mackrodt, Lecture Notes in Physics, Vol. 166, Springer, Berlin, 1982, p. 3.
[78] A.B. Lidiard, J. Chem. Soc. Faraday Trans. II, 85 (1989) 341.
[79] C. Noguera, A. Pojani, F. Finocchi, and J. Goniakowski, in Chemisorption and Reactivity on Supported Clusters and Thin Films: Towards an Understanding of Microscopic Processes in Catalysis, Eds. R.M. Lambert, G. Pacchioni, NATO ASI Series E, Vol. 331, Kluwer, Dordrecht, 1997, p. 455.
[80] U. Eichler, C.M. Kölmel, and J. Sauer, J. Comput. Chem., 18 (1996) 463.
[81] M. Sierka and J. Sauer, Faraday Discuss., 106 (1997) 41.
[82] P. Sherwood, A. de Vries, S.J. Collins, S.P. Greatbanks, N.A. Burton, M.A. Vincent, and I.H. Hiller, Faraday Discuss., 106 (1997) 79.
[83] F. Maseras and K. J. Morokuma, J. Comput. Chem., 16 (1995) 1170.
[84] D. Bakowies and W.J. Thiel, J. Phys. Chem., 100 (1996) 10580.
[85] V.A. Nasluzov, E.A. Ivanova, A.M. Shor, G.N. Vayssilov, U. Birkenheuer, and N. Rösch, J. Phys. Chem. B, 107 (2003) 2228.
[86] Y. Zhang, T.-S. Lee, and W. Yang, J. Chem. Phys., 110 (1999) 46.
[87] V.E. Henrich and P. Cox, The Surface Science of Metal Oxides, Cambridge University, Cambridge, 1994.
[88] C. Noguera, J. Phys. Condens. Matter, 12 (2000) R376.
[89] K.M. Neyman, G. Pacchioni, and N. Rösch, in Recent Developments and Applications of Modern Density Functional Theory, Ed. J. Seminario, Elsevier, Amsterdam, 1996, p. 569.
[90] K.M. Neyman, V.A. Nasluzov, and N. Rösch, unpublished.
[91] N. Rösch, K.M. Neyman, and U. Birkenheuer, in Adsorption on Ordered Surfacers of Ionic Solids and Thin Films, Eds. H.-J. Freund and E. Umbach, Springer Series in Surface Sciences, Vol. 33, Springer, Berlin, 1993, p. 206.
[92] M. Schlüter and L. J. Sham, Adv. Quant. Chem., 21 (1990) 97.
[93] S. Schintke, S. Messerli, M. Pivetta, F. Patthey, L. Libioulle, M. Stengel, A. De Vita, and W.-D. Schneider, Phys. Rev. Lett., 87 (2001) 276801 and references therein.
[94] O. Robach, G. Renaud, and A. Barbier, Surf. Sci., 401 (1998) 227.
[95] S. Cai, K.M. Neyman, H. Knözinger, and N. Rösch, Surf. Sci., 479 (2001) 169.
[96] A.V. Matveev, K.M. Neyman, I.V. Yudanov, and N. Rösch, Surf. Sci., 426 (1999) 123.
[97] A. Kirfel and K. Eichhorn, Acta Cryst. A, 46 (1990) 271.
[98] J. Ahn and J. W. Rabalais, Surf. Sci., 388 (1997) 121.
[99] R. Baxter, P. Reinhardt, N. López, and F. Illas, Surf. Sci., 445 (2000) 448.
[100] G. V. Lewis and C. R. A. Catlow, J. Phys. C, 18 (1985) 1149.
[101] G. Pacchioni, Surf. Rev. Lett., 7 (2000) 277.
[102] K.M. Neyman and N. Rösch, Ber. Bunsenges. Phys. Chem., 96 (1992) 1711.
[103] G. Pacchioni, K.M. Neyman, and N. Rösch, J. Electron Spectrosc. Relat. Phenom., 69 (1994) 13.
[104] K.M. Neyman, S.Ph. Ruzankin, and N. Rösch, Chem. Phys. Lett., 246 (1995) 546.
[105] F. Illas, G. Pacchioni, A. Pelmenschikov, L.G.M. Pettersson, R. Dovesi, C. Pisani, K.M. Neyman, and N. Rösch, Chem. Phys. Lett., 306 (1999) 202.
[106] J.L. Whitten and H. Yang, Surf. Sci. Rep., 24 (1996) 59.
[107] G. Pacchioni, T. Minerva, and P.S. Bagus, Surf. Sci., 275 (1992) 450.
[108] J.-W. He, C.A. Estrada, J.S. Corneille, M.-C. Wu, and D.W. Goodman, Surf. Sci., 261 (1992) 164.
[109] C.R. Henry, C. Chapon, and C. Duriez, J. Chem. Phys., 95 (1991) 700.

[110] P. Ugliengo and A. Damin, Chem. Phys. Lett., 366 (2002) 683.
[111] R. Wichtendahl, M. Rodriguez-Rodrigo, U. Härtel, H. Kuhlenbeck, H.-J. Freund, Surf. Sci., 423 (1999) 90.
[112] R. Wichtendahl, M. Rodriguez-Rodrigo, U. Härtel, H. Kuhlenbeck, H.-J. Freund, Phys. Stat. Sol. (a), 173 (1999) 93.
[113] H. Knözinger, in Adsorption on Ordered Surfacers of Ionic Solids and Thin Films, Eds. H.-J. Freund and E. Umbach, Springer Series in Surface Sciences, Vol. 33, Springer, Berlin, 1993, p. 257.
[114] A. Zecchina, E. Escalona Platero, and C. Otero Areán, J. Catal., 107 (1987) 244.
[115] E.A. Paukshtis, Infrared Spectroscopy in Heterogeneous Acid-Base Catalysis, Nauka, Novosibirsk, 1992 (in Russ.).
[116] L.M. Kustov, V.B. Kazansky, S. Beran, L. Kubelková, and P. Jirů, J. Phys. Chem., 91 (1987) 5247.
[117] S. Bates and J. Dwyer, J. Phys. Chem., 97 (1993) 5897.
[118] K.M. Neyman, V.A. Nasluzov, and G. M. Zhidomirov, Catal. Lett., 40 (1996) 183.
[119] J.H. Lunsford, in Handbook of Heterogeneous Catalysis, Eds. G. Ertl, H. Knözinger, and J. Weitkamp, Vol. 4, Wiley-VCH, Weinheim, 1997, p. 1843.
[120] C. Li, G. Li, and Q. Xin, J. Phys. Chem., 98 (1994) 1933.
[121] A.M. Ferrari, S. Huber, H. Knözinger, K.M. Neyman, and N. Rösch, J. Phys. Chem. B, 102 (1998) 4548.
[122] S. Huber and H. Knözinger, J. Mol. Catal. A, 141 (1999) 117.
[123] J.B. Nicholas, A.A. Kheir, T. Xu, T.R. Krawietz, and J.F. Haw, J. Am. Chem. Soc., 120 (1998) 10471.
[124] N. Rösch, G.N. Vayssilov, and K.M. Neyman, in Nanostructured Host/Guest Systems, F. Schüth et al. (eds.), Wiley-VCH, 2003, p. 339.
[125] K.I. Hadjiivanov and G.N. Vayssilov, Adv. Catal., 47 (2002) 307.
[126] J. Sauer, P. Ugliengo, E. Garrone, and V.R. Saunders, Chem. Rev., 94 (1994) 2095.
[127] R.A. van Santen, Catal. Today, 38 (1997) 377.
[128] G.N. Vayssilov and N. Rösch, J. Phys. Chem. B, 105 (2001) 4277.
[129] G.N. Vayssilov, M. Staufer, T. Belling, K.M. Neyman, H. Knözinger, and N. Rösch, J. Phys. Chem. B, 103 (1999) 7920.
[130] W. Loewenstein, Am. Mineral., 39 (1954) 92.
[131] D.H. Olson, Zeolites, 15 (1995) 439.
[132] M. Sierka, U. Eichler, J. Datka, and J. Sauer, J. Phys. Chem. B, 102 (1998) 6397.
[133] N.O. Gonzales, A.K. Chakraborty, and A.T. Bell, Catal. Lett., 50 (1998) 135.
[134] D. Nachtigallova, P. Nachtigall, M. Sierka, and J. Sauer, Phys. Chem. Chem. Phys., 1 (1999) 2019.
[135] D. Nachtigallova, P. Nachtigall, and J. Sauer, Phys. Chem. Chem. Phys., 3 (2001) 1552.
[136] K. Pierloot, A. Delabie, M.H. Groothaert, and R.A. Schoonheydt, Phys. Chem. Chem. Phys., 3 (2001) 2174.
[137] L.A.M.M. Barbosa and R.A. van Santen, Catal. Lett., 63 (1999) 97.
[138] A.A. Shubin, G.M. Zhidomirov, A.L. Yakovlev, and R.A. van Santen, J. Phys. Chem. B, 105 (2001) 4928.
[139] M.J. Rice, A.K. Chakraborty, and A.T. Bell, J. Phys. Chem. B, 104 (2000) 9987.
[140] D. Berthomieu, S. Krishnamurty, B. Coq, G. Delahay, and A. Goursot, J. Phys. Chem. B, 105 (2001) 1149.
[141] P. Treesukol, J. Limtrakul, and T.N. Truong, J. Phys. Chem. B, 105 (2001) 2421.
[142] J.L. Lievens, J.P. Verduijn, A.J. Bons, and W. J. Mortier, Zeolites, 12 (1992) 698.

[143] K. Hadjiivanov and H. Knözinger, Catal. Lett., 58 (1999) 21.
[144] K. Hadjiivanov, P. Massiani, and H. Knözinger, Phys. Chem. Chem. Phys., 1 (1999) 3831.
[145] G.N. Vayssilov and N. Rösch, J. Catal., 186 (1999) 423.
[146] K. Hadjiivanov and H. Knözinger, J. Phys. Chem. B, 105 (2001) 4531.
[147] A.M. Ferrari, P. Ugliengo, and E. Garone, J. Chem. Phys., 105 (1996) 4129.
[148] A.M. Ferrari, K.M. Neyman, and N. Rösch, J. Phys. Chem. B, 101 (1997) 9292.
[149] A. Zecchina, S. Bordiga, C. Lamberti, G. Spoto, L. Carneli, and C. Otero Arean, J. Phys. Chem., 98 (1994) 9577.
[150] S. Bordiga, C. Lamberti, F. Geobaldo, A. Zecchina, G. Turnes Palomino, and C. Otero Arean, Langmuir, 11 (1995) 527.
[151] M. Katoh, T. Yamazaki, and S. Ozawa, Bull. Chem. Soc. Jpn. 67 (1994) 1246.
[152] S. Huber and H. Knözinger, Appl. Catal. A, 181 (1999) 239.
[153] T.A. Egerton and F.S. Stone, J. Chem. Soc. Faraday Trans. I, 69 (1973) 22.
[154] R.I. Soltanov, E.A. Paukshtis, and E.N. Yurchenko, Kinet. i Katal., 23 (1980) 164.
[155] J. Klinowski, S. Ramdas, and J.M. Thomas, J. Chem. Soc., Faraday Trans. 2, 78 (1982) 1025.
[156] K. Hadjiivanov and H. Knözinger, Chem. Phys. Lett., 303 (1999) 513.
[157] G.N. Vayssilov, A. Hu, U. Birkenheuer, and N. Rösch, J. Mol. Catal. A, 162 (2000) 135.
[158] A. Zecchina, C. Otero Arean, G. Turnes Palomino, F. Geobaldo, C. Lamberti, G. Spoto, and S. Bordiga, Phys. Chem. Chem. Phys., 1 (1999) 1649.
[159] T. Yamazaki, I. Watanuki, S. Ozawa, and Y. Ogino, Langmuir, 4 (1988) 433.
[160] A.Y. Khodakov, L.M. Kustov, V.B. Kazansky, and C. Williams, J. Chem. Soc., Faraday Trans., 89 (1993) 1393.
[161] A.M. Ferrari, K.M. Neyman, S. Huber, H. Knözinger, and N. Rösch, Langmuir, 14 (1998) 5559.
[162] S. Huber and H. Knözinger, Chem. Phys. Lett., 244 (1995) 111.
[163] M. Rep, A.E. Palomares, G. Eder-Mirth, J.G. van Ommen, N. Rösch, and J.A. Lercher, J. Phys. Chem. B, 104 (2000) 8624.
[164] G.N. Vayssilov, J.A. Lercher, and N. Rösch, J. Phys. Chem. B, 104 (2000) 8614.
[165] G.N. Vayssilov and N. Rösch, Phys. Chem. Chem. Phys., 4 (2002) 146.
[166] B.E. Mills, R.L. Martin, and D.A. Shirley, J. Am. Chem. Soc., 98 (1976) 2380.
[167] I. Yudanov, G. Pacchioni, K. Neyman, and N. Rösch, J. Phys. Chem. B, 101 (1997) 2786.
[168] K.M. Neyman, S. Vent, G. Pacchioni, and N. Rösch, Il Nuovo Cimento D, 19 (1997) 1743.
[169] I.V. Yudanov, S. Vent, K.M. Neyman, G. Pacchioni, and N. Rösch, Chem. Phys. Lett., 275 (1997) 245.
[170] K.M. Neyman, C. Inntam, V.A. Nasluzov, R. Kosarev, and N. Rösch, Appl. Phys. A, submitted.
[171] V.V. Rivanenkov, V.A. Nasluzov, A.M. Shor, K.M. Neyman, and N. Rösch, Surf. Sci., 525 (2003) 173.
[172] A.V. Matveev, K.M. Neyman, G. Pacchioni, and N. Rösch, Chem. Phys. Lett., 299 (1999) 603.
[173] A.M. Ferrari, C. Xiao, K.M. Neyman, G. Pacchioni, and N. Rösch, Phys. Chem. Chem. Phys., 1 (1999) 4655.
[174] S. Cai, K.M. Neyman, A. Hu, and N. Rösch, J. Phys. Chem. B, 104 (2000) 11506.
[175] K.M. Neyman, S. Vent, N. Rösch, and G. Pacchioni, Top. Catal., 9 (1999) 153.

[176] K.M. Neyman, N. Rösch, and G. Pacchioni, Appl. Catal. A, 191 (2000) 3.
[177] L. Giordano, G. Pacchioni, A.M. Ferrari, F. Illas, and N. Rösch, Surf. Sci., 473 (2001) 213.
[178] C. Di Valentin, L. Giordano, G. Pacchioni, and N. Rösch, Surf. Sci., 522 (2003) 175.
[179] L. Giordano, G. Pacchioni, F. Illas, and N. Rösch, Surf. Sci., 499 (2002) 73.
[180] J.F. Goellner, K.M. Neyman, M. Mayer, F. Nörtemann, B.C. Gates, and N. Rösch, Langmuir, 16 (2000) 2736.
[181] V.A. Nasluzov, V.V. Rivanenkov, A.M. Shor, K.M. Neyman, and N. Rösch, Chem. Phys. Lett., (2003), in press.
[182] K.M. Neyman, C. Inntam, V.A. Nasluzov, and N. Rösch, to be published.
[183] A. Hu, K.M. Neyman, M. Staufer, T. Belling, B.C. Gates, and N. Rösch, J. Am. Chem. Soc., 121 (1999) 4522.
[184] K.M. Neyman, V.A. Nasluzov, J. Hahn, C.R. Landis, and N. Rösch, Organometallics, 16 (1997) 995.
[185] J.B. Jou, H.C. Lu, T. Gustafsson, and E. Garfunkel, Surf. Sci., 293 (1993) L887.
[186] G. Haas, A. Menck, H. Brune, J.V. Barth, J.A. Venables, and K. Kern, Phys. Rev. B, 61 (2000) 11105.
[187] N. Lopez, F. Illas, N. Rösch, and G. Pacchioni, J. Chem. Phys., 110 (1999) 4873.
[188] A.E. Mattsson and D.R. Jennison, Surf. Sci., 520 (2002) L611.
[189] K.H. Hansen, T. Worren, S. Stempel, E. Lægsgaard, M. Bäumer, H.-J. Freund, F. Besenbacher, and I. Stensgaard, Phys. Rev. Lett., 83 (1999) 4120.
[190] E.A. Soares, M.A. Van Hove, C.F. Walters, and K.F. McCarty, Phys. Rev. B, 65 (2002) 195405.
[191] V. Musolino, A. Selloni, and R. Car, J. Chem. Phys., 108 (1998) 5044.
[192] V. Musolino, A. Selloni, and R. Car, Phys. Rev. Lett., 83 (1999) 3242.
[193] A. Bogicevic and D.R. Jennison, Surf. Sci., 515 (2002) L481.
[194] J.R.B. Gomes, F. Illas, N. Cruz Hernández, J.F. Sanz, A. Wander, and N.M. Harrison, J. Chem. Phys., 116 (2002) 1684.
[195] J.R.B. Gomes, F. Illas, N. Cruz Hernández, A. Márquez, and J.F. Sanz, Phys. Rev. B, 65 (2002) 125414.
[196] C. Verdozzi, D.R. Jennison, P.A. Schultz, and M.P. Sears, Phys. Rev. Lett., 82 (1999) 799.
[197] N. Tanaka, H. Kimata, T. Takashima, and T. Kizuka, Surf. Rev. Lett., 5 (1998) 723.
[198] B.C. Gates, Catalytic Chemistry, Wiley-VCH, New York, 1992.
[199] I. Efremenko, J. Mol. Catal. A, 173 (2001) 19.
[200] W.M.H. Sachtler, Acc. Chem. Res., 26 (1993) 383.
[201] G. Mestl and H. Knözinger, in Handbook of Heterogeneous Catalysis, Vol. 2, Eds. G. Ertl, H. Knözinger, and J. Weitkamp, Wiley-VCH, Weinheim, 1997, p. 707.
[202] C. Li and A. J. Freeman, Phys. Rev., B 43 (1991) 780.
[203] G. Pacchioni and N. Rösch, Acc. Chem. Res. 28 (1995) 390.
[204] G. Pacchioni, S. Krüger, and N. Rösch, in: Metal Clusters in Chemistry, P. Braunstein, L. A. Oro and P. R. Raithby (Eds.), Wiley-VCH, Weinheim 1999, pp. 1392-1433.
[205] J.B. Bucher, D.C. Douglas, and L.A. Bloomfield, Phys. Rev. Lett., 66 (1991) 3052.
[206] M. Bäumer and H.-J. Freund, Progr. Surf. Sci., 61 (1999) 127.
[207] S. Andersson, P.A. Brühwiler, A. Sandell, M. Frank, J. Libuda, A. Giertz, B. Brena, A. J. Maxwell, M. Bäumer, H.-J. Freund, and N. Mårtensson, Surf. Sci., 442 (1999) L964.
[208] G. Panjabi, S. Salvi, B. Phillips, L.F. Allard, and B.C. Gates, private communication.
[209] P.S. Kirlin, F.B.M. van Zon, D.C. Koningsberger, and B.C. Gates, J. Phys. Chem., 94 (1990) 8439.

[210] C.J. Papile and B.C. Gates, Langmuir, 8 (1992) 74.
[211] P. Gisdakis, S. Antonczak, and N. Rösch, Organomet., 18 (1999) 5044.
[212] A.M. Argo, J.F. Odzak, F.S. Lai, and B.C. Gates, Nature, 415 (2002) 623.
[213] A.M. Ferrari, L. Giordano, N. Rösch, U. Heiz, S. Abbet, A. Sanchez, and G. Pacchioni, J. Phys. Chem. B, 104 (2000) 10612.
[214] A. Sanchez, S. Abbet, U. Heiz, W.-D. Schneider, H. Häkkinen, R.N. Barnett, and U.J. Landman, J. Phys. Chem. A 103 (1999) 9573.
[215] G.A. Somorjai, Introduction to Surface Chemistry and Catalysis, Wiley, New York, 1994.
[216] G. Pacchioni and P.S. Bagus, Surf. Sci., 269/270 (1992) 669.
[217] P.S. Bagus, G. Pacchioni, and M.R. Philpott, J. Chem. Phys., 90 (1989) 4287.
[218] W.T. Tysoe, G.L. Nyberg, and R.M. Lambert, J. Chem. Soc., Chem. Commun., (1983) 623.
[219] W. Sesselmann, B. Woratschek, G. Ertl, J. Kuppers, and H. Haberland, Surf. Sci., 130 (1983) 245.
[220] P.M. Holmblad, D.R. Rainer, and D.W. Goodman, J. Phys. Chem. B, 101 (1997) 8883.
[221] I.M. Abdelrehim, K. Pelhos, T.E. Madey, J. Eng, and J.G. Chen, J. Mol. Catal., A 131 (1998) 107.
[222] T.M. Gentle and E.L. Muetterties, J. Phys. Chem., 87 (1983) 2469.
[223] T.G. Rucker, M.A. Logan, T.M. Gentle, E.L. Muetterties, and G.A. Somorjai, J. Phys. Chem., 90 (1986) 2703.
[224] H. Hoffmann, F. Zaera, R.M. Ormerod, R.M. Lambert, J.M. Yao, D.K. Saldin, L.P. Wang, D.W. Bennett, and W.T. Tysoe, Surf. Sci., 268 (1992) 1.
[225] C.H. Patterson and R.M. Lambert, J. Am. Chem. Soc., 110 (1988) 6871.
[226] R.M. Ormerod and R.M. Lambert, J. Phys. Chem., 96 (1992) 8111.
[227] R.M. Ormerod, R.M. Lambert, H. Hoffmann, F. Zaera, J.M. Yao, D.K. Saldin, L.P. Wang, D.W. Bennet, and W.T. Tysoe, Surf. Sci., 295 (1993) 277.
[228] G. Pacchioni and R.M. Lambert, Surf. Sci., 304 (1994) 208.
[229] S. Abbet, A. Sanchez, U. Heiz, and W.-D. Schneider, J. Catal., 198 (2001) 122.
[230] A. M. Ferrari, L. Giordano, G. Pacchioni, S. Abbet, U. Heiz, J. Phys. Chem. B, 106 (2002) 3173.
[231] M.J.S. Dewar, Bull. Soc. Chem. Fr., 18 (1951) C71.
[232] J. Chatt and L.A. Duncanson, J. Chem. Soc., (1953) 2939.
[233] J.H. Hardesty, J.B. Koerner, T.A. Albright, and G.Y. Le, J. Am. Chem. Soc., 121 (1999) 6055.
[234] J.F. Goellner, B.C. Gates, G.N. Vayssilov, and N. Rösch, J. Am. Chem. Soc., 122 (2000) 8056.
[235] G.N. Vayssilov and N. Rösch, J. Am. Chem. Soc., 124 (2002) 3783.
[236] H. Miessner, I. Burkhardt, D. Gutschick, A. Zecchina, C. Morterra, and G. Spoto, J. Chem. Soc., Faraday Trans. 1, 85 (1989) 2113.
[237] H. Miessner, J. Am. Chem. Soc., 116 (1994) 11522.
[238] B. Hayden, in Chemisorption and Reactivity of Supported Clusters and Thin Films, R.M. Lambert and G. Pacchioni (eds.), Kluwer, Dordrecht, The Netherlands, 1997, p 215.
[239] T.P. Dougherty, W.T. Grubbs, and E.J. Heilweil, J. Phys. Chem., 98 (1994) 9396.
[240] E.A. Wovchko and J.T. Yates, Jr., J. Am. Chem. Soc., 118 (1996) 10250.
[241] D. Barthomeuf, Catal. Rev., 38 (1996) 521.
[242] A.I. Serykh, O.P. Tkachenko, V.Yu. Borovkov, V.B. Kazansky, M. Beneke, N.I. Jaeger, and G. Schulz-Ekloff, Phys. Chem. Chem. Phys., 2 (2000) 5647.

[243] A.M. Ferrari, K.M. Neyman, T. Belling, M. Mayer, and N. Rösch, J. Phys. Chem. B, 103 (1999) 216.
[244] O. Alexeev, B.C. Gates, Top. Catal., 273 (2000) 273.
[245] S. Kawi, B.C. Gates, in Clusters and Colloids, Ed. G. Schmid, VCH, Weinheim, 1994, p. 299.
[246] B.C. Gates, in Catalysis by Di- and Polynuclear Metal Cluster Complexes, R. D. Adams and F.A. Cotton (Eds.), Wiley-VCH, Weinheim, 1998, p. 509.
[247] A.M. Ferrari, K.M. Neyman, M. Mayer, M. Staufer, B.C. Gates, and N. Rösch, J. Phys. Chem. B, 103 (1999) 5311.
[248] B.C. Gates, private communication.
[249] W.A. Weber and B.C. Gates, J. Phys. Chem. B, 101 (1997) 10423.
[250] G.N. Vayssilov and N. Rösch, to be published.
[251] G.N. Vayssilov, B.C. Gates, and N. Rösch, Angew. Chem. Int. Ed. Engl. 42 (2003) 1391.
[252] B.K. Teo, Acc. Chem. Res., 13 (1980) 412.
[253] J. Libuda, M. Frank, A. Sandell, S. Andersson, P.A. Brühwiler, M. Bäumer, N. Mårtensson, and H.-J. Freund, Surf. Sci., 384 (1997) 106.
[254] M. Heemeier, M. Frank, J. Libuda, K. Wolter, H. Kuhlenbeck, M. Bäumer, and H.-J. Freund, Catal. Lett., 68 (2000) 19.
[255] I.V. Yudanov, R. Sahnoun, K.M. Neyman, and N. Rösch, J. Chem. Phys., 117 (2002) 9887.
[256] I.V. Yudanov, R. Sahnoun, K.M. Neyman, N. Rösch, J. Hoffmann, S. Schauermann, V. Johánek, H. Unterhalt, G. Rupprechter, J. Libuda, and H.-J. Freund, J. Phys. Chem. B, 107 (2003) 255.
[257] K. Hermann, P.S. Bagus, and C.J. Nelin, Phys. Rev. B, 35 (1987) 9467.
[258] G. te Velde and E.J. Baerends, Chem. Phys., 117 (1993) 399.
[259] L.G.M. Pettersson and T. Faxen, Theor. Chim. Acta, 85 (1993) 345.
[260] U. Gutdeutsch, U. Birkenheuer, S. Krüger, and N. Rösch, J. Chem. Phys., 106 (1997) 6020.
[261] U. Gutdeutsch, U. Birkenheuer, and N. Rösch, J. Chem. Phys., 109 (1998) 2056.
[262] D. Loffreda, D. Simon, and P. Sautet, Surf. Sci., 425 (1999) 68.
[263] N. Lopez and J.K. Nørskov, Surf. Sci., 477 (2001) 59.
[264] A.M. Bradshaw and F.M. Hoffmann, Surf. Sci., 72 (1978) 513.
[265] X. Guo and J.T. Yates, Jr., J. Chem. Phys., 90 (1989) 6761.
[266] A. Matveev, M. Staufer, M. Mayer, and N. Rösch, Int. J. Quantum Chem., 75 (1999) 863.
[267] W.K. Kuhn, J. Szanyi, and D.W. Goodman, Surf. Sci., 274 (1992) L611.
[268] S. Krüger, S. Vent, and N. Rösch, Ber. Bunseges. Phys. Chem., 101 (1997) 1640.
[269] S. Krüger, S. Vent, F. Nörtemann, M. Staufer, and N. Rösch, J. Chem. Phys., 115 (2001) 2082.
[270] J. Libuda and H.-J. Freund, J. Phys. Chem. B, 106 (2002) 4901.
[271] T. Dellwig, G. Rupprechter, H. Unterhalt, and H.-J. Freund, Phys. Rev. Lett., 85 (2000) 776.
[272] H. Unterhalt, G. Rupprechter, and H.-J. Freund, J. Phys. Chem. B, 106 (2002) 356.
[273] G. Rupprechter, H. Unterhalt, M. Morkel, P. Galletto, L. Hu, and H.-J. Freund, Surf. Sci., 502-503 (2002) 109.

J. Leszczynski (Editor)
Computational Materials Science
Theoretical and Computational Chemistry, Vol. 15

Index

This Page Intentionally Left Blank